# HIGH SPEED FORMING 2016

## PROCEEDINGS OF THE 7th INTERNATIONAL CONFERENCE

APRIL 27-28, 2016

DORTMUND, GERMANY

**Edited by:**

A. E. Tekkaya
M. Kleiner




# Preface

The “International Conference on High Speed Forming” has developed into a major event for impulse forming, its processes, and its applications. Since the first ICHSF in Dortmund in 2004, the latest developments in the analysis of high speed forming and joining processes, tools and machines as well as material characterization have been introduced at the biannual conferences with growing interest and impact. I am especially proud to recognize that the last ICHSF 2014 in Daejeon/Korea has strengthened the ties between the European, American, and Asian impulse forming communities.

The objectives of the 7$^{th}$ ICHSF are to offer a platform for innovative presentations from international universities, research institutes, and companies and to support discussions and the informal exchange of experiences and knowledge between scientists, practicing engineers, manufacturers, and industrial operators.

I cordially thank all authors, co-authors, sponsors, and participants of the conference for their valuable contributions. Moreover, I would like to express my gratitude to the members of the scientific committee, which is co-chaired by my esteemed colleague Glenn Daehn from the Department of Materials Science and Engineering of the Ohio State University. Special thanks go to the local organizing committee of the IUL.

Like their six predecessors, the conference proceedings will be available through the online repository “Eldorado” of TU Dortmund University.

I am particularly honored to welcome you to Dortmund.

Dortmund, April 2016

A. Erman Tekkaya

# Scientific Committee:

### Chairmen

| | |
|---|---|
| Prof. A. Erman Tekkaya | Germany |
| Prof. Glenn S. Daehn | USA |

### Members

| | |
|---|---|
| Dr. Gilles Avrillaud | France |
| Dr. Charlotte Beerwald | Germany |
| Prof. Alexander Brosius | Germany |
| Prof. Jian Cao | USA |
| Prof. Laurent Dubar | France |
| Dr. Koen Faes | Belgium |
| Prof. Sergey Golovashchenko | USA |
| Prof. Werner Homberg | Germany |
| Prof. Hoon Huh | Korea |
| Prof. Brad Kinsey | USA |
| Prof. Matthias Kleiner | Germany |
| Prof. Paulo Martins | Portugal |
| Prof. Eckhart Uhlmann | Germany |
| Dr. Christian Weddeling | Germany |
| Prof. Michael Worswick | Canada |

Institute of Forming Technology and Lightweight Construction
Technische Universität Dortmund
Prof. Dr.-Ing. M. Kleiner
Prof. Dr.-Ing. A. E. Tekkaya

# Table of Contents

**Preface** ..... v

## Simulation and Optimization

**A Coupled 3D/2D Axisymmetric Method for Simulating Magnetic Metal Forming Processes in LS-DYNA**
P. L´Eplattenier, I. Çaldichoury ..... 3

**3D Impacts Modeling of the Magnetic Pulse Welding Process and Comparison to Experimental Data**
J.-P. Cuq-Lelandais, G. Avrillaud, S. Ferreira, G. Mazars, A. Nottebaert, G. Teilla, V. Shribman ..... 13

**Mathematical Optimization for the Virtual Design of Process Chains with Electromagnetic Forming**
M. Rozgič, M. Stiemer ..... 23

**Process Design for Electromagnetic Forming of Magnesium Alloy AZ31 Using FE Simulation**
E. Uhlmann, L. Prasol, H. Roehrs ..... 33

## Innovative Processes

**Combined Working Media-Based Forming on a Pneumo-Mechanical High Speed Forming Machine**
E. Djakow, W. Homberg, D. Tabakajew ..... 47

**Numerical and Experimental Investigation of Joining Aluminium and Carbon Fiber Reinforced Composites by Electromagnetic Forming Process**
A. Zajkani, M. Salamati ..... 59

**Detachment of Conductive Coatings by Pulsed Electromagnetic Field**
V. Mironov, A. Tatarinov, M. Kolbe, V. Gluschenkov ..... 69

## Process Analysis

**Analytical 1D-calculation of a 1-turn Coil Parameters for the Magneto-Forming Technology**
O. Mansouri, O. Maloberti, D. Jouaffre, M. Hamzaoui, J. Derosiere, D. Haye, J. P. Leonard, P. Pelca ..... 81

**Analytical and Numerical Investigation of Tube Compression with a Multi-Turn, Axisymmetric Coil**
A. Nassiri, S. Zhang, K. Reisert, B. Kinsey ..... 91

**Determination of Forming Speed at a Laser Shock Stretch Drawing Process**
S. Veenaas, F. Vollertsen, M. Krüger, F. Meyer, M. Hartmann ..... 105

**Electrohydraulic Forming of Light Weight Automotive Panels**
A. V. Mamutov, S. F. Golovashchenko, J. J. Bonnen, A. J. Gillard, S. A. Dawson, L. Maison ..... 115

**Increase of the Reproducibility of Joints Welded with Magnetic Pulse Technology Using Graded Surface Topographies**
A. Rebensdorf, S. Boehm ..... 125

**Effect of Conductivity of the Inner Rod on the Collision Conditions During a Magnetic Pulse Welding Process**
T. Sapanathan, K. Yang, R. N. Raoelison, N. Buiron, D. Jouaffre, M. Rachik ..... 137

# Tools and Machines

**Efficient Coil Design by Electromagnetic Topology Optimization for Electromagnetic Sharp Edge Forming of DP980 Steel Sheet**
M. K. Choi, H. Huh, M. H. Seo, Y. Kang ..... 149

**Electrodynamics of Magnetic Pulse Welding Machines: Global and Local Electrical Analogues**
R. Bouzerar, F. Bougrioua, I. Tekaya, N. Foy, M. Hamzaoui, V. Bourny, O. Durand-Drouhin, D. Jouaffre, D. Haye ..... 159

**Qualification of CuCr1Zr for the SLM Process**
E. Uhlmann, A. E. Tekkaya, V. Kashevko, S. Gies, R. Reimann, P. John ..... 173

# Material Testing

**Material Constitutive Behavior Identification at High Strain Rates Using a Direct-Impact Hopkinson Device**
X. Guo, C. Sow, C. Khalil, T. Heuzé, G. Racineux ..... 185

**A Study to Improve the Crash Performance of Plastic Materials Considering the Strain Rate and Fracture Characteristic**
H. Y. Kim, C. A. Lee, J. H. Bamg, B. C. Cho, D. Y. Kim, D. Y. Ha ..... 193

**A New Experimental Technique for Applying Impulse Tension Loading**
Z. S. Fan, H. P. Yu, H. Su, X. Zhang, C. F. Li ..... 203

**Development of an Interrupted Pulse Expanding Ring Test**
J. Imbert, M. Worswick ..... 213

**Development of Vibration During the Electromagnetic Ring Expansion Test**
K. Yang, G. Taber, T. Sapanathan, A. Vivek, G. S. Daehn, R. N. Raoelison, N. Buiron, M. Rachik..... 223

**Experimental and Numerical Prediction of the Static and Dynamic Forming Properties of Ti6Al4V**
P. Verleysen, J. Galan-Lopez..... 235

**Influence of Different Strain Rates on the Flow Curve and the Formability of Thin Aluminium and Tinplate Sheets**
M. Linnemann, T. Lieber, C. Scheffler, V. Psyk, R. Müller, D. Landgrebe ..... 245

# Joining and Welding

**Influence of the Wall Thicknesses on the Joint Quality During Magnetic Pulse Welding in Tube-to-Tube Configuration**
J. Lueg-Althoff, B. Schilling, J. Bellmann, S. Gies, S. Schulze, A. E. Tekkaya, E. Beyer ..... 259

**Impact Welding Structural Aluminium Alloys to High Strength Steels Using Vaporizing Foil Actuator**
B. Liu, A. Vivek, G. S. Daehn ..... 269

**Effects of Surface Coatings on the Joint Formation During Magnetic Pulse Welding in Tube-to-Cylinder Configuration**
J. Bellmann, J. Lueg-Althoff, G. Goebel, S. Gies, E. Beyer, A. E. Tekkaya ..... 279

**Benchmarking and Refining the Vaporizing Foil Actuator Spot Welding Process**
A. Vivek, S. M. Wright, B. C. Liu, S. R. Hansen, R. C. Brune, B. P. Thurston, G. A. Taber, T. Lee, Y. Mao, T. J. Dittrich, G. S. Daehn..... 289

**Electromagnetic Pulse Welded Aluminium to Copper Sheet Joints: Morphological and Mechanical Characterization**
K. Faes, I. Kwee..... 299

**The Influence of Thermal and Mechanical Effects on the Bond Formation During Impact Welding**
C. Pabst, P. Groche ..... 309

**A Study on the Critical Thickness of the Inner Tube for Magnetic Pulse Welding Using FEM and BEM**
H. Geng, J. Cui, G. Sun, G. Li ..... 321

# Simulation and Optimization

# A Coupled 3D/2D Axisymmetric Method for Simulating Magnetic Metal Forming Processes in LS-DYNA

**P. L'Eplattenier*, I. Çaldichoury**

Livermore Software Technology Corporation, Livermore, CA, USA
*Corresponding author. Email: pierre@lstc.com

## Abstract

*LS-DYNA is a general purpose explicit and implicit finite element program used to analyse the non-linear dynamic response of three-dimensional solids and fluids. It is developed by Livermore Software Technology Corporation (LSTC). An electromagnetism (EM) module has been added to LS-DYNA for coupled mechanical/thermal/electromagnetic simulations, which have been extensively performed and benchmarked against experimental results for Magnetic Metal Forming (MMF) and Welding (MMW) applications. These simulations are done using a Finite Element Method (FEM) for the conductors coupled with a Boundary Element Method (BEM) for the surrounding air, hence avoiding the need of an air mesh.*

*More recently, a 2D axisymmetric version of the electromagnetic solver was introduced for much faster simulations when the rotational invariance can be assumed.*

*In many MMF and MMW applications though, the rotational invariance exists only for part of the geometry (typically the coil), but other parts (typically the workpiece or the die) may not have this symmetry, or at least not for the whole simulation time.*

*In order to take advantage of the partial symmetry without limiting the geometry to fully symmetric cases, a coupling between 2D and 3D was introduced in the EM. The user can define the parts that can be solved in 2D and the ones which need to be solved in 3D and the solver will assume the rotational invariance only on the 2D parts, thus keeping the results accurate while significantly reducing the computation time.*

*In this paper, the coupling method will be presented along with benchmarks with fully 3D and fully 2D simulations, comparing the accuracy of the results and the simulation times.*

## Keywords

Simulation, Finite element method (FEM), Electroforming

# 1 Introduction

A 3D electromagnetism module has being developed in LS-DYNA for coupled mechanical/thermal/electromagnetic simulations (L'Eplattenier et al, 2008).

More recently, a new 2D axi-symmetric version of this solver was introduced, allowing much faster simulations (L'Eplattenier et al, 2015). In this 2D solver, the EM equations are solved in a 2D plane, and the 2D EM fields, Lorentz force and Joule heating are then expanded to 3D elements by rotations around the axis. This allows the coupling of the 2D EM with 3D mechanics and thermal, thus keeping all the LS-DYNA 3D capabilities available. The user needs to provide a 3D mesh with rotational symmetry, either on the full 360 degrees or a small slice.

Both the 3D and the 2D-EM eddy-current problems are solved using a coupled FEM-BEM method, based on differential forms. They can be coupled to different external circuits, including imposed currents, imposed voltage or (R,L,C) circuits. They both work in serial and MPP (L'Eplattenier et al, 2010) and allow contact between conductors (L'Eplattenier et al 2012).

Many applications show a partial rotational invariance. It would be interesting to take it into account to reduce the computation time while still solving the non-axisymmetric parts in 3D to keep a good accuracy. A coupling between 2D and 3D was thus introduced in the EM solver. The user can define the parts that can be solved in 2D and the ones which need to be solved in 3D and the solver will assume the rotational invariance only on the 2D parts.

In this paper, the coupling method will be presented along with benchmarks with fully 3D and fully 2D simulations, with comparisons on the accuracy of the results and the simulation times.

# 2 Presentation of the 3D/2D Coupled EM Model

## 2.1 The 3D Eddy Current Solver

The electromagnetic equations are solved using a coupled Finite Element Method (FEM) and Boundary Element Method (BEM). Note that the following demonstration is just a brief summary of what is presented in details in (L'Eplattenier et al, 2008).

In the eddy current approximation of the Maxwell equations, we can introduce a scalar potential $\varphi$ and a vector potential $\vec{A}$ and get all the EM fields from the evolution of these potentials. They satisfy the following evolution equations:

$$\nabla . \sigma \vec{\nabla} \varphi = 0 \tag{1}$$

$$\sigma \frac{\partial \vec{A}}{\partial t} + \vec{\nabla} \times \frac{1}{\mu} \vec{\nabla} \times \vec{A} + \sigma \vec{\nabla} \varphi = \vec{j}_s \tag{2}$$

Where σ is the electrical conductivity, μ the permeability and $\vec{j_s}$ a source current. When projecting these equations against form based basis functions (Rieben et al, 2006), and integrating over a volume, we get the following finite element equations:

$$\int_{\Omega} \sigma \vec{\nabla}\varphi . \vec{\nabla} W^0 d\Omega = 0 \tag{3}$$

$$\begin{aligned} &\int_{\Omega} \sigma \frac{\partial \vec{A}}{\partial t} . \overrightarrow{W}^1 d\Omega + \int_{\Omega} \frac{1}{\mu} \vec{\nabla} \times \vec{A} . \vec{\nabla} \times \overrightarrow{W}^1 \, d\Omega = \\ &- \int_{\Omega} \sigma \vec{\nabla}\varphi . \overrightarrow{W}^1 d\Omega + \int_{\Gamma} \frac{1}{\mu} \left[\vec{n} \times \left(\vec{\nabla} \times \vec{A}\right)\right] . \overrightarrow{W}^1 d\Gamma \end{aligned} \tag{4}$$

Where $W^0$ are the so called 0-form basis function and $\overrightarrow{W}^1$ the 1-form (Rieben at al, 2006). The last term in this last equation is computed using a BEM (Ren et al, 1990):

$$\vec{A}(\vec{x}) = \frac{\mu_0}{4\pi} \int_{\Gamma} \frac{1}{|\vec{x} - \vec{y}|} \vec{k}\,(\vec{y}) dy \tag{5}$$

$$\begin{aligned} &\left[\vec{n} \times \left(\vec{\nabla} \times \vec{A}\right)\right](\vec{x}) \\ &\quad = \frac{\mu_0}{2} \vec{k} - \frac{\mu_0}{4\pi} \int_{\Gamma} \frac{1}{|\vec{x} - \vec{y}|^3} \vec{n} \times \left[(\vec{x} - \vec{y}) \times \vec{k}(\vec{y})\right] dy \end{aligned} \tag{6}$$

We can notice in particular in Eq. 5 the 3D kernel:

$$G^0_{3d}(\vec{x}, \vec{x}') = \frac{1}{|\vec{x} - \vec{x}'|} \tag{7}$$

## 2.2 2D Eddy Current Solver

We now introduce a cylindrical system of coordinates (r,θ,z) and consider that we have some axi-symmetric conditions, i.e. that the fields depend only on r and z. We consider an axisymmetric situation where the currents are toroidal (along $\overrightarrow{e_\theta}$) and the B field poloidal (along ($\overrightarrow{e_r}$, $\overrightarrow{e_z}$)). This corresponds to a purely azimuthal vector potential (L'Eplattenier et al, 2015):

$$\vec{A}(\vec{r}) = A(r, z)\overrightarrow{e_\theta} \tag{8}$$

Since $\vec{A}$ is homogeneous to $\vec{\nabla}\phi$ (see **Eq. 2**), we must also have $\vec{\nabla}\phi$ azimuthal and (axisymmetric). We thus have:

$$\phi(r,\theta,z) = \phi(\theta) \tag{9}$$

$$\vec{\nabla}\Phi = \frac{1}{r}\frac{\partial\phi}{\delta\theta}\overrightarrow{e_\theta} \tag{10}$$

The FEM part of the 2D is very similar to the FEM of the 3D part, except that the integration is over 2D faces compared to 3D solids. The BEM part, though, is quite different since one point in the (r,z) plane actually represents a whole circle around the axis. Eq. 5 for example reads:

$$\vec{A}(r,z) = \iiint r'dr'dz'd\theta' \frac{k(r',z')\overrightarrow{e_{\theta'}}}{|x(r,\theta,z) - x'(r',\theta',z')|} \tag{11}$$

And the integration over θ' leads to:

$$\begin{aligned} A(r,z) &= \vec{A}(r,z).\overrightarrow{e_\theta} \\ &= \iiint r'dr'dz'd\theta' \frac{k(r',z')\overrightarrow{e_{\theta'}}.\overrightarrow{e_\theta}}{|x(r,\theta,z) - x'(r',\theta',z')|} \\ &= \iint dr'dz'k(r',z')G(r,z;r',z') \end{aligned} \tag{12}$$

Where $G(r,z;r',z')$ is the 2D kernel which involves elliptic integrals. These different kernels due to the extra integration over θ in 2D are the main differences between 3D and 2D.

## 2.3 3D/2D Eddy Current Solver

In the new coupled 3D/2D model, the user can choose which parts are to be handled in 3D and which are to be handled in 2D. Again, the FEM system is not very complicated, the 3D parts having their own FEM matrices and system, and same for the 2D. The real coupling between the 3D and 2D comes from the BEM equations, since all the parts interact with each other. A typical BEM matrix is thus composed of 4 blocks as represented below:

$$P = \begin{bmatrix} P_{3d-3d} & P_{3d-2d} \\ P_{2d-3d} & P_{2d-2d} \end{bmatrix} \tag{13}$$

Where $P_{3d-3d}$ represents all the interactions between the 3D parts, and is computed the same way as in section 2.1, and similarly, $P_{2d-2d}$ is computed as in section 2.2. The coupling parts, $P_{3d-2d}$ and $P_{2d-3d}$ are computed by projecting the 3D basis functions onto the local 2D plane (or its normal depending on the type of basis function) and using a kernel

very similar to the 2D one – the only difference being only one integral over the angle θ of the 2D basis function, instead of 2, hence a factor 2π. In other words, the 3D bases see the 2D ones as if they were a sum of 3D basis function all around the axis, with a rotational invariance. The 2D basis functions on the other hand see the 3D ones as their "in plane only" (or "out of plane only" depending on the kind of basis function) components in the rotational plane used for the 2D.

# 3 Numerical Results

## 3.1 Turning 3D into 2D

The case presented here features a spiral type coil with imposed current and a 1 mm thick Aluminium sheet forming on a conical die as shown on Fig. 1. The experiment was performed at the Department of Mechanical Engineering, University of Waterloo, Ontario, Canada (L'Eplattenier et al, 2009). Fig. 2 shows a comparison between the numerical and experimental final shape of the sheet, which shows a very good agreement. More details on the experimental/simulation comparisons can be found in (L'Eplattenier et al, 2009).

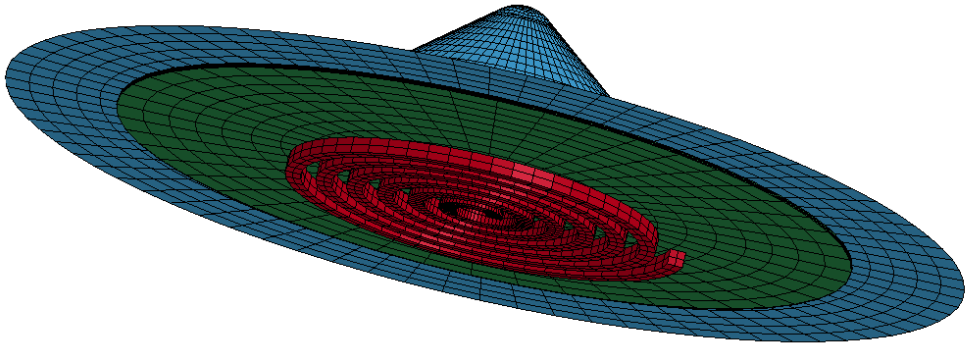

***Figure 1**: Magnetic metal forming with spiral coil. 3D setup*

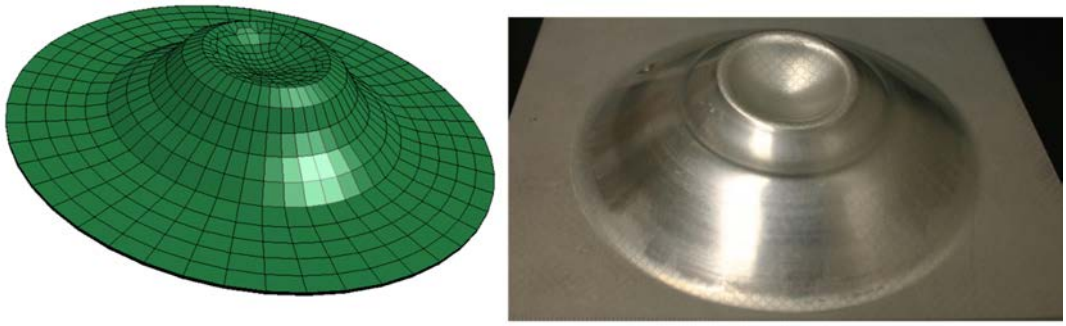

***Figure 2**: Magnetic Metal Forming: 3D numerical result (left) and experimental (right) final shape of the sheet*

This case has been chosen because it allows us to illustrate how the 2D axi-symmetric solver can be used in order to significantly reduce the calculation time. In order to transform a specific part in 2D, a 3D slice of the conductor must be provided along with some segment sets that define the plane where the EM-2D calculation is done as well as where the current flows in and out (See **Fig. 3**). **Fig. 4** and **Fig. 5** then offer some comparison of the results between the 2D setup and the 3D setup. The results appear to be very similar; the discrepancies may be explained by the 3D effects of the pitch in the spiral shaped coil. However, while the complete 3D run took about 20 minutes on 1 CPU, the 2D axi-symmetric problem only took 10 seconds.

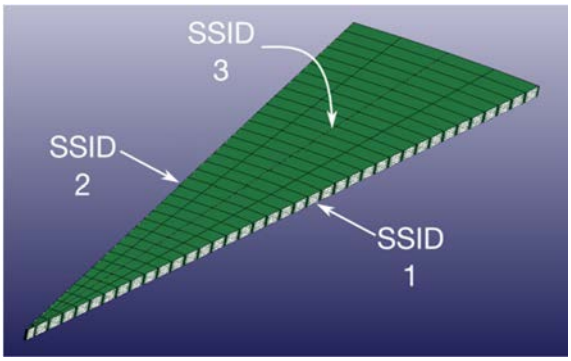


***Figure 3**: Example of a 2D axisymmetric part made of 1/32th of the full cylinder*

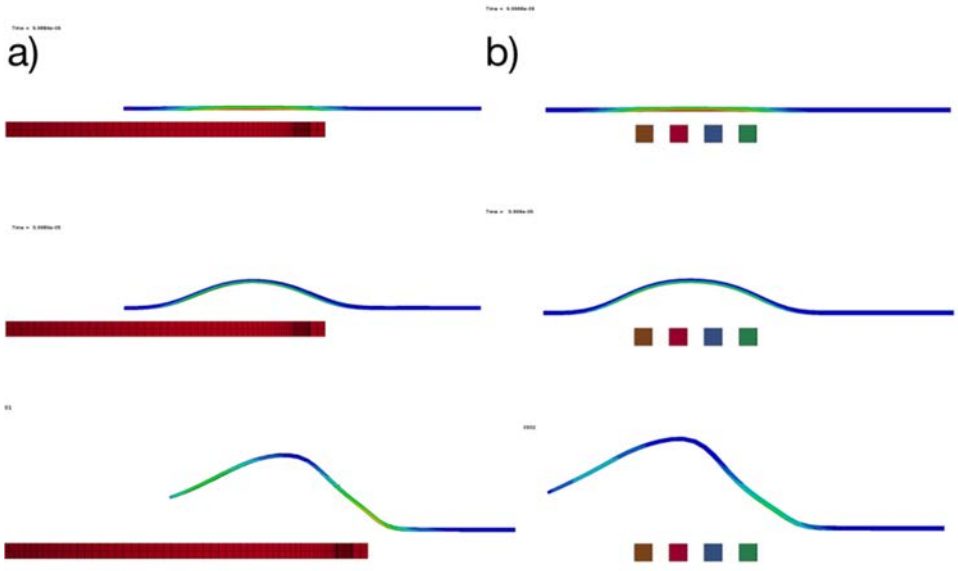


***Figure 4**: Lorentz force fringes at different times in a cross section of the workpiece. Comparison of the displacements between 3D, a) and 2D b)*

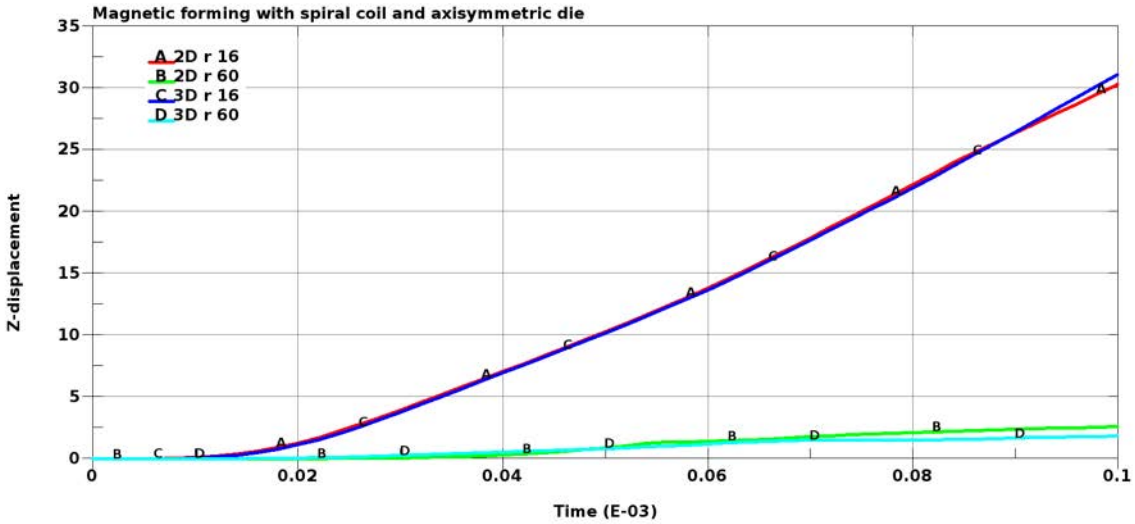


***Figure 5**: Comparison of displacements between 2D and 3D for two points along the workpiece's radius, one close to the center (radius = 16 mm), one further away (radius = 60 mm)*

## 3.2 Mixing 3D and 2D Parts

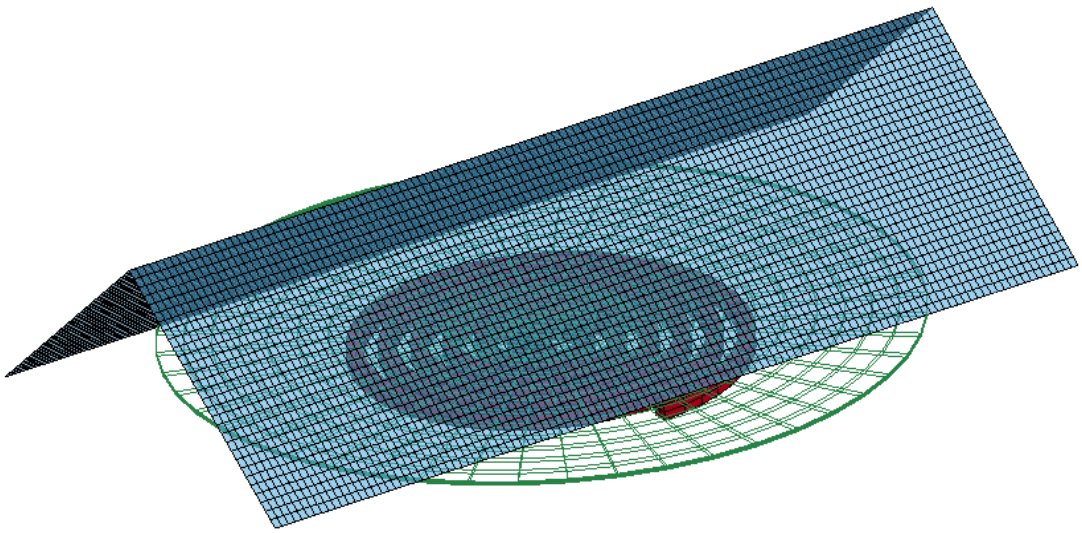

***Figure 6**: Magnetic metal forming with spiral coil and non-axisymmetric die. 3D setup.*

The previous case had the advantage of presenting an axi-symmetric coil, workpiece and die, thus allowing the problem to be fully reduced to 2D. However, it many instances, any of those parts could present some 3D features that cannot be reduced to a 2D equivalent. For this reason, the new method allows users to combine 2D parts with 3D parts. In this example, the previously described case has been slightly modified by using a different shape for the

die as shown on **Fig. 6**. In such a configuration, the workpiece can no longer be reduced to an axi-symmetric part since it will not keep its rotational invariance during its deformation. However, it is still possible to use the 2D solver for the coil. **Fig. 7** offers a view of the final shape of the workpiece. The somewhat strange shape is due to the rebound of the sheet against the die. **Fig. 8** offers a comparison between displacements for the fully 3D and the 2D-3D mixed case. Again, good agreement between the results is found but with a significant reduction in the calculation times for the 2D-3D configuration which took about 7 minutes on 1 CPU compared to the 20 minutes for the 3D case.

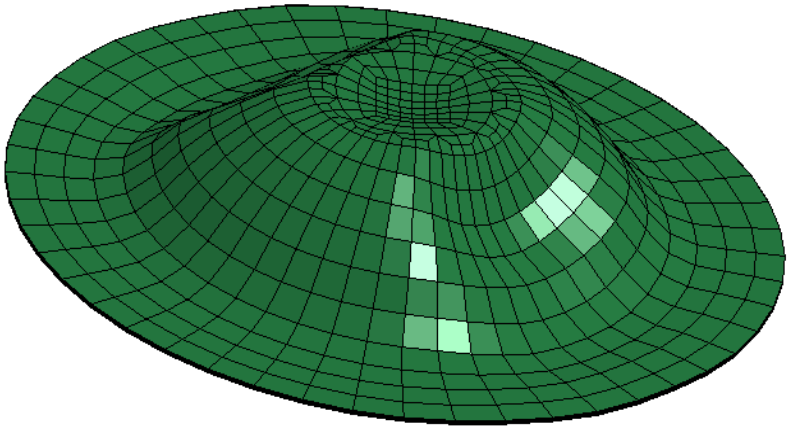

***Figure 7**: Final shape of the sheet after forming against the non-axisymmetric die*

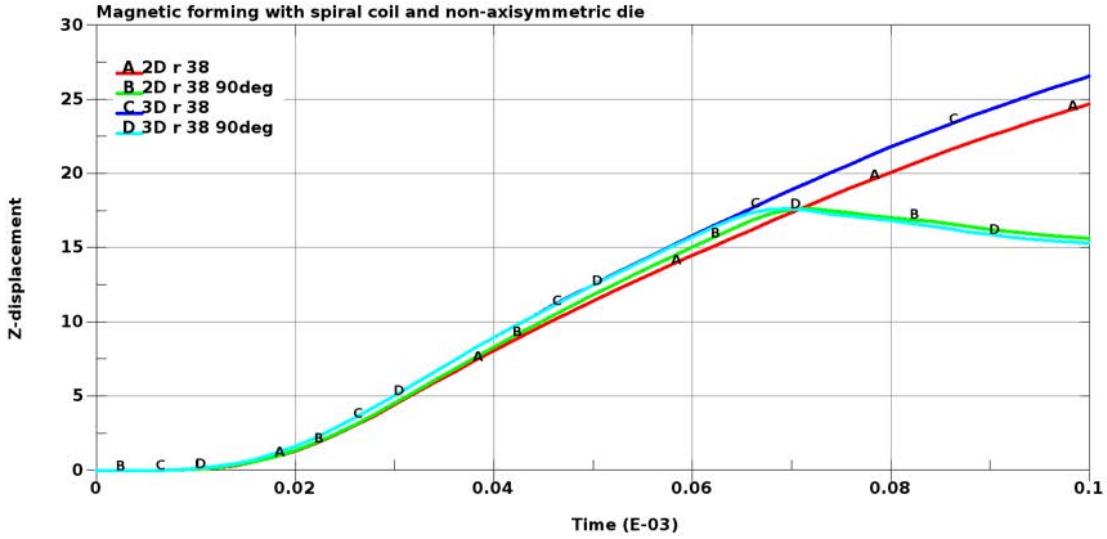


***Figure 8**: Comparison of displacements between 3D and 3D mixed with 2D for two points with the same radius but shifted by an angle of 90 degrees*

# 4 Conclusion

The development of the axi-symmetric solver arose from a need by users to reduce their calculation times in their EM metal forming and welding simulations. Indeed, in certain configurations, it was possible to accelerate the output of the desired result by a factor ten. However, it was so far limited to perfectly axi-symmetric cases. The newly developed extension that allows for mixing between 2D and 3D parts suddenly expands tremendously the range of application that the axi-symmetric solver can have. The signification reduction of calculations costs that it proposes will allow users to bring more flexibly in their setting up of model, give them more opportunities to conduct trial runs but also permit them to potentially couple the EM solver with LS-Opt for optimization purposes.

# References

L'Eplattenier, P, Imbert, J. & Worswick, M., Introduction of an Electromagnetism Module in LS-DYNA for Coupled Mechanical-Thermal-Electromagnetic Simulations. Steel Research Int, Vol 80 no.5, 2009.

L'Eplattenier, P, Ashcraft, C & Ulacia, I An MPP version of the Electromagnetism Module in LS-DYNA for 3D Coupled Mechanical-Thermal-Electromagnetic Simulations, ICHSF 2010, Columbus, OH, USA

L'Eplattenier, P & Caldichoury, I Simulation of a Railgun: A Contribution to the Validation of the Electromagnetism Module in LS-DYNA v980, 12th International LS-DYNA conference, Dearborn, MI, June 3-5 2012. Available under www.dynalook.com

L'Eplattenier, P & Caldichoury, I, Recent Developments in the Electromagnetic Module: a New 2D Axisymmetric EM solver, 10th European LS-DYNA conference 2015, Wurzburg, Germany, 2015. Available under www.dynalook.com

Ren, Z & Razek, A, New Technique for Solving Three-dimentional Multiply Connected Eddy-current Problems, IEE Proceedings, 137, No 3, 1990

Rieben, R & White, D, Verification of High-order Mixed Finite Element Solution of Transient Magnetic Diffusion Problems, IEEE Transactions on Magnetics, 42, No1 pp25-39, 2006

# 3D Impacts Modeling of the Magnetic Pulse Welding Process and Comparison to Experimental Data

**J.-P. Cuq-Lelandais*, G. Avrillaud, S. Ferreira, G. Mazars, A. Nottebaert, G. Teilla, V. Shribman**

Bmax, 30 boulevard de Thibaud, ZI de Thibaud, 31100 Toulouse Cedex 9 – France
Website: www.bmax.com
*Corresponding author. Email: jean-paul.cuq@bmax.com – Tel.: +335 34 61 16 68

## Abstract

*Magnetic Pulse Welding (MPW) is a solid state (cold) welding process known to present several advantages. When properly designed, such an assembly is stronger than the weakest base material even for multi-material joining. These high quality welds are due to an almost inexistent Heat Affected Zone which is not the case with fusion welding solutions. Another advantage is a welding time that is under a millisecond. In order to define the MPW parameters (mainly geometry, current and frequency), recent developments have made it possible to adapt welding windows from the Explosive Welding (EXW) for use in MPW. Until now, these welding windows have been simulated only in 2D geometries showing how the impact angle and the radial velocities progress in a welding window. The aim of this paper is to present our most recent development, which builds on this analysis to develop a 3D model in order to deal for example with local planar MPW. Simulation results will be presented and then compared to experimental data for a multi-material join case.*

## Keywords

Magnetic pulse welding (MPW), Dynamic simulations, Welding windows

# 1 Introduction

High Pulse Power (HPP) processes are drawing ever more attention from industry, in particular in the case of Magnetic Pulse Welding of two different materials or in complex geometries. Conventional processes that rely on melting of the materials, is only rarely able to successfully assemble such different materials. The reasons for this are related to strong differences in the respective material properties, such as their melting points or thermic expansion rates. This in turn leads to strong residual stresses and therefore potential cracks. Moreover, thick layers of intermetallic materials are created in proximity to the interface during the re-solidification step. This results in a brittle and mechanically weak heat affected zone and thus a limited quality assembly between the two materials (Kapil 2015).

Solid state welding solutions, such as Explosive Welding (EXW) and Magnetic Pulse Welding (MPW), are known to bond material without or with a very limited solid to liquid phase change during the process. Both processes are based on a high velocity oblique impact. This way, the heat affected zone is negligible and leads to high quality welds when the welding parameters are properly chosen.

The MPW process consists in a fast discharge (several microseconds) of a high current in a coil, inducing strong Lorentz forces in the part to be accelerated. This process is currently available at Bmax alongside a number of other industrial HPP technologies, such as Magnetic Pulse Forming/Crimping or Electro-Hydraulic Forming.

When compared to EXW, and when thicknesses are not too large, the MPW solution is more suitable for mass production for obvious production rate, cost and safety reasons. MPW can also be adapted to a wide range of geometries (tubular or planar) and to various weld sizes (up to more than a meter in length). One of the necessary preconditions for MPW is to control the evolution of impact parameters as these are essential to achieving a high quality weld in geometries other than 2D. This requirement motivated the recent development presented in this paper, based on 3D impact modeling. These simulations make it possible to apply the technology on 3D geometries and to analyze the welding process, in a strong multi-physics model, with a reduced calculation time. This allows us to greatly shorten the fine-tuning phase of the process to obtain the proper welding parameters that are necessary to optimize the joining strength.

To begin with, a short explanation of the MPW theory is presented. This includes how a welding window is built and gives the appropriated ballistic conditions to bond two given materials. This in turn provides the basis for a simulated prediction of the potential welded zones.

For this purpose, 2D and 3D multi-physical simulations are performed with dynamic explicit LS-DYNA code. A post-processing program developed by Bmax is used to define the ballistic history of the collision model and to plot it in the welding window graph. The method is first demonstrated in a 2D geometry showing a comparison between multi-physical simulations and experimental results (Cuq-Lelandais and al., 2014).

The method is then extended to a 3D geometry case with the same welded materials. In this case, a planar welding example is used. The ballistic results are shown in the

Welding Window and compared to the experimental equivalent test. Moreover, this latter is projected on the geometry to directly identify the potential welded area.

# 2 Welding Window Theory and Numerical Methodology

## 2.1 Theoretical Background

Cold welding between two parts is achieved using an oblique impact at high speed. In the case of MPW, a high current discharge (hundreds of kA) flows through a coil, inducing Lorentz forces on the part to move. This strong and short loading causes the part acceleration within few microseconds on about a millimeter standoff distance. It can reach several hundreds of m/s at impact with the parent part. Extensive studies on the EXW method showed welding is achieved for a given range of impact angles and velocities, referred to as the Welding Window (Grignon, 2003 and Kapil, 2015). The impact welding process implies multi-physical and dynamic phenomena, including mechanical, thermal and thermodynamics fields. To obtain a strong welding, several necessary conditions must be achieved. Whereas the welding windows for the EXW plot collision angle versus collision point velocity ($V_c$), Cuq-Lelandais and al. (2014) have proposed to plot the more practical collision angle ($\alpha$) versus normal impact velocity ($V_n$) for MPW (see Fig. 1).

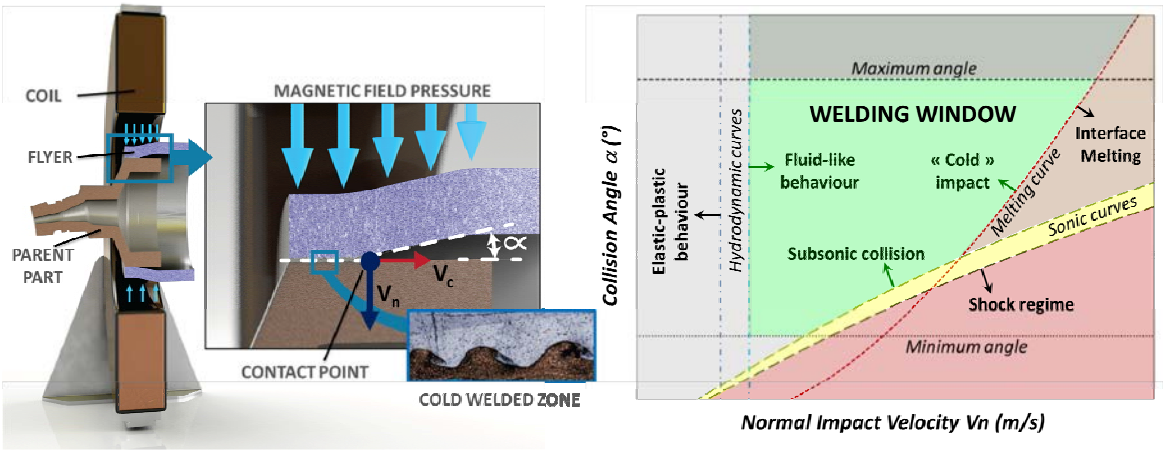


***Figure 1**: MPW oblique impact process and a typical theoretical Magnetic Pulse Welding Window*

- **Jetting conditions:** The collision point has to be subsonic compared to the local materials speed of sound to generate a jet. A supersonic case leads to an oblique shock wave behind the collision point.
- **High Pressure/hydrodynamic regime:** If the velocity is not high enough to provide a fluid-like behavior, the parts are only bent following an elastic-plastic regime.
- **No fusion during the collision:** The process has to remain "cold". If the pressure is too high, the materials can locally melt and then re-solidify, implying issues to those in the traditional welding processes.

Contrary to the EXW method, the impact collision history in MPW is transient due to the non-constant magnetic pressure. For this reason it is necessary to develop a numerical method to predict the evolution of these parameters and thus determine the potential welded/unwelded zones to optimize the joining parameters, in particular when the geometry becomes complex. Such analysis is demonstrated in the following example in a 2D axisymmetric geometry.

## 2.2 Numerical Ballistic Analysis – 2D Axisymmetric Example

This case study examines the MPW of an aluminum alloy outer tube on a steel anvil. The coil surrounds the outer tube and is loaded with an imposed current pulse, inducing the outer tube acceleration. The calculation is run with the LS-DYNA® code (Hallquist, 2015). This latter is the only commercial code available to perform parallel 3D Magneto-Hydro-Dynamic (MHD) with a strong coupling with high speed mechanics, electromagnetics (Eddy currents) and thermal effects (including Joule effects and electrical conductivity equation of state) (L'Eplattenier, 2009). This model provides a complete analysis of the collision history, which can be reported on the Welding Window graph (see Figures 2 & 3). For comparison purposes, experimental welded zones can be identified by using a cross section micrography. Welding starts only 0.5 mm after the first impact point (entry zone). It can be seen that two zones have been bonded with a smooth interface, leaving a central region unwelded. The welded lengths measured are in good agreement with the simulation which exhibit a similar behavior.

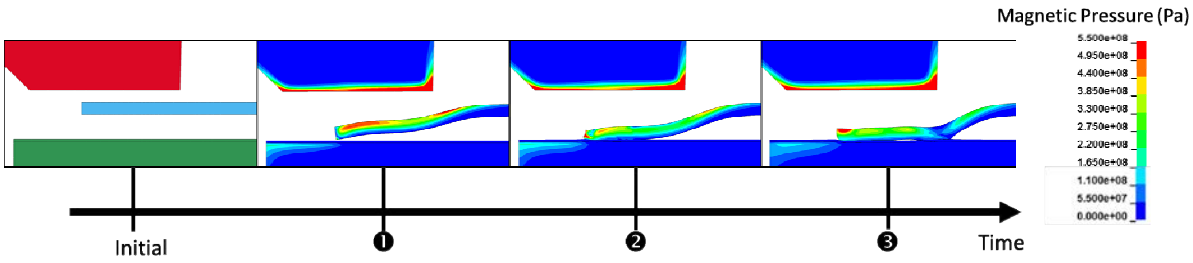


***Figure 2**: 2D cylindrical MPW impact Simulation – Magnetic pressure contours at different times*

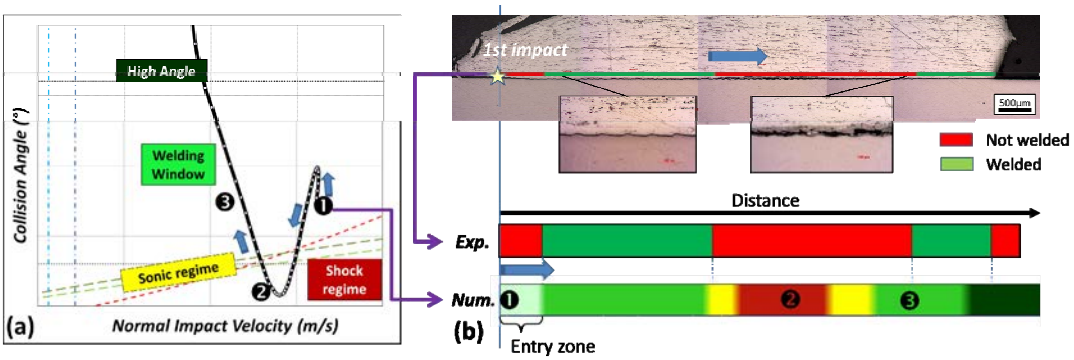


***Figure 3**: Simulation ballistic results on the Aluminum/Steel Welding Window graph (a) - Experimental/Numerical comparison of the welded zones (b)*

## 2.3 Results Interpretation – Eulerian Calculations

In this case, the deformed shape of the tube is not optimized and presents large variations of the collision angle. The ballistic path goes out of the Welding Window when the collision angle becomes too weak (flat impact), and comes back later on, in the last third of the impacted zone.

The local impact behavior in both welded and unwelded zones can be compared to impact simulations as shown in Figure 3 where the collision point is followed at different times.

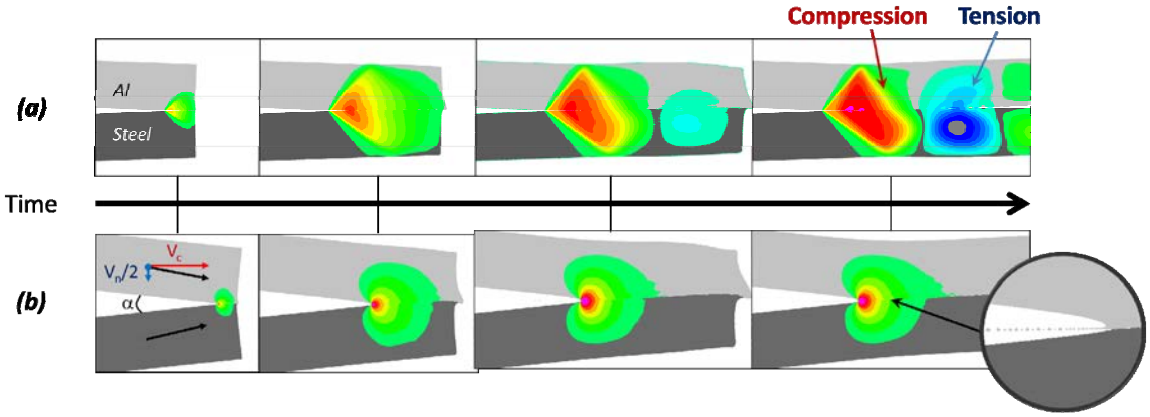


***Figure 4**: Simulations of the impact local behavior for different collision angles α at the same impact velocity: (a) = 4° angle; (b) = 12° angle – Fringes = Pressure*

When the angle is low (Fig.4-a), the collision point velocity is higher than the materials speed of sound. It results in a shock behavior, similar to a Mach cone, and no jet is generated. In addition, the reflected waves create a tensile state just behind the collision point, tending to peel off the parts. This can be considered as a bounce back in the central zone, which can affect the weld quality since it may propagate the tensile waves to the already bonded zones (Cuq-Lelandais and al., 2014). In the areas suitable for welding, the collision angle is higher and the corresponding simulation presents a cardioid pressure field, maximum at the collision point, with jetting. As it can be seen on the Fig. 4-b, the jet does not appear at the first impact, but only after a certain rise time in impact pressure. This inertia can explain why welding does not occur immediately in the entry zone, even if the ballistic conditions are good in the welding window.

This 2D example shows a good agreement between the welding windows theory, the simulations and the corresponding experimental test. The numerical results make it possible to explain the welded zones distribution and lengths, thanks to the ballistic analysis on the welding window graph.

# 3 3D Case Analysis – Planar Welding

The ballistic interpretation of a MPW impact validated in 2D geometries can be applied on a 3D case. In this work, a planar welding setup is presented, which is used to bond two metallic plates along a double weld straight line, as it can be seen in Figure 5.

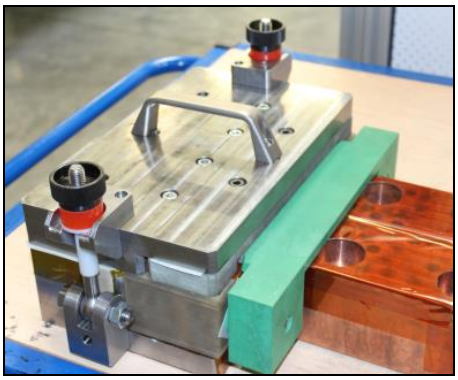

***Figure 5**: Planar MPW setup*

## 3.1 Planar Welding – Numerical Model

The model of the geometry and a cross section of the line to be welded are shown in Figure 6. The electrical pulsed loading delivered into the coil (IN/OUT on the figure 6-a) is calculated by an RLC circuit solver. The mesh is fine enough to accurately estimate the magnetic field diffusion (5 cells in the skin depth). This model contains about 700,000 elements to represent all the components. The model is run by coupling the electromagnetic solver with an explicit mechanical analysis using massive parallel computing, which reduces the calculation time. This case takes about one day to complete on 32 CPUs (Intel® Xeon® x7560).

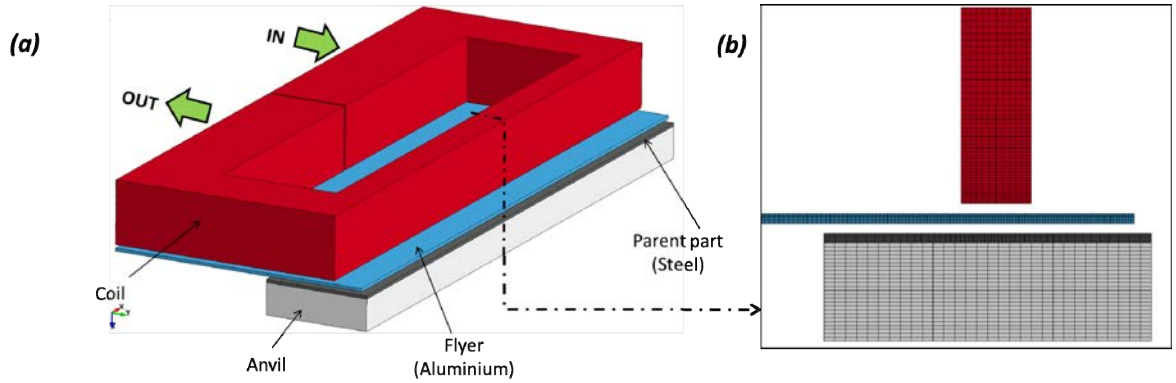


***Figure 6**: Planar MPW simulation model. (a) = 3D overview – (b) = Active zone cross section*

## 3.2 3D Multi-Physical Dynamic Behavior

The model presented in 3.1 provides a full 3D analysis, including electromagnetic effects, induced current in the flyer or the magnetic pressure distribution. Figure 7 exhibits for the model current densities (a) and Lorentz forces (b) at current peak. The current density in the coil is at its highest at the edges, whereas for the flyer it is located at the center of the coil (Fig. 7-a). The resulting Lorentz forces on the flyer show (Fig 7-b) a maximum at the center of the coil. However, significant forces on the flyer are applied next to the sides of the coil leading to substantial deformations in these regions.

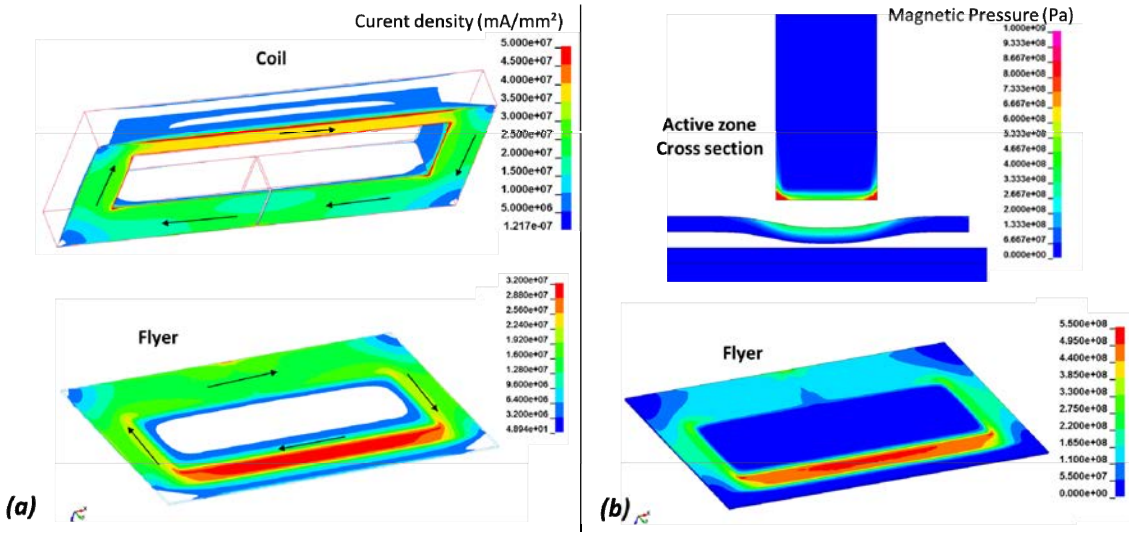


***Figure 7**: Planar MPW simulation at the quarter of period. (a) = Current densities (coil & flyer view) – (b) = Magnetic Pressure (model median cross section and 3D flyer view)*

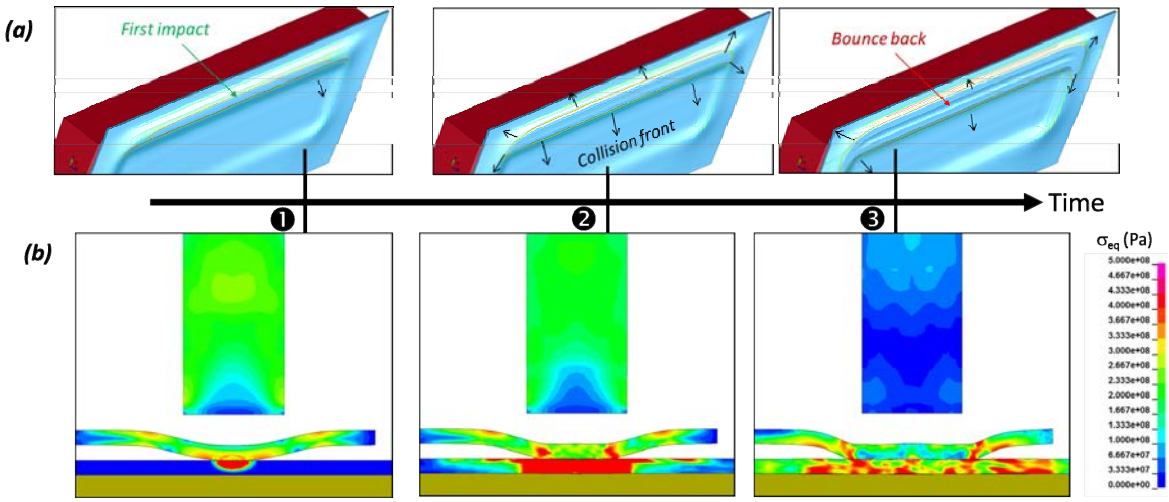


***Figure 8**: Planar MPW impact evolution at different times: upper = Flyer deformation and impact – lower = Equivalent stresses on the 2D active zone cross section*

Also, 3D modelling makes it possible to analyze mechanical stresses on the parent part and the coil. The 2D median cross section equivalent stresses are presented in Figure 8, showing two distinct behaviors. First, when the impact velocity is high (2), the stresses concentrate only around the collision point. On the other hand, when the impact velocity is reduced, the stress field shows a bending, with two tension/compression zones across the thickness. The stresses in the coil are checked in order to always keep them below the material yield stress, ensuring adequate life time for industrial uses.

## 3.3 3D Ballistic Results

Furthermore, a global ballistic post-processing can be performed similarly to the 2D case. Such analysis appears to be helpful in revealing the favorable zones where welding between the two plates can be achieved. Consequently it can be used to adapt the coil shape and the gaps in order to increase the welding area and thus the strength of the assembly.

The analysis can be run on the whole impacted area, as can be seen in Figure 9 where only half of the model is shown. This provides a characterization of the main ballistic data. For a 3D analysis, the impact time contours on the geometry make it possible to draw the collision front evolution. In this case, 2 symmetric linear fronts start at the center of the coil location, where the impact velocity is the highest but normal to the parent part (no angle). They expand then on both sides and the impact velocity reduces progressively, while the angles increase.

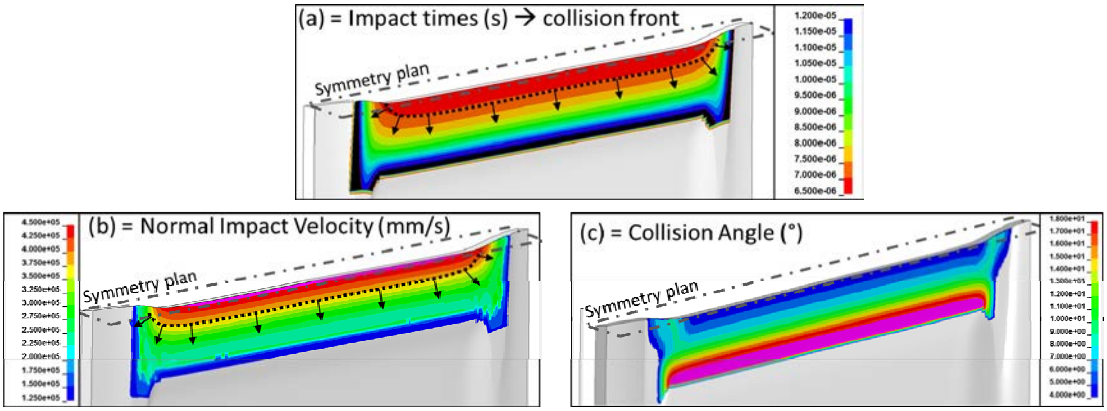


***Figure 9**: 3D ballistic analysis on the impacted zone for half of the model: (a) = Impact time contours – (b) = Normal impact velocity contours – (c) = Collision angle contours*

Concerning the Welding Window ballistic curve, if a 2D analysis is suitable as the collision is curvilinear; it becomes harder to draw it for a 3D problem where the collision follows a surface. As one can plot the main ballistic parameters on the geometry, it is possible to directly project the Welding Window and interpret the weldability in terms of zones. Figure 10 gives the Welding Window projection applied to the planar MPW case. The zones where appropriate conditions for welding are reached appear as green. This latter can be compared to the experimental test (upper picture). In this picture, all the

unwelded flyer zones have been removed. The simulation gives a good evaluation of the experimental welded lateral half-length: 7.9 vs. 7.7 cm measured on the sample.

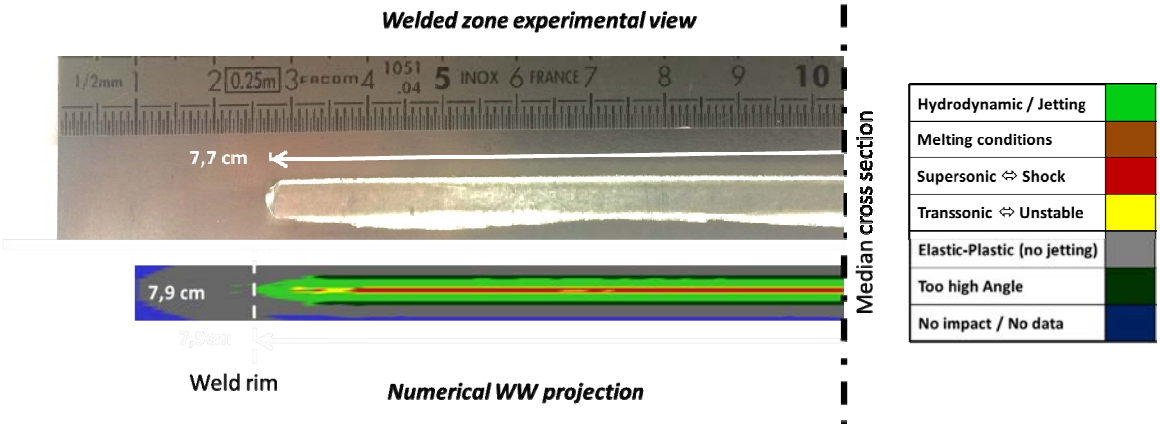


***Figure 10**: Experimental/Numerical comparison of the welded lengths in the impacted zone – Welding Window projection on the geometry*

In addition, 2D cross section analysis can be done, leading to a more classical interpretation as for the 2D cylindrical case. Experimental axial welded length is compared to the ballistic curve results taken in the median cross section as performed in paragraph 2.2 (see Figure 11 - right). They are also quite closely correlated with the theoretical Welding Window.

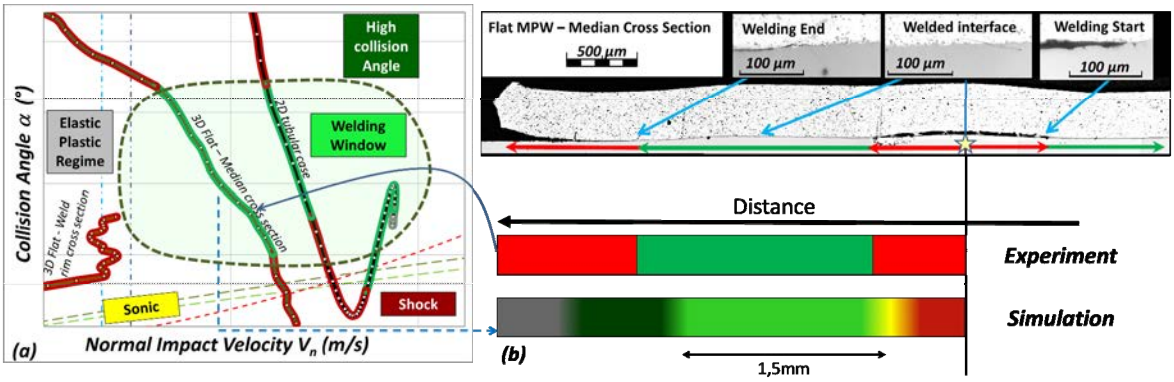


***Figure 11**: Experimental/Numerical comparison of the welded lengths on the 2D median cross section (b); Experimental welded zone retro-projection on the Welding Window (a)*

An additional curve is taken from a cross section on the rim of the welded zone (see white dashed line in Figure 10). This allows us to accurately characterize a boundary of the Welding Window. This lower velocity limit is in good agreement with the theoretical elastic-plastic/hydrodynamic vertical limit.

More generally, the comparison between numerical and experimental ballistic data in 2D and 3D can be useful to refine the Welding Windows, especially for high angles and

velocities. Figure 11 (left) illustrates this by projecting the experimental welded/unwelded lengths on the corresponding ballistic curve. In this case, three curves are processed. The 2D tubular case and the 2D cross sections from the planar MPW case give complementary results, as their respective ballistic curves are located in different regions of the graph.

# 4 Conclusion

This paper demonstrated the most recent modeling developments performed at Bmax dedicated to Magnetic Pulse Welding. The work is based on the post-processing of 3D impact conditions. The simulations are performed using the multi-physical LS-DYNA® code that makes it possible to accurately model induced Lorentz forces leading to high velocity impacts. The resulting collision parameters, angle and velocity, can be compared with the theoretical and experimental Welding Window for the combination of 2 materials. Two possibilities have been demonstrated, depending on the complexity of the case. For simple geometries, ballistic data can be plotted in the welding window graph as the collision point follows a curvilinear path. For a more complex 3D case, where it is no longer possible to easily use the results, the Welding Window can be reciprocally projected on the geometry. This provides a direct observation of predicted welded zones. This method has been validated using several experimental results associated to micrographs, in different geometries (cylindrical and planar). In both cases, simulated MPW data have shown a good match between experimental and theoretical welding windows. These tools provide not only the ability to efficiently refine the welding windows, but also to optimize coils and gaps in order to increase welding areas and thus the strength of assemblies. In addition this method facilitates a better understanding of the related physical phenomena. Practically, this analysis can be extended to more complex shapes, more in line with customer's requirements.

# References

Kapil A., Sharma A., 2015, Magnetic Pulse Welding: An efficient and environmentally friendly multi-material joining technique, Journal of Cleaner Production, 100 p.35.

Grignon F., Benson D., et al, 2003, Explosive welding of aluminum to aluminum: analysis, computations and experiments. Int J. Imp. Eng., 30 p 1333.

Cuq-Lelandais J.-P., Avrillaud G., et al, 2014, Weldability Windows Simulations for Magnetic Pulse Welding (MPW) processes, 6th International Conference on High Speed Forming, Daejeon, South Korea.

Hallquist J.O., 2015, LS-DYNA® Theory Manual.

L'Eplattenier P. et al., 2009, Introduction of an electromagnetic module in LS-DYNA for coupled mechanical-thermal-electromagnetic simulations, Steel Research Int. 80 p5.

# Mathematical Optimization for the Virtual Design of Process Chains with Electromagnetic Forming

**M. Rozgič, M. Stiemer***

Institute for the Theory of Electrical Engineering, Helmut Schmidt University / University of the Federal Armed Forces Hamburg, Germany
*Corresponding author. Email: m.stiemer@hsu-hh.de; Tel.: +49 40 6541 2769

## Abstract

*In this work, a framework for virtual process design for coupled processes including electromagnetic impulse forming is presented. Virtual process design is here understood as the computer based identification of suitable geometry and process parameters to reach a predefined forming result via physically feasible process paths. Implementation of this concept relies on three pillars: a physical process model, its implementation within a numerical simulation, and a mathematical optimization algorithm. This methodology is particularly applied to a combination of deep drawing and subsequent electromagnetic forming (EMF). In this case, the model is given by an anisotropic elasto-viscoplastic material model augmented by damage evolution and coupled with the magneto-quasistatic approximation to Maxwell's equations. For constrained mathematical optimization, an inner point algorithm is applied. With this method for virtual process design at hand, several technological problems are addressed including tool coil design and the identification of ideal electrical parameters of the tool coil circuit. Employing this framework requires the identification of the material model described above. It turns out that a high precision identification of material parameters can be achieved with basically the same mathematical algorithm as derived for process identification.*

## Keywords

Metal forming, Design optimization, Finite element method

# 1 Introduction

Contemporary forming technology has to cope with increasing demands resulting from requirements of light-weight construction on the one hand, and from the claim for high-strength parts on the other hand (Stiemer et al., 2011). To satisfyingly consider such opposing trends, the invention of new processes is required that extend the forming limits of classical quasi-static forming such as deep-drawing. A viable method to reach this goal are process combinations of a classical quasi-static forming method and a subsequent impulse forming process (Vohnout, 1998). Due to different damage mechanisms acting during the quasi-static and during the high-speed phase, the overall formability is increased even if both processes act on similar strain paths (Kiliclar et al., 2016). However, for certain process combinations such as deep-drawing and subsequent EMF, an increase in formability can only be achieved if all parameters of the combined process are carefully tuned (Taebi et al., 2012). Hence, a successful process control requires the identification of suitable process and geometry parameters, such as parameters describing the blank holder adjustment, tribological conditions, punch force and velocity on the quasi-static side, and tool shape and position or the discharging current on the electromagnetic side.

An experimental adjustment of these parameters is very time consuming. The high competition in modern markets forces technological solutions to be found in an increasingly short period. Hence, computer based methods become more and more important, since they allow for a reduction of expensive experiments required for a parameter identification process. In an ideal setting, only a final experimental verification of virtually identified technological solutions would remain.

In this work, virtual process design is understood as the computer based identification of suitable geometry and process parameters to reach a predefined forming result via physically feasible process paths. Implementation of this concepts relies on a physical process model, its implementation in a finite element simulation, and a mathematical optimization algorithm. The methodology developed here is particularly applied to a combination of deep drawing and subsequent EMF of aluminum EN AW 5083. In this case the model is given by a combination of an anisotropic elasto-viscoplastic material model (Vladimirov et al., 2010) augmented by damage evolution with the magneto-quasi-static approximation to Maxwell's equations (Vladimirov et al., 2014). For constrained mathematical optimization, an inner point algorithm is applied. With the method for virtual process design at hand, several technological problems can be addressed including tool coil design and the identification of ideal electrical parameters of the tool coil circuit. Employing this framework for virtual process design requires the identification of the material model described above. It turns out that the identification of material parameters in a high precision can be achieved with basically the same mathematical algorithm as derived for process identification.

In the following Chapter 2, a short introduction into the here exemplarily considered type of process combinations is given. Then, in Chapter 3, the mathematical framework of the method is sketched. In the main part of this work, Chapter 4, some concrete technological applications are discussed. The article ends with some conclusions in Chapter 5.

## 2 Combination of Quasi-static and Impulse Forming

EMF is a contact free impulse forming method yielding strain rates over 1000 $s^{-1}$. It is suited for electrically good conducting materials such as copper, aluminum, and even steel (see, e.g., Daehn 2006, or Psyk et al., 2011). In EMF, forming is triggered by Lorentz forces resulting from the interaction of eddy currents induced in the work piece by a pulsed magnetic field with the triggering magnetic field itself. The latter results from the discharging current of a capacitor bank into a tool coil close to the work piece. In the case of sheet metal forming, it acts most efficiently when applied to small areas as part of a process chain combined with a classical quasi-static process (Vonhout, 1998). In this particular context, classical forming limits of quasi-static processes can be extended yielding a broader range of applications (Psyk et al., 2011). In Fig. 1, a combined process setup for cup forming is depicted as an example. It consists of deep drawing followed by an electromagnetic calibration close to the bottom edge of the die. The tool coil is incorporated in the punch. This type of process combination will frequently be considered as an example in the following.

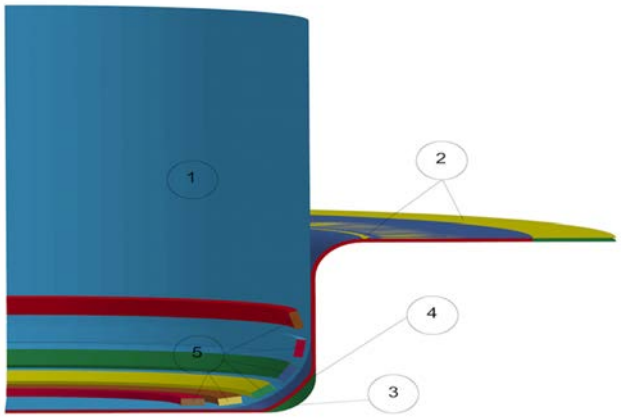


***Figure 1**: Example of a process chain combining deep drawing and EMF: (1) punch, (2) blank holder, (3) die, (4) work piece, (5) tool coils (CAD model by Kiliclar, IFAM, Aachen)*

Several problems arise in the design of process chains including EMF: Particularly, it has turned out that an increase in formability can only be achieved if the process parameters are carefully tuned (Taebi et al., 2012). Moreover, the design of suitable, sufficiently stable and long living tool coils yielding the optimum Lorentz force is technologically challenging.

## 3 Mathematical Concepts

The paradigm followed in this work relies on a physical model of the combined process, which is capable of predicting the outcome of the process. Then, a process simulation is

developed that is based on the physical model. Separation of physical modeling and numerical implementation is essential for a control of the accuracy of the process simulation. The next step is a quantitative validation of the simulated process result. The corresponding value could be the quadratic mean deviation between the shape resulting from the forming process as computed via simulation and an ideal shape (Taebi et al. 2012). The function that assigns to each set of certain process parameters of interest such a quantitative validation of the forming process is called an *objective function.* From the mathematical point of view, process identification can be considered as finding a local or even global extremum of the objective function. The case of a local extremum corresponds to the situation that only fractions of the parameter space are searched for, while the search of a global extremum refers to consideration of the whole space of suitable parameters. The latter is a more difficult task, and in many cases only local optima can satisfyingly be found by numerical algorithms (Nocedal, J. and Wright, S., 2006). Optimization problems resulting from parameter identification are typically constrained: all parameters are subject to bounds resulting from physical or technical considerations (Tarantola, A., 2005).

In this chapter the three mathematical pillars of a framework for virtual process design, the process model, its numerical simulation, and the mathematical optimization are individually discussed in case of a process combination of deep drawing and subsequent EMF as described in Chapter 2.

## 3.1 Process Models

Corresponding to the different physical nature of the individual constituents of the coupled process, both mechanical and electromagnetic fields have to be mathematically described. On the mechanical side, one model is employed that is both suitable for the quasi-static and for the high speed regime. This flexibility is achieved by an elasto-viscoplastic material model including strain rate effects and material anisotropy due to Vladimirov et al. (2010), which is coupled with a damage model to separate viable strain paths from those leading to material failure (Vladimirov et al. 2014). In this approach, a Hill-type plastic anisotropy model is employed. Further, a Perzyna rate dependent formulation is coupled with rate independent Kuhn-Tucker conditions, to model both regimes. Kiliclar et al. (2012) demonstrated the suitability of the model for the simulation of aluminum EN AW 5083.

On the electromagnetic side, the magneto-quasistatic approximation to Maxwell's equations is relevant. Since the wavelengths at typical field excitations for EMF (e.g., 50 kHz) are much longer than the size of a forming device, and since induction is the relevant coupling process between tool coil and work piece, displacement currents may be omitted.

## 3.2 Numerical Simulation

As the considered process relies on different physical models, various discretization techniques have to be considered to obtain a fast simulation scheme. In the context of the commercial software LS-DYNA, a boundary element solver for the air between tool coil and

work piece, coupled with Nédélec edge finite elements for conducting material, is available. On the mechanical side, standard vertex based 3d volume elements can be used.

While LS-DYNA allows for a direct numerical solution of the coupled partial differential equations of the underlying model, it is sometimes more efficient not to solve the linear system of equations resulting from the finite element method directly, but to hand the assembled matrices over to the mathematical optimization routine. In the optimization step, compliance with the finite element system then defines a set of constraints for any critical state of the objective function. The latter guarantees that only physically feasible states are considered for optimization of the objective function, without solving the finite element system. This leads to an enormous gain in efficiency as Rozgič and Stiemer (2014) indicated. However, most commercial code that is employed as a black box solver lacks the flexibility to be employed in such a way.

## 3.3 Mathematical Optimization

The identification of suitable parameters is controlled by an exterior mathematical optimization algorithm. Here, the inner point method as implemented within IPOPT by A. Wächter and L. T. Biegler (2006) is employed. A complete algorithmic variant is depicted in Fig. 2, which relies on a use of LS-DYNA as black box solver. In this case, the mathematical model equations are solved and the objective function is computed from the identified state. This is not as efficient as the method described in the preceding section, where feasibility of the state was only established indirectly via constraints, but it is often more convenient to employ the finite element solver in its original fashion instead of accessing its internal data.

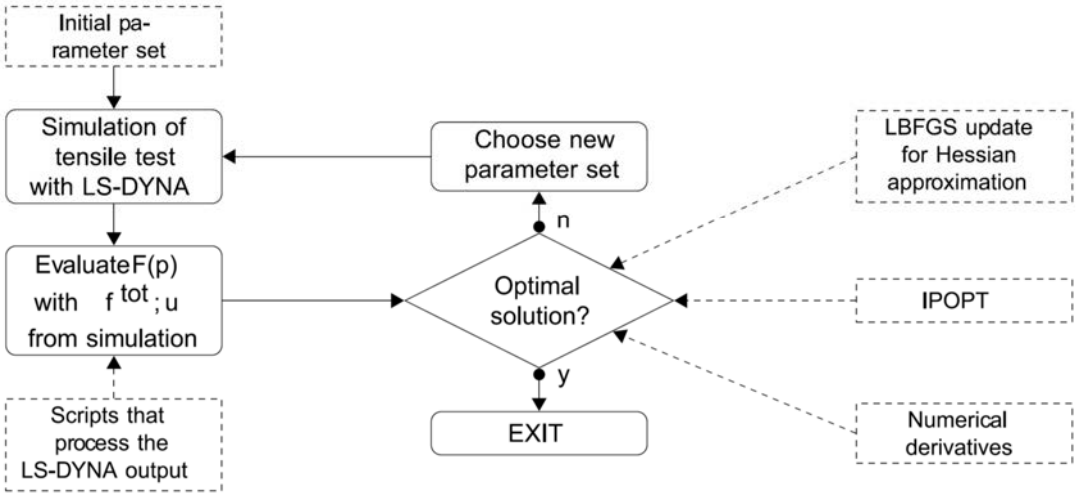


***Figure 2**: A flow chart of the process parameter identification algorithm (Kiliclar et al. 2016)*

# 4 Technological Applications

In this chapter typical technological applications of the method outlined before are presented including both process and model identification.

## 4.1 Identification of Material Parameters

Applications of the method described above to the identification of the underlying material model have been presented in Kiliclar et al. (2016), and, in more detail, in Rozgič et al. (2016). In the identification process simple experiments (e.g., uni-axial stress-strain curves etc.) are carried out and their outcome is compared to simulation results. As objective function a distance function between simulation result and experimental data can be taken. Via optimization those internal parameters of the material model are identified that yield the best agreement between experiments and simulation. The material model parameters obtained by the previously outlined procedure refer to quasi-static strain rates only. However, results by Clausen et al. (2004) show, that EN AW 5083 under high strain rates exhibits an increase in yield stress, but not in hardening. Therefore, the obtained results can be extended to high-strain rates by a linear extrapolation of the model's damage threshold (Kiliclar et al. 2016). This approach is validated by comparison to tensile tests with strain rates up to 1000 $s^{-1}$.

## 4.2 Identification of Current Parameters

Taebi et al. (2012) offered a first approach to the identification of ideal current parameters for the EMF step. The objective is to find those parameters for the pulse that make the bottom radius of a round cup formed from a disc-shaped metal sheet under axi-symmetric conditions as small as possible, such that no damage occurs. In that work, a damped cosine has been assumed as current function in the tool coil with amplitude $I_0$, angular frequency $\omega$, damping parameter $\beta$, and phase angle $\varphi$:

$$I(t) = I_0 e^{\beta t} \cos(\omega t + \varphi) \tag{1}$$

While phase and damping have been held on a constant level, a two parameter optimization for the angular frequency and the amplitude has been performed. Forming limits were not included via a physically motivated damage model, but by a phenomenological approach resorting to so called forming limit surfaces, which account for rate dependency by rescaling a quasi-static forming limit curve according to the phenomenological Johnson, Cook (1985) damage model. These results have been experimentally validated.

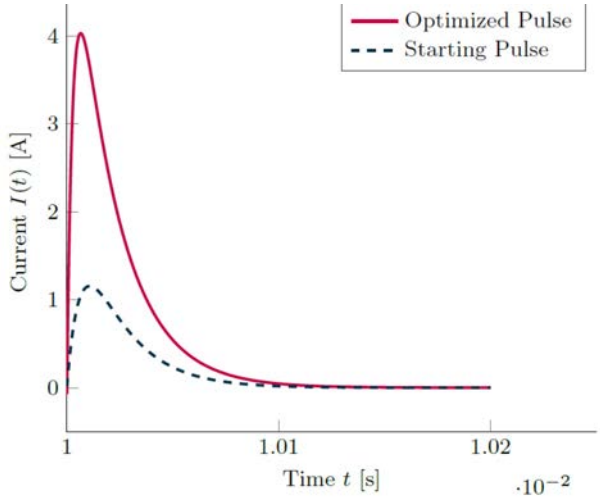


***Figure 3**: Current I(t) for the identified parameters $I_\alpha = 65570$ A and $I_\beta = 64868$ A, as well as the corresponding exponential factors $\alpha = 6879\ \mathrm{s}^{-1}$ and $\beta = 973\ \mathrm{s}^{-1}$ (Rozgič et al. 2016)*

Although a damped cosine seems to be a natural adjustment for the coil current, there are severe disadvantages connected to such an arrangement: The opposite sign of the second half-wave yields coil abrasion, since the work piece has already moved so far that it cannot bind a significant amount of momentum. Hence, the complete momentum resulting from the Lorentz force is absorbed by the tool coil, which makes the tool windings bend up and eventually break (Gies et al. 2012). This leads to the demand of avoidance of second half-waves. A technical approach to this claim is the construction of electrical supply circuits that prevent the second half wave. To analyze such approaches numerically, Rozgič et al. (2016) approximated the damped cosine with removed second half-wave by a double exponential pulse, which can quite conveniently be treated within the mathematical framework described above. To obtain the optimized characteristics of single pulse excitations, Rozgič et al. (2016) identified the two amplitudes $I_\alpha$ and $I_\beta$, as well as the corresponding exponential factors $\alpha$ and $\beta$ in the pulse representation

$$I(t) = I_\alpha e^{-\alpha t} + I_\beta e^{-\beta t} \tag{2}$$

Starting and resulting pulse of the parameter identification process are displayed in Fig. 3. For the complete set of data, see Rozgič et al. (2016).

## 4.3 Identification of Coil Parameters

An interesting application is the numerical identification of geometry parameters of the tool coil embedded in the punch employed for deep drawing.

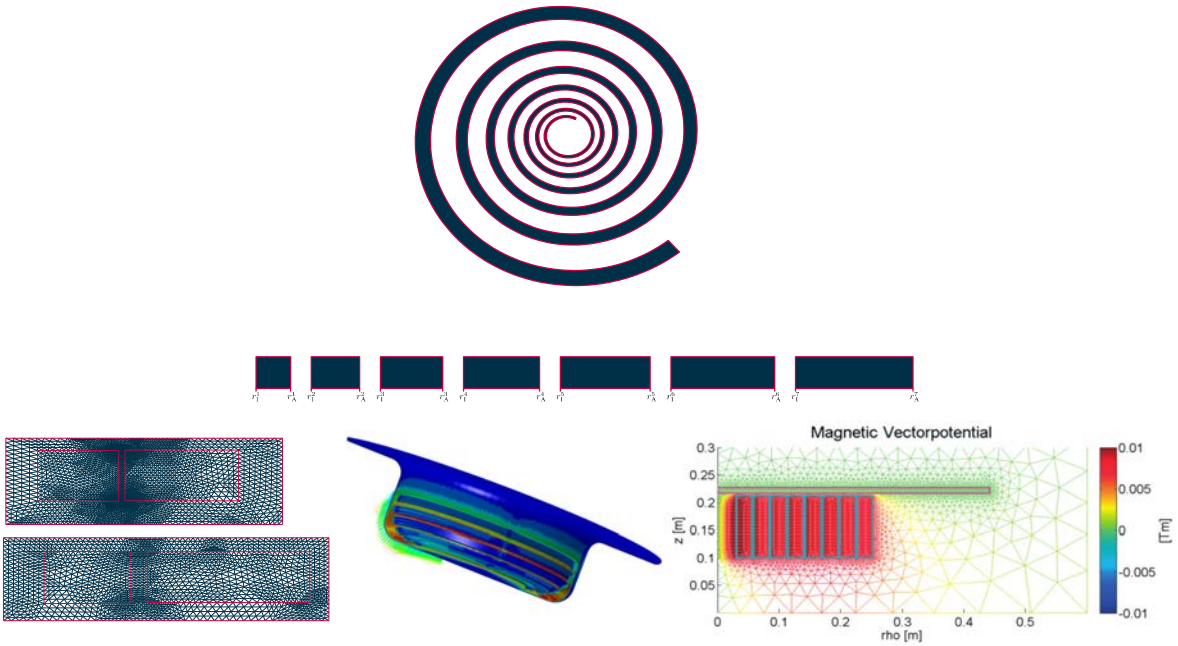


***Figure 4**: Components of an algorithm for the identification of coil geometry parameters: tool coil (top), axi-symmetric adaptation of the tool coil (middle), meshes of different geometries (down, left), 3d field computation (down, middle), axi-symmetric field computation (down right)*

A sketch of such an algorithm is depicted in Fig. 4. Here, the problem arises that different geometries may lead to different mesh structures after discretization, and, hence, to different instances of optimization problems that cannot easily take part in a common parameter search. There are several approaches to overcome this difficulty: in case of consideration of only small geometrical deviations during parameter variation, the mesh structure does not need to be altered, and just a displacement of the mesh vertices has to be done. The structure of the resulting optimization problems is consequently not changed (see the two grids on the left hand side in Fig. 4). However, if large geometrical variations or even topology changes shall be taken into account, it could be helpful to consider a new mathematical approach, where optima to whole classes of optimization problems are searched for. The key to such an approach are uniformity properties of all members in such a family, which could be deduced if the optimization problem is considered as a continuous problem in a certain function space, which is only discretized, after analytical conditions for optimality have already been applied on the continuous level.

## 4.4 Identification of Quasi-static and of High-speed Parameters

Finally, parameter sets should be considered that both define electromagnetic and mechanical quantities. It will be interesting to investigate in what cases a splitting between the quasi-static regime and the impulse forming regime is always possible during

optimization. Such a split always applies when strain paths are relevant where the full quasi-static forming limit can be exhausted before additional formability is gained by the fast forming method, since in this case both processes can be optimized independently of each other. The existence of such strain paths has been shown by Kiliclar et al. (2016).

# 5 Conclusions

In this work, a mathematical optimization scheme is coupled with a numerical process simulation to establish an environment for the automated identification of geometry and process parameters. The parameters are identified as stationary points of a suitable objective function under constraints and can be considered as the outcome of a virtual design process, since the identified process is described by these parameters.

To obtain efficient algorithms that allow to treat large problems, the finite element solver should not be employed as primary solver, but only as prepare-unit for the optimization method, which, hence, assumes the role of the solver. The idea behind this is to choose a rather simple objective function, such as, e.g., a distance function between an optimum part and a part that corresponds to the currently chosen parameters. The system of partial differential equations governing the technological processes is here just interpreted as side conditions to the optimization algorithm. Hence, a large speed up can be achieved. However, if an existing commercial code shall be employed as black box solver, this method can usually not be applied, since the required data are often not available.

By the virtual environment presented here, many important technological questions can be tackled: The identification of electrical current parameters in the EMF step minimizing drawing radii under the site condition that damage is avoided, the identification of parameters of the material model, the design of suitable tool coils, and, as intended in near future, complete sets of parameters including deep drawing parameters as well as electromagnetic parameters.

# Acknowledgments

This work is based on the results of the research project PAK343-2; the authors would like to thank the German Research Foundation (DFG) for its financial support. Further, the authors are indebted to the Institute of Forming Technology and Lightweight Construction (IUL) at the TU-Dortmund and the Institute of Applied Mechanics (IFAM) at RWTH Aachen University.

# References

Clausen, A.H., Børvik, T., Hopperstad, O.S. and Benallal, A., 2004. Flow and fracture characteristics of aluminium alloy AA5083–H116 as function of strain rate, temperature and triaxiality. Materials Science and Engineering: A, 364(1), pp. 260-272.

Daehn, G.S., 2006. High-velocity metal forming.

Johnson, G.R., Cook, W.H., 1985. Fracture characteristics of three metals subjected to various strains, strain rates, temperatures and pressures. Eng. Fracture Mechanics 21(1), pp. 31-48.

Kiliclar, Y., Demir, O.K., Vladimirov, I.N., Kwiatkowski, L., Brosius, A., Reese, S. and Tekkaya, A.E., 2012. Combined simulation of quasi-static deep drawing and electromagnetic forming by means of a coupled damage–viscoplasticity model at finite strains. ICHSF 2012, pp. 325 - 334.

Kiliclar, Y., Demir, O.K., Engelhardt, M., Rozgič, M., Vladimirov, I.N., Wulfinghoff, S., Weddeling, C., Gies, S., Klose, C., Reese, S., Tekkaya, A.E., Maier, H.J., Stiemer, M., 2016. Experimental and numerical investigation of increased formability in combined quasi-static and high-speed forming processes. International Journal of Materials Processing Technology, submitted (January 19, 2016).

Nocedal, J. and Wright, S., 2006. Numerical optimization. Springer Science & Business Media.

Psyk, V., Risch, D., Kinsey, B.L., Tekkaya, A.E., Kleiner, M., 2011. Electromagnetic forming – A review. Journal of Materials Processing Tech. 211 (5), pp. 787-829.

Rozgič, M. and Stiemer, M., 2014. Numerical Comparison of Optimization Methods for Process Parameters Identification in Forming Technology. Proc. Appl. Math. Mech., 14, pp. 797–798.

Rozgič, M., Stiemer, M. Kiliclar, Y., Reese, S. Engelhardt, M., Klose, Ch., Maier, H.J., Demir, O.K., Tekkaya, A.E., 2016. Mathematical Optimization for virtual process design and material identification in high speed forming, in preparation.

Stiemer, M., Brosius, A., Tekkaya, A.E., 2011. Leichtbau und hochfeste Werkstoffe fordern die Umformtechnik heraus. MaschinenMarkt 37, pp. 24 – 27.

Taebi, F., Demir, O.K., Stiemer, M., Psyk, V., Kwiatkowski, L., Brosius, A., Blum, H., Tekkaya, A.E., 2012. Dynamic forming limits and numerical optimization of combined quasi-static and impulse metal forming. Computational Materials Science 54, pp. 293-302.

Tarantola, A., 2005. Inverse problem theory and methods for model parameter estimation. SIAM.

Vladimirov, I.N., Pietryga, M.P., Kiliclar, Y., Tini, V., Reese, S., 2014. Failure modelling in metal forming by means of an anisotropic hyperelastic-plasticity model with damage. International Journal of Damage Mechanics 23, pp. 1096–1132.

Vladimirov, I.N., Pietryga, M.P., Reese, S., 2010. Anisotropic finite elastoplasticity with nonlinear kinematic and isotropic hardening and application to sheet metal forming. International Journal of Plasticity 26, pp. 659–687.

Vohnout, V.J., 1998. A Hybrid Quasi-Static / Dynamic Process for Forming Large Sheet Metal Parts from Aluminum Alloys. PhD thesis, The Ohio State University.

Wächter, A.; Biegler, L.T., 2006. On the implementation of a primal dual interior point filter line search algorithm for large-scale nonlinear programming. Math. Prog., 106(1), pp. 25-57.

# Process Design for Electromagnetic Forming of Magnesium Alloy AZ31 Using FE Simulation

**E. Uhlmann, L. Prasol*, H. Roehrs**

Institute of Machine Tools and Factory Management, TU Berlin University, Germany
*Corresponding author. Email: prasol@iwf.tu-berlin.de

## Abstract

*Magnesium wrought alloys are outstanding lightweight materials due to their low density and high specific strength. The low formability of magnesium wrought alloy AZ31 at room temperature is increased by electromagnetic forming in comparison to quasi-static forming. For a detailed study of electro-magnetic process a coupled FE simulation must be performed. In this paper the process design for electromagnetic forming of magnesium wrought alloy AZ1 using FE simulation is presented.*

*The complexity of an electromagnetic forming process requires the illustration of magnetic, thermal and structural dynamic domains. Moreover, it is also necessary to illustrate the electromagnetic resonant circuit RLC. Short processing time and the strong dependence of the physical domains to each other requires a coupled FE simulation.*

*The illustration of resonant circuit and the resulting formation of magnetic field is carried out in two-dimensional rotationally symmetric model in ANSYS MAPDL using a suitable material model. As a result time-dependent and location-dependent eddy currents and Lorentz forces are estimated.*

*Subsequently, the transmission of the estimated Lorentz forces and joule heat generation rates to ANSYS LS-DYNA is done. Due to the rotational symmetry of 2D ANSYS MAPDL model a transformation of the loads on 3D structures can be realized. The formation of an optimum deformation of a work piece in dependence of a defined die has been carried out. Here, the influence of different coil designs, die materials and geometries and RLC parameters was investigated.*

## Keywords

Electromagnetic forming, FE simulation, Magnesium wrought alloy AZ31

# 1 Introduction

The idea of using the power of pulse magnetic fields was introduced in the year 1958 when the first patent for an application of electromagnetic advices was presented in the United States of America. Since 1990s interest on electromagnetic forming has been increasing due to rising demands on flexibility, efficiency and sustainability of industrial production processes and products (Hahn, 2004). Electromagnetic forming processes can contribute an important part to meet the requirements mentioned above as they provide advantages in comparison to conventional processes (Psyk et al., 2011):

- Forming process is realized without any mechanical contact of work piece surfaces,
- Scrap minimization is a result of very high process repeatability,
- Short process $t_p$ time enables high production rates and
- Electromagnetic forming processes can be realized without lubricants, whereby the environmental impact and sustainability increase.

It is also crucial that process conditions of electromagnetic forming modify mechanical behaviour of various materials. In particular, the formability of lightweight material magnesium alloy AZ31 is increased considerably by high strain rates (Ulacia et al, 2009; Ulacia et al., 2011, Feng et al., 2014, Uhlmann et al., 2014, Ahmad and Shu, 2015). These advantages are faced with a high process complexity due to numerous, interdependent factors. Without process simulation the interpretation of an electromagnetic forming process is dependent on time-intensive process design (Azab et al., 2003).

Process design of an electromagnetic forming process for a defined component is presented within this paper. Main aspects of this paper are

- Development of an appropriate simulation model,
- Design of manufacturing process for a complex component and
- Evaluation of electromagnetic forming process for a complex component made of magnesium alloy AZ31.

# 2 State Of Art

## 2.1 Electromagnetic Forming

Electromagnetic forming includes all production methods using the dynamic effect of a pulsed magnetic field directly for machining of a work piece (Neubauer et al., 1988). The duration of the magnetic pulse is only a few microseconds. The effect of the forming process occurs due to the inertia of the work piece with a time offset, but the energy conversion occurs abruptly. Therefore, electromagnetic forming is classified as method of high speed forming (Lange, 1993).

Electromagnetic forming is based on the physical effect of induction. The required energy for the forming process is stored in capacitors by charging them to a high voltage $U$. By discharging the capacitors over a high-current switch, the arising large currents $I(t)$ generate an intense magnetic field $H(t)$ outside the tool coil with the magnetic flux density $B = \mu H$. This magnetic field $H(t)$ induces eddy currents $I_{eddy}(t)$ in the work piece which are

running in the opposite direction compared to the primary currents $I(t)$ in the tool coil (Lange, 1993, Finkenstein, von, 1967).

Due to the short process time $t_p$ and high frequencies $f$ of the discharging process the induced eddy currents $I_{eddy}(t)$ are running near the surface of the sheet metal. It´s justified by the skin effect. Consequently, the resulting Lorentz forces $F_L(t)$ which depend on the primary magnetic field $H(t)$ are acting for a short time $t_p$ of 50 to 100 µs on the work piece. The acting Lorentz $F_L(t)$ forces are converted as a magnetic pressure on the work piece surface (Winkler, 1993).

## 2.2 Process Dependent Mechanical Behaviour of Magnesium Alloy AZ31

Material which is machined by electromagnetic forming is subjected with strain rates up to $10^4$ $s^{-1}$ and different mechanical stress states. Additionally, a local temperature increase is observed within the workpiece as a result of resistance heating and forming temperature due to the adiabatic character of the electro-magnetic process (Psyk et al., 2011). Within the framework of scientific studies the influence of different parameters at different loading conditions was investigated in detail (Ulacia et al., 2010, Ulacia et al., 2011, Feng et al., 2014, Ahmad and Shu, 2015, Kurukuri et al., 2015). In particular, the influence of strain rates in the range of $10^{-4}$ to $10^4$ $s^{-1}$ and work piece temperatures of 20 to 400°C at tensile and compression conditions were investigated. As a result the following statements with regard to the formability of Mg alloy AZ31 can be derived:

- Yield stress $Y_f$ increases with increasing strain rates, i.e. magnesium alloy AZ31 exhibits positive strain rate sensitivity (Ulacia et al., 2011, Feng et al., 2014, Ahmad and Shu 2015, Kurukuri et al., 2015). Strain rate sensitivity is more pronounced at tension (Ulacia et al, 2010, Ahmad and Shu, 2014, Kurukuri et al., 2015).
- Hardening of AZ 31 depends on strain rates (Ulacia et al., 2011, Ahmad and Shu, 2014, Kurukuri et al., 2015)
- Strain rate sensitivity is temperature-dependent (Ulacia et al., 2011)
- Magnesium alloy AZ31 is anisotropic and exhibits a tensile-compression-asymmetry at room temperature. With increasing strain rates tensile-compression-asymmetry increases (Ulacia et al., 2012).
- Perpendicular anisotropy increases with increasing strain rates (Ulacia et al., 2011), while mechanical behaviour of planar anisotropy at high stain rates is not conclusive answered. ULACIA ET AL. exhibit an increase of planar anisotropy (Ulacia et al., 2010) while ULACIA ET AL. also shows an decrease (Ulacia et al., 2011) or influence of planar anisotropy by high strain rates (Kurukuri et al., 2015).

The dependence of strain rates on the yield stress Yf can be described mathematically by a material model for thermo-viscoplastic behaviour. Cowper and Symonds (Cowper and Symonds, 1952), Perzyna (Perzyna, 1966), Johnson and Cook (Johnson and Cook, 1983) as well as Zerilli and Armstrong (Zerilli and Armstrong, 1985) suggest constitutive models for description of electromagnetic forming process assuming

isotropic hardening. The description of the tensile-compression-asymmetry can be realized using yield criterion of Cazacu (Cazacu et al., 2006).

## 2.3 Simulation of Electromagnetic Forming Process

The process behavior during electromagnetic forming can be described by electrodynamic, thermodynamic and continuum mechanical field equations using vector analysis (Azab et al, 2003, L´Eplattenier et al., 2008). The description of an electromagnetic forming process requires the mapping of a

- Circuit model (RLC resonant circuit),
- Electromagnetic model,
- Mechanical model and
- Optional thermal model.

The *circuit model* can be formulated by applying the 2nd KIRCHHOFF's law on the resulting equivalent circuit as an ordinary differential equation (Winkler, 1973). The *electromagnetic model* is based on the solution of the quasi-static approximation of MAXWELL's equations (L´Eplattenier, 2008). As a result of the electromagnetic model the estimated magnetic force density (Cao et al., 2015) is being transferred to the *mechanical model*. Here, the LORENTZ force $F_L(t)$ acts as a body force and is integrated in the mechanical model in the momentum balance. The solution of the thermal model is based on the conservation of energy. By estimating the JOULE heating rate in the electromagnetic model and additionally the forming temperature within the work piece both quantities are being used for the *thermal model.*

The solution of the resulting differential equations is done by FE method. In particular, it has to be taken into account in which way the respective models are being coupled. In general, there are different types of model domains, i.e. which domains are being coupled. Furthermore, the coupling strategy is also important. There are four model domains:

1. Reduced models (only mechanical model),
2. Basic models (electrodynamic model and mechanical model),
3. Extended models (electrodynamic model, mechanical model and thermal model or circuit model) and
4. Extensive models (circuit model, electrodynamic model, mechanical model and thermal model).

The models of the category two up to four can be coupled via different strategies (Pérez et al., 2009). A distinction is made between *loose* coupling (estimation of electrodynamic domain for a defined number of steps and transfer as boundary condition to mechanical domain), *sequential* coupling (bilateral exchange of load data and state variables after each time step with an update of the domains) and *direct* coupling (field variables of different domains are solved simultaneously in a combined system of equations). *Reduced models* use only the mechanical domain to calculate displacements (Imbert et al., 2005, Wang et al., 2006). *Basic models* with a coupling of electrodynamic and mechanical models are presented by (Oliveira, 2005, Correira et al., 2008, Unger et al.,

2008) with a *loose coupling* and by (Mamalis et al., 2006) with a *sequential coupling*. *Extended models* are presented by (Meriched et al., 2000, Xu et al., 2015). *Extensive models* are presented by (Bessonov and Golovashchenko, 2006; Ulacia et al., 2008, Doley and Kore, 2014, Cao et al., 2015). Most of the presented papers deal with the investigation of aluminum. Only (Ulacia et al., 2008; Doley and Kore, 2014; Xu et al., 2015) take investigations of AZ31 into account.

# 3 Approach

In the context of this paper the approach in the process design for an electromagnetic forming process is presented for complex work piece made of magnesium alloy AZ31 at room temperature, **Fig. 1**. The complexity of an electromagnetic process thus requires in the first step, the conceptual design of an appropriate simulation model using an appropriate material model. The process design for an electromagnetic forming process for complex work piece geometry by varying the parameters

- tool coil geometry,
- die material and
- die geometry

concerning system parameters – capacity $C$ and charging voltage $U$ – is the aim of the investigation. The process-related potential of the electromagnetic forming process with respect to work piece feasibility is shown. The evaluation of the permissible material strength in the areas with maximum stress is based on experimentally determined reference values.

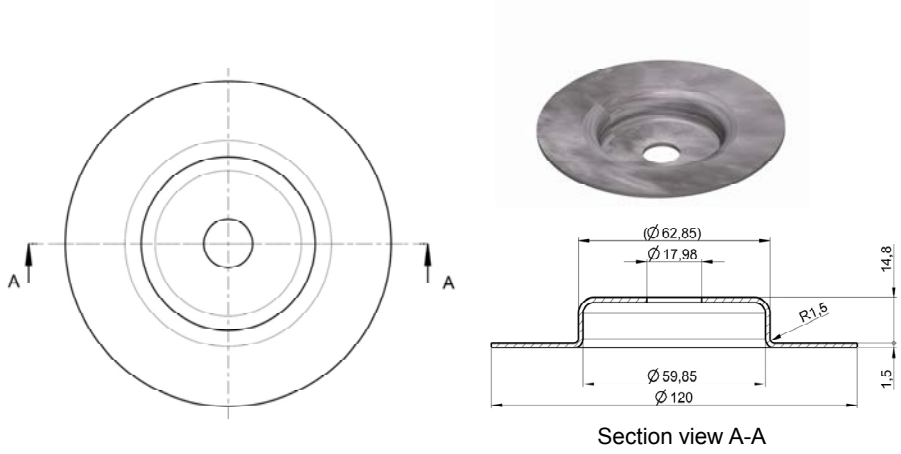


***Figure 1**: Anticipated work piece geometry*

# 4 Simulation Concept

The simulation concept shown in **Fig. 2** was used to combine an accurate estimation of LORENTZ forces and JOULE heat generation rates – *implicit 2D* model – as well as an accurate deformation and dynamic behaviour of the work piece while interacting with the

die during the forming process – *explicit 3D* model. The PERZYNA model has been implemented in the implicit 2D simulation – domain *simplified mechanics*. The required parameter for the PERZYNA model has been adapted to temperature and strain rate dependent flow curves.

Flow curves have been experimentally determined by the Bundesanstalt fuer Materialpruefung und -forschung (BAM), Berlin, Germany. In the context of explicit 3D simulation the Johnson-Cook model with experimentally determined characteristics has been used in the domain Complex Mechanics (Feng et al., 2014).

The choice of different materials models, which have a minimal discrepancy between the determined deformations, is justified by the ANSYS structure and validation results. ANSYS MAPDL granted only the use of PERZYNA model as a strain rate dependent model. As part of the material model validation it has been shown that the experimentally determined parameters up to 1000 $s^{-1}$ does not describe the material behaviour with sufficient accuracy. A rotationally symmetrical tool coil was used to validate the material model (Uhlmann and Prasol, 2013). Rather, the numerical results showed that strain rates up to 2500 $s^{-1}$ occur during electromagnetic forming process. In the literature comparable material data up to strain rates of 3000 $s^{-1}$ is presented by (Feng et al., 2015) for the JOHNSON-COOK model. Only ANSYS LS-DYNA granted the usage of JOHNSON-COOK model as a strain rate and temperature dependent material model.

A two-dimensional, rotationally symmetrical model is used in ANSYS MAPDL to determine the loads – Lorentz forces and Joule heating rates – within a forming process without a dominant die. A three-dimensional model in ANSYS LS-DYNA is used to simulate the deformation process within the die. Both models are coupled with a loose algorithm. Within the implicit 2D model the estimation of magnetic field H(t) and tool coil current I(t) is realized with a direct coupling of model blocks circuit and electromagnetic field. This results in the determination of parameters Lorentz force and Joule heating rate which are passed in each time step as boundary conditions to the model blocks simplified mechanics and simplified thermal field. The mesh morphing of the deformed work piece structure is performed simultaneously at each time step. Within implicit 2D model an accurate estimation of Lorentz forces is realized by estimation of inductance L in each time step. Due to the forming process a permanent change of inductance L occurs which has to be taken into account. Temperature dependence of material parameters is also taken into account.

In the explicit 3D model a transient structural mechanical simulation is done. Model block thermal field is directly coupled with model block complex mechanics which considers also Joule heating rates and deformation heating rates due to the adiabatic process. To enable this coupled thermal structural analysis defined keywords have to be add to LS-DYNA .k-file before solving.

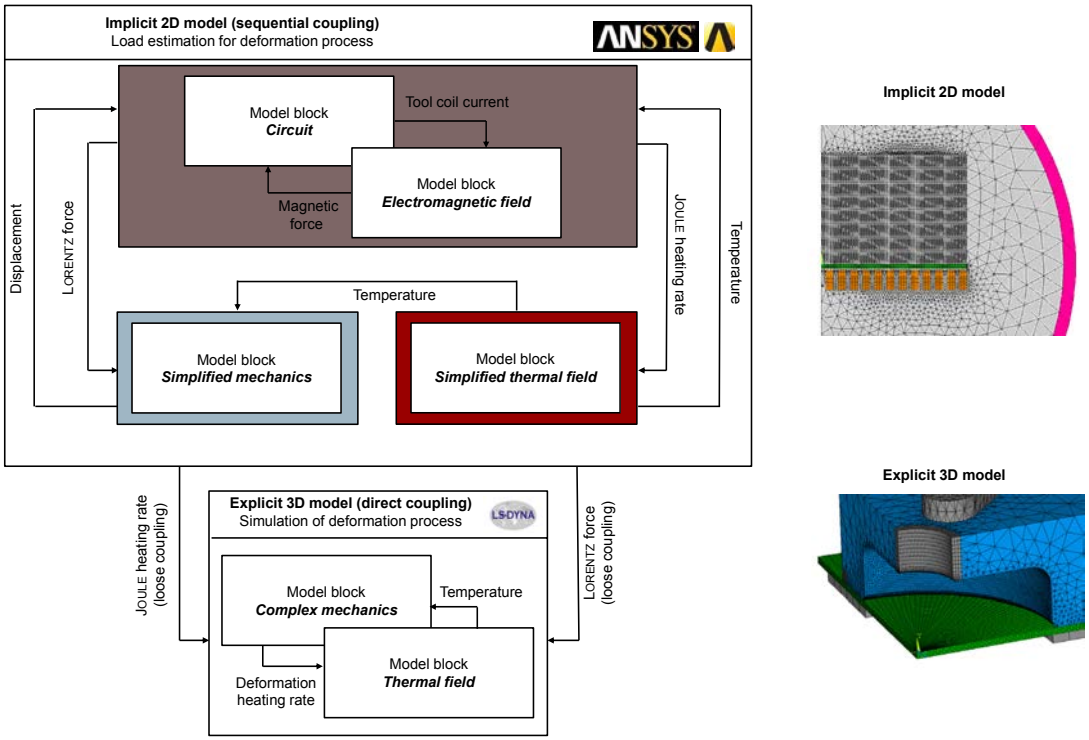


***Figure 2**: Schematic representation of the simulation concept*

# 5 Results

Following, the presented results are based on preliminary investigations. In advance the tool coil geometry, the die material and the blank holder force has been optimized. The adapted tool coil geometry is shown in **Fig. 3**.

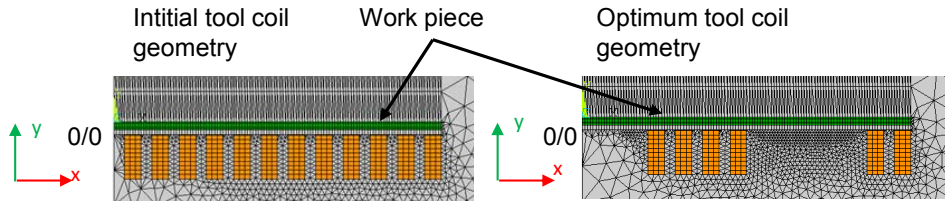


***Figure 3**: Optimum tool coil geometry*

Steel has been found to be optimum material due to its mechanical properties. Depending on the provided charging energy $E$ and the charging voltage $U$ arising optimum blank holder pressures has been identified. The blank holder pressures can be found in the following charts **Fig. 4** to **Fig 8**.

In dependence of the die height $h$ it is possible to realize a work piece contour which aims the contour of the work piece shown in **Fig. 1**. The percentage values given in **Fig. 4** and **Fig. 8** describe the degree of die filling, estimated as the ratio of the numerical integrals of the curves for actual and desired contour (**Fig. 1**) in the portion between $r$ = 8.99 mm and $r$ = 35 mm. Basically, a decrease of the die height causes an increase in the desired work piece geometry.

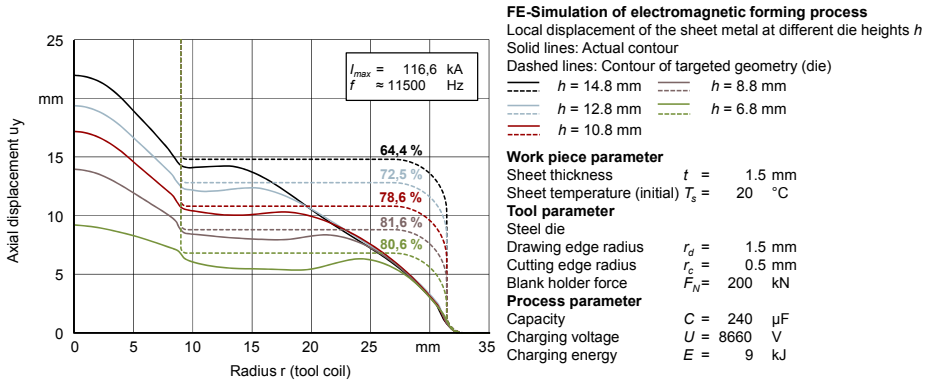


***Figure 4**: Displacement $u_y$ for different die heights h (simulation time = 300 µs)*

The principle strain $\varphi_1$ limits the maximum material stress in the plane strain condition. Due to instability of the membrane this condition is located in the region of the drawing edge $r_d$ and the cutting edge $r_c$. The dependence of $r_d$ is shown in **Fig. 5**. The cutting edge $r_c$ *i*s constant $r_c = 0.5$ mm. Increasing drawing edge $r_d$ causes a decrease in the principal strain. Due to this an increasing material stability in this area is expected. The cutting edge $r_c = 0.5$ mm causes material failure due to the high principle strain. In general instability of membrane causes material failure during electromagnetic processes (Uhlmann and Scholz, 2003).

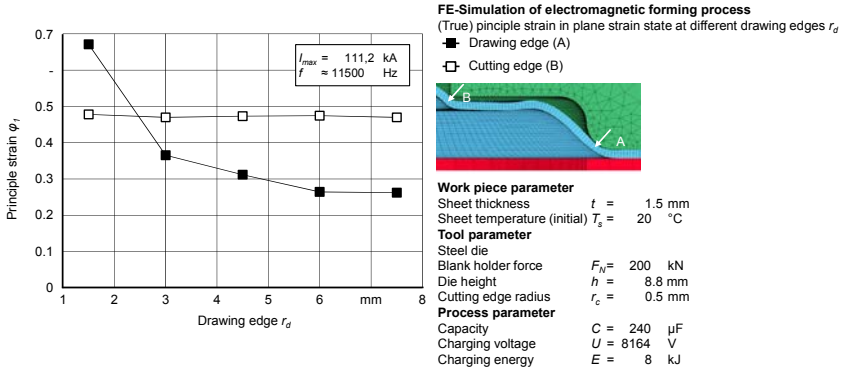


***Figure 5**: Principle strain $\varphi_1$ in dependence of drawing edge $r_d$ ($r_c$ ist constant)*

**Fig. 6** shows the secure (true) principle strains $\varphi_1$ measured by electromagnetic forming. For the investigations the experimental setup presented by (Uhlmann and Prasol, 2014) has been used. Due to the uniform force effect on the forming area and instability of membrane (drawing edge, cutting edge) the influence of electromagnetic forming on the maximum allowable principle strains in the material can be investigated.

The comparison of the numerically determined (true) principle strains $\varphi_1$ in the area of the drawing edge radius $r_d$ (**Fig. 5**) with the experimentally determined (true) principle strains $\varphi_1$ (**Fig. 6**) shows an exceed of permissible (true) principle strains $\varphi_1$ at the determined current values $I_{max}(t)$.

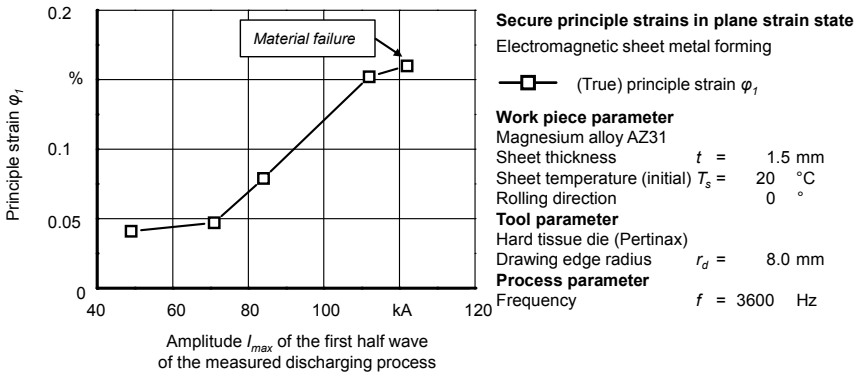


***Figure 6**: Experimentally measured principle strain $\varphi_1$*

To decrease the principle strain $\varphi_1$ at the drawing edge $r_d$ it is necessary to decrease the charging energy $E$. The influence of charging energy $E$ or the tool coil current $I_{max}(t)$ is shown in **Fig. 7**. Charging energy $E$ = 6 kJ leads to (true) principle strain $\varphi_1$ = 0.15. There is no material failure expected at the drawing edge. Maximum (true) principle strain $\varphi_1$ at the cutting edge $r_c$ is $\varphi_1$ = 0.28 which leads to material failure.

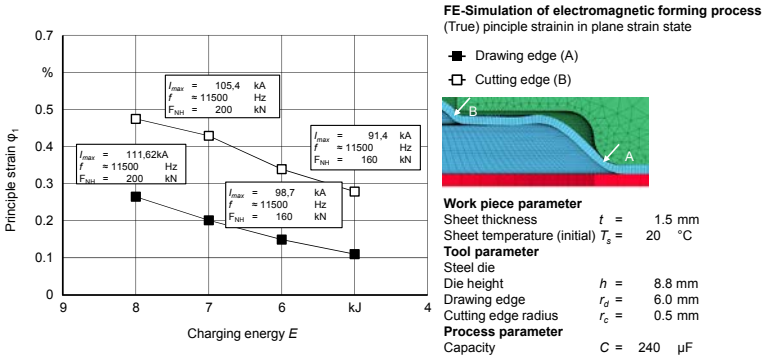


***Figure 7**: Principle strain $\varphi_1$ in dependence of charging energy E or tool coil current I(t)*

The corresponding work piece deformations are shown in **Fig. 8**. The forming process with charging energy $E$ = 6 kJ achieves a die filling of 78.7 % with die height $h$ = 8.8 mm. The deviation from the targeted drawing edge $r_d$ = 1.5 mm at $r_d$ = 6 mm is about 75%. The deviation from the targeted work piece height $h_w$ = 14.8 mm to realizable heights $h$ = 8.8 mm is approximately 41%.

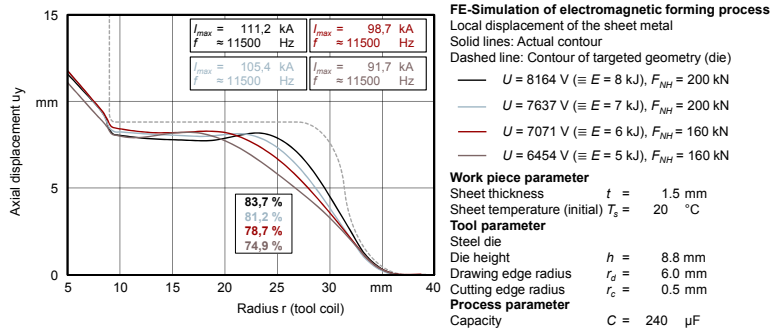


***Figure 8**: Displacement uy for different charging energies E while drawing edge rd = 6 mm (simulation time = 300 µs)*

# 6 Conclusion

In the context of this paper, the process design using FE simulation for production of complex three-dimensional work piece geometry made of magnesium alloy AZ31 by electro-forming forming at room temperature was presented. For this purpose, in the first step a suitable simulation concept was developed. Within the framework of simulation an adjusted tool coil geometry as well as an adjusted blank holder has been identified. Depending on the charging energy defined blank holder forces has been determined.

By varying the die height $h$, the drawing edge radius $r_d$ and the cutting radius $r_c$ a suitable work piece geometry was identified without material failure. Die filling of 78.7 % was achieved. The deviation of the targeted work piece height $h_w$ in relation to initial geometry is 41 %. The deviation of the targeted drawing edge $r_d$ in relation to initial drawing edge $r_d$ is 75 %

# Acknowledgement

The authors would like to thank the Arbeitsgemeinschaft industrieller Forschungsvereinigungen – AiF – (Federation of Industrial Research Associations) for funding this research within the project 18443 N1 .

# References

El-Azab, A., Garnich, M., Kapoor, A., 2003. Modeling of the electromagnetic forming of sheet metals: state-of-the-art and future needs. Journal of Materials Processing Technology 142, pp. 744-754.

Ahmad, I. R.; Shu, D. W., 2015: Experimental and Constitutive Study of Tensile Behavior of AZ31B Wrought Magnesium Alloy. Journal of Engineering Mechanics 141 (3), pp. 04014124.

Bessonov, N., Golovashchenko, S., 2004. Numerical Simulation of Pulsed Electro-magnetic Stamping Process. In: Kleiner, M. (Eds.), High Speed Forming 2004, Proceedings of the 1st International Conference, Dortmund, Germany.

Cao, Q., Han, X., Lai, Z., Xiong, Q., Zhang, X., Chen, Q., Xiao, H., Li, L., 2015. Analysis and reduction of coil temperature rise in electromagnetic forming. Journal of Materials Processing Technology 225, pp. 185-194.

Cazacu, O; Plunkett, B.; Barlat, F., 2006. Orthotropic yield criterion for hexagonal closed packed metals. International Journal of Plasticity 22 (7), pp. 1171-1194.

Correia, J. P. M., Siddiqui, M. A., Ahzi, S., Belouettar, S., Davies, R., 2008. A simple model to simulate electromagnetic sheet free bulging process. International Journal of Mechanical Science 50, pp. 1466-1475.

Cowper, G. R., Symonds, P. S., 1952. Strain-hardening and strain-rate effects in the impact loading of cantilever beams. Providence, Rhode Island, USA, Brown University, Devision of Applied Mechanics, Technical Report No. 28.

Doley, J. K.; Kore, S. D., 2014. FEM Study on Electromagnetic Formability of AZ31B Magnesium alloy. Huh, H.; Tekkaya (Eds.), Proceedings of the 6th International Conference, (ICHSF), Daejon, Korea, 2014, pp. 273-280.

L'Eplattenier, P., Cook, G., Ashcraft, C., 2008. Introduction of an Electromagnetism Module in LS-DYNA for Coupled Mechanical Thermal Electromagnetic Simulations. Kleiner, M., Tekkaya, A.E. (Eds.), Proceedings of the 3rd International Conference (ICHSF), Dortmund, Germany, pp. 85-96.

Feng, F., Huang, S., Meng, Z., Hu, J., Lei, Y., Zhou, M., Wu, D., Yang, Z., 2014. Experimental study on tensile property of AZ31B magnesium alloy at different high strain rates and temperatures. Materials and Design 57, pp. 10-29.

Finckenstein, E. v., 1967. Ein Beitrag zur Hochgeschwindigkeitsumformung rohrförmiger Werkstücke durch magnetische Kräfte. Dissertation, Universität Hannover.

Hahn, R., 2004. Werkzeuge zum impulsmagnetischen Warmfügen von Profilen aus Aluminium- und Magnesiumlegierungen. In: Berichte aus dem Produktionstechnischen Zentrum Berlin, Hrsg.: Uhlmann, Dissertation, Technische Universität Berlin, Stuttgart: Fraunhofer IRB.

Imbert, J. M., Winkler, S. L., Worswick, M. J., Oliveira, D. A., Golovashchenko, S., 2005. The Effect of Tool-Sheet Interaction on Damage Evolution in Electromagnetic Forming of Aluminium Alloy Sheet. Journal of Engineering Materials and Technology 127, pp. 145-153.

Johnson, G. R., Cook, W. H., 1983. A constitutive model and data for metals subjected to large strain, high strain rates and high temperatures. Proceedings of the 7th International Symposium on Balistics, Vol. 21, Den Haag, The Netherlands.

Kurukuri, S., Worswick, M. J., Ghaffari Tari, D., Mishra, R. K., Carter, J. T., 2015. Rate sensitivity and tension - compression asymmetry in AZ31B magnesium alloy sheet. Philosphical Transactions of the Royal Society 327, p. 20130216.

Lange, K., 1993. Umformtechnik, Band 4, Sonderverfahren, Prozeßsimulation, Werkzeugtechnik, Produktion. Heidelberg, New York, London: Springer.

Mamalis, A. G., Manolakos, D. E., Kladas, A. G., Koumoutsos, A. K., 2006. Electromagnetic Forming Tools and Processing Conditions: Numerical Simulation. Materials and Manufacturing Processes 21, pp. 411-423.

Meriched, A., Féliachi, M., Mohellebi, H., 2000. Electromagnetic Forming of Thin Metal Sheets. IEEE Transactions on Magnetics 36 (4), pp. 1808-1811.

Neubauer, A., Strope, H., Wolf, H., 1988. Hochgeschwindigkeitstechnologie der Metallbearbeitung. In: Berlin: VEB Verlag Technik.

Oliveira, D. A., 2005. Electromagnetic forming of aluminium alloy sheet: Free-form and cavity fill experiments and model. Journal of Materials Processing Technology 170, pp. 350-362.

Pérez, I., Aranguren, I., Gonzáles, B., Eguia, I., 2009. A new coupling method. International Journal of Material Forming 2 , pp. 637-640.

Perzyna, P., 1966. Fundamental Problems in Viscoplasticity. Advances in Applied Mechanics 9, pp. 243-377.

Psyk, V., Risch, D., Kinsey, B.L., Tekkaya, A.E., Kleiner, M., 2011. Electromagnetic forming – A review. Journal of Materials Processing Technology 211 (5).

Ulacia, I., Imbert, J., Salisbury, C.P., Arroyo, A., Hurtado, I., Worswick, M.J., 2008. Electromagnetic Forming of AZ31B Magnesium Alloy Sheet: Experimental Work and Numerical Simulation. Kleiner, M.; Tekkaya, A. E. (Eds.), Proceedings of the 3rd International Conference (ICHSF), Dortmund, Germany, pp.191-200.

Ulacia, I., Hurtado, I., Imbert, J., Salisbury, C.P., Worswick, M.J., Arroyo, A., 2009. Experimental and Numerical Study of Electromagnetic Forming of AZ31B Magnesium Alloy Sheet. Steel Research International 80 (5), pp. 344-350.

Ulacia, I., Dudamell, N.V., Gálvez, F., Yi, S., Pérez-Prado, M. T., Hurtado, I., 2010. Mechnical behavior and microstructural evolution of a Mg AZ31 sheet at dynamic strain rates. Acta Materialia 58, pp. 2988-2998.

Ulacia, I., Salisbury, C.P., Hurtado, I., Worswick, M.J., Arroyo, A., 2011. Tensile characterization and constitutive modeling of AZ31B mangesium alloy sheet oder a wide range of strain rates and temperatures. Journal of Materials Processing Technology 211, pp. 830-839.

Ulacia, I., Yi, S., Pérez-Prado, M., Dudamell, N., Gálvez, D., Letzig, D., Hurtado, I., 2012. Texture Evolution of AZ31 Magnesium Alloy Sheet at High Strain Rates. Materials Science Forum, pp. 706-709.

Uhlmann, E., Scholz, M, 2003. Zerteilen von Aluminiumblechen durch Impulsmagnetfelder. Tagungsberichtsband zum „2. Kolloquium Elektromagnetische Umformung“, Kleiner, M. (Ed.), Dortmund, Germany.

Uhlmann, E., Prasol, L., 2013. Holistic approach to pulse magnetic forming of magnesium alloy AZ31 at low forming temperatures. Archenti, A., Maffei, A. (Eds.), Proceedings of the NEWTECH, Volume 2, Stockholm, Sweden, pp. 9-24.

Uhlmann, E., Prasol, L., Kawalla, R., Schmidt, C., Becker, T., 2014: Extension of formability of the magnesium wrought alloy AZ31B-O at room temperature by pulse magnetic forming. Huh, H.; Tekkaya (Eds.), Proceedings of the 6th International Conference (ICHSF), Daejon, Korea, pp. 21-30.

Unger, J., Stiemer, M., Schwarze, M, Svendsen, B., Blum, H., Reese, S., 2008. Strategies for 3D simulation of electromagnetic forming process. Journal of Materials Processing Technology 199, pp. 341-362.

Wang, L., Chen, Z. Y., Li, C. X., Huang, S. Y., 2006. Numerical simulation of the electromagnetic sheet metal bulging process. International Journal of Advanced Manufacturing Technology 30, pp. 395-400.

Winkler, R., 1973. Hochgeschwindigkeitsbearbeitung – Grundlagen und technische Anwendungen elektrisch erzeugter Schockwellen und Impulsmagnetfelder. VEG Verlag Technik Berlin.

Zerilli, F. J.; Armstrong, R. W., 1985. Constitutive Equation for HCP Metals and High Strength Alloy Steels. ASME Publications 48, pp. 121-126.

Xu, J. R., Cui, J. J., Lin, Q., Li, Y., Li C. F., 2015. Magnetic pulse forming of AZ31 magnesium alloy shell by uniform pressure coil at room temperature. International Journal of Advanced Manufacturing Technology 77 (1-4), pp. 289-304.

# Innovative Processes

# Combined Working Media-Based Forming on a Pneumo-Mechanical High Speed Forming Machine

**E. Djakow*, W. Homberg, D. Tabakajew**

Chair of Forming and Machining Technology, Faculty of Mechanical Engineering, Warburger Straße 100, 33098 Paderborn, Germany
*Corresponding author. Email: ed@luf.uni-paderborn.de, Tel.: +49 5251/605347

## Abstract

*Quasi-static working media-based forming processes (WMF) permit the production of complex sheet metal parts with relatively little expense. The associated need for very high pressures and hence complex tools and machines for the production of fine geometrical details is often problematic. The use of high speed forming processes (HSF) can offer many benefits, including a reduced financial outlay on equipment and better part properties in this case. But these processes also have disadvantages, of course, such as if they are used for the production of complex large-surface parts. Consequently, a combination of both approaches would be ideal. This paper describes a new approach to combining high pressure sheet metal forming (HPF) and pneumo-mechanical HSF for the production of complex sheet metal parts.*

## Keywords

Pneumomechanical high speed forming, Working media-based process, Hydroforming

## 1 Working Media-based Forming Process

The working media-based forming processes (WMBP) are considered to be processes with a high innovation potential and are frequently used for the production of complex, multifunctional components in a large number of industrial fields. The WMBP include all processes in which a working medium (fluid) or a flexible non-compressible material is used in the processing of metallic semi-finished parts The fluid – mostly an oil in water emulsion – “transfers” the pressure to the semi-finished part, either directly or indirectly, and thus leads to the uniform forming. The pressure effect can be achieved through

either internal or external working media sources, on a quasi-static or dynamic basis (Homberg, 2001 and Lange, 1993). The most important representatives of these technologies with their typical process characteristic are presented in Figure 1. The WMBP can essentially be divided into two groups with respect to the forming velocity:

- **Quasi-static working media-based forming process**
- **Dynamic working media-based forming process**

**Classification of working media based forming process**

| Forming velocity | Quasi-static | | | | | | | | | Dynamic | | | | | | | | | | | | |
|---|---|---|---|---|---|---|---|---|---|---|---|---|---|---|---|---|---|---|---|---|---|---|
| Working media | Flexible tools or working medium | | | | Working medium | | | | Accelerated rigid masses | Working medium with | | | | | | | | Working energy | | | | |
| | | | | | | | | | | Force associated effect | | | | Energy associated effect | | | | | | | | |
| Semi-finished part | Blank | | Tube | | Blank | | Tube | | Blank | Blank | | Tube | | Blank | | Tube | | Blank | | Tube | | |
| Working media contact directly=D indirekctly = I | D | I | D | I | D | I | D | I | D | D | I | D | I | D | I | D | I | D | I | I | | |
| Process examples | HYDROMEC | Guerin Rubber Pad Forming | Variform | Tube expanding with water bag | High pressure sheet metal forming (HBF) | Verson Hydroforming | Tube Hydroforming | Hydroforming with membran | Petro-Forge Machins DYNAPAC | Hydropunch Mazukin | Hydropunch Chachin | Hydropunch Tominaga | Hydropunch with membran | Electrohydraulical Fomring (EHF) | | EHF with Membran | | Explosive forming | | Explosive forming EHF with mebran | Electromagnetic forming with plunger | | EMF | EMF |
| Energy transmission media | Fluids, sand, rubber | | | | Fluids | | | | Rigid body | Fluids, sand, rubber | | | | Fluids, sand, rubber | | | | Air | | | | |
| Pressure generation | Tool movement | | | | Pressure intensifier | | | | Mass movement | Plunger movement | | | | Electrical discharge explosion | | | | Magnetic fields | | | | |
| Pressure duration | t > 10s | | | | t> 10 s | | | | 10e-3<t<10e-1s | 10e-4<t<10e-3s | | | | t<10e-5s | | | | t<10-5s | | | | |
| Maximal pressure | $p_{max}$<100MPa | | | | $p_{max}$<600MPa | | | | $p_{max}$<1000MPa | $p_{max}$<300MPa | | | | $p_{max}$<10.000MPa | | | | $p_{max}$<500MPa | | | | |

**Characteristic of working media based forming process**

***Figure 1**: Classification and characterization of working media-based forming processes (based on the work of Homberg, Beerwald, Lange and Mamutov)*

The use of working media-based forming processes (Fig.1) generally has numerous technical and economic advantages but also certain disadvantages. So the idea of combining several processes in order to create a new process is only logical. That is the way in which certain research work related to this topic was performed in the past (Mamutov, 2001).

One promising process chain, i.e. the combination of quasi-static/classic deep-drawing, has thus already been tested with electromagnetic high-speed forming in the PAK 343 and EMF-G3RD projects (Psyk, 2007 and Demir, 2014). The results of the projects have shown, on the one hand, that the existing forming limits of aluminum alloys and steel can be effectively extended by the correct sequence of forming processes. Additionally, in work by

Golovashchenko, a further promising approach is shown, improving the precision and complexity of components by combining the classical deep drawing process with an electrohydraulic high speed forming process, for more details see (Golovashchenko, 2011). This same combination method is also described in the work of Mamutov, where the so called pre-forming of the semi-finished parts is performed by deep drawing with a flexible working medium such as polyurethane. In this case, the calibration is performed by means of an electromagnetic forming process (Mamutov, 2001). Based on the research work conducted and the existing process characteristics of the WMF, it can be stated that, in the known variants, the combination partners differ significantly in terms of pressure generation, transmission and duration, as well as in terms of the process characteristics. There are only a few combinations where the same working medium and the same forming machine is used for the combined forming process. This paper thus presents a possible approach to combined working media-based forming processes where the advantages of quasi-static high pressure sheet metal forming and pneumo-mechanical high speed forming are combined on one and the same high speed forming machine (the so called Hydropunch machine), see Figure 2.

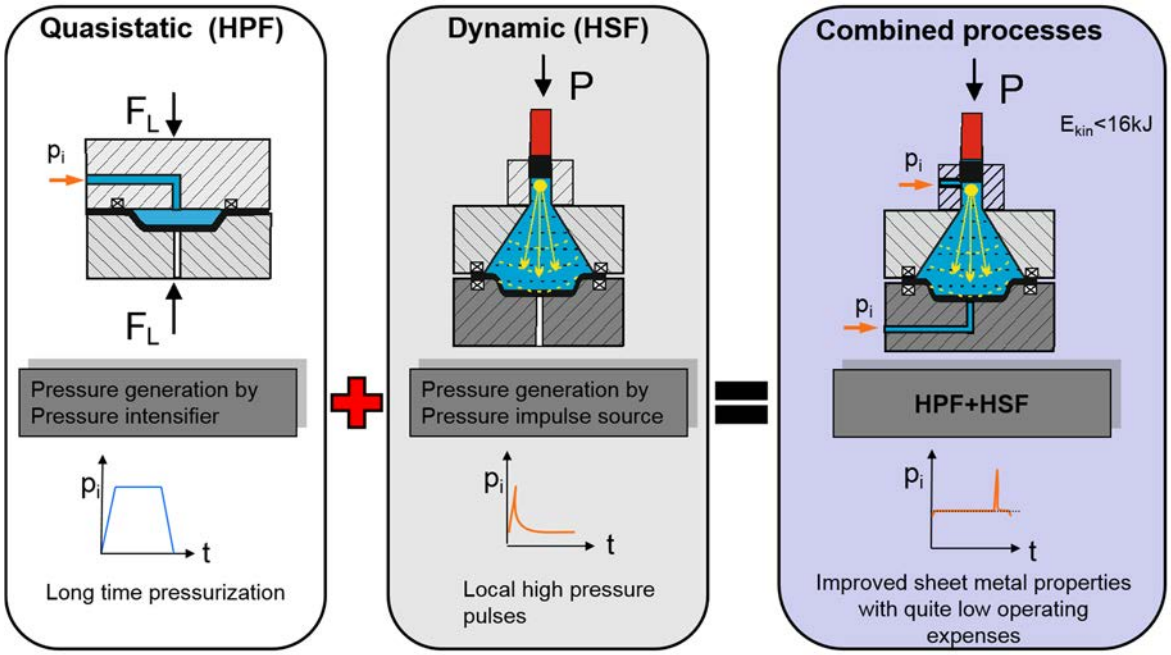


***Figure 2**: Concept for a combined working media forming process*

## 2 Potential Process Routes on the Combined Hydropunch Machine

The combination of quasi-static (pre)forming with high-speed forming processes like pneumo-mechanical HSF inside a single machine opens up new possibilities for process design. Hence it is possible to influence the strain distribution and preform geometry of the part in such a way as to positively affect the course and result of a subsequent high speed

forming step. In this work, two different process strategies for combining quasi-static and dynamic forming process are presented, see Figure 3.

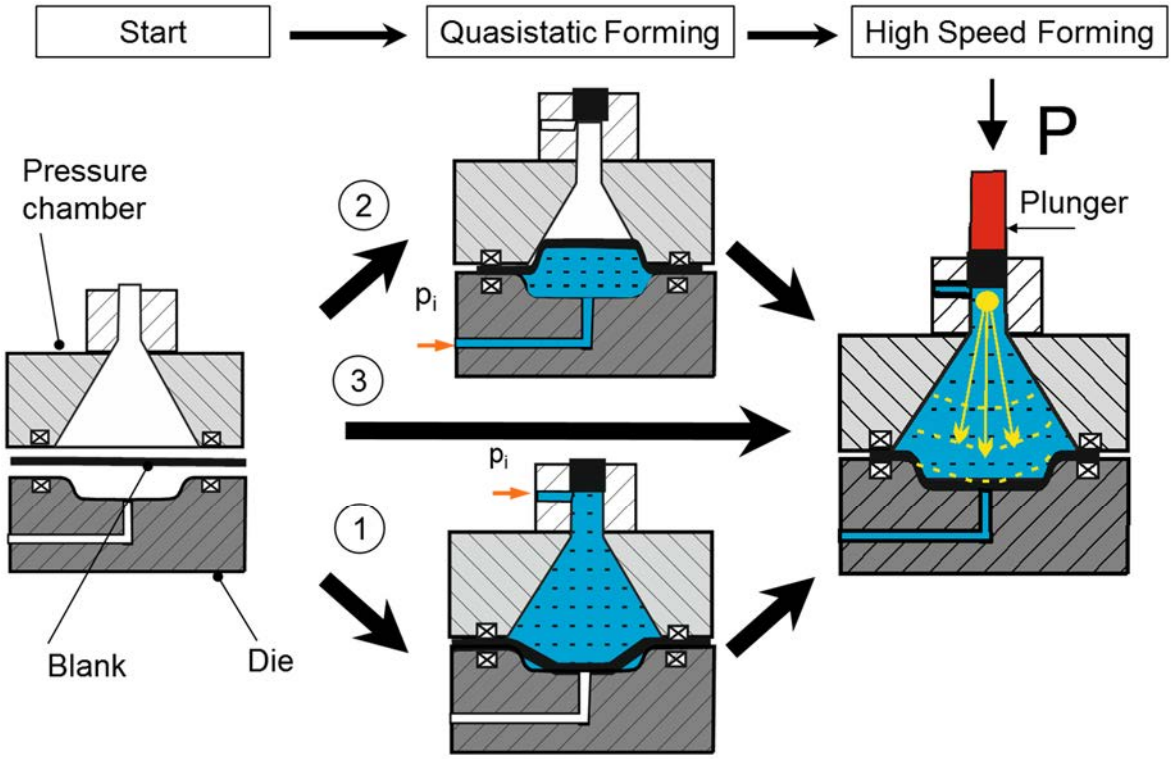


***Figure 3**: Sequence of positive and negative preforming and dynamic calibration*

The first strategy (1) is characterized by preforming the semi-finished part quasi-statically in the positive forming direction (towards the forming die). The subsequent dynamic forming step is then used to calibrate the part. The deformation zone is quite small and is limited to the areas without contact between the sheet and die.

The second strategy (2) also employs quasi-static preforming. In contrast to this, the preforming takes place in the negative forming direction (towards the conical pressure chamber). The main aim of the negative preforming with the help of reverse drawing is to achieve a preform inline which permits the desired geometry to be obtained without thinning. This strategy permits the extension of the existing forming limits.

Other possible process strategies consist of a combination of the two variants described above. Here, the quasi-static or dynamic processes can be used either independently (3) or together on the same Hydropunch machine.

# 3 Numerical Model of Combined Working Media-based Forming

In order to determine the effect of the different quasi-static preforming operations on the course and result of pneumo-mechanical HSF, intensive experimental and theoretical

research work was performed at the Chair of Forming and Machining Technology (LUF). One focus of this research work is achieving a reliable simulation of the process combination.

Furthermore, the forming of a workpiece with combined hydrostatic and hydrodynamic forming processes is influenced by a large number of parameters, including the locally acting pressure, the working media, the type of pressure chamber and the plunger geometry. In order to understand these process phenomena, to determine the interaction between key process parameters, and also to support/optimize the development of the new combined machine, use was made of FEA based on a coupled Euler Lagrange model (CEL). Here, both quasi-static and dynamic processes are represented in a single model. The modelling was carried out using the Finite Element Method and the explicit calculation type in Abaqus 6.14. The finite element mesh in the CEL model is represented by a stationary cube in which Euler and Lagrange elements move and interact with each other, see Figure 4. Here, the EC3D8R elements make it possible to model the Euler problems which are completely or partially filled with the working medium or material. The unfilled areas of the grids are automatically designated with the void material model. The volume fraction is recalculated in each iteration step and fed to the next calculation step, for more details see (Abaqus, 2014 and Smojver, 2010).

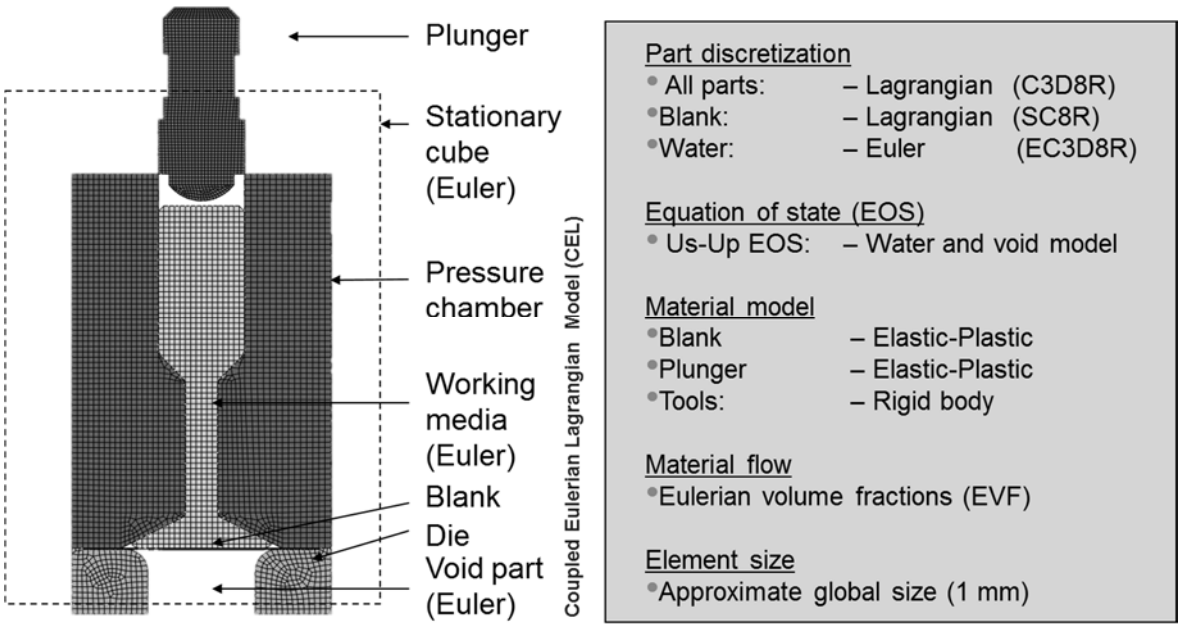


***Figure 4**: Numerical model of combined working media-based forming process*

In the first approach, the Us-Up equations of states were used to model the water movement, where the properties for the Us-Up EOS for water have been taken from (Vovk, 2008). These equations describe the working pressure states within a working medium as a function of the incompressibility, density and viscosity of the working medium. Furthermore, for modelling the preforming and forming operations of the semi-finished sheet metal parts, use was made of a simplified material model by Johnson Cook. The

necessary Johnson Cook coefficients, the static and dynamic material density and also the Gruneisen coefficient were taken from (Vovk, 2007 and Zaizew, 2013). This material model makes it possible to determine material hardening during the quasi-static forming process as well as the plastic effects during dynamic forming. Due to the low forming speed during the quasi-static and pneumo-mechanical high speed forming processes, both the thermal effects in the material and the cavitation on the surface of the semi-finished part are neglected. These are also being examined in ongoing work at the LUF.

The CEL model that was developed was used for a detailed analysis of the influence and interaction of the process parameters with the pressure and distribution during pneumo-mechanical high speed forming or calibration processes and was conducted in addition to the experimental investigations into the influencing parameters and the work on drawing up the concept for the new machine and process design. Initially, the pneumo-mechanical forming process was examined numerically with regard to the influence of the plunger and pressure chamber geometry on the pressure effect and the pressure distribution. In order to validate and calibrate the simulation results and to determine the pressure distribution and effect, use was made of a phenomenological approach (Homberg, 2012). This approach is based on the determination of the resulting local spherical dent and radius R in a multiply-bulged sheet metal part. The radius height of the dent is a (local) indicator of the acting pressure. According to the Laplace formulation for spherical elements, the acting pressure can be calculated using the following equation:

$$P = \frac{2\,\sigma\,t}{R} \tag{1}$$

With $\sigma$ = tensile strength, t=thickness of the semi-finished part, R= radius of the spherical dent, see also Fig. 5.

# 4 Influence of Plunger Geometry Through Contact with Working Media

Due to the fact that the required pressure pulse with PMF is generated through the plunger dipping into the water-filled pressure chamber, it is obvious that the contact geometry of the plunger and the chamber geometry will influence the course and result of pneumo-mechanical forming processes. For this reason, dulled and staged plunger geometries were used during the investigation into the influence on the pressure effect and the pressure distribution. Analyzing the results of appropriate experimental and simulation-oriented research work, it can be seen that, while maintaining the same plunger impact velocity and process parameters, a dulled plunger geometry leads to a higher pressure and higher sheet deformation in the center of the blank than staged geometries, see Fig. 5. Analyzing the forming height distribution of the deformed parts during the experimental validation, it can be seen that the absolute and simulated pressure levels in the working area tally well in qualitative terms. Depending on the plunger geometry, the modeling process shows pressures approximately 12% to 18% higher in the center of the workpiece than the

analytical pressure calculation in accordance with the Laplace formulation. Based on the present experimental and analytical results, it can be stated that the dulled plunger geometry leads to higher pressure effects under the same impact velocity. The staged and dulled geometries have no influence, or only a minor influence, on the pressure distribution and the impulse duration. The radial deviation of the forming height is thus less than 5 %.

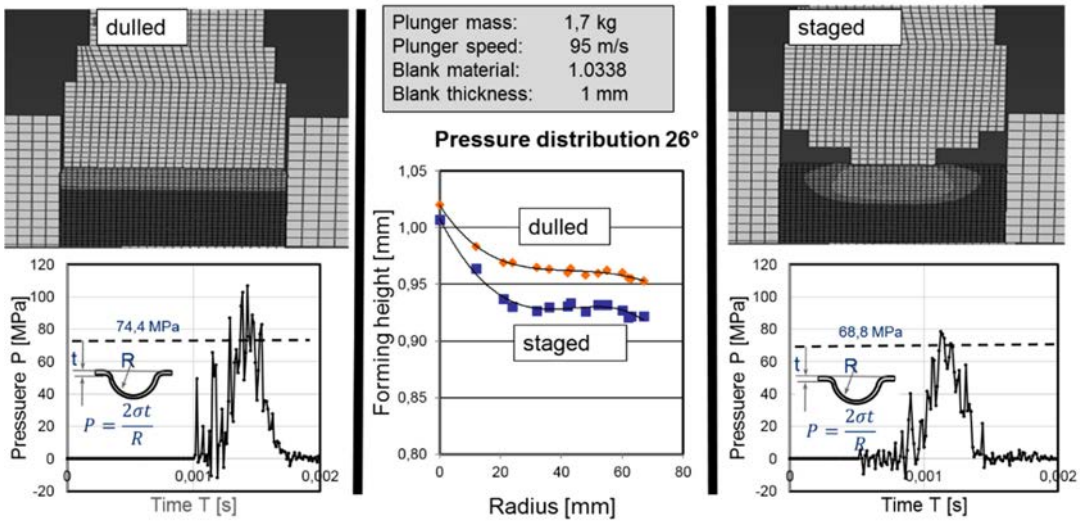


***Figure 5**: Influence of two different plunger top geometries of pressure pulse*

Taking into account the knowledge that shock waves are strongly influenced in their propagation behaviour by the surrounding compartment, it is necessary to examine this effect during PMF. Fig. 5 shows the result of a corresponding FEA investigation by way of an example. It can be seen that decreasing the pressure chamber angle leads to a decrease in the pressurized zone. Increasing the angle from 45° to 65° leads to a homogeneous pressure distribution in the radial direction on the part surface. But, increasing the angle to above 45 ° reduces the dent height or pressure by up to 20 %.

Furthermore, the experimental investigation of the forming height or the pressure distribution reveals the same trend as in the simulation. Here the results show that, with a pressure chamber angle of 26°, the highest pressures are clearly reached in the center of the workpiece up to a radius of 20 mm. Then, the forming height or pressure remains lower and constant with the result in a decreased forming height. The percentage deviation of the forming height between the inhomogeneous and homogeneous area is around 5%. A further increase in the impact velocity of the plunger up to 110m/s leads to a more inhomogeneous pressure distribution, which can be seen from the inhomogeneous sheet forming. Here, the highest pressures are also reached in the center and up to a radius of 20 mm. So it can be stated that, as a function of the pressure chamber angle, there is a definite limit at which the inhomogeneous pressure effect stagnates. The investigation of these limits and the optimization of significant process parameters is the subject of ongoing research work.

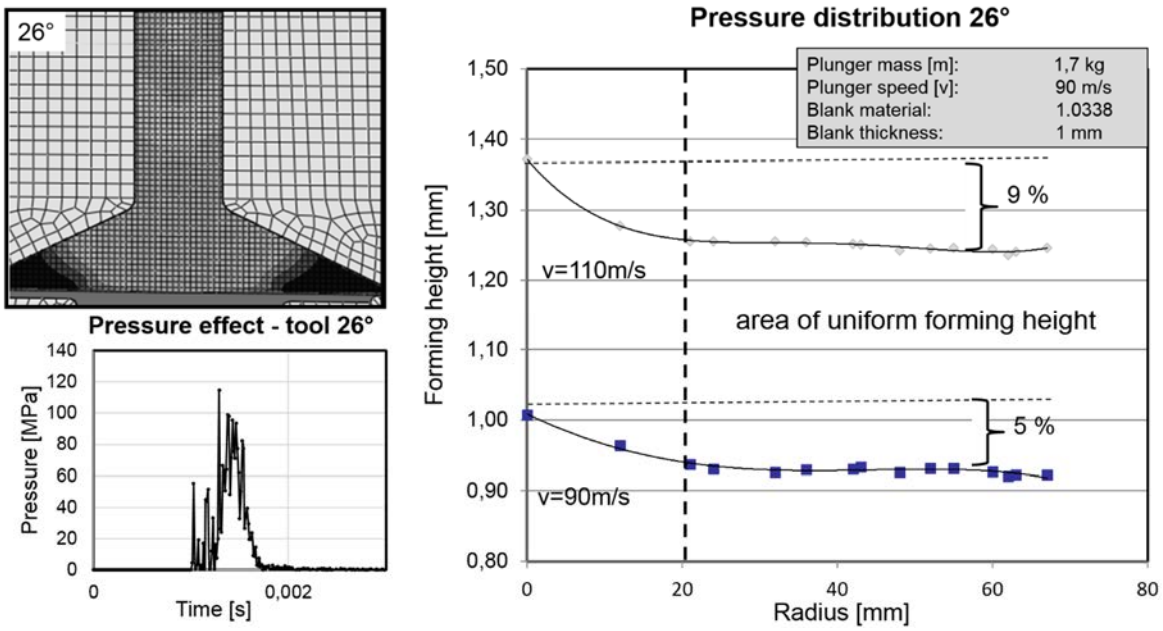


***Figure 6**: Influence of the pressure chamber geometry pressure effect and distribution*

# 5 Setup of the new Combined Hydropunch Machine

To validate the theoretical results, and enable a detailed experimental investigation of the process combination, it is necessary to have a special experimental setup. For this reason, a new experimental machine was built, based on both the described results of the simulations performed and the experimental and theoretical research work carried out at the LUF. Here, high-pressure sheet metal forming and the pneumo-mechanical high speed forming process (Hydropunch) were selected as procedural representatives for the combined forming process. The following requirements have to be taken into account on the new machine:

- the combined machine has to allow different process sequences of positive preforming (form fill) and negative preforming operations (reverse drawing) as well as dynamic calibration;
- the sequential forming has to take place in the same tool, with the same clamping device
- the new pneumo-mechanical machine has to permit sequential and separate application of the quasi-static and dynamic sheet metal forming processes; and
- the same sealing principle for the pressure chamber has to be used for quasi-static and dynamic processes;

Figure 7 shows the setup of the combined pneumo-mechanical high speed forming machine (CPMF) with a tool unit for symmetrical and non-symmetrical sheet metal forming. Based on the fundamental principles of pneumo-mechanical high speed forming machines from Mazukin J.G. (1961), Tominaga H. (1967), Chachin B. A. (1972), Zuravskij J.A. (1994), Bragin A.P. (1995), and Kosing OE (1997), Frolov E. A (2008), Vovk A. (2004), the new CPMF machine consists of two pressure generation units (hydraulic and pneumatic),

a vertically arranged acceleration tube and a two-part forming tool. The forming tool consists of a conical pressure chamber and a die with the base plates. By comparison to spherical or rectangular pressure chamber shapes, the conical chamber shape makes for a more homogeneous pressure distribution on the part surface during the forming processes (Vovk 2008). In contrast to other hydroforming and PMF machines, no expensive presses are used for locking the tool. Here, the two halves of the forming tool are clamped during the preforming and forming process with the help of two locking rings. This type of mechanical locking makes it possible to attain the forces from quasi-static forming pressure process up to 10 MPa as well as dynamic pressures of up to 175 MPa locally. Furthermore, by contrast to all other systems, the new machine with its newly developed hydraulic and venting system in the lower and upper forming tool permits bidirectional preforming as well as the required venting of the tool cavity for PMF. This means that the combined machine, which was developed at LUF, permits a combination of the advantages of quasi-static high pressure sheet metal forming and pneumo-mechanical high speed forming on one and the same forming machine.

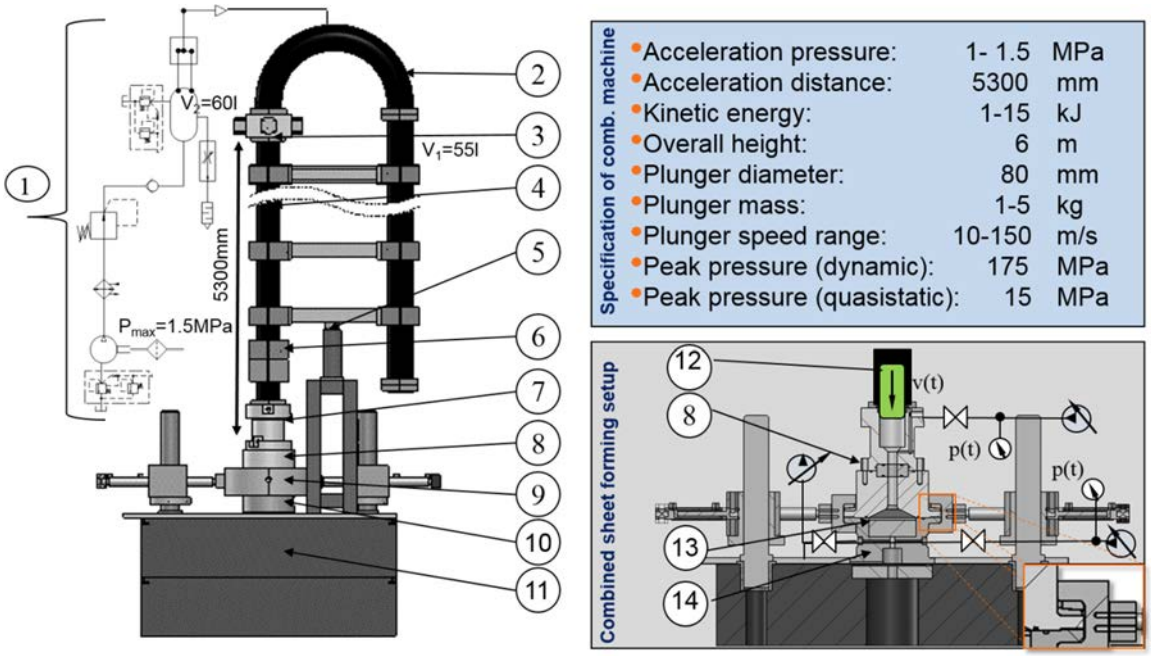


***Figure 7**: Pneumo-mechanical setup: 1 – pressure generation unit with secondary pressure tank; 2 – primary pressure tank; 3 - release mechanism; 4 – acceleration tube; 5 – lifting device; 6 – light barrier; 7 – tube adapter: 8 pressure chamber; 9 – locking ring; 10 – lower tooling adaptor (die); 11 machine bed; 12 – plunger; 13 – base plates; 14 – vent port.*

The principle of the so-called Hydropunch machine or the alternative method for the pressure wave generated in a working medium by means of an accelerated plunger was developed by Mazukin J.G. in 1961(Bragin, 2007). The principle is that, for the generation of pressure waves in the working medium which is enclosed in a pressure chamber, the working medium

is loaded through impulse generation by a fast-flying plunger. The plunger dips into the working medium, reaching the desired speed at the end of the accelerating tube, and thus generates very short and high pressure pulses up to several dozen MPa due to the kinetic movement of the plunger and the incompressible properties of the working medium. In order to accelerate the plunger in the new machine, use is made of compressed air pressure. The maximum acceleration pressure is 1.5 MPa, the length of the acceleration tube is 5.3 m and the diameter used is 80 mm. At the lower end of the tube there is a device for measuring the plunger speed in order to determine the plunger energy. Below the measuring device a ventilation system is located, in order to limit the proportion of compressed air in front of the plunger during the downward movement. The measurement of the pressure distribution and the pressure effect is performed using a phenomenological approach, more details of which are given in (Homberg, 2012). The quasi-static working media pressures are generated by means of a pneumatically driven high-pressure pump from the Maximator company. The transmission ratio amounts to 1:44 MPa. During the dynamic processes, a technical vacuum is created in the cavity of the lower die which amounts to 0.005MPa.

# 6 Technologically-oriented Research Work

Besides the support for machine design, basic research regarding the effect and interaction of parameters on the course and result of the PMF process was carried out at LUF. By way of example, one result shows that the thickness distribution of an equally formed conical part can be strongly influenced by the selected preforming strategy, see Fig. 8. Here, the investigation into the thickness distribution showed that, due to higher stretch forming, the classical PMF process leads to a 25 % thinning of the base material. In this case of classical PMF, the highest thickness variations obviously occur directly on the drawing radius. Then, the thinning level remains homogeneous in the radial direction on the blank, at 21%. The same thickness profile is also attainable with the negative preforming (RD) strategy, but with a lesser thinning of the base material. In contrast to a single PMF forming operation, negative preforming leads to a wall thickness reduction of only 8% or so. Furthermore, the positive preforming strategy shows that both the thickness profile and the thinning can be optimized. The positive preforming permits a uniform thickness reduction profile extending from the drawing radius to the center of the workpiece. However, the positive preforming strategy compensates the thinning for the same degree of forming by up to 5%. Moreover, analyzing the forming height distribution of the deformed parts, it can be seen that the resulting forming, as well as the sheet thickness distribution can be readily approximated by the CEL-Model developed, see Fig. 8. The resulting deviation between the experimental investigation and the simulation results is lower than 12%.

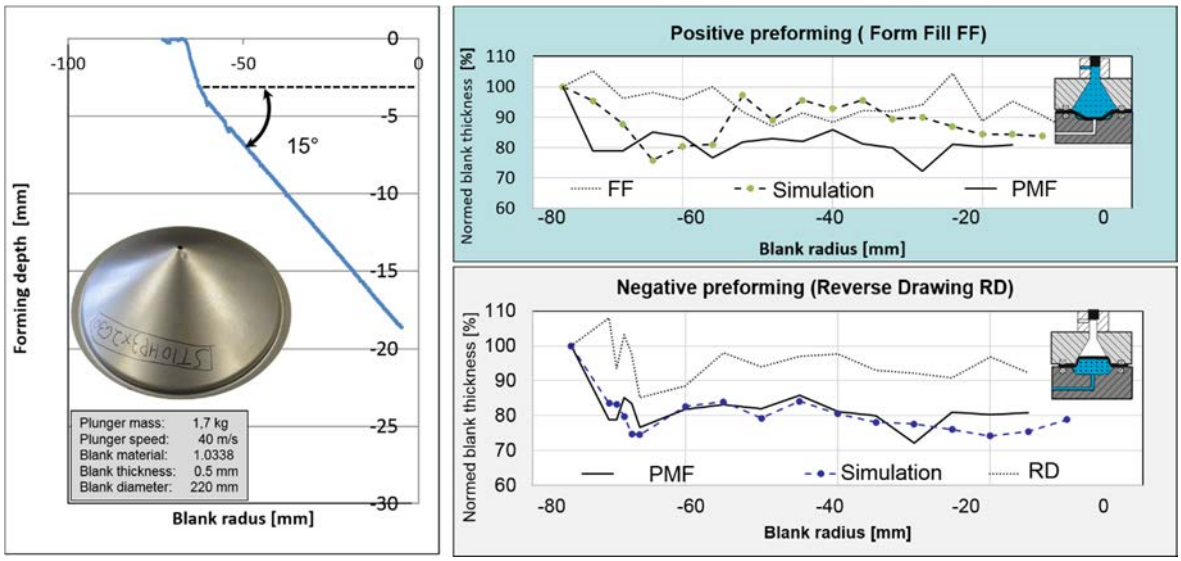


***Figure 8**: Influence of the preform strategies onto thickness distribution and profile*

# 7 Conclusion

This paper presents a possible process combination of quasi-static and high-speed-working media-based forming processes, where the advantages of quasi-static high pressure sheet metal forming and pneumo-mechanical high speed forming are combined using a special high speed forming machine. It presents new forming strategies for the preforming, forming and calibration of the sheet metal parts by means of the working media. Moreover, the paper shows validated numerical results for the influence of significant process parameters, such as the pressure chamber angle and plunger geometry, on the pressure distribution when using the pneumo-mechanical forming high speed processes. So the variation of the chamber angle showed that the chamber angle, for example, can effectively increase the homogeneity of the pressure distribution during the forming. A comparison of positive and negative preforming strategies, showed that it is possible to achieve lower and uniform thickness reduction with the aid of the two above-mentioned strategies compared to the conventional quasi-static or dynamic processes. To conclude, the combined forming processes have a high potential for producing complex geometries through the optimal use of the formability of the material employed.

# References

Abaqus Analysis User Manual, Version 6.14. Dassault Systémes, 2014.

Beerwald, C.: Grundlagen der Prozessauslegung und –gestaltung bei der elektromagnetischen Umformung. Dissertation, Dortmund 2004

Benson, D.J., S. Okuzawa, "Contact in a Multi-Material Eulerian Finite Element Formulation," Computer Methods in Applied Mechanics and Engineering, no. 193, pp. 4277-4298, 2004

Bragin A.P. Gidrodynamicheskaja shtampovka na press-pushkah kak odno iz napravlenij impulsnoj obrabotki materialov davleniem. Awiaziono kosmichskaja technika i technologij 2007, Kharkov, Ukraine, 2007

Demir, O.K., Weddeling, C., Ben Khalifa, N., Tekkaya, A. E., 2014. Avoiding Bending in Case of Uniaxial Tension with Electromagnetic Forming. In: Proceedings of the 6th International Conference on High Speed Forming - ICHSF 2014, 26-29 May, Daejeon, Korea

Golovashchenko, S.F., Bessonov, N.M., Ilinich, A.M.: Two-step method of forming complex shapes from sheet metal, Journal of Materials Processing Technology, Volume 211, Issue 5, 1 May 2011, P 875-885

Homberg, W.; Djakow E. Akst O.: Some aspects regarding the use of a pneumo-mechanical high speed forming process, Proceedings ICHSF 2012, Dortmund, Germany, 25 April 2012

Lange, K: Umformtechnik – Handbuch für Industrie und Wissenschaft, Band 4: Sonderverfahren, Prozeßsimulation, Werkzeugtechnik, Produktion, 2. Auflage, Springer-Verlag 1993

Mamutov A.V.:Vitezhka tonko lisitowih materialow polyurethanom kombinirowanim kwasistatisticheskim i magnitno impulsnim nagruzheniem, St-Petersburg 2001

Neugebauer, R.: Hydro-Umformung, Springer-Verlag, Berlin Heidelberg, 2007

Neugebauer, R.; Bräunlich, H.: Forming of double blanks with compressed medium. Society of Automotive Engineers Special Publications Band 1686. Detroit 2002. S. 49-55.

Psyk, V.; Beerwald, C.; Henselek, A.; Homberg, W.; Brosius, A.; Kleiner, M.: Integration of Electromagnetic Calibration into the Deep Drawing Process of an Industrial Demonstrator Part. Key Engineering Materials, Vol. 344 (2007), pp. 435-442, Trans Tech Publications, Switzerland.

SME, Fundamental Manufacturing process Study, Product ID: DV03PUB28,2002

Smojver I.,Ivancevic: Coupled Euler Lagrange Approach using Abaqus explicit in the bird strike aircraft damage analysis, Simulia Custemer Conference 2010

Vovk, A.: Verfahrensentwicklung zur Fertigung qualitätsgerechter Bauteile mit dem Hydro-Impuls-Umformen von Blechen, Dissertation, Magdeburg, 2008

Zaizew W.E., Sukaylo W.A., Korbach W.G., Hodjko A.A.:Modelirowanie processa swobodnoj rastqzhki trubchatoj zagotowki pri gidrodynamischeskoj shtampovke. Wisnik NTU ISSN 2079-5459, Vol 42, Ukraine, 2013

# Numerical and Experimental Investigation of Joining Aluminium and Carbon Fiber Reinforced Composites by Electromagnetic Forming Process

**A. Zajkani*, M. Salamati**

Department of Mechanical Engineering, Imam Khomeini International University, Qazvin, Iran
*Corresponding author: Email: zajkani@eng.ikiu.ac.ir

## Abstract

*Carbon fiber reinforced composites became so popular in automotive, aerospace, marine and military industries in past years, because of their high strength, low weight and subsequently high specific strength. The basic challenges of producing the CFRP components are their forming and joining techniques. In this study, a finite element analysis is carried out by the purpose that the optimum geometries to be selected for manufacturing an electromagnetically assisted joining by forming system of two aluminium and CFRP sheets. Electromagnetic forming is one of the high speed forming technologies that uses the Lorentz force as a forming pressure. High speed and usually one-step forming process are some of its advantages while, the necessity of high electrical conductivity of the work-piece is an important restriction. Aluminium deformed in this study, so that its behaviour is assumed to be dependent on the strain rate. Also, the hardening behaviour of aluminium is described by the Johnson-Cook material model. The joining by forming system is modelled in the finite element code by means of the ABAQUS 6.13 FEM software. The magnetic pressure pulse of the coil is described by the VDLOAD subroutine to apply it to the lower surface of the aluminium field shaper. Under influence of this force, the punch bulges the aluminium sheet into the hole on the CFRP sheet and a cavity on die helps the bulged region to form a mechanical interlock. In the experimental investigations, predrilled CFRP sheets with different diameter holes and locations are used. The effect of geometrical parameters such as metal thickness are studied on the quality of joints. The most important parameter to be considered here, is the tensile strength of the joints. Therefore, the joint samples had been applied under tensile test in order to consider failure modes, experimentally.*

## Keywords

Joining, Fiber reinforced plastic, Finite element method (FEM)

# 1 Introduction

Electromagnetic forming is a forming technology that utilizes electromagnetic force as forming force. In this high- speed forming technology, a severe, transient magnetic field is applied to the work-piece and the forming process takes place. EMF is a precise method for forming and joining of the metals and other materials that are able to overcome some technical problems such as spring-back, wrinkling and low formability of materials in other forming methods. Due to the very high speed forming process, strain rate is so high. Therefore, forming limit diagrams can be extended in which the formability of the material is increased significantly (Seth et al., 2005) and spring-back and wrinkling are reduced (Podmanabhan, 1997).

Usually EMF is used for forming of materials of high electrical conductivity, but by using some techniques such as using driver materials it can be used for forming materials of lower electrical conductivity. The magnetic field produced in the coil induces eddy currents in the nearby work-piece that flows in the opposite direction to that of discharge current which causes the mutual repulsion between the work-piece and the forming coil (Walke et al., 2014). This method has now been applied in the automotive, aerospace, military and electronics industries.

Ultra-lightweight materials had been developed in the last 20 years, rapidly, especially in aerospace and automotive industries, because these materials have a great strength to weight ratio and can reduce the energy consumption significantly. One of these lightweight materials is carbon fiber reinforced plastics (CFRP). CFRP has higher specific strength and specific stiffness, higher fatigue strength and higher resistivity in a corrosive environments than metals (Huang et al., 2013). There are two types of CFRP laminates generally: Thermosets and thermoplastics. Thermosetting CFRPs are more applicable than thermoplastic CFRPs for the automotive and aerospace applications as well as the fire-resistant structures. These advantages appear from their non-reversible phase transition polymer matrix and longer fatigue life under a cyclic tension tensile condition (Huang et al., 2013). However thermosetting CFRPs have some disadvantages such as poor formability and no welding capability.

Spot joints are of high importance in industries such as automotive and aerospace, since a car body contains almost 4000 spot joints for example. Since thermosetting CFRPs don't have welding capability, so heat sources such as laser, ultrasonic and friction can't be applied for joining them, these techniques are only available for joining of thermoplastic composites. So special methods for joining of CFRPs must be introduced.

In this study a joining by forming system is introduced in order to join metal-CFRP and CFRP-CFRP sheets. Moreover, the system is designed to be able to join any ductile metal sheets to CFRP sheets without respect to their electrical conductivity. In this system a ductile metal sheet is enforced into the hole on a predrilled CFRP sheet. The die cavity helps it to form a mechanical interlock. In order to prevent the trial and error procedure in a manufacturing system, a finite element analysis is carried out by ABAQUS 6.13 FE package. The optimum geometries and sizes for different system parts such as die, blank-holder, field shaper and punch are selected. There are generally three ways to finite element analysis of

the EMF process, first is loosely coupled scheme that is used in some works such as (Oliveira et al., 2003). The other method is a fully coupled scheme that is used by (Svendsen et al., 2005) and (Stiemer et al., 2006), and the last method that is simpler in comparison to the former methods used by (Correia et al., 2008), (Imbert et al., 2006) and (Uhlmann et al., 2004). In this method, which is used in the present work, analysis is divided into two different sections: electromagnetic analysis and mechanical analysis, and the pressure resulted by electromagnetic analysis is applied on the work-piece as mechanical force.

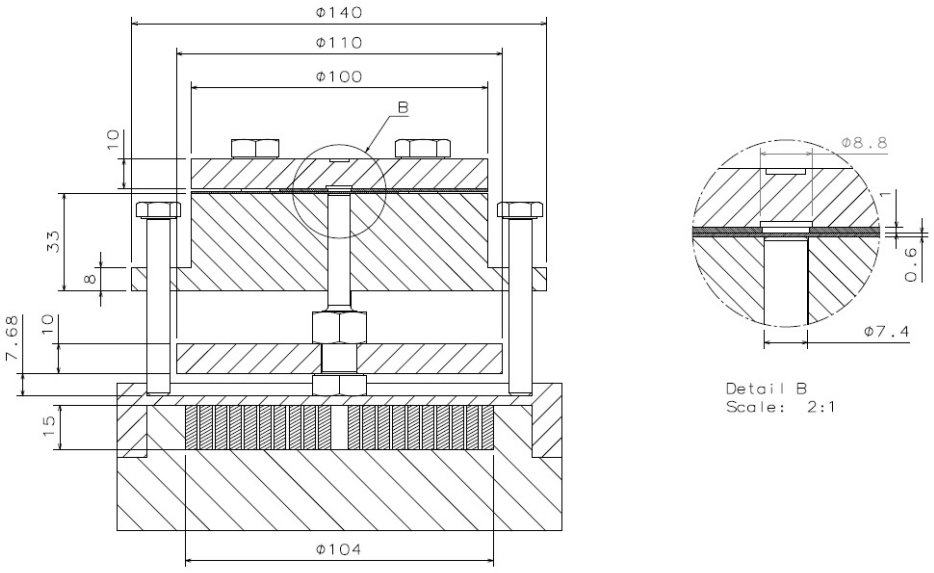


***Figure 1**: The joining by forming system*

After FE analysis and selecting best geometries for system, the parts are manufactured and experimental tests were carried out on the aluminium sheets of 0.6, 1 and 2mm thickness. After joining process, the specimens were applied under tensile test and their tensile strength was obtained.

# 2 Finite Element Analysis

Finite element analysis is carried out in order to find and select the best geometries and sizes for different system parts. First, it is necessary to define the electromagnetic pressure produced in the coil. The current in the coil is defined by Eq. 1 (Correia et al., 2008):

$$I(t) = I_0 e^{-t/\tau} \sin \omega t \tag{1}$$

where $I_0$ is maximum intensity of the discharge current, because the field shaper is a disk, a cylindrical coordinate system can be used, thus the magnetic field density **B** possesses a radial component $B_r$ and an axial component $B_z$ which are given as follows:

$$\frac{-1}{\mu_0\sigma_w}\left(\frac{\partial^2}{\partial r^2}+\frac{1}{r}\frac{\partial}{\partial r}+\frac{\partial^2}{\partial z^2}-\frac{1}{r^2}\right)B_r+\frac{\partial B_r}{\partial t}=0 \tag{2.a}$$

$$\frac{-1}{\mu_0\sigma_w}\left(\frac{\partial^2}{\partial r^2}+\frac{1}{r}\frac{\partial}{\partial r}+\frac{\partial^2}{\partial z^2}\right)B_z+\frac{\partial B_z}{\partial t}=0 \tag{2.b}$$

The boundary conditions to solve Eqs.2 are:

$$\boldsymbol{B}=\boldsymbol{B_0}+\boldsymbol{B_1} \qquad at\ z=d_g+u_2(t) \tag{3.a}$$

$$\boldsymbol{B}=0 \qquad at\ z=d_g+u_2(t)+h \tag{3.b}$$

Where $u_2(t)$ is vertical deflection of the field shaper and $d_g$ is the initial gap between coil and the field shaper. For solving these equations the approach used in (Correia et al., 2008) is used in this study too. For more information this approach can be found.

The equations are solved by a VDLOAD subroutine and temporal distribution of electromagnetic pressure is obtained. This pressure is applied to the lower surface of aluminium field shaper as mechanical force in ABAQUS/Explicit. Field shaper is used in order to translate the electromagnetic force produced in coil to the steel punch. Due to the low size of the punch in comparison to the coil size, if not to use the field shaper, most amount of the produced pressure will be wasted and sufficient force to move the punch will not be prepared.

The CFRP sheet modelled, is an 1mm thickness 3ply laminate with epoxy 5052 resin and [0/90] direction fibers.

Aluminum sheet is the part that deforms plastically in this study, so that its behaviour is assumed to be dependent on the strain rate. Also, the hardening behaviour of aluminium is described by the Johnson-Cook material model. Johnson-Cook parameters are listed in **Table 1**.

| Parameter | A (MPa) | B (MPa) | n | T melt (K) | T transition (K) | m | C | $\dot{\varepsilon}_0$ (1/s) |
|---|---|---|---|---|---|---|---|---|
| Quantity | 324.1 | 113.8 | 0.42 | 925 | 293.2 | 1.34 | 0.002 | 1.0 |

***Table 1**: Johnson-Cook parameters for aluminium sheet*

Die, blank-holder and the set of punch and field shaper assumed as rigid bodies and the boundary conditions are applied to constrain the die and blank-holder's motion in any direction and the set of punch and field shaper's motion in radial direction.

In the simulation, contact conditions are needed to be considered between the Aluminum sheet and other parts (CFRP, die, blank-holder and punch) as well as the field shaper and blank-holder and CFRP with die. Coulomb friction law has been used with a friction coefficient of 0.2 for aluminum sheet, and the other contacts assumed to be frictionless. The geometrical parameters used for FE simulations are summarized in **Table 2**.

| Work-piece material | Thickness (mm) | Electrical conductivity (MS/m) | Density (Kg/m$^3$) | Young's modulus (GPa) | Poisson ratio |
|---|---|---|---|---|---|
| Aluminium 1050 | 0.6 | 34.45 | 2.7e3 | 80.7 | 0.33 |
| Epoxy 5052 CFRP | 1 | 1 | 1.4e3 | $E_1$= 133.86 | $v_{12}$=$v_{13}$=0.301 |
| | | | | $E_2$=$E_3$= 7.706 | $v_{23}$=0.396 |

***Table 2**: Material properties of aluminium and CFRP sheets in FE analysis*

The aluminum and CFRP sheets are meshed by CPS4R elements which is a four node bilinear plane stress quadrilateral element with reduced integration. A dynamic explicit time integration scheme is employed in ABAQUS/Explicit. The simulation process time is fixed 220 μs.

The aluminum material that is formed into the CFRP hole forms a mechanical interlock by CFRP sheet after the collision with the die cavity. The predicted conditions of the interlock and its strains, stresses and corresponding displacements are shown in **Fig. 2**.

After the finite element analysis, the optimum geometries for manufacturing the system parts were selected and system were manufactured by milling and turning processes.

# 3 Experimental Procedure

CFRP sheets became so popular in last years because of their special characteristics and great strength to weight ratio. There are two different types of CFRPs: thermosets and thermoplastics. Two basic challenges about thermosetting CFRPs are their no welding capability and brittleness, thus special methods are needed to forming and joining of these materials. Usually adhesive bonds and mechanical fasteners are used to joining process of CFRP sheets.

The system introduced in this study has three main parts: die, blank-holder and set of punch and field shaper. Metal and CFRP sheets lie between die and blank holder. The die is clamped to the blank-holder by four M10 bolts to hold the sheets strongly. Blank-holder is a 33mm height and 120 mm diameter disk made of steel ST37. It has a through all hole in center that is the path for punch motion and has four threaded holes for clamping die. Die is a 10mm height and 120 mm diameter disk made of steel ST37. The die has hollows in both sides with different diameters to be capable to link sheets with two different hole sizes. There are an 1mm depth and 8.8 mm diameter cavity at one side and an 1mm depth and 6.6 mm diameter cavity at the other side. These sizes are determined by the finite element analysis. The other part of the system is the set of punch and field shaper. The field shaper is an aluminum disk by 10 mm height and 110 mm diameter drilled and threaded at center. The punch is an 80mm M12 steel bolt that is clamped to the field shaper by a nut and 50 mm of its end has been turned and surface finished. **Fig. 3** shows the schematic set of joining by forming system by arranged parts and EMF apparatus system which assembled parts is fixed over the coil.

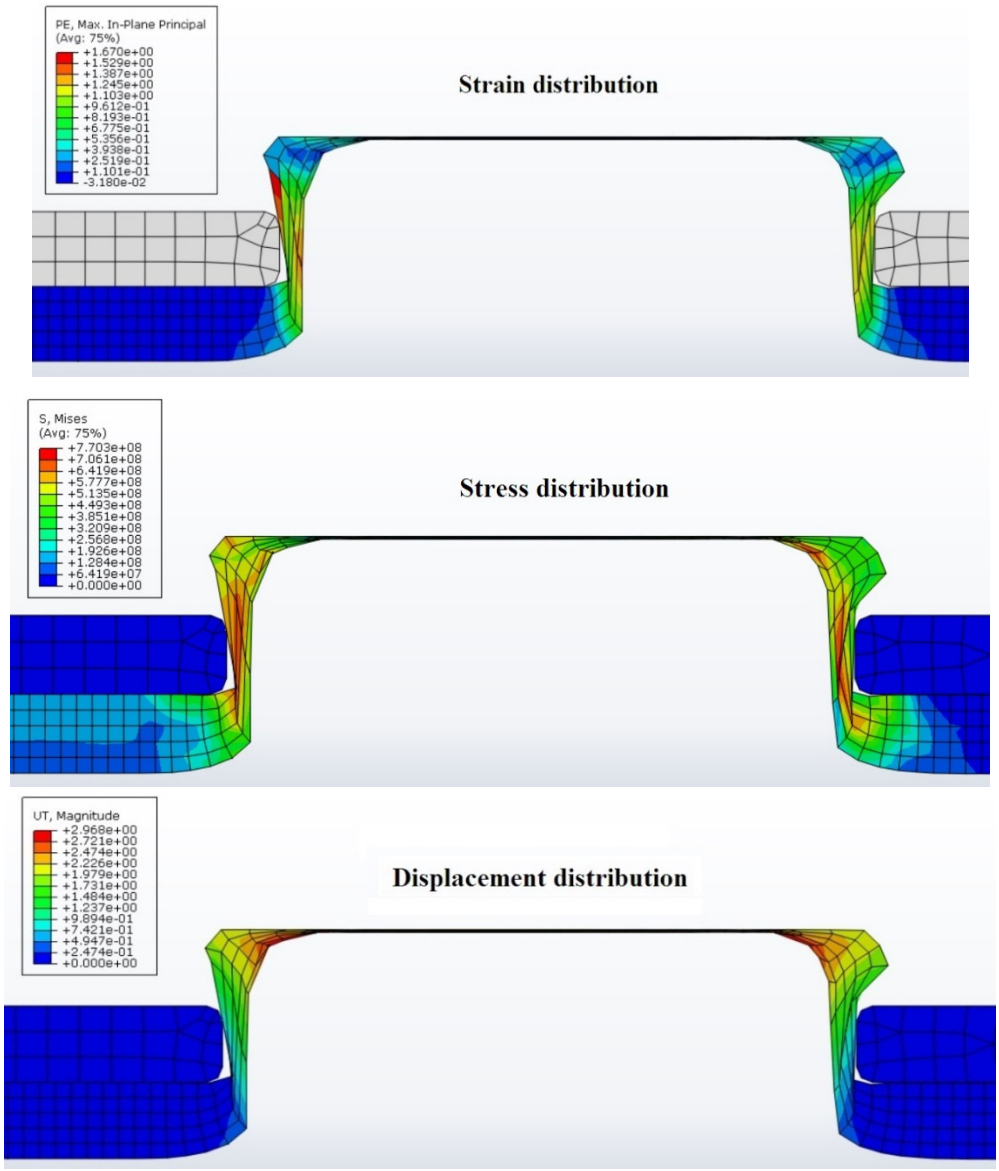


***Figure 2**: FE simulation results*

**Fig. 4** illustrates the joined CFRP and Aluminum samples and the universal tensile test machine. First the set of punch and field shaper lies on the coil, then blank-holder and die stand on the set of punch and field shaper in ways that punch enters the hole on the blank-holder. Clearance between the punch and this hole is very low (about 0.05 mm) that constrains the radial motion of punch with high accuracy. In order to adjust the height of the blank-holder from punch, four 100mm M8 bolts are used, by adjusting the height of these bolts, the gap between the blank-holder and punch can be adjusted. By appropriate adjustment of this height the punch can easily move in vertical direction. Initial gap between the coil and field shaper is secured by the M12 bolt (punch) head, this gap is 8 mm.

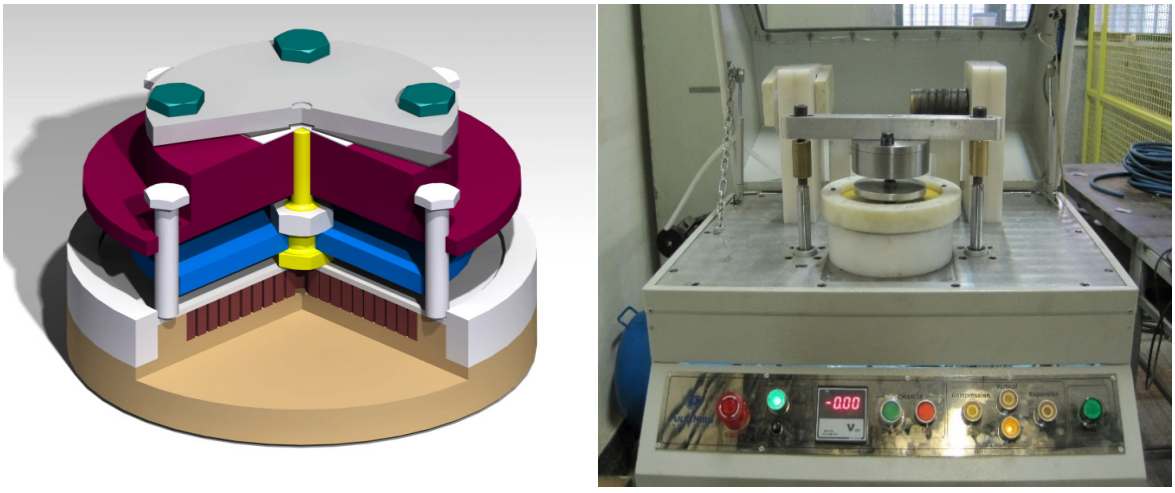

a) b)

***Figure 3**: The set of EMF system with assembled parts; a). Schematic set. b). Actual set*

For experimental tests aluminum 1050 sheets by 0.6, 1 and 2 mm thickness were used. The CFRP sheets were 1mm thickness 3ply epoxy 5052 resin and [0/90] fibers direction. Since drilling and cutting of CFRPs are so challenging processes that may cause problems such as delamination and local fiber rupture, so selecting an appropriate method for this processes are of high importance. Laser cutting and water jet cutting are some good techniques for cutting and drilling. Laser cutting may cause local temperatures which may cause resin suffering (especially in thermosetting CFRPs), so water jet cutting were used for cutting and drilling processes. The basic characteristics of these sheets were summarized in **Table 2.**

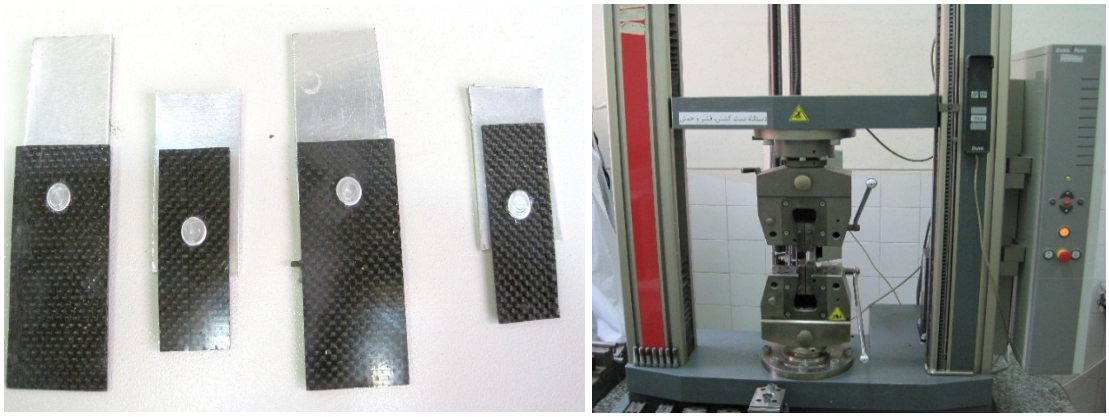

***Figure 4**: a). The joined CFRP and Aluminium samples, b). Tensile testing machine*

The experiments were carried out by voltages between 4 to 5.5 KV voltages, in lower voltages the mechanical interlock were not formed and in higher voltages, the aluminum sheet fails. After tests, the specimens were applied under tensile test, the apparatus for tensile test were Zwick/ Roell Z100 (**Fig. 4b**).

For 0.6 mm sheets, mechanical interlock were created in range of 4 to 4.2 KV voltages, in higher voltages the aluminum sheet fails in the interlock location. The tensile strength of these specimens was only in the range of 200N for different discharge voltages. These joints have no good characteristics because of very low thickness of aluminum at neck zone.

As illustrated in **Fig. 5** the best range of voltage for 1mm sheets were obtained at 4.4 to 4.8KV. The best joint were in case of 4.4 KV, in this case the joint strength was 774.22N and failure mode was aluminum neck fracture, The CFRP sheet was entirely safe and no signs of fracture or delamination had be seen on it, this means that by increasing the thickness of deforming part, a more quality joint can be produced, in other hand the weakest joint was the case of 4.8 KV, the strength of this joint was only 299.73N, failure mode was similar to former specimen, but in this case the neck thickness of aluminum was very low because of the high energy of process, so the failure takes place in very low forces.

In case of 2mm sheets the results were so better than 0.6 and 1mm specimens, so it can be resulted that the thickness of deforming material is a high effective parameter on joint quality, it is evident somehow, since as **Fig. 3** in FE analysis shows, material flow results thinning in joint neck, and when initial thickness is higher, after necking phenomenon, the sheet thickness in neck zone is sufficient to joint be strength enough. In the case of 2 mm aluminum thickness, the joint strength was 1494.38N for 5.2KV and 1742.18N for 5.5KV.

Increasing the velocity of punching process through exposing a high strain rate EMF pressing causes to strike metallic sheet by more plastic flow rate inside die cavity. So, it provides forming by stronger mechanical interlock between the metal sheet and CFRP laminate. Generally, using the conventional methods in low punching velocity such as hydraulic press may perform small size in joining as well as low quality. According to the finite element simulations for a conventional press, in order to obtain similar characteristics with the EMF process, large -amplitude holding forces (about three or four times than EMF process) by heavy apparatus are needed to be used.

One of the most important capabilities of this system is joining two CFRP sheets by means of a small aluminum dummy tape. For this purpose, two predrilled CFRP sheets lie on each other and an aluminum dummy tape lies under them. Other characteristics of the process are as former. **Fig. 6** shows joining two CFRP sheets by this method and the aluminum dummy tape can be seen. Mainly, it is the biggest advantage of this system, whereas the thermosetting CFRP has no welding capability. So, it is necessary to join them by another consumable material. Accordingly, in this method the consumable material is very small in size and is an inexpensive and cost-effective method to join two CFRP sheets.

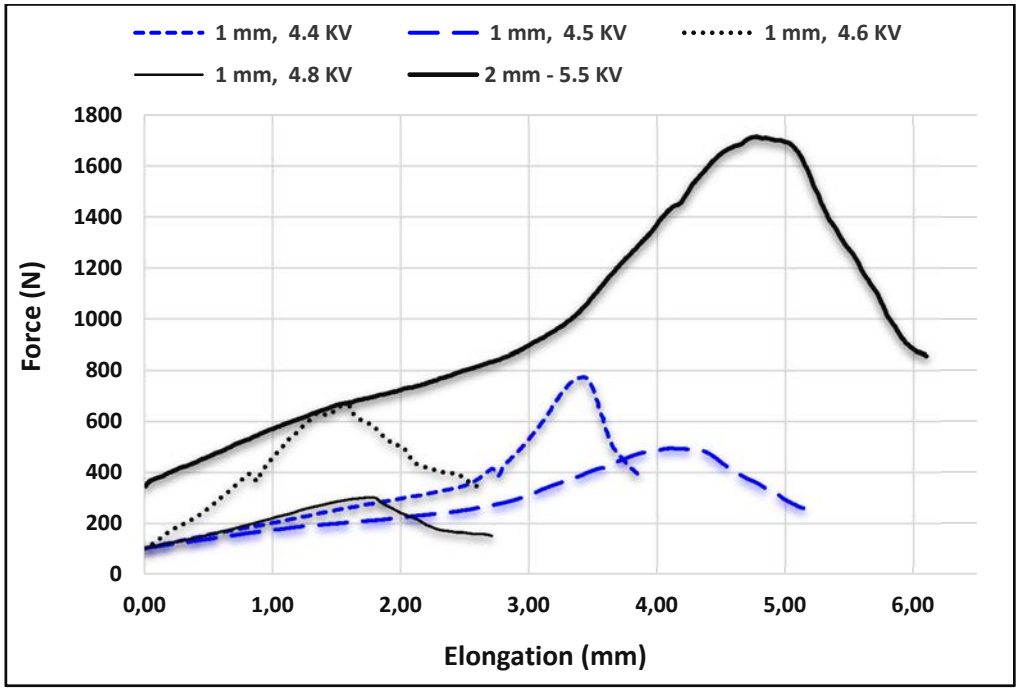


***Figure 5**: Force-Strain (elongation) diagrams for 0.6 mm and 1mm Al sheet*

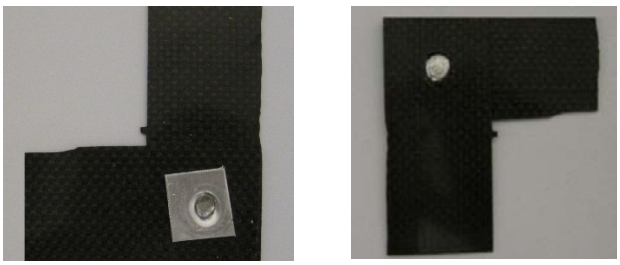

***Figure 6**: Joining two CFRP sheets by an aluminium dummy tape*

# 4 Conclusions

In this study, a finite element analysis was carried out by the purpose that the optimum geometries to be selected for manufacturing an electromagnetically assisted joining by forming system. Aluminium and CFRP sheets were used for experiments, and after joining process, the specimens were applied under universal tensile test. The joining by forming system were designed in order to overcome the restriction of necessity of high electrical conductivity of work-pieces in EMF process. So, it can be used to join any ductile materials. Another advantage of the system is its capability to link two CFRP sheets by a small dummy tape, whereas the CFRPs have no welding capability. Actually, conventional methods are inexpensive for joining them rather than the high speed joining process, which has no need to any additional equipment. Moreover, by having the advantages along with capability of

joining two or more different sheets, it is a convenient method to joining a wide range of dissimilar materials and any geometries.

If the stronger material is substituted for the punch such as annealed steels, it would be more convenient to apply the method for the steel metallic joining parts.

# References

Correia, JPM., Siddiqui, MA., Ahzi, s., Belouettar, S., Davies, R., 2008. A simple model to simulate electromagnetic sheet free bulging process. International Journal of Mechanical Sciences 50, pp. 1466-1475.

Huang, Z., Sugiyama, S., Yanagimoto, J., 2013. Hybrid joining process for carbon fiber reinforced thermosetting plastic and metallic thin sheets by chemical bonding and plastic deformation. Journal of Materials Processing Technology 213, pp. 1864-1874.

Imbert, J., Worswick, M., Golovashchenko, S., 2006. Contributing factors to the increased formability observed in electromagnetically formed aluminium alloy sheet. In: Tekkaya, A.E., Daehn, G.S., Kleiner, M. (Eds.), High Speed Forming 2006, Proceedings of the 2nd International Conference, Dortmund, Germany, pp. 3-12.

Oliveira, DA., Worswick, M J., Finn, M., Newman, D., 2003. Electromagnetic forming of aluminium alloy sheet: free-form and cavity fill experiments and model. Journal of Materials Processing Technology 142, pp. 744-754.

Podmanabhan, M., 1997. Wrinkling and spring-back in electromagnetic sheet metal forming and electromagnetic ring compression. MS Thesis, The Ohio state university.

Seth, M., Vohnout, VJ., Daehn, GS., 2005. Formability of steel sheet in high velocity impact. Journal of Materials Processing Technology 168, pp. 390-400.

Stiemer, M., Unger, J., Svensden, B., Blum, H., 2006. Algorithmic formulation and numerical implementation of coupled electromagnetic inelastic continuum models for electromagnetic metal forming. International Journal for Numerical Methods in Engineering, 68, pp. 1301-1328.

Uhlmann, E., Jurgasch, D., 2004. New impulses in the forming of magnesium sheet metals. In: Tekkaya, A.E., Daehn, G.S., Kleiner, M. (Eds.), High Speed Forming 2004, Proceedings of the 1st International Conference, Dortmund, Germany, pp. 229-241.

Walke, GA., Kulkarni, A., Vasudevem, R., 2014. Finite element analysis and parametric study of electromagnetic forming process. International Journal of Engineering Research and Technology.

# Detachment of Conductive Coatings by Pulsed Electromagnetic Field

**V. Mironov[1*], A. Tatarinov[1], M. Kolbe[2], V. Gluschenkov[3]**

[1] Laboratory of Powder Materials, Riga Technical University, Latvia
[2] West Saxony University of Applied Science Zwickau, Zwickau, Germany
[3] Samara State Aerospace University, Russia
[*]Corresponding author. Email: viktors.mironovs@gmail.com

## Abstract

*The paper presents results of studies on the detachment of conductive coatings from the metal substrate by pulsed electromagnetic field (PEMF). It is known that at the boundary of a metal substrate and an electrically conductive coating having different electrical conductivities sharp changes of PEMF strength arise. This effect has been used to remove a copper layer from a steel substrate. Experimental studies were carried out in the Riga Technical University (Latvia), West Saxony University of Applied Science Zwickau, (Germany) and the Samara Aerospace University (Russia). Generators of pulsed current with power capacity from 1 to 60 kJ with discharge rates from 10 to 100 kHz were used. Treatment of coatings was performed using both flat and cylindrical inductors. The influence of a number of factors on the efficiency of the separation of conductive coating (Cu, Al), such as the thickness and material properties of the coating and substrate, the strength of adhesion of the coating to the substrate, the electrical parameters of the equipment and the inductor system, are shown. Examples demonstrating the main application potential of the method include: deleting of a thin conductive coating induced on metallic and non-metallic products by spraying; separation of layers of metal sheets after their joint rolling or punching; removal of conductive membranes used in the magnetic pulse compression of powders.*

## Keywords

Pulsed electromagnetic field, Conductive coatings, Separation

# 1 Introduction

The method of materials processing by means of a pulsed electromagnetic field (PEMF) has been widely known since early 1970-ths. It is based on the transformation of electrical power, accumulated in a capacitive or inductive storage into a pulse magnetic field (PMF) that performs plastic strain work in a deformed product or accelerating a solid. The theoretical fundamentals of the PMF method were developed in works of G. Knopfel [1], H. Dietz [2], V. Mihailov [3], D. Montgomery [4], R. Winkler [5] and others. In 1980-ths, advances in the practical use of PMF were especially significant for metals deforming. Investigations of that period performed by D. Bauer [6], H. Wolf [7], L. Himenko [8] and V. Gluschenkov [9] are widely known.

From the beginning of 2000-ths, center of the highest activity in the field of PEMF appeared in Germany [10-12], USA [13], China [14], Russia [15] and other countries. Among the most successful technological applications of PEMF the following ones should be mentioned: crimping of tubes made of aluminum and copper alloys, forming shells, calibration of tubular blanks, performing of separation and assembly operations. A large number of publications were devoted to application of PEMF for compression and deformation of powder materials [16-18].

The present work considers some features of REMF use for detachment of electrically conductive coating from the base. Frequently, such detachment presents a rather complicated task. The difficulty is caused by to strong adhesion between the coating and the base, a tiny thickness of the coating, a necessity to preserve both the coating and the base undamaged and by other factors. PEMF can be an effective tool in fabrication of metallic foils, separation of metal sheets, removal of technological shells and membranes, and etc.

The simplest approach is realized by the pulsed electro-dynamic method, where interaction of parallel pulsed currents flowing simultaneously in the coating and basic substrate are used. However, achievement of qualitative exfoliation of coatings is complicated in practice due to the non-uniformity of currents upon the cross-sections of layers, as well as possible melting of the coating. The PEMF method based on influence on the conductive coating by a flat or cylindrical inductor seems more realistic.

# 2 Experiments

Experimental studies were carried out using two layouts of PEMF application to the objects: a) impact by penetrating field with positioning the inductor at the substrate side (Fig.1A) and b) attraction method, where the inductor is located at the coating side (Fig.1B).

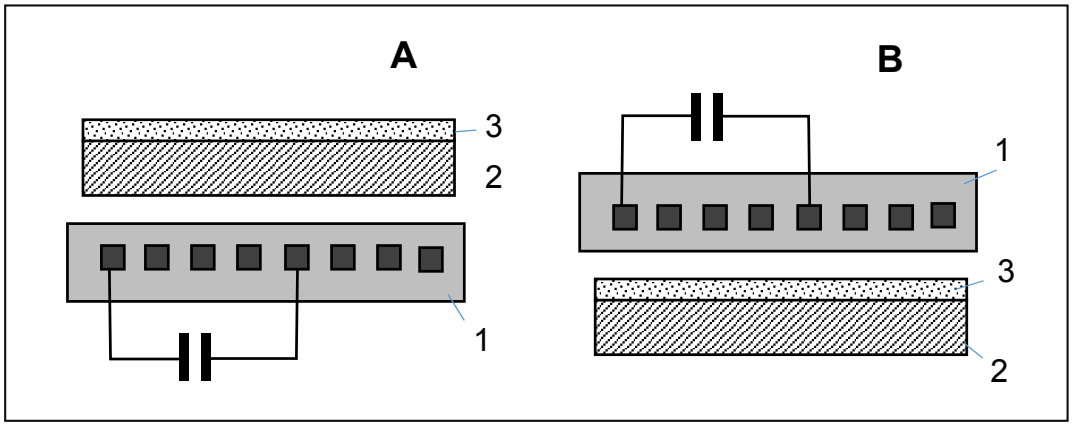


***Figure 1**: Experiment layouts according to penetrating PEMF method with the inductor positioned at the substrate side (A) and attraction method with inductor at the coating side (B). 1 – PEMF inductor; 2 – substrate; 3 – coating*

The experiments were carried out, partially, on the specially designed pulsed magnetic equipment MIU-15 (Fig.2), parameters of which are given in Table 1. Both flat and cylindrical inductors were used.

***Figure 2**: Pulsed electromagnetic equipment MIU-15 (left) and inductor arrangement (right)*

| Model | Energy max., kJ | Voltage range, kV | Frequency limit, kHz | Case size (inches) | Weight (lbs) |
|---|---|---|---|---|---|
| MIU-50 | 50 | 5 - 20 | 40 | 61x53x69 | 2640 |
| MIU-15 | 18 | 1 - 20 | 55 | 45x28x61 | 1100 |
| MIU-10 | 10 | 1 - 10 | 55 | 33x37x49 | 770 |
| MIU-3 | 5 | 1 - 6 | 33 | 25x29x32 | 220 |
| MIU-1 | 1,25 | 1 - 7,5 | 70 | 26x15x20 | 110 |

***Table 1**: Main parameters of equipment line MIU used in experiments*

# 3 Methodology

When PMF of a certain intensity is exposed on a metal coating, electromagnetic field $H_2$ produced by eddy currents $i_2$ is induced in its conductive layer. Interaction of eddy currents with electromagnetic field $H_1$ from the inductor results in forces $F_2$ acting on the coating with area $S_2$.

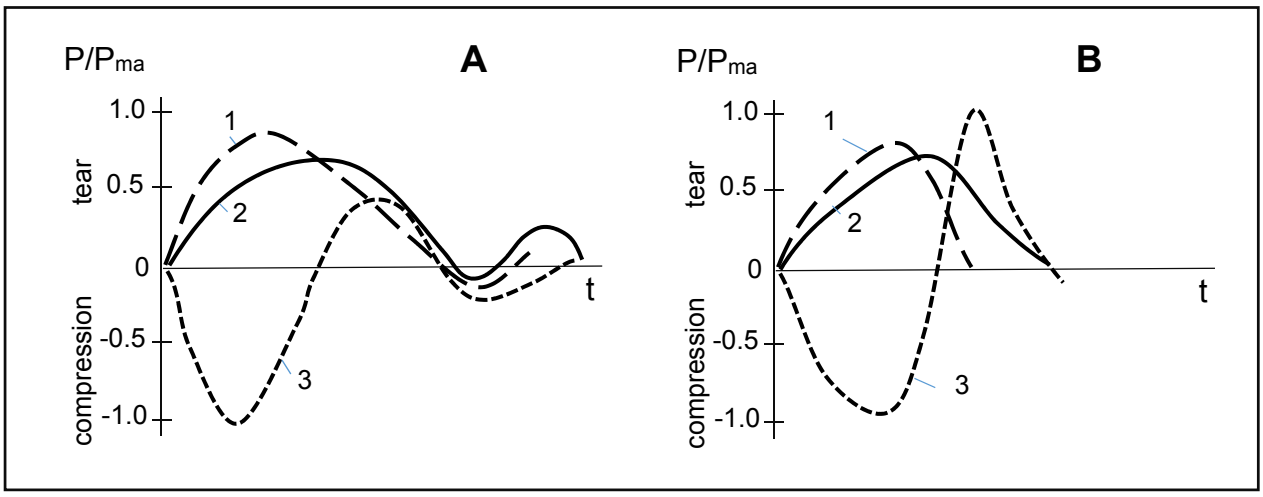


***Figure 3**: Changes of magnetic induction on external (1) and internal (2) sides of steel substrate and pressure of PMF (3) onto coating in the cases of: A - penetrating field according to Fig.1A; B – attraction according to Fig.1B.*

In the case of the layout depicted in Fig.1A (penetrating PEMF), pressure $p_2$ onto the coating is determined by intensity $H_1$ of the fast growing PMF and the degree of its damping by passing through the basic substrate that is characterized by the field attenuation coefficient $K_c$. Pressure $p_2$ is expressed as

$$p_2 = \mu_0 H_1 K_c, \quad (1)$$

where $\mu_0$ is the magnetic constant.

The value of $K_c$ is a complex function dependent on the parameters of discharging circuit (generator-inductor) and the materials and thicknesses of the base and the coating.
In this case, the thinner is the base and the lower is its electrical conductivity, the smaller is attenuation of the field. The attenuation effect is absent at all, if the base is made of non-metal material. Changes of magnetic induction on external and internal sides of steel substrate and pressure of PMF onto the coating in the case of penetrating field are shown in Fig.3A.

For realization of the layout of direct impact of PMF according to Fig.1B, it is necessary to create slow increasing PMF in the coating and then to decrease the external field of the inductor with high speed (Fig.3B). A rising electro-dynamic force pulls the coating towards the inductor, causing its detachment from the base. The coating is detached more easily, if the adhesion strength $\sigma_c$ between the coating and the base is lower.

Such a method can be realized by using a "crowbar" system in the PEMF arrangement. The main criterion of the process efficacy is the quality of the detached coating, first of all absence of damages and defects of surfaces of the coating and base. In the process of the coating removal, duration and strength of PMF, the electrical and mechanical properties of the coating and base materials, as well as the adhesion strength of the coating to the substrate, are the most significant.

# 4 Results and Discussion

## 4.1 Process of Separation of Metal Layers

At joint press forming of multiple layers of metals, their grip due to adhesion, formation of burrs and other factors is observed. For comparison, separation of the layers was performed by two PEMF methods discussed above in section 3.

The process of detachment is more technological in the case of "attraction" method, when PEMF is imposed to the coating directly from the inductor as depicted in Fig.1B, and thus it may be implemented directly on the conveyor line. Separation process is particularly effective for coating with high conductivity and using bases made of steel (Fig.4). However, this requires high discharge frequency (above 50 kHz for a copper coating) and, therefore, increases the voltage level of the equipment (10 kV). All this has a significant impact on the longevity of the inductor. In addition, damage was observed on the surface of the detached coating.

***Figure 4****: Example of detachment of copper coating (thickness 0.1 mm) from stainless steel base (thickness 1.1 mm): A – separated base and coating; B – macrostructure of coating surface*

If penetrating field is imposed to the coating from the base side (Fig.1B), the process is carried out under reduced discharge voltage (1 kV) and lower frequency (below 30 kHz). This method is effective in the case of a small thickness of the base (3-5 mm) and its low conductivity. The best effect was achieved by using of stainless steel or textolite as the base materials.

The separation of "stuck" thin walled copper foil and a steel base after stamping operation was conducted by means of a flat inductor and a PEMF equipment MIU. A billet was put in the active zone of a coil inductor (Fig.5). PEMF in this case was directed orthogonally to the coating surface.

***Figure 5****: Inductor's arrangement for separation of metal layers.*

The MIU parameters were: accumulated energy – up to 1kJ; charge voltage – 1…7 kV; natural frequency – 80 kHz. The spiral coil inductor has 12 turns with sizes: ID = 20 mm, OD= 600 mm, inductance – 5.3 μH. Separation of metal layers in the billet of a diameter of 30 mm was performed when the power of MIU reached 100 – 500 J. In some cases, deformation of the copper foil occurred in its plane. It is explained by the non-uniformity of PEMF distribution upon the cross section of the inductor due to the "fossa" or the inactive zone in the center of the inductor's coil.

To record the separation process visually, a highspeed - thermo - camera FLIR SC7300 was applied (Fig.6).

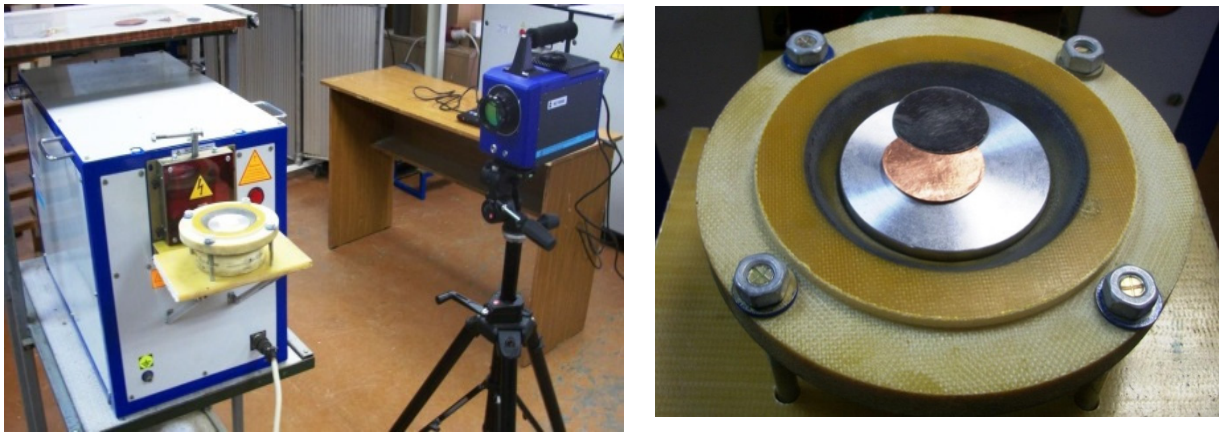

***Figure 6**: Recording of separation mechanism of thin layers in PEMF: setup and billet positioned in inductor.*

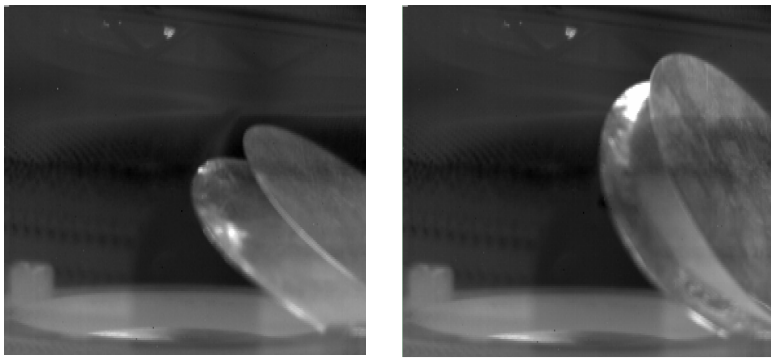

***Figure 7**: Example of recording of separation of copper foil and steel plate.*

Fig. 7 illustrates snapshots of separation of a copper foil from a steel plate of 65 mm diameter. The time-interval between frames was 8 milliseconds.

## 4.2 Process of Removal of Deposited Coating

In this experimental study, the method of separating of a thin foil (Cu-Ni) from steel substrates was used. The foil coating was obtained by vacuum sputtering. The coating was exposed to PEMF from the inductor's side (Fig.1A). Detachment of the coating layer was produced by single pulses using the equipment MIU-15 with above mentioned parameter. A removal case is shown in Fig.8.

## 4.3 Removal of Technological Casing

In the pulsed magnetic compression of powdered materials, technological casing made of materials with a high electrical conductivity (copper, aluminum) are used.

To remove the casing after pressing sleeves of 40 mm in diameter, PEMF method with an inductor positioned in the annular cavity of the preform was used. The method allowed removal of the tubular and annular casings made of Cu without damage that made possible to reuse them. To increase the efficiency, additional measures may be undertaken, such as pre-coating the inner surface of the casing before PEMF by a separating layer of paraffin.

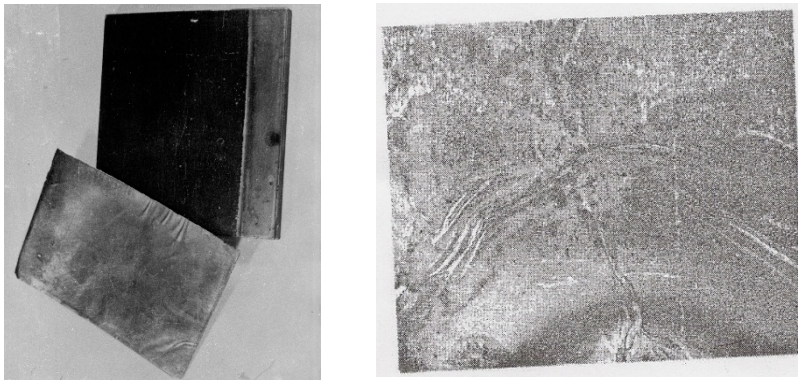

***Figure 8****: Example of removal of Cu-Ni coating (thickness 0.15 mm) from stainless steel base (thickness 1.1 mm) by direct impact on the coating with discharge current above 1kA: A – separated base and coating; B – macrostructure of coating surface*

# References


1. Knopfel, G. Sverhsilnie impulsnie magnitniepolja. (Superstrong pulsed magnetic fields) Moscow, Mir. 1972. (in Russian).
2. Dietz, H., Lippmann, H., Schenk, H. Theorie des Magneform Verfahren: Erreichbarer Druck. ETZ. Ausg. A, 1967, Bd.88, H.8, S.217-222.
3. Mihailov,V. Impulsnie electromagnitnie polja. (Pulsed electromagnetic fields) Harkov, 1979. (in Russian).
4. Montgomery, D. Poluchenie silnih impulsnih magnitnih poljej (Obtaining of powerful pulsed magnetic fields), Moscow, 1971. (in Russian)..
5. Winkler, R. Hochgeschwindigkeitsbearbeitung. Verlag Technik, Berlin, 1973, 456 S.
6. Bauer, D. Erwärmung der Werkstücke bei Magnetumformung.-Bänder, Bleche, Rohre, 1968, Bd.9, N.11, S.673-676.
7. Wolf H. Pulververdichten durch elektromagnetische Kräfte. Herstellungsmöglichkeiten für Werkzeugaktivelemente. Fertigungstechnik u. Betrieb. 1980. N 9. S. 558-560.
8. Bely I, Fertik S.,Himenko,L. Spravochnik po magnitno-impulsnojo abrabotke metallov (Handbook on pulsed magnetic processing of metals), Harkov, 1977. 168 p. (in Russian).

9. Glushenkov, V., Karpuhin, V. Tehnologija magnitno-impulsnojo abrabotki materialov (Technology of pulsed magnetic processing of materials). Samara,2014. 193c..(in Russian).
10. Jäger, A., Tekkaya, A. E., Online measurement of the radial workpiece displacement in electromagnetic forming subsequent to hot aluminium extrusion. In: Tekkaya, A. E., Daehn, G.S., Kleiner, M. (Eds.), High Speed Forming 2012, Proceedings of the 5th International Conference, Dortmund, Germany, pp. 13-22.
11. Jablonski, J.,Winkler,R. Analysis of the electromagnetic forming process. International Journal of Mechanical Sciences.Vol.20, (5), 1978, pp. 315–325.
12. Psyk, V., Risch, D., Kinsey, B. L., Tekkaya, A. E., Kleiner, M., Electromagnetic forming – A review. Journal of Materials Processing Technology 211 (5), pp. 787-829.
13. Chelluri, B., Knoth, E. Powder Forming Using Dynamic Magnetic Compaction, 4th International Conference on High Speed Forming, pp. 26–34, 2010.
14. Huang S.Y.,Meng Z.H., Li Y.C., Zhang B., and Ouyang W. Investigation of the density uniformity of pressed parts by low voltage electromagnetic compaction. Acte metallurgica, Vo1. 17, No. 6, 2004, pp.805-811.
15. Karpuhin,V., Glouschenkov,V. Pulse-Magnetic Technology of Joining Materials. In Proc. Of Int. Conf. JOM-10, Helsingor (Denmark), 2001, p. 365-370.
16. Mironov,V. Pulververdichtung mit Magnetimpulsen -Planseeberichte. Pulvermetallurgie1, 1976, Bd. 24, S. 175-190.
17. Dorozhkin, N., Mironov, V., Kot, A. Elektrofizicheskie metody poluchenija pokrytij iz metallicheskih poroshkov (Electrophysical methods of obtaining of coatings from metal powders). Riga, Zinatne, 1985, p. 131. (in Russian)
18. Mironovs,V., Boiko,I., Kolbe, M. Application of Pulse Electromagnetic Field for Joining of Powder Details, In Abstracts of 9th International Conference „Mechatronic Systems and Materials - MSM-2013”, Vilnius, Lithuania, pp.170 – 172.

# Process Analysis

# Analytical 1D-calculation of a 1-turn Coil Parameters for the Magneto-Forming Technology

**O. Mansouri[1*], O. Maloberti[1], D. Jouaffre[2], M. Hamzaoui[3], J. Derosiere[4], D. Haye[2], J. P. Leonard[5], P. Pelca[6]**

[1] ESIEE Amiens, France ; [2] PFT Innovaltech, Saint-Quentin, France ; [3] LTI-UPJV, Saint Quentin, France ; [4] BASIS-EP, Saint-Quentin, France ; [5] INDUXIAL, Albert, France ; [6] CLAL France, Bornel, France
[*]Corresponding author. Email: mansouri@esiee-amiens.fr

## Abstract

*In this paper, we will present an analytical modelling of a one-turn coil dedicated to magnetic-pulse technologies. The goal is to be able to determine the main useful parameters of an inductor by calculating the magnetic vector potential "A" diffusion. The concerned parameters are electromagnetic (electromagnetic fields, magnetic flux and electric current densities), electrical (resistance and inductance, maximum field coefficient) and electromechanical (Lorentz force density and maximum force coefficient). The results obtained will then be compared to numerical computations performed onto some test cases. In order to get an approximate but robust analytical solution, it is proposed to assume an axial symmetry and to solve the problem in the harmonic working condition before studying the transient state.*

## Keywords

Magnetic pulse forming and welding, Analytical methods, Bessel functions

## 1 Introduction

Electromagnetic problems are usually divided into three categories: low, intermediate, and high frequency. At low frequencies, static conditions are assumed; at high frequencies, wave equations are used. Both of these regions have been studied extensively. However, in the intermediate frequency range, where diffusion equations are used, only a few problems have actually been solved. The induction problems concerning the magnetic pulse technology fall

into this intermediate frequency region (Jackson, 1999). The magneto-forming is a shaping process for conducting materials. It takes profit from the Lorentz force effects that the oscillating magnetic field produces on a metal in which eddy currents are induced. The stake is the evaluation of this force through the fields and currents.

This paper proposes an analytical method in order to calculate the electromagnetic fields and densities that are generated by the current pulse in the inductor used in the magneto-forming technology. Different geometries of inductors are used to generate electromagnetic pulses. In several applications the single turn coil is preferable to the multi-turn coil because it is more robust (Psyk et al., 2011) and (Wilson et al., 1965). Single turn coils are used in pulsed magnetic technologies for which both magneto-harmonic and transient magnetic analyses are required. We suggest studying one single turn coil example made of a conducting massive coil. Due to a cut within the toroïdal coil between the two terminals, it is rigorously a 3D component with no axial symmetry. Because this cut is very small, we would like to investigate the possibility to reduce this geometry into an equivalent 2D and then 1D axi-symmetrical model, giving with good approximation the solution. Since the coil is highly conducting and the source is varying very quickly in time (from 10 to 100 kHz), we suggest computing the model with time harmonics in order to analyse the eddy currents, skin effects and induced Lorentz forces.

In the following we will first derive the general 1D Partial Differential Equation (PDE) in cylindrical coordinates, then solve the problem in the harmonic working condition, finally give the results onto the main electromagnetic fields, densities, and electrical and electromechanical parameters, before concluding.

# 2 Theory

The equations for the vector potential $\vec{A}$ can be derived from the Maxwell's equations:

$$\vec{\nabla} \wedge \vec{H} = \vec{j} + \frac{\partial \vec{D}}{\partial t} \tag{1}$$

$$\vec{\nabla} \wedge \vec{E} = -\frac{\partial \vec{B}}{\partial t} \tag{2}$$

$$\vec{\nabla} \cdot \vec{B} = 0 \tag{3}$$

$$\vec{\nabla} \cdot \vec{E} = \frac{\rho}{\varepsilon} \tag{4}$$

The medium is assumed to be linear, isotropic and homogeneous; the following relationships between $\vec{D}$ and $\vec{E}$, and $\vec{B}$ and $\vec{H}$ hold: $\vec{B} = \mu\vec{H}$ (5), $\vec{D} = \varepsilon\vec{E}$ (6); $\mu$ and $\varepsilon$ are respectively the absolute magnetic permeability and dielectric permittivity. The current density $\vec{j}$ can be expressed in terms of the Ohm's law: $\vec{j} = \sigma\vec{E}$ (7); where $\sigma$ is the electric conductivity.

**Eq. 6** and **Eq. 7** may be substituted into **Eq. 1** to obtain the curl of $\vec{H}$ in terms of $\vec{E}$:

$$\vec{\nabla} \wedge \vec{H} = \sigma\vec{E} + \frac{\partial \varepsilon \vec{E}}{\partial t} \tag{8}$$

The term $\sigma\vec{E}$ is much greater than $\partial\left(\varepsilon\vec{E}\right)/\partial t$, so the latter may be neglected for frequencies below about ten megacycles per second (Dodd et al., 1968) and (Dodd, 1967). The magnetic induction field $\vec{B}$ may be expressed as the curl of a magnetic vector potential $\vec{A}_i$, **Eq. 9** replacing **Eq. 9** in **Eq. 2** and **Eq. 7** give **Eq. 10** and **Eq. 11.**

$$\vec{B} = \vec{\nabla} \wedge \vec{A}_i \tag{9}$$

$$\vec{\nabla} \wedge \vec{\mathrm{E}} = -\frac{\partial}{\partial \mathrm{t}} \vec{\nabla} \wedge \vec{\mathrm{A}}_{\mathrm{i}} = -\vec{\nabla} \wedge \frac{\partial \vec{\mathrm{A}}_{\mathrm{i}}}{\partial \mathrm{t}} \tag{10}$$

$$\vec{j} = \sigma\vec{E} = -\sigma\frac{\vec{A}_i}{\partial t} - \sigma\vec{\nabla}V \tag{11}$$

where *V is* an electric scalar potential. The coil may be driven by a voltage generator with an applied voltage *V*. The total electric field $\vec{E}$ is thus the sum of the source field $\vec{E}_s = -\vec{\nabla}V$ and the induced field $\vec{E}_i = -\partial_t\vec{A}_i$. In the following, we investigate the possibility to look after a total magnetic potential $\vec{A}$ responsible for the total electric field $\vec{E}$ and the total electric current density $\vec{j}$ such that:

$$\vec{E} = -\frac{\partial \vec{A}}{\partial t},\ \vec{j} = -\sigma\frac{\partial \vec{A}}{\partial t} \text{ and } \vec{B} = \vec{\nabla} \wedge \vec{A} \tag{12}$$

By using the Coulomb gauge $\vec{\nabla}.\vec{A} = 0$, **Eq. 12**, **Eq. 9** and **Eq. 5** into **Eq. 1**, we obtain:

$$\Delta\vec{A} - \mu\sigma\frac{\partial \vec{A}}{\partial t} = 0 \tag{13}$$

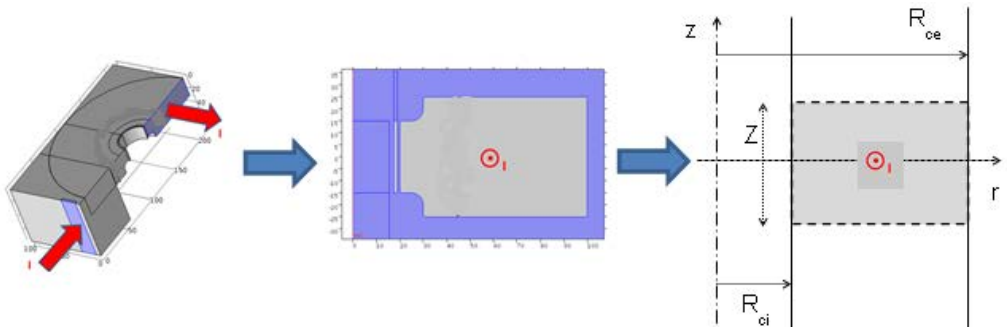


***Figure 1**: Geometry of the 3D geometry and its 2D reduced model*

Fig.1 shows the inductor in 3, 2 and 1 dimensions respectively. The present analytical model is made on the basis of a 1D scheme. In 1D axial symmetric model only the (orthoradial) components $A\Phi$ and $j\Phi$ are present in the magnetic vector potential $\vec{A}$ and in the current density $\vec{j}$ . Then, we obtain the homogeneous Partial Differential Equation (PDE) **Eq. 14** of the inductor in cylindrical coordinates *(r,ϕ,z)* while neglecting both the *z* and *ϕ* dependences.

$$\frac{\partial^2 A_\phi}{\partial r^2} + \frac{1}{r}\frac{\partial A_\phi}{\partial r} - \frac{A_\phi}{r^2} - \mu\sigma\frac{\partial A_\phi}{\partial t} = 0 \tag{14}$$

# 3 Harmonic Model

Assuming that both the voltage *V* and the total current *I* are sinusoidal functions of time, $V \equiv Ve^{i(\omega t+\varphi)}$ and $I \equiv Ie^{i\omega t}$ . Then the vector potential is likewise a sinusoidal function of time, $A_\phi \equiv A_\phi e^{i\omega t}$ , with $A_\phi$ a complex magnitude. **Eq. 14** is then written as follows:

$$\frac{\partial^2 A_\phi}{\partial r^2} + \frac{1}{r}\frac{\partial A_\phi}{\partial r} - \frac{A_\phi}{r^2} - i\omega\mu\sigma A_\phi = 0 \tag{15}$$

## 3.1 General Solution of the Homogeneous PDE

By using the global form of vector potential *A*, we consider that the total current density is included in the vector potential equation. For this, The 1D PDE and its solution in the harmonic working condition are given in **Eq. 16** and **Eq. 17.** (μ is the magnetic permeability of the coil, σ is the electrical conductivity of the coil, ω is the angle velocity of the current, $\alpha^2 = \mu\sigma\omega$. **Eq. 16**, is called the modified Bessel equation, for which the solution is given by **Eq. 17** (Andrew Gray et al., 1985) and (Figueiredo Jardim et al., 1989).

$$r^2\frac{\partial^2 A_\phi}{\partial r^2} + r\frac{\partial A_\phi}{\partial r} - (1 + ir^2\alpha^2)A_\phi = 0 \tag{16}$$

$$A_\emptyset(r,\omega) = C_1 J_1(\alpha_1 r) - i * C_2 K_1(\alpha_2 r) \tag{17}$$

With $\alpha_1 = \alpha.r.e^{(\frac{3\pi}{4}i)}$ and $\alpha_2 = \alpha.r.e^{(\frac{\pi}{4}i)}$, and where $J_1$ is the Bessel function of order 1 and first kind, and $K_1$ is the modified Bessel function of order 1 and second kind. The constants $C_1$ and $C_2$ can be determined from the boundary conditions and constraints (see next section).

## 3.2 Complete Solution with Limit Conditions and Constraints

We now need a limit condition on the surface field, and a total current constraint, and we assume that the inductor has a finite equivalent length $Z_2$ along the z axis (even if no z dependence is considered, see § 3.3).

$$I = \int_{R_{ci}}^{R_{ce}} \int_{-Z_2/2}^{+Z_2/2} j dr dz = -\sigma Z_2 i\omega \int_{R_{ci}}^{R_{ce}} A_\emptyset(r,\omega) dr \quad (18)$$

$$I = \oint Hdl = H_z(R_{ci},\omega)Z_2 = \frac{B_z(R_{ci},\omega)Z_2}{\mu_0} = \frac{Z_2}{\mu_0}\left(\frac{A_\emptyset(R_{ci},\omega)}{R_{ci}} + \partial_r A_\emptyset(R_{ci},\omega)\right) \quad (19)$$

After some mathematical operations, we get:

$$C_1 = \frac{C_{12}K_0(\alpha_2 R_{ci}) - C_{22}(K_0(\alpha_2 R_{ce}) - K_0(\alpha_2 R_{ci}))}{K_0(\alpha_2 R_{ci})\left(J_0(\alpha_1 R_{ce}) - J_0(\alpha_1 R_{ci})\right) - J_0(\alpha_1 R_{ci})(K_0(\alpha_2 R_{ce}) - K_0(\alpha_2 R_{ci}))} \quad (20)$$

$$C_2 = \frac{C_{22}\left(J_0(\alpha_1 R_{ce}) - J_0(\alpha_1 R_{ci})\right) - C_{12}J_0(\alpha_1 R_{ci})}{K_0(\alpha_2 R_{ci})\left(J_0(\alpha_1 R_{ce}) - J_0(\alpha_1 R_{ci})\right) - J_0(\alpha_1 R_{ci})(K_0(\alpha_2 R_{ce}) - K_0(\alpha_2 R_{ci}))} \quad (21)$$

where:

$$C_{12} = \frac{I\alpha_2}{\sigma Z_2 \omega} \quad (22)$$

$$C_{22} = -i\frac{I\mu_0}{Z_2\alpha_2} \quad (23)$$

## 3.3 How to Include the Z Dimension

The analytical model is calculated in one dimension for which the total length $Z$ of the inductor should tend to the infinite. To qualify this modeling, we have compared the results to 2D numerical results obtained with the Finite Element method. The discrepancy between analytical and numerical results is mainly due to the finite $Z$ dependence of the actual electromagnetic fields and densities. In order to reduce this error, we must take the dimension « Z » into account. In the 2D numerical simulations, we can observe that the current density $j$ is expanding along the direction z with a longer equivalent length $Z_2=(Z+2\Delta Z)$, including the edges of equivalent length $\Delta Z$ at both sides (Fig. 2). As a conclusion, we propose to use $Z_2$ instead of $Z$ inside the previous solution. The absolute and relative difference $2\Delta Z$ between $Z_2$ and $Z$ can be expressed and estimated as a function of $R_{ci}$ and $Z$ : $\Delta Z = (Z_2\text{-}Z)/2 = f(Z,Rci)$ (24). The first analysis consists in adjusting the value of $\Delta Z$ for a fixed radius $R_{ci}$ and various coil length $Z$, in order to fit the 2D numerical data. We observe that $\Delta Z$ depends only very slightly on the length Z, but the relative error $\Delta Z/Z$ is rapidly decreasing when the length is increasing, rendering the 1D assumption more relevant (Fig. 2). Next analysis might consider the dependence of the relative error $\Delta Z/Z$ on the radius *Rci*; which should be easier to interpret thanks to an analytical 2D model.

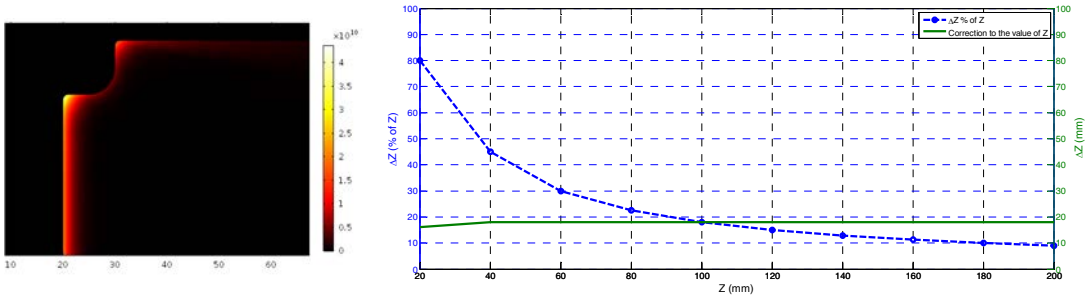


***Figure 2**: Numerical computation of the current density distribution and variation of the ΔZ correction factor according to the length Z of inductor.*

### 3.4 How to Compute Electrical and Electromechanical Parameters

The magnetic vector potential solution $\vec{A}$ in Eq. 17 can be used to compute the whole electromagnetic fields $\vec{B}$, $\vec{H}$, $\vec{E}$ and $\vec{j}$ thanks to Eq. 12, Eq. 5 and Eq. 7. As a consequence, it becomes finally possible do deduce global quantities such as the Joule losses Pj=∫∫∫(j2/(2σ))d3x, the equivalent coil resistance R (Eq. 25), the stored magnetic energy Wm-Wm0=∫∫∫(jA/2)d3x, the equivalent coil inductance L (Eq. 26), the maximum field coefficient Kb (Eq. 27) and the maximum force density coefficient Kf (Eq. 28).

$$P_j = \iiint_{coil} \frac{1}{2}\sigma(\omega A)^2 r dr d\emptyset dz \text{ and } R = \frac{2P_j}{I^2} \quad (25)$$

$$W_m = W_{m0} + \iiint_{coil} \frac{1}{2}\sigma\omega A^2 r dr d\emptyset dz \text{ and } L = \frac{2W_m}{I^2} \quad (26)$$

$$B_{max} = max\{|\vec{B}\cdot\overrightarrow{u_z}|\} \text{ and } K_b = \frac{B_{max}}{(I/(Z*(R_{ce}-R_{ci})))} \quad (27)$$

$$f_{max} = max\{|\vec{f}\cdot\overrightarrow{u_r}|\} \text{ and } K_f = \frac{f_{max}}{\omega(I/(Z*(R_{ce}-R_{ci})))^2} \quad (28)$$

## 4 Simulation and Experimental Results

The geometrical parameters of the inductor are given in the Appendix; the coil length is: *Z=20…200 mm*; the current peak is: *I=825(Z[mm]/30) kA* (*I/(Z*(Rce-Rci))* stays constant, the reference current being 825 kA when *Z=30 mm*); the frequency is: *F = 20 kHz*.
In the following, we will analyze the results on *j*, *B* and *f* obtained as follow:

$$\vec{j} = j\overrightarrow{u_\varphi} = -\sigma\omega A\overrightarrow{u_\varphi} \quad (29)$$

$$\vec{B} = B\overrightarrow{u_z} = \left(\frac{A}{r} + \frac{\partial A}{\partial r}\right)\overrightarrow{u_z} \quad (30)$$

$$\vec{f} = f\overrightarrow{u_r} = real(j.B^*)\overrightarrow{u_r} \quad (31)$$

## 4.1 Electromagnetic Fields and Densities

**Fig. 2**, **Fig. 3** and **Fig. 4** show the results obtained for the magnitude of the current density |j|, the flux density |B| and the Lorentz force density |f| respectively (complex modules).

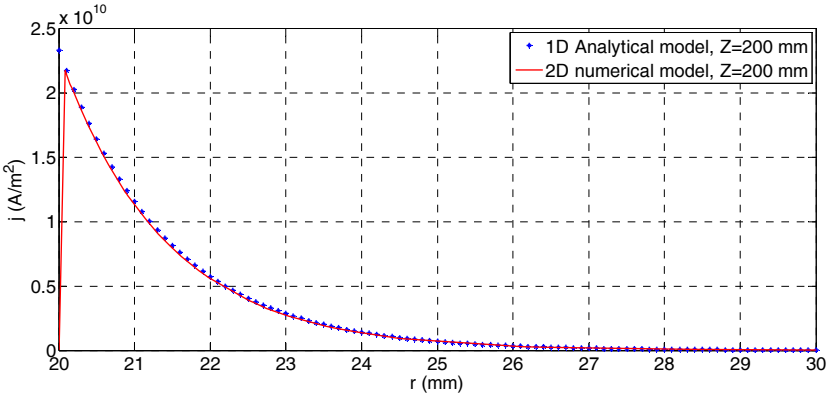


***Figure 3**: Current density distribution inside the coil (Z = 200 mm)*

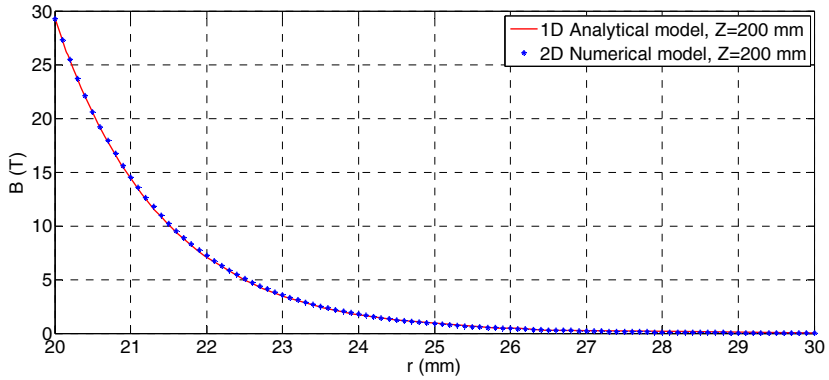


***Figure 4**: Magnetic flux density distribution inside the coil (Z = 200 mm)*

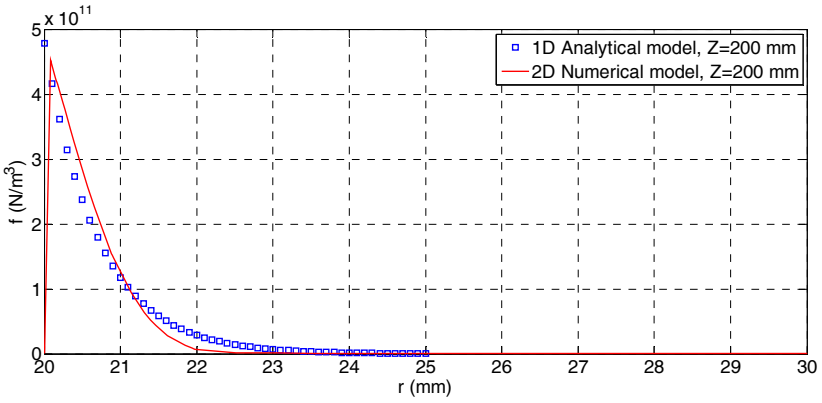


***Figure 5**: Lorentz force density distribution inside the coil (Z = 200mm)*

Fig. 3, Fig. 4 and Fig. 5 show an interesting agreement between numerical and analytical calculations for the main tendency due to the skin effect. The discrepancy is due to the dependence on z coordinate but this last can however be reduced thanks to the $\Delta Z$

correction factor (see Fig. 2 and Fig. 6). Either any disparity between the two methods or any deterministic relationship between $\Delta Z$, $R_{ci}$ and $Z$ can be improved and found by a 2D resolution.

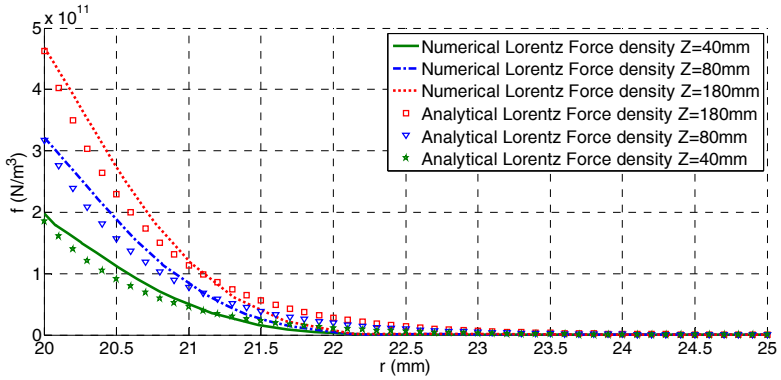


***Figure 6**: Lorentz force density distribution inside the coil (Z = 40, 80 and 200 mm)*

Finally, it is possible to go further in the modelling technique by either considering:

1) the reduced potential $\vec{A}_i$ and the source field inside **Eq. 13** to **Eq. 16**,
2) the transient effect by solving the time dependent **Eq. 14**,
3) the z dependence by solving the 2D PDE coming from **Eq. 13**,
4) any second or third region to model a field shaper or a tube to deform.

## 4.2 Electrical and Electromechanical Parameters

In this section Fig. 7 and Fig. 8 show the results obtained for the electrical (equivalent coil resistance $R$ and inductance $L$) and electromechanical (maximum field coefficient $K_b$ and maximum force density coefficient $K_f$) parameters respectively (see **Eq. 25**, **Eq. 26**, **Eq. 27** and **Eq. 28**).

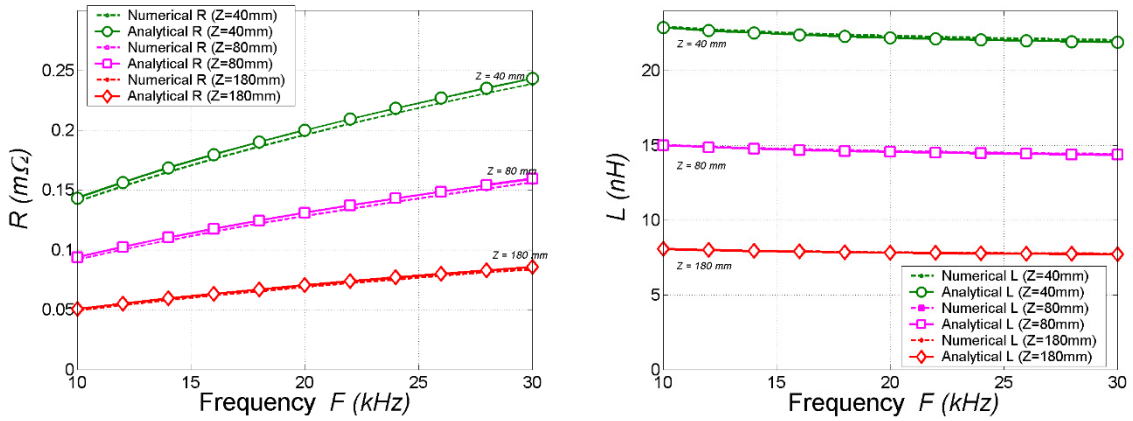


***Figure 7**: The equivalent coil resistance and coil inductance defined by **Eq. 25** and **Eq. 26** as a function of the frequency F (Z = 40, 80 and 180 mm).*

As expected, we can see on figures Fig. 7 that the resistance is increasing while increasing the frequency (skin effect resistance) and decreasing while increasing the coil length or section. For similar reasons, the inductance is decreasing while increasing the frequency (skin effect inductance) and also decreasing while increasing the coil length or section.

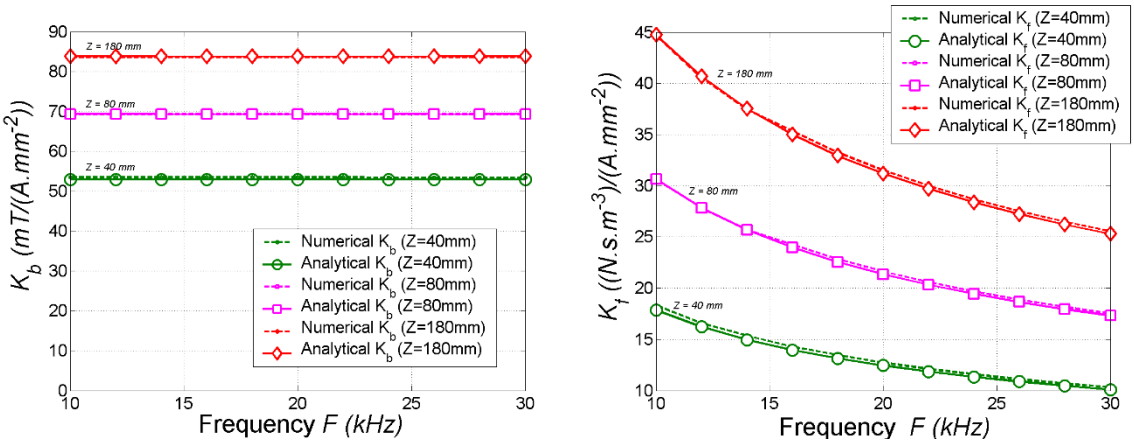


***Figure 8**: The maximum field coefficient and the maximum force density coefficient defined by **Eq. 27** and **Eq. 28** as a function of the frequency F (Z = 40, 80 and 180 mm).*

In the same time, we can see on figures Fig. 8 that the maximum field coefficient stays constant whatever the frequency is (no skin effect dependent) and that this coefficient is increasing while increasing the coil length but with a limit around 101 mT/(A.mm$^{-2}$) which corresponds to the perfect infinite coil. Finally the maximum force density coefficient is decreasing while increasing the frequency and increasing while increasing the coil length but still with a limit around 65 (N.s.m$^{-3}$)/((A.mm$^{-2}$)$^2$).

The figures Fig. 7 and Fig. 8 permit to check that the 1D model proposed is also able to compute the main electrical and electromechanical parameters as a function of the frequency $F$ and the coil length $Z$. All the main parameters are correctly computed but unfortunately, an unknown initial stored energy $W_{m0}$ is necessary to get the correct inductance value. This might be due to the choice of the total magnetic vector potential instead of the reduced potential $\vec{A}_i$ inside **Eq. 13** to **Eq. 16**.

# 5 Conclusion

Starting from the general 1D Partial Differential Equation (PDE) and using a series development in a space of well-chosen base functions, it is possible to get a simple analytical solution. This method might ease the couplings between electrical, electromagnetic and mechanical effects. This method will help for: 1) the magnetic pulse process simulation, 2) the inductor sizing and optimization, 3) the choice of optimal working conditions.

# Acknowledgments

We would like to express our gratitude to the Picardie Region, the Technopole and IndustriLab who gave a financial support to this work under the project "COILTIM".


# References


Jackson, J. D., 1999, Classical Electrodynamics, Third Edition, John Wiley & Sons, Inc.

Psyk, V., Risch, D., Kinsey, B. L., Tekkaya, A. E., Kleiner, M., 2011, Electromagnetic Forming – A review, Journal of Materials Technology 211 (2011) 787 – 829.

Wilson, M. N., Srivastava, K. D., 1965, Design of Efficient Flux Concentrators for Pulsed High Magnetic Fields, The Review of Scientific Instruments, Vol. 36, N° 8, August 1965,

Dodd, C. V. and Deeds, W. E., 1968, Analytical Solutions to Eddy-Current Probe-Coil Problems, J. Appl. Phys. 39, 2829,1968.

Dodd, C. V., 1967, A Solution to Electromagnetic Induction Problems, M. S. Thesis, University of Tennessee, Oak Ridge National Laboratory, 1967.

Andrew Gray, M.A., G. B. Mathews, M.A., 1985, a treatise on bessel functions and their applications to physics, Macmillan and co. and New York. 1985.

Figueiredo Jardim, R., Laks, B., 1989, Kelvin functions for determination of magnetic susceptibility in nonmagnetic metals, J. Appl. Phys. 65(12), 15 June 1989.


# Appendix A Geometrical and Physical Parameters

## A.1 Parameters of the Coil Geometry

| Name | Value | significance |
|---|---|---|
| $R_{ci}$ | 20 mm | Internal coil radius |
| $R_{cii}$ | 30 mm | Intermediate coil radius |
| $R_{ce}$ | 100 mm | External coil radius |

***Table 1**: Parameters of the coil geometry*

## A.2 Parameters of the Materials

| Name | Value | significance |
|---|---|---|
| $\mu_0$ | $4\pi.10^{-7}$ H.m$^{-1}$ | Vacuum magnetic permeability |
| $\sigma_c$ | 10 % IACS* | Coil electrical conductivity |
| $\sigma_{Cu}$ | 5.8 e$^7$ S.m$^{-1}$ | Copper electrical conductivity |

***Table 2**: Parameters of the materials (@20°C)*

*IACS: International Annealed Copper Standard (100 % IACS = $\sigma_{Cu}$)

# Analytical and Numerical Investigation of Tube Compression with a Multi-Turn, Axisymmetric Coil

**A. Nassiri, S. Zhang, K. Reisert, B. Kinsey***

Department of Mechanical Engineering, University of New Hampshire, USA
*Corresponding author. Email: brad.kinsey@unh.edu

## Abstract

*While some Finite Element software packages exist that are capable of modelling the electromagnetic forming process and estimating the corresponding process parameters (e.g., magnetic pressure and workpiece velocity), there is a lack of simplified and accuracy analytical modelling tools for this purpose. In this study, a coupled analytical model was created to predict the magnetic pressure generated by a multi-turn, axisymmetric coil and the corresponding tube radial displacement and velocity. In the proposed model, at each time increment, the magnetic field geometry is updated in response to the tube deformation. To assess the proposed analytical model, numerical simulations were conducted where the pressure distribution from the analytical model was applied. The results show good agreement between analytical and numerical results.*

## Keywords

Forming, Modelling, Electromagnetic tube compression

## 1 Introduction

The electromagnetic forming (EMF) process is an innovative high speed forming technology widely used in aerospace and automobile industries. It is a safer process than explosive forming and can be easily performed to shape hollow profiles and sheet metal parts made of electrically conductive materials. The setup of EMF includes a fast acting, high power switch; a capacitor bank; a coil; workpiece(s); and additional application specific components, e.g., a mandrel and field shaper for tubular workpieces.

In contrast to the quasi-static forming process, the pressure pulse in EMF causes high strain rate in the workpieces with the entire process being completed O(100μs). The capacitor bank and switch constitute the pulsed power generator. The electrical energy is quickly dissipated into the coil with a damped sinusoidal current trace. A magnetic field is generated, and eddy currents are induced in the workpiece, which flow in the opposite direction to the coil current. These two opposite currents and magnetic fields cause a repulsive Lorentz force between the workpiece and the coil (see Fig. 1). If the Lorentz force is sufficient, the workpiece is plastically deformed or sheared (Nassiri et al., 2014), i.e., if the stress induced is greater than the yield or shear strength of the material, respectively.

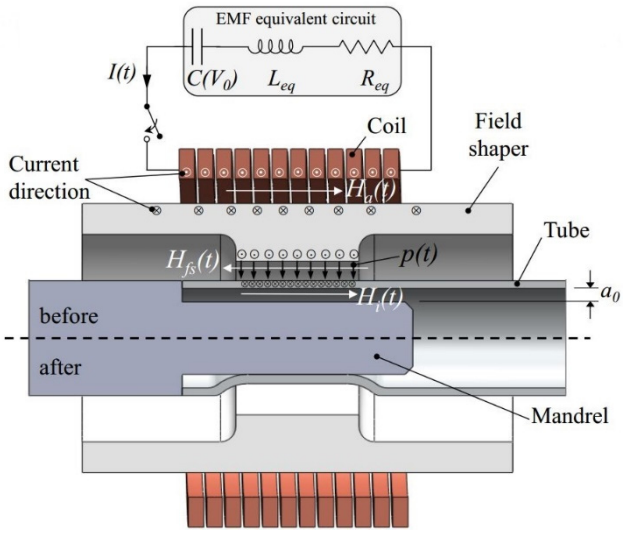


***Figure 1**: Schematic of the Electromagnetic Forming (EMF) process (Geier et al., 2013)*

Numerical simulations of the EMF are beneficial to assess the process as opposed to time consuming and costly experimental investigations. Weddeling et al. (2015) and Lorenz et al. (2014) used two software packages to model the entire EMF process through coupled electromagnetic (ANSYS) and mechanical (LS-DYNA) simulations. Alternatively, Nassiri et al., (2015b) used Abaqus/Explicit for interface investigations during impact welding by simply inputting velocity into the simulations to solve the mechanical component and observed a wavy morphology at the interface. While FEA simulations of the EMF process are effective for estimating the critical process parameters numerically, analytical models can also be effective and less computational and time intensive. Thibaudeau and Kinsey (2015) presented an analytical model to calculate the initial workpiece acceleration, velocity and position during a sheet EMF process with the assumption of rigid body motion of the workpiece. In the analytical model by Hahn et al. (2016), rigid-plastic theory was assumed to represent the material behaviour in response to the forming pressure in magnetic pulsed welding. Finally, similar to the work presented in this paper, Weddeling et al. (2015) numerically and analytically predicted the radial forming displacement during tube compression while also validating the results through experiments.

In this research, an analytical model for determining the pressure distribution applied to the workpiece and the subsequent workpiece radial position and velocity for a multi-turn, axisymmetric coil with field shaper was investigated. In the model, at each time increment, the magnetic field is automatically updated in response to the tube deformation. Compared to previous analytical modelling efforts (Thibaudeau and Kinsey, 2015, Nassiri et al., 2015a, Weddeling et al., 2015, Hahn et al., 2016), a rigid body or a rigid-plastic material assumption was eliminated. Alternatively, plastic deformation of the workpiece during the forming process was taken into account at each time increment. In addition, the coupling factors between the coil, field shaper, and workpiece were experimentally measured and incorporated into the analytical model. The analytical model was then numerically verified using the Abaqus/Explicit to calculate radial position and velocity of the workpiece. Good agreement between the analytical and numerical model results was obtained.

# 2 Analytical Model

The basic EMF process consists of three fundamental parts: a capacitor bank to store energy, a coil to create the magnetic field, and a workpiece to be formed. Based on the multi-physics nature of the EMF process, the analytical model was divided into three stages. First electrical theory was used to determine the primary current and voltage out of the capacitor bank and passing through the coil. Second, the magnetic field distribution and the effective magnetic pressure that was developed on the workpieces were calculated from electromagnetic analyses. Lastly, classical mechanics theory was used to determine the velocity of the workpiece caused by the effective magnetic pressure. Since the magnetic field distribution strongly depends on the gap distance between the field shaper and workpiece, the magnetic and mechanical processes were coupled. To calculate the workpiece displacement, a simplified plasticity model was incorporated into the algorithm. At each time increment, the magnetics field geometry was updated with an incremental displacement of the workpiece and hence the model includes the new gap between the field shaper and workpiece. See the flowchart of the model in Fig. 2.

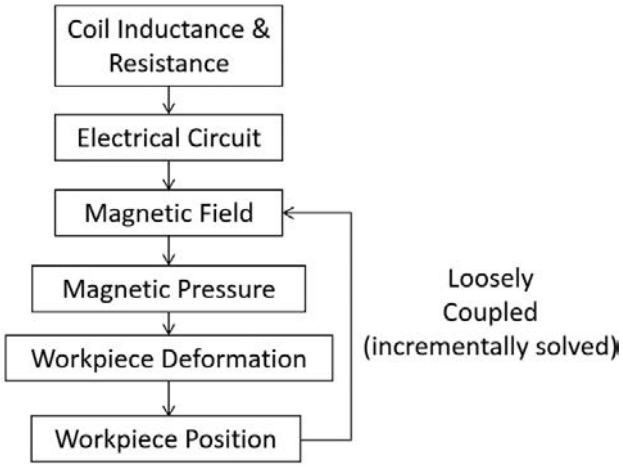


***Figure 2**: Flowchart of the analytical model*

In this study, a commercially purchased multi-turn, axisymmetric coil (Poynting, model: SMU-K100-4/65) was used. The workpiece was a Cu101 tube with a length of 100mm, wall thickness of 0.88mm and outer diameter of 25.36mm. In tube compression processes, usually, a "field shaper" is positioned between the coil and workpiece to concentrate the magnetic field generated (see Fig. 3a and 3b).

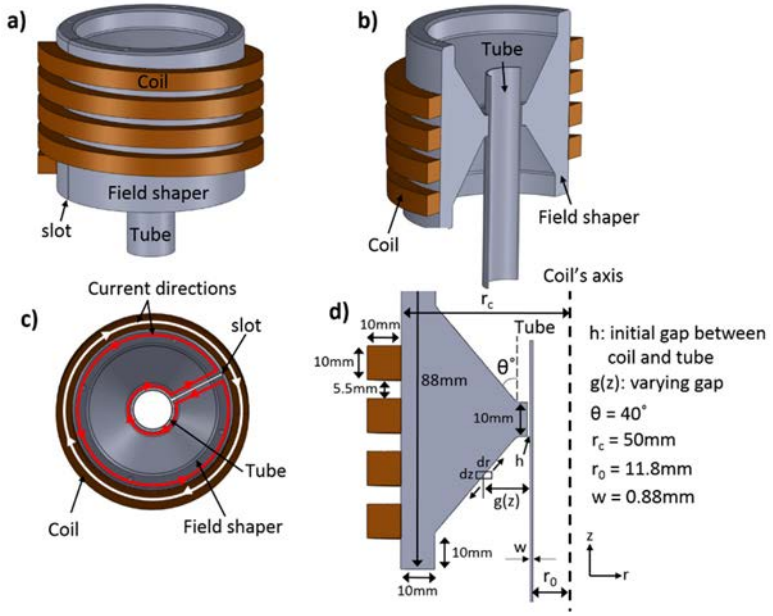


***Figure 3**: Schematic of multi-turn, axisymmetric coil with field shaper and tube: a) full view, b) half view, c) current directions, and d) cross-section*

A quick discharge of the capacitor bank causes a damped sinusoidal current flowing through the coil which induces a related electromagnetic field. Then, in the field shaper which acts as a short circuited second winding of a current transformer, a secondary current is induced. Due to the skin effect and Lenz' law this induced current flows opposite to the coil current at the outer surface of the field shaper (Psyk et al., 2011). At the axial slot, the current is directed to the inner surface of the field shaper in which the current direction is the same as in the coil (see Fig 3c). Compared to the outer surface of the field shaper, the inner area is much smaller, resulting in a higher current density and higher field strength. For this analysis, a series of elements were generated along the surface of the field shaper. The elements were equally spaced, dz, in the axial direction (i.e., z-direction) and the width of each element, dr, was equal to the skin depth (see Fig 3d).

## 2.1 Electrical Theory

The electrical circuit, consisting of the capacitor bank, coil, field shaper and workpiece, can be represented by ideal electrical elements and circuits (see Fig. 4). As is clear from Fig. 4, both the primary and induced circuits are coupled with the secondary circuit through the mutual inductances (i.e., $M_1$ and $M_2$) which are a measure of induction between the two circuits. A "coupling factor" ($k$) represents the loss of magnetic flux with a value between

$0 \leq k \leq 1$. In this study, the two coupling factors (i.e., $k_1$ and $k_2$ corresponding to $M_1$ and $M_2$ respectively) were experimentally measured by placing a Rogowski coil in two different locations in the experimental set-up and calculating the ratios of the secondary to primary current ($k_1 = 0.78$) and induced to secondary current ($k_2 = 0.91$). Applying Kirchhoff's voltage law and summing the voltages around the primary circuit, a differential equation is obtained with respect to time, $t$ (Ogata, 2004)

$$\frac{1}{C_m}\int i_p\, dt + i_p R + L\frac{di_p}{dt} = 0 \tag{1}$$

where $C_m$ is the capacitance of the machine, $i_p$ is the current in the primary circuit, $R = R_m + R_c$ is the total resistance, and $L = L_m + L_c$ is the total inductance. Note that the resistance and inductance of the machine, $R_m$ and $L_m$, can be determined experimentally with a known capacitance by calculating the damped natural frequency and damping ratio of the RLC circuit. Resistance and inductance of the coil, $R_c$ and $L_c$, are functions of the material properties (i.e., resistivity of the coil), the geometry of the coil, current condition (i.e., the angular frequency), and the cross-sectional area of the coil contained from the skin depth to the surface of the coil. For detailed information see Nassiri et al. (2015a) and Zhang et al., (2004).

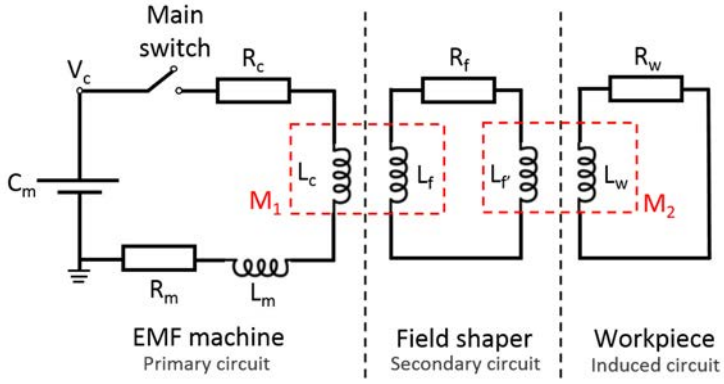


***Figure 4**: Configuration of three circuits and two coupling systems*

To solve the differential equation, i.e., Eq. (1), the initial conditions were specified from the charged capacitor bank with the main switch closing at $t = 0$;

$$i_p(0) = 0, \qquad \frac{di_p}{dt}(0) = \frac{V_i}{L} \tag{2}$$

where $V_i$ is the initial voltage in the capacitor bank

$$V_i = \sqrt{\frac{2E}{C_m}} \tag{3}$$

where E is the total energy stored in the machine. The solution of the differential equation, Eq. (1), yields the variation of the primary circuit current with time and can be expressed as

$$i_p(t) = \frac{V_i}{\sqrt{1-\zeta^2}} \sqrt{C_m/_L}\; e^{-\zeta\omega_n t}\, sin\, \omega_n \sqrt{1-\zeta^2}\, t \tag{4}$$

where $\omega_n$ is the natural frequency and $\zeta$ is a damping factor of the circuit. Lastly, capacitor voltage can be calculated by integrating the current out of the capacitor

$$V_c(t) = \int -i_p(t)dt \; + \; V_i \tag{5}$$

## 2.2 Magnetic Theory

The magnetic field produced from a given axisymmetric coil can be determined with respect to the physical location of the tube and the gap distance between the field shaper and tube. As is clear from Fig 2d, because of the tapered geometry of the field shaper, the gap distance is varied along the thickness of the field shaper (i.e., $g(z)$). The magnetic flux density, $\vec{B}$, produced by the coil induces eddy current in the workpiece with a current density, $\vec{J}$ . The current density, $\vec{J}$, is related to the magnetic field, $\vec{H}$, through a partial derivative in the radial direction. A Lorentz force is created which acts as a volume force, $\vec{F}$, (Nassiri et al. 2015a)

$$\vec{F} = -\mu_m \vec{H} \frac{\partial \vec{H}}{\partial r} = \; -\frac{1}{2}\mu_m \frac{\partial(\vec{H}^2)}{\partial r} \tag{6}$$

The body force, $\vec{F}$, is integrated through the thickness of the tube to determine the pressure acting on the tube surface

$$\mathrm{P} = \int_0^w \vec{F} dr = \frac{1}{2}\mu_m H_{gap}^2 \tag{7}$$

where the integration limit, $w$, is the tube thickness (see Fig. 3d) and $H_{gap}$ is the gap magnetic field strength. In this study, the penetrated magnetic field was neglected due to the skin effect. Also, the air space between the coil and workpiece was not considered in the magnetic calculation because its permeability is close to that of free space. The magnetic field strength, $H_{gap}$, is the resultant field of a superposition of magnetic field strength from many current carrying differential elements, $dH_{gap}$ (see Fig 2d). For the axisymmetric coil investigated in this study, only the magnetic field strength along the coil's axis is of interest (i.e., tangential to the workpiece because this will create a force in the radial direction according to the cross product $\vec{F} = \vec{J} \times \vec{B}$ ) (Al-Hassani, 1975),

$$H_z = \frac{i}{2\pi}\left[\frac{g(z)-r}{(g(z)-r)^2+z^2} + \frac{g(z)+r}{(g(z)+r)^2+z^2}\right] \quad (8)$$

where $g(z)$ is the varying gap between the coil element and the workpiece and $i$ is the current in the element. As is clear from Eq. (8), the magnetic field strength strongly depends on the radial gap between the field shaper and workpiece.

## 2.3 Mechanical Theory

Knowing that the workpiece in the forming process is plastically deformed, a simple plasticity model was employed to evaluate the exact deformation of the workpiece in each time increment. Longitudinal and hoop stresses can be easily calculated by knowing the applied external pressure and radius of the workpiece, $r$, (see Fig 3d).

$$\sigma_L = \frac{Pr}{2w} \;\; \& \;\; \sigma_H = \frac{Pr}{w} \quad (9)$$

The effective stress, assuming von Mises yield criterion was calculated as

$$\bar{\sigma} = \sqrt{{\sigma_H}^2 + {\sigma_L}^2 - \sigma_H\sigma_L} \quad (10)$$

The effective stress, strain and strain-rate relation was defined as

$$\bar{\sigma} = C'\bar{\varepsilon}^n\dot{\varepsilon}^m \quad (11)$$

where $C'$ is the strength coefficient and $n$ and $m$ are the strain and strain-rate hardening exponents respectively. In this study, these parameters were obtained (i.e., $C' = 480\ MPa$, $n = 0.01$, and $m = 0.04$) from Split-Hopkinson Pressure Bar experimental tests on Cu101 (Bragov et al., 2006). The strain rate term in this equation was simply used to shift power hardening curve based on the strain rate in the test. From Eq. (11), $\bar{\varepsilon}$ was calculated. Neglecting the longitudinal strain ($\varepsilon_L = 0$) and considering $d\varepsilon_H + d\varepsilon_t = 0$ (note that this assumption was confirmed experimentally by measuring the axial elongation), the effective strain was evaluated, again assuming von Mises yield criterion, as

$$\bar{\varepsilon} = \frac{2}{\sqrt{3}}\varepsilon_H \quad (12)$$

Finally, the hoop strain, $\varepsilon_H$ was calculated from

$$\varepsilon_H = ln\frac{r_{i-1}}{r_i} \quad (13)$$

To obtain the radial location change from time increment, $i-1$, to $i$, at each axial location. An updated gap between the field shaper and workpiece was then calculated inside a loop by knowing the gap at the previous step and the current incremental displacement of the workpiece. Integrating Eq. (8) over the entire coil thickness yields

$$H_{gap} = \int_0^z \int_0^r H_z dr dy \tag{14}$$

Substituting Eq. (14) in Eq. (7) yields a pressure distribution acting on the workpiece at each time increment. From the radial position data, the velocity of the workpiece was also determined.

# 3 Numerical Simulations

To validate the analytical result, numerical simulation was performed on the commercial FEA package Abaqus/Explicit. A two dimensional, axisymmetric model was used in this study. The dimensions of the model were exactly the same as mentioned in the analytical modelling section, i.e., length of 100mm, tube thickness of 0.88mm, and outer tube diameter of 12.68mm (see Fig. 5). As in the analytical model, Eq. (11) was also utilized as the material model for Cu101 for the numerical simulations.

For boundary conditions, only the bottom end was fixed in all directions, the top end was free to move. This is consistent with an experimental set-up available for this process. The deformation area was at the middle of the tube where the pressure distribution obtained from analytical model was applied (see Fig. 5). The numerical analysis with the pressure distributions response at both 2.4kJ and 3.6kJ energy discharges were performed. The element type was 4 node, bilinear, axisymmetric, quadrilateral element (CAX4R) with 14400 elements (24 elements through the thickness) in the deformation area (which is 20 mm long based on the pressure distribution) and 1920 elements in the top and bottom areas. A mesh sensitivity analysis was also performed to assure that the mesh density used was not affecting the numerical result.

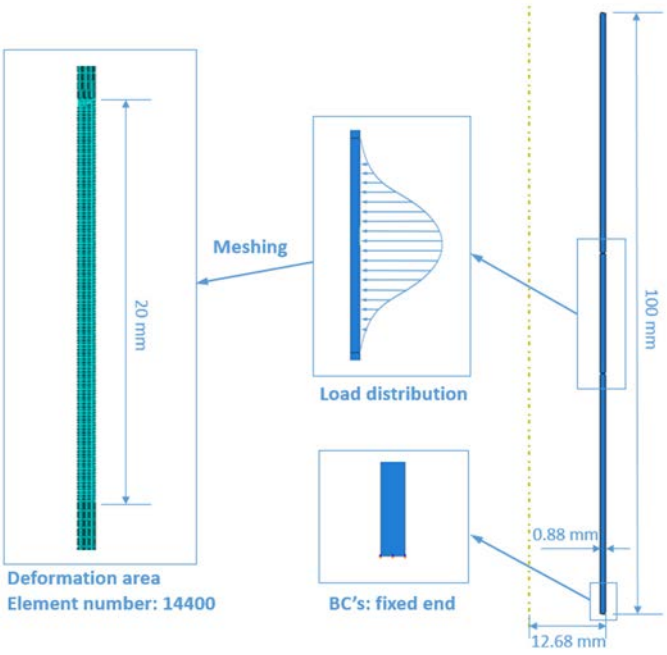


***Figure 5**: Schematic of FEA model*

# 4 Results

Results from the analytical model include electrical, magnetic, and mechanical predictions. The electrical analysis determines the electrical parameters of the coil and the electrical response of the EMF machine. The predicted circuit response at 2.4kJ energy discharge is shown in Fig. 6 while the spatial magnetic pressure distribution along the workpiece with respect to time is shown in Fig. 7. Clearly for such a coil, the pressure pulse from the first half cycle of the current pulse is more significant than the later oscillations. Thus, the forming event occurs during this timeframe.

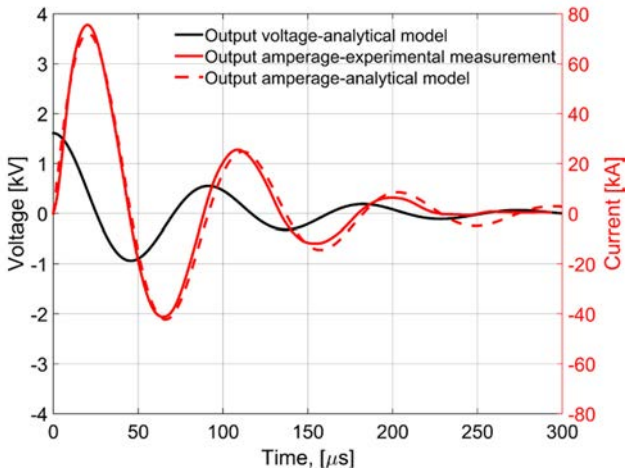


***Figure 6**: Predicted current and voltage during discharge*

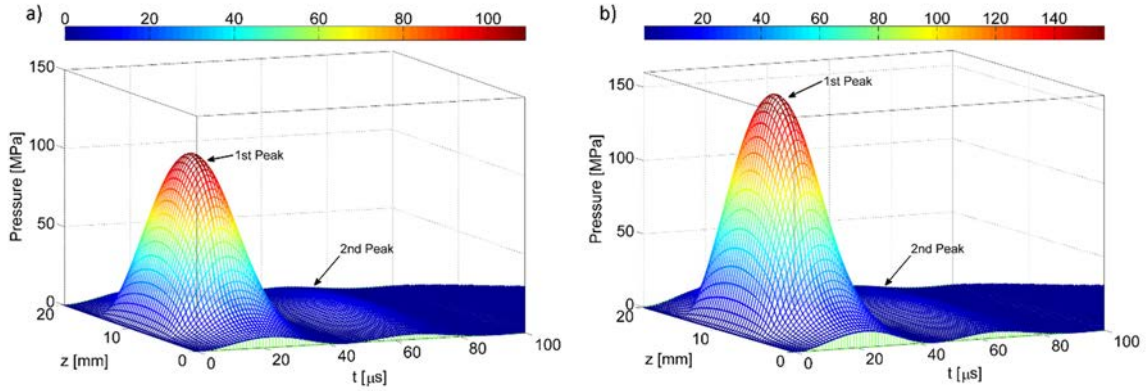


***Figure 7**: Predicted pressure distribution along the tube with time for a) 2.4kJ and b) 3.6kJ cases*

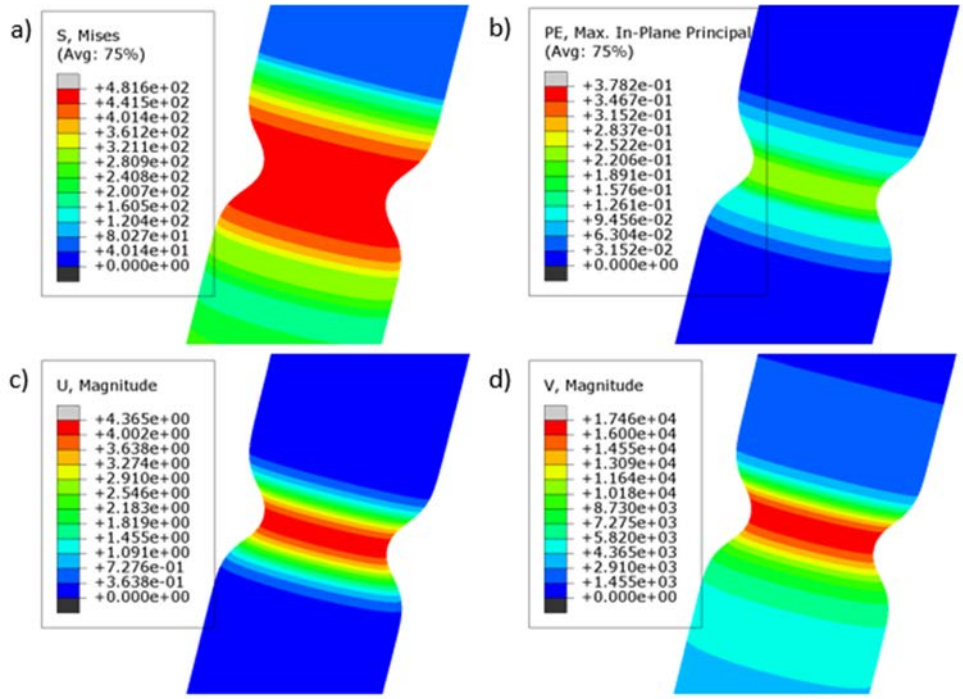


***Figure 8**: FEA results: a) von-Mises stress, b) plastic strain c) radial displacement, and d) radial velocity*

Fig. 8 shows the FEA results for the 3.6kJ energy discharge case with respect to the von-Mises stress, plastic strain, radial displacement, and velocity. Due to the boundary condition that only bottom end was fixed, the results in the axial direction are not perfectly symmetric, e.g., in the non-deformation area. In this case, the axial displacement was only 0.12mm and 0.14mm for 2.4kJ and 3.6kJ energy discharge cases respectively.

Fig. 9 shows the predicted velocity from analytical model and numerical simulations with good agreement demonstrated. The peak velocity from the numerical analyses were 107m/s and 153m/s for 2.4kJ and 3.6kJ energy discharges respectively compared to 106m/s

and 159m/s from the analytical model. The error between these values are 0.9% and 3.9% respectively. The time of the peak velocity is numerically predicted later in the process, but this parameter is less critical for the effectiveness of the process.

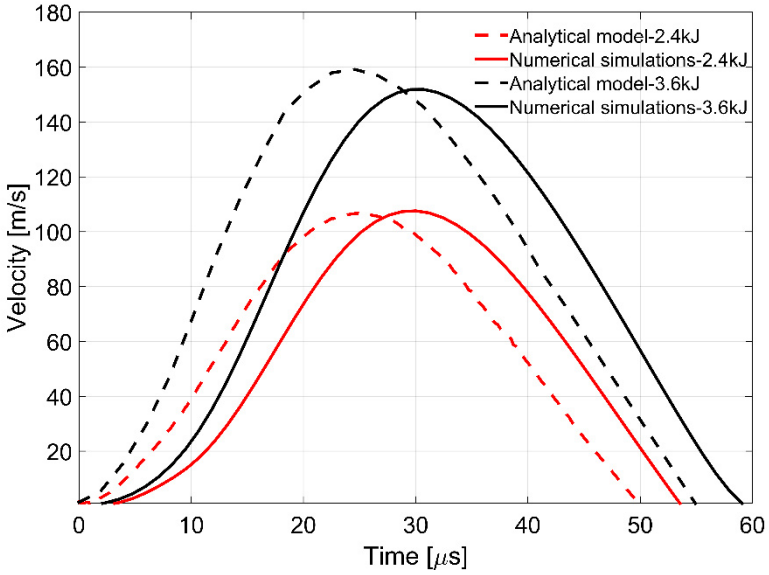


***Figure 9**: Velocity results from the analytical model and numerical simulations*

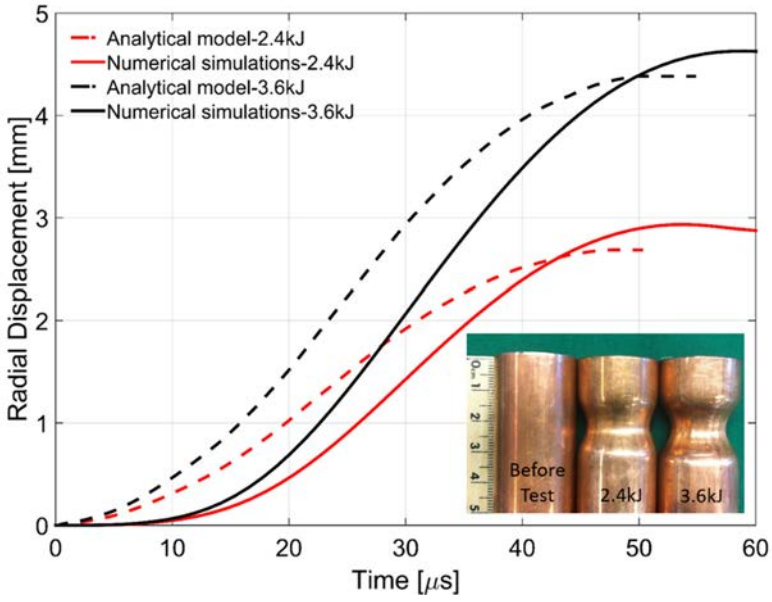


***Figure 10**: Radial displacement from the analytical model and numerical simulations*

The comparison between the predicted radial displacements from the analytical model and numerical analysis is shown in Fig. 10. Again, good agreement is obtained with the peak values being 2.68 mm and 4.38 mm for the analytical model and 2.87 mm and 4.52 mm for the numerical simulations that correspond to 6.6% and 3% differences for the 2.4 kJ and

3.6kJ cases respectively. The data shows that the analytical model approximate the numerical results well. The inset of Fig. 10 includes pictures from experimental tests with Cu101. The slot in the field shaper of the coil (see Fig. 3) causes the process to not be perfectly axisymmetric around the entire perimeter. Also, note that wrinkling is present in the deformed samples.

Some factors used in the modelling efforts were experimentally measured which could account for the discrepancies between the results. For example, the system inductance and resistance were physically measured, but these vary due to resistance heating during the experiments which was not accounted for in the models. The measurement devices and experiment tools may have calibration errors and contribute to the deviations as well. Additionally, the simplification of the material model, used in both modelling efforts, could cause errors. Finally, the analytical model includes various assumptions and simplifications, e.g., the yield criterion and strain assumptions. Therefore, it is difficult to get a precise match between numerical simulations and analytical model results.

# 5 Conclusions

In this study, an analytical model was set up for the EMF process using a multi-turn, axisymmetric coil and assessed by numerical simulations in Abaqus/Explicit. The results show good agreement between the analytical model and numerical simulations. Compared to the previous analytical modelling efforts, this model incorporates the experimentally determined coupling coefficients in the system and work hardening deformation of the workpiece instead of a rigid body or perfectly plastic material assumption. Therefore, the analytical model is able to predict not only the magnetic pressure distribution on the workpiece, but also the subsequent workpiece velocity and radial displacement. Also, the computational time of the analytical model is considerably less than the FEA simulations.

# Acknowledgments

Funding from the U.S. National Science Foundation (CMII-0928319 and CMMI-1537471) is gratefully acknowledged as well as discussions with Yannis Korkolis regarding the analytical model.

# References

Al-Hassani, S.T.S., 1975, Magnetic Pressure Distributions in Sheet Metal Forming, Conference on Electrical Methods of Machining, Forming, and Coating, pp. 1–10.

Bragov, A.M., Lomunov, A.K., Abramov, A.V., Konstantinov, A.Y., Sergeichev, I.V., Braithwaite, C., Proud, W.G., Church, P.D., Cullis, I.G. and Gould, P., 2006. The dynamic response of Copper 101 under high-rate loading. In Journal de Physique IV (Proceedings) (Vol. 134, pp. 311-315). EDP sciences.

Geier, M., José, M.M., Rossi, R., Rosa, P.A.R., Martins, P.A.F., 2013. Interference-Fit Joining of Aluminium Tubes by Electromagnetic Forming. Advanced Materials Research 853, pp. 488-493.

Hahn, M., Weddeling, C., Lueg-Althoff, J., Tekkaya, A. E., 2016. Analytical approach for magnetic pulse welding of sheet connections. Journal of Materials Processing Technology, 230, pp. 131-142.

Lorenz, A. Lueg-Althoff J. Goebel, G. Weddeling, C. Beyer, E. Tekkaya, A.E. 2014. Influence of axial workpiece positioning during magnetic pulse welding of aluminum-steel joints. 6th International Conference on High Speed Forming.

Mamalis, A. G., Manolakos, D. E., Kladas, A. G., Koumoutsos, A. K., 2004. Electromagnetic forming and powder processing: Trends and developments. Applied Mechanics Reviews, 57(4), pp. 299-324.

Nassiri, A., Chini, G., Kinsey, B., 2014. Spatial stability analysis of emergent wavy interfacial patterns in magnetic pulsed welding. CIRP Annals-Manufacturing Technology, 63(1), pp. 245-248.

Nassiri, A., Campbell, C., Chini, G., Kinsey, B., 2015a. Analytical Model and Experimental Validation of Single Turn, Axi-symmetric Coil for Electromagnetic Forming and Welding. Procedia Manufacturing, 1, pp. 814-827.

Nassiri, A., Chini, G., Vivek, A., Daehn, G., Kinsey, B., 2015b. Arbitrary Lagrangian–Eulerian finite element simulation and experimental investigation of wavy interfacial morphology during high velocity impact welding. Materials & Design, 88, pp. 345-358.

Ogata, K., 2004. System Dynamics, 4th ed. Pearson Prentice Hall, New Jersey.

Psyk, V., Risch, D., Kinsey, B.L., Tekkaya, A.E., Kleiner, M., 2011. Electromagnetic forming – A review. Journal of Materials Processing Technology 211 (5), pp. 787-829.

Thibaudeau, E., Kinsey, B. L., 2015. Analytical design and experimental validation of uniform pressure actuator for electromagnetic forming and welding. Journal of Materials Processing Technology, 215, pp. 251-263.

Weddeling, C., Demir, O. K., Haupt, P., Tekkaya, A. E., 2015. Analytical methodology for the process design of electromagnetic crimping. Journal of Materials Processing Technology, 222, pp. 163-180.

Zhang, P., Kimchi, M., Shao, H., Gould, J.E., Daehn, G.S., 2004. Analysis of the Electromagnetic Impulse Joining Process a Field Concentrator. AIP Conference Proceeding, pp. 1253-1258.

# Determination of Forming Speed at a Laser Shock Stretch Drawing Process

**S. Veenaas[1*], F. Vollertsen[2], M. Krüger[1], F. Meyer[1], M. Hartmann[1]**

[1] Bremer Institut für angewandte Strahltechnik GmbH, Klagenfurter Str. 2, 28359 Bremen, Germany
[2] BIAS - Bremer Institut für angewandte Strahltechnik and University of Bremen, 28359 Bremen, Germany
[*]Corresponding author. Email: veenaas@bias.de

## Abstract

*Laser shock forming is a new high speed forming process based on TEA-CO2-laser induced shock waves. In former publications laser shock forming was already presented as a process which can be used for deep drawing, stretch drawing and cutting of thin copper and aluminum sheets. The process utilizes an initiated plasma shock wave on the target surface, which leads to the sheets forming. Several pulses can be applied at one point in order to achieve a high forming degree without increasing the energy density beyond the ablation limit. During the process, pressure peaks in the range of some MPa can be achieved. In order to classify the process in the framework of high speed forming processes, the temporal varying deformation velocity due to different materials have been identified based on a stretch drawing process by using different pulse energies. Therefore a new high speed measurement system based on the shadowing effects is designed and its suitability is shown. The determined strain rate of 520 s-1 meets one of the criteria for the classification of laser shock stretch drawing as a high-speed forming process.*

## Keywords

Forming speed, Strain rate, Laser shock forming

# 1 Introduction

The trend towards miniaturization, especially in the electronics industry and medical technology, continues. Geiger et al. (2011) recognized that innovative ideas and new developments in this field have great potential to intensify this trend. Thus, for example in each generation of smart phones more functions are integrated with nearly unchanged dimensions of the device itself. Hoffmann (2006) stated that the trend of miniaturization includes the necessity to produce small high quality components in fast and reliable manufacturing processes. Krause (1995) demonstrated that forming processes are particularly suitable for mass production of micro metal parts, due to the short production times, possibility of automation and the improvement of the material properties e.g. by work hardening.

The potential to realize short process times is also provided by high-speed forming. First applications were already made in the 19th century. Munroe (1888) for example described how the detonation of explosive material over a stamping die can be used for engraving processes. Due to the required safety measures and the long setup times, the use of explosive materials is not suitable for mass production. One possible alternative is laser shock forming. There are different possibilities for laser shock processes. Laser shock forming using a TEA-$CO_2$-laser is a well-known process, such as the works of Schulze Niehoff et al. (2005). Due to thermo- and field emission electrons are irradiating out of the surface. Collision processes between these highly energetic electrons and atmosphere molecules are producing ions, which are absorbing the ongoing laser radiation. Miziolek et al. (2006) described that these free ions and electrons absorb energy by inverse bremsstrahlung absorption and can produce further ions and electrons by impact processes until an optical breakdown and thus a plasma formation is achieved. The inverse bremsstrahlung increases with the square of the wavelength accomplishing a nearly complete absorption of the longer wavelength of $CO_2$-laser light by the plasma. This process offers the possibility of high speed mass production of micro parts. Wielage (2011) characterized the process and identified the fundamentals of the process design for the manufacturing of small metal parts. Vollertsen et al. (2009) demonstrated, that the production of micro components result in so-called size effects, which are leading to difficulties in scaling down the forming processes to the micro range. To use laser shock forming for industrial processes, an accurate understanding of the process is necessary for using it effectively and economically.

An important process parameter is the strain rate of the forming process. For the measurement of the strain rate, the deformation velocity has to be determined. Wielage determined also the strain rate for a laser shock bending process for different pulse energies using a high speed camera. The determined strain rates are in the range from $1 \cdot 10^3 \cdot s^{-1}$ to $2 \cdot 10^3 \cdot s^{-1}$. Due to the size of the high speed camera, the accessibility to the process is not given. Numerous studies show, that different high speed measuring systems are known which have extremely high operational costs, such as the works of Fenton et al. (1998) and Bessonov et al. (2004). Beerwald (2005) described a modified system for high speed measurement of strain rates in the electromagnetic forming, based on the measurement setup

of Finkenstein et al. (1967). This is an optical measurement principle which is based on the shadowing effect, wherein a line laser is used as a light source. In this work, a measurement method for the determination of the deformation velocity in a laser stretch drawing process is designed, implemented and validated. Actual systems are restricted to the measurement direction and the accessibility to the process. Therefore in this investigation the measurement principle based on the shadowing effect will be used and the feasibility of this method for the micro range will be investigated.

# 2 Method

## 2.1 Measurement Principle

A schematic representation of the technique, which is used in this study, is shown in Figure 1. The Setup consist of three major parts: the measurement laser, the specimen which will be deformed and the sensor. The measurement laser, which is a diode laser with a wavelength of 650 nm and an average output power of 10 mW, is irradiating directly onto the sensor surface. The sensor, a position sensitive device (PSD-sensor) from First-Sensor, is providing an analogue voltage value proportional to the amount of laser light irradiating onto it. The measurement frequency of the PSD-sensor is 250 kHz. The specimen is placed between the measurement laser and the PSD-senor. When the specimen is deformed the amount of laser light irradiating on the PSD-sensor is reduced, thus decreasing the analogue signal in the same manner.

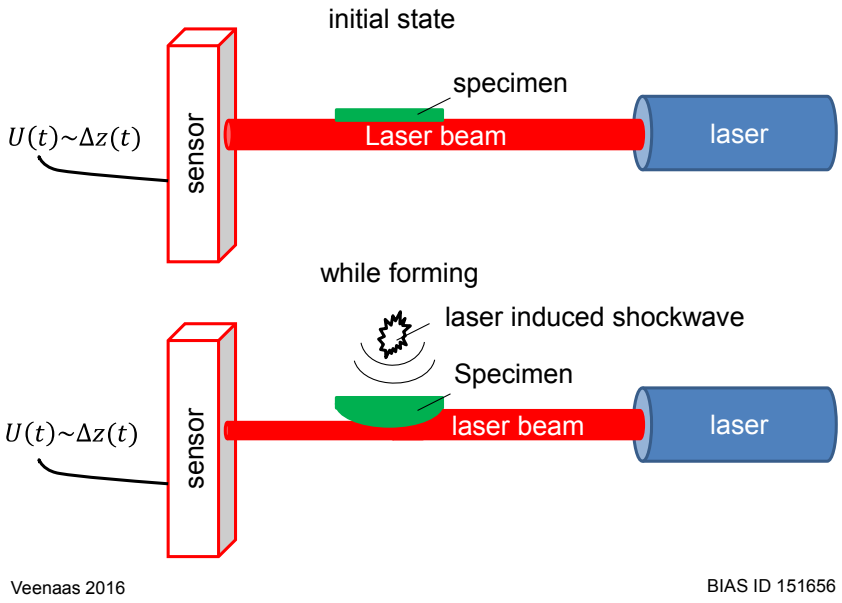


***Figure 1**: Schematic representation of the measurement principle*

## 2.2 Measurement Setup

The experimental setup is shown in **Figure 2**. The used laser is a TEA-$CO_2$ Laser (TEA = Transverse Excitation at Atmospheric Pressure) with a wavelength of 10.6 µm, a maximum pulse energy of 6 J and a pulse duration of 100 ns. The laser is irradiating onto the surface of the specimen.

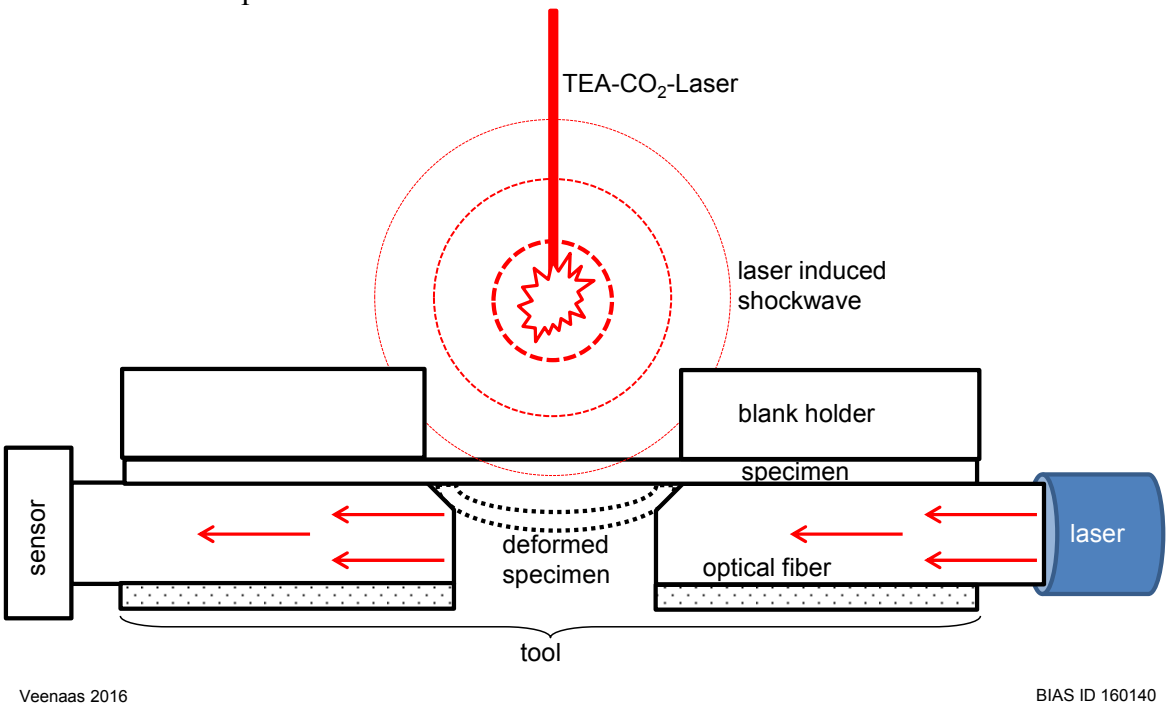


***Figure 2**: Experimental setup*

As shown in **Figure 2**, the measurement system is integrated into the forming tool. The laser is guided through an optical fibre. This optical fibre ensures the correct alignment of sensor and laser, which makes the measurement system more stable against disturbances. The chamfer at the optical fiber is needed for the forming process. Due to this chamfer the measurement range of the sensor is reduced, because of a different refraction behaviour of the laser light. The calibration of measurement system is done with a micro forming machine by using a punch with a round geometry for the shadowing. The travel speed of the punch is 1 m/s. The standard deviation of the measurement system is 2 %.

The height of the formed cups is measured with a contact free optical 3D laser scanning microscope (Keyence VK-X210).

## 2.3 Determination of Strain Rate

To determine the strain rate it is necessary to measure the strain itself. As shown in **Figure 3** from a cross section the deformation area D is measured which is the diameter of the dome. This value is taken as a reference for the determination of the average strain. Beginning at the edge of the dome the length of the center layer L is measured, using Olympus Image

Analysis Software Stream Enterprise. The center layer L is compared to the deformation area D for the calculation of the average strain. In this case an ideal stretch drawing process is assumed.

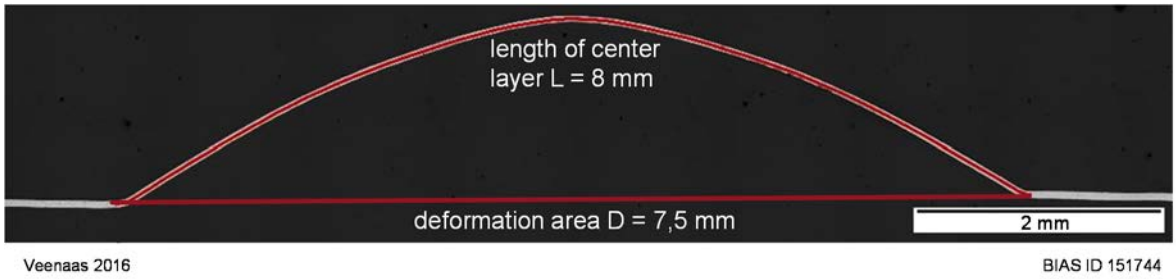


***Figure 3**: Cross section of a formed dome and strain determination method*

Using this average strain the strain rate is calculated by:

$$\varepsilon = \frac{(l_1 - l_0)}{l_0} \tag{1}$$

$$\dot{\varepsilon}(t) = \frac{\mathrm{d}\varepsilon}{\mathrm{d}t} = \frac{d}{dt}\left(\frac{l(t) - l_0}{l_0}\right) \tag{2}$$

# 3 Results

In **Figure 4** the parts produced by laser shock stretch drawing are shown. Only the aluminum sheets with a thickness of 50 µm and the copper sheets with a thickness of 20 µm are leading to evaluable results. For aluminium sheets with a thickness of 20 µm the used laser pulse energy is too high, thus the material is breaking. For the copper sheets with a thickness of 50 µm the height of the formed cup was too low, thus the shadowing of the sensor was not evaluable.

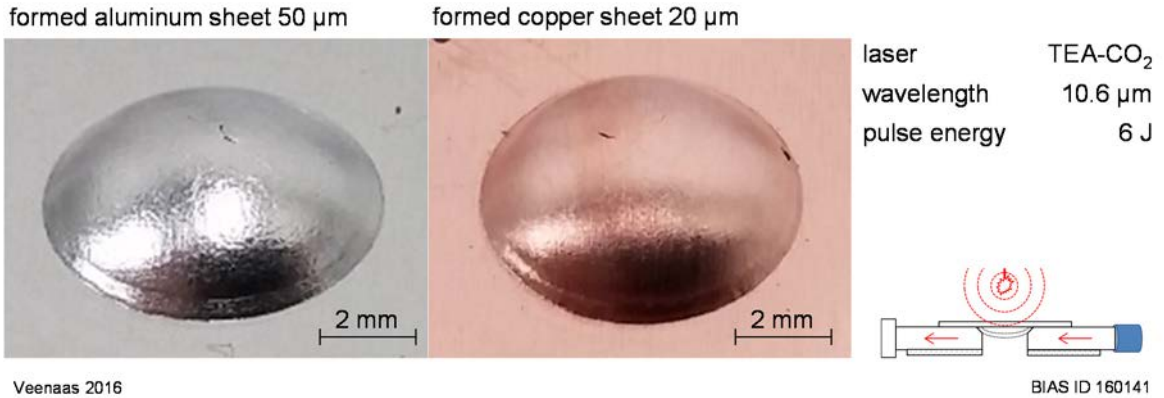


***Figure 4**: Laser shock stretch drawn cup out of Al99.5 (left) and E-Cu 58 (right)*

A representable voltage over time signal recorded by the PSD-sensor during the laser induced forming process is shown in **Figure 5**. It can be seen that the signal is decreasing exponentially over time. The value drops from 1.14 V to 0.97 V in a time period of 128 ms.

The height of the formed cup, measuring 1.29 mm, was determined using a 3D laser scanning microscope. Using the measured height $h_{cup}$ and the time for the forming process $t_{form}$ the deformation velocity $v_{form}$ can be calculated by:

$$v_{form} = \frac{h_{cup}}{t_{form}} \tag{3}$$

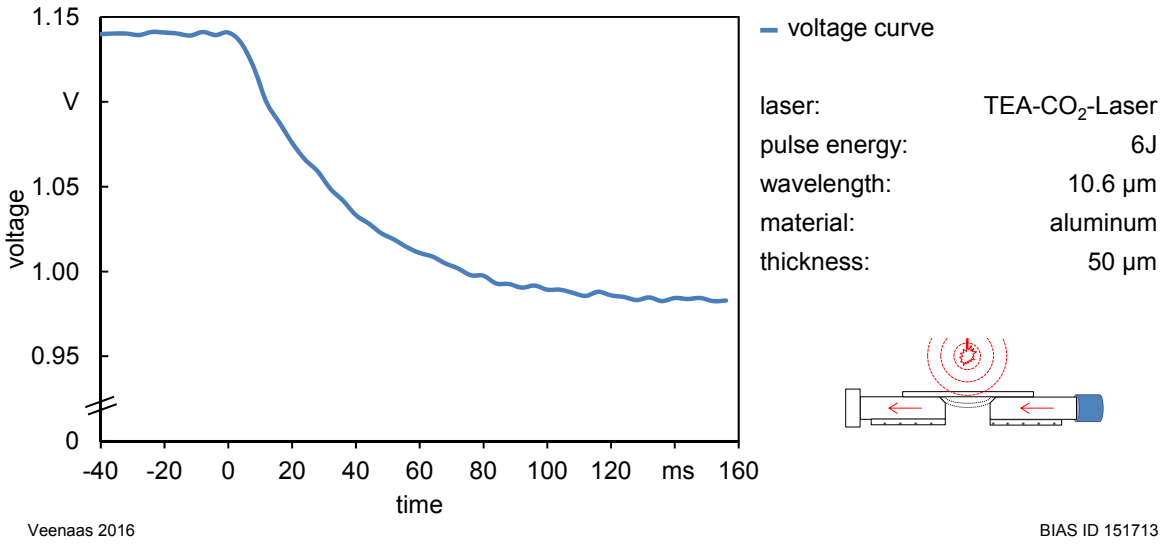


***Figure 5**: Voltage over time signal for Al99.5 with a thickness of 50 µm*

As described in section 2.2 the chamfer in the forming tool, the measured decrease of the signal does not represent the correct forming value. For the determination of the correct forming value the reduced signal due to the chamfer has to be compensated. Therefore an exponential function is used to determine the absolute value for the time period of forming, this is shown in **Figure 6**. Due to this exponential fit, the forming behaviour can be observed and an estimation of the total forming time $t_{form}$ and height can be made.

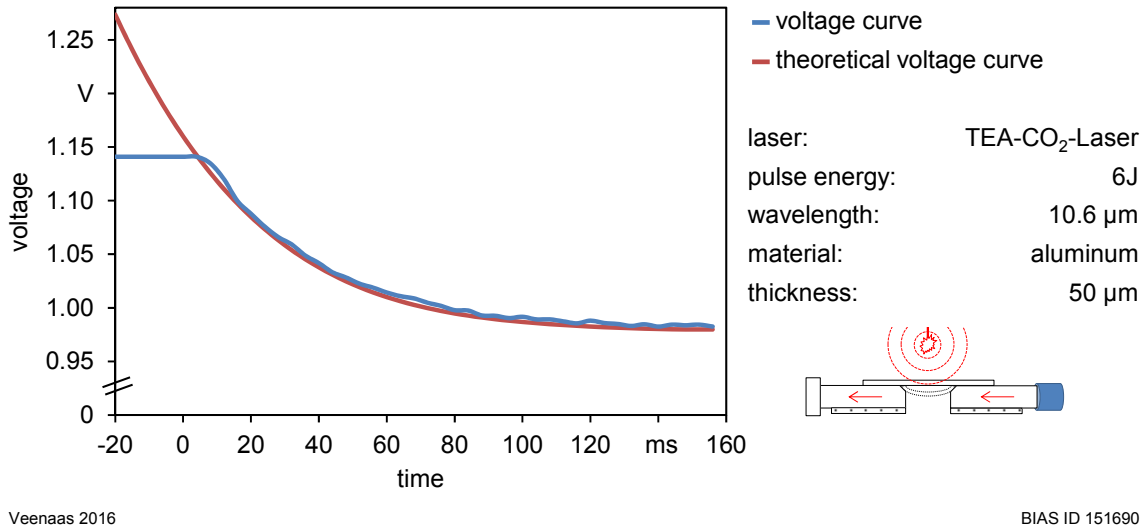


***Figure 6**: Exponential fit of the signal*

By using this procedure the time period of forming is increased to 148 ms, which is reducing the average deformation velocity of the forming process. Using equation 3, the corrected forming velocity of an Al99.5 sheet with a thickness of 50 µm and a copper sheet with a thickness of 20 µm can be seen in **Figure 7**. In this figure different pulse energies were used. Based on this data it can be seen, that the average deformation velocity is increasing with increasing pulse energies. For calculating the deformation velocity a uniform movement of the material is assumed. Therefore the determined deformation velocities are average deformation velocities of this process.

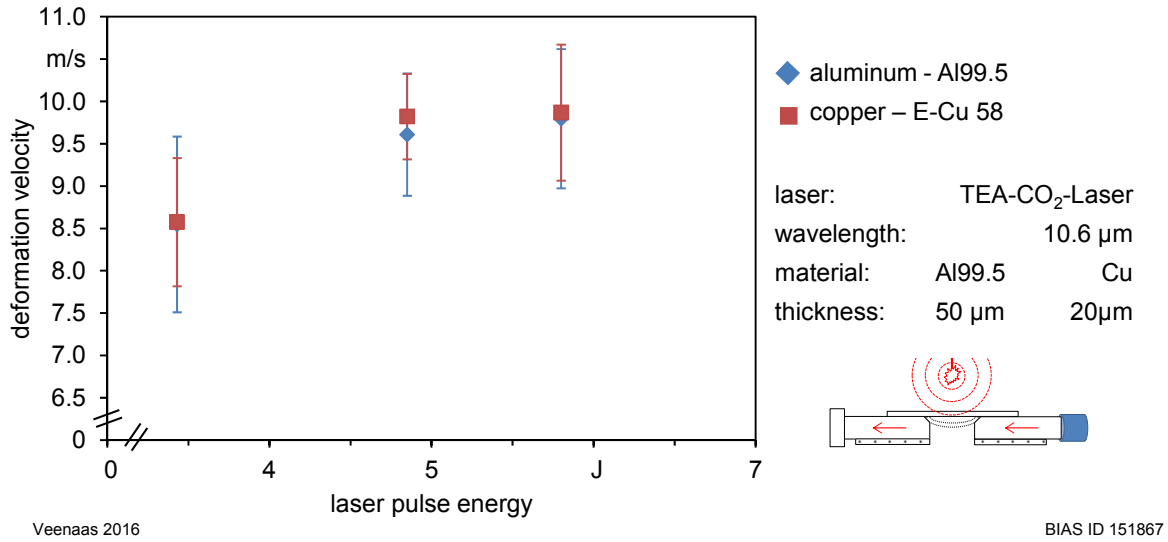


***Figure** 7: Deformation velocity and dome height of Al99.5 with a thickness of 50 µm*

For an Al99.5 sheet with a thickness of 50 µm and for the E-Cu 58 sheet with a thickness of 20 µm the strain rate is in the same range and could be determined as $\dot{\varepsilon} \approx 520\ s^{-1}$.

# 4 Discussion

Wielage stated that for the definition of a high speed forming process, in addition to the workpiece speed and the pressure rise time, the strain rate can be used. To be classified as high-speed forming the strain rate has to be inside the range of $10^2\ s^{-1}$ to $10^7\ s^{-1}$. The determined strain rate of $520\ s^{-1}$ meets this criteria for classification of laser shock stretch drawing as a high-speed forming process. This value is a function of the measured deformation and the resulting strain on one hand, as well as the measured forming time on the other. The determined strain rate compared to the strain rate which Wielage determined for a laser shock bending process is lower. This can be explained by the different forming conditions, during the process. For a bending process, the deformation energy is lower than the deformation energy in an axially symmetric stretch drawing process. Thus more energy is left for the deformation of the bending part, which leads to a higher deformation velocity. On the other hand, for the stretch drawing process more deformation energy is needed for

the forming process, which leads to a lower deformation velocity and hence to lower strain rates.

Figure 7 shows the average deformation velocity as a function of the pulse energy. It is shown, that the average deformation velocity is increasing with increasing pulse energies. However, this behaviour is not linear. With an increase from 5 J to 6 J the average deformation velocity is nearly the same. The average deformation velocity is calculated by the dome height and the time for the forming process. Due to work hardening, the increase of dome height using pulse energies from 5 J to 6 J is also smaller, which is also influencing the average deformation velocity.

**Figure 5** shows the Voltage over time signal of the measurement sensor. Based on the exponential decrease of the signal, it can be seen, that the forming of the sheet does show the same behaviour. Due to the laser induced shock wave the deformation velocity of the material reaches the highest value at the beginning of the forming process. The signal of the sensor is based on the area of shadowing, which is a result of the forming of the cup. The form of the cup is cone-shaped, thus the area which is shadowed should be increasing with increasing deformation of the cup. This behaviour cannot be observed in the signal sequence. Because of the optical fibre, the measurement width is 3 mm which is reducing the described effect. Also the deformation velocity during the process is more significant than the effect of shadowing, thus the signal is showing an exponential decrease. Therefore the deformation at the beginning does have the highest value, which is than exponentially decreasing.

Due to the chamfer at the forming tool, the beginning of the forming process cannot be observed. By using an exponential fit this behaviour can be extrapolated. This procedure enables the determination of the beginning and the end of the forming process. Thus the average strain rate and deformation velocity can be calculated using this information. Due to the exponential behaviour of the deformation velocity, the maximum strain rate cannot be calculated. Therefore the strain and forming behaviour during the process must be known, which is not investigated yet. For this reason only an average value for the strain rate is determined.

Measurement systems for high-speed measurements are widely used in the industry and serve different applications. The achieved temporal resolution and the accuracy of these systems are suited for high speed forming processes. However, a necessary condition is the accessibility of the measurement system on the axis which will be measured. For example a laser triangulation must be installed under the forming tool to measure the sample from below. In addition, it would be necessary to decouple the system from the workbench to avoid vibrations and shock waves on the position-sensitive triangulation. This problem does not occur when using the present measurement system based on the shadowing effect. The integration of this sensor into the tool is leading to stable measurement conditions, which are not affected by vibrations. Also the accessibility for different measurement systems is give, thus this system can be used in combination with e.g. optical strain measurement systems.

Due to the calibration with a micro forming machine the uncertainty of measurement is below 2.5 % for deformation velocities of 1 m/s. The uncertainty of measurement for

higher deformation velocities is in the same range, due to the qualitative progress of the voltage curve for different velocities.

# 5 Conclusion

- The measurement system, based on the shadowing effect, is well suited for the determination of the deformation velocity during a laser shock stretch drawing process.
- The uncertainty of the measurement is below 2.5 % for absolute average deformation velocities of 1 m/s.
- The strain rate of 520 $s^{-1}$ classifies laser shock stretch drawing as a high-speed forming process.

# Acknowledgements

This work has been funded by the Project VO530/65-2 “Fügen durch Hochgeschwindigkeitsumformen durch laserinduzierte Schockwellen”. The authors would like to thank the Deutsche Forschungsgemeinschaft for their financial support within the project.

# References

Beerwald, C., 2005. Grundlagen der Prozessauslegung und -gestaltung bei der elektromagnetischen Umformung, Aachen: Shaker Verlag

Bessonov, N., Golovsachenko, S., 2004. „Numerical Simulation Pulsed Electromagnetic Stamping Processes“ in Proceedings of ICHSF - 1st International Conference on High Speed Forming, Dortmund

Fenton, G., Daehn, G., 1998. „Modelling of electromagnetically formed sheet metal,“ in Journal of Materials Processing Technology

Finckenstein, E. v., 1967. Ein Beitrag zur Hochgeschwindigkeitsumformung rohrförmiger Werkstücke durch magnetiscche Kräfte, Hannover: Universität Hannover

Geiger, M., Kleiner, M., Eckstein, R., Tiesler, N., Engel, U., 2001. Microforming, CIRP Annals – Manufacturing Technology

Hoffmann, H., 2006. Tensile Test of very thin Sheet Metal and, CIRP Annals – Manufacturing Technology

Krause, W., 1995. Fertigung in der Feinwerk- und Mikrotechnik, Wien: Carl Hanser Verlag München

Miziolek, A. W., Palleschi, V., Schechter, I., 2006. Laser Induced Breakdown Spectroscopy, 1st ed., Cambridge University Press, Cambridge

Munroe, C., 1888. „Modern Explosives“ Scribners Magazin, Vol. 3/5,, pp. 563-577

Schulze Niehoff, H., Vollertsen, F., 2005. Non-thermal Laser Stretch-Forming, Sheet Metal 2005, Advanced Materials Research, Vol. 6-8 (433-440)

Vollertsen, F., Biermann, D., Hansen, H., Jawahir I., Kuzman, K., Size effects in manufacturing of metallic components, CIRP Annals - Manufacturing Technology, Vol. 58/2, 2009.

Wielage, H., 2011. Hochgeschwindigkeitsumformen durch laserinduzierte Schockwellen, Bremen: BIAS Verlag

# Electrohydraulic Forming of Light Weight Automotive Panels

**A. V. Mamutov[1], S. F. Golovashchenko[1*], J. J. Bonnen[2], A. J. Gillard[3], S. A. Dawson[1], L. Maison[3]**

[1] Mechanical Engineering Department, Oakland University, U.S.A.
[2] AGC Automotive America's Research, U.S.A.
[3] Ford Research & Advanced Engineering, U.S.A.
[*]Corresponding author. Email: golovash@oakland.edu; Tel.: +1 248 370 4051

## Abstract

*This paper describes the results of development of the electrohydraulic forming (EHF) process as a near-net shape automotive panel manufacturing technology. EHF is an electro-dynamic process based upon high-voltage discharge of capacitors between two electrodes positioned in a fluid-filled chamber. This process is extremely fast, uses lower-cost single-sided tooling, and potentially derives significantly increased formability from many sheet metal materials due to the elevated strain rate. Major results obtained during this study include: developing numerical model of the EHF; demonstrating increased formability for high-strength materials and other technical benefits of using EHF; developing the electrode design suitable for high volume production conditions; understanding the limitations on loads on the die in pulsed forming conditions; developing an automated fully computer controlled and robust EHF cell; demonstration of electrohydraulic springback calibration and electrohydraulic trimming of stamped panels; full scale demonstration of a hybrid conventional and EHF forming process for automotive dash panel.*

## Keywords

Electrohydraulic forming, High voltage discharge, Automotive panels

# 1 Introduction

According to the general trend of decreasing vehicle weight, advanced high strength steels (AHSS) and aluminum alloys (AA) are being used more and more in automotive body construction. In order to achieve formability levels offered by mild steels and bakehardenable steels, further development is necessary in sheet metal forming technologies. Electrohydraulic forming (EHF) is capable of achieving such improvements for both AHSS and AA. EHF also offers significant reducing in tool cost because only a one-sided die is required. Compared to popular electromagnetic forming processes, EHF does not impose any special requirements to electrical conductivity of the deformed material or necessity to be positioned close to the coil. EHF also allows several pulses to be produced in one tool without necessity to use several coils and several sets of dies.

In EHF, an electrical energy, stored in a high-voltage capacitor, is discharged across a gap in water enclosed in a discharge chamber. A small volume of liquid between the tips of the electrodes is vaporized and then forms a plasma channel. Electrical current continues to go through the channel thus converting the electrical energy into the internal energy of plasma bubble, which happens over a very short period of time, usually less than 100 microseconds. This leads to explosive expansion of the channel with forming high velocity shock waves in the liquid, which form a blank into a die.

EHF technology was developed in early 50-s mostly as a method of producing low volume parts at low cost. Yutkin (1955), Bruno (1968), and Davies and Austin (1970) reviewed early applications and research results on EHF. A significant advantage of EHF compared to traditional sheet metal forming technology is that it does not require two matching dies: a punch is usually replaced by the liquid transmitting pressure from the discharge channel to the surface of the blank. Bruno (1968) described a number of industrial examples where EHF machines storing 36kJ, 60kJ, 150kJ and 172kJ were employed. However, due to the necessity to fill the chamber with liquid at the beginning of each forming cycle and evacuate the liquid at the end of it, the cycle time for EHF was in the range of several minutes. Sanford (1969) described a hybrid technology where static hydroforming was used to bulge sheet metal into the die cavity followed by EHF which provided higher pressure level and filled the details of the die cavity. According to Sanford (1969), a typical cycle time for such a hybrid process is 10 minutes.

More recently, Balanethiram and Daehn (1994) reported increased forming limits after forming into a conical die compared to Forming Limit Diagrams of copper and AA6061-T4: the maximum strain for plane strain conditions was increased factor of 2.5 for copper and factor of 5 for AA6061-T4. Significant improvements in formability of AA 6111-T4 (approximately factor of 2.5), 5754 and 5182 (approximately factor of 3) after formation into conical dies and elongated corner die (V-shape) using electromagnetic forming technology were reported by Imbert et al ( 2005 ) and Golovashchenko (2007 ).

Very limited attempts have been made to simulate the EHF process. Golovashchenko and Mamutov (2005) presented results of bulging into an open round die. Vohnut et al (2010) reported results of pulsed loading in closed volume assuming energy equivalence to the explosive forming.

The objective of the research project reported in this paper is to develop EHF process as a near-net shape automotive panel manufacturing technology suitable for mid volume production of full-scale parts.

# 2 Developing Numerical Model

Numerical modeling is crucial for designing an optimal technological process in reasonable time. During work on the project, significant progress was made in developing a numerical model of the EHF process. The developed multiphysics numerical approach includes expanding discharge channel, compressible liquid as a pressure transmitting medium, deformable blank which interact with a rigid die. Each individual model was developed using the capabilities of LS-DYNA commercial code.

The plasma channel was modelled in LS-DYNA as an adiabatically expanding bubble of ideal gas. The electric energy is assumed to be introduced uniformly through the channel volume. The energy deposited in the channel was obtained experimentally for the specific configuration by measuring electrical current and voltage during discharge. The liquid was assumed ideally compressible. Modelling of sheet metal blank formation into a designated shape was conducted using an elastic-plastic shell. To eliminate the issue of mesh distortion, the Arbitrary Lagrange Eulerian (ALE) solver with Multi-Material capability available in LS-DYNA was employed. The details of the developed numerical approach are described in (Mamutov et al, 2015).

Simulation of full process chain of multistage EHF of the license plate area of a decklid has been performed. The chamber and the one-sided die are shown in **Fig.1**.

The evolution of the shape of the discharge channel and deformation of the blank during the first EHF stage are shown in **Fig.2**. Progress of blank formation after each discharge is illustrated in **Fig.3**.

# 3 Enablers of EHF Technology

The formability of AHSS in pulsed forming conditions was investigated experimentally and also using numerical simulation. The results show that significant improvements in formability is observed for DP780 and DP980 when forming into conical and v-shape dies using EHF from a flat sheet. The observable failure modes are in good correlation with the results of numerical simulation. The results of these researches are explained in details in (Gillard et al, 2013) and also in (Golovashchenko et al, 2014c).

A series of tests on electrodes were conducted to study the viability of Electro-Hydraulic Forming for production applications. As a result, the recommendation on electrodes material and design were obtained which is explained in details in (Bonnen et al, 2013).

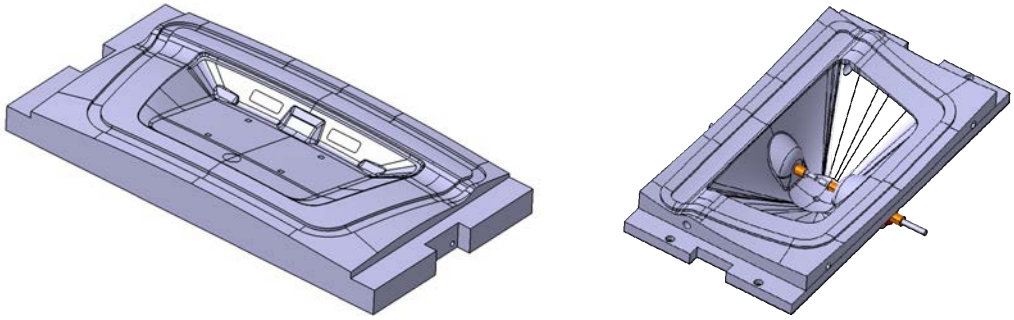


***Figure 1**: Geometry of the die (a) and the chamber (b)*

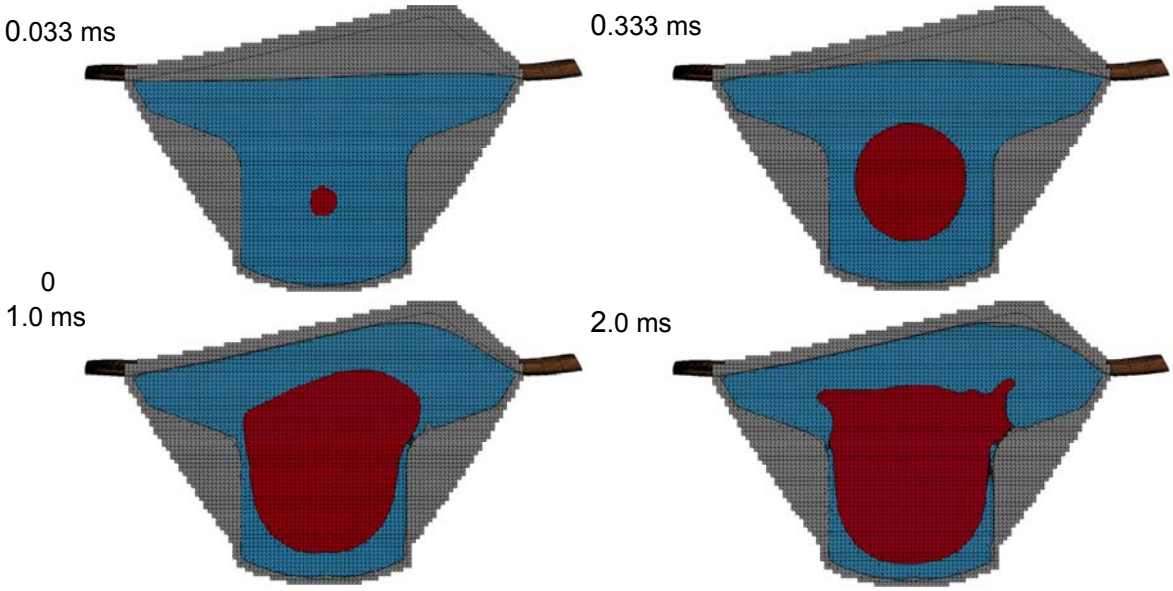


***Figure 2**: Channel expansion and deformation of the blank during the first discharge*

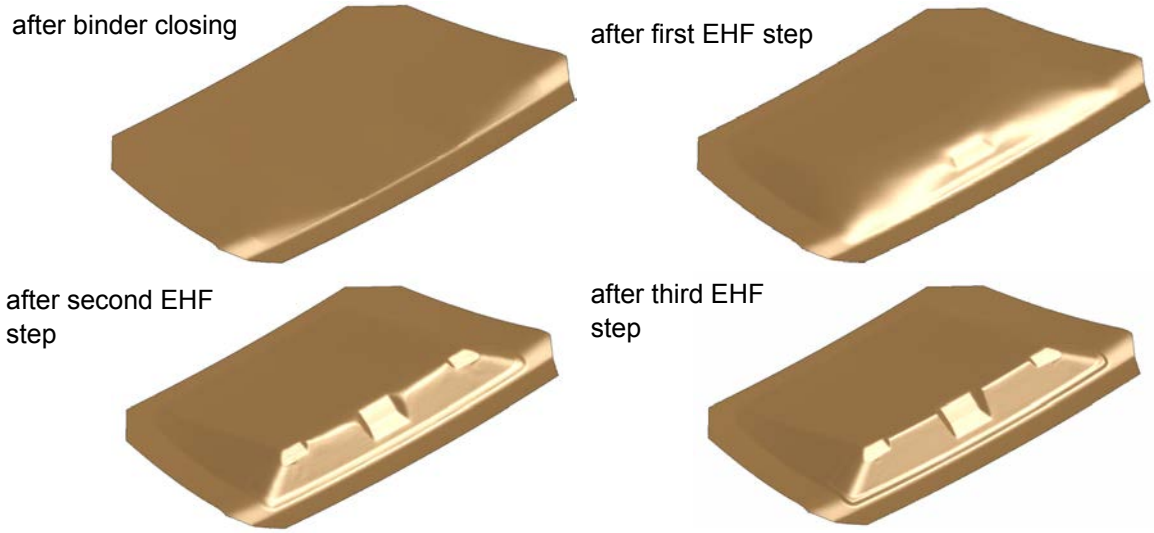


***Figure 3**: Changing of blank geometry*

The extensive research was performed regarding correct simulation of impact behavior which is crucial for the robust die tooling design. As a result, the recommendation on choosing the contact algorithm were obtained and verified experimentally. The results are described in details in (Ibrahim et al, 2014).

With appropriate discharge energy that ensures filling all the die features, the final shape of a blank, formed by EHF, matches the die. The factor that is affecting the final shape is the springback. EH calibration, the operation which is similar to a conventional restrike operation, except that the pressures are much higher, was demonstrated as an efficient method to reduce springback in the formed parts comparing with the conventional forming. The results are published in (Golovashchenko et al, 2014b).

Another demonstrated extension of EH technology was the EH trimming which enables trimming operations without a punch and also significantly reduces formation of a bur in comparison with conventional trimming methods. The results are published in (Golovashchenko et al, 2014a). The additional research on cutting edge loads during EH trimming is published in (Tang et al, 2014).

# 4 Demonstration of EHF Automation Cell

The fully automated cell was created to demonstrate the possibility to use EHF at production rates. Multiple tasks were completed to overcome different challenges, to increase robustness, and decrease the cycle time. The major task, which required several iterations during the overall development, was to integrate all the components (the gantry, hydroforming, electric pulse generator, safety system, vacuum pump, hydraulic press, and water/air management system) into an automated system and to establishing remote control via the Ethernet and feedback using variety of sensors. The humidity rising during continuous operation increases the risk of an unplanned internal arc or discharge. Solving this issue required reorganization the components in space, establishing proper ventilation and using a commercial de-humidifier. The electrical isolation and grounding of the electric pulse generator was improved to increase robustness and electrical safety. Filling the chamber with water and water draining after discharges is the major factor that slows down the productivity of EHF. To solve this issue, the custom Fluid Handling Systems (FHS) was designed, manufactured, and built into the cell. The new FHS increased the fluid drain and fill rates over an order of magnitude from 26 to 380 liters/min. FHS also integrates the high pressure functionality to increase the production rate of both EHF and hybrid forming of EHF combined with traditional sheet hydroforming. The increased fluid drain had required optimization of the size of the water/air ports going into the chamber/die. Experiments and numerical simulation were performed to find the optimal ports size that does not constrict the flow too much and, at the same time, does not reduce efficiency of the process. The chamber diaphragm was introduced to ensure that clean fluid was always in contact with the blank and to ensure that any fluid contaminated with electrode erosion products was confined to the region around the electrodes.

The part used for demonstration and the automated cell are shown in **Fig.4**.

***Figure 4**: License plate and automated cell for its production*

Operation of the EHF cell includes the following steps: 1) the gantry retrieves the blank from sheet metal stack; 2) the gantry places the blank on the blank holder surface located between the die and the EHF chamber; 3) the press is closed, and the lock beads clamped the blank; 4) the chamber is filled with water; vacuum is drawn on the die preventing potential air pockets between the blank and the die surface; EHF pulses are applied; 5) water is drained down, and vacuum is released; 6) fully formed part is picked up by the gantry and moved to the stack of stamped parts. There were four discharges applied for each part with increasing voltage up to 12 kV (14.4 kJ) for the last calibrating discharge which ensured filling all the radii and repeatable resulting parts' shape matching the die geometry.

The EHF cell was able to produce over 100 parts formed in two batches over a total running time of approximately 3 hours. It was capable of running an 8 hour shift without maintenance. Further details can be found in report (Golovaschenko, 2013).

# 5 Full Scale Demonstration of a Hybrid Conventional and EH Forming Process for Automotive Dash Panel

The fabrication of tooling for the full-scale demonstration of the dash panel (**Fig.5**) forming process was the major effort of the project. This part imposes significant formability challenges because it has very deep and wrinkling prone central area and can be produced only from mild steel when using a conventional stamping approach.

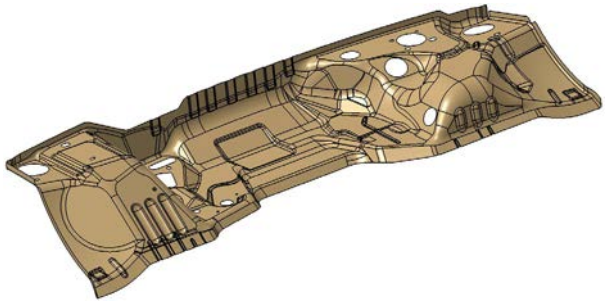

***Figure 5**: Geometry of the dash panel after trimming and flanging*

The tool set included the following dies: the preforming die and the final shape die for EHF forming. The preforming die was designed and fabricated as a triple action tool schematically shown in **Fig.6**.

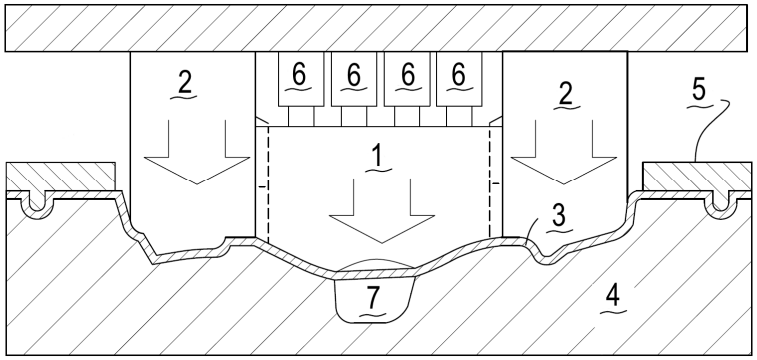


***Figure 6**: Geometry of the dash panel after trimming and flanging*

The approach (patented, Golovashchenko et al 2015) is that the central punch 1 was fabricated separately from the side punches 2. At the beginning of the process, the flat blank 3 is positioned inside the tool on top of the lower preforming die 4 using guiding pins. After closing the binder 5 and clamping the periphery of the part, the central punch backed by cylinders 6 (which may be hydraulic, pneumatic or nitrogen) starts drawing the blank in the central region of the part. Once the central punch reaches its home position, the upper die continues to travel downward, allowing the side punches to form the rest of the panel while the central punch is held in its position by the cylinders. After the side punches complete their stroke, the press stops and dwells with all punches in the home position. Water is then pumped into the metal gainer pocket 7 region to reverse form the pocket (which can be also performed as an EHF operation). The components of the preforming die are shown in **Fig.7**.

a) b)

***Figure 7**: Assembled upper (a) and lower (b) preforming dies*

The shape of the blank after finishing the preform operation is shown in **Fig.8**.

***Figure 8**: Preformed blank*

The EHF tooling includes the die and the multielectrode chamber shown in **Fig.9a**. **Fig.9b** shows the EHF chamber and die assembly installed in a 150 ton hydraulic Beckwood press. The sequence of steps for the final forming stage using EHF was the following: the partially formed part is placed in the die and located by two guide pins; the chamber and die are closed; the chamber is filled with fluid; each of the electrodes in each subchamber is pulsed sequentially.

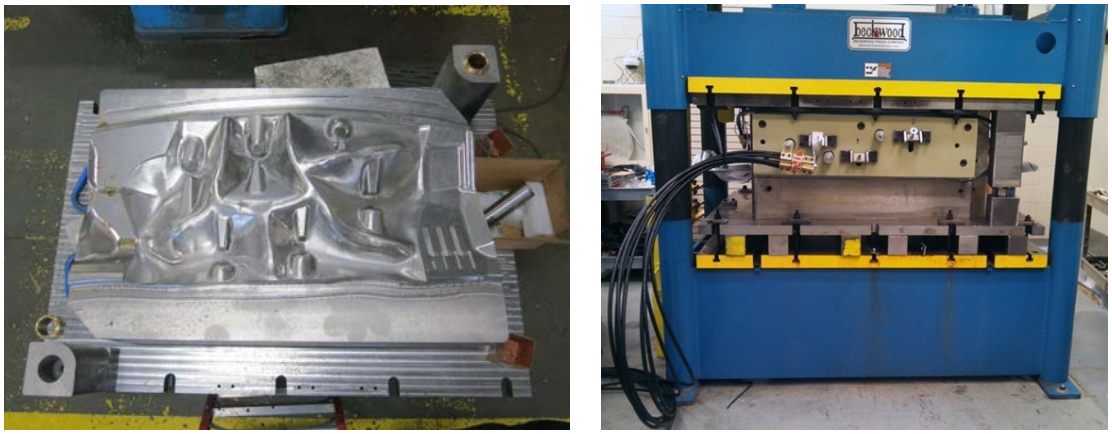

a) b)

***Figure 9**: EHF chamber prior to the installation of electrodes (a) and EHF tooling in closed position during the tryout process (b)*

The final shape of the dash panel after finishing EHF step is shown in **Fig.10**.

***Figure 10**: The fully formed dash panel (1.5 mm DP600) after EHF forming*

# 6 Conclusions

As a result of the performed study, important enablers have been developed advancing the EHF technology as a method of producing near-net shape automotive panels of AHSS. That includes:

1. Reducing of the cycle time due to the development of the water/air management system; extension of the electrode life and minimizing of the electrode system maintenance based on electrode erosion study. This made possible to create a fully automated and robust production cell with suitable for industrial production.
2. Developing a complete simulation tool based on LS-DYNA code which enables simulation-driven design of the EHF tooling.
3. Detailed study on contact algorithms used in FEM which enables precise simulation of impact loadings and correct choosing the appropriate tools materials during design.
4. Extensive study on material formability which confirms benefits of using EHF to improve formability of AHSS over conventional stamping.
5. The possibility to perform calibration to reduce springback and to perform trimming operation was demonstrated.
6. The full-scale demonstration of the dash panel forming process using combined conventional-EHF process was performed to demonstrate the maturity of the technology.

# Acknowledgments

This research work was supported by Advanced Manufacturing Office of US Department of Energy under Award No. DE-FG36-08GO18128, by Ford Research & Advanced Engineering and by United States Steel Corporation.

# References

Balanethiram, V.S., Daehn, G..S., 1994. Hyperplasticity: increased forming limits at high workpiece velocity. Scripta Metallurgica et Materialia, 30, p.515-520.

Bonnen, J.J.F., Golovashchenko, S.F., Dawson S.A., and Mamutov, A.V., 2013, Electrode Erosion Observed in Electro-Hydraulic Discharges Used In Pulsed Sheet Metal Forming, Journal of Materials Engineering and Performance, V. 22, Issue 12, pp. 3946-3958.

Bruno, E.J., 1968, High-velocity forming of metals. American Society of Tool and Manufacturing Engineers, Dearborn, Michigan, USA.

Davies, R., Austin, E.R., 1970, Development in high speed metal forming, Industrial Press Inc.

Gillard, A.J., Golovashchenko S.F., and Mamutov, A.V., 2013, Effect of quasi-static prestrain on the formability of dual phase steels in electrohydraulic forming, Journal of Manufacturing Processes, V.15, Issue 2, pp. 201-218.

Golovaschenko, S.F., 2013, "Electrohydraulic Forming of Near-Net Shape Automotive Panels". United States. doi:10.2172/1094831. http://www.osti.gov/scitech/servlets/purl/1094831.

Golovashchenko, S.F., 2007, Material formability and coil design in electromagnetic forming, Journal of Materials Engineering and Performance, 16, N.3, p.314-320.

Golovashchenko, S.F., Gillard, A.J., and Mamutov, A.V., 2014c, Formability of dual phase steels in electrohydraulic forming, Journal of Materials Processing Technology. V.213, Issue 7, pp.1191-1212.

Golovashchenko, S.F., Gillard, A.J., Mamutov, A.V., and Ibrahim R., 2014b, Pulsed Electrohydraulic Springback Calibration of Parts Stamped from Advanced High Strength Steel, Journal of Materials Processing Technology. V. 214, Issue 11, pp. 2796–2810.

Golovashchenko, S.F., Gillard, A.J., Mamutov, A.V., Bonnen J.J.F., and Tang Z., 2014a, Electrohydraulic Trimming of Advanced and Ultra High Strength Steels, Journal of Materials Processing Technology. V. 214, Issue 4, pp. 1027-1043.

Golovashchenko, S.F., Mamutov, V.S., 2005. Electrohydraulic Forming of Automotive Panels. In: Proc. of 6th Global Innovations Symposium: Trends in Materials and Manufacturing Technologies for Transpotation In-dustries, TMS, February 13-17, San Francisco, Califor-nia, USA, p.65-70.

Golovashchenko, S.F., Narainen, R., Bonnen, J.J.F., Mamutov, A.V., Dawson, S.A., Diveto A., 2015, Deep Draw manufacturing Process, US Patent number 9044801, 06/02/2015.

Ibrahim, R., Golovashchenko, S., Smith, L.M., Mamutov, A., Bonnen, J., Gillard, A., 2014, Analysis of Dynamic Loads on the Dies in High Speed Sheet Metal Forming Processes, Journal of Materials Engineering and Performance, V.23, Issue 5, pp 1759-1769.

Imbert, J.M., Winkler, S.L., Worswick, M.J., Oliveira, D.A., and Golovashchenko, S.F., 2005. The effect of tool-sheet interaction on damage evolutionin electromagnetic forming of aluminum alloy sheet. Journal of Engineering Materials and Technology 127, p.145-153.

Mamutov, A.V., Golovashchenko, S.F., Mamutov, V.S. and Bonnen, J.J.F., 2015, Modeling of electrohydraulic forming of sheet metal parts, Journal of Material Processing Technology, V.219, pp. 84–100

Sanford, J.E., 1969. High velocity takes off again. Iron Age, N3, p.91-95.

Tang, Z., Golovashchenko, S.F., Bonnen, J.F., Mamutov, A.V., Gillard, A.J., Bonnen, D., 2014, Analysis of loads on the shearing edge during Electrohydraulic Trimming of AHSS steel in comparison with conventional trimming, Journal of Materials Processing Technology, V.214, Issue 12, pp. 2843–2857.

Vohnout, V.J., Fenton, G.., Daehn, G.S., 2010, Pressure heterogenity in small displacement electrohydraulic forming process. In: Proc. of 4th International Conference on High Speed Forming, March 9-10, Columbus, Ohio, USA, p.65-74.

Yutkin, L.A., 1955, Electrohydraulic Effect, Moscow, Russia, Mashgiz (in Russian).

# Increase of the Reproducibility of Joints Welded with Magnetic Pulse Technology Using Graded Surface Topographies


## A. Rebensdorf*, S. Boehm

Institute for Production Technologies and Logistics, Department for Cutting and Joining, University of Kassel, Germany
*Corresponding author. Email: a.rebensdorf@uni-kassel.de



## Abstract

*The reproducibility of individual welding methods depends to large extents on the material properties. This is especially the case for impact welding as tests have shown that the surface properties influence the joint formation. With the aim to influence the formation and position of the lower curve of the welding process window, this paper focuses on how the surface topography influences an asymmetrical impact. Additionally, relevant process parameters (e.g. collision speed, collision angle, jet formation) will be included and disturbance contours that are placed transversely to the collision vector will be examined. A high-speed camera was used to measure the collision speed as well as the collision angle. The specific surface topographies were created using belt grinding (cutting with geometrically undefined edges) and laser ablation (non-cutting process, local vaporization of materials through pulsed laser beams). The tests exemplarily show a strong correlation between the surface geometries and the joint. The disturbance contours that were introduced transversely to the collision vector shift the lower weld seam boundary, whereas a reduction of the discharge energy leads to a relative strength of the joint of 1.0.*

*In sum, this paper offers fundamental insights into the mechanisms of the joint formation when using magnetic pulse welding and shows the influence of the surface topographies on the conflict between relevant procedural parameters and the possibility to shift the lower procedural window.*



## Keywords

Surface topography, Lower weld seam boundary, Reproducibility

# 1 Introduction

## 1.1 Motivation

Constructions with multi-material-design (mixed materials) have long since been established in production of means for transportation, but especially in the automotive and aerospace industries, as they enable a weight reduction of structures. Here, the joining techniques for the joining of mixed materials are of increasing importance, as they have to meet the current and constantly growing future demands on these structures (for example high rigidity and reduction of weight).

Within the field of linear joining techniques for similar and dissimilar materials (e.g. St/Al or Al/Cu) that can be applied without heat and which are an alternative to adhesive bonding, Magnetic Pulse Welding (MPW) is the only option. With a processing time of under 25 µs, especially in serial productions with thin metal sheets (sheet thickness up to 3 mm), MPW enables the production of coalesced joints of similar and dissimilar materials with low distortion and without filler material. The elliptical weld formation can be realized as a short linear seam (Manogaran et al., 2014) or as a seam with a length of up to 3.000 mm (Schäfer and Pasquale, 2011), (Aizawa et al., 2012). Because of its technological and metallurgical advantages, MPW is especially suited for aluminum-steel-joints, which are increasingly requested.

However, the challenge lies in adapting the process to the specific material and constructional characteristics and design. Thus, in order to receive high-quality joints, the process window should take these characteristics into account and should be expanded if possible. Here, the reproducibility of the procedure plays an important role. Although it has been proven that the procedure is reproducible in (Geyer et al., 2014), as well as (Rebensdorf and Boehm, 2015), some issues still remain and show that especially through the influence of the surface topography, the lower process window can be shifted.

## 1.2 State of the Art and Aim of the Work

Metal welding processes are classified according to the norm DIN 1910:2008 and organized in higher categories. Thus, MPW belongs into the category of pressure welding processes in which coalescent joints are achieved through the movement of mass.

The physical context for impact welding processes can be explained with the basic mechanisms of explosion welding (EXW), as EXW has comparable impact conditions to MPW. This can also be described as an asymmetrical impact welding process. During the impact, the flyer meets the target with a collision angle of β at the collision point/ stagnation point S. The geometrical relationship of the flyer plate velocity (vp) and the collision angle (ß) results in the collision speed (vc) according to Crossland (1982).

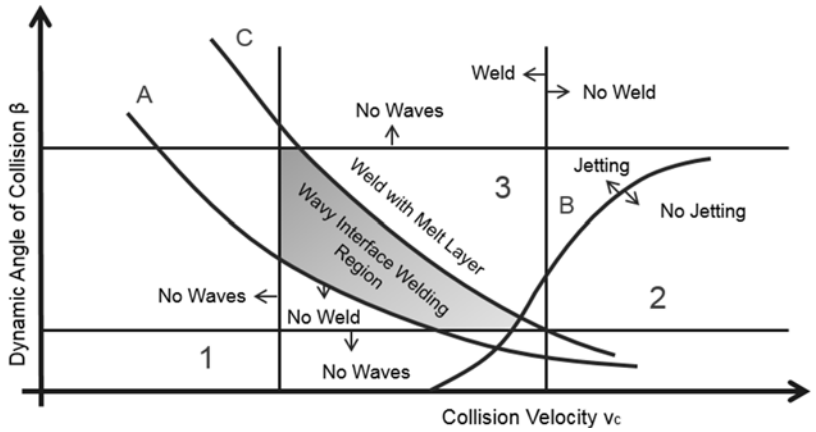


***Figure 1**: General process window for impact welding (experimental investigation of explosion welding) (Crossland, 1982), (Deribas and Zakharenko, 1974), (Walsh et al., 1953), (Mousavi et al., 2013).*

Due to the non-linear behavior of the impact process in MPW, no distinct depiction of the welding process window has been able to established itself. Although similarities to EXW are sought for (Verstraete et al, 2011), the depiction on the β-vc-level is difficult as the angles and velocities vary during impact.

Within the scientific field, there are currently two approaches in dealing with the dependence of the process speed during joint formation in MPW. The first approach assumes that the same procedural limits as for EXW apply in this case too. The second approach, however, presumes that the joint is formed under lower speed and pressure than are known from EXW.

A joint formation using MPW is discussed in (Goebel et al., 2010) in areas of the welding process window in which a joint could not have been formed with EXW. In addition, this publication shows that a joint can be formed with less processing speed than in EXW. In (Goebel et al., 2010), the central element is suggested to be a metastable wave formation process as initiator for the formation of the weld seam, wave initiation in dependence to the Reynold number in (Pai et al., 2013) is also referred to. Göbel et al. prove the difference in the welding process window between MPW and EXW with the help of scientific publications. On the basis of these publications, Göbel et al. assumes that the flyer velocity normal to the target surface is between 30 m/s – 250 m/s. In (Ben-Artzy et al., 2008), however, impact velocities of 250 m/s – 500 m/s were listed from scientific publications and in (Desai et al., 2010) velocities of 400 m/s were presented. These correspond to the velocities of 300 m/s – 650 m/s for EXW as presented in (Goebel et al., 2010) and, therefore, contradict Göbel`s basis of argumentation.

Within the priority program 1640, workgroup 9, of the German Research Foundation (DFG), these theses were taken up and examined. The main focus was on the reproducibility of the Magnetic Pulse Welding technology when the impact is asymmetric and on the influence of the surface topography on the joint formation. Thus, the research focused on specific process variables, collision speed and angle. Here, could be shown the direct effect changes of these variables had on the quality of the weld.

# 2 Experimental Setup

## 2.1 Sample Material, Preparation and Testing Methods

To define the real collision speed and angle, a high-speed camera, produced by the company PCO AG, was used. The camera system HSFC-Pro with its four CCD-camera modules allows to take four pictures in 3 ns.

Assumptions were made to define the influencing variables for MPW. The determination of the process velocities was specifically related to the physical conditions for uniformly accelerated motion (formula 1).

$$v_p(t) = \frac{2(s_1 - v_0 t - s_0)}{t} + v_0 \quad (1)$$

$v_p$ = flyer plate velocity in m/s
$v_0$ = initial velocity in m/s
s = distance in m
t = time in s

The analytical calculation of the flyer plate velocities results from the geometrical dimensions of the impact conditions and is shown exemplary in figure 2, figure 3 shows the procedure.

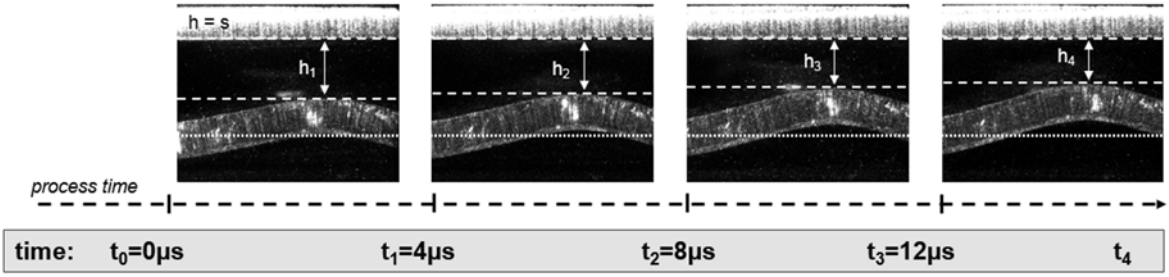


***Figure 2**: Exemplary depiction of the determination of the flyer plate velocities*

The collision angles changed during the process and were evaluated with the help of image correlation (figure 3).

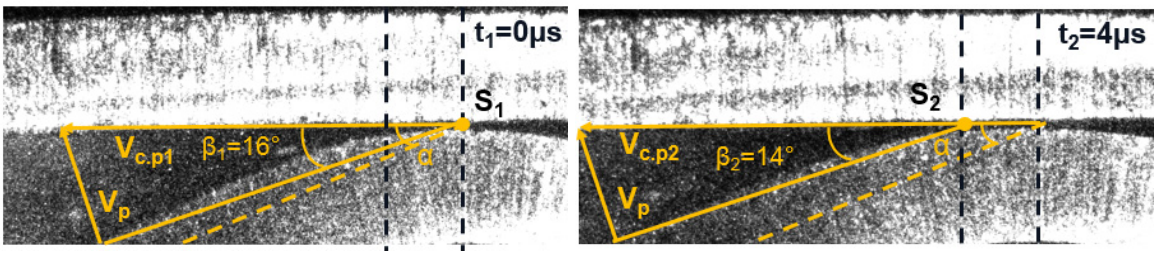


***Figure 3**: Exemplary depiction of the determination of the collision angle*

Subsequently, the calculation of the collision point velocity was done according to Crossland (1982) as follows:

$$V_{cp} = Vp \frac{\cos\frac{1}{2}(\beta-\alpha)}{\sin\beta} \quad (2)$$

$v_{cp}$ = collision point velocity in m/s
ß = collision angle
α = set angle before welding

Here, the material combination EN AW-1050 / S235 JR was examined. The aluminum alloy consisted to 99.4% of aluminum and to 0.44% of iron (Fe) as well as to 0.05% of silicon (Si). The mechanical properties included a tensile strength of 109 N/mm² and a yield strength of 102 N/mm². The steel S235JR had, apart from being to 99.3% of iron (Fe), a proportion of 0.22% of manganese. With a yield to tensile ratio of 1.12, the tensile strength was 380 N/mm².

The system BlueWave 48-16 (max. discharge energy of 48 kJ as well as a max. possible impulse of up to 480 kA) with a flat coil of max. 500 kA and web thickness of 10 mm was used for this project (Geyer et al., 2014). For the variation of the parameters, an acceleration distance (s) of 1.0mm to 2.5mm was examined and varied in steps of 0.5 mm. The discharge energy (E) of the capacitors was varied in steps of 2 kJ, ranging from 11 kJ to 17 kJ. To determine the quality of the weld, tensile tests in accordance to the norm DIN EN ISO 14273 were performed. Five welds were examined per test series. The sample dimensions were (100x40x1.5) mm with an overlapping length of 30 mm. The crucial variable for the assessment of the influencing variables was the determined relative strength of the weld (σ) which is based on the dimensions of the weaker material.

Several disturbance variables were taken into account within this research project. For one, the anisotropy of periodic surface irregularities on the flyer, caused by the roller, to the collision vector was varied. Secondly, the kinematic and phenomenological characteristics of the material flow behavior, as caused by disturbance contours that were induced transversely to the welding direction according to (Lysak and Kuzmin, 2012), were also included (figure 4). The roughness on the surface of the target was created with the CleanLaser CL50. Furthermore, laser ablation was performed on the flyer to minimize the influencing variables and the accompanying dispersion.

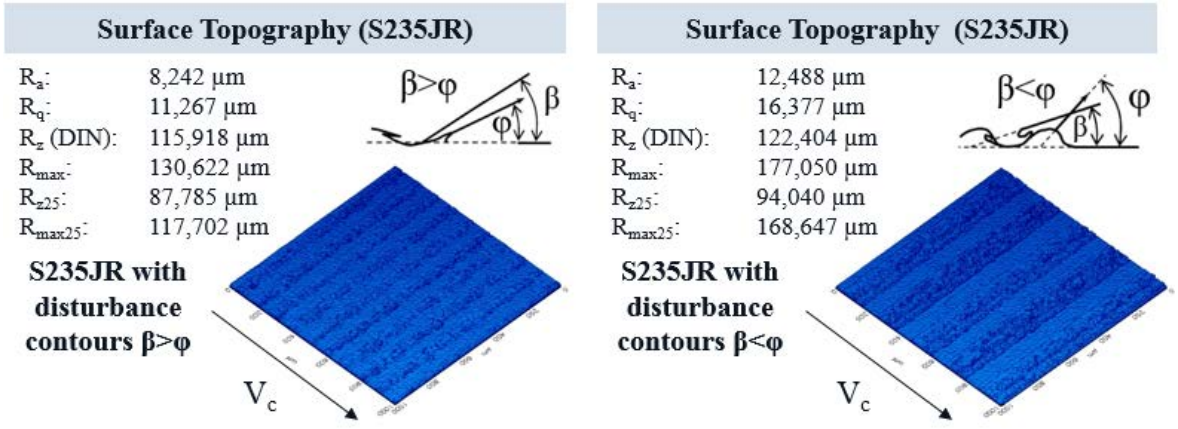


***Figure 4**: Recording of the surface topography, taken with white-light interferometer, MicroProf manufactured by the company Fries Research & Technology GmbH.*

## 2.2 Magnetic Pulse Welding Process Window

Before examining the processing speed, the influence of the acceleration distance and the discharge energy on the weld was evaluated. Figure 5 (A) shows the results of the direction dependent periodic surface irregularities with 0° (parallel) to the collision vector.

It is striking that when the acceleration distance is 1.0mm and the selected minimal discharge energy is 11kJ, there is a relatively low dispersion of strength. If the acceleration distance is increased to up to 2.5mm, the joint strength decreases. On the other hand, an increase in discharge energy leads to abandonment of the lower welding border.

The acceleration distance of s=1.5mm shows the best results and, thus, the least dispersion, for 11kJ as well as 17kJ.

If the roller direction of the aluminum is changed (90° to the collision vector), the discharge energy of 11kJ is not enough anymore to transgress into the stable process window (figure 5, B).

Even if the energy is increased to 13kJ, an improvement can only be seen at an acceleration distance of s=1.0mm. Within the overall context, an acceleration distance of 1.5mm shows the best results when the discharge energy is varied.

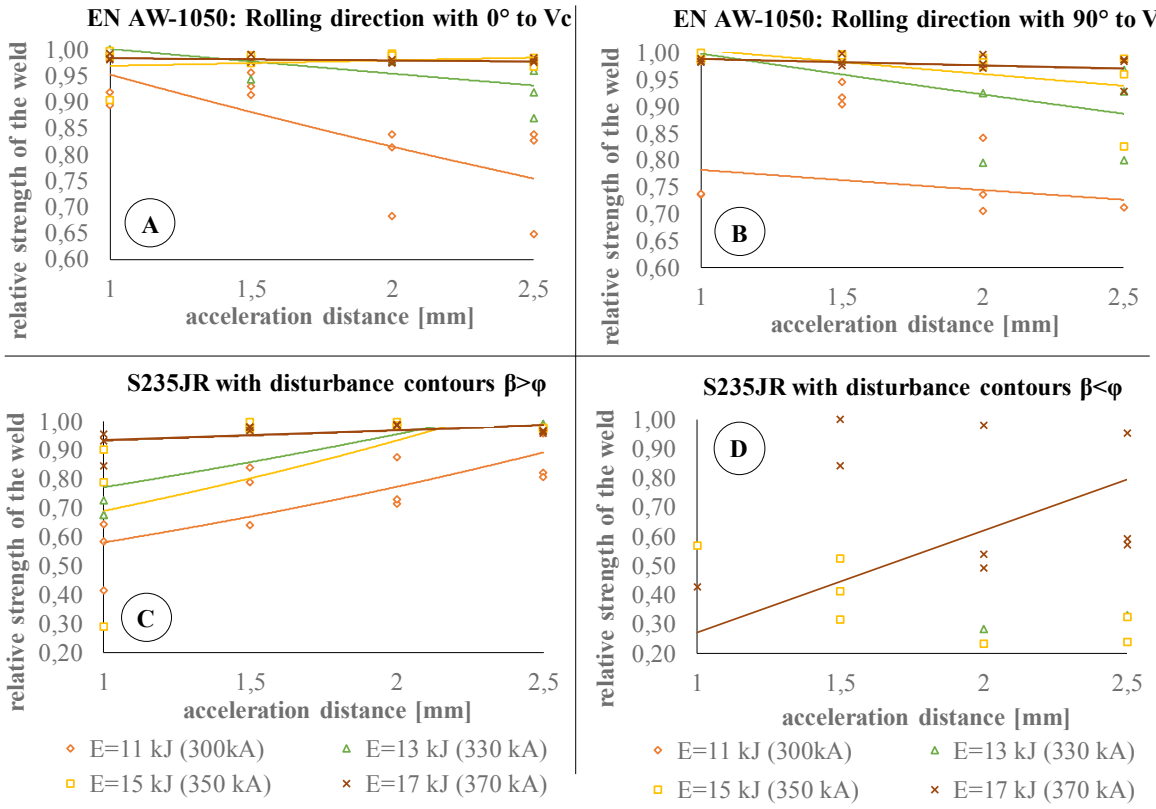


***Figure 5**: Influences on the relative strength of the joint in correlation to the acceleration distance and discharge energy*

This phenomenon became clear, when disturbing contours according to (Lysak and Kuzmin, 2012) were induced. Here, the aluminum alloy EN AW-1050 with surface

irregularities, as caused by the roller, with 90° to the collision vector (Picture 5, C) was tested.

Tests that were performed without induced disturbing contours, with low discharge energy and an increased acceleration distance and which resulted in decreased strength (figure 5, C compare figure 5, A), show opposite results as in figure 7. In comparison, the test series E=11kJ showed an increase in strength with increasing acceleration distance. An increase in energy to 13kJ lead to hardly any dispersion and relative strengths σ=1.0.

This effect became clear, when the relation between the critical angle of the induced disturbance contours and the collision angle was changed from β>φ (figure 5, C) to β<φ (figure 5, D). As a result, all test series showed high dispersion and the strengths of the joint only increased at 17kJ with increasing distance.

Besides showing the influence of the process parameters – acceleration distance as well as discharge energy – the results show a direct influence of the non-linear behavior of the impact process in MPW.

# 3 Experimental Work

## 3.1 Effects of the Flyer Plate Velocities during Joint Formation

Contrary to the cited scientific publications, the effect of the relative strength of the joint of σ=1.0 was examined, as a realized joint – without direct proof of quality – is not enough to define the effects of the influencing variables.

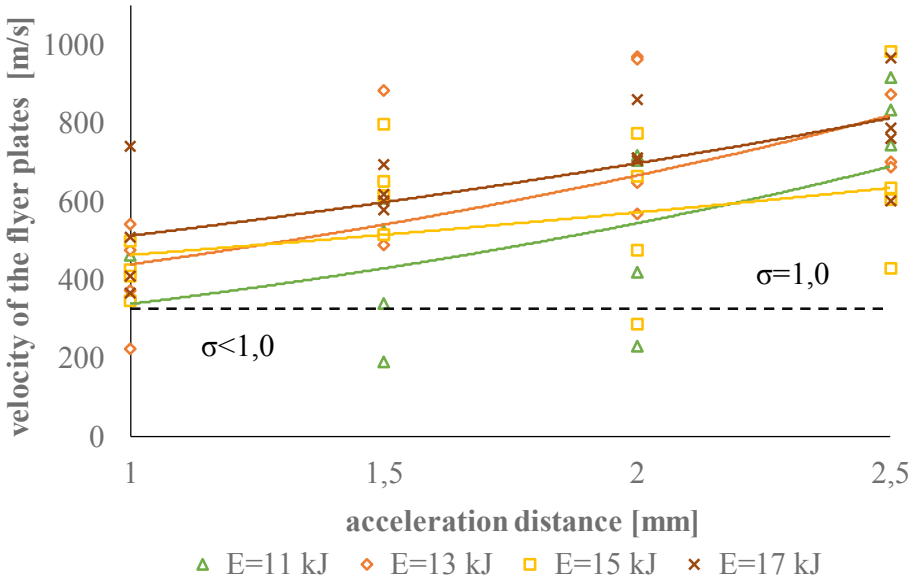


***Figure 6**: Influence of the acceleration distance and the discharge energy on the flyer plate velocities*

The tests showed that in order to achieve a strength of the joint of σ=1.0 (comparable to a weaker base material of joining partners), flyer plates velocities of at least 300 m/s had

to be achieved. A complete overview of the results of this test series, in correlation to the identified flyer plate velocities, is shown in figure 6.

The necessary flyer plate velocities Vp ≥ 300 m/s do not necessarily lead to an optimal joint. Figure 7 exemplarily shows the fracture surface of S235JR as target. Etching according to Adler clearly shows the actual area of connection to the joining partner aluminum, thus, pointing to failures in the joint. The acceleration distance was 2.0mm and the discharge energy 11kJ. The maximum tensile force was 4.590 N, resulting in a relative strength of the joint towards the weaker base material (EN AW-1050) of 0.67. The strength of the joint was low although flyer plate velocities were 420 m/s.

***Figure** 7: Fracture image analysis of the target S235JR, test series 9.3, Etching according to Adler*

## 3.2 Effects of the Collision Point Velocity and the Relative Strength ($V_{cp}$ - σ)

Collision point velocities were taken as the basis to define the influence of the processing speed. Figure 8 shows the collision point velocities in correlation to the relative strength of the joint.

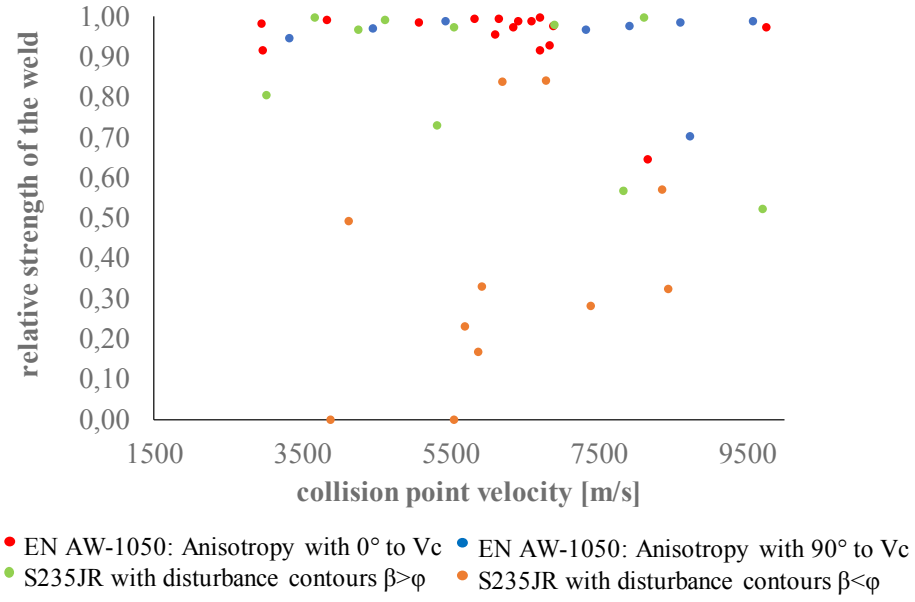


***Figure** 7: Correlation of the collision point velocities with the relative strength of the joint*

Four test series with the respective influencing variables were examined. The results show no direct connection between the collision point velocity and the quality of the joint. Especially when the roughness was such that its angle (φ) was bigger than the collision angle (β) (φ>β), no high strengths of the joint could be realized (figure 8).

## 3.3 Effects of the Collision Angle and the Relative Strength (β - σ)

The results in figure 9 show the influence of the surface topography. However, the decisive influencing parameter for MPW are not the collision point velocity but the collision angle which constantly changes during the process (see figure 9).

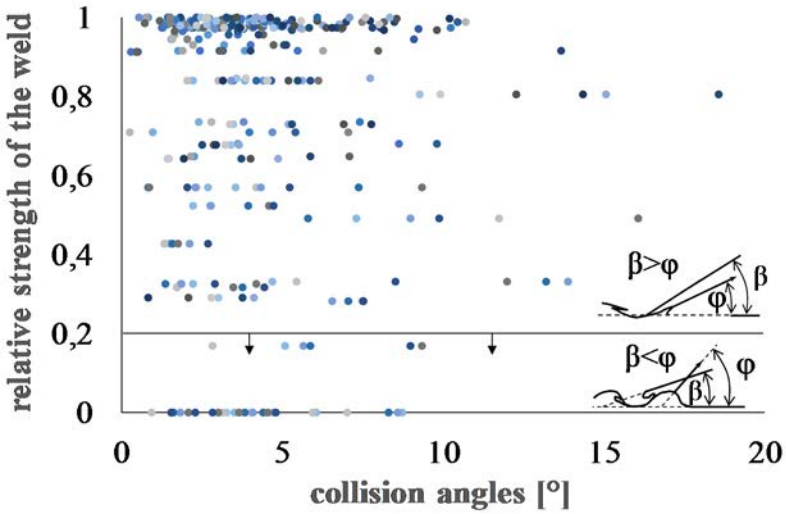


***Figure 8**: Correlation of the collision angle and the relative strength of the joint*

If the collision angle is below the angle of the roughness which needs to be passed, failures in the joint can occur. This information offers a new approach to MPW which has been disregarded in scientific publications so far.

However, this effect can be used; if there is enough information about the exact kind of roughness, wave formation can be realized even for difficult welding combinations such as aluminum and steel. Figure 10 (left) shows a wavy interface without induced disturbance contours transverse to the collision vector. The wavy interface (figure 10, left) was created with an acceleration distance of 2.5mm and a discharge energy of 17kJ. With flyer plate velocities of up to 966 m/s, collision point velocities of 11.237 m/s and collision angles of $\beta \leq 8{,}071$, the joint achieved a relative strength of 0.98.

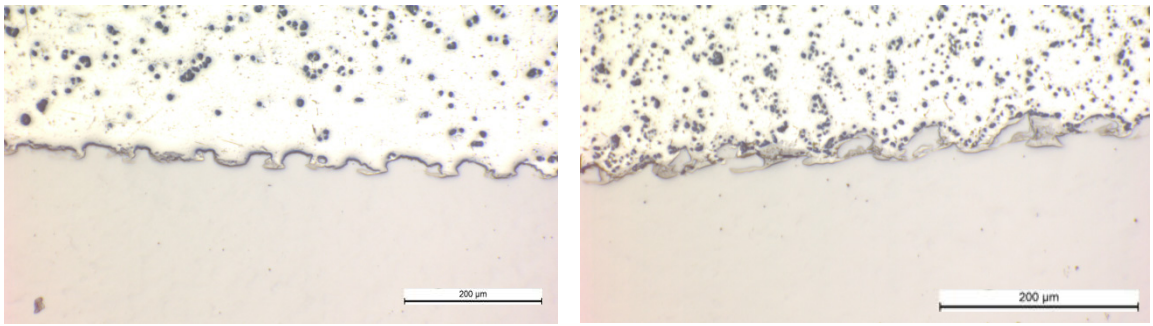


***Figure 9:*** *(left) EN AW-1050 (0° to Vc) / S235 JR, Pl.-No.: 6962;*
*(right) EN AW-1050 / S235JR β<φ, Pl.-No.: 7505*

Figure 10 (right), on the other hand, shows a target with a laser structured surface β<φ (S235JR). The acceleration distance was s=2.5mm and the energy E=17kJ. The flyer plate velocities were 602 m/s, collision point velocities were 4.632 m/s and collision angles were $\beta \leq 9.804$. The relative strength of the joint was 0.97.

These results allow the conclusion that, besides applying specific surface modifications, the interface of the magnetic pulse weld can be adjusted with regard to the surface topography. This allows to prevent critical weld seam irregularities (e.g. joint failures) and, thus, enables to increase the quality of the joint (e.g. waviness in its various forms for fatigue strength stressed parts).

# 4 Conclusion

These results show at which points good reproducibility can be achieved. Apart from specifically shaping the surface topography, a controlled handling of the process-specific parameters is possible and will lead to high-quality welds. All in all, the following insights could be gained:

- To achieve a relative strength of the joint of σ=1,0, flyer plate velocities of more than 300 m/s are necessary.
- When the acceleration distance is $1.0\ \text{mm} \leq d \leq 1{,}5\ \text{mm}$, collision angles of $5.1° \leq \beta \leq 9.1°$ are realized.
- There is a connection between the relative strength of the joint and the collision angle.
- If the collision angles are from $4{,}8° \leq \beta \leq 10{,}3°$, the resulting interface is wavy (surface topography of target with $0.587 \leq Ra \leq 1.823$).
- Collision point velocities have an indirect influence on the joint formation. However, the collision angle is decisive.
- Optimal process parameters for rel. strength of the joint σ=1:
    - Flyer plate velocities ($v_p$): ≥ 695 m/s
    - Collision angle (ß): $6.1° \leq \beta \leq 9.3°$
    - Collision point velocities ($v_{cp}$): ≥ 6.777 m/s

# 5 Acknowledgments

This work was funded by the publicly sponsored Project BO 1980/18-1 “Untersuchungen zur Reproduzierbarkeit des Magnetpulsschweißens beim asymmetrischen Aufschlag“. The authors would like to thank the German Research Foundation (DFG) for their financial support within the project.

# References

Aizawa, T., Kashani, M. & Okagawa, K., 2012. Welding and forming of sheet metals by using magnetic pulse welding (MPW) technique: ICHSF. 4th international conference on high speed forming.

Ben-Artzy, A., Stern, A., Frage, N. & Shribman, V., 2008. Interface phenomena in aluminum-magnesium magnetic pulse welding. Science and technology of welding and joining, 13(4), page 402-408.

Crossland, B., 1982. Explosive welding of metals and its application. Clarendon Press, Oxford.

Deribas, A. A. & Zakharenko, I. D., 1974. Surface effects with oblique collisions between metallic plates: Combustion Explosion and Shock Waves, Vol. 10, page 358–367.

Desai, S. V. et al., 2010. Scaling Relationships for Input Energy in Electromagnetic Welding of Similar and Dissimilar Metals: J. Electromagnetic Analysis & Applications, page 563–570.

Geyer, M., Rebensdorf, A. & Böhm, S., 2014. Influence of the boundary layer of magnetic pulse welds between aluminum and steel. 6th International Conference on High Speed Forming.

Göbel, G. et al., 2010. Dissimilar Metal Joining: Macro- and Microscopic Effects of MPW: ICHSF. 3th international conference on high speed forming, page. 179–188.

Lysak, V. & Kuzmin, S., 2012. Lower boundary in metal explosive welding. Evolution of ideas: Journal of Materials Processing Technology, page 150–156.

Manogaran, A., Manoharan, P., Priem, D., Marya, S. & Racineux, G., 2014. Magnetic Pulse spot welding of bimetals. Journal of Materials Processing Technology, 2014, S. 1236-1244.

Mousavi, A. A. A., Al-Hassani, S. T. S. & Barrett, L. M., 2013. Experimental Investigation of Explosive/Impfact Welding-Experiments wit a Gas Gun. ftp://ns1.ystp.ac.ir/YSTP/4/1/Papers/318.PDF, 12.02.2013.

Pai, V.; Luk'yanov, Y. L.; Kuzmin, G. Y. I. V., 2013. Wave formation in a high-velocity symmetric impact of metal plates.

http://download.springer.com/static/pdf/785/art%253A10.1007%252Fs10573-006-0094-7.pdf?auth66=1360852123_5ded8271bafc33e0504d3713d2c7fd65&ext=.pdf, 12.02.2013.

Rebensdorf, A. & Böhm, S., 2015. Prospects for using Magnetic Pulse Technology to make Steel-Aluminium Connections, Insight Edition @ Daimler AG 2015, Bremen, 24. – 25.06.2015.

Schäfer, R. & Pasquale, P., 2011. Material hybrid joining of sheet metals by electromagnetic pulse technology. Key Engineering Materials, page 61-68.

Verstraete, J., De Waele, W. & Faes, K., 2011. Magnetic Pulse Welding: Lessons to be learned from Explosive Welding. Sustainable Construction and Design 2011, Ghent University, Laboratory Soete, Belgium, page 458–464.

Walsh, J., Shreffer, R. & Willig, E., 1953. Limiting Conditions for Jet Formation in High Velocity Collisions: Journal of Applied Physics, Vol 24, page 349–359.

# Effect of Conductivity of the Inner Rod on the Collision Conditions During a Magnetic Pulse Welding Process

**T. Sapanathan[1*], K. Yang[1], R. N. Raoelison[1, 2], N. Buiron[1], D. Jouaffre[3], M. Rachik[1]**

[1] Sorbonne universités, Université de Technologie de Compiègne, Laboratoire Roberval, CNRS UMR 7337, Centre de Recherche Royallieu, CS 60319, 60203 Compiègne cedex, France
[2] Université de Bourgogne Franche Comté, IRTES-LERMPS, Université de Technologie de Belfort Montbéliard, 90100 Belfort, France
[3] PFT INNOVALTECH, 02100 Saint-Quentin, France
[*]Corresponding author. Email: thaneshan.sapanathan@utc.fr

## Abstract

*The Magnetic Pulse Welding (MPW) process involves a high speed collision between the flyer and inner rod. Conductivity of the inner rod may play a significant role in the collision speed and collision angle. The collision conditions were investigated with varying conductivity of the inner rod in this study. Coupled mechanical-electromagnetic 3D simulations were carried out using LS-DYNA package to investigate the effect of conductivity of the inner rod on the collision patterns during the MPW process. The simulation involves a welding process with a tube and a rod using a one turn coil with a separate field shaper. The electrical conductivity was varied to a wide range to investigate the influence on the collision condition. Moreover, in order to verify the independency of the collision condition with the mechanical properties of the inner rod, two cases including aluminum alloy AA2024-T351 and copper with appropriate Johnson-Cook parameters were used for the rod. In the entire simulations aluminum alloy was used as the tube material. It was identified that the impact velocity is almost consistent for each case and the impact angles vary between negative and positive values according to the angular measurement convention used in this study. Although, influence of the conductivity of the inner rod is not significant for the investigated current flow while it may sometime delay the incidence of collision at lower frequencies than the critical frequency ($F_{Crit}$). Optimizing the collision conditions in the MPW process can help to identify the suitable materials for prescribed welding conditions.*

## Keywords

Magnetic pulse welding, Numerical modelling, Collision velocity

## 1 Introduction

Interface characterization is used to ensure the weldability of the materials in various joining applications. The wavy interface produced during the collision is a unique feature of the impact welding that was also experimentally evidenced to identify potentially permanent weld while defective joints appear with the degradation and highly deformed interfaces (Baaten et al., 2010). In the literature, the notion of weldability is described and experimentally confirmed depending on the development of interfacial waves and the research works on this subject result in the identification of suitable parameters for weld creation. Early studies revealed that jetting and hydrodynamic conditions at the interface govern the weldability windows for impact welding processes. Suitable conditions for weld formation were also theoretically established using a correlation between collision angle and impact velocity which served as a reference for further development to describe the welding range.

The welding range may consist of several different zones, viz., pre-critical zone (no welding), wavy zone (welding zone) and unfavorable zone including waveless zone, anomalous wave zone, melt solidification zone and supersonic zone (Lysak and Kuzmin, 2012). But waveless interface without apparent deformation, wavy morphology and interface deterioration are practically evidenced at the interface and they allow a pragmatic distinction of a successful welding range (Raoelison et al., 2013, Nassiri et al., 2015). In accordance with the aforementioned reason, the weldability in impact welding is currently related to the morphology of the interface and particularly with the wavy shape. Moreover, the major criteria of bonding used in an impact welding remains the transition from smooth to wavy morphology.

Although, formation of wavy interface and its characteristics such as high amplitude and large wavelength are considered as an indication of a strong bonding (Zamani and Liaghat, 2012, Xu et al., 2013), recent research studies reported that these parameters may not be crucial for the formation of bonding. In contrast, jetting and ejection of materials from the interface are identified as required phenomena to create a successful bonding, which mainly depend on the collision conditions such as collision speed and collision angle (Groche and Pabst, 2015). These ejected materials may consist of oxides or solid parent materials (Kakizaki et al., 2011, Pabst and Groche, 2014) that may also include burnt properties which depend on the temperature of the interface (Pabst and Groche, 2014). Negative or zero degree collision angles may hinder the weld formation and that could weaken the welding due to the accumulation of the ejected materials at the interface. At the same time, very high impact velocity (i.e. higher than the speed of sound in the material), the jetting phenomenon becomes impossible because the gap closure speed is higher than

that of the jet, which traps the ejected material in place (Lysak and Kuzmin, 2012, Groche and Pabst, 2015). Therefore it is important to determine the collision conditions at the interface to obtain the favorable welding conditions.

During a magnetic pulse welding the conductivity of individual parts and the conductivity difference between the welding components can influence the impact conditions and the associated ejection phenomena during the weld formation by influencing the collision speed and the collision angle. This could be a main difference between MPW and other impact welding processes. This study presents an investigation on the effect of the conductivity of the inner rod during a weld formation in a magnetic pulse welding process for materials with various electromagnetic properties.

# 2 Methods

Coupled electromagnetic-mechanical simulations with 3D models (**Fig. 1a**) are used to investigate the welding conditions in terms of collision speed and collision angle while varying the conductivity of the inner rod. The input current obtained for the coil using a Rogowski probe for 8 kV input voltage from a custom made generator is used in the simulation. The current curve and specifications of the main working area are respectively given in **Fig. 1b** and **1c.**

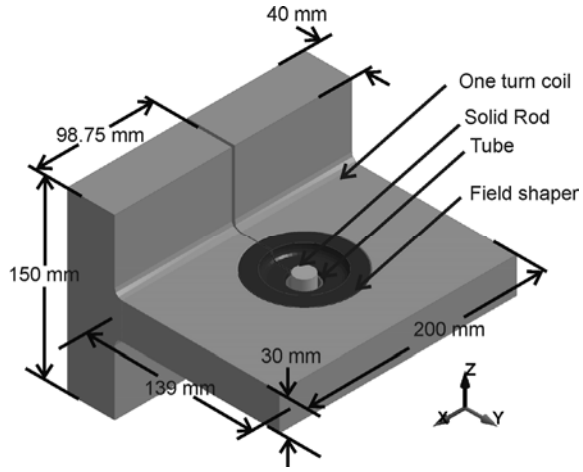


(a)

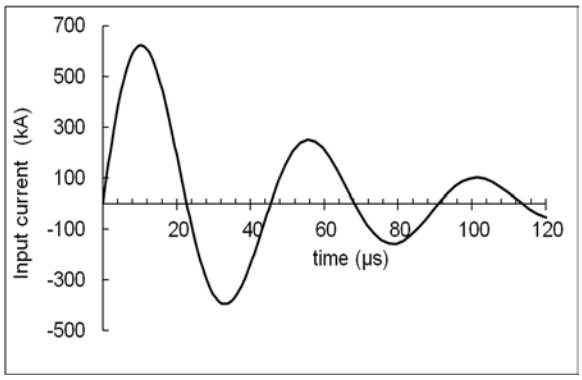


(b)

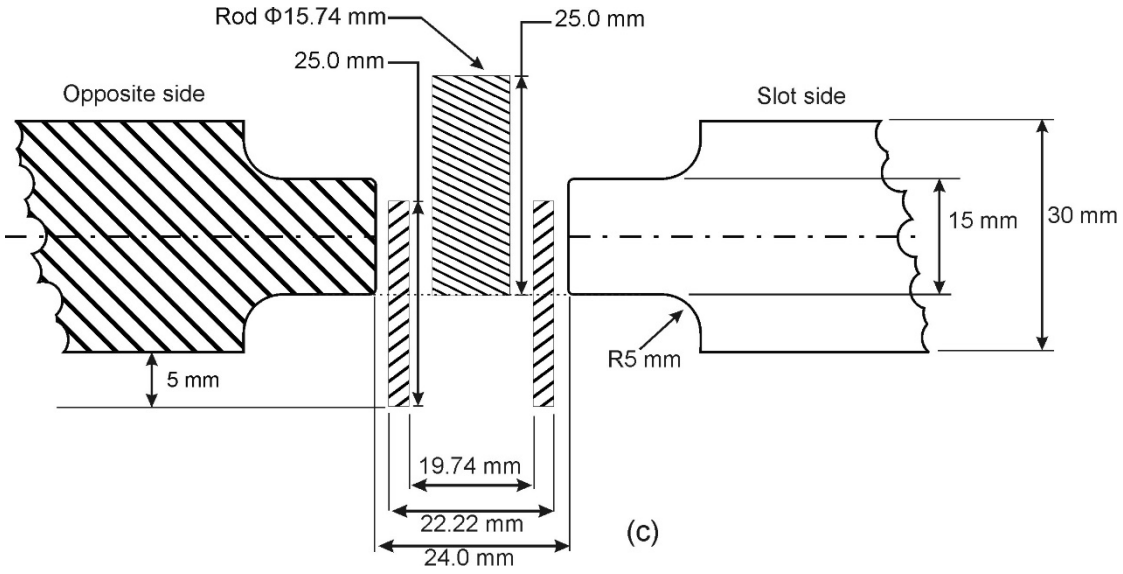


***Figure 1**: 3D model (a) and the input current (b) used in the numerical simulations, and the schematic illustration of the test case (c).*

Mechanical and electromagnetic properties used for each component in the welding assembly are given in **Table 1**. Material behavior of the deformable parts under high strain rate was defined in the simulations using Johnson-Cook material model (Eq. 1) and the corresponding parameters obtained from literatures for aluminum (Mabrouki et al., 2008) and copper (Johnson and Cook, 1985) are provided in **Table 2.**

| Material | Components | Density ($kg.m^{-3}$) | Young's modulus (GPa) | Poisson's ratio | Electrical conductivity (IACS%) |
|---|---|---|---|---|---|
| AA2024 – T351 | Tube or Rod | 2700 | 73 | 0.33 | 5%, 30%, 60%, 90% |
| Commercially pure copper | Tube or Rod | 8900 | 124 | 0.34 | 5%, 30%, 60%, 90% |
| Copper Alloy | Field shaper | 7900 | 210 | 0.29 | 46% |
| Steel | Coil | Rigid | | | 7% |

***Table 1**: Mechanical and electromagnetic properties of components and their materials used in this model, where 100% IACS is equivalent of 5.8001 × $10^7$ $S.m^{-1}$.*

| Johnson-Cook parameters | *A* (MPa) | *B* (MPa) | *C* | *n* |
|---|---|---|---|---|
| Aluminum alloy AA2024-T351 | 352 | 440 | 0.0083 | 0.42 |
| Commercially pure copper | 90 | 292 | 0.025 | 0.31 |

***Table 2**: Johnson-Cook parameters used for the constitutive behavior of aluminum alloy AA2024-T351 and commercially pure copper during the simulations.*

$$\bar{\sigma} = (A + B\bar{\varepsilon}^n)\left[1 + Cln\left(\frac{\dot{\bar{\varepsilon}}}{\dot{\bar{\varepsilon}}_0}\right)\right] \quad (1)$$

The following 9 cases (**Table 3**) were investigated in the simulation for impact velocity and the collision angle at the onset of impact. Although, the simulation did not include the microscopic interfacial effect to capture the welding effect, these models are sufficient to obtain the impact conditions. Automatic surface to surface contact was prescribed between workpieces to capture the contact behavior during the collision. The collision angles were calculated based on the angle between the velocities component ($V_r$ and $V_z$) from the simulations. The sign conventions used in the angle and velocity predictions are provided in **Fig. 2**. A high magnification view near the top edge of the tube shown in **Fig. 2b** represents the possible in-flight kinematics of the flyer tube.

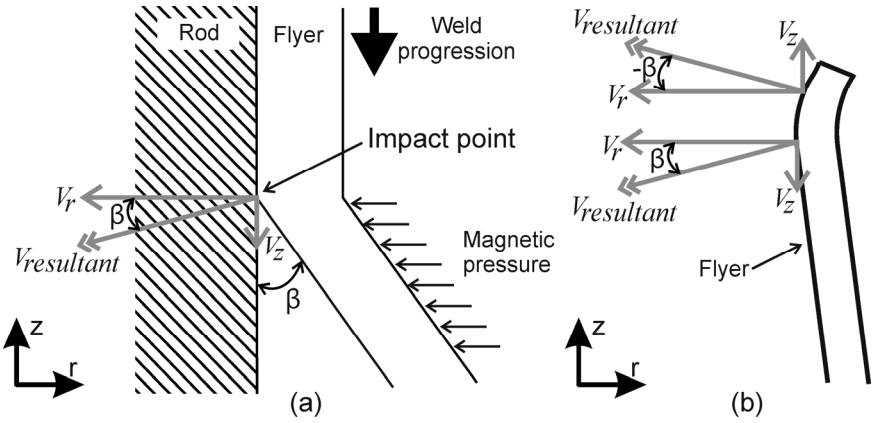


***Figure 2**: (a) Sign convention used for velocity and angle predictions in this study and (b) a detailed view of the positive and negative angles near the top edge of the flyer.*

The simulations were carried out using LS-DYNA® package with the solver version R8. The electromagnetic-mechanical multi-physics solver uses both finite element method (FEM) and boundary element method (BEM) (Çaldichoury and L'Eplattenier, 2012). These simulations provide an ideal condition to investigate the conductivity effect on the collision conditions, where the representations of materials are not 100 percent accurate with the reality. However, conductivity values are carefully chosen within the reality of conductivity limits (5% - 90 % IACS) in this study.

Moreover, solution time steps are important input parameters that govern the convergence of a simulation. In an electromagnetic-mechanical coupling, that requires for both electromagnetic and mechanical time steps for a simulation. In general, the electromagnetic time step, $\Delta T \leq p^2/2D$, where $p$ and $D$ are characteristic mesh size and characteristic diffusion time. The characteristic diffusion time $D$ is determined by, $D = 1/\mu\sigma$, where $\mu$ and $\sigma$ respectively denote magnetic permeability and electric conductivity of the conductor. The mechanical time step ($\Delta t$) is always smaller than the electromagnetic time step, $\Delta t \ll \Delta T$.

| | Case 1 | Case 2 | Case 3 | Case 4 | Case 5 | Case 6 | Case 7 | Case 8 | Case 9 |
|---|---|---|---|---|---|---|---|---|---|
| Tube material and conductivity | Al, 30% | Al, 30% | Al, 30% | Al, 30% | Al, 30% | Al, 30% | Al, 30% | Al, 30% | Cu, 30% |
| Rod material and conductivity | Al, 5% | Al, 30% | Al, 60% | Al, 90% | Cu, 5% | Cu, 30% | Cu, 60% | Cu, 90% | Cu, 30% |

***Table 3**: Mechanical behavior of material and electromagnetic properties considered for the corresponding material in various simulation cases.*

# 3 Results and Discussion

Although, validation procedure for the numerical model is still in progress, the preliminary observations of the overall final shape for a welded sample obtained under similar experimental setting **(Fig. 3b)** corroborate the predicted final deformed shape of the samples (**Fig. 3a)**. Further measurements and interfacial observations for the particular case are required to validate the numerical model. Sample shown in Fig. 3b, is obtained from a pool of previous experiments and details of welded samples obtained under various parameters with their weld variances could be found elsewhere (Raoelison et al., 2015). Mechanical strength of those welds were characterised using push-out and torsion-shear tests (Raoelison et al., 2013).

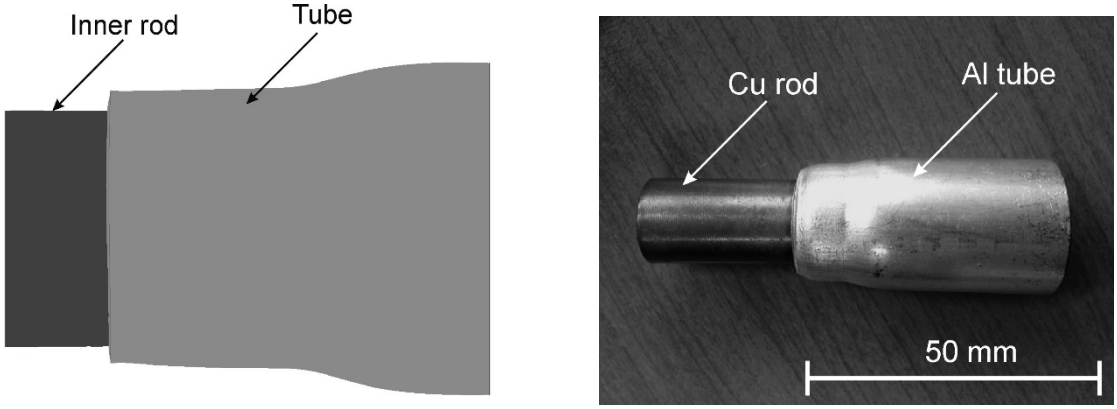


***Figure 3**: Final shape of the welded specimen from numerical simulations in comparison with MPW sample; (a) weld region of the numerical model at the end of the simulation (b) magnetic pulse welded Al/Cu sample*

The impact velocity was calculated inside of the tube along the longitudinal direction. Sudden change of velocity was used to identify the onset of the impact velocity. Immediately at the onset of the impact, the resultant velocity of the tube rapidly reduces. Based on the calculation of the resultant velocity, and angle of attack [$tan^{-1}$ *(Vz/ Vr)*] were calculated for the corresponding onset time.

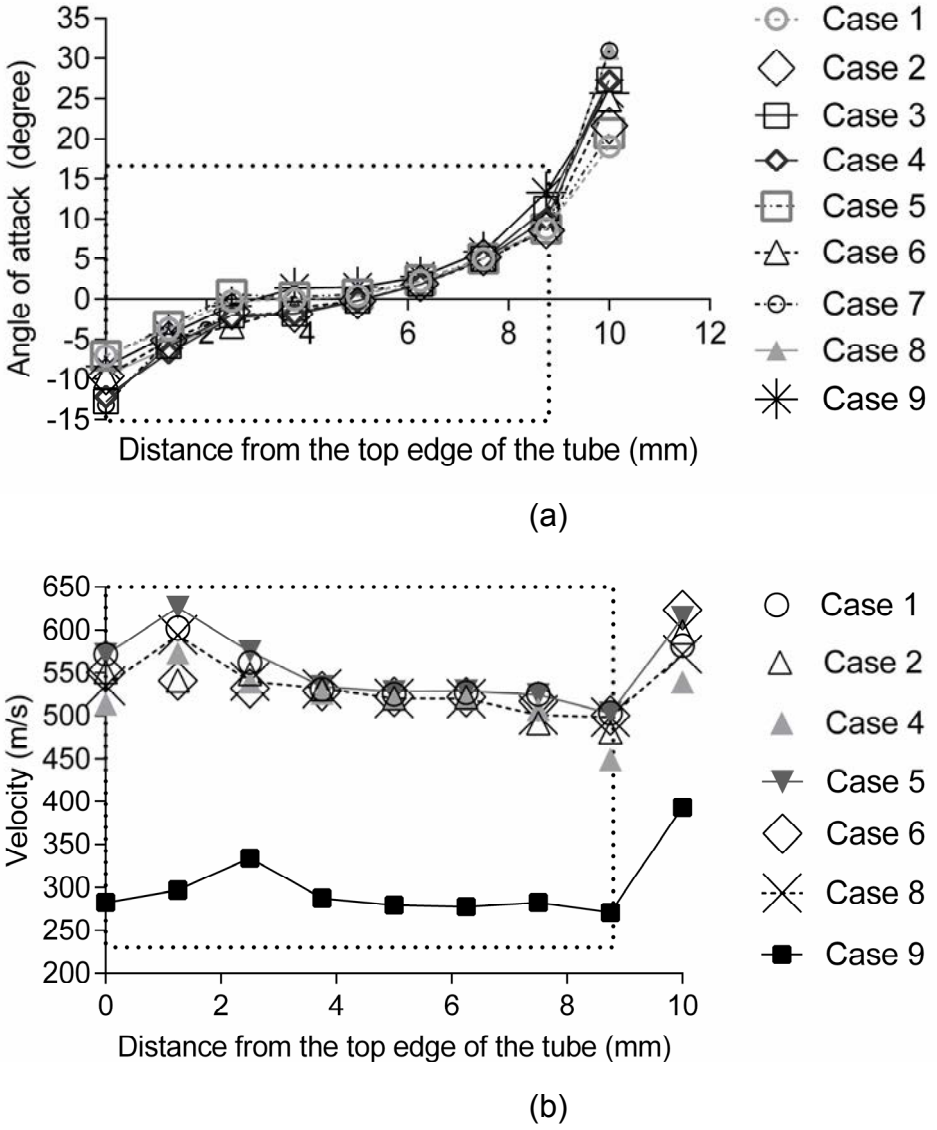


***Figure 4**: Impact angles along the longitudinal distance from the top edge of the tube for the simulation cases of 1 to 9 in (a) and instantaneous resultant velocity at those corresponding points during the onset time of the impact in (b). The boxed regions in (a) and (b) well represent the onset of impact.*

The impact velocity is plotted against the longitudinal distance from the top edge of the tube (**Fig. 4b**) and results indicate almost consistent throughout the entire weld length (~0 - 9 mm). Impact angle measured with the radial direction and positive sign convention used for the anti clockwise impact angles. Impact angles obtained along the longitudinal directions corresponding to those impact velocity points in Fig. 4b, shown in **Fig. 4a**. The impact angles vary between positive and negative in the impact region according to the sign convention (Fig. 2) used in this study. Outside of the boxed regions in Fig 4a and 4b do not represent the impact because the tube was not able to come in contact with the rod in those

outside regions. It's also in agreement with the experimental case where ~9 mm tube length was in contact with the rod (Fig. 3b).

There are almost very similar behaviors observed for the same electrical conductivity cases, regardless of the parts' mechanical parameters. That is, pairs of (Case 1 and Case 5), (Case 2 and Case 6), (Case 3 and Case 7) and (Case 4 and Case 8) show a close agreement in comparison with other results. However, the variations were not significant in these case studies. A control case was considered with the mechanical properties of copper tube (Case 9), impact angles obtained from this case deviate from other cases of 1-8. Moreover the velocity was consistent for all the cases of 1-8 and that significantly differs from the Case 9 as expected.

Although these case studies indicate that the influence of the conductivity of the inner rod on the impact angle and impact velocity is not apparent, the influence was identified as highly depended on the current frequency. That is, one could neglect the conductivity of the inner rod when considering various materials for welding at higher frequencies than that of a critical frequency ($F_{Crit}$) that can be obtained by equating the onset of collision time and the diffusion time for the magnetic field to reach the inner surface from the outer, through thickness direction of the flyer tube. At those higher frequencies ($>F_{Crit}$) the impact occurs before the full diffusion of magnetic field through thickness from the exterior to the inner surface of the tube while at lower frequencies ($<F_{Crit}$) impact may occur after the full diffusion of magnetic field through thickness of the tube, hence those events fully depend on the individual input current frequency.

Therefore, this study was further extended to investigate diffusion time and magnetic field at various locations. The magnetic field is parallel to the axis of tube and it diffuses through thickness from the outer surface of the tube. Magnetic field in the tube can be calculated for a particular position along the *z* axis using Eq. 2 in a cylindrical coordinate system.

$$B(t,d) = b\exp\left(-\alpha t - \frac{d}{\delta}\right)\sin(\omega t - \frac{d}{\delta}) \qquad (2)$$

where *t, d, δ, b, α* and *ω* are respectively time and distance from the external surface, skin depth, amplitude factor, time damping constant and angular frequency. Constants *b, α* and *ω* are decided by the source current. In this equation, the terms "*exp (-αt – d/δ)*" and "*sin (ωt – d/δ)*" respectively denote the damping and periodic components. The magnetic field diffusion reaches a particular point when "*(ωt – d/δ=0)*". Based on these aforementioned equations, the diffusion time for the inner surface of the tube (when *d=1.24* mm, equivalent to the thickness of the tube and the electrical conductivity of 30 IACS% for all the cases) can be estimated as ~10.7 µs. This diffusion time to the inner surface is identified as just 1 µs before impact time. However, the full diffusion of the current requires extra time; the influence of the initial diffusion within the 1 µs is negligible.

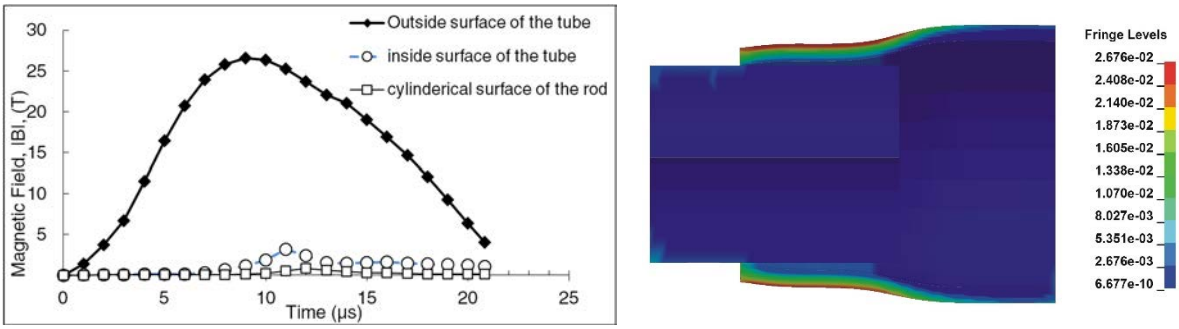


(a) (b)

***Figure 5**: Magnetic field strength obtained for the Case 2 along the mid plane of the field shaper at various locations against time in (a) and magnetic flux density in kilo Tesla obtained along the longitudinal section at 11 µs in (b).*

Magnetic field strength at the locations of the outer surface of the tube, inner surface of the tube and the cylindrical surface of the rod against time for the first half period of the input current are shown in **Fig. 5a**. These results clearly indicate the shielding effect of the tube during the diffusion time that blocks almost 100% of the magnetic field reaching inside the tube. **Fig. 5b** explains the magnetic field diffusion through thickness just after the diffusion reaches the inner surface of the tube at 11 µs.

# 4. Conclusions

This study was carried out to investigate the influence of the conductivity of inner rod on the collision velocity and collision angle during a magnetic pulse welding process. The simulations were performed under the same process conditions with varying material properties. The impact velocities were captured at the onset of the collision and the impact angles were determined from the direction of the velocity at the onset. It was identified that the impact velocity is almost consistent for each case within the contact region, while the impact angles vary between negative and positive values according to the angular measurement convention used in this study. This study also clearly shows that the impact velocity changes from a positive $z$ with $r$ coordinate to negative $z$ with $r$ coordinate during the welding process. However, the influence of the conductivity of the inner rod on the impact angle and impact velocity are not well captured within the resolution of the data points, and which is identified as highly influenced by the diffusion time and the magnetic field strength at the inner surface of the flyer tube before the onset of the collision. Moreover, this study reveals at high current frequencies, higher than the critical frequency ($F_{Crit}$), one can neglect the effect of conductivity of the inner rod during a magnetic pulse welding process.

## Acknowledgments

Authors would like to acknowledge the "Région Picardie" and "Le fonds européen de développement régional (FEDER)" for their financial support and "Plateforme Innovaltech" for its collaboration.

## References

Baaten, T., N. Debroux, W. De Waele and K. Faes, 2010. Joining of copper to brass using magnetic pulse welding. 4th International Conference on High Speed Forming, Dortmund.

Çaldichoury, I. and P. L'Eplattenier, 2012. EM Theory Manual. Electromagnetism and Linear Algebra in LS-DYNA, Livemore Software Technology Corporation.

Groche, P. and C. Pabst, 2015. Numerical simulation of impact welding processes with LS-DYNA. 10th European LS-DYNA Conference, Würzburg, Germany.

Johnson, G. R. and W. H. Cook, 1985. *Fracture characteristics of three metals subjected to various strains, strain rates, temperatures and pressures*. Engineering fracture mechanics 21(1), pp. 31-48.

Kakizaki, S., M. Watanabe and S. Kumai, 2011. *Simulation and experimental analysis of metal jet emission and weld interface morphology in impact welding*. Materials transactions 52(5), pp. 1003-1008.

Lysak, V. and S. Kuzmin, 2012. *Lower boundary in metal explosive welding. Evolution of ideas*. Journal of Materials Processing Technology 212(1), pp. 150-156.

Mabrouki, T., F. Girardin, M. Asad and J.-F. Rigal, 2008. *Numerical and experimental study of dry cutting for an aeronautic aluminium alloy (A2024-T351)*. International Journal of Machine Tools and Manufacture 48(11), pp. 1187-1197.

Nassiri, A., G. Chini, A. Vivek, G. Daehn and B. Kinsey, 2015. *Arbitrary Lagrangian–Eulerian finite element simulation and experimental investigation of wavy interfacial morphology during high velocity impact welding*. Materials & Design 88, pp. 345-358.

Pabst, C. and P. Groche, 2014. Electromagnetic Pulse Welding: Process Insights by High Speed Imaging and Numerical Simulation. 6th International Conference on High Speed Forming, South Korea.

Raoelison, R., N. Buiron, M. Rachik, D. Haye, G. Franz and M. Habak, 2013. *Study of the elaboration of a practical weldability window in magnetic pulse welding*. Journal of Materials Processing Technology 213(8), pp. 1348-1354.

Raoelison, R. N., T. Sapanathan, N. Buiron and M. Rachik, 2015. *Magnetic pulse welding of Al/Al and Al/Cu metal pairs: Consequences of the dissimilar combination on the interfacial behavior during the welding process*. Journal of Manufacturing Processes 20, Part 1, pp. 112-127.

Xu, Z., J. Cui, H. Yu and C. Li, 2013. *Research on the impact velocity of magnetic impulse welding of pipe fitting*. Materials & Design 49, pp. 736-745.

Zamani, E. and G. H. Liaghat, 2012. *Explosive welding of stainless steel–carbon steel coaxial pipes*. Journal of Materials Science 47(2), pp. 685-695.

# Tools and Machines

# Efficient Coil Design by Electromagnetic Topology Optimization for Electromagnetic Sharp Edge Forming of DP980 Steel Sheet

**M. K. Choi[1], H. Huh[1*], M. H. Seo[2], Y. Kang[2]**

[1] School of Mechanical, Aerospace and Systems Engineering, KAIST, Daejeon, Korea
[2] Steel Solution Center, POSCO, Incheon, Korea
[*]Corresponding author. Email: hhuh@kaist.ac.kr

## Abstract

*This paper proposes a design method of the tool coil by topology optimization for the electromagnetic sharp edge forming process. Topology optimization is an approach that optimizes material configuration in a given domain to meet the design requirements. The design problem for the tool coil is defined as enhancing efficiency of the forming process and optimization problem is set to be maximization of the Lorentz force induced on the tool coil. A new topology optimization formulation based on the numerical methods for electromagnetism using FEM and BEM is developed for maximization of the Lorentz force. Optimum design of the tool coil is obtained by the topology optimization using the element density approach. The optimized result is compared with other coils which have different configurations to show the effectiveness of the proposed method. The idea of applying topology optimization to the design of the tool coil is successful and this formulation deals effectively for the optimization problems.*

## Keywords

Coil design, Topology optimization, Electromagnetic sharp edge forming

## 1 Introduction

Auto industries recent trend is to develop lightweight vehicles for both improvement of both efficiency and crashworthiness of auto-body with the use of advanced high strength steels (AHSS). DP980 steel is one of the AHSS materials with ultimate tensile strength of higher than 980 MPa. However, the application of DP980 steel sheet to auto-body is limited with

conventional deep drawing processes due to its poor formability in many cases of manufacturing of automotive parts.

Electromagnetic forming (EMF) is one of the innovative forming methods to improve the formability of a material. There are advantages of EMF with a material of poor formability. In EMF, the workpiece is accelerated to high strain rates so the mechanical properties and the formability of the workpiece material can be improved compared to the quasi-static ones (Psyk et al., 2011). In addition, forming force can be applied locally and it is possible to perform EMF in hard-to-reach areas by utilizing a suitable tool coil (Psyk et al., 2011). EMF can be combined with conventional deep drawing for sharp edge forming process which consists of pre-forming by conventional deep drawing and making a sharp corner radius of a workpiece electromagnetically.

Many researchers have conducted investigations on the feasibility of the electromagnetic sharp edge forming process over the last years. Vohnout (1998) showed that combination of higher strains and more complex geometries of a door inner and a hood part can be realized using combined deep drawing and electromagnetic calibration. Psyk et al. (2007) studied sharpening of a feature on an automotive stamping and found that the process was feasible. Imbert and Worswick (2011) showed that hybrid conventional/electromagnetic forming process using a specially designed coil could be successful in corner filling process for aluminum alloy sheet parts.

Most of the research works about electromagnetic sharp edge forming process are, however, limited to the application of aluminum alloys. In general, electromagnetic forming is suitable for materials with a high electrical conductivity. The application of DP980 steel sheet to EMF seems to be challenging because DP980 steel sheet has low electrical conductivity and very high flow stress. Choi et al. (2014) developed a method for optimization of electromagnetic sharp edge forming process of DP980 steel sheet and the process was feasible. However, they suggested that the efficiency of the electromagnetic energy delivery would have to be enhanced to accommodate industrial settings.

In order to enhance the efficiency of the electromagnetic energy delivery, optimum coil design is necessary. The coil is an important component of any EMF process since it delivers the electrical energy to form the workpiece. However, only a small part of the charging energy is used for the plastic deformation resulting in a comparable bad efficiency of the EMF process. Thus the optimum design of the tool coil is conducted to enhance the efficiency of the forming process.

This paper proposes a design method of the tool coil by topology optimization for the electromagnetic sharp edge forming process. Topology optimization is an approach that optimizes material configuration in a given domain to meet the design requirements. In this paper, design requirement for the tool coil is defined as enhancing the efficiency of the forming process and optimization problem is set to be maximization of Lorentz force induced in the tool coil. In order to solve the optimization problem, a new topology optimization formulation is developed for Lorentz force maximization. Optimum design of the tool coil is obtained using the topology optimization. Then the optimized result is compared with the other coils which have different configurations to show the effectiveness of the proposed method.

# 2 Optimization Formulation

## 2.1 Problem Description

Electromagnetic sharp edge forming of DP980 steel sheet where optimum coil will be applied is described in Fig. 1. Conventional square cup drawing with a punch radius of 30 mm is conducted for pre-forming of the process. Then electromagnetic sharp edge forming is applied to the pre-formed workpiece to obtain a sharp edge with a punch radius of 10 mm (Choi et al., 2014). In order to form the sharp edge of DP980 workpiece with the electromagnetic sharp edge forming process, efficient tool coil is necessary due to low electrical conductivity and high flow stress of DP980 steel sheet.

The design objective of the tool coil is to find an optimal configuration of the tool coil that maximizes the efficiency of the process. The efficiency of the process is defined as the ratio of the deformation energy to the stored electrical charging energy. The deformation energy in this process is determined by the Lorentz force in the radial direction. Thus, the optimum tool coil which maximizes the Lorentz force in the radial direction will be obtained.

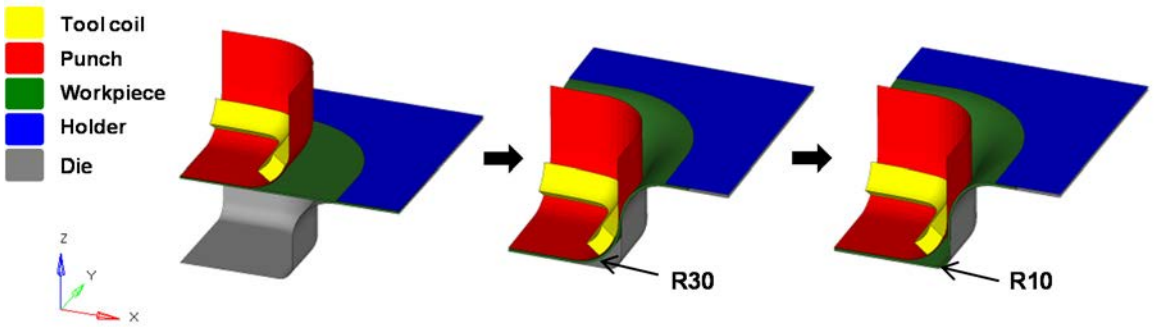


***Figure 1**: Schematic of electromagnetic sharp edge forming of DP980 steel sheet*

## 2.2 Numerical Methods for Electromagnetism

The optimization formulation for the Lorentz force maximization is based on the numerical methods used in LS-DYNA EM module (L'Eplattenier et al., 2008). Governing equations of electromagnetism are Maxwell's equations. Maxwell's equations in terms of scalar and vector potential with Eddy current approximation can be expressed as follows:

$$\nabla \cdot (\sigma \vec{\nabla} \phi) = 0 \tag{1}$$

$$\sigma \frac{\partial \vec{A}}{\partial t} + \vec{\nabla} \times (\frac{1}{\mu} \vec{\nabla} \times \vec{A}) + \sigma \vec{\nabla} \phi = \vec{j}_s \tag{2}$$

where $\phi$ is the electric scalar potential, $\vec{A}$ is the magnetic vector potential, $\sigma$ is the electrical conductivity, $\mu$ is the magnetic permeability and $\vec{j}_s$ is the source current density.

The potential equation can be solved by a finite element method using differential forms elements (Ren and Razek, 1996). There are four forms of basis function called 0-forms, 1-forms, 2-forms and 3-forms, defined on the solid hexahedral element. Equation (1) is projected on the 0-forms basis functions, $W^0$, which are scalar basis functions that have a gradient. Equation (2) is projected on the 1-forms basis functions, $\vec{W}^1$, which are vector basis functions that have a curl. The weak formulations are obtained by applying the boundary conditions and integration by part as follows:

$$\int_\Omega \sigma \vec{\nabla}\Phi \cdot \vec{\nabla} W^0 d\Omega = 0 \tag{3}$$

$$\int_\Omega \sigma \frac{\partial \vec{A}}{\partial t} \cdot \vec{W}^1 d\Omega + \int_\Omega \frac{1}{\mu} \vec{\nabla} \times \vec{A} \cdot \vec{\nabla} \times \vec{W}^1 d\Omega = -\int_\Omega \sigma \vec{\nabla}\Phi \cdot \vec{W}^1 d\Omega + \int_\Gamma \frac{1}{u} \left[ \vec{n} \times \left( \vec{\nabla} \times \vec{A} \right) \right] \cdot \vec{W}^1 d\Gamma \tag{4}$$

where $d\Omega$ is an element of volume $\Omega$, $\Gamma$ is the boundary of volume $\Omega$ and $\vec{n}$ is the outer normal to the boundary. After decomposing the scalar and vector potential on the 0-forms and 1-forms basis function, the finite element equations can be derived as follows:

$$\mathbf{S^0}(\sigma)\phi = 0 \tag{5}$$

$$\mathbf{M^1}(\sigma)\frac{\partial a}{\partial t} + \mathbf{S^1}(\frac{1}{\mu})a = -\mathbf{D^{01}}(\sigma)\phi + \mathbf{S}a \tag{6}$$

with the stiffness matrix of the 0-forms $\mathbf{S^0}$, the mass matrix of the 1-forms $\mathbf{M^1}$, the stiffness matrix of the 0-forms $\mathbf{S^1}$ and the derivative matrix of the 0-1-forms $\mathbf{D^{01}}$. The finite element matrices can be found in L'Eplattenier et al., 2008.

The last term $\mathbf{S}$, the outside stiffness matrix, cannot be directly computed. It can be computed from a definition of a BEM system. The BEM system is used for solving equations in the air. In order to compute the last term of the FEM system, a surface current $\vec{k}$ is introduced on the surfaces of the conductors from the Biot−Savart equation.

$$\vec{A}(x) = \frac{\mu_0}{4\pi} \int_\Gamma \frac{1}{|x-y|} \vec{k}(y)\, dy \tag{7}$$

Using new technique proposed by Ren and Razek (1990), Equation (8) can be expressed as follow:

$$\vec{n} \times (\vec{\nabla} \times \vec{A})(x) = \frac{\mu_0}{2} \vec{k}(x_0) - \frac{\mu_0}{4\pi} \int_\Gamma \frac{1}{|x-y|^3} \vec{n} \times [(\vec{x}-\vec{y}) \times \vec{k}(y)]\, dy \quad \text{where } x \to x_0 \in \Gamma \tag{8}$$

After discretization of vector potential with 1-form basis functions and surface current with 1-form surface basis functions $\vec{V}^1 = \vec{n} \times \vec{W}^1$, the BEM system equations can be derived as follows:

$$\mathbf{P}k = \mathbf{D}a \tag{9}$$

$$\mathbf{S}a = \mathbf{Q}k = \mathbf{Q}_{\mathbf{s}}k + \mathbf{Q}_{\mathbf{d}}k \tag{10}$$

with the BEM matrices which can be found in L'Eplattenier et al., 2008.

The FEM system Equation (6) is coupled with the BEM system Equation (9) and (10). Time integration is done with implicit backward Euler method. The global system equations are expressed as follows:

$$\mathbf{P}k_{n+1}^{t+1} = \mathbf{D}a_{n}^{t+1} \tag{11}$$

$$\left[\mathbf{M^1}(\sigma) + dt\mathbf{S^1}(\frac{1}{\mu})\right]a_{n+1}^{t+1} = \mathbf{M^1}(\sigma)a^{t} - dt\mathbf{D^{01}}(\sigma)\phi^{t+1} + dt\mathbf{Q}k_{n+1}^{k+1} \tag{12}$$

Equation (5) is solved only when a voltage is imposed with the Dirichlet condition. Equation (11) is solved using a pre-conditioned gradient method and Equation (12) is solved using a direct solver.

Once the scalar potential and the vector potential have been determined, the Lorentz force can be computed. The Lorentz force is cross product of the current density $\vec{j}$ and the magnetic flux density $\vec{B}$. In terms of vector potential, the Lorentz force generated on the workpiece can be expressed with the topological derivative matrix as follows:

$$\vec{F} = \vec{j} \times \vec{B} = \sigma\left(-\frac{d\vec{a}_i}{dt}\right) \times \left(-\mathbf{T}^{12}\vec{a}_i\right) \tag{13}$$

## 2.3 Topology Optimization Formulation

In order to obtain optimal configuration of the tool coil by topology optimization, the element density approach is adopted. For electromagnetic topology optimization, the electric conductivity is assumed to vary from 0 to $\sigma_0$ with element density $x$ as follows:

$$\sigma = \sigma_0 f(x) = \sigma_0 \cdot x^p \tag{14}$$

where $\sigma_0$ is the electric conductivity of a material and $p$ is the penalization power. In addition, the BEM system is utilized for numerical methods for electromagnetism. The boundary element determines the boundary of the conductor and air, which has importance in computation of vector potential. When the finite element of the conductor becomes close to 0, the element is regarded as air and new boundary elements might be created. Therefore, the boundary element density function is considered for every face element. When element $E_1$ and $E_2$ share a face element F, the boundary element density is expressed as follows:

$$\rho_F = \left|x_{E_1} - x_{E_2}\right| \tag{15}$$

Design variables are determined as densities of elements in the domain. The topology optimization problem for the tool coil is set with the design variables: finding the element densities of the coil domain which maximize the sum of the Lorentz force generated on the workpiece subject to the mass constraint. It is expressed as follow:

$$\begin{aligned} &\textit{Find}: && \vec{x} = \left[ x_1, x_2, \cdots, x_j, \cdots, x_m \right]^{\mathrm{T}} \\ &\textit{Maximize} && F = \sum_{i=1}^{n} \left| \sigma \left( -\frac{d\vec{a}_i}{dt} \right) \times \left( -\mathbf{T}^{12} \vec{a}_i \right) \right| \\ &\textit{Subject to} && h(x_j) = \sum_{j=1}^{m} x_j v_j - M \le 0 \end{aligned} \tag{16}$$

where $\vec{x}$ is the element density vector for the coil domain, $m$ and $n$ is the number of elements of the coil domain and the workpiece, respectively. $v_j$ is the volume of element $j$ and $M$ is the constrained mass of the coil.

The topology optimization problem is solved by the method of moving asymptotes (Svanberg, 1987) which is a gradient based optimizer. In order to use the MMA, the sensitivity analysis of the objective function and the constraint function with respect to the element density are necessary. The sensitivity of the objective function can be computed as follows:

$$\begin{aligned} \frac{d}{dx_j} F &= \frac{d}{dx_j} \left[ \sum_{i=1}^{n} \sigma \left( -\frac{d\vec{a}_i}{dt} \right) \times \left( -\mathbf{T}^{12} \vec{a}_i \right) \right] \\ &= \sum_{i=1}^{n} \left( \sigma \frac{d}{dx_j} \left( -\frac{\vec{a}_i^{\,t} - \vec{a}_i^{\,t-1}}{dt} \right) \times \left( -\mathbf{T}^{12} \vec{a}_i^{\,t} \right) + \sigma \left( -\frac{\vec{a}_i^{\,t} - \vec{a}_i^{\,t-1}}{dt} \right) \times \frac{d}{dx_j} \left( -\mathbf{T}^{12} \vec{a}_i^{\,t} \right) \right) \end{aligned} \tag{17}$$

The sensitivity of the objective function is in terms of the vector potential and the sensitivity of the vector potential. The sensitivity of the vector potential is obtained from the global system equations using the FEM and BEM matrices as follows:

$$\begin{aligned} &\frac{\partial \mathbf{M^1}(\sigma)}{\partial x_j} \frac{(a_{n+1}^{t+1} - a^t)}{dt} + \mathbf{M^1}(\sigma) \frac{\partial}{\partial x_j} \left[ \frac{(a_{n+1}^{t+1} - a^t)}{dt} \right] + \mathbf{S^1}(\frac{1}{\mu}) \frac{\partial a_{n+1}^{t+1}}{\partial x_j} \\ &= -\frac{\partial \mathbf{D^{01}}(\sigma)}{\partial x_j} \phi^{t+1} - \mathbf{D^{01}}(\sigma) \frac{\partial \phi^{t+1}}{\partial x_j} + \mathbf{Q}_s(\rho) \frac{\partial k_{n+1}^{t+1}}{\partial x_j} + \mathbf{Q}_d(\rho) \frac{\partial k_{n+1}^{t+1}}{\partial x_j} + \frac{\partial \mathbf{Q}_s(\rho)}{\partial x_j} k_{n+1}^{t+1} + \frac{\partial \mathbf{Q}_d(\rho)}{\partial x_j} k_{n+1}^{t+1} \\ &\text{where} \quad \frac{\partial \phi^{t+1}}{\partial x_j} = \mathbf{S^0(x)}^{-1} \left( -\frac{\partial \mathbf{S^0(x)}}{\partial x_j} \phi^{t+1} \right) \\ &\qquad \frac{\partial k_{n+1}^{t+1}}{\partial x_j} = \mathbf{P}(\rho)^{-1} \left( \mathbf{D}(\rho) \frac{\partial a_n^{t+1}}{\partial x_j} + \frac{\partial \mathbf{D}(\rho)}{\partial x_j} a_n^{t+1} - \frac{\partial \mathbf{P}(\rho)}{\partial x_j} k_{n+1}^{t+1} \right) \end{aligned} \tag{18}$$

# 3 Coil Design Optimization

## 3.1 Topology Optimization of the Tool Coil

The topology optimization problem is defined for the design of the efficient tool coil. The coil domain for the electromagnetic topology optimization problem is described in Fig. 2. The gap between the tool coil and the workpiece is set to 1 mm. A part of the tool coil is considered for the coil domain since it is assumed that the tool coil has a constant cross section along the edge of the workpiece and the optimal configuration of the cross section of the tool coil is necessary for the coil design. Coil current flows through the RLC circuit connected part and the Lorentz force is generated on the workpiece. The optimal location of the Lorentz force applied to the workpiece for successful electromagnetic sharp edge forming is studied by Choi et al. (2014), and the corresponding optimal region of the workpiece is considered for the optimization problem. As for input parameters, the electrical conductivities are $5.75\times10^7\ \Omega^{-1}\ m^{-1}$ for the tool coil and $6.99\times10^6\ \Omega^{-1}\ m^{-1}$ for the workpiece. The RLC values of the equivalent circuit are set to be 6 mΩ, 230 nH and 380 μF, respectively and the voltage of 12 kV is imposed as a capacitor voltage. The constrained mass of the coil is set to half of mass of the coil domain.

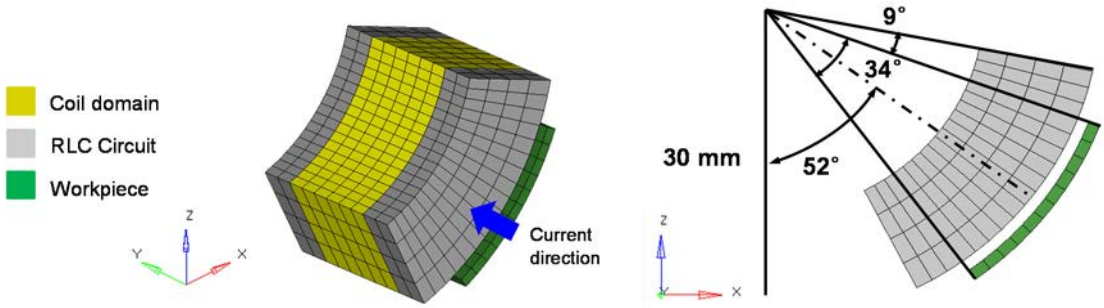


***Figure 2**: The coil domain for the electromagnetic topology optimization problem*

The optimal distribution of densities of the tool coil is shown in Fig. 3. Densities of the elements near the workpiece are higher than that of the elements far from the workpiece. The objective and constraint function values converge after 6th iteration.

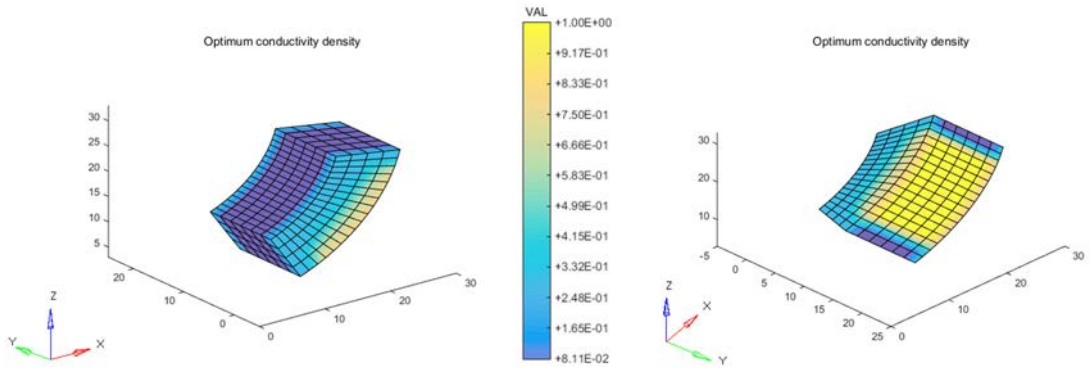


***Figure 3**: The optimal distribution of densities of the tool coil*

## 3.2 Efficiency of the Optimum Tool Coil

Optimal configuration of the tool coil is obtained by solving the electromagnetic topology optimization problem. Based on the optimal configuration, optimum design for efficient tool coil is obtained as shown in Fig. 4. The coil thickness is determined as 5 mm according to the constraint of cross section area since 4 kA/mm$^2$ is allowed for a copper conductor without overheating or mechanical damage (Kim et al, 2014). Outer radius is 29 mm which determines the gap between the tool coil and the workpiece as 1 mm.

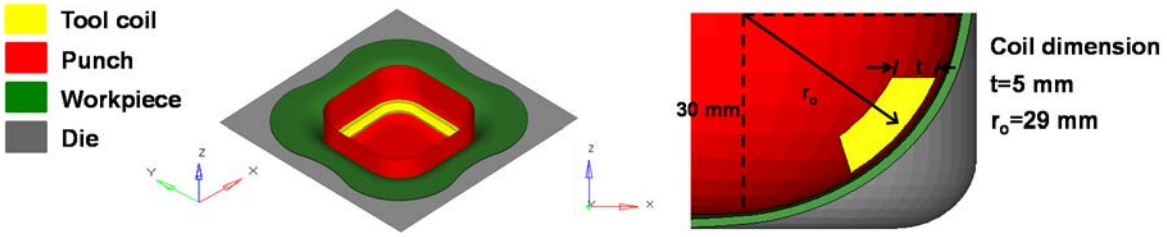


***Figure 4**: The optimum design for the efficient tool coil*

Numerical analysis of electromagnetic sharp edge forming of DP980 steel sheet is conducted to investigate the efficiency of the optimum tool coil. For the numerical analysis, LS-DYNA EM module is employed. Electromagnetic parameters described in Section 3.1 are used for input parameters of the numerical analysis. The efficiency of the optimum tool coil is compared with other coils which have different configurations. Various configurations of the tool coil are shown in Fig. 5. The dimensions of each tool coil are determined according to the constraint of cross section area.

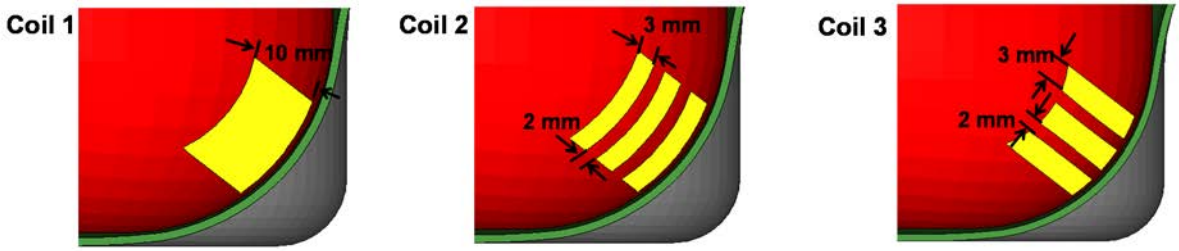


***Figure 5**: Various configurations of the tool coil for the comparison of the efficiency*

After the numerical analysis, the section profile along the x-z plane is obtained as shown in Fig. 6 with various configurations of the tool coil. It is confirmed that the amount of the deformation is largest for the optimum tool coil. The enhancement of the efficiency by the optimum tool coil appears quite significant compared with various configurations of the tool coil.

In order to investigate why the optimized coil provides efficiency improvement, distributions of the maximum current density during the process in each coil are compared as shown in Fig. 7. Unit for the current density is mA/mm$^3$. The current density of the optimized coil has the largest value among other coils although the resistance of the optimized coil is the largest and total current flowing through the coil is the smallest among

other coils. In addition, the current density of the optimized coil is concentrated at the region which is close to the workpiece. This can lead to high induced current density and high magnetic flux density on the workpiece which is related to the Lorentz force.

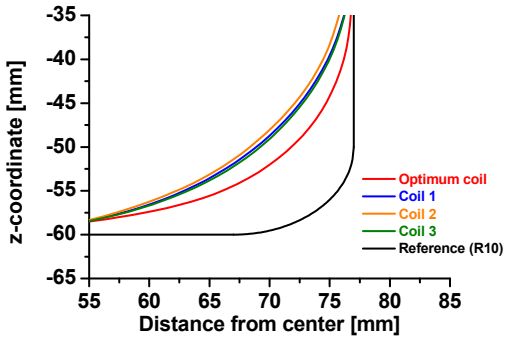


***Figure 6**: Section profile along the x-z plane with various configurations of the tool coil*

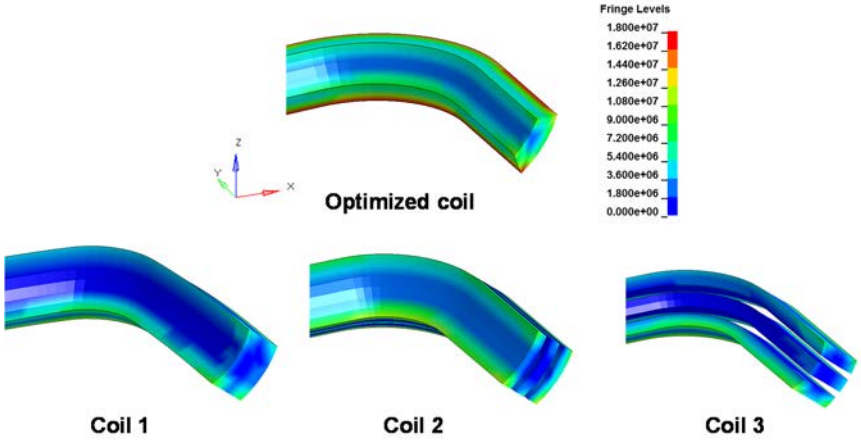


***Figure 7**: Distributions of current density with various configurations of the tool coil*

Induced current density and magnetic field on the workpiece with various configurations of the tool coil are compared as shown in Fig. 8. The result by the optimized coil is the largest and the resultant Lorentz force will also be the largest, thus the optimized coil can provide improvement of the efficiency.

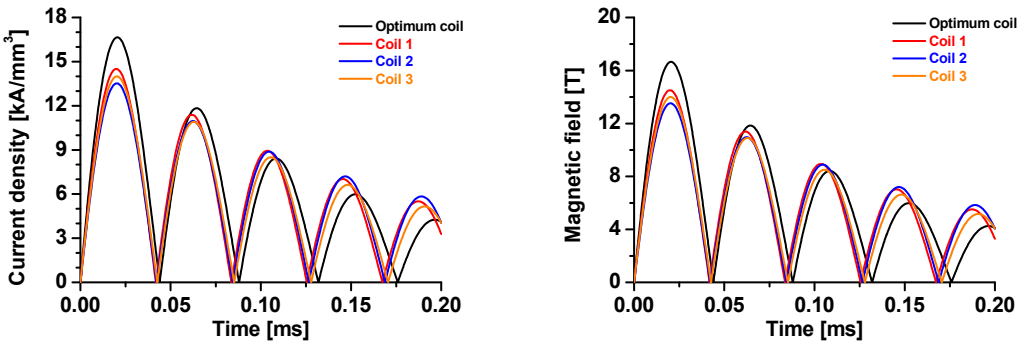


***Figure 8**: Induced current density and magnetic field on the workpiece with various configurations of the tool coil*

# 4 Conclusion

This paper introduces a design method of the efficient tool coil by topology optimization. Topology optimization formulation is based on the numerical methods for electromagnetism using the FEM and BEM. Topology optimization problem is defined as maximization of the Lorentz force in the radial direction. Tool coil is treated as electric conductors and the element density approach is used for representing the electric conductivity. The idea of applying topology optimization to the design of efficient tool coil is successful and this formulation deals effectively for the optimization problems.

# References

Choi, M.K., Huh, H., Park, N., Jung, C.G., Nam, J., 2014. Optimization of Combined Deep Drawing and Electromagnetic Corner Fill Process of DP980 Steel Sheet. High Speed Forming 2014, Proceedings of the 6th International Conference, Daejeon, Korea, pp. 281-292.

Imbert, J., Worswick, M., 2011. Electromagnetic reduction of a pre-formed radius on AA5754 sheet, Journal of Materials Processing Technology 211, pp.896-908.

Kim, D., Park, H.I., Lee, J., Kim, J.H., Lee, M.G., Lee, Y., 2014. Experimental study on forming behavior of high-strength steel sheets under electromagnetic pressure, Journal of Engineering Manufacture, pp. 1-12.

L'Eplattenier, P., Cook, G., Ashcraft, C., 2008. Introduction of an Electromagnetism Module in LS-DYNA for Coupled Mechanical Thermal Electromagnetic Simulations. High Speed Forming 2008, Proceedings of the 3th International Conference, Dortmund, Germany, pp. 86-96.

Psyk, V., Risch, D., Kinsey, B.L., Tekkaya, A.E., Kleiner, M., 2011. Electromagnetic forming – A review. Journal of Materials Processing Technology 211 (5), pp. 787-829.

Psyk, V., Beerwald, C., Henselek, A., Homberg, W., Brosius, A., Kleiner, M., 2007. Integration of Electromagnetic Calibration in to the Deep Drawing Process of an Industrial Demonstrator Part, Key Engineering Materials 344, pp. 435-442.

Ren, Z., Razek, A., 1990. New technique for solving three-dimentional multiply connected eddy-current problems, IEEE Proceedings, Vol. 137, No. 3.

Ren, Z., Razek, A., 1996. Computation of 3-D electromagnetic field using differential forms based elements and dual formulations, International Journal of Numerical Modeling: Electronic Networks, Devices and Fields 5, pp. 81-98.

Svanberg, K., 1987. The method of moving asymptotes – A new method for structural optimization, International Journal for Numerical Methods in Engineering 24, pp. 359-373.

Vohnout, V.J., 1998. A Hybrid Quasi-Static/dynamic Process for Forming Large Sheet Metals Parts from Aluminum Alloys, Ph.D. Thesis, The Ohio State University.

# Electrodynamics of Magnetic Pulse Welding Machines: Global and Local Electrical Analogues

**R. Bouzerar[1,4], F. Bougrioua[1], I. Tekaya[1,4*], N. Foy[1], M. Hamzaoui[2], V. Bourny[2,3], O. Durand-Drouhin[4], D. Jouaffre[5], D. Haye[5]**

[1] Laboratoire Physique des Systèmes Complexes, EA 4663, Université de Picardie Jules Verne, Amiens, France
[2] Laboratoire des Technologies Innovantes, EA 3899, Université de Picardie Jules Verne, Amiens, France
[3] ESIEE, 14 Quai de la Somme, Amiens, France
[4] Laboratoire de Physique de la Matière Condensée, EA 2081, Université de Picardie Jules Verne, France
[5] PFT Innovaltech, Lycée Condorcet, Rond-Point Joliot-Curie, Saint-Quentin, France
[*]Corresponding author. E-mail: issyan.tekaya@u-picardie.fr

## Abstract

*In this paper, a theoretical, experimental and numerical study of MPW machines is carried out. While it is known that such machines are very complex by nature because of the coupling between different parts, we used simple electrical analogues to describe its dynamics. A RLC circuit modeling the whole machine is depicted and experimental results are shown. A further study including numerical simulations allows to compute the current distribution and estimate the magnetic field within the coil but also the magnetic pressure generated in the process, all using a 2D model and reasonable assumptions. A late theoretical study opens the way for innovative experimental measurements regarding the kinetics of the deformations of metallic tubes, but also their mechanical behavior before the welding process, making use of their capacitive properties.*

## Keywords

Magnetic pulse welding, Electrodynamics, Electrical analogues

# 1 Introduction

Magnetic pulse technologies and especially their application to welding or forming (Broeckhove, 2010, Daehn, 2002, Psyk et al., 2011), are an important application of electromagnetism attracting the attention of both the academic and industrial communities. Because of their complexity, these technologies and related research give an interesting example of cross-disciplinary theme since it can be regarded as an application of electromagnetism and high deformation mechanics leading to potential biological risk. There is no need to stress the extreme importance of electromagnetism (Griffith, 1999) in our modern societies, so deeply permeated with its applications as telephony or radio broadcasting. But the significant development of electromagnetic technology has deeply modified the radiation bath exerted on individuals, leading to unavoidable questioning about its harmfulness. This ambient bath is particularly intense around electromagnetic sources such as the magnetic pulses machines we focus on in our study. The evaluation of the impact of electromagnetic radiation on both users' health (biological effects of radiations) and material environment (electronic devices being sensitive to electromagnetic pulses) is the first type of fundamental questions raised by the study of electromagnetic machines. These investigations can certainly profit by a better knowledge of the machine dynamics and its malfunction. More precisely, this second fundamental questioning regards the operation of such machines in connection to their structure. As any industrial machine, magnetic pulse machines convert electrical power into work (mechanical deformations of pieces), this process being accompanied with multiple sources of loss. Magnetic forming or welding machines, as schematized on **Fig. 1**, consist mainly of a power generator, that is a set of high voltages capacitances, providing, through a spark-gap (power switch), the extremely high current intensities necessary to produce the high magnetic pulses or equivalently the magnetic stresses required to deform hard conductive materials.

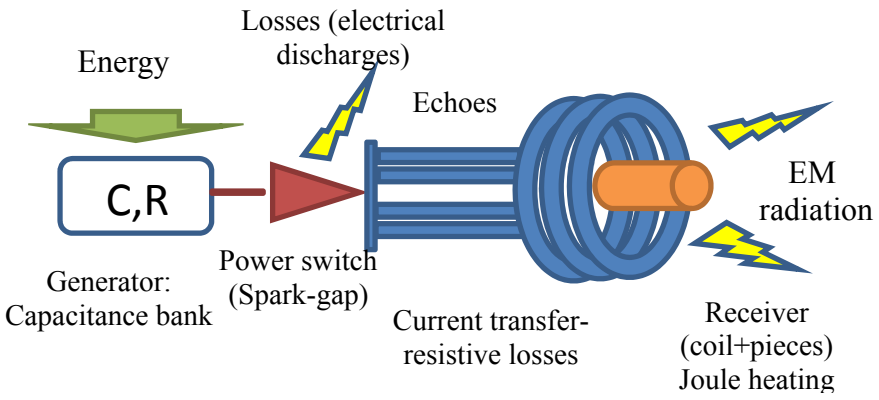


***Figure 1**: Typical structure of magnetic pulse machines indicating its main components and localization of the main EM radiation sources.*

This figure gives a simplified chart of the sources of energy loss. Electrical echoes in the current transfer lines result in both a distortion of the current pulses and substantial

resistive losses. EM radiation is produced especially by the spark-gaps (e.g. through electrical discharge) and the receiver (coil) fed by the very intense and short current pulses. A better understanding of such processes would help mastering the influence of the 'electromagnetic noise' on the machine dynamics and its optimization of the mechanism of the plastic deformation of pieces. The development of the underlying theory and its experimental validation is an essential step to understand the way the machine configuration and its structure influences the deformation process as well as a possible optimization of the welding or forming process through adaptation of the operating conditions to the mechanical properties of the tubes. In the search for relevant answers to these questions, we unavoidably have to face the structural complexity of these machines, manifesting in the coupling between its parts. To avoid the usual difficulties associated with the study of complexity, we carried out a global characterization of the machine and tried in a second step to capture its main structural and functional features through global electrical analogues, that is analogues of the whole machine. The necessary incorporation of the deforming tubes to the 'naked' machine analogue is not an easy task. Corrective attempts to the global analogues of the machine are proposed and discussed according to their interest in the understanding of the machine dynamics.

# 2 Electrodynamical Characterization: Results

A MP machine obviously underlies a more or less complex electrical circuit controlling its electrodynamic behavior. Aiming to build up a predictive and reliable framework accounting for the electrodynamics of MP machines, we thus need a global characterization of the electrical operating of these machines. Apart from a better understanding of their electrical features in view of their optimization, that framework allows also a monitoring to prevent their malfunction and over all, to assess their electrical structure. The electrical structure can be defined as the minimal set of parameters necessary to build the simplest global analogue of the machine, that is, the simplest electrical circuit accounting faithfully for its operating. The analogue provides the right interpretation of electrical measurements carried out on the machines. These parameters are of course intimately connected to the components of the machine and can be constrained by efficiency requirements.

To approach these questions and assess these parameters, we carried out such a complete characterization of the MP 25 9 magnetic pulse system developed by Pulsar (Ould Ahmed, 2012). In a first step, we have studied the 'unloaded' machine, that is, without insertion of the pieces to be deformed within the coil. The simplest global analogue of a MP machine as schematized in figure 1, consists in a classical RLC circuit corresponding to 3 parameters accounting for energy dissipation (combining the resistance of the transfer lines and the coil), the electrical energy stored in the power stage (bank capacitance) and the magnetic energy delivered by the coil (coil inductance). Other features as the coil geometry (dimensions, flat or massive) as well as special configurations of the machine's components are incorporated in these parameters. Uncontrolled coupling between the components might be responsible for deviations from the ideal operation of the machine (as defined in its

performance specifications). The typical current pulse (in kA) delivered by the machine is presented in **Fig. 2** below.

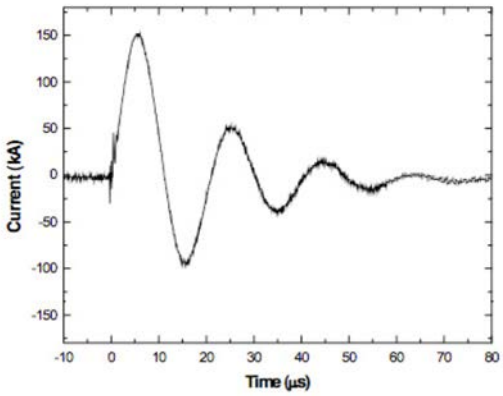


***Figure 2**: Profile of the current – pulse delivered by an MP machine (model MP 25 9 from the Pulsar Company). The pulse duration is typically 80 µs.*

Its profile evokes clearly a damped oscillator, which is the signature of a RLC circuit. The shots have thus been treated with a current profile,

$$I(t) = I_0 e^{-t/2\tau} \sin(\Omega t - \varphi) \qquad (1)$$

characterized by its maximal value $I_0$, the pulse duration $\tau$ (typically a few tenth microseconds), $\Omega$ the angular frequency and a phase angle $\varphi$ accounting for the date of the rise of the current pulse.

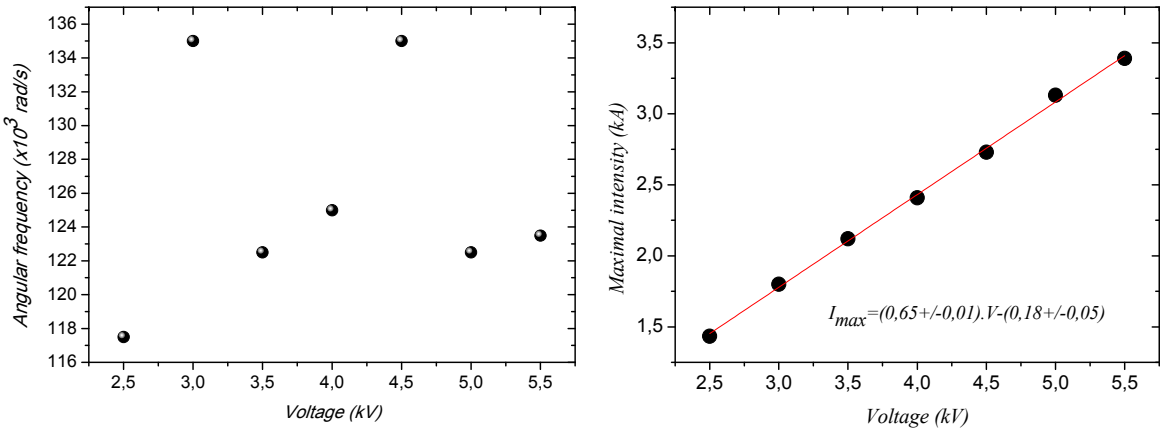


***Figure 3**: Dependence of the angular frequency (rad/s) – left panel - and maximal intensity (kA) – right panel - upon the feeding voltage V (kV) of the power stage.*

The dependence of the maximal intensity and the angular frequency upon the applied voltage across the power stage is presented on **Fig. 3** above. The evolution of the pulse duration and phase-angle is recapped on the left and right panels of **Fig. 4** below.

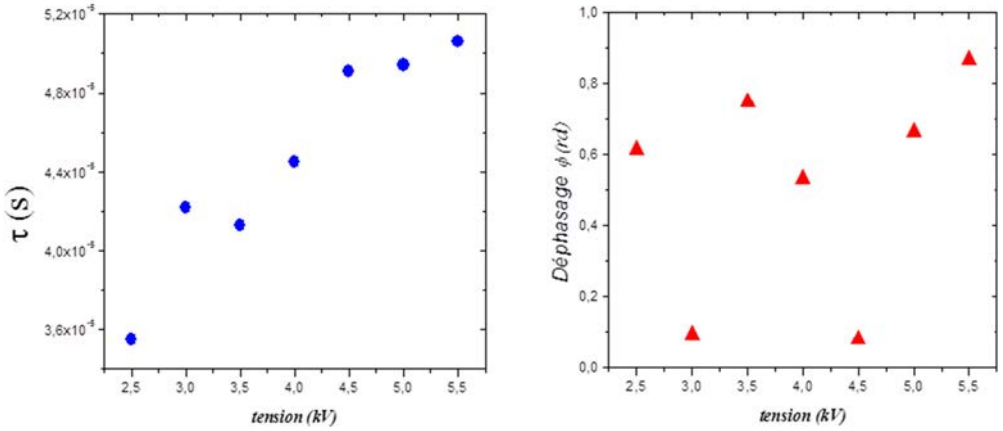


***Figure 4**: Dependence of the pulse duration (in s) – left panel – and the phase-angle (rad) – right pane – upon the feeding voltage (in kV) of the power stage.*

The angular frequency, the maximal current and the pulse duration are rather well defined with typical values of about 1,25 $10^5$ rad/s (or equivalently a frequency of 20 kHz) for the angular frequency and typical pulse duration varying slightly around 80 μs when the voltage doesn't exceed 6 kV. The pulse duration is defined as the time required for the measured intensity to vanish. The control of the current shape of the pulse through the feeding voltage is quite well ensured. This can be better appreciated on figure 3-b where the linear dependence is very well defined. The residue at zero-voltage has no physical meaning: it just indicates a systematic shift of the voltage measured across the power stage. Only the phase angle exhibits spread values, evidencing its random nature. This randomness manifests the difficulty with controlling the shot initiation, that is, their unsynchronized nature. The interpretation of these data is facilitated by the current pulse shape. As suggested by **Eq. 1**, the electrical structure of the MP system derives straightforwardly from a simple RLC circuit. Its parameters can then be assessed from the presented data. Considering the simplest case of as single shot initiated at a time $t_0$, the electrical behavior of the machine is modeled by the equation,

$$\frac{1}{C}\int I(t)dt + RI(t) + L\frac{dI(t)}{dt} = V(1-\theta(t-t_0)) \qquad (2)$$

where $V$ is the constant feeding voltage of the power stage, $I$ is the corresponding electric current and $R$, $L$ and $C$ are respectively the resistance, inductance and capacitance of the circuit. To avoid needless mathematical difficulties associated with the spark-gap operation, we have assumed here a rough discharge of the bank capacitance through a Heaviside

function $\theta(t-t_0)$ jumping at time $t_0$. Solving this equation requires an additional derivative leading to the Green equation,

$$\frac{1}{C}I(t)+R\frac{dI(t)}{dt}+L\frac{d^2I(t)}{dt^2}=-V\delta(t-t_0) \tag{3}$$

A simple Fourier transform followed by an integration in the complex plane leads to the current pulse ($t > t_0$),

$$\begin{cases} I(t)=\dfrac{4\pi V}{L\Omega}e^{-(t-t_0)/2\tau}\sin(\Omega(t-t_0)) \\ \Omega=\sqrt{\omega_0^2-1/4\tau^2}\ ,\tau=\mathrm{L/R},\omega_0=1/\sqrt{\mathrm{LC}} \end{cases} \tag{4}$$

This solution clearly accounts for the pulse shape given in Eq. 1 with a phase-angle $\varphi = \Omega t_0$. **Fig. 5** shows a plot of the measured current with its corresponding fit to a damped sine.

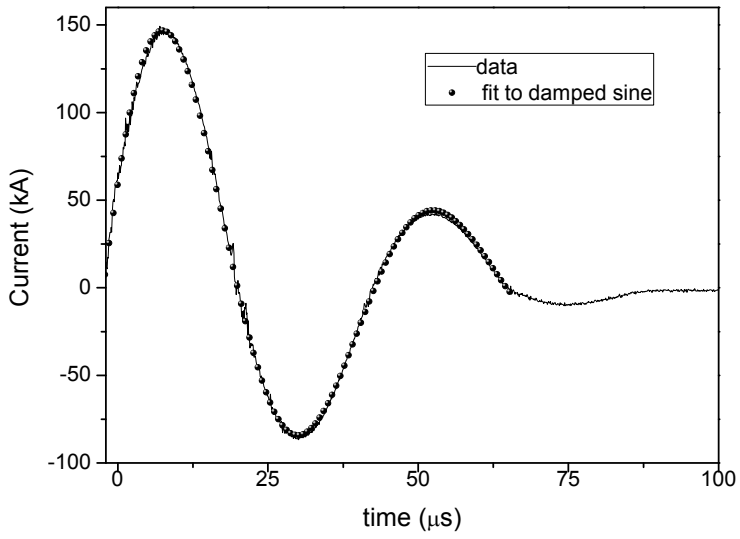


***Figure 5**: Plot of the experimental data (current (kA) vs. time (μs)) and its fit to a damped sine.*

The plot shows a good fit quality. We noticed that all our data can be fitted with a damped sine as our model suggests, but the quality of the fit is reduced at the last part before the end of the pulse, reflecting the high level of operation complexity of the spark-gaps power switches. This demonstrates that a more complete characterization of the machine is needed.

Comparison to the experimental data gives the following variations of the parameters in the applied voltage range,

$$\Omega/2\pi \simeq 20\ kHz,\ R \simeq 42-58\ \Omega,\ C \simeq 3{,}34.10^{-8}\ F,\ L \simeq 1{,}87\ mH$$

Taking into account the dispersion on the phase-angle values, the shot initiation dates vary within the time interval $t_0 \approx 4-6\ \mu s$. The assessment of the global resistance and the coil inductance are rather reasonable but the capacitance is questionable when compared to the expected (DC) capacitance of the power stage being a few hundredth microfarads. To solve this disagreement, we have to keep in mind that our model gives the effective parameters associated with the machine. The capacitance of the total circuit combines the power stage capacitance and additional contributions arising from the transfer line or any component of the machine. In our case, the additional contribution is attached to the coil slit (separation between two parts of the coil) which, being small, dominates the overall capacitance. Such perturbations regard in fact all the components of the machine, the critical ones being the capacitance and the coil inductance which determine the current (and magnetic) pulse duration and the working frequency $\omega_0$. A too high shift of this working frequency can affect the quality of the welding or forming processes. Prior to any trial, an adequate preparation of the machine is thus necessary. This optimization of the configuration can only be reached through a careful characterization of the system.

# 3 Estimation of the Magnetic Fields: Theoretical and Numerical Modeling

The magnetic pulse is delivered by the coil excited by the current pulse studied in the previous section. In the present section, we enunciate a tentative assessment of the magnetic field created by the coil. This study follows logically the first step dedicated to the MP system electrodynamic characterization and consists in both the numerical computation of the current distribution (Foy, 2013) within the coil bulk and the magnetic field (intensity) distribution created by the coil. To achieve this goal despite the complexity of the situation, a simplified model was derived from reasonable assumptions. The first simplification regards the dimensionality of the numerical model restricted to 2D, allowing handling simpler boundary conditions. In a 2D space, the magnetic field reduces to a (pseudo-) scalar, being in fact the component of the field perpendicular to the coil plane.

The Maxwell-Ampère equation then reads,

$$J.\nabla B = \mu_0 \vec{j} + \frac{1}{c^2}\partial_t \vec{E}, J = \begin{pmatrix} 0 & 1 \\ -1 & 0 \end{pmatrix} \quad (5)$$

The left-hand side of this equation corresponds to the usual curl term and *J* the right angle is the rotation matrix in the plane. *B* and *E* represent the magnetic field and the electric field, respectively. From this equation we deduce the field gradient, expressed as a function of the displacement current (derivative of the electric field) and the conduction current (Ohm's law)

$$\nabla B = -\mu_0 J.\left(\int_{-\infty}^{+\infty} \sigma(t-t')\,\vec{E}(t')dt' + \varepsilon_0 \partial_t \vec{E}\right) \quad (6)$$

A time-Fourier transform of this expression leads to the (Fourier amplitude) electric field,

$$\begin{cases} \vec{E}_\omega = \frac{1}{\mu_0(\sigma(\omega)+\varepsilon_0 i\omega)} J.\nabla B_\omega = i\omega J.\nabla\varphi_\omega \\ \varphi_\omega = \frac{B_\omega}{\mu_0(i\omega\sigma(\omega)-\varepsilon_0\omega^2)} \end{cases} \quad (7)$$

In the expression of the potential $\varphi_\omega$ , $\sigma(\omega)$ is the complex conductivity of the coil material, that is, the FT of the response function σ(t) in **Eq. 6**. Within the approximation of quasi-steady regime ($\omega \ll \sigma/\varepsilon_0$) in which propagation effects are negligible, we are led to simpler equations,

$$\begin{cases} \varphi_\omega \simeq \frac{B_\omega}{\mu_0 i\omega\sigma(\omega)} \\ E_{\omega x} = \partial_y(B_\omega/\mu_0\sigma(\omega)) \\ E_{\omega y} = -\partial_x(B_\omega/\mu_0\sigma(\omega)) \end{cases} \quad (8)$$

These equations state that the current stream lines are perpendicular to the isolines of the potential $\varphi$. The main difficulty of the model relies on skin effect. Understanding its influence on the fields and the current distribution doesn't require solving these equations in the whole frequency range. For practical use, the low (LF) and high (HF) frequency limits of **Eq. 7**, detailed in **Eq. 9**, provide the relevant information.

$$\begin{cases} \vec{E}_\omega \simeq J.\nabla\varphi_\omega^{LF} \\ \varphi_\omega^{LF} \approx \frac{B_\omega}{\mu_0\sigma_{DC}}, \sigma_{DC} = \sigma(0) \end{cases} \quad \begin{cases} \vec{E}_\omega \simeq J.\nabla\varphi_\omega^{HF} \\ \varphi_\omega^{HF} \approx \frac{B_\omega}{\mu_0\sigma(\omega)} \end{cases} \quad (9)$$

The threshold separating these two regimes is given by the characteristic frequency $\sigma/\varepsilon_0$, which is about 1,6 MHz for Fe and about 300 kHz for stainless steel. Handling these limits separately allows avoiding difficulties with the treatment of the rigorous equations. In most MP systems, the operating frequencies being a few tenth kHz are low enough (compared to $\sigma/\varepsilon_0$ ) to justify the restriction to the LF limit. The LF limit equations were thus solved through a finite element (FE) method implemented within the Matlab software (using PDE Toolbox). The mesh was composed of 8496 triangles, 4405 nodes and 316 edges. We used a full integration method. The LF solution obtained for an excitation current $I = 10^5$ A, which is a realistic value for our shots, is presented on **Fig. 6** below.

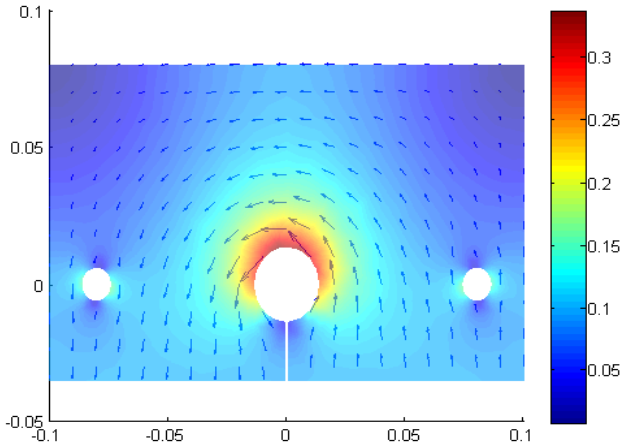


***Figure 6**: Distribution of the current stream lines with the coil material and corresponding variation of the electric field intensity.*

This figure gives the space variation of the electric field amplitude within the coil bulk as well as the current streamlines. Using the Biot-Savart law, we derived from this current distribution the magnetic field amplitudes generated by the coil for different types of metallic materials. To match the 3D realistic situation, we inserted the coil thickness $h$ along the axis (in our case $h$ = 1.5 cm) in a frequency-scaling law obeyed by the Fourier amplitude of the magnetic field,

$$\vec{B}(\omega) = \frac{\mu_0}{4\pi}\sigma_{DC} h \sqrt{\omega}\,\vec{B}(1\ rad/s) \qquad (10)$$

This relation allows to deduce the solution at any (low enough) frequency from the simulation at a fixed frequency of 1 rad/s. The variation ranges of the magnetic field generated by the coil are reported in **Table 1** along with the corresponding magnetic pressure evaluated at the operating frequency of the machine, that is 20 kHz.

| Material | Variation range (Teslas) | Magnetic pressure (kPa) |
|---|---|---|
| **Stainless steel** | **0,097 - 0,16** | **3,7 - 10** |
| **Iron** | **0,97 - 1,62** | **37 - 100** |
| **Copper** | **5,8 - 9,72** | **13330 - 37600** |

***Table 1:** Variation range of the magnetic field intensity (Teslas) for different metallic materials and corresponding magnetic pressure (kPa).*

Obviously, the great difference between these values reflects the importance of the choice of the metallic compound (its conductivity). These values seem reasonable. While all of these materials (especially stainless steel and iron) would of course not be relevant for these applications, this table only shows estimates for such materials in order to compare

them. Nevertheless, our ideal model assumes a 'perfect' coil, that is, without defects. An extension of the model to more realistic coils with bulk defects might be interesting to evaluate field inhomogeneities, since these alterations of the magnetic field can deeply affect the welding/forming process and its quality.

# 4 Welding Configuration: Insertion of Metallic Tubes

This section is devoted to a preliminary study of the local electrical analogue associated with the deformable pieces coupled to the coil generator. In welding configuration, the metallic coaxial tubes to be deformed are inserted in the coil. This additional component modifies the structure of the global electrical analogue of the machine. The additional circuit associated with the {coil + pieces} subsystem plays in fact the role of the receiver (of the energy delivered by the MP system) and can have a complex structure. The main difficulty with the identification of that structure arises mainly from the electromagnetic coupling between the coil and the metallic pieces. The simplest approach to the problem consists in a parallel self/capacitor device. The capacitor reflects the geometrical configuration of the coaxial tubes: this is a cylindrical capacitor with a capacitance given by the usual formula $C = 2\pi\varepsilon_0 l / Ln(R_2 / R_1)$, for tubes of length $l$ and radii $R_2$ for the external tube, $R_1$ for the internal tube. The inductance component accounts for the eddy current excited within the tubes and the magnetic energy stored within. A resistance modeling the dissipative effects can be added. This minimal electrical analogue accounts for the mutual inductance coupling between the coil generator and the tubes (transformer configuration) and controlling the energy transfer to the tubes. It is clear that the knowledge of this magnetic coupling is of great importance, especially with respect to efficiency questions. Indeed, the impedance introduced by this additional circuit varies very rapidly because of the fast deformation kinetics of the tubes: we have to deal with strongly time dependent components, making it difficult to ensure impedance matching between the power stage and the coil generator stage. This type of unsteady circuit, whose structure varies rapidly with time, is very difficult to handle because of a lack of both theoretical and experimental knowledge. From an experimental point of view, a deeper electrical characterization is clearly needed. Up to now, our theoretical and experimental investigations pointed out some research directions. Retaining the only capacitance of the tubes, we built up a simplified model of the local electrical analogue incorporating the coupling between the electrical degrees of freedom (charge $Q(t)$) and the mechanical ones (deformation $x(t)$). This model is depicted in **Fig. 7** where the spring models the elastic properties of the tubes and $e(t)$ is the voltage between the tubes (plates of the capacitor). This voltage is a residue of the inductance of the tube (not explicit in this model), that is, the voltage induced by the varying magnetic flux through the tube.

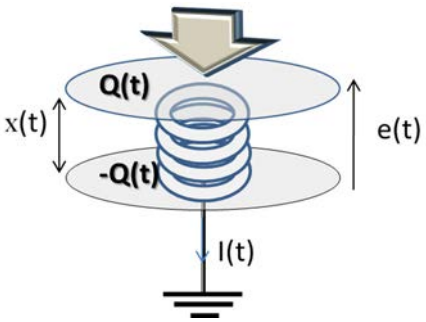


***Figure** 7: Schematic view of the simplest electrical analogue of two coaxial elastic tubes evidencing the coupling between the mechanical and electrical degrees of freedom.*

Ignoring in a first step the dissipation, the dynamics of such a system derives from the Lagrangian,

$$L(x,\dot{x}) = \frac{1}{2}M\dot{x}^2 - \frac{1}{2}k(x(t)-\bar{x})^2 + F_m(t)x(t) - \frac{1}{2}C(x(t))e(t)^2 \qquad (11)$$

The first terms give the mechanical contribution including the magnetic force $F_m$, the last one, giving the electrical energy stored in the deformable pieces, generates the coupling between the mechanical and electrical degrees of freedom. It admits series expansion in powers of the deformation $\Delta(t) = x(t) - \bar{x}$, leading to the dynamical equation corrected by a dissipative force,

$$\begin{cases} \ddot{\Delta} + \omega_0^2(t)\Delta + \eta\dot{\Delta} = F_m(t) - \frac{1}{2}\frac{\partial C}{\partial x}(\bar{x})e(t)^2 \\ \omega_0^2(t) = \frac{k}{M} + \frac{1}{M}\frac{\partial^2 C}{\partial x^2}(\bar{x})e(t)^2 \end{cases} \qquad (12)$$

This equation has a complex structure, as could be expected. It evidences the influence of the voltage *e(t)* on both the 'resonance' frequency of the tube and the magnetic pressure force. The consequence of these effects on the dynamics of the tube is made simpler for a constant voltage: the resonance frequency is simply shifted. At high enough voltage, the matching between the mechanical resonance frequency of the tube and the operating frequency of the machine (required for high quality welding) is lost. On the other hand, it strengthens the magnetic force exerted on the tube (since the derivative is negative). As the induced voltage depends in a complex way upon the current pulse and its derivative, the Fourier spectrum of the deformation is strongly altered. A deeper understanding of these effects requires additional experimental studies and can profit by the measurement of the deformation kinetics law (Deroy, 2015). A fundamental application of this preliminary investigation devoted to the identification of electrical analogues of the pieces inserted in the coil generator, concerns a new type of spectroscopy of the tubes. Our proposal exploits the natural configuration of the pieces and the coil in the welding machine. We expect two different configurations of the device:

- Deformation spectroscopy mode: the tubes are excited by a ‘low amplitude’ modulated magnetic field. This mode allows in situ mechanical testing of the tubes prior to any welding process.

- Deformation kinetics of the tubes in the welding regime. This application should lead to a more complete understanding of the plastic deformation kinetics of the tubes.

The implementation of these techniques will certainly lead to relevant global electrical analogues of any MP system, especially in view to optimize the welding or forming process.

# 5 Conclusion

We carried out a theoretical, experimental and numerical study of MPW machines.

The classical setups of such machines are depicted, and because of their inherent complexity, electrical analogues are used in order to ease their physical description.

A first magnetic pulse system is treated as a RLC circuit, with its components being experimentally and separately characterized. The main parameters of such a circuit can then be deduced. While the coil inductance and global resistance can be considered reasonable, a problem lies with the capacitance. This is due to the fact that only the bank (power stage) capacitance was taken into account in our early model, while other contributions, such as the capacitance arising from the coil slit, were not included.

A further study, using numerical tools, allowed for the computations of current distributions within the coil bulk, along with the magnetic field such currents create within the coil. Using the electromagnetism equations (namely, the Maxwell-Ampère equation) for a 2D model, we calculate the corresponding Fourier transforms of such solutions so that two limits appear: low and high frequencies. We show that low frequencies are of interest for us on MP machines and solve the LF equations using a PDE toolbox in Matlab. We then get the values of the current distributions within the coils and corresponding magnetic fields, and the magnetic pressure values they generate.

The last part of our paper deals is of theoretical nature, and deals with the true configuration of the machine, that is when metallic tubes are inserted. Using the Lagrangian formalism, the dynamics of the tubes are modeled, taking into account their capacitive properties. While this part is only theoretical, it may lead to two interesting measurement processes: a deformation spectroscopy mode, allowing in situ mechanical testing of the tubes without any welding, and another mode, which should allow for a greater understanding of the process of plastic deformation of the tubes.

# Acknowledgments

We wish to thank the Région Picardie for its support.

## References

Broeckhove J., 2010. Experimental research on magnetic pulse welding of dissimilar metals. Ph.D. Thesis, Ghent University, Belgium.

Daehn G. S., 2002. High Velocity Sheet Metal Forming: State of the Art and Prognosis for Advanced Commercialization, Ohio State University Press.

Deroy J., Avrillaud G, Ferreira S., Jeanson A.C., 2015. Comparison between experimental and simulated velocities in MPW geometry. In: I2FG Dortmund 2015, Dortmund, Germany.

Foy N, 2013. Soudage par impulsions magnétiques. Physics M.S. internship report, Université de Picardie Jules Verne, Amiens, France.

Griffith D.J., 1999. Introduction to electrodynamics. Prentice Hall, New Jersey.

Ould Ahmed S.M., 2012. Electrodynamique des machines de soudure à impulsions magnétiques. Physics M.S. internship report, Université de Picardie Jules Verne, Amiens, France.

Psyk, V., Risch, D., Kinsey, B.L., Tekkaya, A.E., Kleiner, M., 2011. *Electromagnetic forming – A review*. Journal of Materials Processing Technology 211 (5), pp. 787-829.

# Qualification of CuCr1Zr for the SLM Process

**E. Uhlmann[1], A. E. Tekkaya[2], V. Kashevko[1*], S. Gies[2], R. Reimann[1], P. John[1]**

[1] Institute for Machine Tools and Factory Management IWF, Technische Universität Berlin, Germany
[2] Institute of Forming Technology and Lightweight Construction, TU Dortmund University, Germany
[*]Corresponding author. Email: kashevko@iwf.tu-berlin.de

## Abstract

*Working coils for electromagnetic forming processes need to comply with a wide list of requirements such as durability, efficiency and a tailored pressure distribution. Due to its unique combination of high strength and high electrical conductivity CuCr1Zr meets these requirements and is a common material for coil turns. In combination with conventional coil production processes like winding or waterjet cutting the use of this material is state of the art. A promising approach for coil production is the use of additive manufacturing (AM) processes. In comparison to conventional manufacturing processes, AM offers tremendous advantages such as feature-integration e.g. undercuts or lattice structures. However, this increased design freedom only leads to improved working coils if copper alloys with high strength and high electrical conductivity such as CuCr1Zr can be processed. Due to the high thermal conductivity and reflectivity the use of suchlike materials in additive manufacturing processes is challenging. Considering the effects of the required pre- and post-processing treatments for additive manufactured parts the need for research is further increased. The objective of this paper is to develop a method for the qualification of CuCr1Zr for the selective laser melting (SLM) process. This comprises the powder characterization, the process parameter identification and the microstructure investigation of the generated test geometries.*

## Keywords

Electromagnetic forming, Additive manufacturing, Selective laser melting

# 1 Introduction

Durability and efficiency are two basic requirements for working coils in electromagnetic forming operations (Belyy et al., 1977). Both aspects are mainly affected by the choice of the coil turn material. While a high yield strength is beneficial to withstand the mechanical loads a high electrical conductivity increases the process efficiency due to lower heating losses (Risch, 2008). A group of materials with a likewise high yield strength and electrical conductivity are low alloyed precipitation hardening copper alloys. With a yield strength in range of 300 to 400 MPa and an electrical conductivity of about 43 MS/m (74% IACS) (Deutsches Kupferinstitut, 2005) CuCr1Zr has a well-balanced property profile for working coils. In combination with conventional coil production processes like winding or waterjet cutting (Golovashchenko, 2006) the use of this material is state of the art.

Selective laser melting (SLM) is an additive manufacturing process and allows a layer by layer production of complex components directly out of metal powder based on CAD-Data. This technology offers tremendous advantages such as feature-integration e.g. undercuts, lattice structures for light weight construction as well as inner cooling channels. Today SLM is applied in the area of rapid prototyping, rapid tooling and rapid manufacturing. The most frequent manufactured products are tools and individual objects for the medical, automobile and aerospace industry (Gebhard, 2013). The relatively small range of suitable materials limits the broader application of the process. Already well known materials for SLM are stainless and tool steels, titanium-, aluminum- and nickel based alloys with powder grain sizes from 10 to 75 µm. To develop new applications for SLM, novel materials have to be qualified (Uhlmann and Urban, 2011). To qualify new materials for the SLM process different approaches were developed which are all based on a similar procedure. In the first stage maximization of the relative specimen density is the main objective. Afterwards, mechanical properties e.g. yield strength are analyzed and adjusted to reach values comparable to those of conventional wrought alloys. This could also include a heat treatment of the specimen. Finally, the process parameter set is optimized in terms of productivity (Uhlmann and Urban, 2012; Kempen et al., 2011; Sehrt, 2010; Ahuja et al., 2014). In the field of SLM few research is focused on the processing of copper alloys. This can mainly be attributed to the difficulties that occur due to the high thermal conductivity and high reflectivity of copper. While the reflectivity of steel is in the range of $R_{\mathrm{Fe}} \sim 0.64$, copper alloys reach values of up to $R_{\mathrm{Cu}} \sim 0.99$ (Pogson et al., 2003). Zhang et al. (2014) reached a relative density of $\rho_{rel}$ = 94.6 % for specimen made of CuCr1Zr using a laser with a maximum power of 375 W. Becker et al. (2011) achieved densities of about $\rho_{rel}$ = 99 % with another cooper alloy Hovadur® K220 (Schmelzmetall AG, 2006). However, they required significantly more laser power in the range of 1000 W. In summary, lack in the state of the art on the processing of CuCr1Zr with SLM was identified. The main issue is to achieve the relative density of $\rho_{rel} \geq 99$ % for CuCr1Zr. The successful processing of CuCr1Zr allows production of working coils for electromagnetic forming and others applications.

# 2 Objectives

Main objective was to develop a knowledge base for processing CuCr1Zr using SLM. This includes the identification of process relevant parameters and copper-inherent characteristics regarding SLM e.g. heat dissipation through high thermal conductivity, oxidation, densification and porosity. Based on this investigation a set of parameters was derived to process CuCr1Zr with a relative part density close to $\rho_{rel} \geq$ 99 % (VDI 3405, 2014). This is the basic requirement for further investigations focusing on mechanical properties or the material performance in electromagnetic forming operations.

# 3 Approach

All specimen were produced on the SLM machine SLM 250$^{HL}$, MTT Technologies GmbH, Luebeck, Germany. An overview of the machine specifications is given in **Figure 1**.


**Machine specifications:**

| | | |
|---|---|---|
| Building space : | 250 mm x 250 mm x 350 mm | |
| Laser (cw): | 400 | W |
| Focal point diameter: | 70 … 300 | µm |
| Layer thickness: | 20 … 100 | µm |
| Particle size: | 10 … 65 | µm |
| Building speed: | 5 … 20 | cm³/h |
| Tolerance: | ± 50 | µm (x, y, z) |

***Figure 1**: Selective Laser Melting machine SLM 250HL*

## 3.1 Powder Characterization

The inert gas atomized powder was classified into the grain size range of 20 to 63 µm and which was supplied by TLS Technik GmbH & Co. Spezialpulver KG, Bitterfeld, Germany. The powder properties were obtained from the suppliers´ inspection certificate following European Standard DIN EN 10204, 2005 and validated by retesting upon receipt. The powder analysis was carried out according to VDI 3405-2, 2013 guidelines. Investigated powder requirements were grain size distribution DIN ISO 4497, 1991, grain morphology DIN EN ISO 3252, 2001 and bulk density DIN EN ISO 3923-1, 2010.

## 3.2 Parameter Identification

A three-stage qualification process was used to identify a suitable set of process parameters, **Figure 2**. Focusing on the most critical part quality indicators e.g. path width, wall thickness or relative density the process window was narrowed down further in each stage while the specimen geometry gets increasingly complex. For every stage a preheating temperature of $T_V$ = 200°C was applied to reduce thermal stress and distortion.

The first stage covered a parameter field of 128 combinations for the production of single melt tracks of one layer thickness $\Delta z$ = 50 µm on a steel (H13, 1.2344) substrate plate. Varied parameters were the focal position $x_F$, which is linked to the beam diameter $d_B$, laser power $P_L$ and scanning velocity $v_s$ with 3 repetitions. Furthermore, a number of reference specimen were produced to assess and eliminate the effect of the specimen position in the test array. The melt tracks were analyzed via reflected-light microscopy. Path width, path uniformity, discolorations and balling were rated. Parameter combinations which yielded promising results were used for the further investigations. The adequate focal position $x_F$ = +1.0 mm ($d_B$ = 80 µm) was determined.

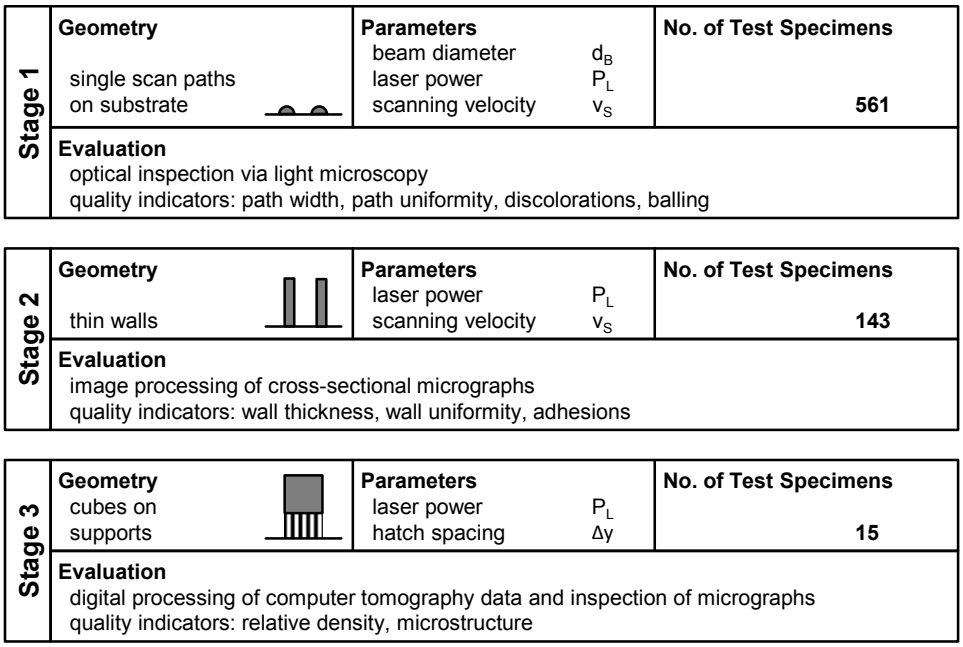


***Figure 2**: Qualification process for CuCr1Zr*

In the second stage were built thin walls with thickness of one melt path width, in the narrowed down parameter field from stage 1. The varied parameters were laser power $P_L$ and scanning velocity $v_s$. The average wall thickness and its standard deviation as wells as number and size of adhesions were analyzed as quality indicators. The final parameter set for thin wall structures (support structures) was determined in this stage.

For the third stage cubes with a dimension 5 x 5 x 5 mm were produced using a further narrowed down parameter field. The varied parameters were laser power $P_L$ and scan spacing $\Delta y$. The specimen were evaluated by digital processing of computer tomography (CT) data. For investigations on this stage 15 combinations were chosen. The evaluation of the results yielded to a parameter combination for the production of dense volumes of CuCr1Zr.

## 3.3 Data Acquisition – Density

The numerical density data was extracted from cross-sectional images by digital image processing. The images were obtained by computer tomography (CT) with a ZEISS METROTOM 800, Carl Zeiss AG, Jena, Germany. The scanning parameters are shown in **Table 1**.

| Parameter | Unit | Value |
|---|---|---|
| Prefilter copper | mm | 0.25 |
| Voltage | kV | 130 |
| Current | µA | 123 |
| Exposure Time | ms | 800 |

| Parameter | Unit | Value |
|---|---|---|
| No. of Projections | - | 2100 |
| Digital Gain | - | 2.5 |
| Binning | - | 1 x 1 |

***Table 1**: Computer tomography (CT) scanning parameters*

The CT-data were obtained as a 3D density field with a spatial resolution of 7 x 7 x 7 µm³/voxel. This density field was sliced into a number of cross-sections which were sequentially evaluated. The optimal threshold to differentiate between material and voids was determined with the Otsu's method (Otsu, 1979). The quotient of pixels identified as material and the total pixel number yielded the relative density $\rho_{\mathrm{rel}}$. The individual results were averaged over all sections in a measured volume of 3 x 3 x 3 mm³ in the center of the cubes. The density determination method by CT was validated by evaluation of micrograph sections and Archimedes' Method.

## 3.4 Data Acquisition – Microstructure

Micrograph sections were produced by manual wet-sanding with grain sizes P50, P800, P1000, P1200 and P2400 on SiC-paper and polishing with diamond suspension with grain sizes 3 µm, 1 µm and 0.25 µm and with a 10 % aqueous iron nitrate solution. Etching was carried out using a Klemm III etchant (100 ml distilled water, 11 ml saturated aqueous sodium sulfate solution, 40 g potassium metabisulfite) for 5 seconds. The produced micrograph sections were digitized using light microscope Olympus BX51, Olympus Corporation and scanning electron microscope ZEISS LEO 1455 VP, Carl Zeiss AG, Jena, Germany.

# 4 Results

## 4.1 Powder Properties

The optical inspection via SEM revealed uniformly spherical grain morphology with a low number of adhering satellite particles, **Figure 3a**. Very few particles exhibit an irregular shape or edges. The particle surface shows an even layer of oxidized material. The cross-sectional micrographs in **Figure 3b** display no inclusions of foreign materials or entrapments of gas (porosity). The microstructure is homogenously and fine as shown in **Figure 3c**.

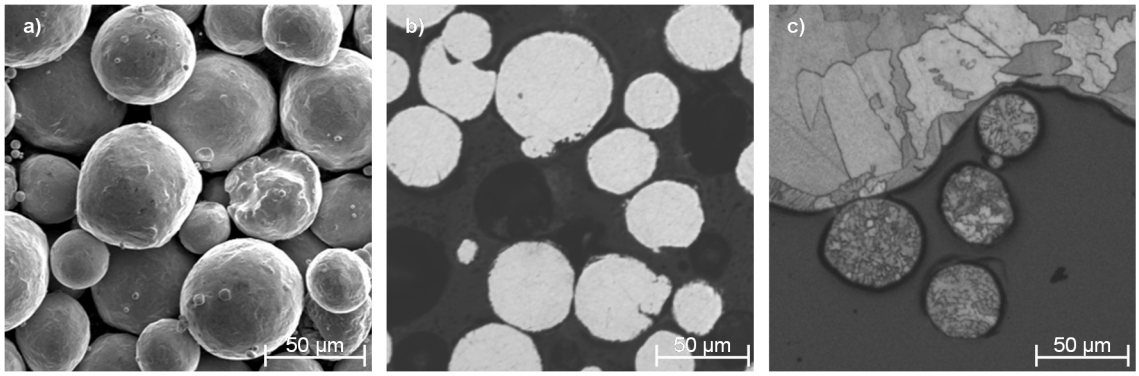


***Figure 3**: Optical powder inspection: a) particle morphology via SEM, b) porosity via microscopy and c) microstructure via microscopy of etched micrograph sections*

## 4.2 Process Stability and Specimen Quality

**Figure 4** shows SLM generated cubes with support structures on a steel substrate plate (H13, 1.2344). Optical inspection of the surfaces by eye reveals no differences in appearance. No discoloration due to overheating could be detected. The bonds of the support structures to the substrate and to the part are adequate which confirms the set of parameters chosen after stage 2. Therefore, the producibility of small-scale copper parts via SLM can be confirmed.

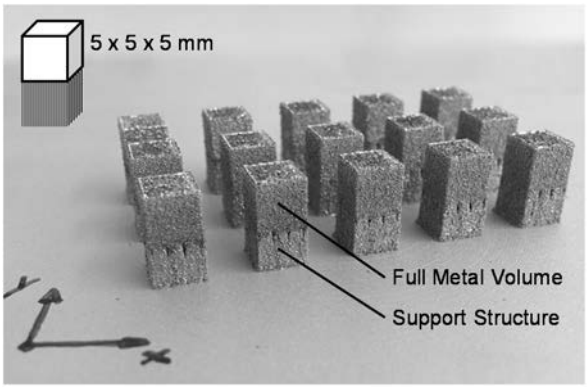


***Figure 4**: SLM generated cubes (5 x 5 x 5 mm³) on support structures*

## 4.3 Densification and Porosity

The analysis of the cubes via CT yields to the data shown in **Figure 5**. Higher laser power $P_\mathrm{L}$ and reduced hatch spacing $\Delta y$ result in increased densities. The highest achieved relative density was $\rho_\mathrm{rel}$ = 99.5 %. This confirms the expectation that the applied energy per volume $E_\mathrm{V}$ is the main influencing factor on the specimens´ density. According to **Eq. 1** the energy per volume $E_\mathrm{V}$ is not only affected by laser power $P_\mathrm{L}$ and hatch spacing $\Delta y$ but also by layer thickness $\Delta z$ as well as scanning velocity $v_\mathrm{s}$.

$$E_\mathrm{V} = P_\mathrm{L}/(v_\mathrm{s} \cdot \Delta y \cdot \Delta z) \quad (1)$$

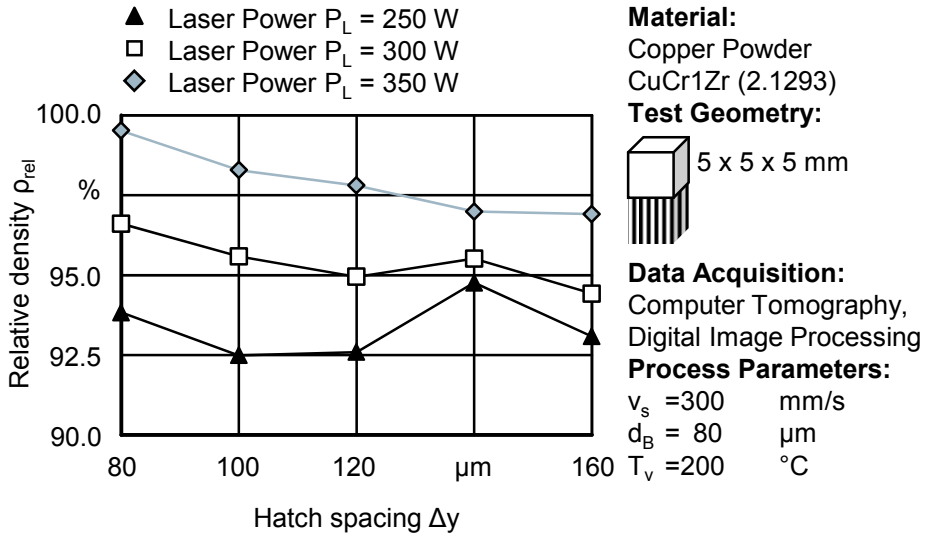


***Figure 5**: Achieved densities as a function of laser power $P_L$ and hatch spacing $\Delta y$*

The further results show an unusual variability at a hatch spacing of $\Delta y$ = 140 µm. The phenomenon cannot be fully explained with the current amount of data but is not expected to have a huge impact on the identification of an optimal parameter set since the results indicate a maximum density $\rho_{\mathrm{rel}}$ at much lower hatch spacing.

## 4.4 Microstructure

The etched micrograph sections in **Figure 6** show randomized grain patterns with grains of distinctly different sizes ranging from 10 µm up to 200 µm. The grains are elongated and show parallel patterns of multiple neighboring grains oriented in the same direction. They cross the boundaries of heat-affected zones of subsequent layers which can be seen as faint, half-circular lines (especially in the top right corner of **Figure 6c**). Some of the grains span multiple layers and seem to have alternating orientations about 45° to the build direction (z-axis). The grain pattern is disrupted by imperfections, such as porosity, and shows a refinement around the pore's edges. These pores span perpendicular to the build direction, which indicates suboptimal layer adhesion as the main reason for porosity. Furthermore, a number of smaller and rounder pores can be seen, which are expected to be caused by irregularities in the powder bed resulting in suboptimal densification and voids in the produced part.

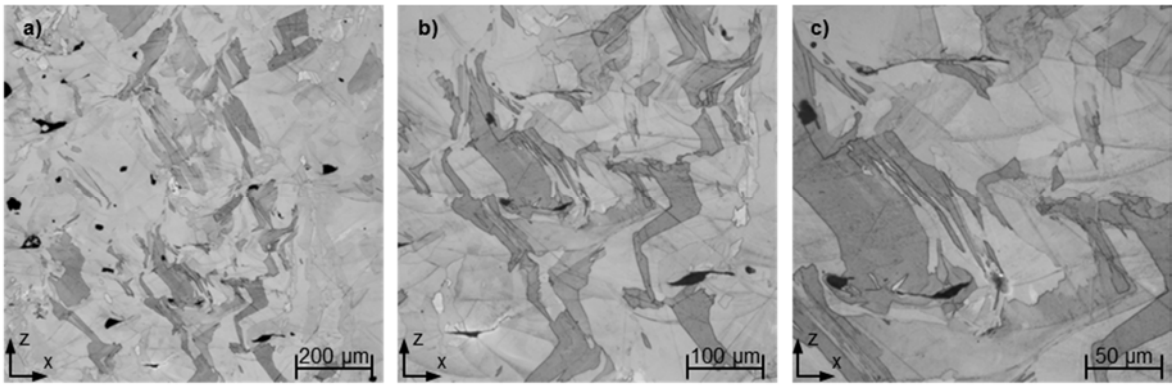


***Figure 6**: Light Microscopy of etched micrograph sections, process parameters: $P_L$ = 350 W, $v_s$ = 300 mm/s, Δy = 80 µm, magnifications: a) 50x, b) 100x, c) 200x*

The SEM-scans in **Figure 7** confirm the assumptions above regarding the grain morphology and interaction with pores. The grains are distinctly elongated along the build direction (z-axis) and describe an alternating angle of ± 45° to it. They stretch over the boundaries of heat-affected zones and are disrupted by pores. Especially **Figure 7a** proves that pores occur between layers. It seems as if the applied energy is insufficient so that the layer is not bonded to the previous layer in some areas. This is supported by the fact that **Figure 7a** shows powder particles that have not been molten inside the pores. Under maximum magnification of 10,000 times the precipitations in the copper alloy become visible. A punctual, homogenous distribution of extremely fine precipitations (diameter $D < 100$ nm) can be seen in the bulk of the material away from the heat-affected zone boundaries. In the vicinity of these boundaries the precipitations are bigger, more prevalent and form lattice structures. The precipitations are not uniformly distributed.

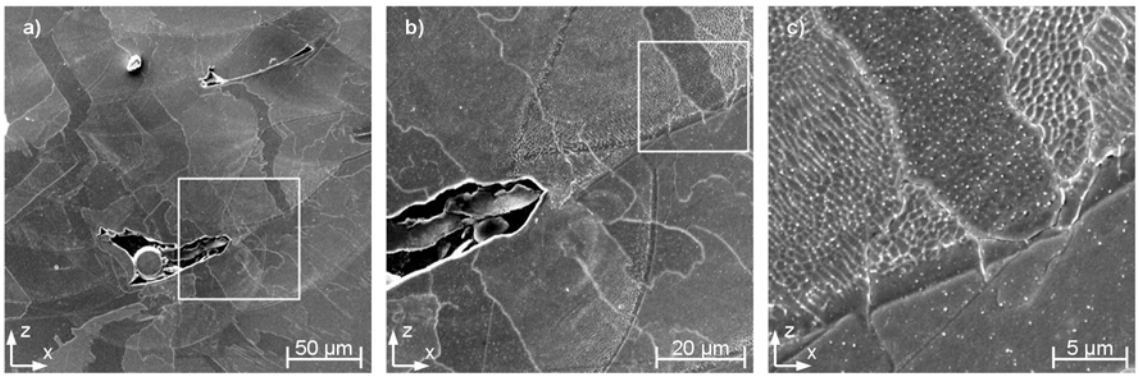


***Figure 7**: SEM of etched micrograph sections, process parameters: $P_L$ = 350 W, $v_s$ = 300 mm/s, Δy = 80 µm, magnifications: a) 1,000x, b) 3,000x, c) 10,000x*

# 5 Conclusions

The identified process parameters facilitate the production of CuCr1Zr parts with a relative density of $\rho_{rel} > 99$ % with a comparatively low maximum laser power of 350 W. This way the limitations of the material-machine-combination determined by Zhang et al. (2014) can be exceeded. Further research where required is needed to investigate the anomalies that occurred with a hatch spacing of $\Delta y = 140$ µm.

The microstructure of CuCr1Zr shows pores that disrupt the homogenous grain patterns and a grain refinement around them. The grains are larger than usual with SLM due to the repeated application of high amounts of energy and the low-alloyed copper. The achieved microstructural state is not optimal for an artificial aging process because the precipitations are dispersed inhomogeneously and concentrated along the boundaries of heat-affected zones. Therefore, a solution annealing step is recommended before aging.

To complete the qualification process for CuCr1Zr analysis of the mechanical e.g. yield stress $\sigma_y$ and physical properties e.g. electrical conductivity $\kappa$ of the specimen are required. This also entails the analysis of the heat treatment procedure on these properties.

# Acknowledgments

This paper is based on results acquired in the projects UH 100/174-1 and TE 508/51-1, which are kindly supported by the German Research Foundation (DFG).

# References

Ahuja, B., Karg, M., Nagulin, K. Y., Schmidt, M., 2014. Fabrication and Charaterization of High Strength Al-Cu alloys Processed Using Laser Beam Melting in Metal Powder Bed. In: 8th International Conference on Laser Assisted Net Shape Engineering LANE 2014. Physics Procedia , S. 135 - 146.

Becker, D., Meiners, W., Wissenbach, K., 2011. Generative Fertigung aus der Kupferlegierung Hovadur® K220 mittels Selective Laser Melting. Fraunhofer Institut für Lasertechnologie ILT, Aachen.

Belyy, I.V., Fertik, S.M., Khimenko, L.T., 1977. Spravochnik Po Magnitno-impul‘ Snoy Obrabotke Metallov. Electromagnetic Metal Forming Handbook. English translation by Altynova, M. M.

Deutsches Kupferinstitut, 2005: Material data specification CuCr1Zr. Online access: https://www.kupferinstitut.de/fileadmin/user_upload/kupferinstitut.de/de/Documents/Shop/Verlag/Downloads/Werkstoffe/Datenblaetter/Niedriglegierte/CuCr1Zr.pdf, last request: 22.12.2015.

DIN EN 10204, 2005. Metallische Erzeugnisse - Arten von Prüfbescheinigungen. Berlin: Beuth.

DIN EN ISO 3252, 2001. Pulvermetallurgie – Begriffe (ISO 3252:1999). Berlin: Beuth.

DIN EN ISO 3923-1, 2010. Metallpulver- Ermittlung der Fülldichte – Teil 1:Trichterverfahren (ISO 3923-1:2008). Berlin: Beuth.

DIN ISO 4497, 1991. Metallpulver; Bestimmung der Teilchengrößen durch Trockensiebung (ISO 4497:1983). Berlin: Beuth.

Gebhardt, A., 2013. Generative Fertigungsverfahren. Additive Manufacturing und 3D Drucken für Prototyping - Tooling - Produktion. Unter Mitarbeit von J.-S. Hötter und M. Fateri. 4. Aufl. München: Hanser.

Golovashchenko, S., 2006. Electromagnetic Forming and Joining for Automotive Applications. In: Proceedings of the 2nd International Conference on High Speed Forming, Dortmund, pp. 201-206.

Kempen, K., Thijs, L., Yasa, E., Badrossamay, M., Verheecke, W., Kruth, J.-P., 2011. Process Optimization and Microstructural Analysis fpr Selective Laser Melting of AlSi10Mg. In: Solid Freeform Fabrication Symposium Proceedings. Solid Freeform Fabrication Symposium, Austin, USA, 08.08. - 10.08.2011.

Otsu, N., 1979. A Threshold Selection Method from Gray-Level Histograms. In: IEEE Transactions on Systems, Man and Cybernetics, vol. 9, no. 1, pp. 62-66, Jan. 1979.

Pogson, S.R., Fox, P., Sutcliffe, C.J., O'Neill, W., 2003. The production of copper parts using DMLR. Rapid Prototyping Journal. Vol.9:334-43.

Risch, D., Nebel, J., Psyk, V., Vogli, E., Tillmann, W., Tekkaya, A. E., 2008. Hybrid Material Design for Coils used in Electromagnetic Forming Processes. In: Proceedings of the 7th International Conference "THE" Coatings in Manufacturing Engineering, pp. 269 – 278.

Schmelzmetall AG. Material data specification HOVADUR® K 220. Issue Nr. 02DE, from 01.04.2006. Online access: http://www.schmelzmetall.com/wp-content/uploads/2015/06/hovadur_k220_vers02_de.pdf, last request: 22.12.2015.

Sehrt, J., 2010. Anforderungen an die Qualifizierung neuer Werkstoffe für das Strahlschmelzen. In: Seminarbericht (2010) 97: Rapid Manufacturing, Universität Duisburg-Essen, Duisburg, Essen.

Uhlmann, E., Urban, K., 2012. Approach for the Qualification of Novel Materials for Selective Laser Melting for the Example of Nickel-based Superalloy Diamalloy 4004NS. Direct Digital Manufacturing Conference 2012, Berlin, 14. - 15.03.2012.

Uhlmann, E., Urban, K., 2011. Markt- und Trendstudie Laserstrahlschmelzen in der generativen Fertigung 2010. Schriftenreihe: Märkte kennen – Trends nutzen, Fraunhofer IPK, pp. 22.

VDI 3405, 2014. Additive manufacturing processes, rapid manufacturing – Basics, definitions, processes. Berlin: Beuth.

VDI 3405-2, 2013. Additive manufacturing processes, rapid manufacturing – Beam melting of metallic parts. Qualification quality assurance and post processing. Berlin: Beuth.

Zhang, D. Q., Liu, Z. H., Chua, C. K., 2014. Challenges Involved in Selective Laser Melting of C18400 Copper Alloy. In: Fraunhofer Direct Digital Manufacturing Conference proceedings.

# Material Testing

# Material Constitutive Behavior Identification at High Strain Rates Using a Direct-Impact Hopkinson Device

**X. Guo, C. Sow*, C. Khalil*, T. Heuzé, G. Racineux**

Research Institute in Civil and Mechanical Engineering (GeM, UMR 6183 CNRS), École Centrale de Nantes (ECN), France
*Corresponding authors. Email: cheikh-tidiane.sow@ec-nantes.fr, chady.khalil@ec-nantes.fr

## Abstract

*Modern numerical simulation techniques allow nowadays obtaining accurate solutions of magnetic pulse and electrohydraulic forming/welding processes. However, one major difficulty persists: the identification of material constitutive equations behavior at levels of high strain rates reached by these processes, and which varies between $10^3$ and $10^5$ $s^{-1}$.*

*To address this challenge, a direct-impact Hopkinson system was developed at ECN. It permits to perform dynamic tests at very high strain rates exceeding the range of the traditional Split Hopkinson Pressure Bars and hence enable us to identify constitutive models for a wide range of strain rates. The alloy used to test this device was Ti-6Al-4V. Strain rates up to $2.5\times10^3$ $s^{-1}$ were attained.*

## Keywords

High strain rate, Inverse analysis, Direct impact Kolsky bar

## 1 Introduction

To further develop electromagnetic or electrohydraulic forming, crimping or welding processes, accurate simulation of theses process is needed. This goes by the study of the material performance at high strain rates and to define a precise dynamic behavior by using constitutive models. The strain rates involved can be up to $10^5\ s^{-1}$. It is well known that the behavior of many metallic materials usually depends on the strain rate; therefore, a good

representation of this behavior is required by the mean of dynamic tests on a wide range of strain rates. The most popular experiment is the classical Split Hopkinson Pressure Bar (SHPB) (Davies 1948; Kolsky 1949) capable to attain strain rates ranging up to $10^4$ $s^{-1}$ (Gorham et al. 1992; Ramesh 2008). For higher strain rates, another system of the SHPB is available: a direct-impact Hopkinson device (Dharan & Hauser 1970). In this device, the incident bar is removed and very high strain rates of the order of $10^5\ s^{-1}$ can be achieved (Dharan & Hauser 1970; Kamler et al. 1995). In the present work, the Ti-6Al-4V alloy is tested at strain rates varying from 3000 to 25000 $s^{-1}$ using a direct-impact Hopkinson device and an elastic-viscoplastic constitutive model is identified by using an inverse identification.

# 2 Direct-Impact Tests on the Ti-6Al-4V at Very High Strain Rate

This device is composed of a transmitted bar, a projectile and three Wheatstone bridges of double gauges mounted on the bar for the measurement of deformations and dispersion monitoring (**Figure 1**). The transmitted bar is 1.2m length and 10 mm diameter. Four projectiles of diameter 15.8 mm and lengths of 500 mm, 125 mm, 60 mm and 30 mm respectively are used.

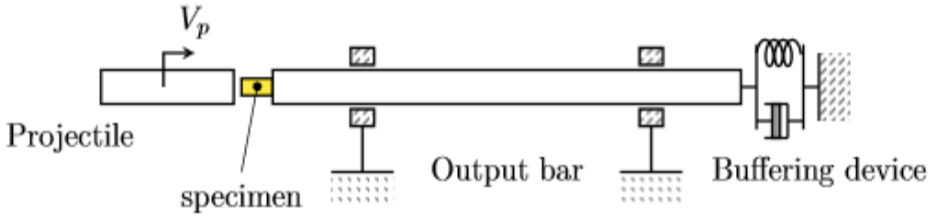


***Figure 1**: Direct impact device*

The higher the objective strain rate is, the lower the length of the projectile must be to avoid crushing the specimen. The bar and the projectiles are made of MARVAL X2NiCoMo18-8-5, with a yield stress of 1800 MPa. The impact velocity of the projectile is measured by two laser diodes. For each objective strain rate, the value of the specimen length $l_s$, the projectile length $l_p$ and its impact velocity $v_p$ should be determined. The maximum values of the expected strain rate $\dot{\varepsilon}_s$ and the allowable strain $\varepsilon_s$ in the specimen can be approximated by the following equation:

$$\dot{\varepsilon}_{smax} \approx \frac{v_p}{l_s} \qquad \varepsilon_{smax} \approx \frac{\dot{\varepsilon}_s 2 l_p}{c_p} \tag{1}$$

where $c_p$ denotes the sound speed in the projectile. $c_p$ is defined by the equation $\sqrt{E/\rho}$. $E$ and $\rho$ are respectively the Young's modulus and the density of the projectile material. The parameters for each objective strain rate (Obj. $\dot{\varepsilon}_S$) are listed in Table 1.

| Test n° | Obj. $\dot{\varepsilon}_s$ ($s^{-1}$) | $v_p$ (m/s) | $l_p$ (mm) | $l_s$ (mm) | $\dot{\varepsilon}_{smax}$ ($s^{-1}$) | $\varepsilon_{smax}$ | Test n° | Obj. $\dot{\varepsilon}_s$ ($s^{-1}$) | $v_p$ (m/s) | $l_p$ (mm) | $l_s$ (mm) | $\dot{\varepsilon}_{smax}$ ($s^{-1}$) | $\varepsilon_{smax}$ |
|---|---|---|---|---|---|---|---|---|---|---|---|---|---|
| T1 | 3000 | 15 | 500 | 5 | 3064 | 0.11 | T7 | 18000 | 36 | 60 | 2 | 17970 | 0.33 |
| T2 | 5000 | 25 | 125 | 5 | 4612 | 0.16 | T8 | 18000 | 30 | 60 | 1.5 | 18350 | 0.16 |
| T3 | 7000 | 28 | 125 | 4 | 6925 | 0.17 | T9 | 20000 | 30 | 60 | 1.5 | 21222 | 0.23 |
| T4 | 10000 | 30 | 60 | 3 | 10740 | 0.17 | T10 | 20000 | 40 | 30 | 2 | 19659 | 0.24 |
| T5 | 12000 | 36 | 60 | 3 | 12040 | 0.25 | T11 | 25000 | 37.5 | 30 | 1.5 | 25050 | 0.25 |
| T6 | 15000 | 30 | 60 | 2 | 15010 | 0.11 | | | | | | | |

***Table 1**: Experimental plan and results*

The elastic strain $\varepsilon_b(t)$ in the transmitted bar and the impact velocity $v_p$ of the projectile are measured. From the recorded strain $\varepsilon_b(t)$, the force $F_s(t)$ applied by the projectile on the specimen is computed by:

$$F_s(t) = E_b S_b \varepsilon_b(t) \tag{2}$$

where $E_b$ is the Young's modulus and $S_b$ is the cross-section of the bar. The results are plotted in Figure 2. The trays observed during the unloading part of these curves arise from the shorter length of the projectile than that of the bar and the mismatch of the generalized wave impedances between the projectile $Z_p = (\rho c S)_p$, the specimen $Z_s = (\rho c S)_s$ and the bar $Z_b = (\rho c S)_b$ (Wang 2007).

When the projectile is long enough, the loading time and the characteristic time are equivalents, as we can see in the Figure 2(a) where the projectile is 500 mm length. As the projectile shorten the actual period of loading of the specimen lasts approximately twice the characteristic time or even longer as is observed in *Figure 2*(b) and Figure 2(d), these results from the different cross-sections of the projectile and the bar. Following this, the specimen undergoes a second compression before the unloading starts. Thus, it is subjected to a higher strain than that of the test T1 as shown in the Table 1, even though the projectile of the test T1 has a greater kinetic energy before impact.

For the direct impact device, the strain rate in the specimen is assessed by the following equation (Gorham et al. 1992; Guo et al. 2014):

$$\dot{\varepsilon}_s(t) = -\frac{v_p + \frac{S_p + S_b}{S_p} C_b \varepsilon_b(t)}{l_s} \tag{3}$$

where $S_p$ is the cross-section of the projectile and $C_b$ the sound speed of the bar. The maximum compressive strain rate $\dot{\varepsilon}_{smax}$ computed by using this equation and the measured compressive strain $\varepsilon_{smax}$ for each test are listed in Table 1. This equation states that the compressive strain rate gets its maximum equal to $v_p/ls$ at the beginning of the impact and is however only valid during the characteristic time (Gorham et al. 1992).

The stress-strain curves are computed using the classical analysis of the Hopkinson tests (Guo 2015). The results are shown in the Figure 3. As the strain rate increases, the curves exhibit a rising strain hardening. However, they are subjected to scattering, as we can

observe through small oscillations. Consequently, the rate dependency is difficult to be assessed on these curves directly. An inverse analysis is carried out for the identification of the constitutive models.

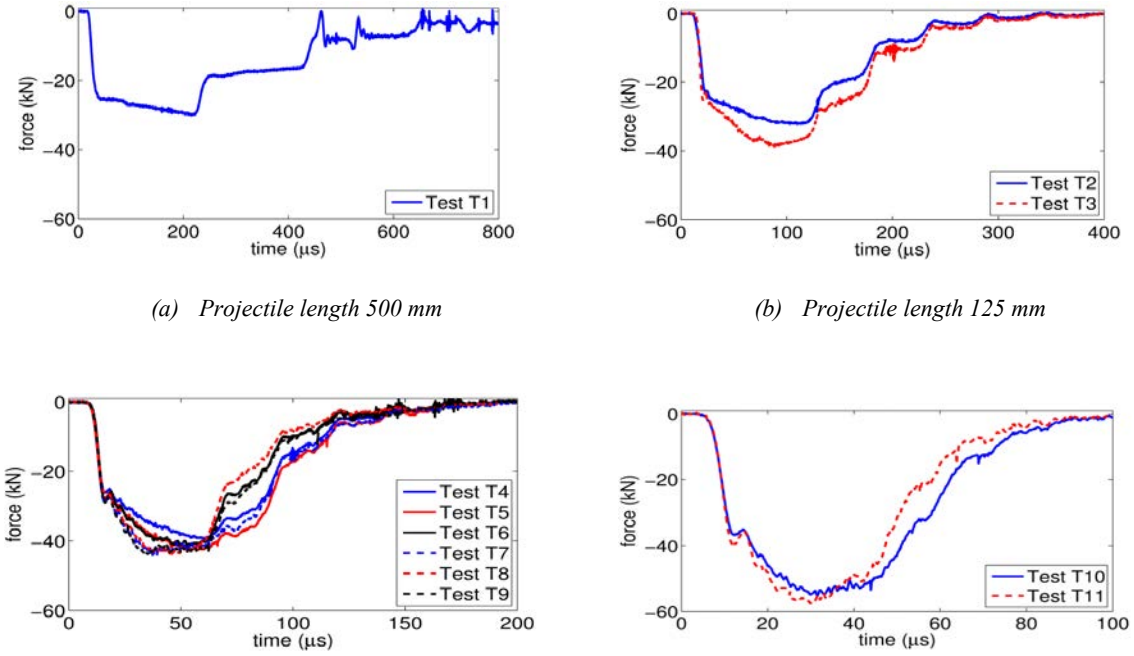


*(a) Projectile length 500 mm*

*(b) Projectile length 125 mm*

*(c) Projectile length 60 mm*

*(d) Projectile length 30 mm*

***Figure 2**: Force on specimen in the direct impact tests*

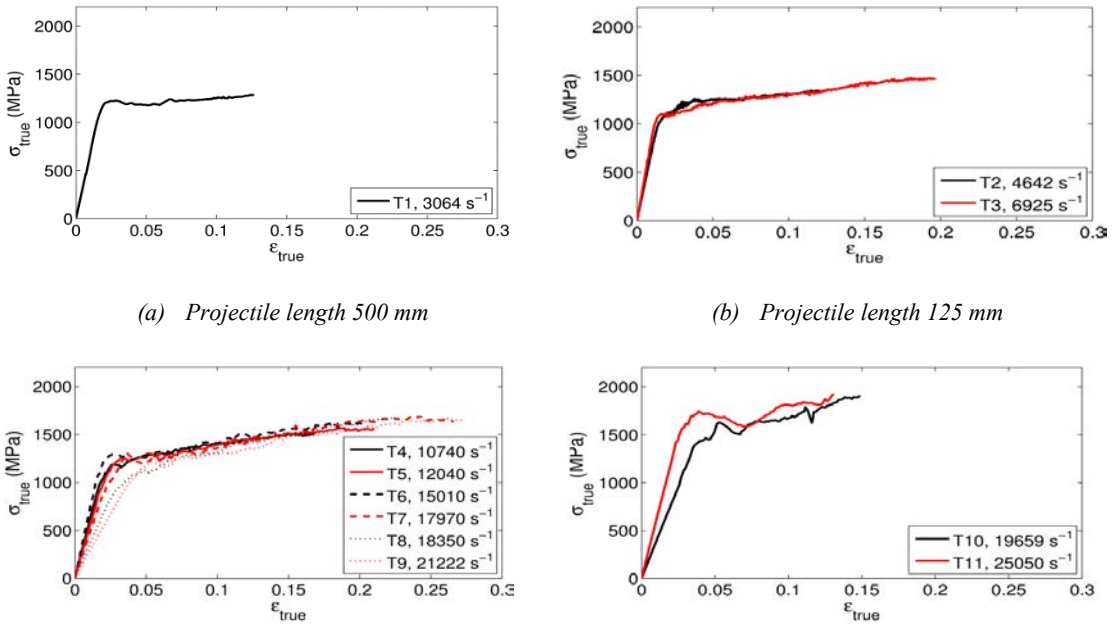


*(a) Projectile length 500 mm*

*(b) Projectile length 125 mm*

*(c) Projectile length 60 mm*

*(d) Projectile length 30 mm*

***Figure 3**: Stress-strain curves of the Ti-6Al-4V*

# 3 Inverse Identification of Elastic-Viscoplastic Constitutive Models

The elastic-viscoplastic constitutive models used to represent the behavior of the material must be able to fit correctly the experimental measurements. They are identified by an inverse procedure that uses a dynamic numerical analysis. No thermal effect is addressed in these identifications. Three models that fit well to this requirement have been chosen:

a) The Johnson-Cook model (Johnson & Cook 1983)

$$\sigma(p,\dot{p}) = (A + Bp^n)(1 + Cln\frac{\dot{p}}{\dot{p}_0}) \quad (4)$$

where $p$ and $\dot{p}$ are the cumulated plastic strain and strain rate respectively. The parameters
$A$, $B$ and $n$ are obtained by quasi-static classical tension test [10]: $A$=955 MPa, $B$=770 MPa and $n$=0.557. The parameter $C$ is the only one to be identified by the inverse process. An axisymmetric 2D Finite Element model in ABAQUS is used to compute the dynamic simulation. The model consists of the projectile, the specimen and the bar.

b) The Zerilli-Armstrong model (Zerilli & Armstrong 1996)

This model is calibrated using a unidimensional FE model in MATLAB developed in (Andriamiseza 2014). Assuming a constant temperature $T$, two variants for bcc and hcp materials are considered in Eq. 5 and Eq. 6 respectively:

$$\sigma_y = K_0 + K_1 p^n + K_2 \dot{p}^{K_3} \quad (5)$$

where $K_0 = C_0$, $K_1 = C_5$, $K_2 = C_1 \exp(-C_3 T)$ and $K_3 = C_4 T$. The parameters, $K_0$, $K_1$ and $n$ have the same value as the parameters $A$, $B$ and $n$ of the Johnson-Cook relation because of the equivalent form of strain hardening. The parameters $K_2$ and $K_3$ have been calibrated inversely.

$$\sigma_y = K_0 + K_1 \dot{p}^{K_2} + K_3 \sqrt{p}\dot{p}^{K_4} \ (hcp) \quad (6)$$

where $K_0 = C_0$, $K_1 = C_1 \exp(-C_3 T)$, $K_2 = C_4 T$, $K_3 = C_2 \exp(-C_3' T)$ and $K_4 = C_4' T$.
$K_0$ is equivalent to the yield stress. Four parameters $K_1$, $K_2$, $K_3$ and $K_4$ are computed during the inverse identification.

The cost function $f(x)$ is defined as the Euclidean norm of the difference between the simulated strain $\varepsilon_{sim}(x,t)$ and the recorded strain $\varepsilon_{\exp}(t)$. The identification is done on each tests of the Table 1. The calibrated strain $\varepsilon_{sim}$ of the tests T1, T4, T6, T8 and T11 are

plotted and superposed to the measured strain $\varepsilon_{exp}$ in the Figure 4(a)-(e). An error bar is plotted associated to each mean value of the parameter *C* for the 2D identification, as shown in the Figure 4(f). At least two repetitions are carried out for each test. The simulated strains of the three different constitutive models fit well to the experimental data at strain rate up to 15000 $s^{-1}$. We observe at the second raising stage when the specimen is plastically deformed that the results are concordant as shown in the Figure 4(a)-(c). A small difference appears at this stage between the calibrated strain of the Johnson-Cook model and the measured one in the Figure 4(d). The Zerilli-Armstrong model fits well the experimental data. The Figure 4(f) indicates that an approximately constant value of the parameter *C* of the Johnson-Cook model is identified at the strain rate ranging from 3000 to 18000 $s^{-1}$. At very high strain rate as observed in the tests T10 and T11, a much greater value of C is obtained. The differences in these two tests may be due to (i) the very short projectile used in the test and/or (ii) the thermal effects not addressed in the identification. More repetitions of these tests must be carried out to clarify the results.

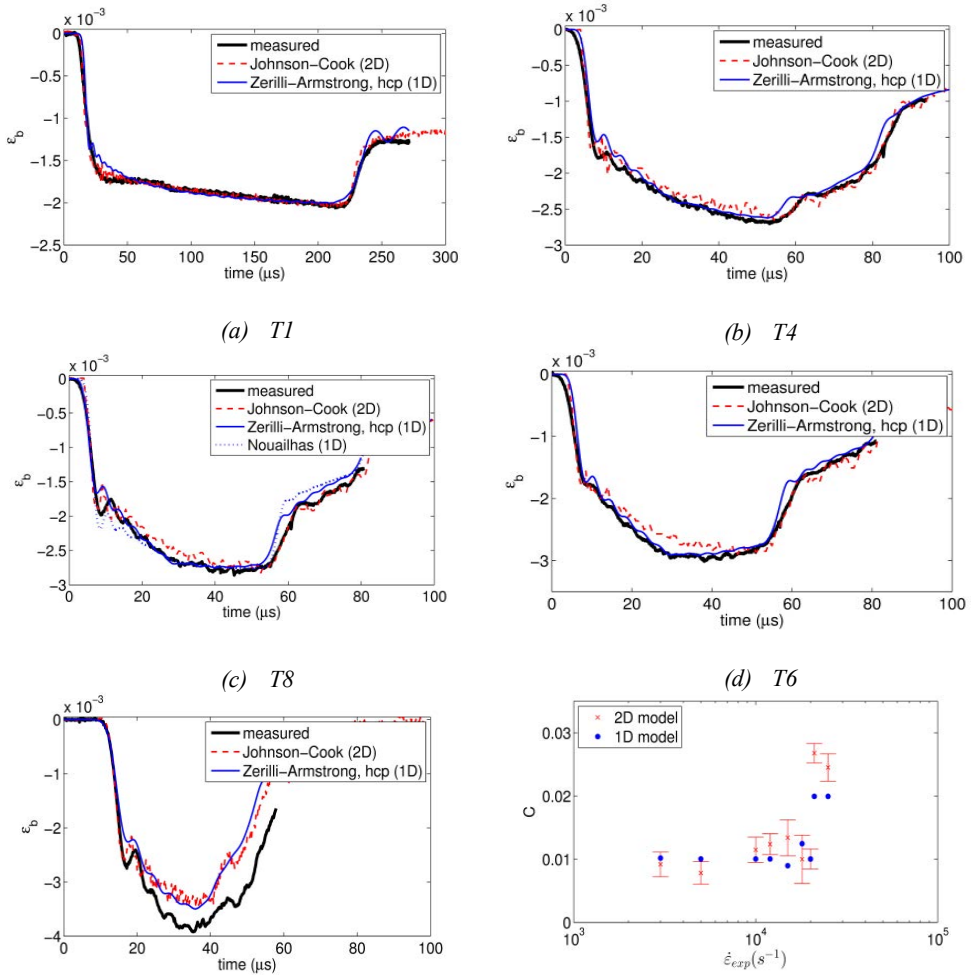


*(a) T1* *(b) T4*

*(c) T8* *(d) T6*

*(e) T11* *(f) Error bars of parameters*

***Figure 4**: Results of identifications*

The stress-strain curves of the identified constitutive models are plotted at the strain rate of 3000 $s^{-1}$ and 18000 $s^{-1}$ and are compared to those obtained from the quasi-static tests in the Figure 5. The Figure 5(a)-(c) show a great raise of the flow stress as the strain rate is increased. This increase is lower when the strain rate goes from 3000 to 18000 $s^{-1}$. For the Johnson-Cook model, the two curves at these two strain rates are very close in the Figure 5(a). Similar observations can be done for the other models.

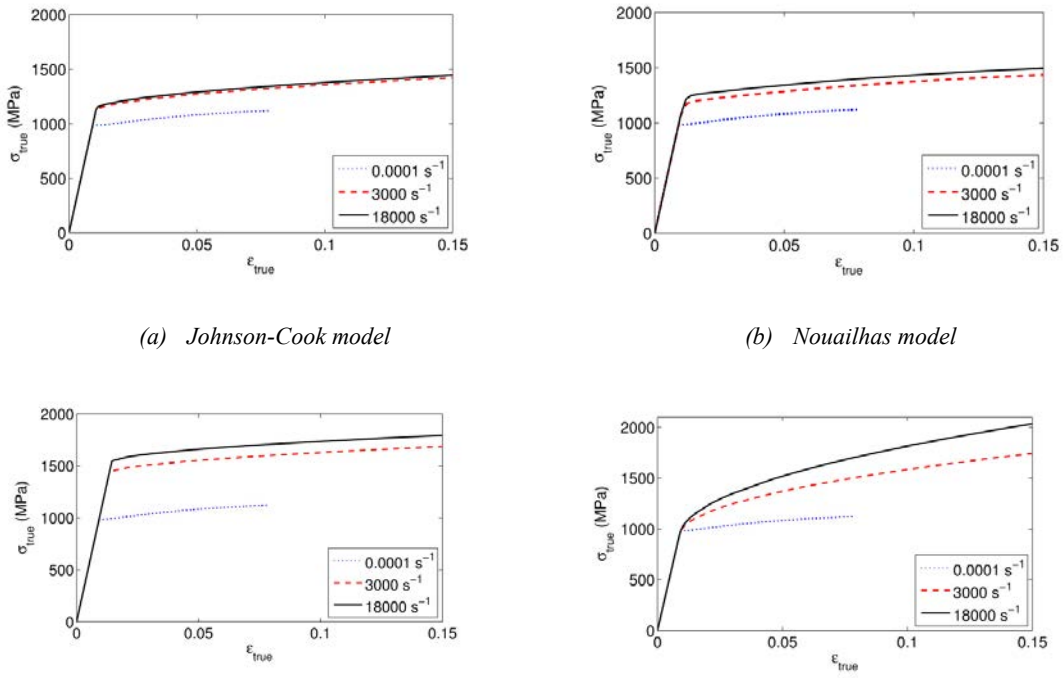


*(a) Johnson-Cook model*

*(b) Nouailhas model*

*(c) Zerilli-Armstrong (bcc)*

*(d) Zerilli-Armstrong (hcp)*

***Figure 5**: Stress-strain curves plotted within the range of $10^{-4}$ to 18000 $s^{-1}$*

# 4 Conclusion

In this work, the Ti-6Al-4V has been tested on a range of strain rate ranging from 3000 to 25000 $s^{-1}$ using the direct-impact Hopkinson device. To identify three elastic-viscoplastic constitutive models, an inverse analysis has been carried out on the experimental data. The three identified constitutive models fit well the experimental data at the strain rate ranging from 3000 up to 18000 $s^{-1}$. However more experimental and numerical research at higher strain rate is required to refine these results.

# References

Andriamiseza, A., 2014. Rapport de stage de Master: Identification de modèles de comportement à haute vitesse de déformation sur des essais de Kolsky à impact direct,

Davies, R.M., 1948. A critical study of the Hopkinson Pressure Bar. Philosophical Transactions of the Royal Society of London. Series A. Mathematical and Physical Sciences, 240(821), pp.375–457.

Dharan, C.K.H. & Hauser, F.E., 1970. Determination of stress-Strain characteristics at very high strain rates. Experimental Mechanics, 10(9), pp.370–376.

Gorham, D.A., Pope, P.H. & Field, J.E., 1992. An improved method for compressive stress-strain measurements at very high strain rates. Philosophical Transactions of the Royal Society of London. Series A. Mathematical and Physical Sciences, 438(1992), pp.153–170.

Guo, X. et al., 2014. Inverse identification at very high strain rate of the Johnson--Cook constitutive model on the Ti-6Al-4V alloy with a specially designed direct-impact Kolsky bar device. Strain, 50(6), pp.527–538.

Guo, X., 2015. On the directimpact Hopkinson system for dynamic tests at very high strain rates. Ecole centrale de Nantes.

Johnson, G.R. & Cook, W.H., 1983. A constitutive model and data for metals subjected to large strains, high strain rates and high temperatures. 7th International Symposium on Ballistics, pp.541–547.

Kamler, F., Niessen, P. & Pick, R.J., 1995. Measurement of the behaviour of high-purity copper at very high rates of strain. Canadian Journal of Physics, 73(5--6), pp.295–303.

Kolsky, H., 1949. An investigation of the mechanical properties of materials at very high rates of loading. Proceedings of the Physical Society. Section B, 62.

Ramesh, K.T., 2008. Part D: Chapter 33. High strain rate and impact experiments. In Springer handbook of experimental solid mechanics. Springer, pp. 1–31.

Wang, L., 2007. Foundations of stress waves, Elsevier BV.

Zerilli, F.J. & Armstrong, R.W., 1996. Constitutive relations for titanium and Ti-6Al-4V. In Proceedings of the conference of the American Physical Society topical group on shock compression of condensed matter. pp. 315–318.

# A Study to Improve the Crash Performance of Plastic Materials Considering the Strain Rate and Fracture Characteristic

**H. Y. Kim[1*], C. A. Lee[1], J. H. Bamg[1], B. C. Cho[1], D. Y. Kim[2], D. Y. Ha[3]**

[1] Department of Mechanical and Biomedical Engineering , Kangwon National University, Korea
[2] Structural Analysis Team, DAS, Korea
[3] CAE Team, HYUNDAI MOBIS, Korea
[*]Corresponding author. Email: khy@kangwon.ac.kr

## Abstract

*The numerical simulation of structural parts made from plastics is becoming increasingly important nowadays. The fact that almost any structural requirement can be combined in a lightweight, durable and cost effective structure is the driving force behind its widespread application. More and more structural relevant parts are being constructed and manufactured from plastics. It is difficult accurately to predict the reliability according to finite element analysis, because plastics materials show the complex material behaviour. Thus, it is demanded for reliable and obvious methods to design these parts and to predict their material behaviour. For the finite element simulations of polymeric materials mathematical models are needed which cover all the phenomena of the material.*

*In this paper, it is possible to describe accurately the mechanical behaviour of thermoplastic materials using a new constitutive model termed as SAMP-1(Semi-Analytical Model for Polymers) in LS-dyna. We performed the high speed tension tests (strain rate: 0.001/s, 0.1/s, 1/s, 50/s, 100/s) for the characterisation of the plastics material. Also, the parameters of the SAMP-1 model were identified by using multi-directional mechanical tests such as uniaxial tension, simple shear, and compression tests. As validation purpose, the SMAP-1 model was compared to the existing models for predicting the stress-strain behaviour in the test specimens and the dynatup impact test.*

## Keywords

High speed tension test, SAMP-1, Finite element method

# 1 Introduction

Automobile interior parts usually consist of plastic and composite materials to keep the vehicle lightweight and to meet quality expectations in appearance. Plastic material is particularly widely used for automobile interiors parts because of the advantages of its lightness, low price, and outstanding formability. However, the various material characteristics exhibited by plastic due to its molecular structure, mixing conditions, manufacturing environment, etc. make it difficult to satisfy the crashworthiness and strength requirements for automobiles(Pawlak et al.,2005; Klompen et al.,1982; Clausen et al., 2011).

With recent improvements in the reliability of forming analyses as well as crash and structural analyses using computer simulation, many studies have been conducted to evaluate the vehicle's structural stability and formability at the stage of research preceding automobile design. However, plastic material has characteristics such as softening, volumetric change, pressure dependence and anisotropy that make it difficult to perform material modelling for crash testing and analysis. For plastic material modelling, the Von-Mises yield criterion and the isotropic hardening model are commonly used, but these are not suitable for accurately simulating the characteristics of plastic. Therefore, for the material modelling of plastic, we need to develop a material model that can represent the characteristics of plastic and a material testing and modelling method for this purpose(Avalle et al., 2010; ).

S. Kolling and three others (2005) conducted a phenomenological analysis of the mechanical characteristics of plastic and applied the characteristics of softening, volumetric change, pressure dependence and strain rate dependence to the material model (Koling et al., 2005). They also applied a damage model to express behaviour under loading and considered fracture strain, triaxiality of stress, and element size as fracture factors in the expression.

Kunio Takekoshi, in collaboration with one other researcher (2012), used the test data for the SAMP-1 material model to present the conversion formulae for true stress and true strain and introduced the procedure for deriving the Poisson's ratio in the plastic region (Takekoshi et al., 2012). In metal materials, the Poisson's ratio is generally assumed to be 0.5 in the plastic region, but in the case of soft plastic, in which softening occurs, the change in the Poisson's ratio results in volumetric change. To take account of this, an analysis was first performed with the initial Poisson's ratio assumed to be 0.5 and based on these results, sequential analyses were performed while adjusting the Poisson's ratio in the plastic region. One disadvantage of this approach, however, is that errors can occur in the process of adjusting the parameter using an unverified analysis model and there is a delay because of the sequential nature of the analyses. One study aiming to improve plastic material testing was performed by F. Grytten and three others (2009). They used a DIC (Digital Image Correlation) technique to obtain and apply the data for true stress, true strain, and Poisson's ratio and performed verification analysis by defining the yield stress for each strain rate (Grytten et al., 2012). Gang-Wook Lee and two others (2006) performed a study of the dynamic characteristics of plastic for collision analysis (Lee et al.,

2006). Based on the sample's deformation, Lee et al. expressed the correlations among true stress, true strain, nominal stress, and nominal strain and presented a series of test/analysis procedures required for establishing the failure criteria of plastic.

In this study, we compared and analysed various material models applicable to plastic and researched methods of application for the SAMP-1(Semi Analytical Model for Plastics-1 model, which uses a phenomenological approach to simulate the material's behaviour. To use the SAMP-1 model, we performed the high-speed tensile test on plastic material and used a range of material tests to derive the material parameters for the SAMP-1 model. We also performed the Dynatup impact test and analysis and compared the results for application in collision analysis.

# 2 Material Characteristics and Experiment

The major characteristics of plastic include anisotropy, pressure dependence, volumetric change, etc. Plastic has a molecular structure in a chained form, and therefore it exhibits different properties depending on the direction. Pressure dependence refers to the phenomenon whereby the material exhibits different properties depending on the pressure applied to the object, and this phenomenon appears in plastic. In the case of metal materials, the mechanical characteristics of the material generally do not change depending on the pressure applied, but plastic material has the characteristic of exhibiting different yield stress depending on the applied pressure. In other words, the yield stress will vary depending on the stress state of the material, and to take account of this pressure dependence in finite element analysis, we need a technique for defining the mechanical characteristics according to varying stress states. Another characteristic of plastic material is that the Poisson's ratio changes in correlation to volumetric change. In the case of metal materials, the Poisson's ratio is generally assumed to be 0.5 in the plastic deformation region following the yield stress, applying the law of constancy of volume whereby the volume does not change. In plastic, however, the Poisson's ratio changes along with the volume changes in the plastic deformation region. The softening behaviour phenomenon caused by this characteristic in plastic can be seen in the stress-strain rate diagram: as the strain rate increases, the stress decreases. In this study we performed material tests with varying stress conditions to take into account the characteristics of plastic material and we performed a high-speed tensile test to evaluate the mechanical characteristics depending on the strain rate. For information in material testing, please refer to **Table 1.** Material tests can be divided into static tests and dynamic tests: static tests include uniaxial tension, uniaxial compression, shear and loading-unloading tests. The loading-unloading test measures the phenomenon whereby the modulus of elasticity decreases as the strain rate of the plastic increases. Dynamic tests included the high-speed tensile test, in which we evaluated the tensile behaviour at the strain rates of 50/s and 100/s. The sample used in the high-speed tensile test is shown in **Fig.1**.

| Quasi-static Test | | | |
|---|---|---|---|
| **Test** | **Specimen** | **Test equipment** | **Output data** |
| Uniaxial tension | ASTM D 638 (type-5) | INSTRON 5882 | Stress-Strain curve |
| Poisson's ratio | ASTM D 638 (type-5) | ARAMIS_DIC | Plastic Poisson's ratio |
| Uniaxial compression | Ref. ASTM & JIS | Cyclic tension/compression tester | Stress-Strain curve |
| Loading-unloading | | | Damage curve |
| Simple shear | ASTM D 7078 | INSTRON 5882 | Stress-Strain curve |
| Destructive | R-notched specimen (R:10mm) | | Load-disp. curve |
| **Dynamic Test** | | | |
| High speed tension | No standard | INSTRON VHS-65/80-25 | Stress-Strain curve |

***Table 1**: Material test*

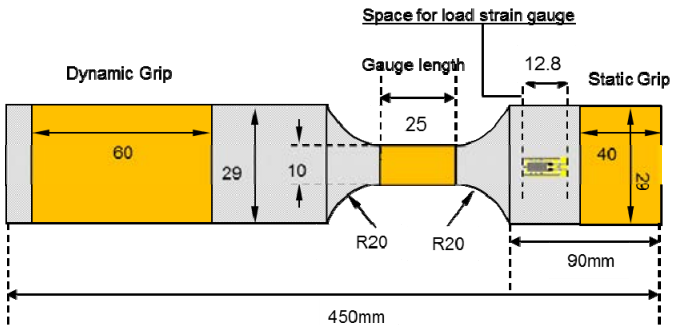


***Figure 1**: Specimen for high speed tension*

The fast-jaws grip system has been adopted as a method of grip in high-speed tensile test. In the fast-jaws grip system, the grip module is not in contact with specimen prior to the test, and eventually comes into contact with specimen and the test proceeds once the actuator reaches its target speed. This system has its merits of preventing materials from being damaged by high pressure on the grip module before the material is tensile-strained, and of ensuring precise test speeds.

In general, a material testing machine adopts two different methods of measuring loads: closed loop and open loop. The closed loop allows testing machines to control speeds while exchanging signals between them and mostly uses the strain gauge load cell while the open loop does not exchange signals between testing machines and usually uses the Piezo load cell. The high-speed tensile test adopts the Piezo load cell that does not exchange signals each other as it occurs within the extremely short period of time. Measuring loads using the Piezo load cell has a drawback of incurring severe load ringing.

To avoid or minimize the load ringing phenomenon caused by vibration between the specimen and jig, and the jig and the load cell, this study has measured loads with the strain gauge attached to top of the specimen as illustrated in **Fig. 2 (a)** below.

A comparison of the results of measuring loads using the load cell and loads at the strain gauge attached to the specimen is illustrated in Fig. 2 (b) below. It is found that the load ringing phenomenon, which occurs in measurements using the load cell, is relieved in load measurements using the strain gauge, which ensures precise measurements of loads.

The results of the plastic material tests are presented in Fig. 3 and Fig. 4. In the high-speed tensile test, to minimize load ringing, a strain rate measuring device was attached to the upper grip of the sample in a manner designed to reduce the ringing that occurs when measuring the load. In addition, to eliminate the noise that occurs when performing the high-speed tensile test measurements, we used the adjacent-averaging method. In the results of the uniaxial tension test, we found that as the strain rate increased, the stress increased while elongation tended to decrease. The measurements of changes in the Poisson's ratio of plastic material showed that the Poisson's ratio tends to decrease over time, and the modulus of elasticity also tends to decrease as the strain rate increases.

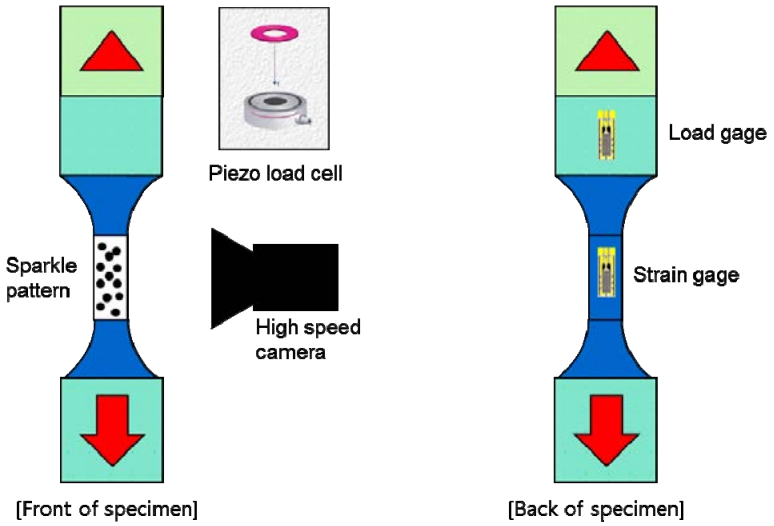


(a) Methods of measuring loads and strain

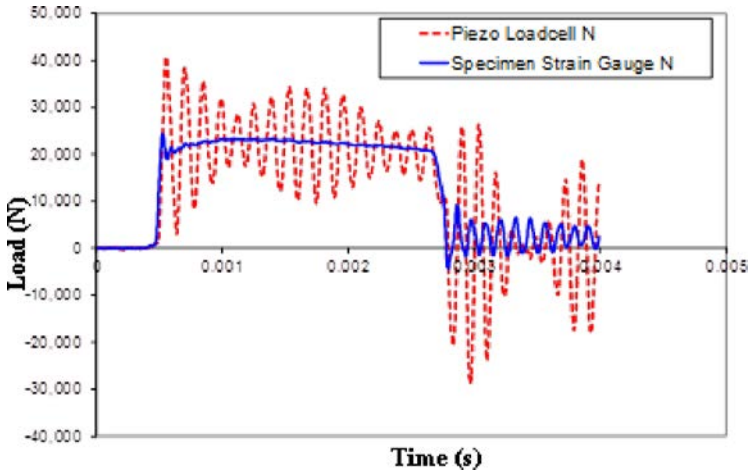


(b) A comparison of the results of measuring loads

***Figure 2**: Load measurement method in high-speed tensile test*

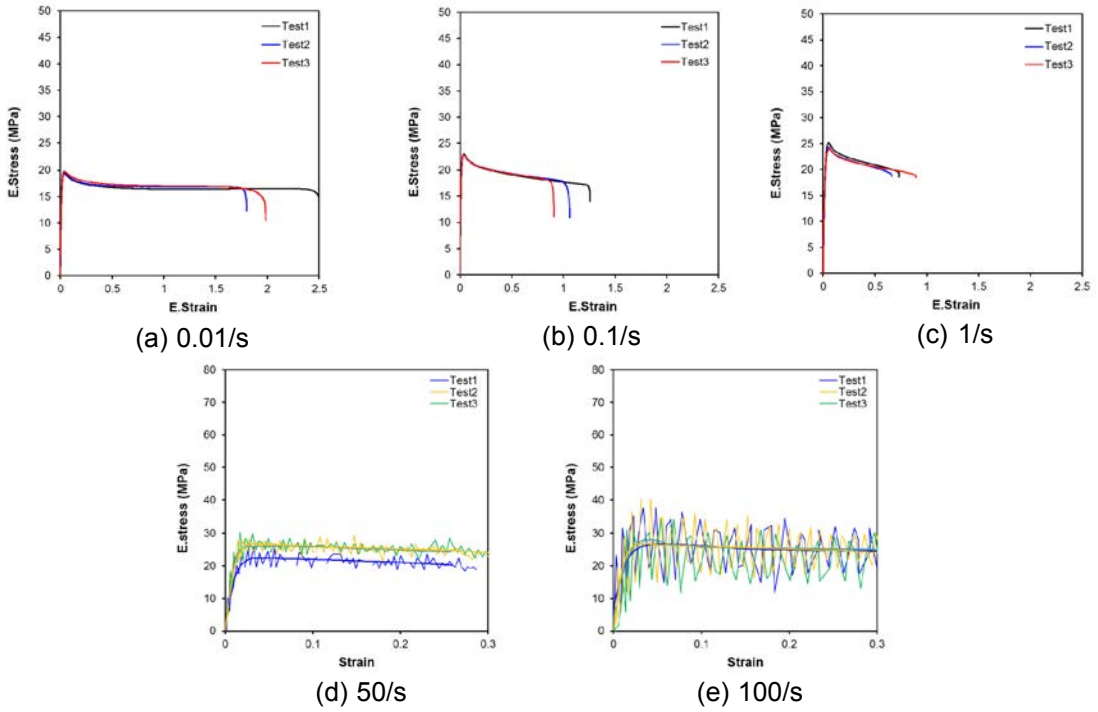


***Figure 3**: Uniaxial tension test result (quasi-static and dynamic)*

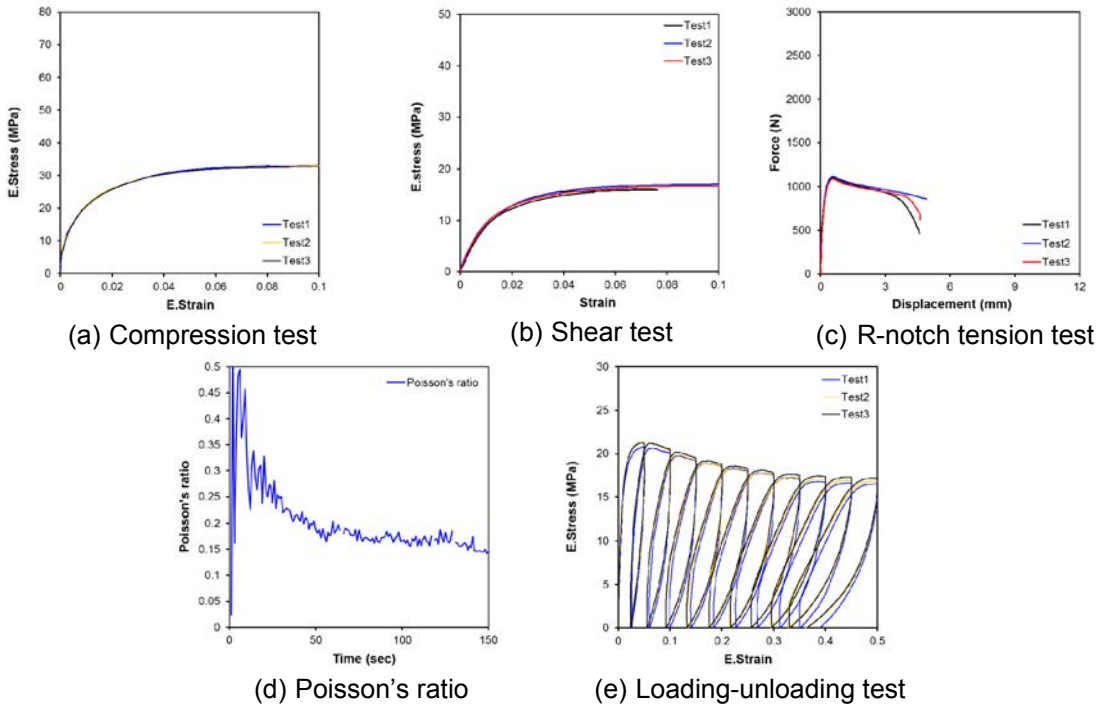


***Figure 4**: Material test result*

# 3 Material Modeling for SAMP-1

The SAMP-1 model (MAT 187) phenomenologically explains the polymer material from a macro perspective. This model, developed by Paul Du Bois, is suitable for non-reinforced plastic and applies a yield surface based on the Isotropic C-1 smooth yield surface. The majority of the parameters required for thermosoftening plastic are approximately taken into account.

The SAMP-1 model can take into account pressure dependence by applying a yield function that can define the yield stress correlating to each pressure, and can apply changes in the Poisson's ratio to express volumetric change and softening in the plastic region. By applying the damage curve based on the plastic deformation rate, we can simulate the behavior when the load is removed, and by applying the stress-strain rate curve for each strain rate and using the Cowper-Symonds model, we can consider the effects depending on speed.

In the SAMP-1 model, the yield surface is internally modified according to the number of the stress-strain rate curves for each mode of the pressure obtained from the material test and the yield criteria is divided into 3 types as shown in Table 2. If only one mode of the material data is applied as the input, the von-Mises yield criterion is applied, whereas if two modes of material data are applied, the Drucker-Prager yield criterion is applied. To apply the yield criterion sought in the SAMP-1 model, it is necessary to apply 3 types of material data—the tensile, compressive and shear modes—and the plastic's characteristic of pressure dependence can be considered approximately. The yield criterion for each condition can be confirmed based on the pressure-stress relation, as shown in Fig. 5.

| Yield criterion | Tension | Shear | Compression | Biaxial |
|---|---|---|---|---|
| **Von-Mises** | O | X | X | X |
| **Drucker-Prager** | O | O | X | X |
| | O | X | O | X |
| | O | X | X | O |
| **SAMP-1** | O | X | O | O |
| | O | O | X | O |
| | O | O | O | O |

***Table 2**: Yield criterion according to the obtained test data*

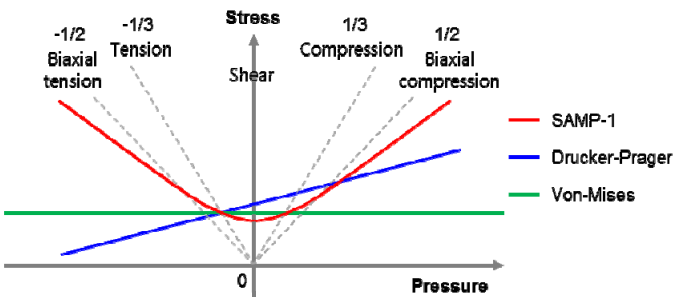


***Figure 5**: Stress-Pressure relationship and differences according to the yield criterion*

# 4 Dynatup Impact Analysis

To perform plastic fracture analysis using the SAMP-1 fracture model in this study, we constructed the Dynatup impact analysis model as shown in **Fig. 6**. We used a 100mm*100mm square shaped sample, with the thickness set at 2.9 mm. The load in the impact shaft was 22.43 kg, and the diameter was set at 12.7mm and the fall speed at 3270mm/sec. To evaluate differences according to the material model, we used the MAT187 (SAMP-1) fracture model and the MAT24 (Von-Mises) model and compared the results. Dynatup impact analyses can be divided into analyses which apply the fracture model and those which do not apply the fracture model and the results for each are shown in **Fig. 7.** Upon measuring the reaction of the impact shaft, it was found that in the case of MAT24 the initial load inclination was similar to the test results but in the load results after a displacement of 5mm, there were significant disparities from the actual test. It was also confirmed that there was a large error in the time point of fracture. By contrast, in the SAMP-1 model, the load and fracture time tended to be similar to those of the actual test.

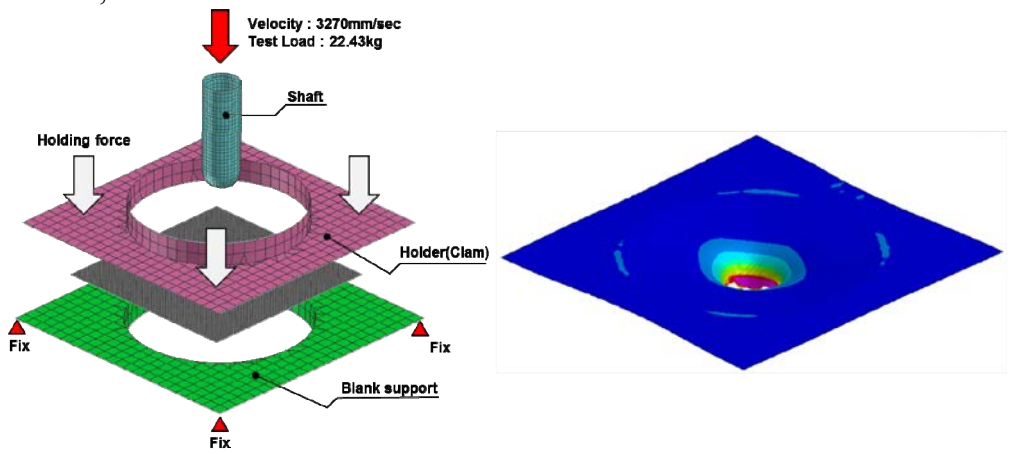


***Figure 6**: Dynatup analysis*

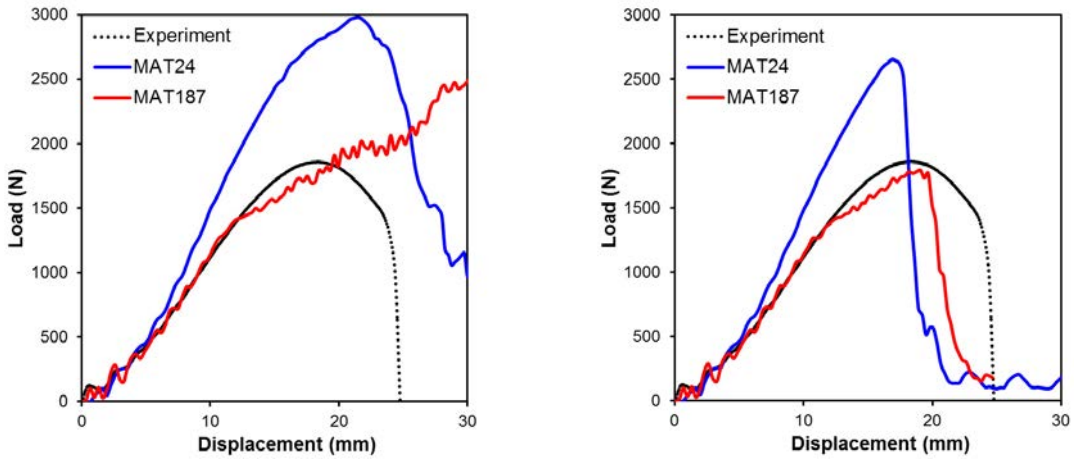


(a) Without fracture model (b) With fracture model

***Figure 7**: Comparison of load-displacement curve*

# 5 Conclusion

In this study, we performed a high-speed tensile test and material tests under varying stress states to analyse the fracture characteristics of plastic, taking account of the strain rate. We also used the Mat187 SAMP-1 model of the LS-dyna analysis program, a material model capable of expressing the behaviour of plastic material, to perform the Dynatup impact analysis and verified the reliability of the material model. Our analysis using the SAMP-1 model yielded simulated results confirmed to be similar to the actual test results and there were few errors in the fracture time point.

# Acknowledgment

This study was made possible by support provided by the analysis team of Hyundai MOBIS and the National Research Foundation of Korea (NRF) BK21Plus project (Kangwon National University, No.22A20130012864)

# References

Avalle M, Peroni M and Scattina A, 2010, Mechanical models of the behaviour of plastic materials: influence of time and temperature, Latin Am J Solids Structs, Vol.7, pp.41–61

Clausen AH, Polanco-Loria M, Berstad T and Hopperstad OS, 2011, A constitutive model for thermoplastics with some applications, In: 8th European LS-DYNA users conference, Strasbourg, France, DYNAmore GmbH

Grytten F, Polanco-Loria M and Daiyan H, 2012, Material parameters identification: an inverse modeling methodology applicable for thermoplastic materials, Polym Engng Sci, Vol.52, pp.438–448

Klompen ETJ, Engels TAP, Govaert LE and Meijer HEH, 2005, Modeling of the postyield response of glassy polymers: influence of thermomechanical history, Macromolecules, Vol.38, pp.1943–1982

Kolling S, Haufe A, Feucht M and Du Bois PA, 2005, SAMP-1: a semi-analytical model for the simulation of polymers, In: 4.LS-DYNA Anwenderforum, Bamberg, Germany, DYNAmore GmbH, pp.A-II-27–A-II-52

Lee K.W., Ha D.Y., Park S.J., 2006, Dynamic Characteristics of Plastics for Crash Analysis, Advanced Materials and Manufacturing in Automotive Engineering, Vol.1, pp.39–46

Pawlak A and Galeski A, 2005, plastic deformation of crystalline polymers: the role of cavitation and crystal plasticity, Macromolecules, Vol.38, pp.9688–9697

Takekoshi K and Niwa K, 2012, Validation and material modeling of polymers by employing MAT_SAMP-1, In: 12th international LS-DYNA users conference, Dearborn, Michigan, USA, DYNAmore GmbH

# A New Experimental Technique for Applying Impulse Tension Loading

**Z. S. Fan[1], H. P. Yu[1,2*], H. Su[3], X. Zhang[1], C. F. Li[1]**

[1] National Key Laboratory for Precision Hot Processing of Metals, Harbin Institute of Technology, China;
[2] School of Materials Science and Engineering, Harbin Institute of Technology, China;
[3] Tianjin Long March Launch Vehicle Manufacturing Co.Ltd., China
[*]Corresponding author. Email: haipingy@hit.edu.cn; Tel.: +86 451 8641 8753

## Abstract

*This paper deals with a new experimental technique for applying impulse tension loads. Briefly, the technique is based on the use of pulsed-magnetic-driven tension loading. Electromagnetic forming (EMF) can be quite effective in increasing the forming limits of metal sheets, such as aluminium and magnesium alloys. Yet, why the forming limit is increased is still an open question. One reason for this is the difficulty to let forming proceed on a certain influence monotonically: the main phenomena causing this increase in formability are considered to due to "body force" effect, inertia effect, changes in strain rate sensitivity. In this study, an impulse tension loading setup is presented. "Body force" effect and strain rate, which are known to be the two key factors leading to higher formability, can now be separated freely by our designed device. Reproducible and adjustable loading rate (80s-1~3267s-1) can be achieved by adjusting the discharge voltage and capacitance. The relation between the discharge voltage and strain rate was obtained with the help of finite element calculations and high-camera measurement results. The results of an exploratory experiment carried out on the designed device are presented for aluminum alloy AA5052 sheet. It shows that this technique could be used to study the dynamic response of sheets.*

## Keywords

Electromagnetic forming, Forming limit, Tension loading

# 1 Introduction

Electromagnetic forming (EMF) is high potential process for sheet metal forming, as it offers many advantages such as higher formability. Yet, why the forming limit is increased is still an open question. One reason for this is the difficulty to let forming proceed on a certain influence monotonically: the main phenomena causing this increase in formability are considered to due to "body force" effect, inertia effect, changes in strain rate sensitivity, or a combination of them. At high velocity forming, the formability is higher than that in traditional stamping. Regazzoni et al. (1987) reported that the glide kinetics should be entirely controlled by drag under the applied stress at very high strain rates. Han and Tvergaard (1995) reported that inertia and finite strain effects are accounted for the dynamic necking of plane strain specimens under rapid deformation. Hu and Daehn (1996) showed that inertial effects are likely to be a first-order factor responsible for enhanced ductility observed in their sheet tensile tests and expanding ring tests. Seth and Daehn (2005) showed that the fragments increase with the increased strain rate in their electromagnetic expanding ring tests. However, which factor is dominant during EMF? From an overview of the-state-of-art of EMF (Psyk et al., 2011), it reveals the necessity for further consideration of these factors. One possible way is the proper decoupling of these influences. Therefore, there is a need of a forming device capable of testing standardized sheet metal specimens at speed precisely within the range of electromagnetic forming and, most importantly, their deformation can be standardized or directly compared to quasi-static and electromagnetic forming results. In this study, an impulse tension loading technique is presented. "Body force" effect and strain rate can now be separated freely by our designed device. The relation between the discharge voltage and strain rate was obtained with the help of finite element model and high-speed camera measurement results. Exploratory experiments of AA5052 Al sheet uniaxial tensile were performed at various strain rates to test the potential application of the designed instrument.

# 2 Experimental Design

## 2.1 Experimental Setup

The schematic diagram of pulsed-magnetic-driven uniaxial tension of AA5052 sheet is shown in Fig. 1. It consists of specimen, flat spiral coil, driver sheet and puller. The specimen is fixed on its one end, while the other one is attached to the puller. Fig. 1(c) shows a photograph of the experimental setup.

The driver sheet was put between coil and puller in order to accelerate the workpiece. The area of coil was covered by the driver sheet. The circle flat spiral coil is made of copper wire, with the rectangular section's dimension at 2.5×16 mm.

The specimens used in the present work were commercially available AA5052 sheets with a thickness of 1 mm. The geometry of the specimen is shown in Fig. 2. The sheet samples were prepared according to an ISO 6892: 1998. The gauged width and length of the tensile specimens were 6 and 25 mm, respectively. In order to determine the strain

distribution after testing, the surface of each sheet sample was firstly printed with 2.5 mm×2.5 mm grids. The experiments were performed using 30 kJ EMF at Harbin Institute of Technology. This system consists of a total of 14 capacitors of 192μF, which can be charged up to 5.0 kV.

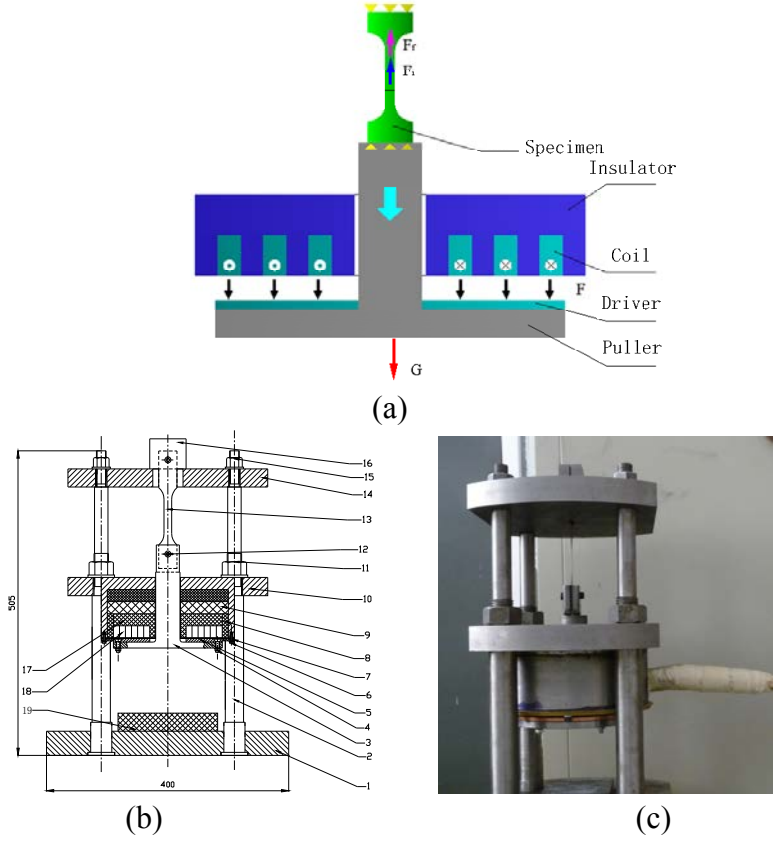


***Figure 1**: (a) Schematic of the pulsed-magnetic-driven uniaxial tension process, (b) configuration of the setup and (c) a photograph of the experimental setup.*

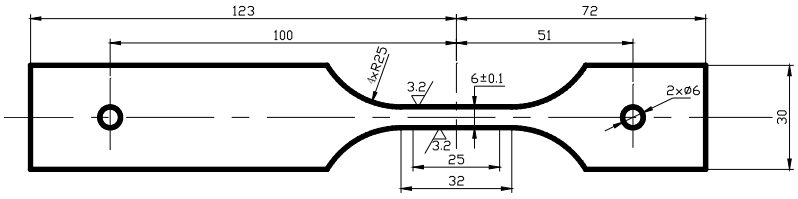


***Figure 2**: Geometry of the specimens (unit, in millimeters)*

## 2.2 Measurement Technique

High-speed camera (Type: FASTCAM SA5 1000K-M2) was used to obtain simultaneous high speed images of the samples during the pulsed-magnetic-driven uniaxial tension process. The images were recorded using 20 μs exposure duration. Tests were performed using the setup sketched in Fig. 3.

***Figure 3**: Pictures of high-speed camera recording the deformation of AA5052 sheet during the pulsed-magnetic-driven uniaxial tension process*

### 2.3 Numerical Simulation

The ANSYS FEA software was used to analyze the deformation law in pulsed-magnetic-driven uniaxial tension. ANSYS/Multiphysics was chosen to simulate the transient electromagnetic phenomena involved in the magnetic pulse forming. The mechanical behavior of the system was modeled using ANSYS/ LSDYNA, an explicit dynamic finite element program. In the simulation process, the electromagnetic field was first computed by solving theMaxwell equations, and then the Lorentz force produced by the electromagnetic model was set as the input data to calculate the deformation of the workpiece in the mechanical model. In the mechanical model, for simplicity, the coil and puller were treated as rigid bodies. In order to model the constitutive response of the material in high-strain rate, the flow stress is determined as a function of the plastic strain, the strain rate, and the temperature using the constitutive equation given by Johnson and Cook (1983):

$$\sigma = [A + B\varepsilon^n][1 + C\ln\left(\frac{\dot{\varepsilon}}{\dot{\varepsilon}_0}\right)][1 - \left(\frac{T - T_{room}}{T_{melt} - T_{room}}\right)^m] \quad (1)$$

where ε is the effective plastic strain; $\dot{\varepsilon}$ is the strain rate; $\dot{\varepsilon}_0$ is the reference strain rate; and T, Troom, and Tmelt are the absolute testing, room, and melting temperature, respectively. In this paper, A=92.4 MPa, B=132 MPa, C=0.025 and n=0.25 are the four material constants which are determined from the experimental data of AA5052 aluminum alloy. The final term on **Eq. 1**, which gives the stress an exponential decay as temperature increases, will be ignored.

## 3 Results and Discussion

### 3.1 High Speed Imaging

A sequence of high speed images showing the dynamic deformation of the AA5052 Al sheet is shown in Fig. 4. As can be seen, uniform deformation stage is about 1.3 ms at discharging voltage of 3kV and capacitor of 768μF. A necking is seen to form on the gauged length of the tensile specimen prior to fracture, as displayed in the image in Fig. 4.

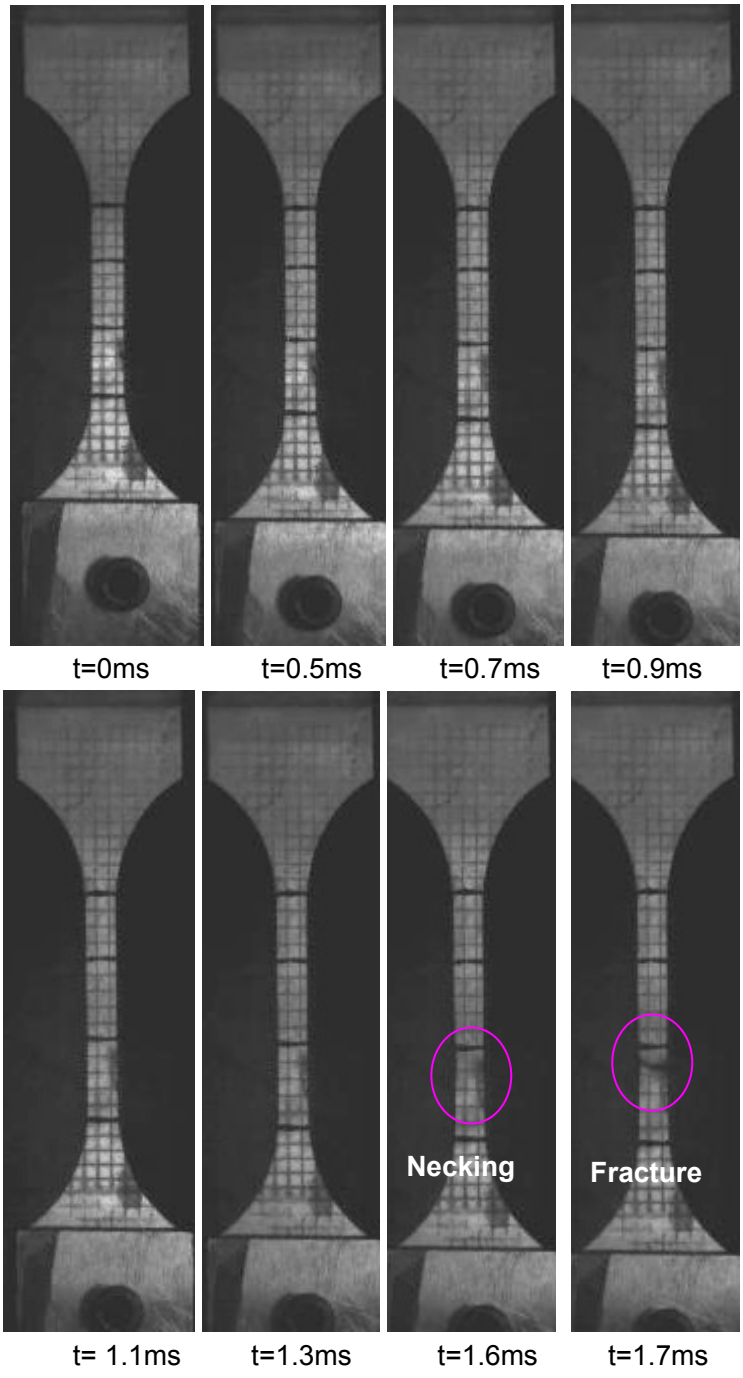


***Figure 4**: High speed image sequences showing the deformation of the AA5052 sheet sample ( 768uF，3kV)*

The length $l$ of two typical points a and b on the sample was measured at different time, as shown in Fig. 5(a). The measured values of length $l_i$ as a function of time t are plotted in Fig. 5(b). The velocity of the sample can be obtained via differential calculation. The velocity varies with the length $l$ under the slope observation in Fig. 5(b). Here, the peak value of velocity was used in this work. The engineering strain rate can be estimated by the following equation:

$$\dot{\varepsilon}=\frac{d\varepsilon}{dt}=\frac{d(\frac{l-l_0}{l_0})}{dt}=\frac{1}{l_0}\cdot\frac{dl}{dt}=\frac{v}{l_0} \tag{2}$$

where $l_0$ is the original length, $v$ is the peak value of velocity. Table 1 shows the resultant data for the velocity of puller and the strain rate, while discharge voltage is varied from 1.85kV to 3.0 kV. As can be seen, the strain rate increases with the discharge voltage at a constant capacitor of 768μF.

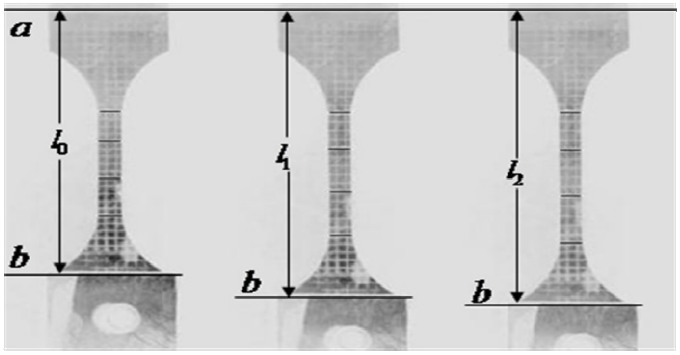


(a)

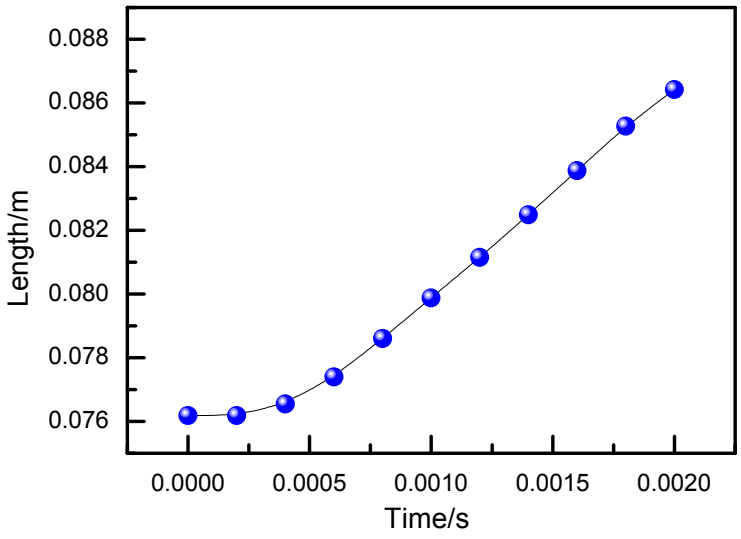


(b)

***Figure 5**: (a) The measured length l of two typical points a and b on the sample, and (b) length li as function of time t (the orginal length l0=76.18mm, 768uF, 3kV)*

***Table 1**: Velocity and strain rate for different discharge voltages*

| Capacitor(μF) | Discharge voltage(kV) | Velocity(m/s) | Strain rate($s^{-1}$) |
|---|---|---|---|
| 768 | 1.85 | 2.75 | 86.15 |
| | 2.00 | 3.05 | 95.41 |
| | 2.50 | 4.48 | 139.92 |
| | 2.75 | 5.72 | 178.81 |
| | 3.00 | 7.00 | 218.75 |

## 3.2 Simulation Results

Fig. 6 shows a sequence of the plastic deformation of the AA5052 Al sheet. As can be seen, deformation process predicted by simulation is similar to that observed through high-speed camera. A necking is also predicted to form in the gauged length of the tensile specimen. Figure 7 shows the velocity variation of typical elements attached to the puller at different discharge voltage and capacitor. As can be seen, the velocity increases rapidly at early stage, reaches to a maximum value and then drops gradually. The maximum value of velocity is selected to evaluate the strain rate. It should be noted that no fracture criterion was used in our current work; therefore, the velocity evolution cannot be used to predict the deform behaviour when necking occurs.

For the purpose of practical application, attempt was made to establish the relationship between the discharge voltage and strain rate. Figure 8 shows strain rate as a function of the square of discharge voltage with respect to different capacitor. For each capacitor, the point distribution shows a linear relationship between strain rate and the square of discharge voltage. As expected from the fitting formulas shown in the inset of Fig. 8, it is estimated that strain rate can range from $130s^{-1}$ to $3267s^{-1}$ by our developed setup, as discharge voltage varies from 1kV to 5kV at a constant capacitor of 1920μF.

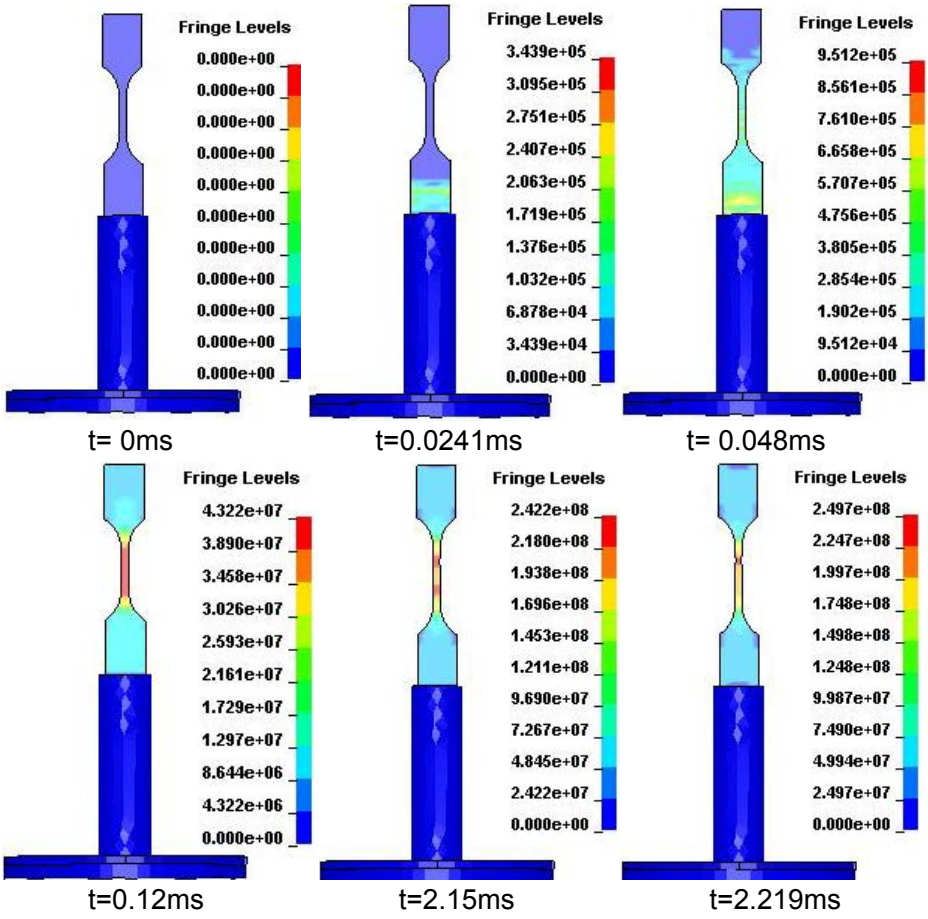


***Figure 6**: Von Mises stress evolution pridicted by numerical simulation ( 768uF，3kV)*

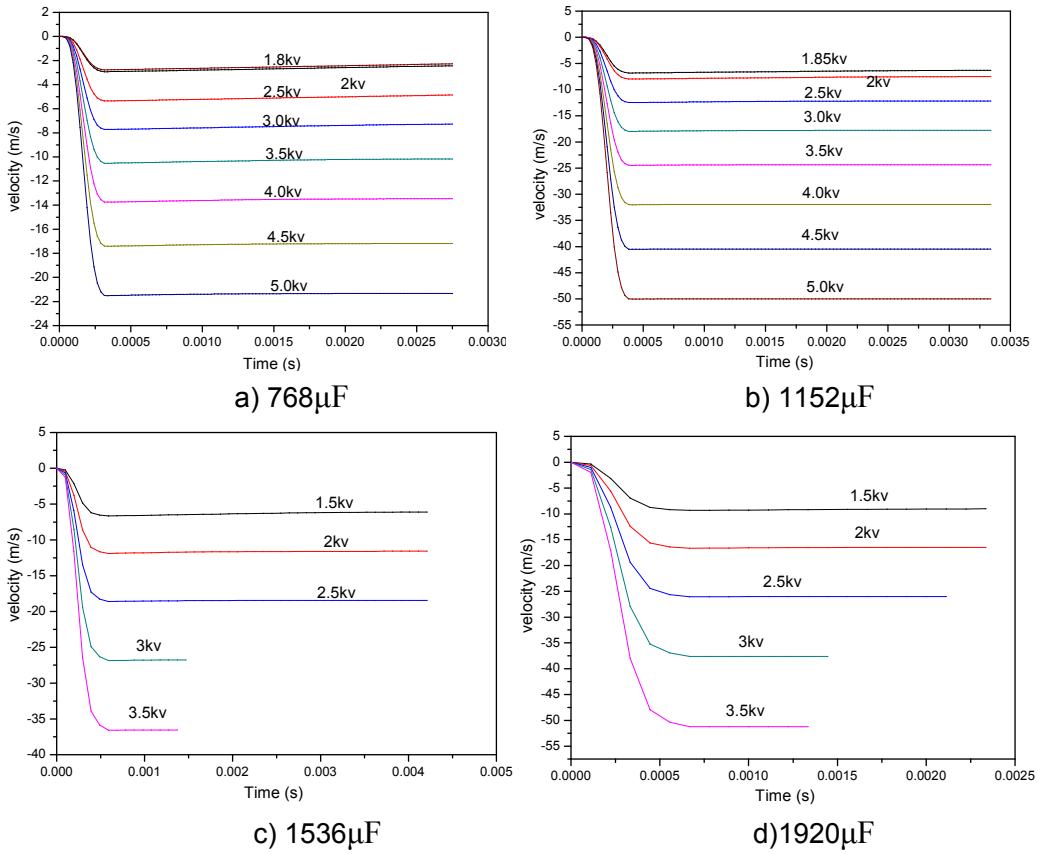


***Figure 7**: Velocity as a function of discharge voltage for four select values of the capacitor: (a) 768μF; (b) 1152μF; (c) 1536μF and (d) 1920μF*

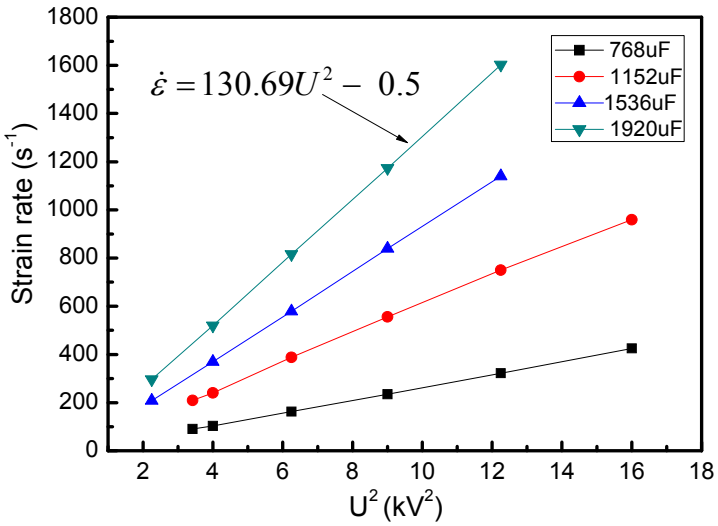


***Figure 8**: Strain rate as a function of the square of discharge voltage with respect to different capacitor*

## 3.3 Experimental Results

For verification purposes, strain rate predicted by simulation was compared to experimental one. Fig.9 displays the comparison results for four selected value of discharge voltage at a constant capacitor of 768μF. It is observed that the errors between the measured and calculated results are less than 10%. The little deviation may be due to the loosely couple method used in this work. The experimental and simulation results have a good agreement. Therefore, one can safely use the relationship between the strain rate and discharge voltage established by simulation.

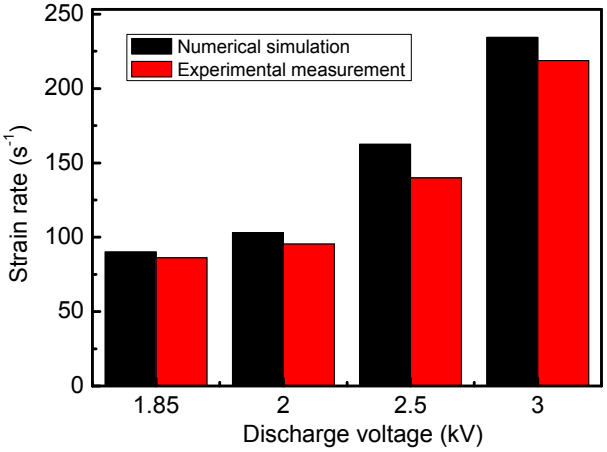


***Figure 9**: Comparison of analytically predicted and experimentally determined strain rate (768μF)*

Experiments of uniaxial tensile were then performed on the designed instrument at various strain rates to investigate the deformation behaviour of AA5052 Al sheet. Fig. 10 shows the deformed samples at different discharge voltage for two selected values of capacitor. It was found that ductility of tensile specimen increases, as the test velocity increases. The results show that the developed instrument is capable of testing standardized sheet metal specimens at speed precisely within the range of electromagnetic forming. What's more, their deformation can be directly compared to quasi-static results.

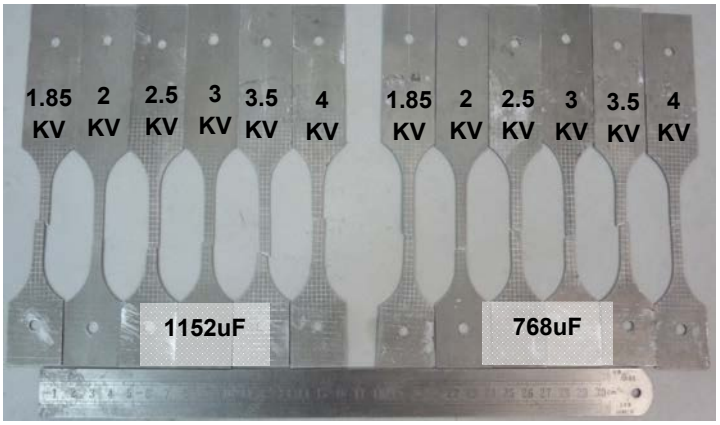


***Figure 10**: Deformed samples of 5052 Al after EMF with different discharge voltage for two selected value of capacitor*

## Conclusion

An impulse tension loading technique is presented, which is based on the use of pulsed-magnetic-driven tension loading. The developed setup can provide reproducible and adjustable loading rate ($80s^{-1}$~$3267s^{-1}$) via the discharge voltage and capacitance. The relation between discharge voltage and strain rate obtained from finite element calculations can be used for the process design. It could be a valuable technique for an investigation of material dynamic response. Also, it is worth to note that more technical details still need to be solved, such as how to measure the force accurately in the designed device.

## Acknowledges

This work was supported by the National Basic Research Program of China (2011CB012805), which is gratefully acknowledged here.

## References

Han, J. B., & Tvergaard, V., 1995. Effect of inertia on the necking behaviour of ring specimens under rapid radial expansion. European journal of mechanics. A. Solids, 14(2), 287-307.

Hu, X., & Daehn, G. S., 1996. Effect of velocity on flow localization in tension. Acta Materialia, 44(3), 1021-1033.

Johnson G., Cook W., 1983. A constitutive model and data for metals subjected to large strains, high strain rates and high temperatures, In: Proceedings of 7th International Conference on Ballistics, pp 541–547.

Psyk, V., Risch, D., Kinsey, B.L., Tekkaya, A.E., Kleiner, M., 2011. Electromagnetic forming – A review. Journal of Materials Processing Technology 211 (5), pp. 787-829.

Regazzoni, G., Kocks, U. F., & Follansbee, P., 1987. Dislocation kinetics at high strain rates. Acta metallurgica, 35(12), 2865-2875.

Seth, M., & Daehn, G. S., 2005. Effect of aspect ratio on high velocity formability of aluminum alloy. Trends in Materials and Manufacturing Technologies for Transportation Industries.

# Development of an Interrupted Pulse Expanding Ring Test


## J. Imbert*, M. Worswick

Department of Mechanical and Mechatronics Engineering, University of Waterloo, Waterloo, Ontario, Canada
*Corresponding author. Email: jmsimber@uwaterloo.ca Tel.: +001 519 888 4567 ext.



## Abstract

*An interrupted pulse electromagnetic (EM) expanding ring test is being developed at the University of Waterloo to study the high rate behaviour of sheet metals. In a classic EM expanding ring test, a ring is expanded radially using the forces induced on the ring by a high frequency high intensity current flowing in a nearby coil. If the driving force and the acceleration of the ring are known, then the stress-strain history of the ring can be determined. Coil currents are typically generated by large capacitor banks that produce a current discharge in the shape of a damped sinusoid. To properly determine the stress of the ring, the forces induced on the ring by the current pulse must be known, which is difficult to do in practice. The approach taken in this work is to interrupt the current by means of an exploding wire switch to eliminate the Lorentz forces and achieve a free flight condition, where the stress can be determined using only the measured velocity and density of the ring. The velocity of the rings was measured using a photon Doppler velocimeter (PDV). With this technique significant periods of free-flight were obtained, with the corresponding stress-strain data. Results for 1.5 mm sheet of AA 5182-O are presented.*



## Keywords

High rate testing, Expanding ring test, Interrupted pulse


## 1 Introduction

The need to reduce vehicle weight has resulted in considerable interest in the application of aluminum alloys and advanced high strength steels in automotive mass production. Unfortunately, these materials exhibit only moderate formability when compared to

traditional low carbon steel alloys. Several researchers have shown that the formability of some of these alloys can be increased using high speed forming techniques (Balanethiram and Daehn, 1994, Imbert et al., 2005 and Imbert and Worswick, 2012). The reasons behind the increased formability are not yet clearly understood. This is in part due to lack of understanding of the material properties at the strain rates that can be encountered during these process, which have been predicted to be in excess of 10,000 s-1, (Imbert et al., 2005, Imbert and Worswick, 2012). This leads to significant limitations on the ability to model these processes. The expanding ring technique is one of a few with potential to generate the stress-strain data at the high rates needed to produce the accurate material models required.

An ideal expanding ring test generates uniaxial tensile stresses and high strain rates within a sample ring, by causing it to expand radially at high speeds (**Fig. 1**). If the ring acceleration is known, the deformation is only radial, and the driving force is known the then stress-strain behaviour is relatively easy to determine.

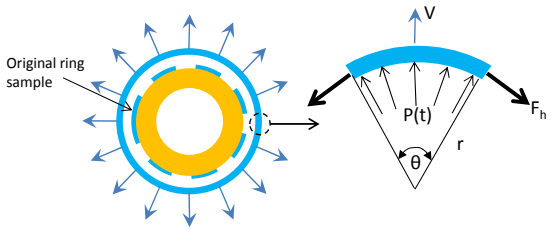


***Figure 1**: Basic principles of the expanding ring test*

The stress, strain and strain rates for an expanding ring are given by (Hoggatt and Recht, 1969, Imbert et al. 2015):

$$\sigma = -\frac{(\rho\theta r\ddot{r}+F_{p(t)})}{A\theta} \quad (1)$$

$$\varepsilon = \frac{\Delta r}{r} \quad (2)$$

$$\dot{\varepsilon} = \frac{\varepsilon}{\Delta t} = \frac{\dot{r}}{r} \quad (3)$$

Where σ=stress, $\varepsilon$= strain,$\dot{\varepsilon}$=strain rate ρ=density, $r = radius$, $\ddot{r}$ = radial acceleration and $F_{P(t)}$ = force generated by the driving pressure P(t). In EM expansion tests, $F_{P(t)}$ are the induced Lorentz forces. If there is no driving force, i.e. free-flight, **Eq. 1** becomes;

$$\sigma = \rho r\ddot{r} \quad (4)$$

The test requires accurate radial acceleration measurements, which are difficult since radial velocities can exceed 100 m/s and test durations are in the order of 50 µs. The advent of the Photon Doppler Velocimeter (PDV) (Strand et al. 2006, Landen et al. 2009) has made these measurements significantly easier to obtain.

Ring expansion tests have been in use since the 1960's (Johnson, 1962, Hoggatt and Recht, 1969), but have never been widely implemented. Currently, the two preferred ways of performing the test are the EM expansion (Gourdin,1989 and Gourdin et al., 1989) and the exploding wire techniques (Rajendran and Fyfe, 1982). In EM expansion, the ring is accelerated by the forces induced on it by a current flowing through a nearby spiral coil. It

is effective for high conductivity, relatively low strength materials. To determine the stress-strain behaviour, the induced forces are needed, which can be very difficult to determine.

In the exploding wire test, the ring is expanded by an elastomer (the "driver") that is itself expanded by vaporizing a wire located in its centre using a high frequency high current pulse (Rajendran and Fyfe, 1982, Johnson et al., 2010). The test eliminates the effects of conductivity, since it does not rely on induced forces. However, the driving force produced by the driver is difficult to determine, as is the exact interaction between the driver and the specimen.

Sheet metal poses challenges to the expanding ring technique, due to the anisotropy of the material and the difficulty of obtaining specimens that accurately represent the properties of the parent sheet metal. To the authors' knowledge, there is not a complete understanding of how to obtain accurate constitutive data from sheet metal using the expanding ring test. This work is part of an effort to develop such a test for AA 5182 and DP 600 sheet metal. Both the EM and exploding wire techniques were studied and tested and it was determined that an interrupted current EM ring expansion test had the greatest potential for being developed into a reliable test (Imbert et al., 2015). By interrupting the current pulse, the ring is allowed to achieve free-flight, thus eliminating the need to determine the induced forces, significantly reducing the uncertainty of the stress-strain behaviour obtained. The following sections describe the test developed, the numerical analysis used to gain insight into the tests and the experimental and numerical results.

# 2 Experimental Methods

## 2.1 Apparatus

A schematic view of the expanding ring apparatus is shown in **Fig. 4**. It consists of a capacitor bank called the magnetic pulse generator (MPG), a coil, Rogowski coils to measure coil and ring currents and a PDV to measure the sample velocity. An aluminum wire is placed in the circuit to act as an exploding switch.

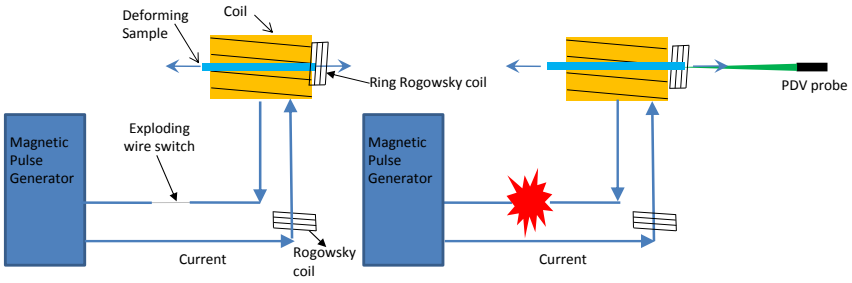


***Figure 4:*** *Schematic of the experimental apparatus*

### 2.1.1 Magnetic Pulse Generator

A Pulsar MPW 20 Research Edition MPG, with a nominal maximum energy capacity of 20 kJ and a maximum charging voltage of 9,000 volts was used. The machine capacitance is

539.7 µF, inductance is 24.35 nH, and resistance is 2.98 mΩ. The nominal shorted discharge frequency was 24.51 kHz. For the present work the MPG was charged to 4.0 kV, which results in a stored energy of 4.3 kJ.

### 2.1.2 Pulse interruption

Interrupting the current pulses used for expanding ring tests, which have frequencies above 10 kHz and peaks currents in the order of 100 kA, is very difficult. Mechanical switches are not capable of handling these conditions. Solid state devices could potentially be used, but the authors were unable to source a device that met the requirements. Gourdin (1989) used a shaped explosive charge switch to interrupt the current by creating an alternate current path. Switches based on exploding aluminum foil were developed by Bealing and Carpenter (1972) to interrupt and shape pulses.

For this research, aluminum wires of 0.8 mm diameter were chosen to interrupt the pulse. The wires ignited once a certain current value was reached, thus opening the circuit. **Fig. 5** shows a current pulse from a discharge using a closed copper circuit, along with five interrupted pulses achieved with the exploding wire switch. The interrupted pulses deliver less energy than the full pulses, due to some energy going to ground as the circuit is opened and, to a lesser extent, the energy consumed by the wire explosion.

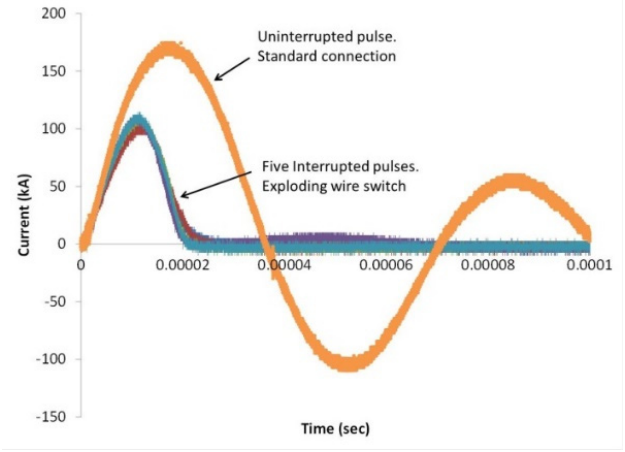


***Figure 5:*** *Comparison of uninterrupted and five interrupted current pulses*

### 2.1.3 Measurements of the Sample Velocity

The sample velocity was measured using an Ohio Manufacturing Institute PDV, which uses a 1550 nm in wave length fibre optic laser. The basic principles of the PDV are given by Strand et al. (2006). The PDV outputs a voltage versus time signal. The frequency spectrum of the signal was calculated using Matlab©. The velocity was calculated using the method outlined in by Strand et al. (2006,) as implemented by Imbert et al. (2015).

### 2.1.4 Coil

A single turn copper coil was designed for this work (**Fig. 7**). The goal of the design was to reduce the coil impedance, maximize strength and minimize out-of-plane sample

deformation. Simulations showed that the rings expanded with the single turn coil had less out of plane deformation when compared to rings expanded with a 3-turn spiral coil (**Fig. 8**).Two coil designs were tested, one with internal grooves (**Fig.7-a**) and one with no grooves (**Fig. 7-b**). The grooved design was morere efficient, but was structurally weaker, so the design with no grooves was chosen. Coils with 38 mm and 25.4 mm outer diameter ("d" in **Fig. 7**) were built to obtain different strain rate histories, as per **Eq. 3**.

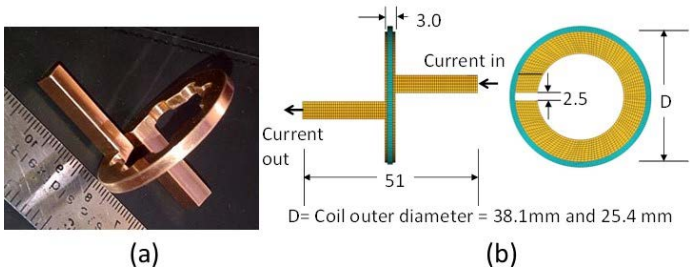


***Figure 7:*** *Coil design developed for present work. All dimensions in mm.*


***Figure 8:*** *Predicted shapes for rings formed with the single turn and a 3-turn spiral coil*

## 2.2 Material and Sample Geometry

The material tested in this work was 1.5 mm sheet of AA 5182-O, which has a nominal yield strength of 130 MPa. Detailed constitutive characterization of this material at strain rates up to 1,000 $s^{-1}$ is reported by Rahmaan et al. (2014). Samples were cut from the stock material and made with a square cross section, of side lengths equal to the sheet thickness.

# 3 Numerical Modelling

Numerical models were used to gain insight into the general behaviour of the rings during the tests. The 38 mm ID ring tests were modelled. An EM capable version of LS-Dyna (L'Eplattenier et al. 2009) was used. The mesh used is shown in Fig. 7-b. Both the coil and ring were modelled with brick elements. The ring was modelled with 5 elements through both thickness and width, which resulted in 6,250 elements. The coil was modelled with 10 elements through thickness and width, for a total of 16,000 elements. An experimentally measured current profile was used as the current input. The rate sensitive modified Voce material model for AA 5182-O developed by Rahmaan et al. (2015) was used. The model provided good predictions of the coil and ring currents (**Fig. 9)** and the final ring geometry (**Fig. 10**).

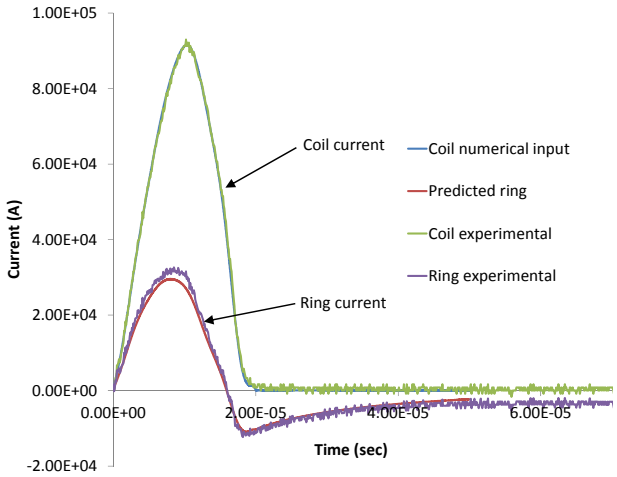


***Figure 9:*** *Measured and predicted coil and ring currents*

The Johnson-Cook (J-C) (Johnson and Cook, 1985) material model was used to study the effects of thermal softening on the ring. Although limited, the J-C model has been shown capable of capturing the general flow stress behaviour of aluminum alloys at rates up to 1,500 $s^{-1}$ (Smerd et al. 2005).The J-C implementation used for this work requires an equation of state (EOS). To the authors' knowledge there is no available J-C and EOS parameter set available for AA 5182-O in the literature. To overcome this, the J-C parameters from Meyer (1996) and EOS parameters from Steinberg (1996) for AA 2024-T351 were used. Both adiabatic and Joule heating were taken into consideration. The authors recognize the limitations of this approach; however, it was deemed acceptable since the goal was to determine if the test could be affected by thermal softening and not to accurately model the AA 5182 behaviour.

# 4 Results and Discussion

Rings formed using the 38 mm and 25.4 mmm coils are shown in **Fig. 10**. The tested samples present a distinctive shape that the numerical simulations indicate is mainly the result of the 2.5 mm gap discussed above (Fig. 10-c).

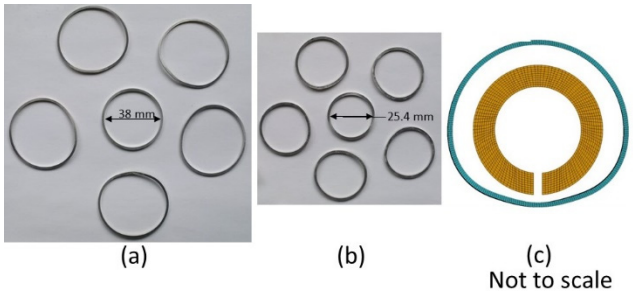


***Figure 10:*** *Rings expanded with (a) the 38 mm and (b) the 25.4 mm diameter coils surrounding an un-deformed ring. The final predicted shape of an expanded ring (c)*

Experimental strain rate and stress data for five samples each tested with the 38 mm and 25.4 mm coil are shown in **Fig. 11**. The stresses are calculated using **Eq. 4**. The point where the current pulse stops and free-flight begins is indicated with a line and shows that a significant period of free-flight was achieved. No stress data is presented prior to free flight, since **Eq. 4** is not valid for that part of the test. There is relatively good repeatability, especially given the nature of this experiment. Data from Smerd et al. (2005) for AA 5182-O at 1,500 $s^{-1}$ at 23 C° and 300 C° is presented for comparison.

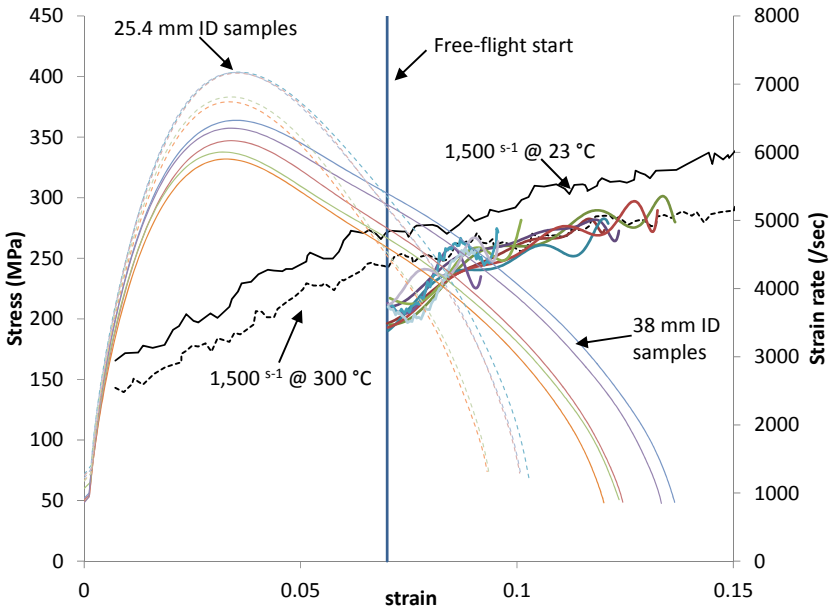


***Figure 11:*** *Strain rate and stress versus true strain for the five 38 mm ID and five 25.4 ID sample. Data for 1,500 $s^{-1}$ from Smerd et al. (2005)*

The highest strains recorded were approximately 7,000 $s^{-1}$ and were experienced by the 25.4 mm ID rings. The highest strain rates for the 38 mm ID rings was approximately 6,000 $s^{-1}$. The highest strain rates were achieved while there was still current in the circuit. The strain rates decrease to approximately 5,000 $s^{-1}$ at the start of free-flight, and to approximately 1,000 $s^{-1}$ at the end of the test. The observed strain rate decay poses some challenges to data fitting for constitutive modelling.

All the experimental stresses obtained are close to each other and closely follow the high temperature data published by Smerd et al. (2005). This suggests the possibility that thermal softening may be affecting the stress response. Since adiabatic heating is not expected to raise the temperature of the samples to a degree where softening will occur, the possibility that Joule heating is affecting the sample was explored.

## 4.1 Joule Heating and Thermal Softening

Joule heating refers to the heat generated on a body by a current flowing through it. Gourdin (1989) recognized that Joule heating could result in thermal softening and designed an interrupted pulse experiment to minimize it. Using ring current measurements and an

analytical analysis Gourdin (1989) concluded that the combined Joule and adiabatic heating effects were minimal. Gourdin's analysis and measurements assumed uniform current distribution through the sample. Henchi et al. (2008) presented numerical simulations that showed that the current distributions within the samples were not uniform. **Fig. 11** shows simulations of the current test, which predict that the current distribution is not uniform.

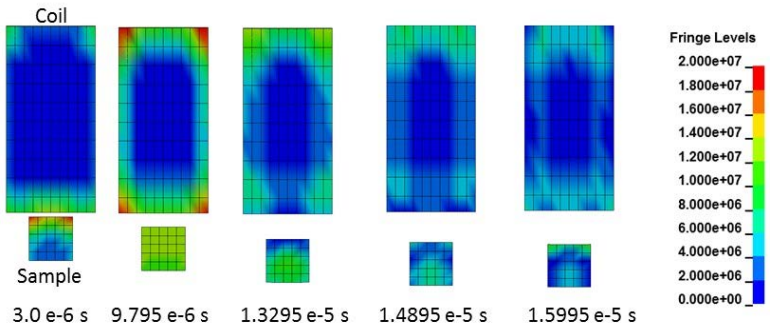


***Figure 11**: Current density distribution of the coil and sample. Contours are of μJ/mm³*

The results shown in Fig. 12 suggest that thermal effects soften the material and make the stress distribution along the ring non-uniform. Although the results are preliminary, if this were the case, it would mean that thermal softening has a significant effect and that the basic assumption of a tensile test, i.e. uniform stress distribution, is violated during an EM expanding ring test (see inset in **Fig. 12**). This would not disqualify the EM expanding ring test from consideration as means to obtain constitutive data, but it means that a methodology combining experimental, finite element and optimization techniques as proposed by Henchi et al. (2008) and Johnson et al. (2010) will likely be needed to extract accurate data from these types of tests. Work is ongoing to confirm these results.

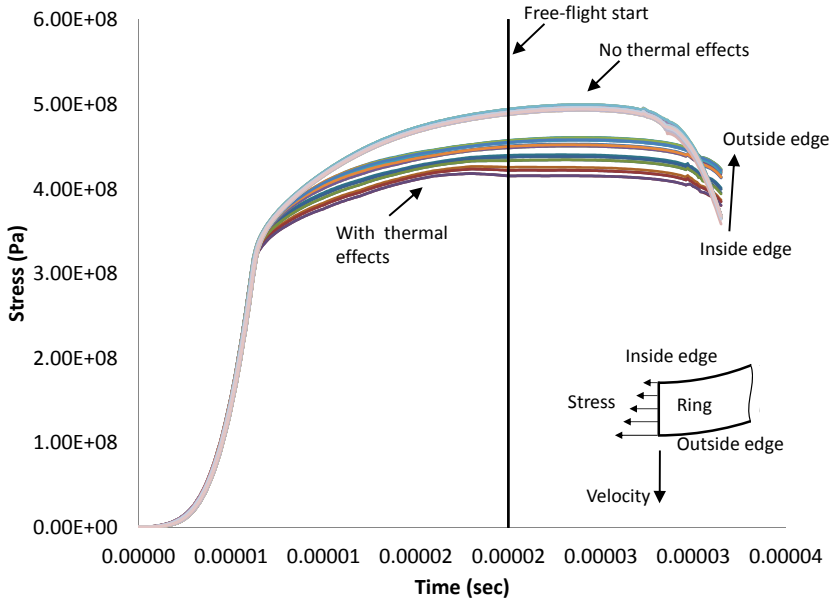


***Figure 12:** Predicted V-M stresses vs. time along the ring cross section from simulations with and without thermal effects. The inset shows an illustration of the stress state.*

# 5 Conclusions

The following conclusions were reached:

1. The interrupted ring expansion test results in free-flight of the ring, from which stress-strain data can be determined without the need to take into account the driving force.
2. The highest strains occur while there is still induced forces on the ring. Thus, the driving force must be taken into account to determine the stress-strain response at the highest strain rates.
3. The strain rates during the test are not constant, which pose a challenge for constitutive fitting.
4. The free flight stress-strain data suggest that thermal softening may be occurring.
5. Simulations suggest that thermal softening is taking place and that the rings present non-uniform stress distributions through the cross section. Work is ongoing to implement more accurate material models, like the one proposed by Bardelcik et al. (2012), which incorporates an exponential hardening term.
6. Given conclusions 2 and 4 finite element and optimization methods will likely be required for accurate data extraction from these types of tests.

# Acknowledgments

The authors greatly appreciate the support of APC, NSERC, CRCS, ORF, Ford Research & Advanced Eng., Amino Corp., Alcoa and ArcelorMittal.

# References

Balanethiram, V.S. and Daehn, G.S., 1994, Hyperplasticity: Enhanced formability at high rates, Scripta Metal. Mater. 30,595-600.

Bardelcik, A., Worswick, M., Winkler, S., Wells, M, 2012. A strain rate sensitive constitutive model for quenched boron steel with tailored properties, I. J. Impact Eng., v.50, 49-62.

Bealing, R, Carpenter, P.G., 1972, Exploding foil devices for shaping megamp current pulses, J. Phys. E., 5, 889-892.

Daehn, G., Zhang, Y., Golowin, , S., Banik, K., Vivek, A., Johnson, J., Taber, G., Fenton, G., Henchi, I., L'Eplattenier, P., 2008, Coupling experiment and simulation in electromagnetic forming using photon Doppler velocimetry 3rd Int. Conf. on High Speed Forming, Dortmund, Germany.

Gourdin, W.H., Weinland, S.L, Boiling, R.M., 1989, Development of the electromagnetically launched expanding ring as a high-strain-rate test technique. Rev. Sci. Instrum., v.60, n.3, pp. 427-432.

Gourdin, W.H., 1989, Analysis and assessment of electromagnetic ring expansion as a high-strain-rate test, J. App. Phys., v. 65, 2, 411-422.

Henchi, P. L'eplattenier, G. Daehn, Y. Zhang, A. Vivek, N. Stander, 2008, Material constitutive parameter identification using an electromagnetic ring expansion experiment coupled with LS-DYNA and LS-OPT, 10th Int. LS-DYNA Users Conf., Dearborn, MI, USA, pp. 14-1-14-10.

Hoggatt, C., Recht,R., 1969, . Stress-strain data obtained at high rates using and expanding ring. Exp. Mechs., 441-448.

Imbert, J.M., Worswick, M.J., Winkler, S.L., Golovashchenko, S., Dmitriev, V., 2005, Analysis of the increased formability of aluminum alloy sheet formed using electromagnetic forming, SAE Trans. J. Mater. Manuf. SAE paper # 2005-01-0082.

Imbert, J., Worswick, M.J., 2012, Reduction of a pre-formed radius in aluminum sheet using electromagnetic and conventional forming, J. Mat. Proc. Tech., 1963-1972**.**

Imbert, J., Worswick, M.J., Rahmaan, T., 2015, Interrupted Pulse Electromagnetic Expanding Ring Test for Sheet Metal, proceedings DYMAT 2015, Lugano.

Johnson, G.R., Cook, W.H., 1985, Fracture characteristics of three metals subjected to various strains, strain rates, temperatures and pressures, Eng. Frac. Mech., V. 21, I.1, 31- 48.

Johnson, P.C., Stein, B.A., Davis, R.S., 1962, Basic parameters of metal behaviour under high strain rate. U.S. Army Mat. Res. A. Rep. No. WAL TR 111.2/20-6.

Johnson, J., Taber, G., Daehn, G., 2010, Constitutive relation development through the FIRE test,4th Int. Conf. on High Speed Forming. Colombus, OH.

Landen, D., Wetz, D., Satapathy, S., Levinson, S., 2009, Electromagnetically driven expanding ring with preheating, IEEE Trans. Mag., v. 45 n. 1, pp. 598-603.

L'Eplattenier, P., Cook, G., Ashcraft, C., Burger, M., Imbert, J., Worswick, M, 2009, Introduction of an electromagnetic module in LS-DYNA, for coupled Mechanical-Thermal-Electromagnetic simulations, Steel Res. Int., v.80, n.5.

Meyers, M. A., 1994, *Dynamic behavior of materials*. John Wiley & Sons.

Rahmaan, T., Bardelcik, A., Imbert, J., Butcher, C., Worswick, M.J., 2016, Effect of strain rate on flow stress and anisotropy of DP600, TRIP780, and AA5182-O sheet metal alloys. I. J. Impact Eng., V. 88, 72-90,

Rajendran, I. Fyfe, 1982, Inertia Effects on the Ductile Failure of Thin Rings, J. App. Mechs., v. 49, pp. 31-36.

Strand, O., Goosman, D., Martinez, C., Whitworth, T, Kuhlow, W., 2006, Compact system for high-speed velocimetry using heterodyne techniques, Rev. Sci. Instrs., **77**.

Smerd, R.,Winkler, S., Salisbury,C., Worswick,M., Lloyd,D., Finn,M.,2005, High strain rate tensile testing of automotive aluminum alloy sheet, I. J. Impact Eng., v.32, 541-560.

Steinberg, D.J., 1996, Equations of State and Strength Properties of Selected Materials, Lawrence Livermore National Laboratory, Originally issued Feb, 1991.

Taber, G., Daehn, G., Vivek, A., 2008, Photonic Doppler Velocimetry Applied to High Strain Rate Electromagnetic Ring Expansion, Ohio State University dissertation.

Warnes, R.H,, Karpp, R.R., Follansbee, P.S., 1985, The freely expanding ring test - a test to determine material strength at high strain rates, J. Phys., C5, n.8, v. 46, 46-8.

# Development of Vibration During the Electromagnetic Ring Expansion Test

**K. Yang[1*], G. Taber[2], T. Sapanathan[1], A. Vivek[2], G. S. Daehn[2], R. N. Raoelison[1, 3], N. Buiron[1], M. Rachik[1]**

[1] Sorbonne universités, Université de Technologie de Compiègne, Laboratoire Roberval, CNRS UMR 7337, Centre de Recherche Royallieu, CS 60319, 60203 Compiègne cedex, France
[2] Department of Materials Science and Engineering, The Ohio State University, 2041 College Road, Columbus, OH 43210, USA
[3] Université de Bourgogne Franche Comté, IRTES-LERMPS, Université de Technologie de Belfort Montbéliard, 90100 Belfort, France
[*]Corresponding author. Email: kang.yang@utc.fr

## Abstract

*Magnetic pulse forming (MPF) techniques work on the principle of Lorentz force induced by eddy current which can cause plastic deformation in a metal workpiece. Lorentz force depends on parameters such as frequency and amplitude of input current, electromagnetic properties of materials and distance between the work piece and coil. The development of vibration as a consequence of elastic strain recovery in a ring expansion process using a MPF technique has been identified and presented in this paper. Coupled mechanical-electromagnetic 3D simulations were carried out to investigate the effect of various magnetic pulse currents in the development of reversal of motion during the MPF process using LS-DYNA package. Ring expansion using a multi-turn helix coil with an applied pulse current, with the rings made of aluminum alloy AA6061 –T6 is investigated for the effect of vibration during the process. The numerical results show good agreement with the experimental work for various currents. The underlying principle of vibration and formability has respectively been studied using force analysis and stress analysis. The results also show that the 5.6kJ energy already increased the formability by ~66 percent in comparison with the quasi-static formability value from the literature.*

## Keywords

Magnetic pulse forming, Elastic strain recovery, Ring expansion

# 1 Introduction

Electromagnetic Pulse forming (EMF) processes can provide competitive advantage with their counterparts in conventional forming processes such as high formability, reduced wrinkling and high productivity. These advantages may benefit the forming industry making the process an alternative to conventional forming techniques and other high speed forming processes. It has been reported that the work piece can experience a very high strain rate of $10^2 – 10^4$ $s^{-1}$ during EMF processes (Johnson et al., 2009) while that may reach up to $10^6 – 10^7$ $s^{-1}$ at the interface during a magnetic pulse welding (MPW) process (Zhang et al., 2010). This high strain rate could play a major role in magnetic pulse processes, which have been successfully utilized in metal forming as well as metal joining (MPW), where the welding occurs with a high impact velocity (Strizhakov, 1991, Göbel et al., 2012, Raoelison et al., 2012, Raoelison et al., 2013, Raoelison et al., 2014).

There was a lack of attention given for the elastic spring back effect in EMF processes, that may be because it has been considered to be significantly reduced in some high velocity forming processes (Baron and Henn, 1964, Padmanabhan, 1997, Zhang, 2003). However, vibration behaviour is observed in the ring expansion process and similar rebound phenomenon and development of negative pressure have been reported in other types of magnetic pulse processes, including sheet forming, tube compression or expansion and electromagnetic welding (Körner et al., 2012, Liu et al., 2014) .

The reversal of direction of radial motion in an electromagnetic ring expansion process is investigated here. Coupled mechanical-electromagnetic 3D simulations were carried out to investigate the effect of various magnetic pulse currents in the development of reversal of motion during the MPF process using LS-DYNA® package with the solver version of R8. The simulation involves a ring expansion using a multi-turn helix coil with an applied pulse current. The numerical results corroborate the experimental finding of vibration and provide insight understanding of the force components that govern the vibration phenomenon. These investigations can be used to optimize the process parameters to control the final dimensions of the expanded ring.

# 2 Experimental and Simulation Methods

## 2.1 Experimental Method and Measurements

Electromagnetic ring expansion has long been promoted as a high strain rate materials' constituent properties test. Gourdin in particular was a pioneer of the technique and made a significant analysis of its application (Gourdin et al., 1989, Gourdin, 1989). The major components of the apparatus used in these experiments are a pulse power supply, a photonic Doppler velocimeter (PDV), and a helical expansion coil. A schematic representation of the apparatus is shown in **Fig. 1**.

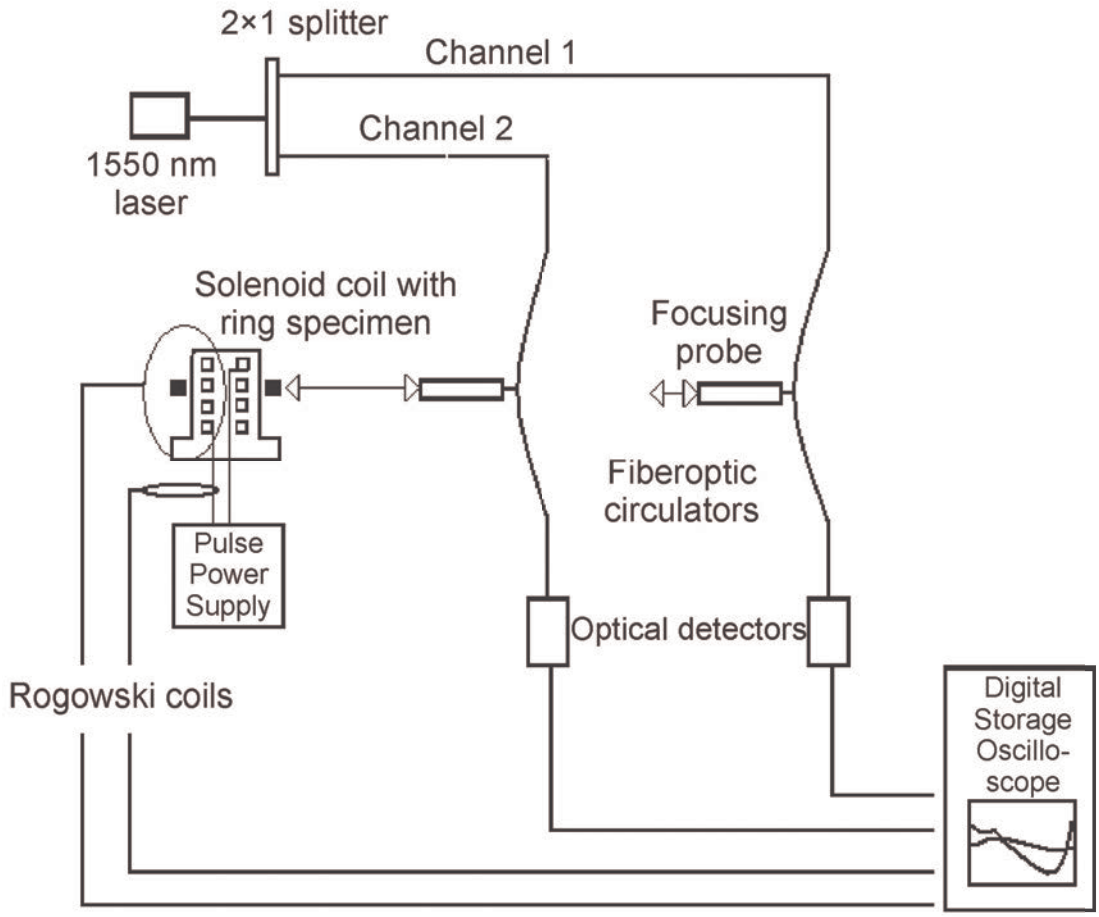


***Figure 1**: Schematic illustration of the photonic Doppler velocimetry (PDV)*

### 2.1.1 Apparatus

The pulse power supply is a commercial capacitor bank made by Maxwell Magneform. It has a maximum capacity of 16 kJ at a maximum charging voltage of 8.66 kV. Only a fraction of the maximum energy was used in these experiments. This unit has eight capacitors, each triggered by an ignitron switch. This supply has a total capacitance of 426 μF and internal inductance of 100 nH and a primary circuit resistance of about 10 mΩ. This gives a quarter cycle rise time into a shorted circuit of about 12 μs. All eight capacitors were used in the circuit in these experiments. The experimental frequency was ~10 kHz due to the influence of the expansion coil in the circuit.

The PDV system constructed at Ohio State University is a significant enabling diagnostic for this type of experimentation (Johnson et al., 2009). This system is a fiber laser based interferometer in which the amount of Doppler shift in light reflected from a moving target is acquired over the time frame of the experiment. Subsequent analysis by Fourier transform yields a velocity over time profile. The technique is relatively simple to deploy and is an agile and robust instrument. The first system was integrated at Lawrence Livermore National Labs in the late 20th century and the method has since become widely

utilized in the shock physics community. As strain rate can be a significant factor in constituent material properties, quantitative data regarding velocity is quite useful.

An archive of presentations from user group meetings is available from (Photonic-Doppler-velocimetry-users-group-meetings-archive, accessed 08/01/2015) and is a comprehensive source of background information. **Fig. 2** is a schematic illustration of an implemented design concept. The helical expansion coil consists of 5 turns of Cu-Zr-Cr 18150 alloy machined from solid round stock. Leads of the same material were brazed to the helix. The coil with leads is potted with epoxy in a fiberglass tube. **Fig. 3** is a 3D illustration of the design.

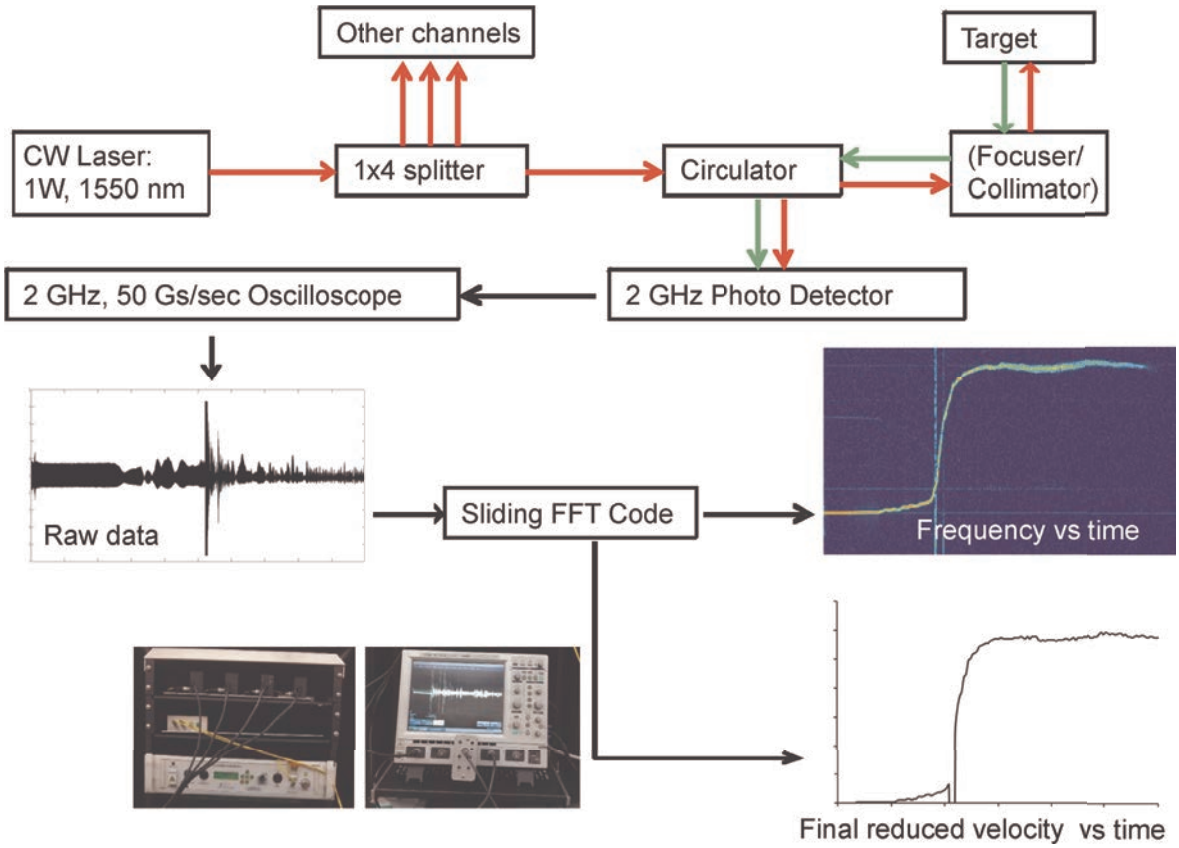


***Figure 2**: Schematic illustration showing an implemented design concept of a PDV system and signal processing unit*

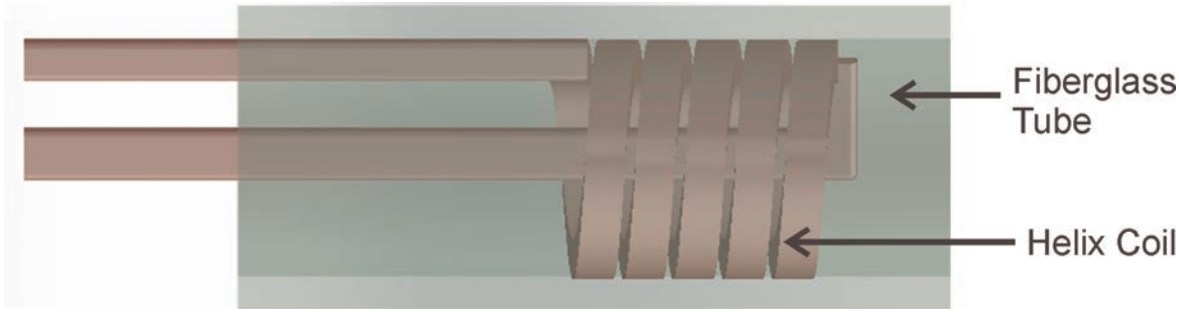


***Figure 3**: An illustration highlighting the features of the helix coil inside a fiberglass tube*

### 2.1.2 Procedure

Ring specimens were machined from aluminum alloy AA6061-T6 tubing. Initial dimensions prior to expansion were 50.8 mm outside diameter, 6.35 mm height, and 1.65 mm wall thickness. Rings were positioned on the expansion coil such that longitudinal displacement due to resultant electromagnetic forces was nil. The PDV probe was focused on the center of the ring height and normal to the radius. Upon discharge of the power supply, the output voltage rise was used to trigger the data acquisition oscilloscope. Data from a 1000:1 voltage probe and a 50 kA per Volt Rogowski integrating current transducer were acquired in addition to the raw PDV signal at a rate of 5 giga-samples per second. Rings were expanded at energies of 3.2 kJ, 4.0 kJ, 4.8 kJ, and 5.6 kJ respectively recalled by test 1 - 4.

## 2.2 Simulation Method and Specifications

A coupled mechanical-electromagnetic numerical simulation is carried out to investigate the development of vibration during a ring expansion test. The magnetic field calculation in LS-DYNA® is governed by Maxwell's equations and Biot–Savart's law. A combination of finite elements with boundary elements (BEM-FEM) is used in the electromagnetic solver of LS-DYNA® (Çaldichoury and L'Eplattenier, 2012). The calculated Lorentz force used in dynamic mechanical computation. The simulations were carried out for experimentally used input currents for four cases as shown in **Fig. 4**.

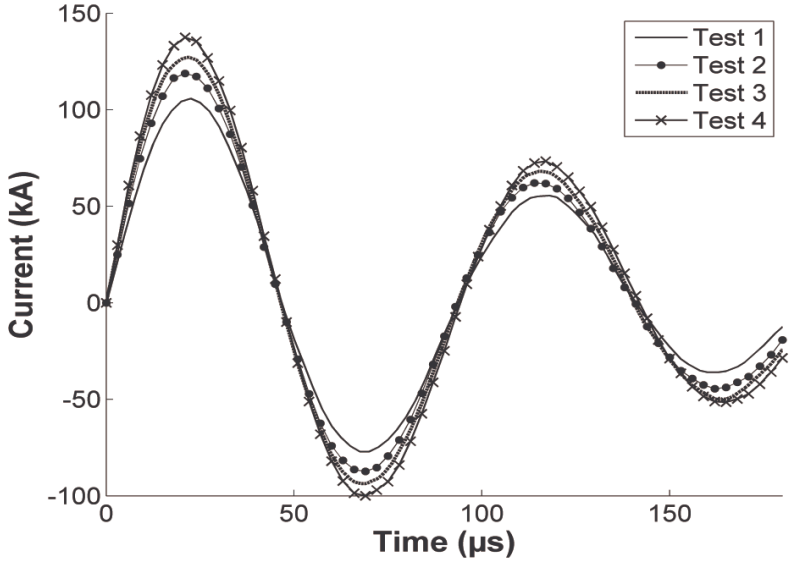


***Figure 4**: Input current used for various cases of simulations*

A meshed numerical model used in this study is also shown in **Fig. 5**, which consists of 8 nodes brick element for both coil and expansion ring. The element size of 0.6 mm along the thickness of the ring was used to sufficiently capture the electromagnetic skin depth effect during the simulation.

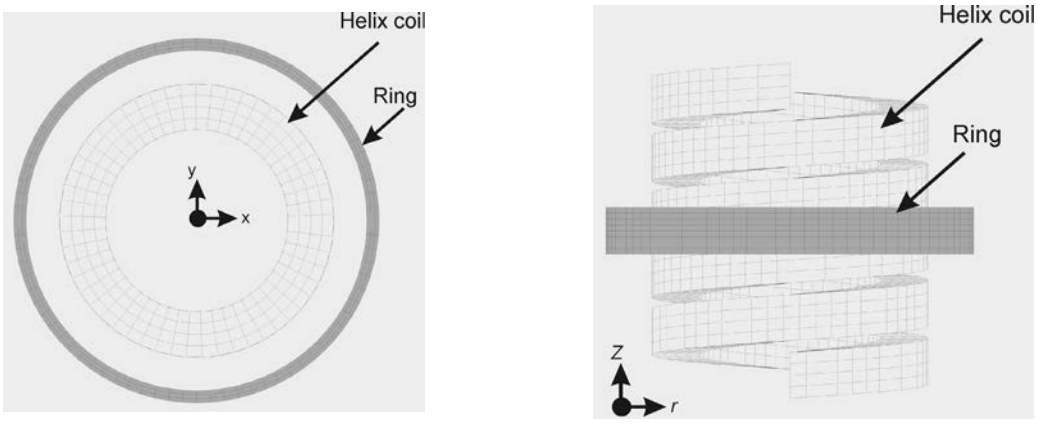


(a) (b)

***Figure 5**: Meshed model used in LS-DYNA simulations (a) top view and (b) side view*

### 2.2.1 Material Model Used in the Simulation

An appropriate constitutive model and material properties are required in the simulation to obtain an accurate test result. Modified Johnson-Cook model was used here to prescribe the material behaviour with integrated high strain rate components as shown in **Eq. 1**.

$$\bar{\sigma} = (A + B\bar{\varepsilon}^{n})\left(1 + \frac{\dot{\bar{\varepsilon}}}{\dot{\bar{\varepsilon}}_0}\right)^{C}(1 - T^{*m}) \quad (1)$$

where, $\bar{\sigma}$ and $\bar{\varepsilon}$ are the von Mises equivalent stress and strain respectively, $\dot{\bar{\varepsilon}}$ is the strain rate. Here $\dot{\bar{\varepsilon}}_0$ is equal to 1/s and $T^*$ is a dimensionless temperature factor. $A$, $B$, $C$ and $n$ are constants, obtained from literature (Anderson Jr et al., 2006). Modified Johnson-Cook parameters (in Eq.1) of the ring material are respectively provided in **Table 1**. Mechanical, electromagnetic and thermal properties of both coil and ring are shown in **Table 2**.

| Johnson cook parameters | *A* (MPa) | *B* (MPa) | *C* | *n* | *m* |
|---|---|---|---|---|---|
| Numerical values for AA6061-T6 | 324 | 114 | 0.002 | 0.42 | 1 |

***Table 1**: Modified Johnson cook parameters used for the ring material, AA6061-T6*

| | Young's Modulus (GPa) | Electrical conductivity (S/m) | Thermal conductivity (W/m·K) | Specific heat Capacity (J/kg·K) | Melting temperature (K) |
|---|---|---|---|---|---|
| Ring (AA6061-T6) | 68.9 | $2.51\times10^{7}$ | 377 | 390 | 1356 |
| Coil (Copper Alloy) | Rigid | $4.64\times10^{7}$ | 323 | 880 | 1348 |

***Table 2**: Material properties of each component of the test*

# 3 Results and Discussion

## 3.1 Experimental and Simulated Velocities

The simulation results show good agreements with the experimental velocities for all the cases (**Fig. 6**) in terms of vibration. The maximum negative velocities of -19.8 m/s, -21.6 m/s, -15.4 m/s and -22.8 m/s are obtained respectively for tests 1, 2, 3 and 4 during the experiments while the simulation results show the maxima of -21.4 m/s, -21.5 m/s, -16.0 m/s and -23.3 m/s respectively. The results also show good agreement in the trend for the entire test, and indicate the elastic-plastic model well predicts the vibration phenomenon during the ring expansion test.

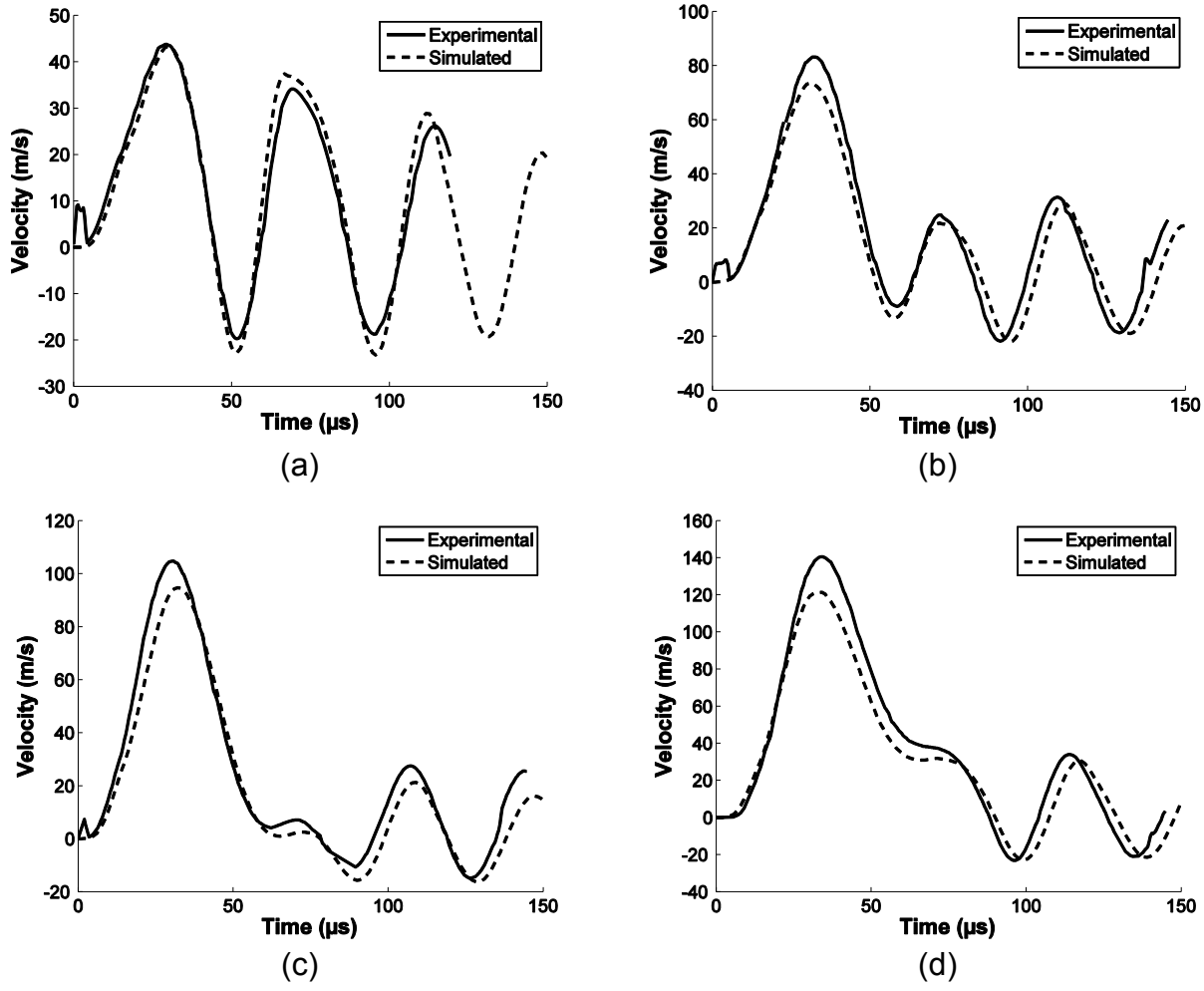


***Figure 6**: Comparison of experimental and simulation results of radial velocity in obtained during test cases of (a) Test 1 (b) Test 2 (c) Test 3 and (d) Test 4*

## 3.2 Analysis of Force Components and Stress During Ring Expansion and Vibration

To better understand the development of negative velocities and the cause of vibration during a ring expansion test, the force components are analysed. In this case, there is no external force on the ring and the model is considered as axisymmetric for the small height of the ring. Moreover, the thickness and height of ring are low enough to be neglected and it can be treated as a one-dimensional problem. The motion of the ring is governed by two forces: the Lorentz force ($F_{Lorentz}$) and inner tensile force (due to the flow stress) ($F_t$). **Fig. 7** shows these forces acting in a differential element. Test 4 is used to explain these forces, shown in **Fig. 8**.

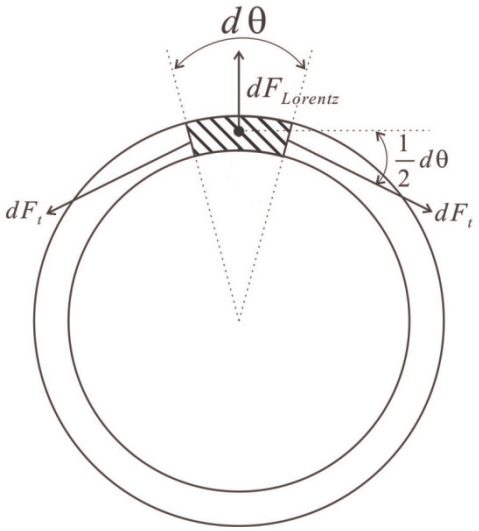


***Figure 7**: Illustration of the force components acting on a differential volume element*

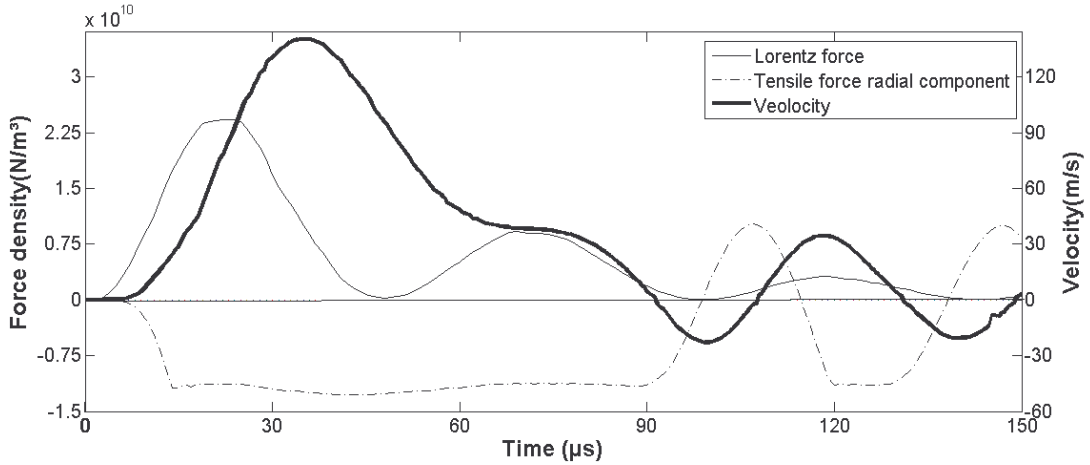


***Figure 8**: Forces components governing the vibration phenomenon during a ring expansion test obtained from simulation results and radial velocity obtained using PDV measurement for test 4*

At the beginning of the test (~ 0 – 40 μs), Lorentz force is large enough to drive the ring to expand and the velocity is continuously increased. After that for a period of ~ 40 – 91 μs (particularly including the second half cycle of the source current, Fig. 4), Lorentz force is lower than radial component of tensile force and ring decelerates to zero velocity. After that, because of the source current became low and the distance between the coil and ring became large, effect of Lorentz force is almost negligible and the velocity is rapidly decreased. Particularly at the end of the full current cycle (~ 95 μs in Fig. 4), tensile force changes its direction (elastic strain recovery), and the velocity accelerates within the negative region.

Negative velocity was firstly observed at 91 μs, the Lorentz force density never became larger than $5\times10^9$ N/m$^3$ afterwards. There were no significant external forces during the vibration which shows that the negative velocities in these ring tests were mainly caused by the elastic stain recovery due to the internal tensile force. Similar behaviours were also observed in those other three tests.

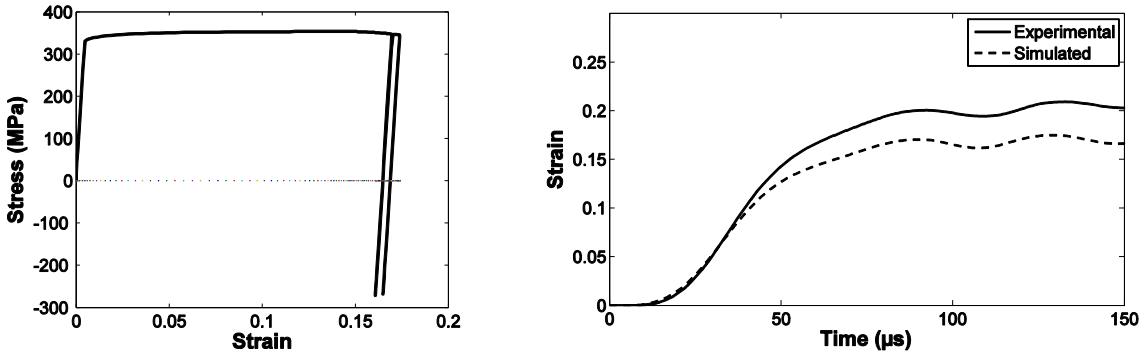


***Figure 9**: Effective equivalent stress against equivalent true strain from simulation in (a) and equivalent true strain with time in (b) obtained for test 4 (true strain calculated using the definition of ln(r/r$_o$), where r and r$_o$ respectively denote instantaneous radius and the initial radius of the ring)*

In these simulations, a simplified elastic-plastic model was used. The deformation involves both plastic and elastic components separately where the spring back effect is caused by the elastic deformation. Moreover, **Fig. 9a** also indicates that the first vibration also has a small additional plastic strain (~0.5%), because during the first vibration, when the velocity was negative the Lorentz force was almost zero while when the velocity turned to be positive the Lorentz force was up to $5\times10^9$ N/m$^3$ in the same direction, which means the magnetic field that provided the required energy to cause the small plastic strain. As a result, there are two ways to decrease the vibration either by increasing the time damping of current or making the direction of Lorentz force different with the direction of velocity.

**Fig. 9b** shows that the maximum strain accommodation during the test 4 (case with 5.6 kJ energy) was 20% in experiments which has ~15% different with the simulation results. This discrepancy is mainly depending on the material model used in the simulation, which requires a fine calibration to improve the accuracy. By using inverse analysis and a calibration with the experimental velocity data the simulations error can be eliminated.

However, the experimental results clearly indicate that the maximum strain is beyond 12%, that was obtained from literature for quasi-static tensile test of AA6061-T6 (Al6061-T6, accessed 08/01/2015). That is in a good agreement with other researchers where the formability of workpiece has been significantly improved during the high strain rate forming techniques.

# 4 Prediction of the Accurate Material Behaviour by Optimisation

Although experimental and numerical results show a good agreement in the tendency and the vibration patterns, there exist small discrepancies between numerical modeling and the experimental measurements. That is, the comparison shows an approximate deviation of 10% in the maximum velocity, in test 2-4. However, numerical simulation of the case 1 closely resembles the experimental observations. But, here one should consider the amount of plastic deformation in these cases, where the test 1 mostly involves elastic deformation and a small amount of plastic strain of ~4%.

The discrepancy could be due to high strain rate effect, while the aforementioned Johnson-Cook parameters (Table 1) may fail to capture the accurate behaviour of the material. This situation also highlights the definite requirement of the material calibration for respective strain rates. Therefore a preliminary calibration work was carried out with varying material parameters as listed in **Table 3** for the test 4.

| Johnson cook parameters | *A* (MPa) | *B* (MPa) | *C* | *n* | *m* |
|---|---|---|---|---|---|
| Material-model 1 | 324 | 114 | 0.002 | 0.42 | 1 |
| Material-model 2 | 275 | 250 | 0.002 | 0.42 | 1 |
| Material-model 3 | 200 | 400 | 0.002 | 0.42 | 1 |

***Table 3**: Modified Johnson cook parameters used for various comparison cases*

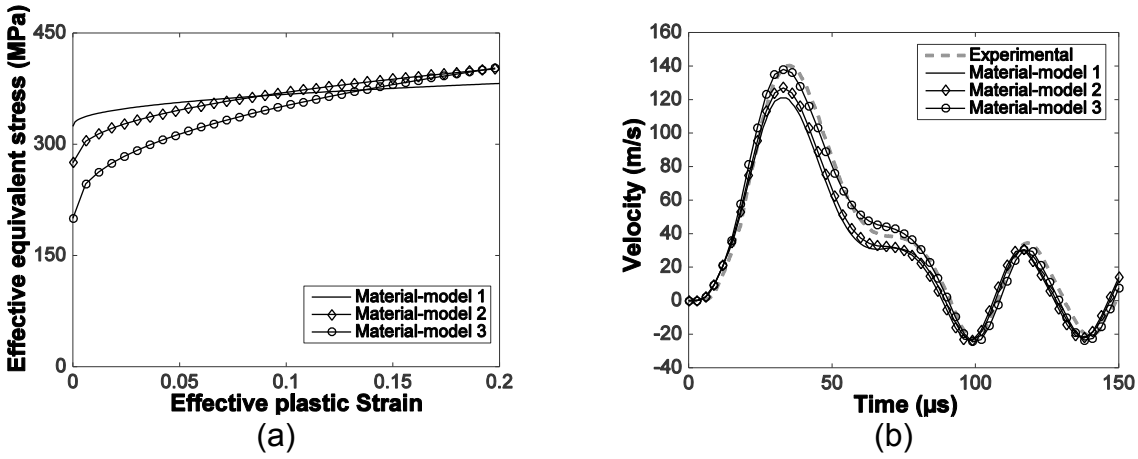


***Figure 10**: (a) Various material models investigated in the numerical simulation of test 4 and (b) comparison of the numerical velocity predictions for those various material-models and experimental velocity obtained using PDV measurement for test 4*

The plastic flow behaviours of the material-models according to the Table 3 used in the simulation are shown in **Fig. 10a**. The predicted velocities using various material-models and the experimental results for the test 4 are shown in **Fig. 10b.**

The results clearly indicate that the material-model 3 agrees well with the experimental simulation (Fig. 10b). However, in order to identify the appropriate material, an accurate optimisation process is required. After that, a cross check of optimization should be utilised for various test cases to identify the single optimum material model. Due to the multi-physics nature of the process, the optimisation computing requires a substantial amount of time to complete the process. Therefore, the proper identification work with optimisation is considered to be performed as a future work.

# 5 Conclusions

Development of vibration as a consequence of elastic strain recovery during an electromagnetic ring expansion test was investigated using experimental and 3D numerical methods. Four test cases were carried out to investigate the effect of various magnetic pulse currents and the underlying reasons for the development of vibration was investigated using various force components, magnitude of Lorentz force and the elastic spring back effect. It was found that the reversal of velocity during the test was caused by the radial component of the elastic tensile force during the ring expansion process. The vibration is a consequence of spring back effect, rather than a consequence of Lorentz force. The external force components are almost negligible at the onset of the reversal of motion. The development of negative velocity and the spring back effects caused a vibration effect at the end of the expansion process. The experimental results corroborate the numerical simulations in terms of overall tendency and capture the vibration patterns. The modified Johnson-Cook model well captures the vibration and the force components explain that the spring back effect was mainly due to the elastic deformation of the material with a negligible plastic deformation. An arbitrary optimisation is utilised for test 4 that improves the accuracy of the predictions and emphasizes the necessity of a proper optimization to identify an optimum constitutive model. These results show the importance of optimizing the process parameters to control the final dimensions of the expanded ring.

# References

Al6061-T6, accessed 08/01/2015, ASM Aerospace Specification Metals. from http://asm.matweb.com/search/SpecificMaterial.asp?bassnum=MA6061t6.

Anderson Jr, C., I. S. Chocron and A. Nicholls, 2006. Damage modeling for Taylor impact simulations. Journal de Physique IV (Proceedings), EDP sciences.

Baron, H. G. and R. H. Henn, 1964. *Spring-back and metal flow in forming shallow dishes by explosives*. International Journal of Mechanical Sciences 6(6), pp. 435-IN435.

Çaldichoury, I. and P. L'Eplattenier, 2012. EM Theory Manual. Electromagnetism and Linear Algebra in LS-DYNA, Livemore Software Technology Corporation.

Göbel, G., E. Beyer, J. Kaspar and B. Brenner, 2012. Dissimilar metal joining: macro-and microscopic effects of MPW. 5th International Conference on High Speed Forming.

Gourdin, W., S. Weinland and R. Boling, 1989. *Development of the electromagnetically launched expanding ring as a high‐strain‐rate test technique*. Review of Scientific Instruments 60(3), pp. 427-432.

Gourdin, W. H., 1989. *Analysis and assessment of electromagnetic ring expansion as a high‐strain‐rate test*. Journal of Applied Physics 65(2), pp. 411-422.

Johnson, J. R., G. Taber, A. Vivek, Y. Zhang, S. Golowin, K. Banik, G. K. Fenton and G. S. Daehn, 2009. *Coupling Experiment and Simulation in Electromagnetic Forming Using Photon Doppler Velocimetry*. steel research international 80(5), pp. 359-365.

Körner, J., G. Göbel, B. Brenner and E. Beyer, 2012. Numerical Simulation of Magnetic Pulse Welding: Insights and Useful Simplifications. 5th International Conference on High Speed Forming, Dortmund, Institut für Umformtechnik - Technische Universität Dortmund.

Liu, X., L. Huang and J. Li, 2014. *An experiment and simulation study of the rebound effect in electromagnetic forming process*.

Padmanabhan, M., 1997. Wrinkling and Springback in Electromagnetic Sheet Metal Forming and electromagnetic Ring Compression, The Ohio State University.

Photonic-Doppler-velocimetry-users-group-meetings-archive, accessed 08/01/2015, from https://kb.osu.edu/dspace/handle/1811/52627.

Raoelison, R., N. Buiron, M. Rachik, D. Haye and G. Franz, 2012. *Efficient welding conditions in magnetic pulse welding process*. Journal of Manufacturing Processes 14(3), pp. 372-377.

Raoelison, R., N. Buiron, M. Rachik, D. Haye, G. Franz and M. Habak, 2013. *Study of the elaboration of a practical weldability window in magnetic pulse welding*. Journal of Materials Processing Technology 213(8), pp. 1348-1354.

Raoelison, R., D. Racine, Z. Zhang, N. Buiron, D. Marceau and M. Rachik, 2014. *Magnetic pulse welding: Interface of Al/Cu joint and investigation of intermetallic formation effect on the weld features*. Journal of Manufacturing Processes 16(4), pp. 427-434.

Strizhakov, Y., 1991. *Calculating and selecting the parameters of magnetic pulsed vacuum welding*. Physical Chemistry Materials and Technology 5(1), pp. 89-91.

Zhang, P., 2003. Joining enabled by high velocity deformation, The Ohio State University.

Zhang, Y., S. Babu and G. Daehn, 2010. *Interfacial ultrafine-grained structures on aluminum alloy 6061 joint and copper alloy 110 joint fabricated by magnetic pulse welding*. Journal of Materials Science 45(17), pp. 4645-4651.

# Experimental and Numerical Prediction of the Static and Dynamic Forming Properties of Ti6Al4V

**P. Verleysen[1*], J. Galan-Lopez[1,2]**

[1] Department of Materials Science and Engineering, Ghent University, Belgium
[2] Department of Materials Science and Engineering, Technical University Delft, The Netherlands
[*]Corresponding author. Email: Patricia.Verleysen@UGent.be

## Abstract

*The strain rate dependence of the plastic yield and failure properties displayed by most metals affects energies, forces and forming limits involved in high speed forming processes. In this contribution a technique is presented to assess the influence of the strain rate on the forming properties of Ti6Al4V sheet. In a first step, static and dynamic tensile experiments are carried out using a classical tensile test device and a split Hopkinson tensile bar facility respectively. Next to uniaxial tensile, also purpose-developed plain strain and shear stress samples are tested. The experimental results clearly show that the mechanical behaviour of Ti6Al4V is strain rate dependent. Indeed, with increasing strain rate, plastic stress levels increase, however, this occurs at the expense of the deformation capacity. Subsequently, to allow simulation of forming processes, Johnson-Cook, Swift and Voce material model parameters are determined. Finally, the influence of the strain rate on the forming limits is assessed using the uni-axial tensile test results. Prediction of the initiation of necking in the Ti6Al4V sheets subjected to multi-axial strain states is based on the Marciniak-Kuczynski model. The thus obtained forming limit diagrams (FLDs) show a non-negligible effect of the strain rate. The reduced ductility at higher strain rates is reflected into an unfavourable downward shift of the FLD. Compared with the experimental data, the static FLD is clearly conservative.*

## Keywords

Dynamic material behaviour, Forming limit diagram, Ti6Al4V

# 1 Introduction

Ti6Al4V is the most widely used titanium alloy, due to the excellent combination of low weight, good mechanical properties and resistance to hostile service conditions such as extreme temperatures and corrosive environments. The mechanical behaviour of Ti6Al4V is determined by the multi-phase microstructure consisting of a harder (and richer) α-phase, which gives its strength, and a softer β-phase, which provides workability (Majorell et al., 2002).

Ti6Al4V is used in the industry in applications such as aircraft components, turbine blades or sports equipment. In many of these applications, the material is subjected to dynamic deformation rates during the production process. Obviously, high rates of deformation are obtained in forming processes such as magnetic pulseforming, hydroforming and explosive forming. However, also in more conventional sheet forming techniques, such as deep drawing, roll forming and bending, locally high strain rates occur. As the strain rate increases, the majority of materials present significantly higher plastic flow stresses, however much lower deformation levels. Materials which experience no strain rate sensitivity at all are rare. Exceptionally, both an increase in flow stress and an increase in elongation values are obtained (Van Slycken et al., 2006). For titanium alloys, both the plastic and failure behaviour are significantly affected by the strain rate. Knowledge of this high strain rate behaviour is indispensable for manufacturers of titanium components. Therefore, in present contribution results are presented of a mixed experimental-numerical study into the dynamic behaviour of Ti6Al4V, aiming at providing data on the properties which affect forming processes.

In a first step, static and dynamic tensile experiments are carried out using a classical tensile test device and a split Hopkinson tensile bar facility respectively. The obtained stress-strain curves show that with increasing strain rate, plastic stress levels increase, however, the deformation capacity decreases. Subsequently, to allow simulation of forming processes, from the tensile tests, Johnson-Cook, Swift and Voce material model parameters are determined (Liang and Khan, 1999). Additionally, static and dynamic tests are carried out using purpose-developed sample geometries aiming at a plane strain and shear deformation mode in the sample. To assess the influence of the strain rate on the forming limits a technique is used based on the Marciniak-Kuczynski model (Marciniak, Kuczynski, 1967). To this purpose only the uniaxial tensile test data are used. Finally, the experimental uniaxial tensile, shear and plane strain data are used to assess the validity of the obtained FLDs ().

# 2 Experimental Programme

## 2.1 Material and Test Samples

The investigated material is Ti6Al4V (ASTM Grade 5) provided by TIMET® (Toronto, Canada) as a sheet with initial thickness of 0.6mm. For the static and high strain rate mechanical tests three different types of samples (Fig. 1) are used:

- In-plane shear sheet sample (Peirs et al., 2011): when the sample is subjected to a tensile load, shear stresses arise in the material between the notches. Note the eccentric position of the notches which leads to an almost pure shear stress state up to large strains.
- In-plane sheet tensile sample (Verleysen et al., 2008): this sample features a 5mm long and 4mm wide gauge section.
- Plane strain sheet sample: the gauge section has a continuously changing width determined by circular arcs with a radius of 2.5mm, the width in the centre is 8mm.

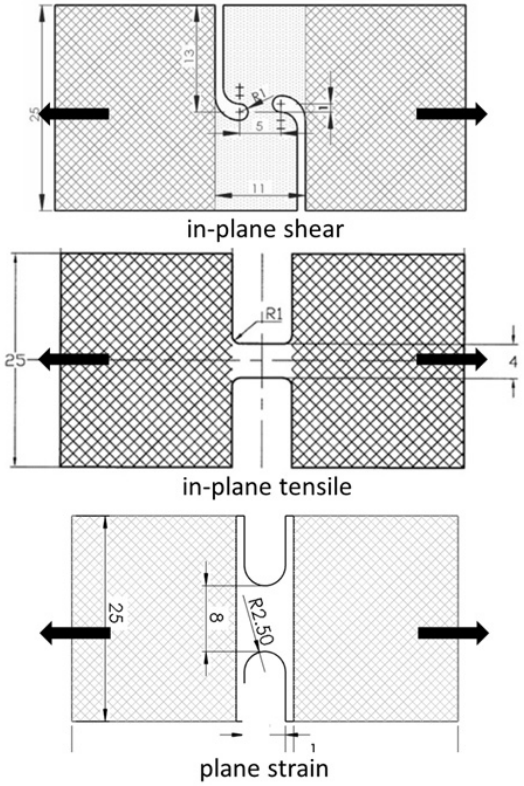


***Figure 1**: Sample geometries used*

The small size of the samples in Fig. 1 guarantees quasi-static equilibrium from the early stage of loading in the dynamic experiments. To exclude effects related to geometry or dimensions of the samples (Verleysen et al., 2008), the samples presented in Fig. 1 are used for both the static and dynamic experiments.

## 2.2 Test Setups

The experimental programme consists of static and high (500–1500/s) strain rate tests at room temperature. The static tests are carried out on a conventional electromechanical Instron® tensile machine. A Split Hopkinson bar (SHB) tensile setup is used for the dynamic

experiments, see Fig. 2. Two tests are carried out for each condition of strain rate and stress state.

The sheet samples are glued in slots made in the Hopkinson bars. To have the same boundary conditions in the static and dynamic tests, in the static tests the samples are also glued in slots of between short bars with the same diameter and material as the Hopkinson bars.

For the static experiments three LVDTs are used to measure the relative displacement of the sample/bar interfaces. Prior to testing, a speckle pattern is applied to the samples. During the tests two cameras record the deforming pattern. For the dynamic tests, Kolsky's theory is used to obtain the force-displacement of the samples subjected to the tensile loading (Kolsky, 1949) Additionally, the sample deformation is recorded by high speed cameras. Local information about the deformation is obtained from the camera images and digital image correlation (DIC). Close to the fracture, large strain gradients occur which give rise to heavily distorted speckle patterns. As a result, the obtained DIC strain might underestimate the actual strain value.

***Figure 2**: Split Hopkinson tensile bar setup at Ghent University. Its total length is 11m, thus enabling loading times of 1.2msec.*

## 2.3 Test Results

Representative static and dynamic curves for the shear, tensile and plane strain tests are presented in Figure 3. From measurements during the tests, the stress in the gauge section is straightforwardly obtained by dividing the force by the gauge area. For the tensile test the

average strain in the gauge section is obtained by dividing the elongation by the initial gauge length. Next to the stress, also the logarithmic strain obtained by DIC is given as a function of the imposed displacement. For all tests, the dynamic stress levels are significantly higher than the static levels. In the shear tests, significant strain hardening is observed. The shear fracture strain at high strain rates is lower than its static counterpart. This is due to the formation of adiabatic shear bands in dynamic shear tests. Also in the tensile experiments fracture strains which are significantly higher in the static tests are observed. In the plane strain tests, however, slightly lower fracture strains are observed in the static tests.

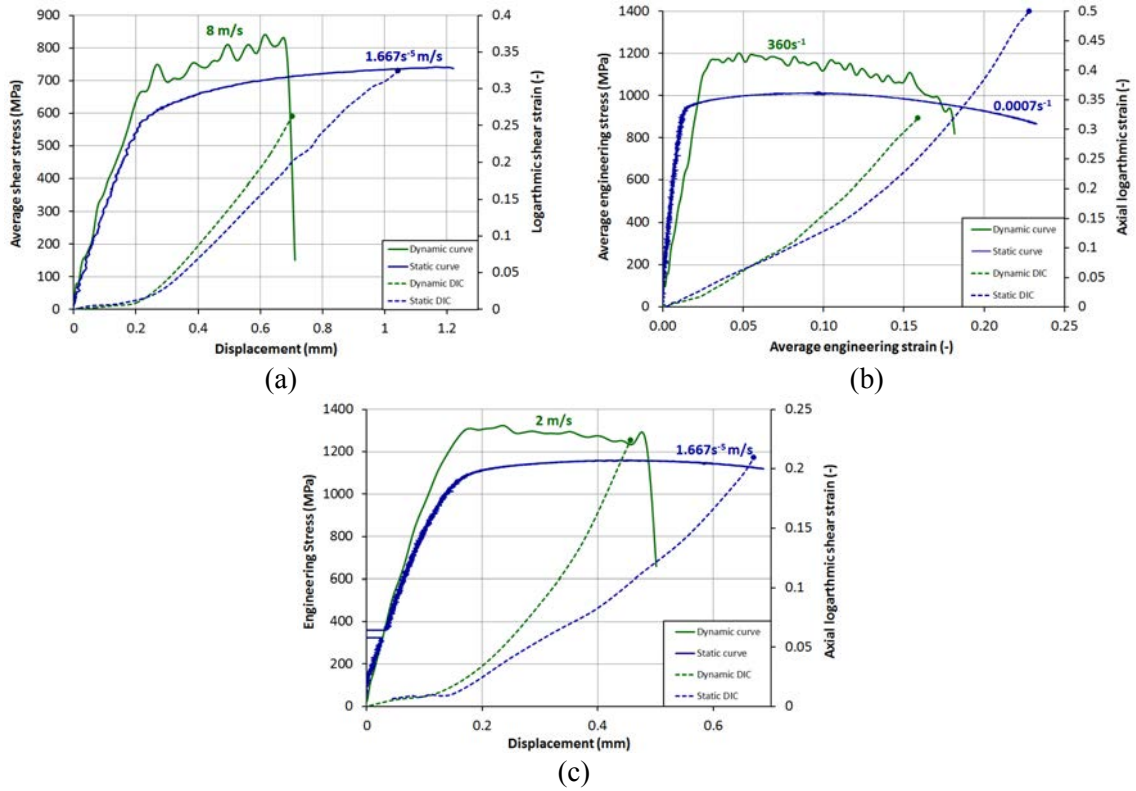


***Figure 3**: Representative static and dynamic stress-strain or stress-displacement curves, and local strain obtained by DIC, from the following tests: shear (a), tensile (b) and plane strain (c). The DIC fracture strain is indicated by a dot.*

# 3 Modelling of the High Strain Rate Behaviour

## 3.1 Hardening Laws

The experimental results are used to model the materials hardening behaviour. Three frequently used models are considered: Voce law, Swift law and the Johnson-Cook model (Liang and Khan, 1999). Voce law describes the relation between the stress $\sigma$ and plastic strain $\varepsilon_p$. The model contains only three parameters $\sigma_0$, K and n which can easily be determined from only one experiment:

$$\sigma = \sigma_0 + K(1 - e^{-n\varepsilon_p}) \quad (1)$$

The Swift law can be written in the following form (Swift, 1952):

$$\sigma = C(\varepsilon_0 + \varepsilon_p)^n \quad (2)$$

the strength coefficient C, ε0 and hardening exponent n are empirical constants.

The Voce and Swift flow rules do not explicitly describe the material's strain rate and temperature dependence. Both can be taken into account by making the model parameters strain rate and/or temperature dependent.

The Johnson-Cook phenomenological model does take into account strain rate and temperature dependent material behaviour (Johnson, Cook, 1983):

$$\sigma = \left(A + B\varepsilon_p{}^n\right)\left(1 + C\ln\frac{\dot{\varepsilon}}{\dot{\varepsilon}_0}\right)\left(1 - \left[\frac{T - T_{room}}{T_{melt} - T_{room}}\right]^m\right) \quad (3)$$

The first term of the right hand side describes the isothermal static material behaviour. Consequently, the parameters A, B and n are determined using the static tensile tests. The strain rate during the static tensile test is the reference strain rate $\dot{\varepsilon}_0$ used in the second term, expressing the strain rate hardening with parameter C. The last factor, including m, represents thermal softening. C and m are calculated using the high strain rate tensile tests (Peirs et al., 2011).

The quasi-adiabatic temperature increase in the specimen during high strain rate plastic deformation is calculated using the following formula:

$$\Delta T = \frac{\beta}{\rho c}\int \sigma d\,\varepsilon_p \quad (4)$$

In this equation ρ is the mass density, c the specific heat and β the Taylor-Quinney coefficient indicating the fraction of plastic work converted into heat. This β-value is usually assumed to have a value between 0.9 and 1. Constant values for c and β can be used regarding the modest temperature range acquired during these tests. During the high strain rate tests the temperature will gradually change from room temperature to approximately 100°C depending on the material.

In table 1 values for the parameters of the Voce, Swift and Johnson-Cook models can be found. The parameters are calculated by a least square method. For the Voce and Swift laws two sets of parameters are given: one for the static behaviour at room temperature and one for a dynamic, adiabatic experiment at $1000s^{-1}$.

In Figure 4 a comparison is made between experimental and modelled stress-strain curves. Both Swift and Voce models succeed in describing the experimental behaviour. Because the Voce model performs better at higher strains, it will be used for calculation of the FLDs in the next section.

| | Voce | | | Swift | | |
|---|---|---|---|---|---|---|
| | $\sigma_0$ (MPa) | K (MPa) | n | C (MPa) | $\varepsilon_0$ | n |
| **Static** | 1007.7 | 389.2 | 4.75 | 1563.8 | 0.0849 | 0.179 |
| **Dynamic** (strain rate 430$s^{-1}$) | 1246.7 | 181.5 | 12.5 | 1532 | 0.0139 | 0.0503 |
| | **Johnson-Cook** | | | | | |
| | A (MPa) | B (MPa) | n | C | m | |
| | 951 | 892 | 0.70 | 0.015 | 0.71 | |

***Table 1**: Values for the Voce, Swift and Johnson-Cook material model parameters. The reference strain rate $\dot{\varepsilon}_0$ for the Johnson-Cook model is $8 \cdot 10^{-5}$/s.*

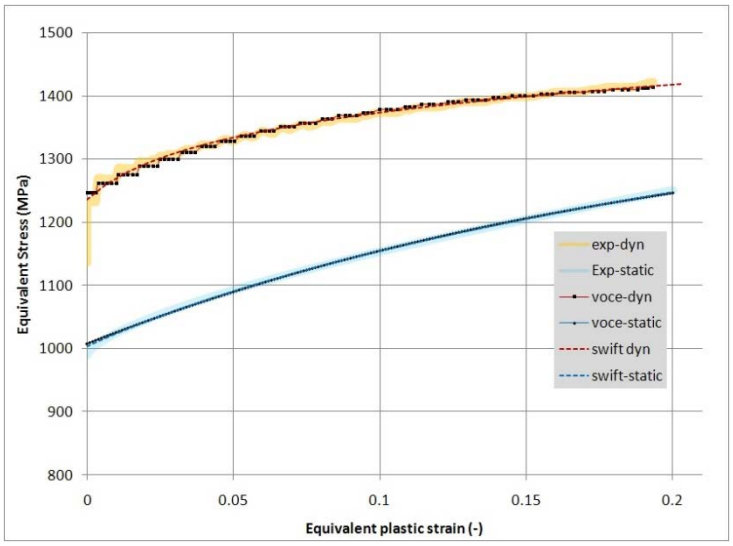


***Figure 4**: Experimental static and dynamic tensile curves for Ti6Al4V and curves simulated with the Voce and Swift hardening law using the parameters given in table 1.*

# 4 Dynamic Forming Limit Diagram

## 4.1 Marciniak-Kuczynski Method

The uniaxial tensile test results at different strain rates are used to predict the forming limits of the studied steel grades. Onset of necking under the multi-axial strain conditions occurring in forming processes is predicted using the well-known Marciniak–Kuczinski model (Marciniak and Kuczynski, 1967). A similar approach is adopted in (Li et al., 2013) to predict the FLD of 22MnB5 in Hot Stamping.

In the Marciniak-Kuczynski (MK) method, it is assumed that an initial imperfection is present in the sheet metal. The imperfection is modelled by a band b of smaller thickness than the surrounding zone a, as schematically represented in Figure 5. The orientation of the band is characterized by the angle $\psi$. The initial imperfection can originate from a real thickness variation, surface roughness, a local variation of the strength or a combination.

Physical meaning of this assumption is given in (Marciniak et al., 1973). The imperfection parameter, $f_0$, is defined as the ratio of the reduced thickness $t_{b0}$ to the initial thickness of the sheet $t_{a0}$ ($f_0=t_{b0}/t_{a0}$). During a biaxial straining process, the imperfection zone deforms more than the uniform zone. Therefore, the strain path of the imperfection zone is continuously ahead of the strain path of the uniform zone. At a certain point, when the strain localization takes place, the difference between the strain path of the imperfection and the uniform zone begins to increase drastically. If the ratio of strain in the zone b to that of the perfect sheet reaches a presumed critical value, the sheet is considered to have failed. This critical value has low impact on the calculated forming limit because the strain in zone a does not change much once there is strain localization in b. The failure strain is calculated for different orientations of b. The lowest failure strain from these calculations is the forming limit. Once the strain localization is detected, the sheet metal is assumed to have failed.

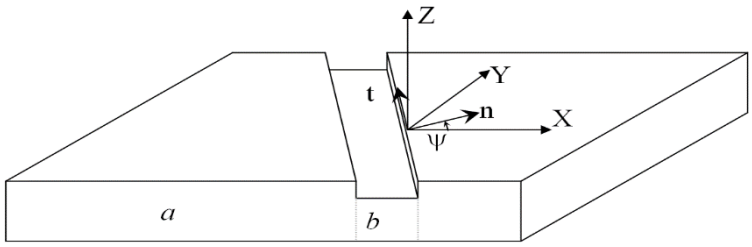


***Figure 5**: Schematic representation of the Marciniak-Kunczynski sheet with imperfection*

For the critical ratio of the strain increment in the region b to that of the region a 4 is chosen. The Voce hardening law fitted to the experimental stress-strain curves (see previous section) and von Mises yield criterion are adopted. Instead of optimizing the imperfection parameter $f_0$, it is set on 0.99.

## 4.2 Static and Dynamic Forming Limit Diagrams for Ti6Al4V

The results of the FLD calculation are shown in Figure 6. A FLD graph for static and one for dynamic ($1000s^{-1}$) deformation can be found. The dynamic FLD is lower than the static one. Certainly, the left-hand side is adversely affected. This can be explained by the lower uniform elongation during dynamic deformation. The right-hand side of the FLD is mainly affected by strain-hardening of the material. At the onset, corresponding with plane strain deformation ($\varepsilon minor = 0$), forming limits are clearly lower for high strain rate deformation, however the slope of the dynamic curves is higher, through which static and dynamic FLDs tend to converge for high strain ratios.

In Figure 6 also experimental data points corresponding with necking in the plain strain and uniaxial tensile tests, together with the (minor, major)-strain at fracture for the shear test, are shown as in (Bruschi et al., 2014). When comparing the position of the experimental data points with the calculated FLDs, it is clear that the static FLD is a conservative approximation. This is not the case for the dynamic FLD. Indeed, the dynamic, experimental shear and tensile strain values are below the corresponding FLD.

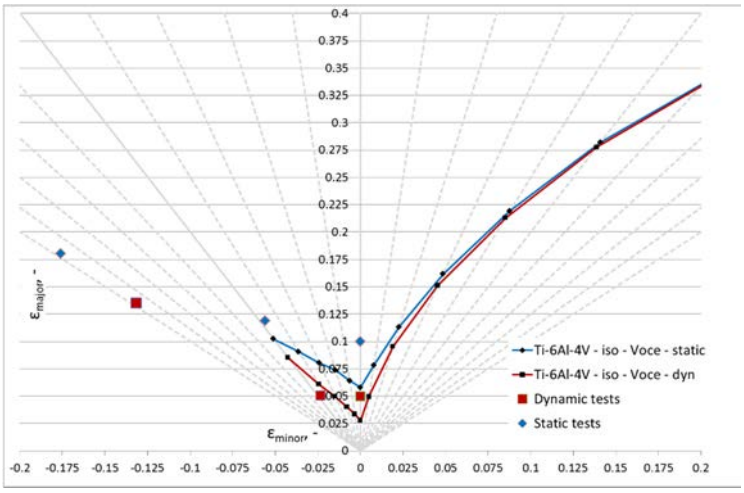


***Figure 6**: Comparison of static and dynamic FLD's for Ti6Al4V*

# 5 Conclusions

The influence of the strain rate on the forming properties of a commercial Ti6Al4V sheet is studied. Static and high strain rate tensile experiments are performed to assess the influence of the strain rate on the mechanical behaviour. Going from static to dynamic loading rates, the plastic stresses increase. Concerning deformation before necking values are roughly halved. Subsequently, the Johnson-Cook and Voce models are used to describe the strain rate and temperature dependent constitutive behaviour of the Ti6Al4V. These constitutive models combined with the corresponding material parameters can be used to calculate the energies and forces occurring in a high speed forming process.

Finally, the influence of the strain rate on the forming limits is assessed. Aiming at multi-axial deformation states, tests are carried out at different strain rates using purpose-developed sample geometries. Additionally, the initiation of necking in the Ti6Al4V sheets subjected to multi-axial strain states is numerically predicted using an algorithm based on the Marciniak-Kuczynski model. The resulting forming limit diagrams show a non-negligible effect of the strain rate. The reduced ductility at higher strain rates is reflected into an unfavourable downward shift of the forming limit diagrams. Comparison of the calculated FLDs with experimental data, shows that a conservative prediction of the FLD is only obtained in the static case.

## Acknowledgments

The authors would like to acknowledge the Interuniversity Attraction Poles Programme (IUAP) of the Federal Science Policy of Belgium and the partners of IUAP-VII-project P7/21 'Multiscale mechanics of interface dominated materials'.

## References

Bruschi, S., Altan, T., Banabic, D., 2014. Testing and modelling of material behaviour and formability in sheet metal forming. CIRP An.-Man. Tech 63 727-749

Li, H., Wu, X., Li, G., 2013. Prediction of Forming Limit Diagrams for 22MnB5 in Hot Stamping Process. J. Mat. Eng. Perf. 22 2131-2140.

Johnson, G.R., Cook, W.H., 1983. A constitutive model and data for metals subjected to large strains, high strain rates and high temperatures. 7th Int. Symposium of Ballistics. The Hague, The Netherlands.

Kolsky, H., 1949. An investigation of the mechanical properties of materials at very high rates of loading. Proc Phys Soc London B 62 676-700.

Liang, R.Q., Khan, A.S., 1999. A critical review of experimental results and constitutive models for BCC and FCC metals over a wide range of strain rates and temperatures. Int. J. Plast. 15, pp. 963-980.

Majorell, A., Srivatsa, S., Picu, R.C., 2002. Mechanical behavior of Ti6Al4V at high and moderate temperatures - Part I: Experimental results. Materials Science and Engineering a-Structural Materials Properties Microstructure and Processing 326(2), pp. 297-305.

Marciniak, Z., Kuczynski, K., 1967. Limit strains in the processes of stretch-forming sheet metal. Int. J. Mech. 9, pp. 609-620.

Marciniak, Z., Kuczynski, K., Pokora, T, 1973. Influence of plastic properties of a material on forming limit diagram for sheet-metal in tension. Int. J. Mech. Sci. 15, pp. 789-800.

Peirs, J., Verleysen, P., Degrieck, J., 2011. Novel technique for static and dynamic shear testing of Ti6Al4V sheet. Experimental Mechanics 52, pp. 729-741

Peirs, J., Verleysen, P., Van Paepegem, W., Degrieck, J., 2011. Determining the stress-strain behaviour at large strains from high strain rate tensile and shear experiments. International Journal of Impact Engineering 38(5), pp. 406-415.

Swift, H.W., 1952. Plastic instability under plane stress. J. Mech. Phys. Solids, 1: 1

Verleysen, P., Degrieck, J., Verstraete, T., Van Slycken, J., 2008. Influence of sample geometry Split Hopkinson Tensile bar on sheet materials. Experimental Mechanics 48, pp. 587-593.

Verleysen, P., Peirs, J., Van Slycken, J., Faes, K., Duchene, L., 2011. Effect of strain rate on the forming behaviour of sheet metals. J. Mat. Proc. Tech. 8, pp. 1457-1464.

Van Slycken, J., Verleysen, P., Degrieck, J., et al., 2006. High-strain-rate behavior of low-alloy multiphase aluminum- and silicon-based transformation-induced plasticity steels. Met. Mat. Trans. A-Phys. Met. Mat. Sc. 37A, pp.1527-1539.

# Influence of Different Strain Rates on the Flow Curve and the Formability of Thin Aluminium and Tinplate Sheets

**M. Linnemann*, T. Lieber, C. Scheffler, V. Psyk, R. Müller, D. Landgrebe**

Fraunhofer Institute for Machine Tools and Forming Technology (IWU), Chemnitz, Germany
*Corresponding author. E-mail: maik.linnemann@iwu.fraunhofer.de

## Abstract

*Due to this high number of produced units and the very thin sheet metals used for beverage cans, precise production processes with high production volumes are necessary. To save expenses, while optimising these processes, numerical simulation methods are exploited. Considering this, it is indispensable to identify the material behaviour as exactly as possible. In practise, often results of quasi static tensile tests are used, although these are insufficient for the precise modelling of the material behaviour during can production, since strain rates of up to $10^3$ $s^{-1}$ can occur, here. Therefore, quasi static and high speed tensile test have been done on specimens featuring the typical materials and thicknesses of semi-finished parts used for beverage can production. The results were compared with similar materials at higher sheet metal thicknesses and authenticated by numerical simulation. It was shown that there is an influence of the strain rate on the material behaviour and it is necessary to determine material characteristics at strain rates, which are close to the process speed. Furthermore, the results were classified in their signification for beverage can production and forming technologies in general.*

## Keywords

Material, Can manufacturing, High speed tensile test

# 1 Introduction

Economic and resource efficient manufacturing becomes more and more important in modern production technologies. This means, that e.g. in order to exploit the volume of the material used for component production as ideally as possible thickness should be preferably low. This plays an important role, especially for mass products as e.g. beverage cans. The number of produced beverage cans in the European Union increased from 45 billion pieces in 2006 to 63 billion pieces in 2014 (Statista GmbH, 2015). Due to this high number of units automated and very quick production processes with high forming speeds are necessary. Nowadays, up to 2000 cans per minute can be produced (Achhammer & Auburger, 2015).

To allow maximum material exploitation, highly accurate dimensions and shape, as well as good reproducibility of the semi-finished and finished products along the complete production chain are necessary. Therefore, the processes are designed by numerical methods. For this purpose, precise material properties are indispensable. In practise, the material properties are usually determined by quasi static tensile tests and strain rate sensitivity of the material behaviour is neglected. However, this is a simplifying approximation of the material behaviour only. Thus, it is not guaranteed to create exact results for high-speed production processes. This is why it is insufficient to represent the realistic behaviour via quasi static tensile test.

# 2 Beverage Can Production

Beverage cans are one of the most important packages for drinks, next to bottles and drink cartons. They appeared on market for the first time in the USA in the 1930's (Ball Europe, 2016). At that time, they looked like usual tin cans and had to be opened by a can-piercer. Until now a lot of developments and improvements have been done. Today beverage cans consist of two parts: the shaft and the cap. In the USA nearly all cans are made of aluminium, while in Germany 90% are made of tin plates (Weddige, 2001). This difference results from local conditions, since the USA has a big aluminium lobby, while Germany has a long steel production tradition. Typical initial thicknesses of the can body, which is formed by deep-drawing and wall ironing **(Figure 1)**, are in the range of 0.1-0.3 mm.

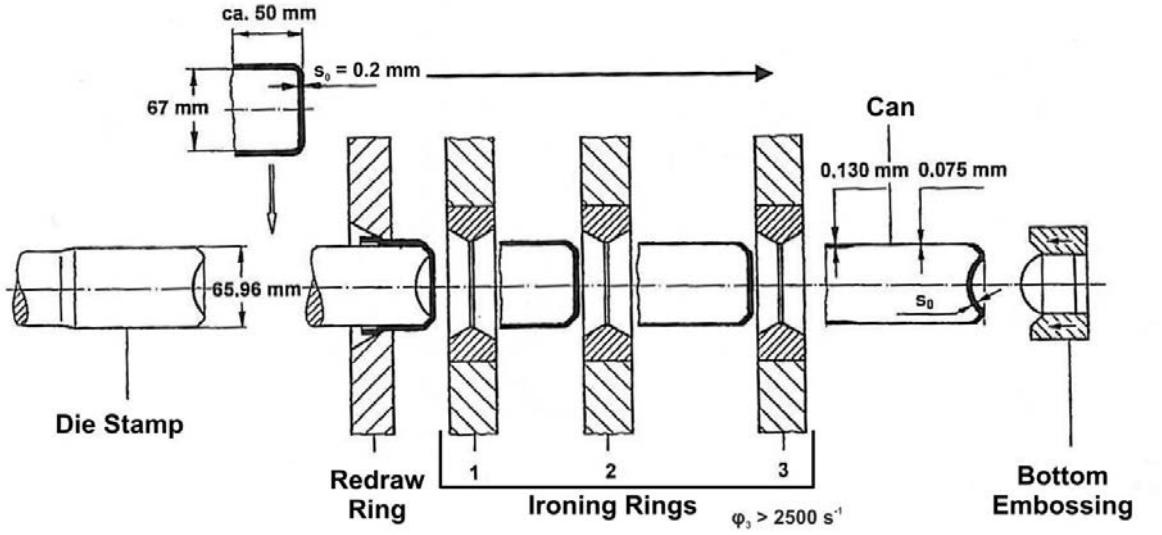


***Figure 1**: Forming Process adapted from Kaup (2003)*

In the production process of can body, small round blanks are formed cups by deep-drawing. Afterwards, these usually pass through 3 ironing rings to form the . Thereby, the wall thickness is reduced to 1/3 of the former thickness and the length increases accordingly. At the end, a die punch shapes the bottom of the can body. During these typical production processes, strain rates in the range of up to $10^3$ $s^{-1}$ can be achieved. (Kaup, 2003)

Nowadays, big efforts are made to optimise manufacturing processes in beverage can production. Main drivers are cost-reduction and an expansion of the market position. In the past, the optimisation was an expensive and time intensive experimental, but with numerical simulation it is more time efficient and related to lower costs, now. The numerical simulation allows designing a virtual model of the production process. Therefore, fundamental knowledge about process parameters and their interactions is necessary. Some of the most important parameters are the forming speed, the behaviour of the tools and the material characteristics of the raw material. With the developed numerical model it is easy to change parameters and check their influence on the production process without doing expensive changes in the real process. To achieve accurate results, this requires precise input data. In forming technologies especially a good material characterisation is needed. Therefore, it is indispensable to perform material test under realistic conditions.

# 3 Experimental Setup

## 3.1 Machine Properties and Test Conditions

All quasi static and high speed tensile tests regarded in this study were carried out at Fraunhofer IWU. For this purpose, two different Zwick/Roell testing machines were used. One machine is a ZPM 1475, which allows measuring a maximum force of 100 kN and operates with a maximum traverse speed of 1 m/min. It is used for quasi static tensile test at

a strain rate of 0.0003 $s^{-1}$, (according to) DIN EN ISO 6892-1 (2009). The elongation is measured by a clip-on extensometer.

For the high speed tests a HTM 16020 is used. It allows measuring a maximum force of 160 kN and operates with a maximum traverse speed of 20 m/s. The selected machine speed of 5 m/s results in a strain rate of 250 $s^{-1}$ for the specimens regarded in this study. The elongation is measured by an optical extensometer. Therefore, black and white marks have to be placed on the specimen **(Figure 2)**.

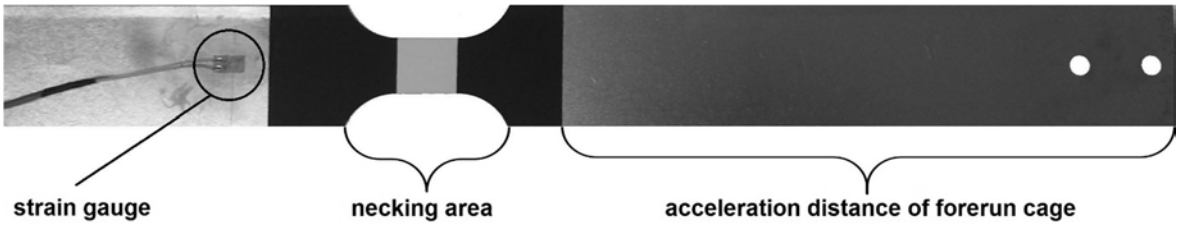


***Figure 2**: Specimen with black/white marks and strain gauge*

Due to the high strain rates, an oscillation, caused by the impact, superposes the measurement signal of the machine integrated load cell. That's why it is indispensable to apply strain gauges. Strain gauges have smaller mass compared to the load cell and can be attached close to the necking area.

## 3.2 Error Calculation

The experimental investigations with strain gauges are sensitive to parameter deviations. Besides of errors in the optical strain measurement, in particular the calculation of the force from the strain gauge can be erroneous. To investigate the impact of parameter deviations, an error calculation study was done (Taylor, 1988). The dependency of the force on the output voltage of the bridge circuit used for measuring the change of the resistance of the strain gauge is computed by **Eq. 1**:

$$F = \frac{E \cdot s_0 \cdot b \cdot U_0}{p \cdot k \cdot 100 \cdot U_B} \tag{1}$$

Here E is the Young's modulus, $s_0$ the sheet metal thickness, b the width of the specimen where the strain gauge is applied to, p a constant which is ½ for half bridges, k the strain gauge constant (2.0 for the applied strain gauge), $U_o$ the measured output voltage and $U_B$ the feeding voltage of the bridge network. Thus there are 5 relevant parameters $x_i$ to be measured. The total differential can be applied to obtain an appropriate estimation of the error **(Eq. 2)**.

$$dF = \sum_{i=1}^{5} \frac{\partial F}{\partial x_i} dx_i \tag{2}$$

The absolute value of the partial derivation is a measure for the relative proportional impact on the total error, the so called participation factor. This factor must be still weighted

with the nominal value of the parameter itself to get the absolute share. The nominal values, used for calculating the participation factors, are E=210,000 N/mm$^2$, $s_0$=0.2 mm, b=44 mm, $U_o$=0.01 V (assumed for a strain of $1.10^{-3}$) and $U_B$=10 V **(Eq. 3)**.

$$\left|E \cdot \frac{\partial F}{\partial E}\right| = \left|s_0 \cdot \frac{\partial F}{\partial s_0}\right| = \left|b \cdot \frac{\partial F}{\partial b}\right| = \left|U_o \cdot \frac{\partial F}{\partial U_0}\right| = \left|U_B \cdot \frac{\partial F}{\partial U_B}\right| = \frac{E \cdot s_0 \cdot b \cdot U_o}{p \cdot k \cdot 100 \cdot U_B} = 18.5 \quad (3)$$

It is obvious that all the parameters have the same impact on the error of the force because the value of the individual participation factors is equal. This is a result of the linear formula and the reason, why the same measurement accuracy should be taken into account for all parameters. This means, that for example the dimensions of the probe should be measured with the same high accuracy as the bridge voltages are measured and imposed.

# 4 Results and Discussion

Based on the force and displacement measurements, taken during the tensile tests, strain-stress-diagrams were created and used to determine the material characteristics yield strength $R_{p0,2}$, ultimate tensile strength $R_m$, and elongation at fracture $A_{20}$ (see ***Table 1***.) and flow curves (see ***Figure 3***).

| | **material** | **thickness [mm]** | **quasi static** | | | **high speed** | | |
|---|---|---|---|---|---|---|---|---|
| | | | $R_{p0,2}$ | $R_m$ | $A_{20}$ | $R_{p0,2}$ | $R_m$ | $A_{20}$ |
| | | | **in N/mm²** | | **in %** | **in N/mm²** | | **in %** |
| 1 | EN AW-5182 | 0.35 | 346 | 411 | 8 | 337 | 395 | 19 |
| | T52BA | 0.16 | 252 | 317 | 38 | 415 | 435 | 38 |
| | T52BA | 0.20 | 227 | 304 | 40 | 407 | 433 | 40 |
| 2 | EN AW-5182 | 1.20 | 150 | 300 | 30 | 160 | 275 | 35 |
| | DC04 | 0.90 | 190 | 320 | 35 | 380 | 510 | 35 |

***Table 1****: Material characteristics (1: beverage can materials, 2: comparative materials)*

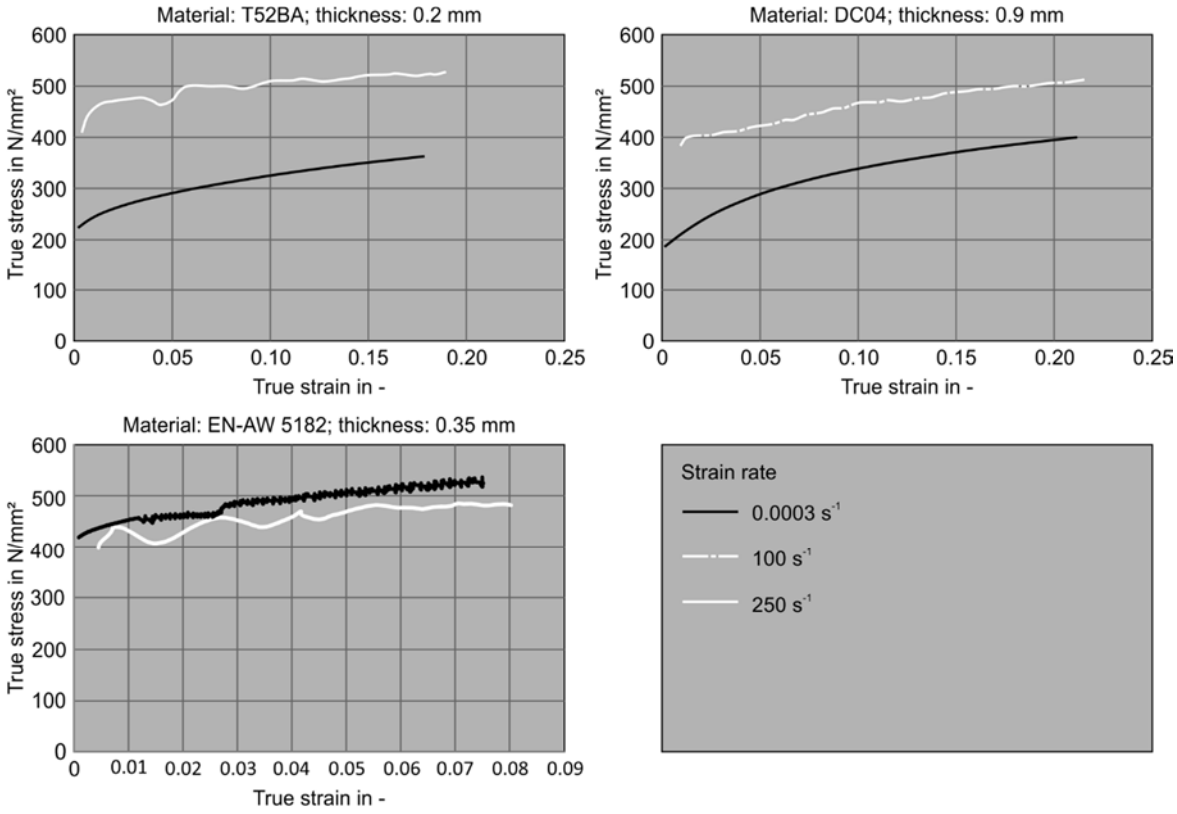


***Figure 3**: Flow curves (from onset of yielding to begin of necking)*

As expected, the measurement on the aluminium and the tin plates reveal significantly different results (see Table 1 and Figure 3). For the tin plates there is no influence of the strain rate on the elongation at fracture. However, there is a significant influence on yield strength and ultimate tensile strength. For both thicknesses of the tin plates the yield strength increases about 170 N/mm² and the ultimate tensile strength increases about 120 N/mm². Furthermore, the measurement results show that there is a difference in the yield strength and the ultimate tensile strength between the different sheet metal thicknesses for both strain rates, which can be explained as a consequence of the rolling process. The tin plate with 0.16 mm contains a stronger deformation and more significant strain hardening compared to the 0.20 mm tin plate.

DC04 - another unalloyed deep drawing steel – shows the same principle behaviour of yield stress and tensile strength for thicker sheets (0.9 mm), as shown in Figure 3 (top, right). DC04 is a low-alloyed steel, which is used for numerous forming applications. Consequently, its behaviour is well known and that is why older measurements performed at Fraunhofer IWU on this material are used as reference, here.

In case of aluminium specimens, the yield stress and the tensile strength at elevated strain rates in the range of 250 $s^{-1}$ are about 10 N/mm² lower than in the quasi-static test (compare Table 1). This is in good agreement with the negative strain rate sensitivity of EN AW-5182 detected by Ostermann (2007). Accordingly, the influence of the strain rate on the material strength can be considered as minor compared to the regarded steel materials. However, there is a big influence on the elongation at fracture. The material characteristics

show that the elongation at fracture increases by nearly 240 % due to the increase in the strain rate (compare Table 1). Both effects are in good agreement with earlier investigations by Meyer et al. (2009).

Certainly, the increased forming limit of the aluminium at elevated strain rates is related to the so called Portevin–Le Chatelier (PLC) effect, which can be seen in the flow curve of EN AW-5182 (Figure 3, bottom, left). As Abbadi et. al (2002) figured out, the PLC effect is a plastic instability typical for aluminium alloys of the 5000 series. It occours if there are diffusing solute atoms within the lattice structure of the alloy. These are typically concentrated at the glide dislocation, because there most space is available. If the material is loaded with stress, the dislocations move along the slip planes. The diffusing solute atoms follow the dislocations and constrict their movement- the stress increases. After a critical stress the dislocation break away from the diffusing solute atoms and the stress suddenly collapses. Then, the process begins all over again. This effect can be seen as serrations in the stress-strain-diagram. If a critical strain rate is exceeded, it is impossible for the diffusing solute atoms to follow the dislocations. Accordingly, stress strain curves for higher strain rates typically do not feature the serration. The movement of dislocations is more homogeneous and thus the specimen can bear higher elongation at fracture. Measurements performed on specimens of the same aluminium alloy (EN AW- 5182) but featuring higher sheet thickness (1.2 mm) show similar effects (see Table 1).

# 5 Numerical Modelling

To enhance the understanding of the experimental results a numerical model for the high speed tensile test specimen with material T52BA 0.2 mm thickness and a velocity of 5 m/s was set up. Due to the short time duration of the experiment the Finite Element software LS-DYNA with its explicit solver was used. The model consists of about 90k full integrated shell elements and features for the specimen material a standard isotropic von Mises plasticity model enhanced by a nonlinear strain dependent damage and failure model (LSTC, 2015). This model (see **Figure 4**) accounts for the effect of damage prior to rupture based on an effective (equivalent) plastic-strain measure $\varepsilon^{p}_{eff}$ without the consideration of the stress state. It is assumed that damage evolution begins at a strain $\varepsilon^{p}_{damage}= 0.3$ and ends with failure corresponding to the determined elongation at fracture with a damage variable $D$=1. The damage variable describes the relation of the void area $A_{damage}$ to the total area $A$ and scales the true stress $\sigma_{damage}$. The relative simplicity of the damage model proved its validity by a successful application for several sheet metal problems at the Fraunhofer IWU. The consideration of the strain rate scaling effect on the yield stress was considered by a strain rate table corresponding to the performed experiments with linear extrapolation beyond the tested strain rates. This was done in order to regard the much higher strain rates in the simulation of beverage can production. The simulation showed that the result of the material test with a strain rate of 250 $s^{-1}$ can be seen as representative for higher strain rates.

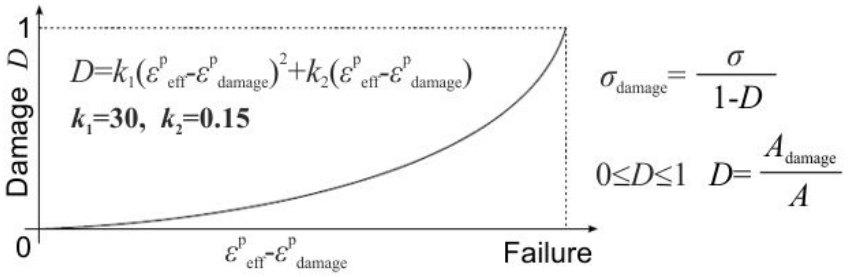


***Figure 4**: Damage evolution curve and model for material T52BA*

The results of the simulation for equivalent plastic strain and temperature are depicted in **Figure 5**. The figure shows a state just before failure occurs. The formation of the crack is triggered by the strain localisation in the specimen. The angle of the crack is 41° to the main axis of the specimen and is a result of the main shear stress. This failure mode is typical for a thin tensile test probe and is in good agreement with the experiment. However, the occurrence of the "arrow" shaped failure mode in Figure 5 is not the only valid mathematical solution for the crack problem. The inclined but straight crack propagation is valid as well and appears in about half of the experimental investigations. This means that from the mathematical fracture mechanics point of view the crack propagation has a bifurcation point in its solution.

It is well-known that the element size in simulations has a significant impact at the failure due to an insufficiently discretised strain field in the localisation zone (Feucht, 2011). To investigate the element size dependency of the failure behaviour, two mesh sizes, one with 50 µm element length in the relevant specimen zone and the other one with 100 µm length were investigated to determine local strains and strain rates. Figure 5 reveals that the global plastic strain in the specimen, determined as average over the parallel section, is at the time of crack initiation around 0.207, whereas the local strains are up to 0.46 for the 50 µm mesh size model and 0.43 for the 100 µm mesh model in the localization zone. The insignificant differences in the local strains indicate that the characteristic length scale of the material is almost achieved by the size of the spatial discretisation. The same can be identified for the strain rate distribution in the specimen where the global strain rate in the specimen is at 5 m/s test velocity 250 $s^{-1}$ whereas the local strain rate in the localization zone can reach values of up to 25,000- 40,000 $s^{-1}$ and even before localisation appears the maximum values are in the range of 500- 650 $s^{-1}$, see **Figure 6**. This figure shows the evolving shear bands, which finally grow together and intensify up to the crack initiation. Shear bands are also slightly visible in the experimental specimen (Figure 5, right).

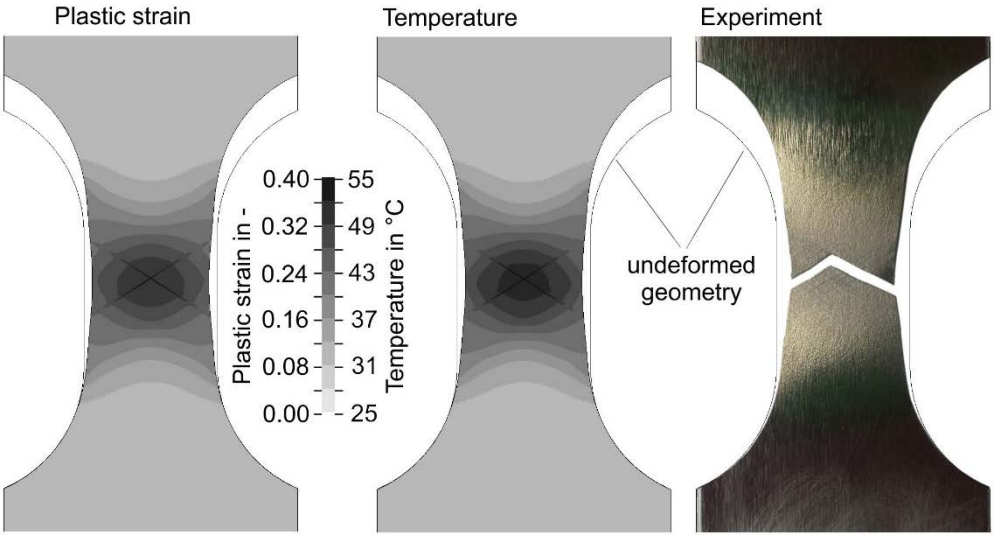


***Figure 5**: Plastic strain and temperature distribution right before crack propagation*

The increase in strain and temperature before rupture is obvious and a result of the localisation. Nevertheless the temperature increase is less than expected. This might be a result of the moderate test velocity of 5 m/s. The average temperature in the middle of the specimen area, where the maximum strain occur, is around 49°C, whereas in the localisation zone around 57°C occur (50 µm mesh size model). The boundary conditions for the coupled thermo-mechanical computation had been assumed as adiabatic. The time history evaluation of a point in the localisation zone is depicted in Figure 6.

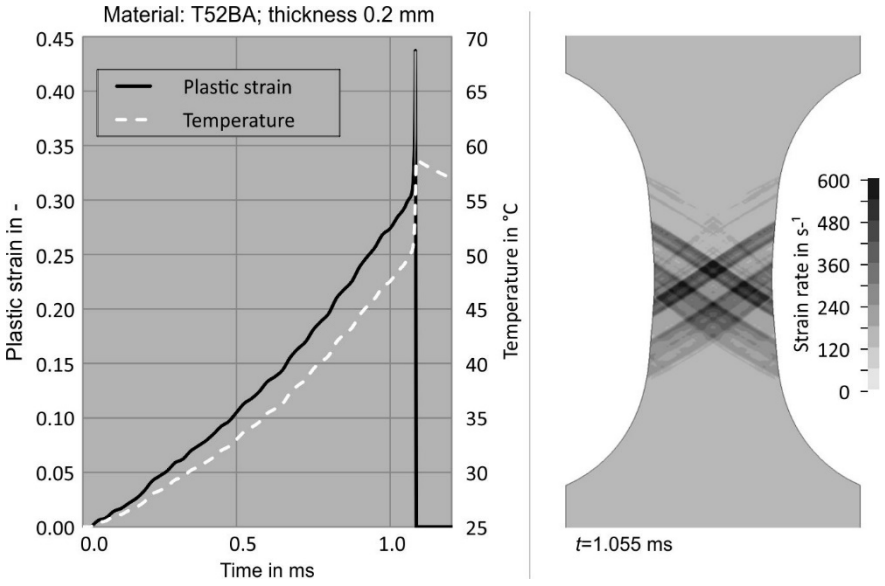


***Figure 6:** Left: plastic strain and temperature evolution for a point in the localisation zone. Right: Strain rate distribution with distinct shear bands before failure.*

# 6 Conclusion

In order to provide fundamental knowledge on the material behaviour of thin sheet metals for the numerical simulation of beverage can production processes, quasi static and high speed tensile tests were carried out. Two different strain rates (0.0003 $s^{-1}$, 250 $s^{-1}$) and two materials relevant for can production (tin plates with thicknesses of 0.2 mm and 0.16 mm and aluminium with a thickness of 0.35 mm) were chosen. The results show that there are severe differences in the behaviour of tin plates and aluminium. However, for both materials the tests have shown that quasi static tensile tests alone are insufficient to describe the material characteristics at higher strain rates, which are definitely relevant for can production. Thus, it is essential to determine the material characteristics for the full range of strain rates occurring during beverage can production in order to create realistic and reliable numerical models.

A look at the T52BA tin plates reveals that for this material at elevated strain rates the yield stress and the tensile strength are higher, resulting in higher forming forces. Consequences for the process design are that bigger machines, which can provide the higher forces, are required and more energy is needed to run them. In addition to this, higher wear of the tool can lead to higher costs for tool maintenance and repair, respectively. On the other hand, there is no measurable influence of the strain rate on the elongation at fracture for the regarded range of strain rates in case of the steel material. Thus, no deterioration of the formability related to the strain rate has to be taken into consideration, when dimensioning the product and the production steps.

The results of the EN AW-5182 show a more favourable behaviour from the point of view of forming technologies. For this material, no increase of the material strength was detected at higher strain rates and within the range of strain rates regarded in this study, even a slight decrease in the strength can be recognised for higher strain rates. This means that the above mentioned disadvantages related to the higher forming forces are not relevant, here. At the same time, the formability, characterised via the strain at failure, significantly increases at higher strain rates, which directly leads to a remarkable increase of the forming limits. Detailed knowledge about this will allow extending the design freedom in can production and enable completely new shapes and details. This general trend also suggests that the use of high speed forming techniques as electromagnetic forming, during which even higher strain rates of up to 104 $s^{-1}$ are reached (Psyk et al., 2011), is predestined for fully exploiting this potential.

# References

Abbadi, M., Hähner, P., & Zeghloul, A. (2002). On the characteristics of Portevin–Le Chatelier bands in aluminum alloy 5182 under stress-controlled and strain-controlled tensile testing. Materials Science and Engineering(A337), pp. 194 - 201.

Achhammer, K.-H., & Auburger, M. (2015, February 25th). Patent No. EP2838834 A1.

Ball Europe. (2016). Retrieved 01 2016, 14, from http://www.ball-europe.com/businesscards/de/911.htm

Feucht, M.; Neukamm, F.; Haufe, A. (2011). A Phenomenological Damage Model to Predict Material Failure in Crashworthiness Applications. In: Recent Developments and Innovative Applications in Comp. mechanics, Müller-Höppe, et al., Springer Berlin Heidelberg.

DIN EN ISO 6892-1. (2009). Metallische Werkstoffe - Zugversuch - Teil 1: Prüfverfahren bei Raumtemperatur. 81. Berlin: Beuth Verlag.

Kaup, B. (2003). Optimierung der Umform- und Gebrauchseigenschaften von tief entkohltem Stahl zur Fertigung von zweiteiligen Getränkedosen. Aachen: Shaker Verlag.

LSTC (2015). LS-DYNA Keyword User's Manual. Volume II. Livermore Software Technology Corporation (LSTC)

Meyer, L. W., Herzig, N., Halle, T., & Abdel-Malek, S. (2009, March 12th). Werkstoffverhalten bei hohen Dehnungsgeschwindigkeiten. Workshop Impulsumformung.

Psyk, V., Risch, D., Kinsey, B. L., Tekkaya, A. E., & Kleiner, M. (2011). Electromagnetic Forming - A Review. Journal of Materials Processing Technology (211), pp. 787 - 829.

Statista GmbH. (2015, September). Absatz von Getränkedosen in Europa nach Bereichen bis 2014 | Statistik. Retrieved 11 02, 2015, from http://de.statista.com/statistik/daten/studie/215739/umfrage/anzahl-der-getraenkedosen-von-bier-und-alkoholfreien-getraenken-in-europa/

Taylor, J. R. (1988). Fehleranalyse. VCH Verlagsgesellschaft, Weinheim-Basel-Cambridge-New York.

Weddige, H.-J. (2001). Stahl im Wettbewerb der Werkstoffe. Freiberg.

# Joining and Welding

# Influence of the Wall Thicknesses on the Joint Quality During Magnetic Pulse Welding in Tube-to-Tube Configuration

**J. Lueg-Althoff[1*], B. Schilling[1], J. Bellmann[2,3], S. Gies[1], S. Schulze[3], A. E. Tekkaya[1], E. Beyer[2,3]**

[1] Institute of Forming Technology and Lightweight Construction, TU Dortmund University, Germany
[2] Institute of Manufacturing Technology, TU Dresden University, Germany
[3] Fraunhofer Institute for Material and Beam Technology, Dresden, Germany
[*]Corresponding author. Email: Joern.Lueg-Althoff@iul.tu-dortmund.de

## Abstract

*The implementation of multi-material concepts, for example, in automotive engineering or aerospace technologies, requires adequate joining techniques. The Magnetic Pulse Welding (MPW) process allows for joining both similar and dissimilar materials without additional mechanical elements, chemical binders, or adverse influences of heat on the joining partners. In this process, an electro-conductive at ('flyer') part is accelerated by Lorentz forces and impacts the inner ('parent') part under high velocity and high pressure, leading to the formation of a metallurgical joint. Besides joining of sheets and tubes to solid cylinders, the connection of two tubes is of particular interest due to the increased lightweight potential. The present paper focuses on the MPW of aluminum (EN AW-6060) to steel (C45) tubes. An experimental study was performed, in which the wall thickness of the parent part was reduced successively. The deformation behavior of both the flyer and parent parts was recorded during the experiments by a two-probe Photon Doppler Velocimeter (PDV). The final shape of the joined specimens was analyzed by a 3D digitizer. An instrumented peel test was used for the determination of the weld quality. It was found that defect-free MPW of aluminum tubes on steel tubes without supporting mandrel is possible.*

## Keywords

Joining, Welding, Magnetic pulse welding

# 1 Introduction

Lightweight design concepts pursue the objective to reduce the weight of components without decreasing their functionality. For example, solid cylinders are replaced by hollow parts whenever possible. In material lightweight concepts, the aim is to choose the optimum material for every single component of a structure. Considering this background, the combination of the described concepts leads to an increasing demand of joining weight optimized parts made from different materials (Gude et al., 2015). Especially the joining of materials with very different physical properties (e.g., melting point and thermal conductivity) is challenging for conventional thermal joining techniques. In many cases, thermally induced defects like cracks and distortion cannot be avoided (Kapil and Sharma, 2015).

Magnetic Pulse Welding (MPW) is an impact welding process used to create solid-state joints without adverse influence of heat. The joint results from the collision of the joining partners at a certain angle $\beta$ at radial impact velocities $v_r$ of up to several hundred m/s and pressures of up to a few thousand MPa. Flat or tubular overlap joints can be fabricated, allowing for the application as a joining process for frame structures or torque tubes (Mori et al., 2013). **Fig. 1** explains the MPW process using the example of a tube-to-tube connection made by electromagnetic compression showing the basic process principle (b), a schematic illustrating the processes at the collision line (a), and an example aluminum-steel joint (c). The process variant of MPW by electromagnetic compression is the one investigated within the presented study.

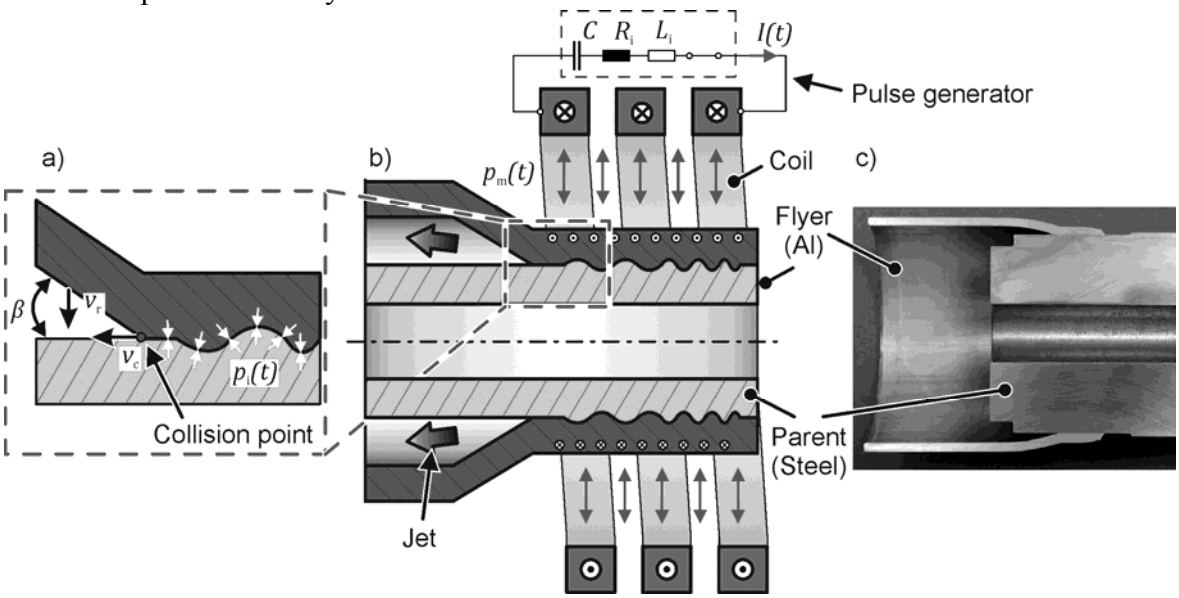


***Figure 1**: a) Processes at the collision zone, b) Process principle of magnetic pulse welding, c) Example of an aluminum-steel joint*

In the following, the MPW process is described briefly. The electric energy stored in a capacitor bank is discharged within several microseconds through a compression coil resulting in a damped sinusoidal current of several hundred kiloamperes. The accompanying

magnetic field induces an opposing secondary current in the electroconductive outer workpiece, the so-called flyer. Lorentz forces, which can mathematically be described by the magnetic pressure $p_m(t)$, are created between coil and flyer resulting in an acceleration of the flyer as soon as the yield stress of the material is exceeded. The flyer and the fixed inner part ('parent') collide under high pressure and at high velocities. The rapid movement of the collision front leads to the formation of a so-called "jet", which cleans the surfaces of the joining parts and leaves them chemically pure, favoring the creation of metallic bonds under the prevailing interface pressure $p_i(t)$.

Due to the mentioned advantages in combination with many unsolved questions, MPW has caused an increasing interest among research institutes and industrial users in recent years. Very active research fields are the expansion of weldable material combinations, the in-depth analysis of the relevant process parameters, an improvement of the tools with regard to durability and numerical simulations to enlighten the actual joining mechanism. (Kapil and Sharma, 2015)

Great effort has been put into analyzing the influence of surface characteristics like roughness (Geyer et al., 2014) and the geometric features of the flyer part, e.g., the wall thickness. However, several researchers have shown interest in the characteristics of the parent. Ben Artzy et al. related the thickness of the parent part to the shockwave characteristics and the interfacial wave formation (Ben-Artzy et al., 2010).

Tamaki and Kojima (1988) investigated several parameters of the MPW process with aluminum flyer tubes (29 mm outer diameter, 1 mm wall thickness) on aluminum parents with different wall thicknesses. They found out, that with an increasing wall thickness of the parent part, the weld quality (defined as the ratio of the welded portion along the circumference to the circumference; measured by peel testing) increases from approx. 50 % at 2 mm up to 100 % for wall thicknesses greater 6 mm. The reasons for this observation were not investigated.

Cui et al. (2016) presented a study of tube-to-tube MPW with aluminum flyer and steel parent (flyer: 20 mm outer diameter, 1 mm wall thickness; parent: 15.2 mm outer diameter, 1.5-4 mm wall thickness). They define a critical parent tube thickness depending on the discharge voltage. Below the critical thickness value, tensile testing of joints results in a separation at the welding zone. Above the critical value the joint fails in the base aluminum. The authors present an analytical approach for the calculation of the plastic deformation of the inner part based on Lame's equations for the stresses in tubes depending on the acting inner and outer pressures.

Usually, joining by forming of tubular workpieces is performed with the help of stabilizing mandrels inserted into the parent part (e.g., Weddeling, 2015). This prevents a deformation of the parent but has the risk of jamming after the process. The objective of this paper is to analyze the deformation behavior of the unsupported parent part and to provide guide values for mandrel-free MPW in tube-to-tube configuration.

# 2 Experimental Setup

## 2.1 Materials and Tools

The deployed flyer parts had an outer diameter of 40 mm and wall thicknesses $s_f$ of 1.5 and 2 mm. They were manufactured out of EN AW-6060 (T66), which is a common alloy for various lightweight applications. Selected tubes were heat-treated at 500 °C for 1 h with subsequent air cooling in order to reduce the strength. The measured yield stress was 60 MPa in the heat-treated and 222 MPa in the T66 state, determined by tensile tests. The parent tubes out of C45 steel had an outer diameter of 32, 33, or 34 mm and a wall thickness $s_p$ of 1-8 mm. The initial standoff $a$ between flyer and parent was 1.5 and 2 mm, respectively. **Fig. 2a** illustrates the geometrical setup.

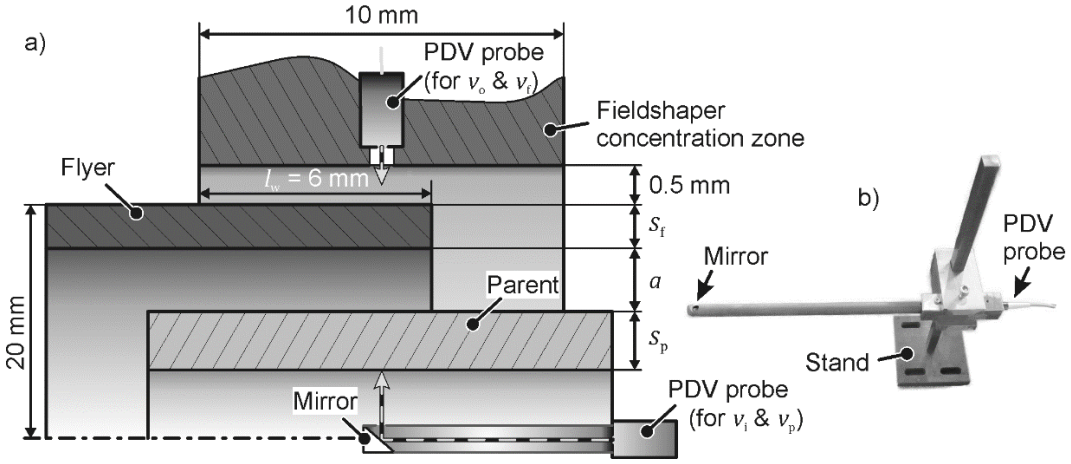


***Figure 2**: a) Experimental setup and PDV measurement devices, b) PDV periscope*

MPW experiments at various discharge energy and frequency levels were performed with a Maxwell Magneform 7000 32 kJ pulse generator. This machine consists of four capacitor banks with different characteristics, which can be used in variable combinations, influencing the properties of the discharge current. The bank configurations 2+3 (A) and 3+4 (B) were used during this study, see **Table 1**. An eight-turn compression coil with an inner diameter of 97 mm and a length of 90 mm in combination with a fieldshaper with a 10 mm long concentration zone and an inner diameter of 41 mm was used. The working length $l_w$ was set at 6 mm.

| | **Maxwell Magneform A (Bank 2+3)** | **Maxwell Magneform B (Bank 3+4)** |
|---|---|---|
| Max. charging energy $E_{max}$ | 12 kJ | 8 kJ |
| Max. charging voltage $U_{max}$ | 8.16 kV | 8.16 kV |
| Inner capacitance $C_i$ | 362 µF | 251 µF |
| Inner inductance $L_i$ | 78 nH | 100 nH |
| Inner resistance $R_i$ | 5.4 mΩ | 6.8 mΩ |
| Resonant frequency $f$* | 29 kHz | 31 kHz |

***Table 1**: Characteristics of the pulse generator configurations*

## 2.2 Measurement Technology

Coil current measurements were conducted for each trial using a Rogowski current probe CWT 3000 B from Power Electronic Measurements Ltd. For recording the radial impact velocities $v_r$ and calculating of the final displacement $h$, a collimator style PDV probe was integrated into the concentration zone of the fieldshaper (Fig. 2a). This idea was first presented by Jäger and Tekkaya (2012) and the concept proved to be suitable for measuring the velocities in MPW experiments (e.g., Lueg-Althoff et al., 2014). In that reference, the technical details of the applied PDV system are described. The deformation behavior of the parent part was monitored by a second, focuser style PDV probe (**Fig. 2b**). The laser beam was directed onto the inner parent surface at the area of impact by a mirror made of polished aluminum, which deflects the laser beam at 90°, see Fig. 2.
The welded specimens were mechanically tested with an instrumented 90° peel testing device integrated into a Zwick Z250 tensile testing machine (see Hahn et al., 2016 for the testing setup) and a straight tensile test. Selected welded specimens were digitized by a GOM ATOS 3D digitizer and micrographs of the joint zone were investigated with a Zeiss Axio Imager.M1m optical microscope.

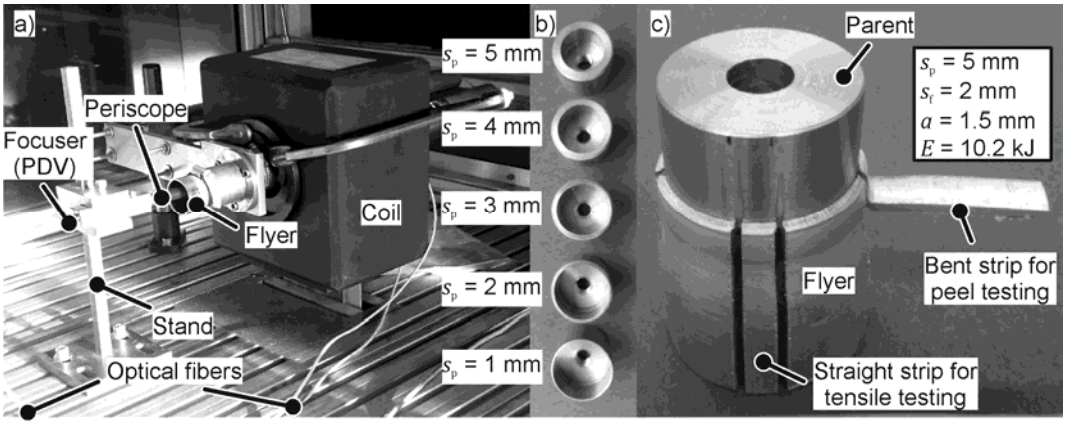


***Figure 3**: a) Experimental setup, b) Parent parts, c) Joined specimen*

# 3 Results and Discussion

## 3.1 Calibration Experiments

The parameters for the experiments were chosen on the basis of successful MPW experiments with solid parent parts and were adapted to the thickness of the flyer part. For every trial, the discharge current $I(t)$ and the PDV recordings were evaluated. The capacitor bank configuration of the pulse generator was chosen in a way that allowed high enough current amplitudes as well as discharge frequencies. The positioning of the periscope PDV probe was done in free compression experiments. **Fig. 4a** shows the result of PDV measurements of a free compression experiment of an aluminum tube (heat-treated state, wall thickness 2 mm) at 3.2 kJ in bank configuration B. There is a sufficient agreement between the graphs

for the inner and the outer tube surface, which confirms that the measurement was performed at the same axial position. The deviation between the peak velocities is 3.4 %.

**Fig. 4.b** shows example current and PDV curves of an MPW experiment; only the first half wave of the current path is depicted at 5.6 kJ (Maxwell configuration B). It can be seen that the acceleration of the flyer begins shortly after the current rises and that it impacts the parent after approx. 15 µs. At this moment, the periscope PDV probe starts recording a movement of the parent part surface. The first peak of the parent part movement is regarded as a measure for the deformation of the parent part. The peak velocity of flyer $v_{f,max}$ and parent $v_{p,max}$ were set into relation for further investigations.

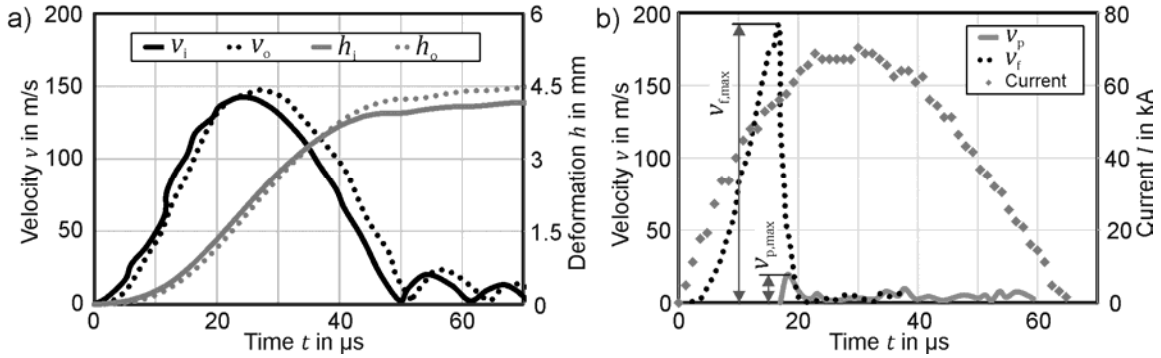


***Figure 4**: a) Measured velocity for a free compression experiment at 3.2 kJ, b) Measured current and velocity curves for an MPW experiment at 5.6 kJ*

## 3.2 Variation of Discharge Energy

In a first set of experiments, welding trials with a fixed flyer wall thickness $s_f$ and standoff $a$ of 2 mm were performed under varying discharge energies and a fixed discharge frequency of 8.7 kHz. **Fig. 5a** shows that an increase of the discharge energy (bank configuration B) leads to an increase of both the velocity of the flyer and the deformation velocity of the parent. The variations of the values at the same energies result from inaccuracies of the relative radial positioning of flyer to parent.

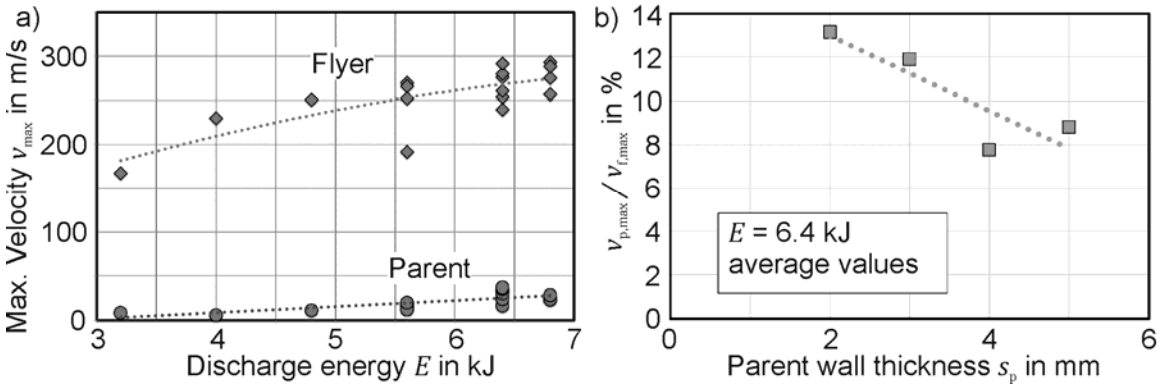


***Figure 5**: a) Peak velocities depending on the discharge energy, b) Ratio of $v_{p,max}$ and $v_{f,max}$ depending on the parent wall thickness*

**Fig. 5b** shows that a decrease of the parent wall thickness $s_p$ leads to an increase of the parent deformation velocity and, thus, to an increase of the ratio $v_{p,max}$ and $v_{f,max}$. It is not possible to determine if the parent is elastically or plastically deformed on the basis of the velocity curve alone. In order to answer this question, selected specimens were digitized with a 3D scanner and the inner contour of the parent part after MPW was compared to a perfect cylinder, see **Fig. 6**. For parent wall thicknesses $s_p$ greater than 3 mm (Fig. 6a), no permanent deformation of the parent was observed. A further reduction of $s_p$ still allows welding to take place; in Fig 6b, residual strips of the flyer material can be seen. However, the parent part experiences a permanent reduction of the radius in the area of impact of up to 0.23 mm. This zone is not distributed uniformly around the circumference due to the non-uniform field distribution (fieldshaper slot) and the mentioned inaccuracies in positioning.

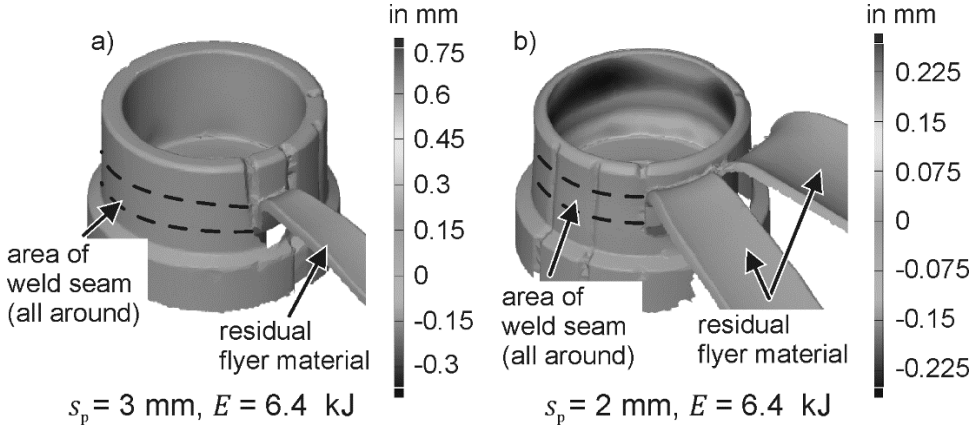


***Figure 6**: 3D scans of parent parts after MPW, Deviation compared to a perfect cylinder*

a)

| $s_p$ in mm | $E$ in kJ | Proof stress $R_{p0.01}$ in MPa | Tensile stress $R_m$ in MPa |
|---|---|---|---|
| 5 | 5.6 | 50 | 61 |
| 4 | 6.4 | 105 | 146 |
| 4 | 6.4 | 92 | 98 |
| 3 | 6.4 | 82 | 120 |
| 3 | 6.4 | 72 | 87 |
| 3 | 6.8 | 95 | 113 |
| 2 | 6.4 | 104 | 147 |
| 2 | 6.8 | 68 | 78 |

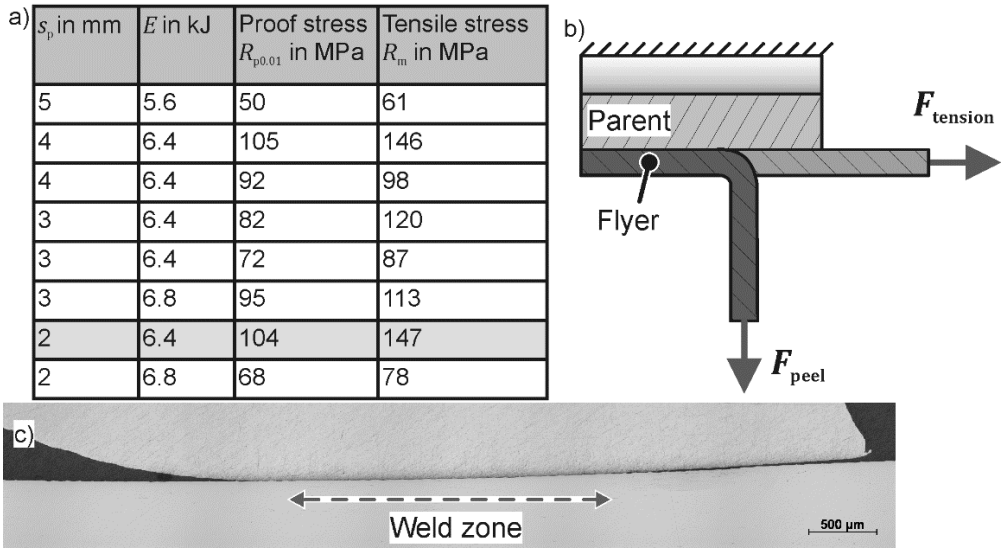


***Figure 7**: a) Results of tensile test, b) Schematic for tensile and peel test, c) Micrograph of welded specimen*

The quality of the welding results was determined in tensile tests. Strips with a width of approx. 6 mm were axially cut off the specimens. The specimens were clamped in a

Zwick Z 250 tensile testing machine and then axially loaded with a tension force. The force and the displacement were recorded. **Fig. 7a** shows that, for the given parameters, successful welding in tube-to-tube configuration by MPW is feasible without using supporting mandrels. The proof stress exceeds the flow stress of the aluminum alloy due to strain hardening mechanisms. The micrograph of a specimen with $s_p = 2$ mm (**Fig. 7c**, specimen refers to shaded row in Fig. 7a) shows an approx. 2.5 mm weld zone starting approx. 2 mm from the free flyer edge.

## 3.3 Variation of Flyer Material, Flyer Wall Thickness, Initial Standoff and Discharge Frequency

In a second set of experiments based on the previous results, several other process parameters were varied. All experiments were carried out in a capacitor bank configuration B (see Table 1), which allows higher discharge energies but limits the discharge frequency to 7.1 kHz. Two different flyer wall thicknesses $s_f$ were used (1.5 and 2 mm). The experiments with $s_f$ = 1.5 mm were performed with an initial standoff $a$ = 2 mm and a discharge energy $E$ of 9.6 kJ, those with $s_f$ = 2 mm were performed with $a$ = 1.5 mm and $E$ = 10.2 kJ. The thickness of the parent part $s_p$ was varied between 1 and 5 mm. **Fig. 8** summarizes the results of the velocity measurements. As seen before, the maximum deformation velocity $v_{p,max}$ of the parent part rises with decreasing $s_p$. The flyer parts out of the softer, heat-treated material reach approx. 10 % higher impact velocities than those in T66 state, which leads to higher deformation velocities of the parent parts and thus to an increasing ratio of $v_{p,max}$ / $v_{f,max}$ (Fig. 8). The increasing velocity ratio is also reflected by an increasing deformation of the parent part.

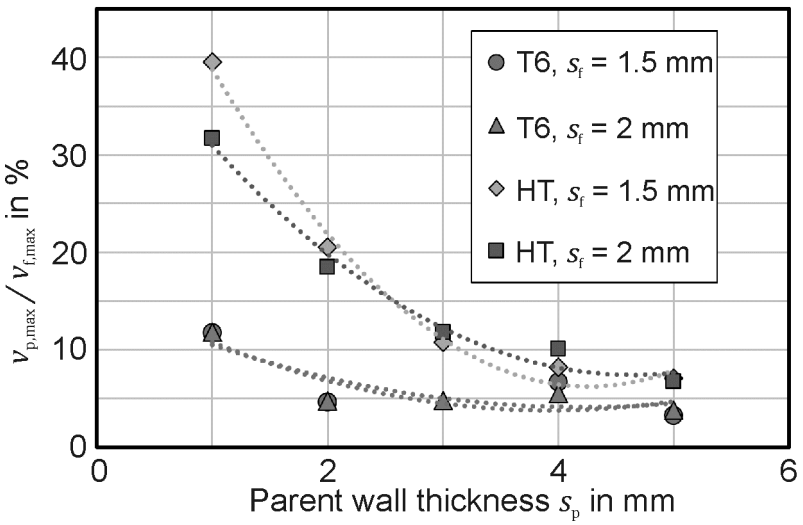


***Figure 8**: Velocity measurements for the second set of experiments, HT = heat treated*

The specimens in T66 state did not undergo welding. Apparently, the reached impact velocities (maximum of 240 m/s for the 1.5 mm specimens) were not high enough for metallurgical bonding. The heat-treated specimens underwent welding and were tested in a 90°

peel test, which applies a very severe loading perpendicular to the weld seam. **Fig. 9a** summarizes the results of this test, the stress values correspond to the width and the thickness of the metal strips. Due to the specific force application, the stress values are below the ones of the 0° tensile test. For the specimen marked with *, the peel test had to be stopped due to a beginning plastic deformation of the parent. The parent parts with $s_p$ = 1 mm wall thickness deformed heavily during the experiments (see **Fig. 9b**), the flyer was basically crimped onto the parent, the joint failed under low loadings.

a)

| $s_p$ in mm | $s_f$ in mm | Maximum stress in MPa |
|---|---|---|
| 5 | 1.5 | 56 |
| 4 | 1.5 | 56 |
| 3 | 1.5 | 52 |
| 5 | 2 | 96 |
| 4 | 2 | 34 |
| 3 | 2 | 40 |
| 2 | 2 | 79* |

b)

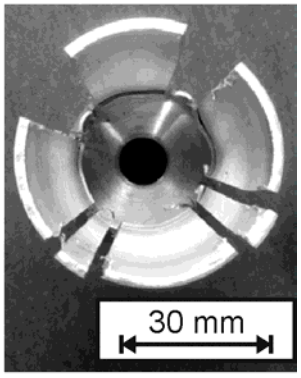


***Figure 9**: a) Results of 90° peel test, flyers were in heat-treated state, b) Deformed thin-walled parent part*

# 4 Conclusions and Outlook

- A periscope-style PDV probe was developed and successfully applied for inline measurement of the deformation of hollow parent parts in MPW.
- Thin-walled steel parent parts of down to the thickness of the aluminum flyer part can be welded by MPW without supporting mandrel.
- Parent wall thicknesses smaller than that of the flyer lead to plastic deformation of the parent, but welding can still be achieved.
- On the basis of the presented study, an estimation of the deformation of hollow mandrels with specific wall-thickness during MPW can be conducted.

For future investigations, an analytical correlation of mechanical parameters of the parent material and the impact conditions is planned in order to predict the deformation behavior. Existing models of shock wave propagation and their influence on the weld formation should be reviewed for the given setup.

## Acknowledgments

The presented results originate from research carried out within the subproject A1 of the priority program 1640 (“joining by plastic deformation”) funded by the German Research Foundation (DFG). The financial support is greatly acknowledged.

## References

Ben-Artzy, A., Stern, A., Frage, N., Shribman, V., Sadot, O., 2010. Wave formation mechanism in magnetic pulse welding. International Journal of Impact Engineering 37 (4), pp. 397–404.

Cui, J., Sun, G., Xu, J., Xu, Z., Huang, X., Li, G., 2016. A study on the critical wall thickness of the inner tube for magnetic pulse welding of tubular Al–Fe parts. Journal of Materials Processing Technology 227, pp. 138–146.

Geyer, M., Rebensdorf, A., Böhm, S., 2014. Influence of the boundary layer in magnetic pulse sheet welds of aluminium to steel. In: Huh, H., Tekkaya, A.E. (Eds.), High Speed Forming 2014, Proceedings of the 6th International Conference, Daejeon, Korea, pp. 51-60.

Gude, M., Meschut, G., Zäh, M.F., Lieberwirth, H., 2015. Chancen und Herausforderungen im ressourceneffizienten Leichtbau für die Elektromobilität – FOREL-Studie, http://plattform-forel.de/wp-content/uploads/2015/05/FOREL-Studie.pdf

Hahn, M., Weddeling, C., Lueg-Althoff, J., Tekkaya, A.E, 2016. Analytical approach for magnetic pulse welding of sheet connections. Journal of Materials Processing Technology 230, pp. 131–142.

Jäger, A., Tekkaya, A.E., 2012. Online measurement of the radial workpiece displacement in electromagnetic forming subsequent to hot aluminium extrusion. In: Tekkaya, A.E., Daehn, G.S., Kleiner, M. (Eds.), High Speed Forming 2012, Proceedings of the 5th International Conference, Dortmund, Germany, pp. 13-22.

Kapil, A., Sharma, A., 2015. Magnetic pulse welding: an efficient and environmentally friendly multi-material joining technique. Journal of Cleaner Production 100, pp. 35-58.

Lueg-Althoff, J., Lorenz, A., Gies, S., Weddeling, C., Göbel, G., Tekkaya, A.E, Beyer, E., 2014. Magnetic pulse welding by electromagnetic compression: Determination of the impact velocity. Advanced Materials Research 966-967, 489–499.

Mori, K., Bay, N., Fratini, L., Micari, F., Tekkaya, A.E., 2013. Joining by plastic deformation. CIRP Annals – Manufacturing Technology 62 (2), pp. 673-694.

Tamaki, K., Kojima, M., 1988. Factors affecting the result of electromagnetic welding of aluminum tube. Transactions of the Japan Welding Society 19 (1), 53–59.

Weddeling, C., 2015. Electromagnetic Form-Fit Joining, Dr.-Ing. Dissertation, Dortmund, Germany.

# Impact Welding Structural Aluminium Alloys to High Strength Steels Using Vaporizing Foil Actuator

**B. Liu*, A. Vivek, G. S. Daehn**

Department of Materials Science and Engineering, The Ohio State University, USA
*Corresponding author. Email: liu.2004@osu.edu

## Abstract

*Dissimilar Al/Fe joining was achieved using vaporizing foil actuator welding. Flyer velocities up to 727 m/s were reached using 10 kJ input energy. Four Al/Fe combinations involving AA5052, AA6111-T4, JAC980, and JSC1500 were examined. Weld samples were mechanically tested in lap-shear in three conditions: as-welded, corrosion-tested with e-coating, and corrosion-tested without coating. In all three conditions, the majority of the samples failed in the base aluminium instead of the weld. This shows that the weld was stronger than at least one of the base materials, both before and after corrosion testing. Galvanic corrosion was not significant since the differences in open cell potential, which represent the driving forces for galvanic corrosion, were small among these materials—no more than 60 mV in all cases. Nonetheless, through corrosion testing, the base materials suffered general corrosion, which accounted for the weakening of the base materials.*

## Keywords

Vaporizing foil actuator welding, Ultra-high strength steel, Aluminium

## 1 Introduction

Vehicle lightweighting has been a major push among automakers, largely due to increasing cost of energy and aggressive fuel efficiency goals (Joost, 2012). Conventional car bodies are mainly made of steel, but their weight can be reduced by substituting components of the car body for materials that provide higher specific strengths, such as structural aluminium alloys and high-strength steels. However, the incorporation of these materials calls for effective joining techniques, and since these materials are often drastically

different from one another, joining them together is often a nontrivial task. Fusion-based welding such as resistance spot welding, which is most common in automotive manufacturing, is usually not suitable for dissimilar joining due to melting point disparities between materials to be welded and the tendency for brittle intermetallic compounds (IMCs) to form in the fusion zone (Qiu et al., 2009). Furthermore, the heat effect from fusion welding also deteriorates the properties of the base material around the weld (Hwang and Chou, 1998). Non-welding techniques, such as fastening coupled with adhesive bonding, provide alternate means of dissimilar joining (Abe et al., 2006; Barnes and Pashby, 2000; Mori et al., 2006). However, fasteners add weight and cost. In high volume production this inhibits the widespread use of fasteners. Solid-state welding techniques such as friction-stir welding and related techniques such as refill friction stir spot welding can join some combinations of dissimilar materials without copious IMCs (Jana et al., 2010; Watanabe et al., 2006; Fukada et al., 2013), but cycle time and geometrical constraints have also limited their application. While many of these techniques have their merits, there is still need for a breakthrough technique that can perform dissimilar metal joining effectively, economically, and flexibly.

In this study, welding was carried out using vaporizing foil actuator welding (VFAW) (Vivek et al., 2013), a solid-state impact welding technique. VFAW is similar to explosion welding (EXW) (Acarer & Demir, 2008) and magnetic pulse welding (MPW) (Manogaran et al., 2014) in that it welds materials in solid-state by means of a high-speed oblique impact that takes place between the two materials being welded. Such an impact forces the oxide films on the colliding surfaces to be ejected in the form of a jet (Abrahamson, 1961), and brings nascent surfaces into atomistically intimate contact, thus creating a metallurgical bond (Mårtensson and Schweitz, 1985). Since impact welding does not require heating and melting, IMC formation can largely be avoided, given appropriate welding parameters. However, in the case where impact energy is excessive, the severe shear deformation near the weld interface may give rise to localized heating and even melting, leading to the formation of IMCs. In many cases, a small amount of IMCs along the weld interface is acceptable, as long as they are thin and discontinuous. It also matters what types of IMCs are present, since some IMCs are more brittle than others (Lei et al., 2015). In any case, understanding the nature and distribution of IMCs present at the weld interface is critical to predicting the properties of the joint.

Another concern with dissimilar joining is galvanic corrosion. In the case of Al/Fe joining, which is highly sought after in the automotive industry, aluminium is often the more anodic element of the pair and is corroded at an accelerated rate. One way to mitigate galvanic corrosion is to create a graded transition joint, where the corrosion potential changes gradually, but this is often difficult or expensive to achieve. A more common way is to use insulating layers to either separate the galvanic couple or isolate the entire joint area from corrosive environment. The former can be done with non-welding techniques, such as fastening coupled with adhesive bonding, or by augmenting the weld with a coating, seal or gasket. Where welding is employed, only the latter strategy against galvanic corrosion is available, typically in the form of a passivation coating, such as e-coating.

The success of impact welding largely depends on two parameters: the angle and speed of the impact. In order to obtain a successful impact weld, these two parameters must fall within some optimal range, known as the welding window (Mousavi and Sartangi 2009). In VFAW, welding typically takes place along the outer perimeter of the active area of the foil actuator, forming a race-track-shaped weld zone (**Fig. 1(a)**). Wavy features can be found at the weld interface, and they are characteristic of impact welding processes (Ben-Artzy et al., 2008). The center of the impacted area is typically not welded because the impact angle is too low. The bonded flyer has a complex shape due to the initial standoff (**Fig. 1(b)**).

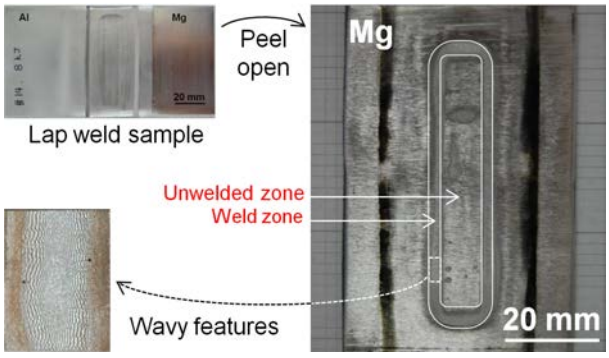


*(a)*


*(b)*

***Figure 1**: (a) Top view of a peeled VFAW joint. (b) Side cross section of a VFAW joint*

## 2 Experimental Method

In this study, four Al/Fe combinations were welded using VFAW:

- AA5052/JAC980
- AA5052/JSC1500
- AA6111-T4/JAC980
- AA6111-T4/JSC1500

The four combinations include two wrought aluminium alloys (AA5052 and AA6111-T4) and two high strength steels (JAC980 and JSC1500). All four alloys are of high interest in the automotive industry. JAC980 is dual-phase steel with minimum ultimate tensile strength of 980 MPa, and JSC1500 is boron steel with minimum ultimate tensile strength of 1500 MPa. JAC980 is galvannealed steel, with a zinc coating. JSC1500 was hot-rolled and was covered with mill scale. To provide a study on the joining of base materials, the surface layers of both steels were removed by surface grinding, in the areas

where welding was to take place. About 0.1 to 0.2 mm of material was removed from each steel plate.

The welding event can be characterized by voltage and current traces using an oscilloscope. Flyer velocities were measured in separate experiments using photonic Doppler velocimetry (PDV) (Strand et al., 2006; Vivek et al., 2014). The welded joints were studied by mechanical testing, cross-sectional microscopy, and corrosion testing.

Six weld coupons were made by VFAW, using the same welding parameters: 10 kJ input energy and 1.6 mm standoff. Of the six weld coupons, two were sectioned and mechanically tested in lap-shear. Sectioning was done by water jet, and each coupon yields two samples for testing, each sample measuring about 1/2 inch (12.7 mm) wide. An additional cross-section of the weld interface of each material combination was mounted and polished for metallography, using standard mounting and polishing procedures.

The remaining four weld coupons were subjected to 30 cycles of corrosion testing according to ASTM B-117 (5% NaCl salt spray, 30 °C, 24 hours/cycle). Of the four weld coupons, two were e-coated (by Electro Prime Inc., using POWERCRON® 6000CX) and two were left bare. After corrosion testing, the four coupons were sectioned by water jet and mechanically tested in lap-shear, the same way as first two weld coupons.

Overall, twelve test cases were explored (four material combinations and three test conditions: as-welded, corrosion-tested with e-coating, and corrosion-tested without e-coating). Four test samples were obtained for each case. A total of 48 samples were tested.

For additional corrosion characterization, the open cell potentials (OCP) of the base materials were measured individually in 5% NaCl solution at room temperature. To prepare for the tests, sheet metals were polished to 1200 fine grit. The Al alloys were polished in ethanol instead of water for 800 grit and beyond. Sample area was 1 $cm^2$. Corrosion pits were measured using optical profilometry.

# 3 Results and Discussion

## 3.1 Flyer Velocity Traces

Flyer velocity traces are shown in **Fig. 2**. The 1.6 mm standoff distance is taken to represent the impact velocity. The impact velocities were 700 m/s for the AA5052 flyer and 727 m/s for the AA6111-T4 flyer.

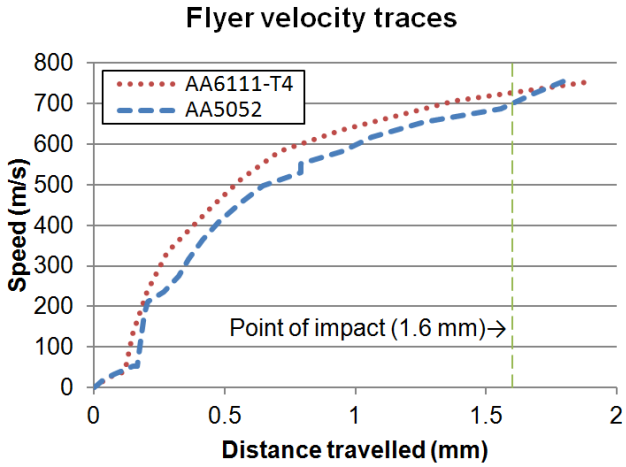


***Figure 2**: Flyer velocity traces*

## 3.2 Mechanical Testing

Mechanical testing results are summarized in **Fig. 3**. Majority (38 out of 48) of the test samples, both before or after corrosion testing, failed in the base aluminium, indicating that the weld, when loaded in lap-shear, was stronger than at least one of the base materials. Failure most frequently occurs near the bent area of the flyer. Of the ten samples that failed along the weld, seven failed prior to mechanical testing, perhaps due to weld defects or damage during sectioning and handing. Only three samples failed along the weld interface during mechanical testing.

After 30 cycles of B-117 corrosion testing, the e-coated AA5052/JAC980 samples only degraded 2.4% in strength. On the other hand, the e-coated AA5052/JSC1500 samples experienced an 18.4% decrease in strength, with two samples failing in the weld and two samples failing in the base Al. If one only counts the samples that failed in the base Al, however, the strength degradation was only 3.4%. The e-coated AA6111-T4 samples suffered more significant strength reduction than their AA5052 counterparts (20.0% for AA6111-T4/JAC980 and 34.0% for AA6111-T4/JSC1500). The uncoated samples underwent more significant strength reduction after corrosion testing: 36.8% reduction for AA5052/JAC980, 35.4% reduction for AA5052/JSC1500, 49.3% reduction for AA6111-T4/JAC980, and 47.2% reduction for AA6111-T4/JSC1500. Nonetheless, in both e-coated and uncoated conditions, majority of the samples still failed in base aluminium, rather than along the weld. This indicates that the strength degradation was largely due to deterioration of the base materials, not of the weld. No significant overall thickness reduction of base materials was detected, but localized corrosion pits did reduce the local cross section and can provide stress concentration.

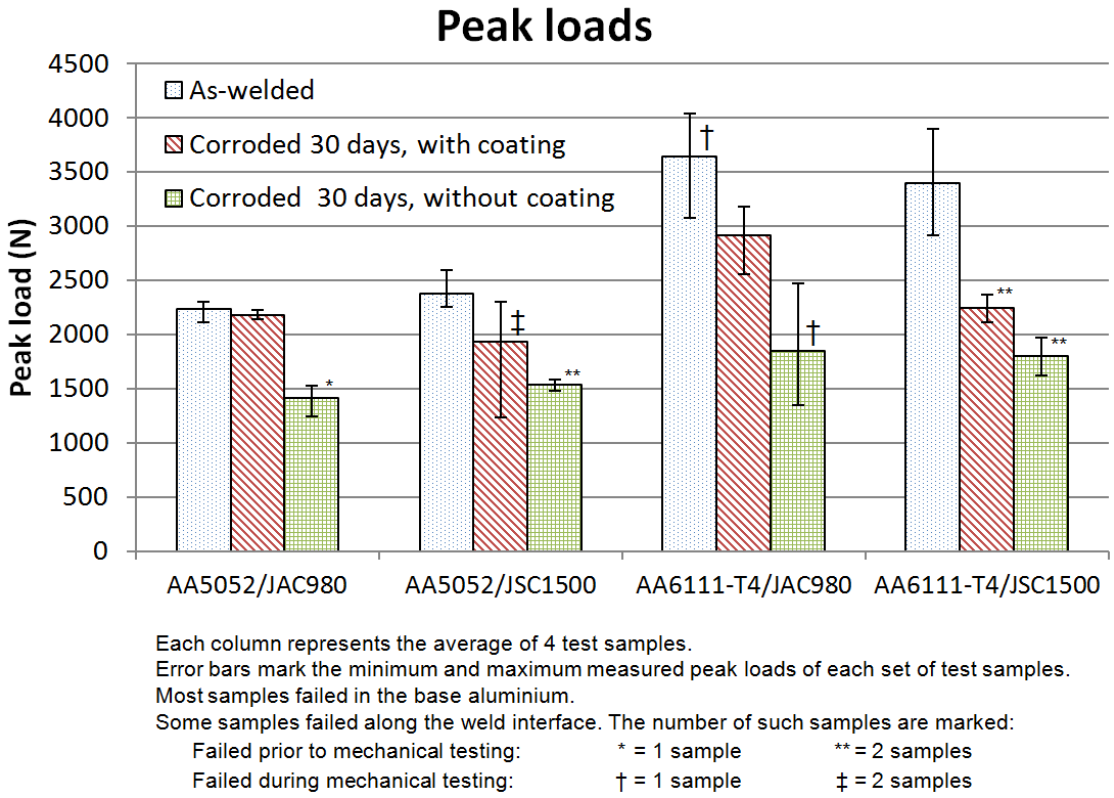


***Figure 3**: Peak loads at various test conditions*

## 3.3 Metallography

Wavy features, which are common to impact welding (Cowan et al., 1971), could be seen at the weld interfaces. The width of each welded area was about 2 mm, viewed from this cross section. The severe shear deformation near the weld interface can sometimes give rise to significant heating and mixing, which can lead to formation of intermediate phases, such as IMCs, especially at the trunks and tails of the waves, where mixing and heating are the most significant (Bahrani et al., 1967). Intermediate phases were present at the interfaces of all four welded material combinations (**Fig. 4**), but all four combinations also have IMC-free regions, which may account for most of the weld's toughness.

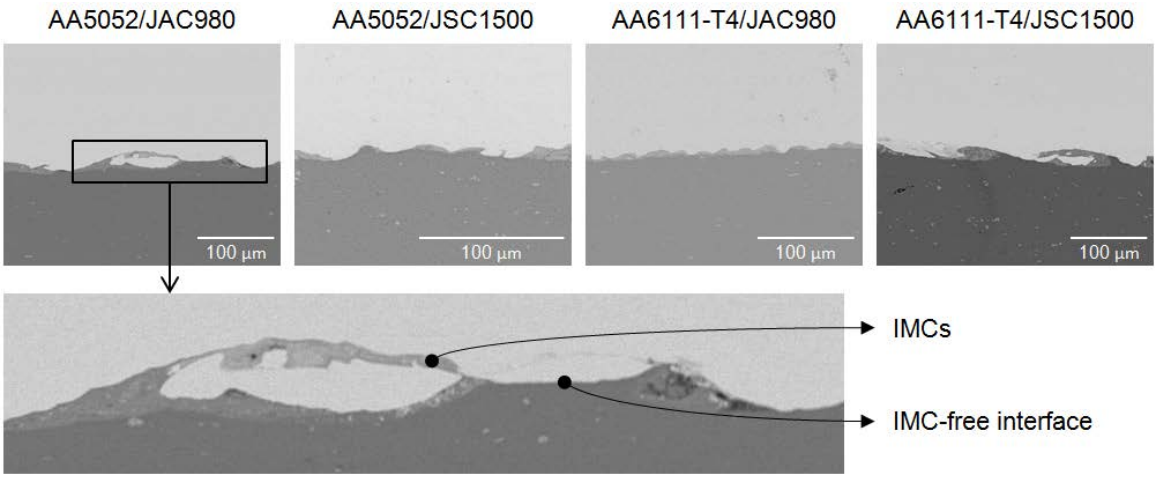


***Figure 4**: Backscattered electron images of weld cross sections*

## 3.4 Corrosion Characterization

Open cell potentials of the base materials are summarized in **Table 1**. Generally, aluminium is expected to be more anodic than steel and susceptible to galvanic corrosion when joined to steel. However, it turned out that the four materials had very similar OCP's, and in some cases, the steel was found to be more anodic than the aluminium. The largest difference in OCP was the one between JAC980 and AA6111-T4, with a magnitude of 0.060 V, which is rather small, for most applications. This is consistent with the fact that no significant galvanic corrosion was observed during corrosion testing of the weld coupons.

| Metal | OCP (V SCE) |
|---|---|
| AA5052 | -0.746 |
| AA6111-T4 | -0.698 |
| JAC980 | -0.758 |
| JSC1500 | -0.690 |

***Table 1:** Open cell potentials of base metals*

Corrosion pits were found near the bent area of the flyer (**Fig. 5**). This could be due to accumulation of salt and moisture in the crevice in this area. In addition, jetted materials from the welding process also could have accumulated here. Jetted materials are a mixture of particles from both base materials, their oxides, and other contaminants. As such, this mixture of materials could affect the corrosion characteristics in the areas where they accumulate. Once corrosion took place and localized corrosion pits formed, they acted as stress concentrators which weakened the base material in mechanical testing.

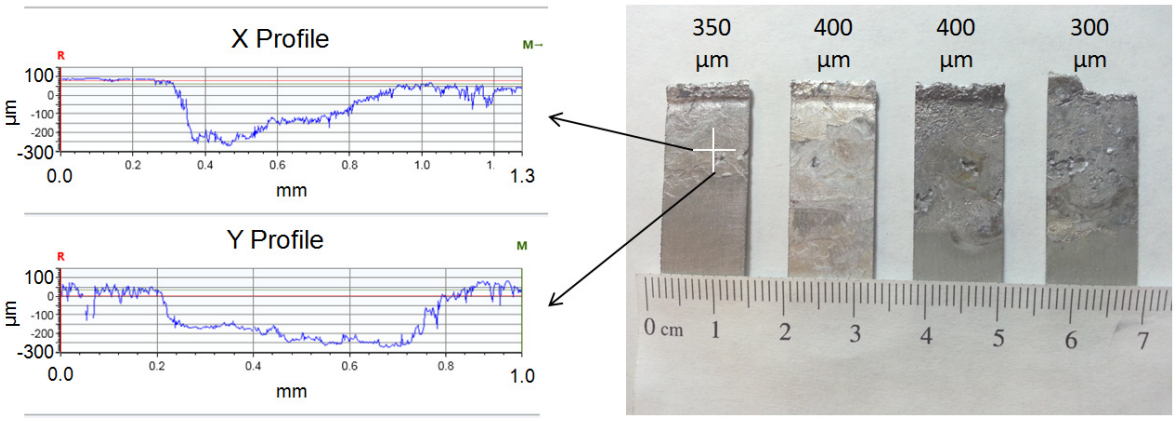


***Figure 5**: Corroded uncoated aluminium, extracted from the four weld combinations (ordered from left to right): AA5052/JAC980, AA5052/JSC1500, AA6111-T4/JAC980, AA6111-T4/JSC1500. Approximate depths of representative corrosion pits are indicated above each sample.*

## Conclusion

Four Al/Fe combinations of automotive aluminium and steel alloys were welded successfully using VFAW. In lap-shear testing, the majority of the test samples failed in the base aluminium, for all three test conditions (as-welded, corrosion tested with e-coating, and corrosion-tested without e-coating). This indicates that the shear strength of the weld exceeds the material strength of the base aluminium. Failure tended to occur in the bent area of the flyer. OCP's of all four materials were found to be very close to one another, and thus the effect of galvanic corrosion was not significant during corrosion testing of weld coupons. Pitting corrosion in the base aluminium near the bent area of the flyer weakened the materials, but the adverse effects of corrosion were mitigated by e-coating. In the case of corrosion testing AA5052/JAC980, the e-coated samples only lost 2.4% of their strength, while the uncoated samples lost 18.4%. Therefore effective isolation of the welded joint from the corrosive environment will be an important strategy against corrosion of dissimilar joints. This suggests that this process can be developed to join aluminium and steel with useful and predictable engineering properties and durability.

## Acknowledgement

The authors are thankful for sponsorship from the U.S. Department of Energy's Vehicle Technologies Office under grant no. DE-EE0006451. Special thanks go to Honda Motor Company for supplying JAC980 and JSC1500 used in this work. Many thanks go to Jichao Li, Benjamin Hanna, and Zhicao Feng for assisting with corrosion characterizations, and to Taylor Dittrich for acquiring SEM images and profilometry measurements.

# References

Abe, Y., Kato, T., Mori, K., 2006. Joinability of aluminium alloy and mild steel sheets by self piercing rivet. Journal of Materials Processing Technology, 177, 417–421. doi:10.1016/j.jmatprotec.2006.04.029

Abrahamson, G., 1961. Permanent periodic surface deformations due to a traveling jet. Journal of Applied Mechanics. Retrieved from http://appliedmechanics.asmedigitalcollection.asme.org/article.aspx?articleid=1394803

Acarer, M., Demir, B., 2008. An investigation of mechanical and metallurgical properties of explosive welded aluminum–dual phase steel. Materials Letters, 62(25), 4158–4160. doi:10.1016/j.matlet.2008.05.060

Bahrani, A. S., Black, T. J., Crossland, B., 1967. The mechanics of wave formation in explosive welding. Proceedings of the Royal Society of London. Series A. Mathematical and Physical Sciences, 296(1445), 123–136. Retrieved from http://rspa.royalsocietypublishing.org/content/296/1445/123.short

Barnes, T. A., Pashby, I. R., 2000. Joining techniques for aluminum spaceframes used in automobiles. Part II - adhesive bonding and mechanical fasteners. Journal of Materials Processing Technology, 99, 72–79. doi:10.1016/S0924-0136(99)00361-1

Ben-Artzy, A., Stern, A., Frage, N., Shribman, V., 2008. Interface phenomena in aluminium–magnesium magnetic pulse welding. Science and Technology of Welding and Joining, 13(4), 402–408. doi:10.1179/174329308X300136

Cowan, G. R., Bergmann, O. R., Holtzman, A. H., 1971. Mechanism of bond zone wave formation in explosion-clad metals. Metallurgical and Materials Transactions B, 2(November), 3145–3155. Retrieved from http://link.springer.com/article/10.1007/BF02814967

Fukada, S., Ohashi, R., Fujimoto, M., Okada, H., 2013. Refill friction stir spot welding of dissimilar materials consisting of A6061 and hot dip zinc-coated steel sheets. Proceedings of the 1st International Joint Symposium on Joining and Welding (pp. 183–187). Woodhead Publishing Limited. doi:http://dx.doi.org/10.1533/978-1-78242-164-1.183

Hwang, R. Y., Chou, C. P., 1998. The Study on Microstructural and Mechanical Properties of Weld Heat Affected Zone of 7075-T651 Aluminum Alloy, 38(2), 215–221.

Jana, S., Hovanski, Y., Grant, G. J., 2010. Friction stir lap welding of magnesium alloy to steel: A preliminary investigation. Metallurgical and Materials Transactions A: Physical Metallurgy and Materials Science, 41(December), 3173–3182. doi:10.1007/s11661-010-0399-8

Joost, W. J., 2012. Reducing Vehicle Weight and Improving U.S. Energy Efficiency Using Integrated Computational Materials Engineering. Jom, 64(9). doi:10.1007/s11837-012-0424-z

Lei, H., Li, Y., Carlson, B. E., Lin, Z., 2015. Cold Metal Transfer Spot Joining of AA6061-T6 to Galvanized DP590 Under Different Modes. Journal of

Manufacturing Science and Engineering, 137(NOVEMBER), 051028. doi:10.1115/1.4029093

Manogaran, A. P., Manoharan, P., Priem, D., Marya, S., Racineux, G., 2014. Magnetic pulse spot welding of bimetals. Journal of Materials Processing Technology, 214(6), 1236–1244. doi:10.1016/j.jmatprotec.2014.01.007

Mårtensson, N., Schweitz, J., 1985. Fundamental aspects of formation and stability of explosive welds. Metallurgical Transactions A, 16(May), 841–852. Retrieved from http://link.springer.com/article/10.1007/BF02814835

Mori, K., Kato, T., Abe, Y., Ravshanbek, Y., 2006. Plastic joining of ultra high strength steel and aluminium alloy sheets by self piercing rivet. CIRP Annals - Manufacturing Technology, 55(2), 283–286. doi:10.1016/S0007-8506(07)60417-X

Mousavi, S. A. A. A., Sartangi, P. F., 2009. Experimental investigation of explosive welding of cp-titanium/AISI 304 stainless steel. Materials Design, 30(3), 459–468. doi:10.1016/j.matdes.2008.06.016

Qiu, R., Iwamoto, C., Satonaka, S., 2009. Interfacial microstructure and strength of steel/aluminum alloy joints welded by resistance spot welding with cover plate. Journal of Materials Processing Technology, 209, 4186–4193. doi:10.1016/j.jmatprotec.2008.11.003

Strand, O. T., Goosman, D. R., Martinez, C., Whitworth, T. L., Kuhlow, W. W., 2006. Compact system for high-speed velocimetry using heterodyne techniques. Review of Scientific Instruments, 77(8), 083108. doi:10.1063/1.2336749

Vivek, A., Hansen, S. R., Daehn, G. S., 2014. High strain rate metalworking with vaporizing foil actuator: control of flyer velocity by varying input energy and foil thickness. The Review of Scientific Instruments, 85(7), 075101. doi:10.1063/1.4884647

Vivek, A., Hansen, S. R., Liu, B. C., Daehn, G. S., 2013. Vaporizing foil actuator: A tool for collision welding. Journal of Materials Processing Technology, 213(12), 2304–2311. doi:10.1016/j.jmatprotec.2013.07.006

Watanabe, T., Takayama, H., Yanagisawa, A., 2006. Joining of aluminum alloy to steel by friction stir welding. Journal of Materials Processing Technology, 178, 342–349. doi:10.1016/j.jmatprotec.2006.04.117

# Effects of Surface Coatings on the Joint Formation During Magnetic Pulse Welding in Tube-to-Cylinder Configuration

**J. Bellmann[1, 2*], J. Lueg-Althoff[3], G. Goebel[2, 4], S. Gies[3], E. Beyer[1, 2], A. E. Tekkaya[3]**

[1] Institute of Manufacturing Technology, TU Dresden, Germany
[2] Fraunhofer Institute for Material and Beam Technology, Dresden, Germany
[3] Institute of Forming Technology and Lightweight Construction, TU Dortmund, Germany
[4] University of Applied Sciences, Dresden, Germany
[*]Corresponding author. E-mail: Joerg.bellmann@tu-dresden.de

## Abstract

*Magnetic Pulse Welding (MPW) is a joining technique favorable for the generation of strong atomic bonded areas between different metals, e.g. aluminum and steel. Brittle intermetallic phases can be avoided due to the high-speed collision and the absence of external heat. The demand for the use of this technique in industries like automotive and plant engineering rises. However, workpieces used in these fields are often coated, e.g. in order to improve the corrosion resistance. Since the weld quality depends on the material's behavior at the collision zone, surface layers in that region have to be taken into account as well.*

*This work investigates the influences of different coating types. Aluminum to steel welding is used as an example system. On the inner steel part (C45) coatings like zinc, nickel and chrome are applied, while the aluminum flyer tubes (EN AW-6060) are anodized, chromated and passivated. Welding tests are performed using two different welding systems with varying discharging frequencies and four geometrical part setups. For all combinations, the flyer velocity during the process is measured by Photon Doppler Velocimetry (PDV). By using the uncoated material combination as a reference, the removal of surface layers due to jetting is analyzed. Finally, the weld quality is characterized in peel tests, shear-push tests and by the help of metallographic analysis. It is found that certain coatings improve the joint formation, while others are obstructive for the performance of MPW. Some coatings have no influence on the joining process at all.*

## Keywords

Joining, Welding, Magnetic pulse welding

# 1 Introduction

The production of modern lightweight designs often requires the use of different materials to fulfil the criteria regarding strength, weight reduction and crash performance. Besides the development of new materials, it is also of great importance to employ suitable joining technologies. Magnetic Pulse Welding (MPW) has a great potential for large-scale industrial production, since it is an efficient, clean, and fast process. It generates strong atomic bonding between two different materials like steel and aluminum without the formation of critical intermetallic phases. **Figure 1** shows the MPW-process for cylindrical parts in three steps. At first, the aluminum flyer tube and the steel parent part are placed into the tool coil (a). Through the discharging of high voltage capacitors through the coil, the resulting current generates a strong magnetic pressure $p_{mag}$ between the flyer tube and the inner side of the coil that consequently accelerates the tube towards the parent part until they collide (b). For certain favorable radial impact velocities $v_r$ and angles $\beta$ between both parts at the collision line that travels with the axial velocity $v_c$, a so called jet is formed. This mass flux contains oxides and surface debris of both joining partners and leaves two juvenile and activated surfaces. Under the high impact pressure welding takes place (c) (Deribas et al., 1975).

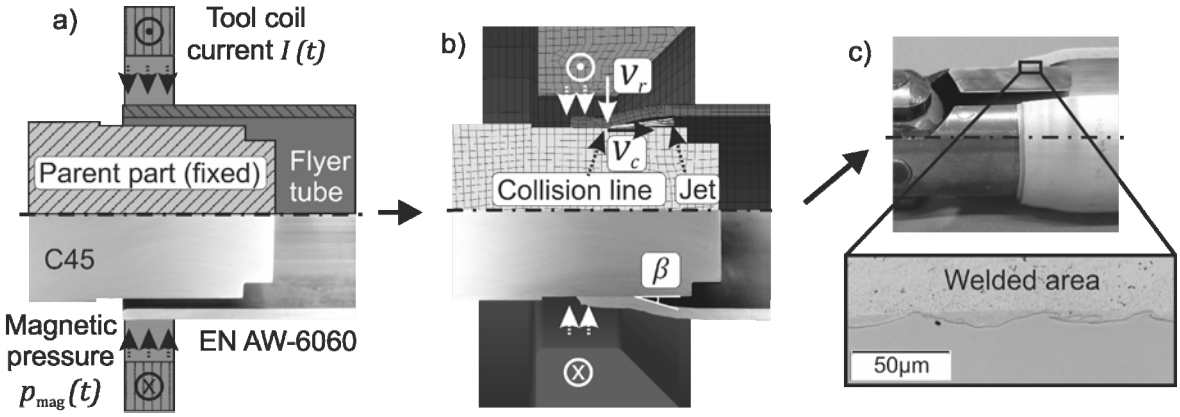


***Figure 1**: Magnetic Pulse Welding of cylindrical parts with a) positioning of flyer tube and parent part in the tool coil, b) forming and joining process, c) macroscopic and microscopic view on the cross section of the welded area*

Welding windows show radial impact velocities $v_r$ and angles $\beta$ that will lead to a welded area (Kapil and Sharma, 2015). This data can be evaluated experimentally or with the help of high velocity impact simulations, as e.g. Cuq-Lelandais et al. (2014) showed. They are valid for the base materials and in most cases do not take surface coatings into consideration. Coatings that are used to improve corrosion resistance or to reduce wear are typically applied on the semi-finished part. This means, every following production step has to cope with these additional layers. Especially in large-scale production, where MPW is nowadays a viable option, an extra process to remove the coating at the joining zone would increase the effort and costs.

The idea of this investigation is to gain an insight which typical industrial coatings are favorable or unfavorable for MPW weld quality. Assuming that other non-fusion welding techniques are influenced likewise, a short literature review is carried out first and reveals three types of interaction between the coatings and the joining partners:

I. Brittle surface coatings: Under high deformation, the layer fractures and the underlying surfaces are welded together due to the high pressure (e.g. Cold roll welding: Zhang and Bay, 1997). A direct welding on these coatings is also possible, but the coating can delaminate (Schäfer et al., 2011).

II. Thick and ductile layers: The layer absorbs a significant portion of the kinetic energy from the flyer during collision (e.g. Explosion welding (EXW): Manikandan et al., 2008).

III. Thin and ductile layers: Although not discussed in literature, thin layers (e.g. only few µm) would still retain chemical features but should probably influence the deformation behavior or the welding process much less than type II.

This paper aims at all three types and will expand the knowledge regarding compatibility of MPW with different coatings as well as the behavior of these surface layers within the process. Therefore, representative industrial coatings are chosen for both joining partners. Additionally, the influence of the pulse generator's discharge frequency is investigated for all coatings listed in **Table 1**.

| **Type** | **Flyer** | **Parent part** |
|---|---|---|
| I. Brittle | Anodized, hard anodized | Zinc, nitrated |
| II. Thick, ductile | - | Nickel |
| III. Thin, ductile | Acid passivated, chromated | Nickel, chrome |

***Table 1**: Typical coatings for flyer and parent part investigated in the present study*

# 2 Experimental Design

## 2.1 Joining Materials and Tools

The experimental investigation of the effect of different surface coatings on the pulse welding process is carried out on two pulse stations as shown in **Table 2.**

| **Setup** | **High Frequency** | **Low Frequency** | **Unit** |
|---|---|---|---|
| Pulse generator | Bmax MPW50/25 | Maxwell-Magneform 7000 | - |
| Capacity | 160 | 362 | µF |
| Maximum charging energy – $E$ | 32 | 12 | kJ |
| Discharge frequency with coil and workpieces - $f_{discharge}$ | 20 | 7 | kHz |
| Coil design | Single turn | 8-turn with field shaper | - |
| Ø Field shaper (see Table 3) | 42 | 41 | mm |

***Table 2**: Comparison of the pulse generators and tool coils*

The experimental setup is depicted in **Table 3**: the width of the field shaper, the working length and the outer diameter of the tube are fixed for all experiments. Varying parameters are the flyer thickness which is changed from $t = 1.5$ mm to $t = 2.0$ mm after half of the experiments, and the gap size $g$ which is set to 1.5 mm and 2.0 mm for both thicknesses. Since the gap is equivalent to the acceleration distance of the flyer, a value of 2.0 mm will lead to higher impact velocities than $g = 1.5$ mm. Furthermore, the collision angle $\beta$ will decrease with a smaller gap.

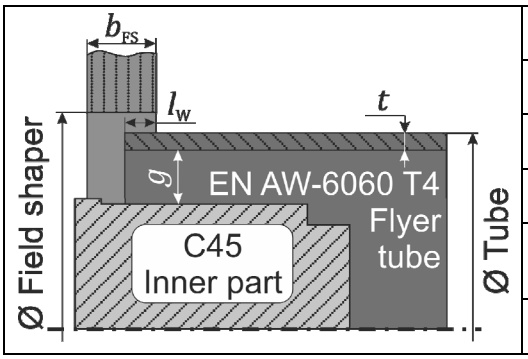


| Definition | Applied values [mm] |
|---|---|
| Width field shaper - $b_{FS}$ | 10.0 |
| Working length - $l_W$ | 6.0 |
| Ø Tube | 40.0 |
| Gap – $g$ (with corresponding Energy $E$) | 1.5 (10.2 kJ); 2.0 (9.6 kJ) |
| Thickness - $t$ | 1.5; 2.0 |

***Table 3**: Geometrical definitions in the experimental setup*

Based on the descriptions given in the introduction, **Table 4** exemplifies the surface coatings that were applied either on the outside of the parent part or on the inside of the flyer tube. To limit the number of surface combinations, all coated flyer tubes are joined to the as-received conditioned steel parts and the as-received aluminum tubes to the coated steel parts. The aim of the acid passivation is to reduce the native oxide layer on the aluminum and preserve this condition with a special passivation until it is joined in the MPW process. The objective is to extend the welded length compared to Al-Pure.

| **Parent part – C45 (St)** | | **Flyer tube – EN AW-6060 (Al)** | |
|---|---|---|---|
| C45, normalized, surface polished (Ra = 1) | | EN AW-6060, T66, heat treated (one hour at 500°C) | |
| **Property** | **Name** | **Property** | **Name** |
| As-received condition | St-Pure | As-received condition | Al-Pure |
| Electroplating nickel 5 µm | St-Ni5 | Anodized 5 µm | Al-An5 |
| Electroplating zinc 5 µm | St-Zn5 | Anodized 10 µm | Al-An10 |
| Electroplating zinc 10 µm | St-Zn10 | Hard anodized 15 µm | Al-HAn15 |
| PVD nickel vanadium 2.5 µm | St-PVD Ni2.5 | Chromated | Al-Cr |
| PVD chrome 1.5 µm | St-PVD Cr1.5 | Acid passivated | Al-AP |
| Nitrated | St-N | | |

***Table 4**: Explanation of surface coatings for steel and aluminum*

## 2.2 Experiment and Evaluation

Every uncoated part is cleaned in acetone to remove passivation oils and dirt before each welding experiment. Afterwards, both parts are positioned and fixed as indicated in Table 3 and the energy level is set to 10.2 kJ for a gap of 1.5 mm and 9.6 kJ for 2.0 mm,

since these are the minimum values to achieve welding at the Maxwell pulse generator. These energy levels are also set at the Bmax pulse generator to guarantee comparability.

The radial deformation velocity of the tube is measured with the PDV-system in the opposite direction of the field shaper's slot with an axial offset of 1.0 mm to the deformed edge of the flyer tube (Jäger and Tekkaya, 2012). After the joining process, flyers are cut once in axial direction to release the compressed tube. If it separates from the parent part during this procedure, the welding has not been successful. In the other case, the samples undergo further mechanical testing as suggested by Shribman (2006) in **Figure 2**. For the tests, stripes with a width of 5.0 (±1.0) mm are cut from the cylindrical part.

With the help of a peel test it is possible to identify the axial position x, where the weld strength is higher than the strength of the base material aluminum and fracture occurs. This value can be interpreted as weld quality along the welding front. The peel test is performed at four positions to the field shaper's slot: 45°, 135°, 225° and 315°. If the samples are not welded or fail during preparation, the value is defined to be zero.

The shear test reveals the shear strength of the welded area A and takes the mechanical properties of the surface coating between both parts into consideration. After the shear test the area A is measured and divided by the applied force $F_{max}$ which gives the shear strength. This is done at four positions in relation to the field shaper's slot: 0°, 90°, 180° and 270°. In addition metallographic analysis is performed on selected samples to identify the location and length of the welded areas. Therefore polished cross sections are prepared for the 90°-position to the field shaper's slot on samples that were not used for the shear test.

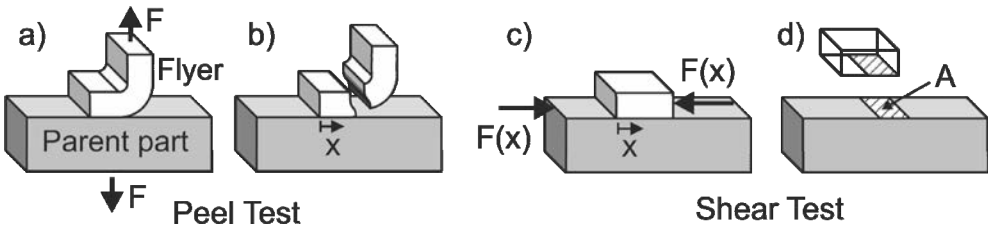


***Figure 2**: Mechanical testing methods for MPW-samples a) during and b) after peel test and c) during and d) after shear test*

# 3 Results

## 3.1 Experimental Results

The deforming behavior of the flyer tube strongly depends on the discharging frequencies of the electrical circuits and thus the pulse generators. If the charging energy is the same, it is obvious that a higher discharging frequency leads to higher flyer accelerations, earlier collisions and higher impact velocities. **Figure 3** shows these effects based on the measured velocities and collision times for all four geometrical combinations of the uncoated aluminum tubes. Furthermore, a gap of 2.0 mm leads to higher impact velocities compared to 1.5 mm since the acceleration distance is longer. The wall thicknesses have

only a small influence on the impact velocity, since the difference between the rigidity of the tube walls is small compared to the magnetic pressure. It was also found that the coatings on the aluminum tube do not affect the acceleration behavior, which is an important requirement for the comparison of the experiments. Using the uncoated parts as references, welding with the same energy was achievable at both discharging frequencies for nickel- and chrome-plated steel parts as well as acid passivated and chromated aluminum tubes. Nitrated and electroplated zinc steel parts and nearly all kinds of anodized tubes were not weldable with the chosen parameters. Within this study, welding of anodized aluminum was only possible for a wall thickness of 1.5 mm with high impact velocities and gaps of 1.5 or 2.0 mm.

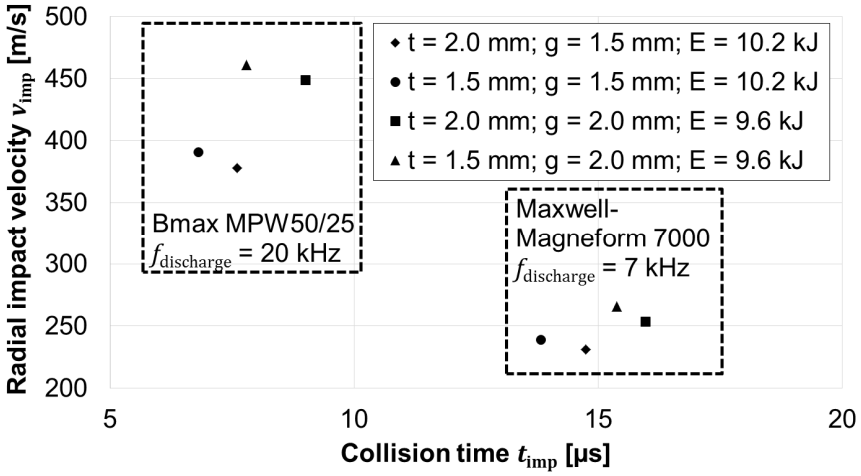


***Figure 3**: Radial impact velocities and collision times for 4 experimental setups and two MPW-machines*

The results of the mechanical testing and the metallographic analysis of the welded samples with a wall thickness t = 1.5 mm and a gap of g = 1.5 mm are plotted in **Figure 4**. The horizontal bars show the position and length of the welded zones in relation to the flyer edges optically measured in the cross section. Furthermore, the failure positions in the base material aluminum during the peel tests are plotted with quadrangles and the corresponding standard deviation. If the standard deviation exceeds the welded area, at least one peel test failed in the weld and not in the base material. Using the uncoated sample as a basis, it can be observed for the coatings in Figure 4 that:

1. **Electroplated nickel clearly enlarges the welded zone**. Due to the deformation of the flyer edge it is possible that welding starts 0.3 mm before the reference point x = 0 and reaches more than 9.0 mm in length. This phenomenon occurred for all investigated wall thicknesses and gaps.
2. The beginning of the welded zone for anodized parts was shifted to 2.0 mm or more, whereas all other coatings show no difference compared to the uncoated sample.
3. The failure position during peel test was located in the last third of the welding for PVD-chromated cylinders and acid passivated and chromated aluminum tubes under high impact speed as well as electroplated nickel parts at both impact velocities.
4. Welding with lower impact velocities **shifted the failure** position for PVD-chromated parts into the first third of the weld and affected a higher spreading.

5. In case of PVD-nickel-plated steel parts, the lower impact velocity improves the weld quality but shows also a high deviation.
6. 5 µm anodized aluminum was only weldable with high impact speeds. Although a wavy interface was achieved, the preparation for the peel test always destroyed the joined zone, suggesting a **strong detrimental effect of anodization**.

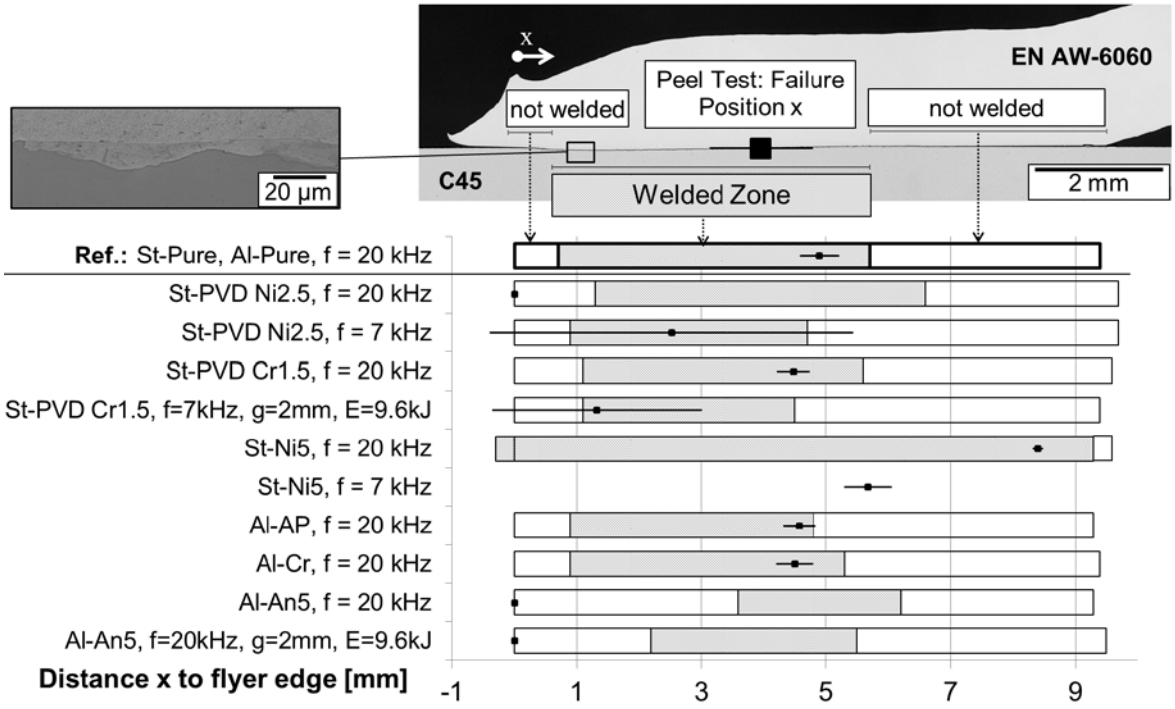


***Figure 4:*** *Welding Results for g = 1.5 mm, t = 1.5 mm and E = 10.2 kJ*

The shear strengths of the welded areas were evaluated for all welded samples with $t = 2.0$ mm and $g = 2.0$ mm. Compared to the shear strength of the uncoated sample with 153 MPa, chromated aluminum tubes have an **increased strength** of 162 MPa. St-PVD Cr1.5 at low impact speeds and St-Ni5 at high impact velocities decrease the shear strength to 120 MPa, whereas the other coatings showed almost no difference compared to the uncoated sample.

## 3.2 Metallographic Results

The metallographic study of selected specimens in **Table 5** shows that:

1. There is a noticeable influence of the impact speed on the weld interface. A comparison between the PVD-nickel-plated steel parts suggests that with increased impact velocity (a vs. b), the height of the formed waves increases. The coating is deformed heavily at the wavy interface (b). This can be found with all welded samples except St-Ni5 (d), where the middle section stays smooth.
2. Except for the PVD-chromed (e) and electroplated nickel (c) parts all samples show areas before and after the welded zone that were bonded first and **separated again** during the joining process as the crack propagation and welded fragments on both base materials show (g).

3. The anodized layer of 5 µm is included in the wavy interface in the first half of the welded zone (i). For a welding gap of 1.5 mm it is also embedded until the end of the weld. For a gap of 2.0 mm the layer is completely removed so that the juvenile steel and aluminum surfaces come into contact (j).
4. The nitrated steel's surface fractures at the collision point, is partially removed, but not welded (h).

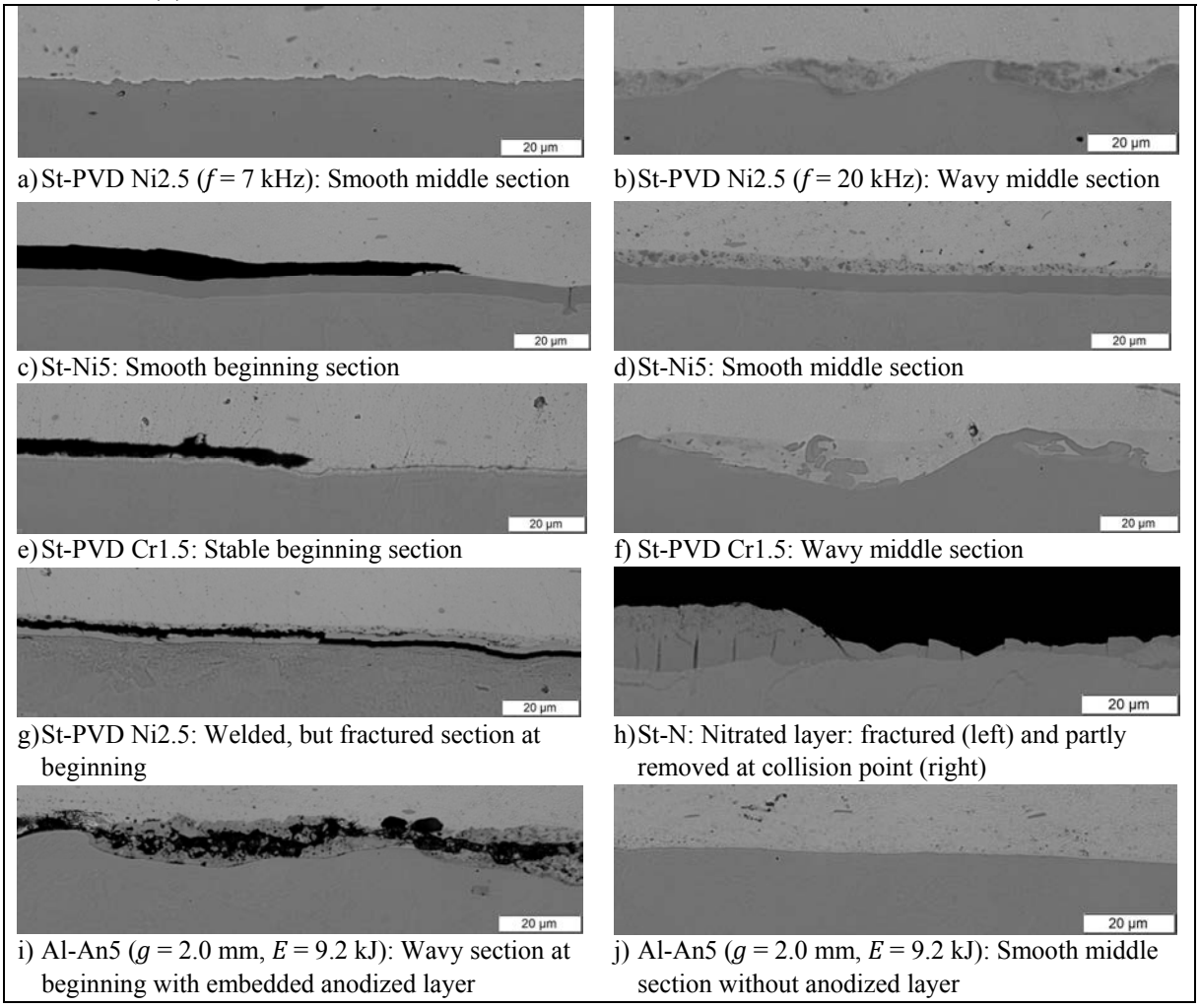


a) St-PVD Ni2.5 ($f$ = 7 kHz): Smooth middle section
b) St-PVD Ni2.5 ($f$ = 20 kHz): Wavy middle section
c) St-Ni5: Smooth beginning section
d) St-Ni5: Smooth middle section
e) St-PVD Cr1.5: Stable beginning section
f) St-PVD Cr1.5: Wavy middle section
g) St-PVD Ni2.5: Welded, but fractured section at beginning
h) St-N: Nitrated layer: fractured (left) and partly removed at collision point (right)
i) Al-An5 ($g$ = 2.0 mm, $E$ = 9.2 kJ): Wavy section at beginning with embedded anodized layer
j) Al-An5 ($g$ = 2.0 mm, $E$ = 9.2 kJ): Smooth middle section without anodized layer

***Table 5:*** *Polished cross sections of selected samples with $g$ = 1.5 mm, $t$ = 1.5 mm, $E$ = 10.2 kJ, $f$ = 20 kHz, welding direction: left to right, scale bar length = 20 µm*

# 4 Discussion

Based on the metallographic observations and the models presented in the introduction it can be predicted that:

1. Brittle surface coatings ("Type I") on the flyer tube can strongly be fragmented by the deformation. In the first part of the joining zone, they are embedded in the weld interface which is bad for welding. Using larger collision angles respectively larger gaps of 2.0 to 2.5 mm helps to remove the fragments by the jet and enables the welding of anodized parts with a layer thickness of 5 µm. Anodization layers of more than 10 µm are not removable by the jet in the given configuration. Brittle coatings on the parent part are

only partly fragmented or delaminated, but not removed by the jet completely. They are unfavorable for the MPW-process in the given configuration.

2. Thick and ductile layers like 5 µm electroplated nickel, ("Type II") seem to absorb a part of the collision energy as described in certain EXW-articles, e.g. by Manikandan et al. (2008). Probably, they also increase the diffusivity. While the uncoated sample shows welding and waves, coated samples show no waves at the same collision conditions. Increasing the impact velocity brings the wave formation back.
   The layer can be used to generate longer weld seams with the same amount of energy. Due to the partial absorption of the collision energy, the elastic forces of the compressed tube are reduced. Thus, internal disruptions ("spallation") that are common in uncoated samples before and after the final weld seam can be avoided with this coating.
3. Thin and ductile surface layers ("Type III") on the parent part are hard to remove by the jet due to the smaller global deformation compared to the flyer tube. It can be stated that ductile and deformable coatings like nickel or PVD-chrome can be embedded in the weld interface without deterioration of the weld quality.
4. The measured impact velocities for discharging frequencies of 20 kHz are approximately 460 m/s, whereas the flyer part in the MPW-setup with the bigger current rise time reaches an impact speed of only 270 m/s. Using the welding window from Cuq-Lelandais (2014) in the $v_r$-$\beta$-plane, it can be seen that for the same collision angle $\beta$, a higher impact speed leads to a wavy interface. Peel and shear tests showed an influence of the surface coating and impact velocity on the joint strength. To study these correlations, further material testing as well as a deeper metallographic analysis is necessary. In general, the welding results are almost independent from the wall thicknesses and gaps, whereas the discharging frequency has a major influence.

# 5 Conclusion

This paper investigates the influence of the surface coating on the welding result during MPW of tubular parts. Using the same amount of energy, two pulse generators with different discharging frequencies are used to join aluminum flyer tubes (EN AW-6060) on steel cylinders (C45). The difference in the acceleration behavior leads to impact velocities of 230 to 270 m/s for the 7 kHz pulse-station and between 400 and 450 m/s for the 20 kHz pulse-station, depending on the wall thickness and the acceleration gap. Three types of surface coatings are defined and systematically investigated in the MPW process:

I. Brittle surface layers: Anodized layers on the flyer part fracture because of the global deformation, but are detrimental for MPW when they stay in the welding interface. To avoid this, welding parameters like the gap must be adapted. Brittle coatings on the parent part (nitrated or zinc-coated surfaces) are strongly fragmented and delaminate from the parent part's base material, too. Due to the lower global deformation of the parent part, the coatings are difficult to remove and thereby detrimental for MPW. Since these coatings are of great importance in industrial production further investigations especially for zinc are necessary.

II. Thick and ductile layers: 5µm electroplated nickel shows a very good performance during MPW and **can even double the weld length** with the same amount of energy compared to uncoated surfaces. It influences the local deformation behavior due to the

kinetic energy loss of the flyer part and reduces wave formation. A wavy interface can be generated with higher impact velocities, but this is not mandatory since the high strength of waveless joints already leads to failure in the base material. A more economic exploitation of the effect would be to reduce the energy in the MPW-process and counteract the decreasing weld length with an interlayer like nickel. Consequently, **pulse generators can be downsized and the tool coils life increased**.

III. Thin and ductile coatings: PVD-nickel, PVD-chrome on the parent part (steel) as well as acid passivated and chromated surfaces on the aluminum tube are deformed and are uncritical for a good welding result.

## Acknowledgments

This work is based on the results of subproject A1 of the priority program 1640 (“joining by plastic deformation”); the authors would like to thank the German Research Foundation (DFG) for its financial support.

## References

Cuq-Lelandais, J.-P., Ferreira, S., Avrillaud, G., Mazars, G., Rauffet, B., 2014. Magnetic pulse welding: welding windows and high velocity impact simulations. In: Huh, H., Tekkaya, A.E. (Eds.), High Speed Forming 2014, Proceedings of the 6th International Conference, Daejeon, Korea, pp. 199–206.

Deribas, A.A., Simonov, V. A., Zakharenko, I.D., 1975. Surface effects with olique collisions between metallic plates. Translated from Fisika Goreniya I. In: Vzyva 10 (3), pp. 409–421.

Jäger, A., Tekkaya, A. E., 2012. Online measurement of the radial workpiece displacement in electromagnetic forming subsequent to hot aluminum extrusion. In: Tekkaya, A.E., Daehn, G.S., Kleiner, M. (Eds.), High Speed Forming 2012, Proceedings of the 5th International Conference, Dortmund, Germany, pp. 13-22.

Kapil, A., Sharma, A., 2015. Magnetic Pulse Welding: An efficient and environmentally friendly multi-material joining technique. In: Journal of Cleaner Production 100, pp. 35–58.

Manikandan, P., Hokamoto, K., Fujita, M., Raghukandan, K., Tomoshige, R., 2008. Control of energetic conditions by employing interlayer of different thickness for explosive welding of titanium/304 stainless steel. In: Journal of Materials Processing Technology 195 (1–3), pp. 232–240.

Schäfer, R., Pasquale, P., Elsen, A., 2011. Material hybrid joining of sheet metals by electromagnetic pulse technology. In: Key Engineering Materials 473, pp. 61–68.

Shribman, V., 2006: Magnetic Pulse Welding of Automotive HVAC Parts. Edited by PULSAR Ltd. Magnetic Pulse Solutions. Yavne, Israel.

Zhang, W., Bay, N., 1997. Cold Welding - Experimental Investigation of the Surface Preparation Methods. In: Welding Journal 76 (8), pp. 326–330.

# Benchmarking and Refining the Vaporizing Foil Actuator Spot Welding Process

**A. Vivek*, S. M. Wright, B. C. Liu, S. R. Hansen, R. C. Brune, B. P. Thurston, G. A. Taber, T. Lee, Y. Mao, T. J. Dittrich, G. S. Daehn**

Department of Materials Science and Engineering, The Ohio State University, USA
*Corresponding author. Email: vivek.4@osu.edu

## Abstract

*Impact spot welding implemented by the vaporizing foil actuator welding method has been studied. With significantly lower input energy levels as compared to resistance spot welding, similar and dissimilar lap welding of aluminium alloys (AA) of types 5052 and 7075 was implemented. The dissimilar welds between 2 mm thick AA5052 and 2.3 mm thick AA7075 were created with 4 kilojoules input energy, whereas the similar welds between 1 mm thick AA5052 sheets required only 0.6 kilojoules. Flyer sheet velocities of approximately 750 m/s were measured with a PDV system. Microhardness measurements, performed across the dissimilar weld interfaces, showed no softening of the base materials due to the welding process. A few distinct welding configurations were investigated for improving process feasibility and obtaining the highest possible weld strength. Lap shear tests and pry tests revealed that the configuration of the starting weld geometry greatly affected weld quality.*

## Keywords

Aluminum, Welding, Photonic Doppler velocimetry

## 1 Introduction

Conventional welding by means of high heat input, fusion and solidification greatly alters the microstructure in the welded region and can be detrimental to the weld's mechanical properties, especially in case of heavily engineered, high specific-strength materials (Hwang & Chou, 1998). The strength of the heat affected zone (HAZ) can be less than one

third the original strength of the base material. Additionally, susceptibility to corrosion is greatly increased after welding certain alloys such as 6xxx and 7xxx series aluminium alloys. Besides, aluminium welding requires high power, resulting in high energy consumption. Fasteners and structural adhesives offer non-welding joining solutions (Barnes & Pashby, 2000; Loureiro et al., 2010). Solid state welding techniques, such as impact welding (Y. Zhang et al., 2011), friction stir welding (Nandan et al., 2008), ultrasonic welding (C. (Sam) Zhanget al., 2009), and roll bonding (Lee et al., 2002) are a few alternatives to fusion based welding and have undergone a certain degree of industrial adaptation so far. Impact welding is of particular interest due to the potentially short cycle time of the process, the possibility to join a wide variety of metal combinations, and the ability to perform the process over varying length scales.

Vaporizing foil actuator welding (VFAW, or VFA welding) is a novel impact welding technique that utilizes the force generated by a thin aluminium foil vaporized by high electric current to launch one piece of metal toward one or more stationary target sheets (Vivek et al., 2013). Explosive welding (EXW) (Grignon et al., 2004) and magnetic pulse welding (MPW) (Watanabe & Kumai, 2009) are previously known and practiced methods of impact welding. Implementation of EXW in traditional factory environment is not possible due to safety regulation in transportation, storage and handling of explosives and because of an inability to automate such process. EXW is mostly used for welding thick plates for the shipbuilding, nuclear, oil and gas and locomotive industries. VFAW operates at the same size scale as MPW while having certain advantages over it. Longevity of the solenoid actuator used for MPW is a major concern, whereas VFAW is designed to have a low-cost consumable actuator for each cycle. With VFAW, pressures generated and achievable flyer sheet velocities are much higher as compared to MPW; therefore, a wider variety of materials can be effectively welded with VFAW. VFAW has been shown to be a significantly more efficient impact welding process as compared to MPW (Hahn et al., 2016). By changing the shape of the foil actuator and the air gap between the flyer and target sheets, welds of different shapes can be created. Circular spot welds are particularly interesting because there are existing spot welding techniques such as resistance spot welding (RSW) and friction stir spot welding (FSSW) against which VFAW can be benchmarked. In this work, spot welding of aluminium alloy type 5052 to itself and to aluminium alloy 7075 has been performed. AA5052 is a wrought aluminium alloy with ultimate tensile strength of about 228 MPa, and AA7075 is a wrought aluminium alloy with ultimate tensile strength of about 572 MPa. The similar material weld strengths have been compared to the FSSW data from Zhang et al. (2011) because they had a similar spot size of 10 mm as the work presented here. The strength data can also be compared to the data from Freeney et al. (2006), who obtained slightly higher weld strength, but their spot diameter was 12 mm.

# 2 Experimental Procedure

A schematic of the basic VFAW process is shown in Fig. 1. A thin aluminium foil as shown in the figure was connected across the terminals of a capacitor bank, which can be

charged up to a certain energy level. Once this energy was discharged through the foil, the foil vaporized rapidly and formed a high temperature gas that could be used to push the flyer sheet. Some degree of confinement is essential; accordingly, the other side the foil was backed by a block of steel approximately 20 mm thick. The flyer sheet has to be separated from the target sheet by an air gap, or standoff, in order to provide room for acceleration and allow for an oblique impact between the two joint members. This standoff was created by inserting an annular spacer or by pre-forming a well of certain depth into the flyer sheet (Fig. 2). The target plate was backed by another block of steel about 20 mm thick. The in-plane dimensions of the flyer as well as the target plates were 40 mm x 120 mm. The two were overlapped by 40 mm along the length and the welding experiment was conducted to create lap-welded specimens. The details of the similar and dissimilar welding are given in the subsections below. Informal pry tests, which involved uninstrumented destruction of the weld using hand tools, were conducted for preliminary screening and determination of suitable welding parameters. If the sample fractured very easily and through the interface, the parameters were changed until the pry test left a weld nugget. The lap-shear strengths of the formal samples were measured on an MTS 831.10 load frame moving with a cross-head speed of 0.1 mm/sec. For each type of sample, five were mechanically tested while one was saved for microanalysis in as-welded condition.

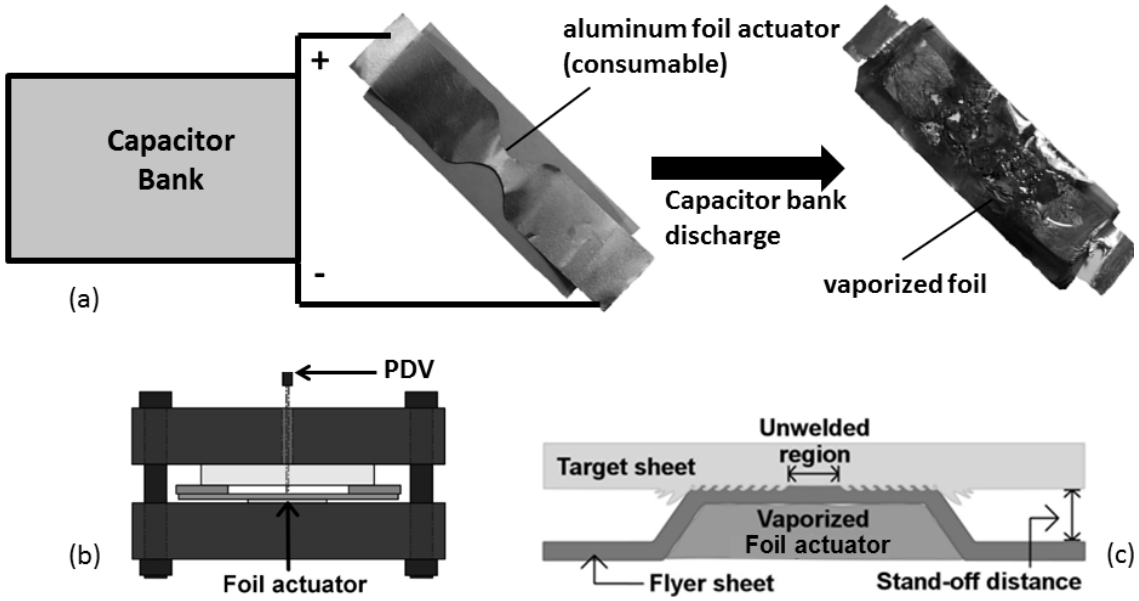


***Figure 1**: Schematics of the VFAW process: (a) the before and after experiment conditions of the foil actuator, (b) stack-up of a typical VFAW assembly, (c) close-up view of the welding operation*

In separate experiments, velocities of both AA5052-H32 and AA7075-T6 as the flyer sheets were measured using the photonic Doppler velocimeter [3]. In this experiment, the target plate had a through hole, which provided a line of sight to the laser focusing probe. With this technique, the evolution of the flyer sheet velocity can be measured with a sub-microsecond temporal resolution. Voltage was measured using a 1000V:1V probe

connected across the terminals of the capacitor bank, and current was measured by a 50kA:1V Rogowski coil.

## 2.1 AA5052 to AA5052

For similar welding of AA5052, 1 mm thick sheets were used as flyer as well as target sheets. Two types of samples with starting geometries as shown in Fig. 2 were created for this combination. Twelve samples were created with circular standoff (type 1) and six were created with a preformed flyer (type 2). In both cases the standoff gap was kept at 2.5 mm. Six of the type 1 samples were flattened in a hydraulic press with a force of 5 kN to remove the gap left by the standoff insert. These samples were created with an input energy of 0.6 kilojoules supplied by a custom-made capacitor bank (fast bank) that supplies a maximum energy of 1.3 kJ and has a short circuit rise time of 5 µs.

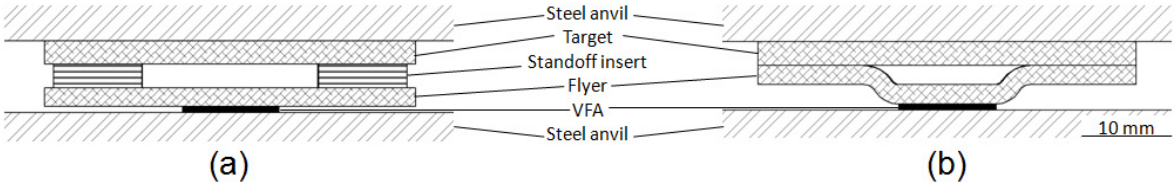


***Figure 2**: Schematic of welding stack up: (a) with standoff insert, (b) with preformed flyer sheet. Length scale is approximate.*

## 2.2 AA5052 to AA7075

For dissimilar welding, of AA5052 to AA7075-T6, 2 mm thick AA5052 sheets and 2.3 mm thick AA7075-T6 sheets were used. Both materials were attempted as flyer sheet. Upon pry tests of welds created, it was found that using AA5052 as the flyer sheet results in stronger welds at an energy level of 4 kJ. These experiments were conducted with a Maxwell Magneform capacitor bank (slow bank) that has a maximum charging energy of 16 kJ and a short circuit current rise time of 12 µs. The standoff distance was provided by a 2.5 mm thick neoprene washer with an inside diameter of 19 mm and outside diameter of 37 mm. Due to the low strength of the neoprene washer, it broke and was ejected from between the flyer sheet and target plate. Six samples were created for this material combination. One of those samples was sectioned along the diameter and microhardness on either side of the weld interface was measured. Vicker's hardness of the base materials away from the interface was also measured.

# 3 Results and Discussion

## 3.1 Diagnostics

The time resolved current and voltage data from a 0.6 kJ shot on the fast bank and a 4 kJ shot on the slow bank are shown in **Fig. 3 (a)**. It can be noted that in the first case the

current reached the maximum value of 40 kiloamperes within 5 μs, while it took 13 μs for the current from the slow bank to reach the peak value of 100 kiloamperes. The voltage trace on the slow bank demonstrated a characteristic spike at the time of foil burst. This phenomenon could not be identified on the fast bank's discharge voltage trace.

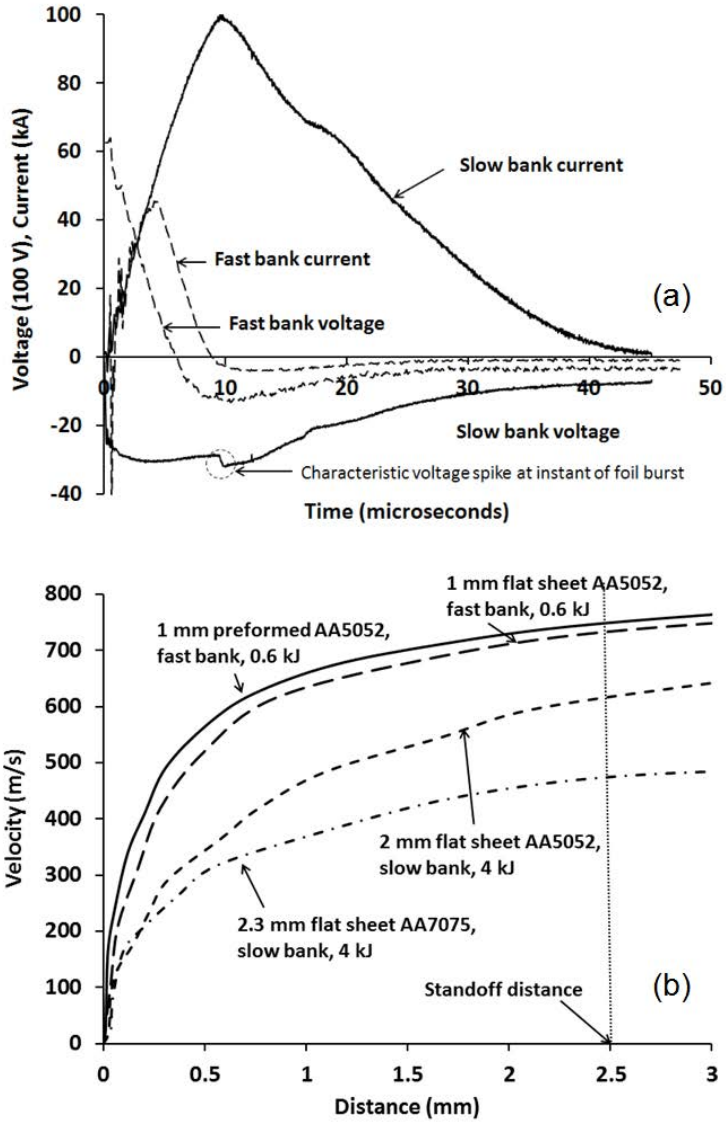


***Figure 3**: diagnostics on different types of experiments: (a) evolution of current and voltage with respect to time, (b) evolution of flyer sheet velocity with distance travelled.*

The evolution of flyer sheet velocities with distance travelled is illustrated in **Fig. 3 (b)**. As the impact with the target sheet occurred at a nominal distance of 2.5 mm, the impact velocities can be estimated as:

a) 1 mm flat sheet AA5052, fast bank at 0.6 kJ: 753 m/s
b) 1 mm preformed sheet AA5052, fast bank at 0.6 kJ: 731 m/s
c) 2 mm flat sheet AA5052, fast bank at 4 kJ: 569 m/s
d) 2.3 mm flat sheet AA7075, fast bank at 4 kJ: 472 m/s

## 3.2 AA5052 to AA5052

By creating spot welds at 0.6 kJ, truly low-energy impact welding of aluminium has been realized. RSW of aluminium consumes nearly one hundred times higher energy (Briskham et al., 2006). The use of a capacitor bank with a fast discharge frequency is important to achieve this energy efficiency. In a separate experiment not discussed here, it was observed that with the faster bank operating at 1 kJ energy level, a 1 mm thick AA5052 sheet can be launched to approximately 750 m/s within 2.5 mm of travel. The same launch carried out with a slower bank (12 μs current rise time) only achieved 400 m/s.

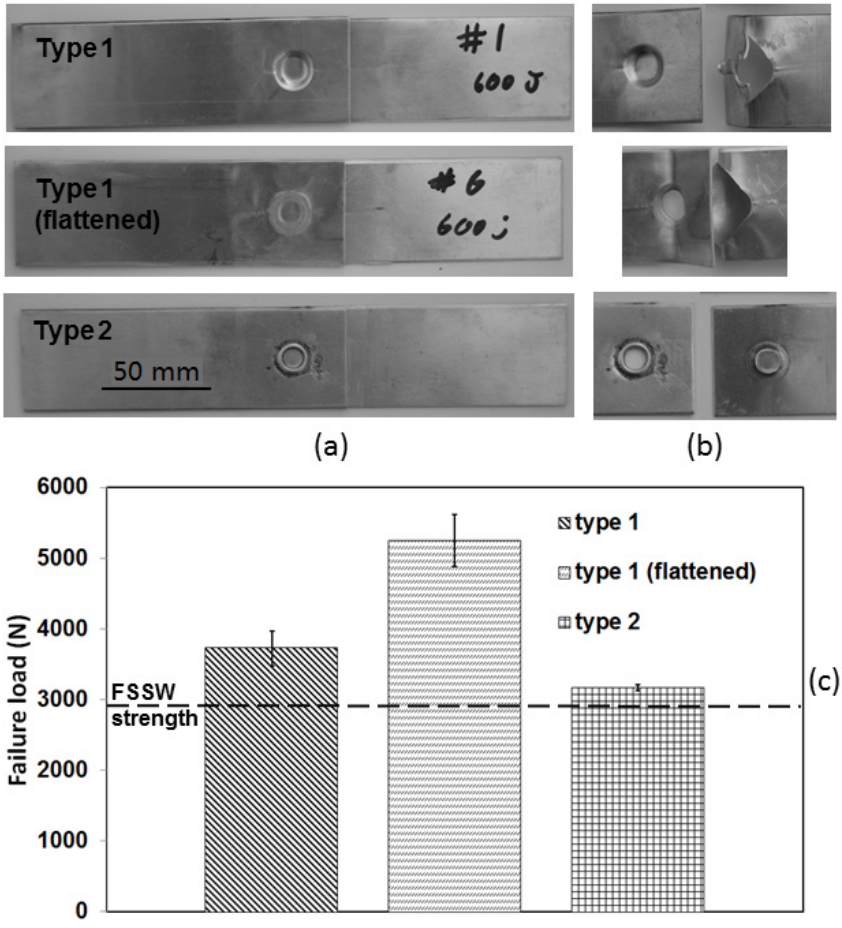


***Figure 4**: Similar alloy welds for AA5052: (a) before mechanical testing, (b) after mechanical testing , (c) failure loads from lap shear tests*

The average diameter of the spot welds was 10 mm. Most of the samples left behind a weld nugget upon mechanical testing. **Fig. 4** shows each type of sample before and after mechanical testing along with a graphical representation of the failure loads. The average failure load of as-welded type 1 samples was 3727 N with a standard deviation of 551 N. The average strength of the flattened type 1 samples was 5250 N with a standard deviation of 816 N. The type 2 samples failed at an average load of 3170 N with a standard deviation

of 39 N. It should be noted that all these failure loads are higher than the ones obtained with FSSW of similar material and spot size, which had lap shear strength of 2900 N (Zhang et al., 2011). The flattened type 1 sample showed the most improvement, where most of the samples sustained almost twice the load that the FSSW samples failed at. This can be attributed to the fact that the flattened type 1 samples had minimal thinning during the welding process and had no HAZ. One of the flattened type 1 samples failed along the interface at a lower load of 3505 N. This could have resulted from an experimental error in aligning the sheets, foil actuator and standoff insert before welding.

## 3.3 AA5052 to AA7075

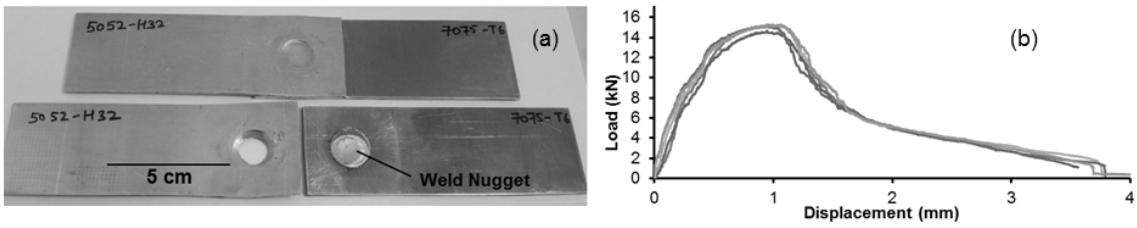


***Figure 5****: (a) A5052/A7075 VFAW spot welded samples before and after lap shear testing, (b) a plot showing variation in load with stroke during lap shear testing of the welded samples.*

**Fig. 5 (a)** shows an impact spot-welded specimen before and after lap shear testing. The load vs. displacement data for each sample is plotted in **Fig. 5 (b)**. The samples failed outside the weld nugget reproducibly at an average load of 15.0 kN with a standard deviation of 286 N. The high strength of these welds can be attributed to three factors: (i) negligible thinning around the welded area, (ii) no HAZ and (iii) effective metallurgical joining with no gaps or cracks at the bond line. The weld cross-section image in **Fig. 6 (a)** depicts the characteristic wavy morphology of an impact welded interface in some parts of the weld. The figure also shows that the flyer sheet retained its original thickness in and around the weld. The microhardness data (**Fig. 6 (b)**) also reveals that the Vicker's hardness on both sides of the weld interface and around the weld nugget remained constant at the base material level, which is 90 HV for A5052 and 205 HV for A7075. This is due to the low external input energy to the weld. It turns out that the input energy for VFAW is not only an order of magnitude smaller than that for RSW, but is also merely a fraction of the energy required for friction spot welding or self-pierced riveting processes (Briskham et al., 2006).

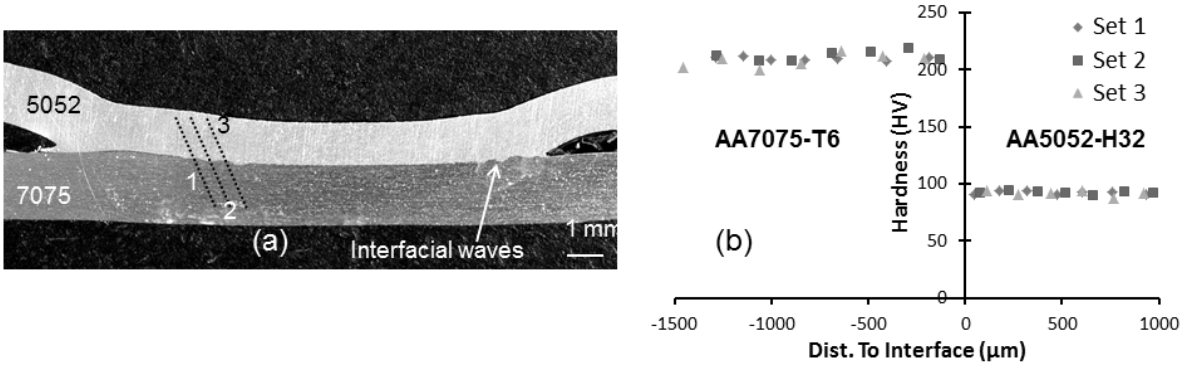


***Figure 6**: (a) Cross-section image of the welded sample depicting the lines along which microhardness testing was performed, (b) Test data showing constant microhardness on either sides of the weld interface.*

# 4 Conclusions

VFA spot welding of AA5052 to itself and to AA7075 was successfully implemented at very low input energies as compared to conventional welding processes. Upon mechanical testing, VFA spot weld samples failed outside the weld nugget and were significantly stronger than similar-sized FSSW. With minimal process-induced changes in geometric and mechanical properties of the base materials, VFAW enables approximately 100% joint efficiency, which sets it apart from other available joining techniques. This motivates further development of the process toward industrial implementation.

# Acknowledgments

The authors are thankful for sponsorship from the ALCOA Foundation's Advancing Sustainability Research Initiative under grant no. GRT00025327. Materials were kindly provided by Honda R&D, North America.

# References

Barnes, T. A., Pashby, I. R., 2000. Joining techniques for aluminum spaceframes used in automobiles. Part II - adhesive bonding and mechanical fasteners. Journal of Materials Processing Technology, 99, 72–79. doi:10.1016/S0924-0136(99)00361-1

Briskham, P., Blundell, N., Han, L., Hewitt, R., Young, K., Boomer, D., 2006. Comparison of self-pierce riveting , resistance spot welding and spot friction joining for aluminium automotive sheet. Sae Sp, 2034, 105. doi:10.4271/2006-01-0774

Grignon, F., Benson, D., Vecchio, K. S., Meyers, M. A., 2004. Explosive welding of aluminum to aluminum: analysis, computations and experiments. International Journal of Impact Engineering, 30(10), 1333–1351. doi:10.1016/j.ijimpeng.2003.09.049

Hahn, M., Weddeling, C., Taber, G., Vivek, A., Daehn, G. S., Tekkaya, a. E., 2016. Vaporizing foil actuator welding as a competing technology to magnetic pulse welding. Journal of Materials Processing Technology, 230, 8–20. doi:10.1016/j.jmatprotec.2015.11.010

Hwang, R. Y., Chou, C. P., 1998. The Study on Microstructural and Mechanical Properties of Weld Heat Affected Zone of 7075-T651 Aluminum Alloy. Scripta Materialia, 38(2), 215–221.

Lee, S. H., Saito, Y., Sakai, T., Utsunomiya, H., 2002. Microstructures and mechanical properties of 6061 aluminum alloy processed by accumulative roll-bonding. Materials Science and Engineering A, 325, 228–235. doi:10.1016/S0921-5093(01)01416-2

Loureiro, A. L., da Silva, L. F. M., Sato, C., Figueiredo, M. A. V., 2010. Comparison of the Mechanical Behaviour Between Stiff and Flexible Adhesive Joints for the Automotive Industry. The Journal of Adhesion, 86(July 2015), 765–787. doi:10.1080/00218464.2010.482440

Nandan, R., DebRoy, T., Bhadeshia, H. K. D. H., 2008. Recent advances in friction-stir welding - Process, weldment structure and properties. Progress in Materials Science, 53, 980–1023. doi:10.1016/j.pmatsci.2008.05.001

Vivek, A., Hansen, S. R., Liu, B. C., Daehn, G. S., 2013. Vaporizing foil actuator: A tool for collision welding. Journal of Materials Processing Technology, 213(12), 2304–2311. doi:10.1016/j.jmatprotec.2013.07.006

Watanabe, M., Kumai, S., 2009. Interfacial morphology of magnetic pulse welded aluminum/aluminum and copper/copper lap joints. Journal of Japan Institute of Light Metals, 59(2), 140–147. doi:10.2464/jilm.59.140

Zhang, C. (Sam), Deceuster, A., Li, L., 2009. A Method for Bond Strength Evaluation for Laminated Structures with Application to Ultrasonic Consolidation. Journal of Materials Engineering and Performance, 18(8), 1124–1132. doi:10.1007/s11665-008-9342-1

Zhang, Y., Babu, S. S., Prothe, C., Blakely, M., Kwasegroch, J., LaHa, M., Daehn, G. S., 2011. Application of high velocity impact welding at varied different length scales. Journal of Materials Processing Technology, 211(5), 944–952. doi:10.1016/j.jmatprotec.2010.01.001

Zhang, Z., Yang, X., Zhang, J., Zhou, G., Xu, X., Zou, B., 2011. Effect of welding parameters on microstructure and mechanical properties of friction stir spot welded 5052 aluminum alloy. Materials and Design, 32(8-9), 4461–4470. doi:10.1016/j.matdes.2011.03.058

# Electromagnetic Pulse Welded Aluminium to Copper Sheet Joints: Morphological and Mechanical Characterization

**K. Faes*, I. Kwee**

Belgian Welding Institute, Belgium
*Corresponding author. Email: Koen.Faes@bil-ibs.be

## Abstract

*This study investigated joining of Al to Cu sheets by electromagnetic pulse welding, which is a solid-state welding process that uses electromagnetic forces to join materials. The interfacial morphology and mechanical properties of the Al/Cu joints were analysed and related to the welding process parameters. The centre section of the Al/Cu joints evolved from a non-welded to a welded zone. The welded zone started with a wavy interface, consisting of thick interfacial layers with defects and evolved to a relatively flat interface without an interfacial layer. Interfacial phases resulted from solid-state mechanical mixing and/or very localised interfacial heating. The interfacial layers had a thickness ranging from 2-39 µm, an interface waviness amplitude up to 11 µm and contained 31-75 wt% Cu. The interfacial layer thickness and the weld length are determined by both the discharge energy and the stand-off distance. A trade-off existed between a homogeneous interface and the maximum weld length when the stand-off distance is changed. The interfacial layer exhibited an increased hardness compared to Al and Cu. A higher tensile force, up to 4,9 kN, was achieved at a higher energy and a lower stand-off distance. One of the factors determining the tensile force was the width of the welded area.*

## Keywords

Welding, Sheet metal, Analysis

## 1 Introduction

Aluminium-copper (Al/Cu) hybrid parts, as a substitution for Cu parts, result in both weight and cost reduction, and are highly relevant in numerous applications related to the electrical, heating and cooling sector (Bergmann et al., 2013; Abbasi et al., 2001).

However, Al to Cu joined by thermal welding processes presents challenges for achieving a good joint quality, due to their highly dissimilar mechanical and thermal properties, which can result in large stress gradients during heating. In contrast, electromagnetic pulse welding is a solid-state welding technology that uses electromagnetic forces to join the materials. In this process, a power supply is used to charge a capacitor bank. When the required amount of energy is stored in the capacitors, it is instantaneously released into a coil, during a very short period of time. The discharge current induces a strong transient magnetic field in the coil, which generates a magnetic pressure that causes one workpiece to impact with another workpiece. Under the correct circumstances, this leads to an atomic bond between the two metal workpieces, in either a tubular or sheet configuration. The objective of the present work is to investigate electromagnetic pulse welding of Al to Cu sheets achieved at different welding conditions. The weld interface and mechanical properties of the resulting Al/Cu sheet joints are analysed and related to the welding process parameters, namely the discharge energy, the stand-off distance, and the overlap between the coil and the Al sheet.

# 2 Experimental Procedure

## 2.1 Set-up of the Electromagnetic Pulse Welding Process

Electromagnetic pulse sheet welding of Al 1050 H14 (sheet dimensions: 50 mm x 50 mm x 1 mm and 48 mm x 50 mm x 1 mm) to Cu (sheet dimensions: 67 mm x 50 mm x 1 mm) sheets was performed using a Pulsar model 50/25 system with a maximum charging energy of 50 kJ (corresponding with a maximum capacitor charging voltage of 25 kV). The total capacitance of the capacitor banks equals 160 $\mu F$. Figure 1 shows the overlap configuration of the Al sheet and Cu sheet in the flat coil. The Al sheet is called the flyer sheet and is located on top of the coil conductor. The Cu sheet is called the parent sheet. The stand-off distance is the distance by which the Al flyer sheet is separated from the Cu parent sheet prior to discharge. The overlap is the overlap distance between the flat coil and the Al flyer sheet. The free length is the part of the Al flyer sheet that is being accelerated.

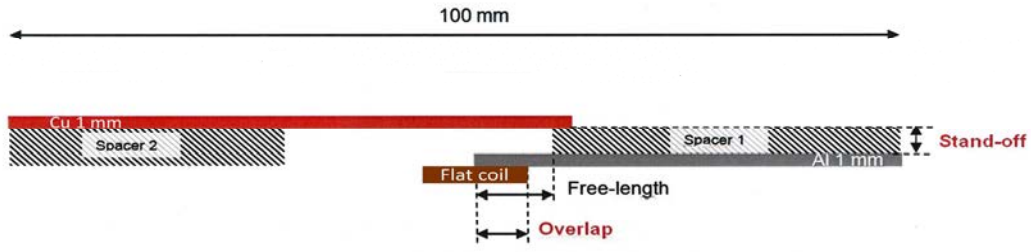


***Figure 1**: Overlap welding configuration of the Al flyer sheet and Cu parent sheet*

## 2.2 Electromagnetic Pulse Sheet Welding Conditions

An overview of the selected welding parameters is shown in Table 1. In total, 27 different welding conditions were tested. The discharge energy, stand-off distance and overlap distance were varied, whereas the free length was fixed throughout all experiments.

| Discharge energy [kJ] | Stand-off distance [mm] | Overlap distance between the flat coil and Al flyer sheet [mm] | Free length [mm] |
|---|---|---|---|
| 10, 12, 14, 16, 18 | 2, 3, 4 | 8, 10 | 15 |

***Table 1**: Selected parameters for electromagnetic sheet welding of Al to Cu sheets*

### 2.3 Weld Characterization

The interfacial morphology and the weld length were assessed by optical microscopy (OM) and Field Emission Scanning Electron Microscopy (SEM). Energy-Dispersive X-ray Spectroscopy (EDX) analysis was conducted to semi-quantitatively identify the chemical composition of the interfacial layer. Subsequently, hardness traverses (micro hardness testing; weight 5,0 gram) and tensile tests were performed.

## 3 Results & Discussion

### 3.1 Weld Interface

Figure 2 (left) shows a typical Al/Cu sheet weld and Figure 2 (right) a typical metallographic cross-section obtained at the centre of the weld. The first impact is at the right extremity of the Al flyer sheet, after which the weld formation advances to the left. In general, all metallographic cross-sections show that Al/Cu sheet joints evolve from a non-welded zone to a welded zone. The weld length corresponds to the length of the welded zone.

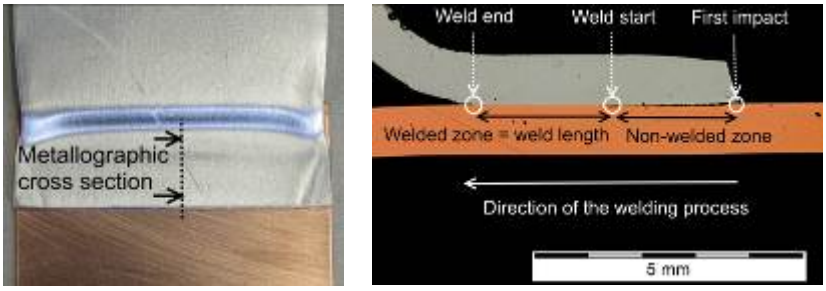


***Figure 2 (left)**: As-welded Al/Cu sheets (discharge energy: 14 kJ, stand-off distance: 2 mm, overlap distance: 10 mm, free length: 15 mm) **(right)** Metallographic cross-section taken at the centre of the welded sample (discharge energy: 10 kJ, stand-off distance: 3 mm, overlap: 10 mm, free length: 15 mm)*

Based on measurements and modelling studies performed by other authors, the evolution of the non-welded to the welded zone can be attributed to the evolution of pure normal Lorentz forces to a combination of normal and shear Lorentz forces (Schäfer and Pasquale; Kore et al., 2007; Kore et al., 2010), the increase of the impact angle (Watanabe et al., 2009) and the change of the impact velocity (Schäfer and Pasquale) during the welding process. The direction and the magnitude of the Lorentz force determine the impact angle between the flyer and parent sheet. The combination of the impact angle and the impact velocity is defined in the so-called welding window, which specifies the requirements of the impact velocity and the impact angle for welding to occur (Göbel et al., 2010; Watanabe et al., 2009; Kore et al., 2010). Under the correct conditions, a jetting

effect can then take place that effectively removes the oxides from the surfaces and allows for atomic bonding to occur (Watanabe et al., 2009).

## 3.2 Interfacial Morphology of the Welded Zone

Figure 3 shows a detailed view of the typical evolution of a welded zone (i.e. the central part of Figure 2, right). At first, a relatively flat interface with a small interfacial layer containing macrocracks and pores is observed (Figure 3a). Subsequently, the interface waviness amplitude, defined as the difference between the maximum and the minimum of a wave, and the thickness of the interfacial layer increase. The interfacial layer becomes strongly porous, with randomly dispersed porosities in different sizes. In addition, transverse microcracks, restricted to the interfacial layer, are noticed (Figure 3b). This is followed by a more homogeneous interfacial layer with a similar interfacial thickness but less porosities (Figure 3c). Further along the weld, the thickness of this homogeneous interfacial layer decreases (Figure 3d) and towards the end of the weld, a small wavy interface and thin interfacial layer without any defects is present (Figure 3e). Finally, the interface becomes relatively flat, without any visible interfacial layers (Figure 3f).

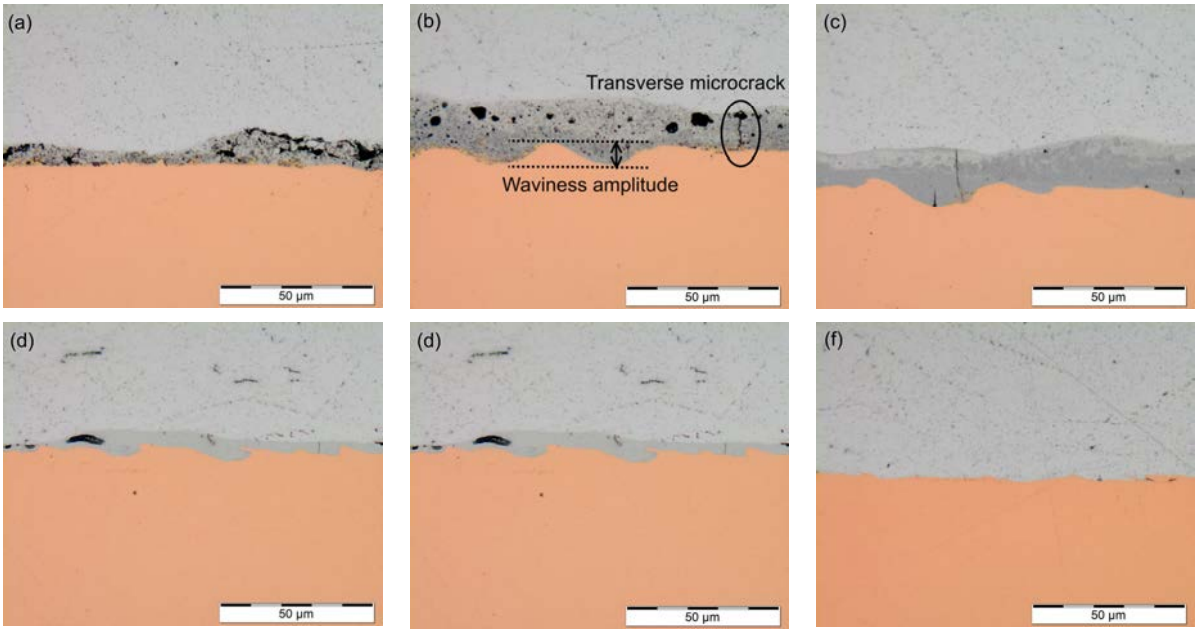


***Figure 3**: Evolution of a typical weld interface from the start (a) to the end (f) of the welded zone (from right to left in Figure 2) (discharge energy: 18 kJ, stand-off distance: 3 mm, overlap distance: 10 mm, free length: 15 mm)*

**Table 2** summarizes the wt% Cu, range of interfacial layer thickness, range of waviness amplitude, and defects present in the different interfacial layers of the welded zone.

| Colour observed by optical microscopy | Position within the welded zone | %wt Cu | Interfacial layer thickness [µm] | Waviness amplitude [µm] | Defects |
|---|---|---|---|---|---|
| Light grey | Mainly at the weld end, sometimes also in the weld middle | ≈31-41 | 2-10 | < 6 | No or small porosities |
| Dark grey, in combination with light grey | Weld middle & weld start | ≈54-62 | 3-26 | 6-11 | Medium-sized porosities, mainly transverse cracks |
| Brown, in combination with light grey and dark grey | Weld start | ≈72-75 | 14-39 | 6-11 | Large porosities, transverse and longitudinal cracks |

***Table 2**: Identification of the wt% Cu, range of interfacial layer thickness, range of waviness amplitude, and defects in the different interfacial layers of the welded zone*

The interfacial layers, found along the weld interface, can be formed by two mechanisms. Firstly, the interfacial phases are formed by solid-state mechanical mixing, during which severe local plastic deformation takes place (Sterb et al., 2010). Secondly, a local temperature rise and localised interfacial heating with subsequent fast cooling can result in interfacial layers (Göbel et al. 2010; Raoelison et al., 2012; Zhang et al., 2011). When using a large discharge energy, melting at the interface can also occur, followed by cooling and solidification shrinkage. Melting can be evidenced by the presence of spherical pores (Figure 4). Such a spherical pore reveals a molten and re-solidified area, which can be an indication that interfacial melting has taken place. In addition, spherical and irregular pores can originate from metallurgical preparations such as grinding and polishing.

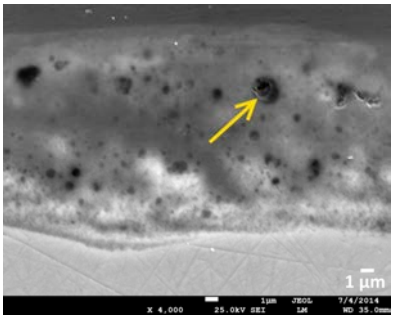


***Figure 4**: Spherical pore within an interfacial layer, revealing a molten and re-solidified area that indicates that localized interfacial melting has occurred (discharge energy: 14 kJ, stand-off distance: 3 mm, overlap: 10 mm, free length: 15 mm)*

The change of the interfacial morphology within the welded zone can be attributed to the continuous variation of the impact velocity and impact angle during the welding process, as found in (Göbel et al., 2010; Göbel et al., 2011; Watanabe et al., 2009). The presence of a higher wt% Cu at the start and the middle of the welded zone possibly indicates that the impact energy at those locations is sufficient to allow more mechanical mixing of Cu with Al and more heating of the materials. In contrast, the presence of less wt% Cu towards the end of the welded zone may indicate that the impact energy decreases, promoting less mixing and less heating of the materials.

## 3.3 Effect of the Welding Process Parameters on the Interfacial Morphology and Weld Length

The thickness of the interfacial layer and hence its structural and chemical composition are determined by both the stand-off distance and the discharge energy. No effect of the overlap distance between the coil and the Al sheet was found in the present study.

At an overlap of 10 mm, a discharge energy of 16 kJ and a stand-off distance of 4 mm, the welded zone consists of a homogeneous weld interface with an interfacial thickness of 5 µm (Figure 5a). At the same overlap and discharge energy, but with a decreased stand-off distance of 3 mm, the welded zone consists of an inhomogeneous weld interface with a large interfacia0 thickness up to 25 µm, many porosities and several transverse microcracks (Figure 5b).

The change of the weld interface for a lower stand-off distance can be attributed to the larger impact velocity for a stand-off of 3 mm. When using a stand-off distance of 4 mm, it is likely that the velocity was already decreasing prior to impact, leading to a lower impact velocity compared to the situation when using a stand-off distance of 3 mm. For this reason, it was assumed that more kinetic energy is available for a stand-off distance of 3 mm that can be transformed into energy for bonding. In that case, also more localised interfacial heating can take place, as observed in (Marya et al., 2004), resulting in a larger interfacial layer thickness.

A similar observation is found for the effect of the discharge energy on the interfacial layer thickness. At the same overlap and stand-off distance, but at a higher discharge energy, the interfacial layer thickness increases and contains more porosities and cracks.

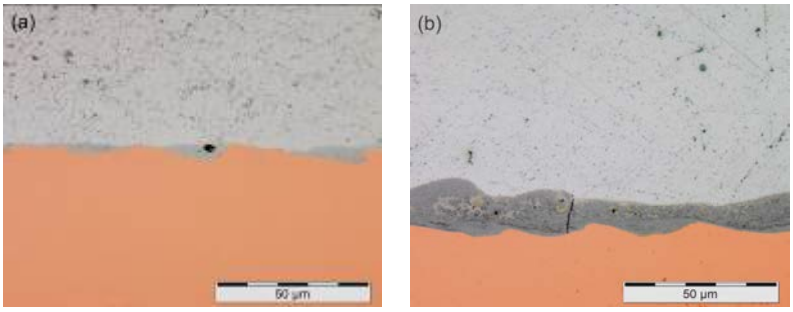


***Figure 5****: Effect of the stand-off distance on the welded zone, obtained with: discharge energy 16 kJ, overlap distance: 10 mm, free length: 15 mm (a) stand-off distance: 4 mm, interfacial thickness: 5 µm (b) stand-off distance: 3 mm, interfacial thickness: 20 µm*

Figure 6 shows the weld length as a function of the discharge energy, for the different combinations of overlap and stand-off distances. Also the weld length is determined by both the stand-off distance and the discharge energy. The maximum weld length is obtained at the optimal stand-off distance of 3 mm, at which the impact velocity and impact angle are situated in a range of the welding window that allows for a maximum jetting effect and hence a maximum weld length. In contrast, the minimum weld length is obtained at a stand-off distance of 2 mm, which indicates that this distance is too small since at the time of impact, the Al flyer sheet has not accelerated yet up to the correct impact velocity. Hence, the impact energy is insufficient to initiate bonding. Medium weld lengths are obtained at a stand-off distance of 4 mm, which indicates that this stand-off

distance is too large, since prior to impact the impact velocity has probably already started to decrease, as discussed previously. A similar observation is found for the effect of the discharge energy on the weld length. At the same overlap and stand-off distance, the maximum weld length is obtained at a discharge energy of 16 kJ, above and below which the weld length decreases.

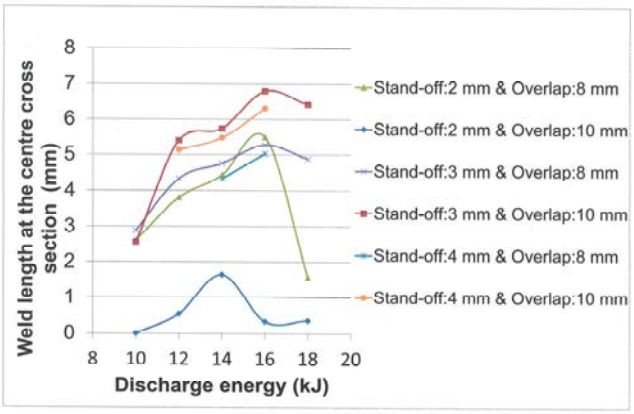


***Figure 6**: Weld length at the centre cross section as a function of the discharge energy for different combinations of the stand-off distance (2-3-4 mm) and the overlap distance (8-10 mm)*

A trade-off exists between a homogeneous interface and a maximum weld length. By decreasing the stand-off distance from 4 to 3 mm, there is change from a homogeneous weld interface with a small interfacial layer thickness to an inhomogeneous interface with a larger interfacial layer thickness (Figure 5) and an increase of the weld length from 6,3 to 6,8 mm (Figure 6). This can possibly be attributed to a higher impact velocity achieved at the stand-off distance equal to 3 mm, which results in more kinetic energy available to be transformed into energy for bonding. As a result, a longer weld length is achieved but also more mechanical mixing, more interfacial heating, which lead to an inhomogeneous interface with a larger interfacial layer thickness.

## 3.4 Mechanical Characteristics

### 3.4.1 Hardness

Figure 7 shows a hardness traverse across an Al/Cu weld interface. The interfacial layer has a higher hardness (370,8 HV) compared to the base materials Al (average hardness 25,8 HV) and Cu (average hardness 52,3 HV). This increase of the hardness can confirm that phase transformations have taken place.

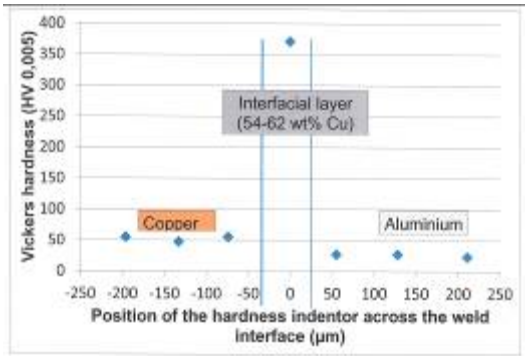


***Figure 7**: Vickers hardness traverse across an Al-Cu weld interface (discharge energy 16 kJ; stand-off distance: 3 mm, overlap distance: 8 mm, free length: 15 mm)*

### 3.4.2 Tensile Force

Figure 8 shows the tensile force as a function of the discharge energy, for different combinations of the stand-off distance and overlap distance. A higher tensile force is achieved at a higher discharge energy and at a lower stand-off distance. Therefore, although energies higher than 10 kJ generally result in a larger interfacial thickness and a larger amount of defects within, the increase of the tensile force at a higher discharge energy shows that the presence of interfacial phases do not necessarily degrade the welds. Instead, interfacial phases can possibly provide additional strength due to their increased hardness compared to the base material. For most welding conditions, the welds with a higher tensile force (4-4,8 kN) have a large interfacial layer thickness (14 to 21 µm), whereas the welds with a lower tensile force (3-4 kN) have a small interfacial layer thickness (4 to 14 µm). The exception are welds obtained at a stand-off distance of 2 mm and an overlap of 10 mm, where all welds exhibit a higher tensile force (4-4,6 kN), but contain a small interfacial thickness (2 to 15 µm).

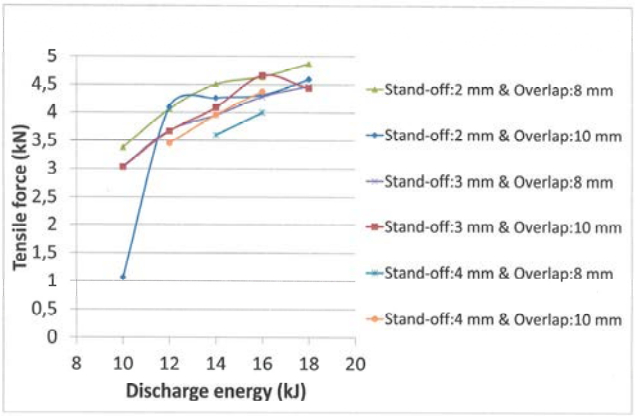


***Figure 8**: Tensile force as a function of the discharge energy for different combinations of the stand-off distance (2-3-4 mm) and the overlap distance (8-10 mm)*

A higher tensile force is achieved for a larger weld width (Figure 9). An increase of the weld width is similarly achieved at a higher discharge energy and a lower stand-off distance of 2 mm. Therefore, the weld width is one of the main factors that determines the

tensile force that the weld can attain. No relation is found between the tensile force and the weld length at the centre of the weld.

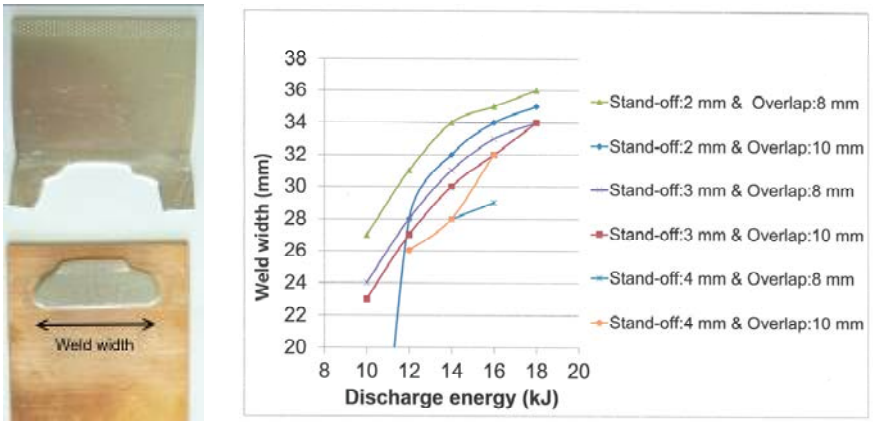


***Figure 9**: (left) Al/Cu weld after tensile testing, showing the weld width (right) Weld width as a function of the discharge energy for different combinations of the stand-off distance (2-3-4 mm) and the overlap distance (8-10 mm)*

# 4 Conclusions

Al to Cu sheets are joined by the electromagnetic pulse technology using different welding conditions. The following conclusions can be drawn from the present experimental study:

- The centre of the Al/Cu sheet joints evolve from a non-welded zone to a welded zone. Based on measurements and modelling studies performed by other authors, this can be explained by the evolution of the direction and magnitude of the Lorentz forces, the change of the impact angle and the change of the impact velocity.
- Interfacial layers along the weld interface can be formed by solid-state mechanical mixing and/or by localised interfacial heating. The welded zone evolves from a thick and wavy interface with defects to a relatively flat interface without visible interfacial phases and defects. The interfacial layer thickness and the weld length are determined by both the discharge energy and the stand-off distance. A trade-off exists between a homogeneous interface with a small interfacial layer thickness and a maximum weld length.
- Higher tensile forces are obtained at a higher discharge energy and at a lower stand-off distance and weld width. The presence of interfacial layers can possibly provide additional tensile strength, due to their increased hardness.

# Acknowledgements

This project has received funding from the European Union's Horizon 2020 research and innovation programme under grant agreement No. H2020-FoF-2014-677660 — JOIN-EM.

# References


Abbasi M., Karimi Taheri A., Salehi M.T., 2001. *Growth rate of interfacial compounds in Al/Cu bimetal produced by cold roll welding process*. Journal of Alloys Compounds 319, pp. 233-241.

Bergmann, J.P., Petzoldt F., Schürer R. Schneider S., 2013. *Solid-state welding of aluminium to copper-case studies.* Welding in the World 57, pp. 541-550.

Doley J.K., Kore S.D., 2011. Study of impact behavior of sheets in electromagnetic pulse welding. In: The 64th Annual Assembly of the International Institute of Welding, Chennai, India. The Indian Institute of Welding, CD-ROM Edition.

Göbel G., Beyer E., Kaspar J., Brenner B., 2011. Dissimilar metal joining: Macro-and Microscopic Effects of MPW. In: Proceedings of the 5th International Conference on High Speed Forming, Dortmund, Germany, pp. 179-188.

Göbel G., Kaspar J., Herrmanssdörfer T., Brenner B., Beyer E., 2010. Insights into interfacial phases on pulse welded dissimilar metal joints. In: Proceedings of the 4th International Conference on High Speed Forming, OH, USA, pp.127-136.

Kore S.D., Date P.P., Kulkarni S.V.,2007. *Effect of process parameters on electromagnetic impact welding of aluminium sheets.* International Journal of Impact Engineering 34, pp.1327-1341.

Kore S.D., Dhanesh P., Kulkarni S.V., Date P.P., 2010. *Numerical modeling of electromagnetic welding.* International Journal of Applied Electromagnetics 32, pp.1-19.

Marya M, Marya S, Priem D., 2004. On the Characteristics of Electromagnetic Welds between Aluminium and Other Metals and Alloys. In: The 57th annual Assembly of the International Institute of Welding, Osaka, Japan.

Raoelison R., Rachik M., Buiron N., Haye D., Morel M., Dos Santos B., Jouaffre D., Franz G., 2012. Assessment of gap and charging voltage influence on mechanical behavior of joints obtained by magnetic pulse welding. In: Proceedings of the 5th International Conference on High Speed Forming, Dortmund, Germany, pp.207-216.

Schäfer R., Pasquale P. *Material hybrid joining of sheet metals by electromagnetic pulse technology.* PST products GmbH, Alzenau, Germany; available at http://www.pstproducts.com/EMPT_sheetwelding_PSTproducts.pdf (accessed 18 January 2016).

Sterb A., Shribman V., Ben-Artzy A., Aizenshtein M., 2014. *Interface phenomena and bonding mechanism in magnetic pulse welding.* Journal of Material Engineering Performance 23, pp.3449-3458.

Watanabe M., Kumai S., 2009. *Interfacial morphology of magnetic pulse welded aluminium/aluminium and copper/copper lap joints.* Materials Transactions 50, pp. 286-292.

Watanabe M., Kumai S., 2009. *High-speed deformation and collision behavior of pure aluminium plates in magnetic pulse welding*. Materials Transactions 50, pp. 2035-2042.

Zhang Y., Suresh Babu S., Prothe C., Blakely M., Kwasegroch J., LaHa M., Daehn G., 2011. *Application of high velocity impact welding at varied different length scales.* Journal of Material Processing Technology 21, pp. 944-985.

# The Influence of Thermal and Mechanical Effects on the Bond Formation During Impact Welding

**C. Pabst*, P. Groche**

Institute for Production Engineering and Forming Machines, TU Darmstadt, Germany
*Corresponding author. Email: pabst@ptu.tu-darmstadt.de

## Abstract

*Impact welding, usually applied as explosion welding or electromagnetic pulse welding, is a highly transient joining process. Strain rates in orders of magnitude far above $10^4$ 1/s and resultant thermal effects occur and influence the formation of the joint significantly. Experimental and microscopic investigations as well as analytical estimations are carried out and presented in this paper in order to gain a more comprehensive understanding of the effective mechanisms and their relevance. In addition to electromagnetic pulse welding, a specially built test rig is used to identify the process window and its change due to modified parameters. The test rig allows to change both impact parameters, angle $\beta$ and velocity $v_c$, independently.*
*It will be shown that the actual formation of the joint and its characteristics are greatly affected by the surrounding gaseous media. Strength and size of the joint can be influenced as well as the location of the process window. Theories will be developed to explain these results and to make them usable for the practical application. Furthermore, experimental results indicate that the compression of the ambient atmosphere in the closing gap between the two specimens evokes highly elevated temperature, which is in good accordance with earlier findings.*

## Keywords

Joining, Impact welding, Bond formation

## 1 Introduction

The discovery of impact welding is traced back to the First World War, when it was found accidentally that shrapnel sometimes stuck to armour (Crossland, 1982). The first industrial application to be developed in the following years was explosion welding (Carl, 1944). The

blast wave of an explosive accelerates a metal sheet (the so-called flyer) up to several hundred meters per second towards a second metal sheet (the so-called target). The metallurgical joint is formed during the impact and does not require melting (Crossland, 1982). This is why impact welding even allows joints between dissimilar metals (Crossland, 1982).

Later, electromagnetic pulse welding has been developed. The force from the blast wave is replaced by electromagnetic forces which are evoked by a strong, pulsed current in a tool coil. The process principles are identical to explosion welding. However, the capacitors of a typical pulse generator deliver a much lower amount of energy than the explosives. This leads to potentially smaller weld areas and smaller material thicknesses for the flyer in electromagnetic pulse welding. This drawback is compensated by the fact that electromagnetic pulse welding is safe and suitable for mass production with cycle times in the range of only few seconds. (Schäfer et al., 2011)

Both processes have in common that the parts to be joined can have almost any shape. Formed sheets as well as tubular structures are possible. Both processes also share the same impact principle. The geometry as well as the force distribution have to be designed in a way that there is a specific angle between the parts during the impact. This leads to a collision line (or collision point in a cross section) travelling across the surface. The normal impact velocity is, as already mentioned, in the range of some hundred meters per second. The angle is usually in the range between 5° and 35°. The velocity of the collision point is in the range of several thousand metres per second and thus always supersonic. The process window for each material combination which has been developed for explosion welding is usually given dependent on the angle and the velocity of the collision point. (Crossland, 1982)

In order to establish a sound weld, a characteristic phenomenon is important: The so-called jetting process (Crossland, 1982). Due to the hydrodynamic flow of material at strain rates far above $10^4$ 1/s (Crossland, 1982) directly at the impact area, superficial layers of both parts are ejected from the closing gap. In earlier scientific investigations the presence of this jet has been proven by high speed imaging, numerical analyses (Wang et al., 2012) and catching the ejected material (Bergmann et al., 1966). A range of experiments has been conducted: The impact has been generated for example by the use of a gun (Turgutlu et al. 1995) or electromagnetic pulse technology (Kakizaki et al. 2011).

The aim of the studies presented in this paper is to provide additional knowledge on the process mechanisms. Currently, the design of impact welding joints is often done empirically and thus is very time consuming. Additionally, a targeted process optimisation and the prediction of the actual weld strength are almost impossible.

# 2 Experimental Setups

For the conducted experiments within this paper, two techniques are utilized: electromagnetic pulse welding and a specially designed test rig.

## 2.1 Electromagnetic Pulse Welding

A pulse generator and a tool coil are the core components of a system for electromagnetic pulse welding. The pulse generator mainly consists of large capacitors which are charged with voltages of several kilovolts. Special switches connect the capacitors to the tool coil and form an oscillating circuit. The damped current reaches several hundred kiloamperes at frequencies mainly in the range between 10 kHz and 50 kHz. The experiments presented in this paper are carried out with a sheet welding coil. The effective part of the coil with a cross section of 5 mm x 5 mm and the position of the sheets to be welded are shown in **Fig. 1**. The distance between the coil and the flyer sheet 0.5 mm, which is determined by an insulation sheet.

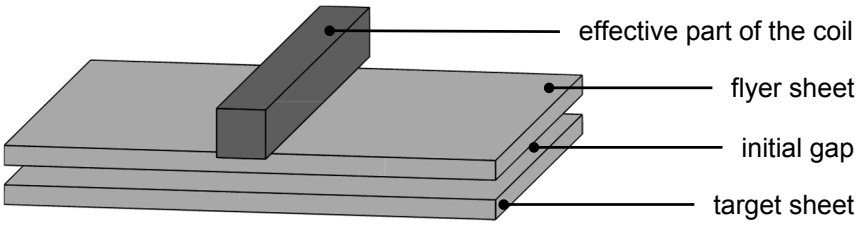


***Figure 1**: Sketch of the electromagnetic pulse welding setup*

A photo of a welded specimen is depicted in **Fig. 2**. Only the material close to the coil is moved due to the spacers and the inertia.

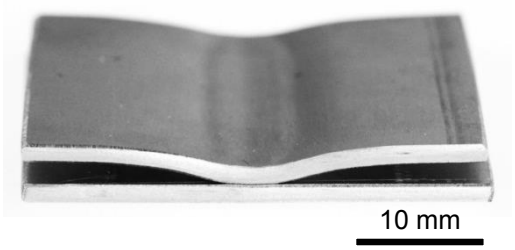


***Figure 2**: Welded specimen*

## 2.2 Test Rig

For basic research, electromagnetic pulse welding exhibits the disadvantage of being transient. This means that the angle at the collision point and its velocity constantly change during the impact (Groche et al., 2014). To overcome this limitation, a special test rig has been developed which is shown in **Fig. 3**. It is capable of colliding specimens at constant and well defined angles and velocities. Each of the two specimens is attached to one aluminium rotor with a diameter of 500 mm. The impact takes place when the acceleration up to 5000 rpm is finished after about 1.5 s. This equals 131 m/s for each specimen and a relative velocity of 262 m/s.

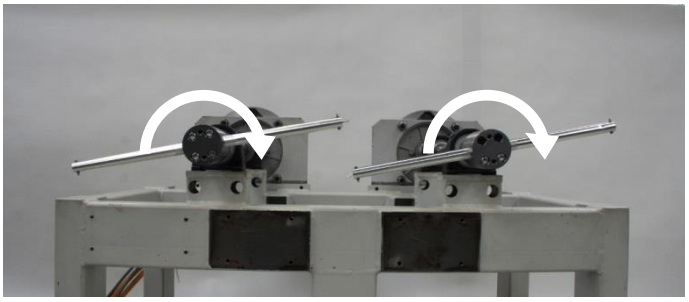

***Figure 3**: Test rig (without housing): Two motors drive one rotor each with one specimen attached at one end*

The impact velocity is directly adjusted by the number of revolutions per minute and the angle is determined by bending one specimen accordingly. After the collision the welded parts of the specimens are torn off at a breaking point, whereas the rest stays attached to the rotors. **Fig. 4** shows the adjusted angle between the specimens (a) and a welded specimen (b) with the end remaining attached to the rotors after the collision.

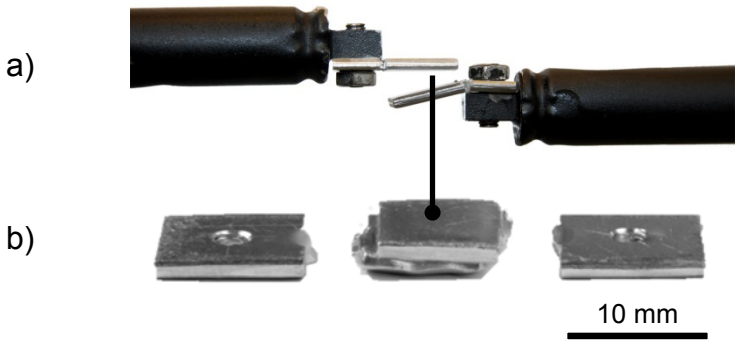


***Figure 4**: Adjustment of the impact angle by bending one specimen (a) and welded sample (b)*

The collision point velocity can be directly calculated from the geometrical relationship between impact velocity and impact angle. Furthermore, these parameters remain constant during the impact. The comparability between electromagnetic pulse welding and the developed test rig has been shown in earlier works by experimental investigations (Groche et al. 2014) and numerical studies (Groche and Pabst, 2015).

# 3 The Influence of the Surrounding Medium During Welding

Investigations in earlier publications have shown that the surrounding gaseous medium has an effect on the process. In (Groche and Pabst, 2014), an effect could be observed when replacing the ambient air by argon. Bergmann et al. (1966) investigated explosion welding of two aluminium sheets in an atmospheric atmosphere and in a vacuum chamber. The alloy remains unspecified. With the help of high speed imaging they found that the velocity of the jet in vacuum is about twice as high as under atmospheric pressure. However, they did not observe any effect on the morphology of the weld in micrographs.

## 3.1 Experimental Setup

In order to investigate the effect of low air pressure, a similar experiment is carried out for electromagnetic pulse welding. The two sheets to be welded are made of commercially pure aluminium (99.5%, EN AW-1050A) in half hard condition (Hx4). The size is 40 mm x 40 mm x 2 mm and the initial distance was adjusted to 2 mm. The working frequency of the system is 19.6 kHz, the charging energy is varied to achieve different peak discharge currents and thus different impact velocities and energies. The peak current is varied between 250 kA, 260 kA, 288 kA and 313 kA. The two aluminium sheets on the coil are covered by an acrylic glass case which allows the process observation. The vacuum is created prior to the discharge and the pressure is approximately 100 mbar.

## 3.2 Process Observation

During the impact, a significant difference could be observed immediately between vacuum and atmospheric pressure: The typical flash during the impact between the two sheets became significantly darker in vacuum, which can be seen in the direct comparison in **Fig. 5**. The tool coil is located at the bottom under an electrical insulation sheet and the two sheet specimens are held down by a fixture from the top. The photos are taken by a conventional camera with a long exposure time to capture the complete process without the need of a trigger signal.

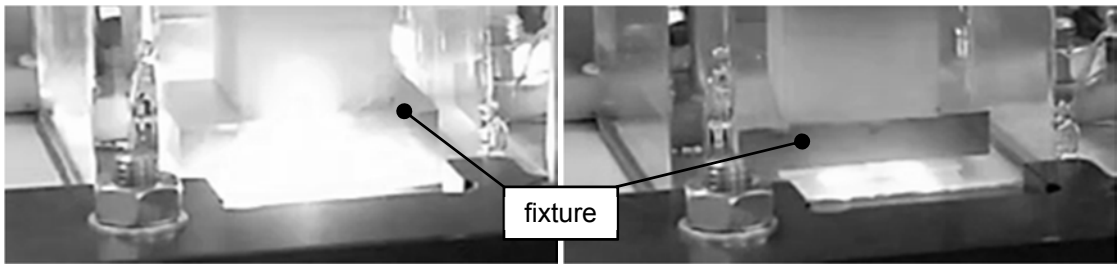


***Figure 5**: The process light at ambient pressure (left) and in vacuum (right).*

This observation is in accordance with former findings and supports an earlier theory on the formation of the light. The authors proposed that the light is caused by the supersonic compression of the surrounding medium, the ambient atmosphere in this case. The compression occurs very fast and is capable of evoking plasma (Koschlig et al., 2008). During the experiments with 250 kA, no light at all could be seen in vacuum, whereas it was still visible at normal pressure. It should be noted that no weld was possible with this current.

## 3.3 Macroscopical and Microscopical Investigation

Peel tests after the welding experiments with low currents (250 kA and 260 kA) showed that the size of the potentially joined area, which can be identified as white surfaces in **Fig. 6**, can be increased drastically in vacuum. This area exhibits the characteristic O-shape for

electromagnetic pulse welding and this setup of the sheets and the coil (Schäfer et al., 2011). At higher currents these areas are welded and thus it was no more possible to damage the weld and estimate its size in the peel test, because the failure occurred in the parent material.

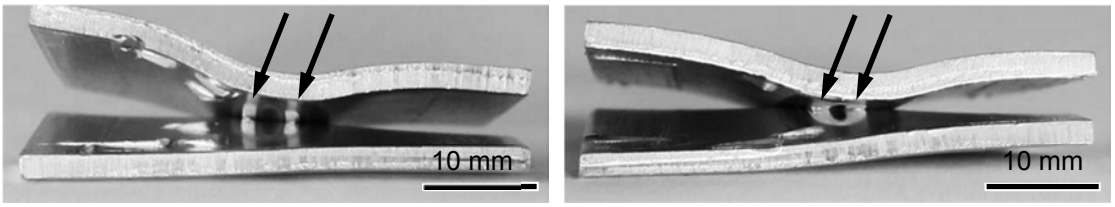


***Figure 6**: Result of the peel test for welded samples at ambient pressure (left) and in vacuum (right) at 260 kA.*

A weld is possible starting at a peak current of 288 kA. Two samples at ambient pressure and in vacuum were used for further, microscopic investigations. The macroscopic overview on the polished cross sections in **Fig. 7** gives a first idea of the size of the actual metallurgical joint.

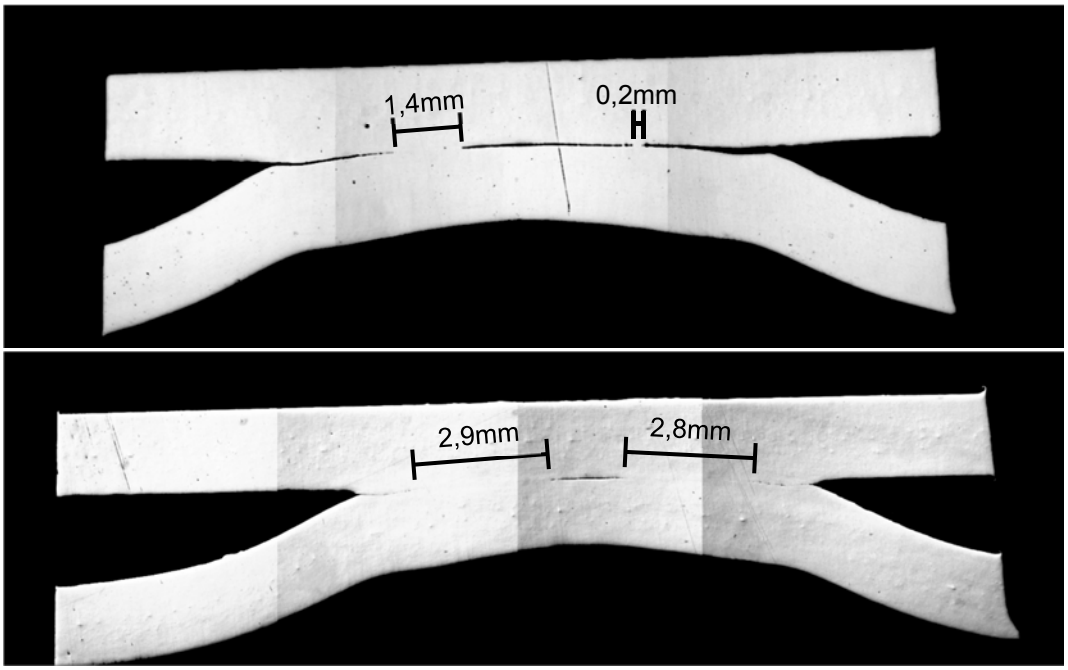


***Figure 7**: Cross section of the samples welded with a peak current of 288 kA at ambient pressure (top) and in vacuum (bottom).*

The total width of the weld is about 1.6 mm at ambient pressure, whereas it reaches about 5.7 mm in vacuum. The distribution of welded and unwelded areas is typical for this setup in electromagnetic pulse welding (Watanabe and Kumai, 2009). In the central area where the first contact occurs, no joint is possible because the impact angle is too small. The collision point then travels symmetrically to the left and the right. Its speed and the angle reach the process window shortly afterwards and a metallurgical joint is formed. Due to the limited size of the effective area of the tool coil and limited process energy in electromagnetic pulse welding compared to explosion welding, the kinetic energy is

transformed steadily into forming energy. The decrease in velocity first stops the bond formation and finally stops the movement. Thus the weld area never spreads across the whole area where both sheets are in contact.

It could be suspected that the difference in the weld lengths is caused by the missing air that has to be pushed out of the continuously closing gap between the two sheets during the process. In this setup, the volume of ejected gas and moved aluminium at the same time is roughly the same. Taking into account that air at normal pressure is by the factor 2250 lighter than aluminium, it can be safely concluded that this effect may be present, but is not relevant. The comparison in **Fig. 8** of the final contours of the two specimens supports this consideration, as there is no clearly visible difference between them.

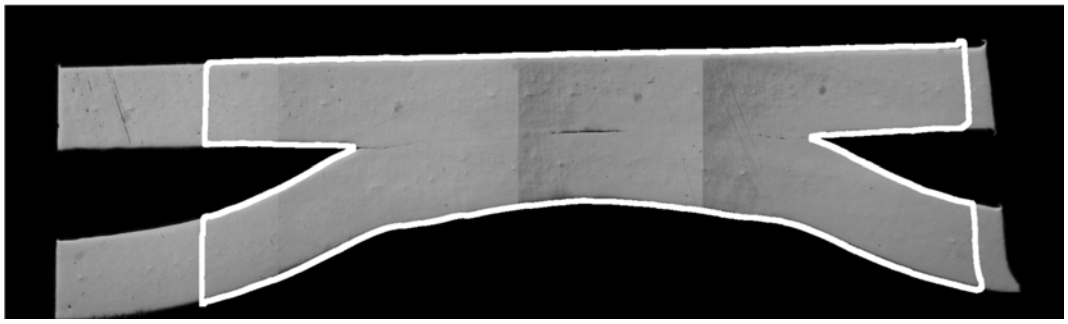

***Figure 8**: Comparison between the vacuum sample and the ambient pressure sample (white contour)*

The micrographs, especially at the unwelded areas, show one main difference between the two samples. The gap in the unwelded areas is in the range of 17 µm up to 50 µm for the atmospheric pressure sample, whereas the vacuum sample exhibits gaps in the range of only 9 µm and below, **Fig. 9**. A closer look at the gaps in the atmospheric pressure sample shows numerous aluminium particles in various sizes from 3000 µm² down to only a few square micrometres. One of these particles is marked in **Fig. 9**. These cannot be observed in the vacuum sample.

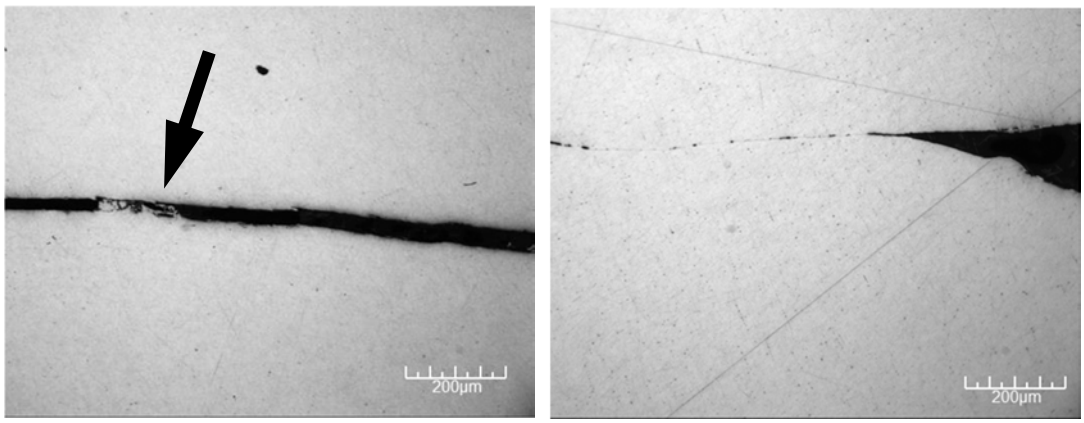


***Figure 9**: The unwelded gap between the two sheets on the very right side of the cross section for the weld at ambient pressure (left) and in vacuum (right)*

### 3.4 Interpretation

It can be concluded that the so-called jet and the process light are two independent phenomena during impact welding. The experiments have shown that it is possible to reduce or even suppress the light but still obtain a weld. As a weld always requires the existence of the jet, it has still to be present. Immediately after the impact, it can be actually seen with the bare eye as a small amount of dust that is expelled from the joint area. Furthermore, the weld quality can be even increased drastically, at least at the lower end of the process window. The reason might be the missing or at least decreased air resistance for the jet, which allows the particles to escape much easier from the closing gap between the sheets. This theory is supported by the presence of aluminium particles between the sheets after the process at ambient pressure. They cannot be found in the specimens which have been welded in vacuum. The findings of Bergmann et al. (1966) about the increased velocity of the jet in vacuum also support this theory. Additionally, their investigations suggest that this effect does not influence the weld quality any more at higher impact energies. A possible explanation is that the jet too has a higher kinetic energy and thus can escape from the gap completely despite the air resistance.

## 4 Estimation of the Temperature in the Weld Area

Impact welded joints, especially at higher energies, often show areas of presumably molten material between dissimilar metals (Göbel et al., 2010) and also similar metals (Stern et al., 2014). One reason is the high strain rate in the impact area. In earlier publications the authors of this paper suggested that the supersonic compression of the surrounding gas is fast enough to also cause extremely high temperatures far above 1000 K and thus create plasma (Groche and Pabst, 2014). This was supported by former analytical investigations on the temperature rise due to the compression of different gases by Koschlig et al. (2008). The experimental verification of this theory is possible but challenging due to the small dimensions and the short duration of the impact process in the range of microseconds. In order to gain first information on the temperatures during the impact ozone measurement is applied. Ozone is sensitive to an increase in temperature. According to Clement (1904), more ozone is generated at higher temperatures, but the decay increases more rapidly. If a significant increase in temperature occurs, this should be detectable by a decrease of the ozone concentration. The experiments are carried out at the developed test rig due to its good accessibility. Furthermore, unwanted effects due to sparkovers between the two sheets in electromagnetic pulse welding are avoided.

### 4.1 Measurement Technique

The air is directly taken from the location where the two specimens collide via a short hose, **Fig. 10**. The ozone measurement device is specially developed for fast data acquisition rates of up to 50 Hz whereas conventional instruments are usually limited to about 2 Hz. However, the device is not capable of providing absolute values of the ozone concentration. In this

application this is not a significant drawback, because only the change in the concentration is relevant. The functional principle can be summarized as follows: The air is driven by an integrated fan via the short hose into the device. There it passes a sensor disc which emits photons proportional to the ozone concentration (chemiluminescence). The photons reach a photomultiplier and the output voltage is measured. The functional principle and the measurement theory are explained in detail in (Zahn et al., 2012).

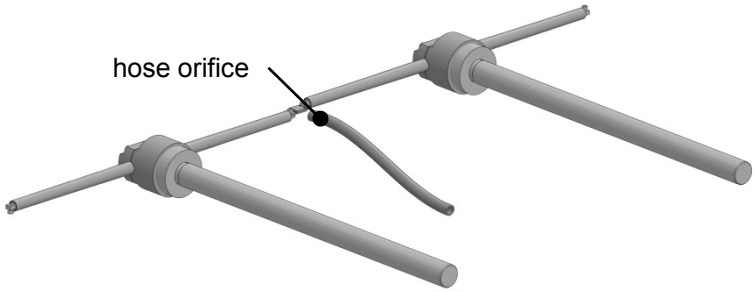


***Figure 10**: 3D drawing of the rotors (without motors) and the location of the hose opening for the ozone measurement*

## 4.2 Experimental Results

The experiments were carried out in summer, which led to a well sufficient amount of natural ambient ozone. **Fig. 11** shows the raw measurement data from a typical experiment at the test rig. The data acquisition frequency was 25 Hz. The temporal axis starts earlier to achieve a stationary state of the measurement.

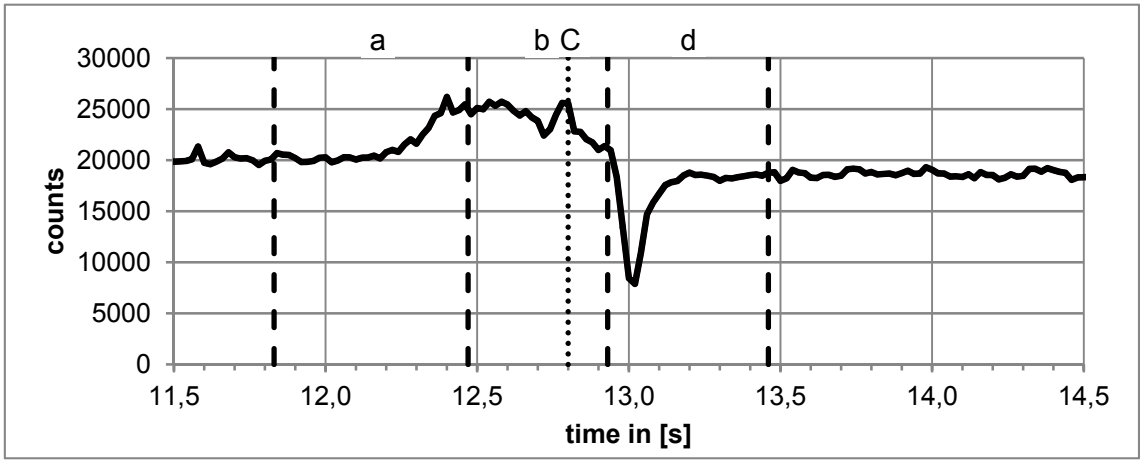


***Figure 11**: Counts over time for a collision experiment at the test rig. The stages of the movement are marked as follows: acceleration (a), constant speed (b), moment of impact (C), deceleration (d).*

When the rotors start after about 11.8 s, the ozone concentration seems to increase shortly afterwards from about 20000 to about 25000 counts for about 0.6 s. This is exactly the time for the acceleration of the rotors, i.e. it takes from the start until the collision takes place. The ozone concentration is delayed by about 0.2 s due to the length of the hose that

the air has to travel. When the collision between the specimens takes place after about 12.8 s the ozone concentration drops rapidly to less than 10000 counts. After this drop, the concentration immediately reaches about 18500 counts and thus almost the initial value of 20000 counts. So far, an explanation has not been found for this deviation of about 1500 counts.

## 4.3 Interpretation

The rise of the concentration within the first second is caused by an aerodynamic effect: The specimens pass the orifice of the suction hose very closely and thus influence the airflow due to air vortices in their vicinity caused by the fast movement of up to 131 m/s. The significant drop of the ozone concentration during the collision indicates that the temperature reaches considerable values. The increased heat leads to excessive ozone decay. Even though absolute values of the ozone concentration cannot be given it appears legitimate to assume temperatures well above 1000 K, which has been proposed by Koschlig et al. (2008). After the impact, the welded parts of the specimens are torn off the rotors. Thus there is no elevated number of counts due to aerodynamic effects at the end, because no sheet specimen passes the orifice of the hose. The rotors are still turning for another 0.5 s until they stop completely. If the test rig's rotors turn with attached specimens, but without any impact, a rise during the acceleration and deceleration can be observed but no drop. The drop can also be found in the data from electromagnetic pulse welding experiments, but here the plateau is not present during the first second before the impact, as was to be expected. **Fig. 12** shows the typical raw measurement data during the weld of two aluminium sheets. The machine setup and the specimens are identical to the vacuum experiments described in chapter 3. The air for measuring the ozone concentration is taken directly next to the impact area of the specimens. Note that the initial ozone concentration is lower and thus the noise seems increased. Also note that the scale of the time axis is different, because the concentration drop lasts longer. This is very likely to be caused by the larger size of the impact area and the higher energy provided by the electromagnetic welding setup compared to the test rig.

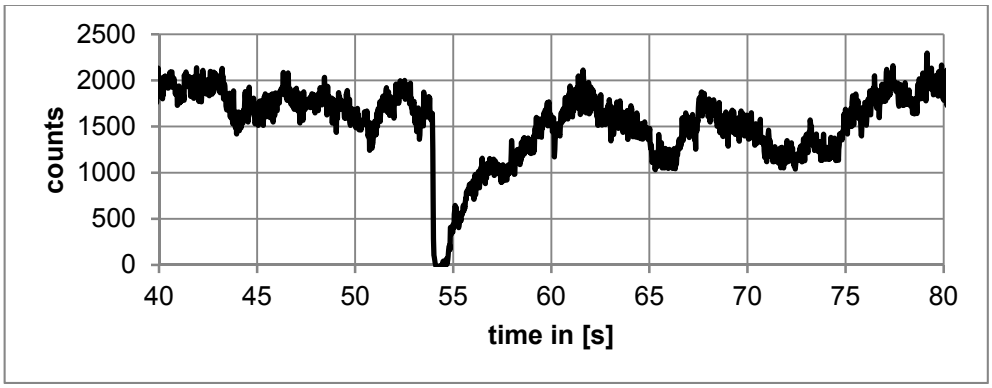


***Figure 12**: Counts over time for electromagnetic pulse welding of two aluminium sheets*

# 5 Summary and Conclusions

The evaluation of the experimental results shows that the ambient atmosphere has a great impact on the quality of the weld, at least at the lower end of the process window. One possible reason is the air resistance that is experienced by the so-called jet. This theory is supported by the micrographs which show particles in the joint area under normal pressure, but no particles can be observed in the vacuum specimens. In literature, it is generally agreed that jetting is crucial for the formation of the bond. The results also show that the process light is independent from the formation of a jet. The advantage of welding in vacuum decreases with increasing impact energies. However, higher energies are known to lead to an increased formation of intermetallic phases that can reduce the strength of the weld. Thus it can be helpful in some applications to evacuate the space between the workpieces. A significant rise in temperature could be proved by ozone measurements. The excessive decay of ozone during the impact can be explained with a highly elevated temperature in the area between the colliding specimens. However, a possible thermal influence of the plasma on the workpieces' surface cannot be quantified by this method.

# 6 Outlook on Future Works

To gain more information on the influence of the surrounding gas more experiments will be conducted with different gases and pressures. It will be also investigated if welds of other material combinations can be improved likewise. Equal attention will be paid on the jetting phenomenon, which is expected to have a great influence on the formation of the joint. High speed imaging will be used to investigate the evolution of the jet. Furthermore, a possible influence of an elevated temperature during the impact due to the incurrence of plasma will be investigated. The gas parameters, i.e. pressure and type, will be chosen carefully in order to distinguish the effects on jet formation and temperature evolution.

# Acknowledgments

The authors would like to thank the German Research Foundation (DFG) for the financial support of the project GR 1818/49 which enabled this paper. Furthermore, the authors thank Baumüller, PCO AG, Acal BFi and PSTproducts for their support during the experimental works. Further thanks go to Boris Schneider from enviscope GmbH and Andreas Zahn from KIT for supporting the ozone measurements.

# References

Bergmann, O. R., Cowan, G. R., Holtzman, A. H., 1966. Experimental Evidence of Jet Formation During Explosion Cladding. In: Transactions of the Metallurgical Society of AIME, Vol. 236, pp. 646-653

Carl, L. R., 1944. Brass welds, made by detonation impulse. In: Metal progress, Vol. 46, pp. 102.

Carpenter, S.H., Wittman, R.H., 1975. Explosion Welding. In: Annu. Rev. Mater. Sci., Vol. 5, pp. 177-199

Clement, J. K., 1904. Über die Bildung des Ozons bei hoher Temperatur. In: Annalen der Physik, Vol. 319, pp. 334-353

Crossland, B., 1982. Explosive welding of metals and its application. In: Oxford series on advanced manufacturing, Oxford University Press, Oxford

Göbel, G., Kaspar, J., Herrmannsdörfer, T., Brenner, B., Beyer, E., 2010. Insights into intermetallic phases on pulse welded dissimilar metal joints. In: 4th International Conference on High Speed Forming, pp. 127-136

Groche, P., Wagner, M. F.-X., Pabst, C., Sharafiev, S., 2014. Development of a novel test rig to investigate the fundamentals of impact welding. In: Journal of Materials Processing Technology, Vol. 214, pp. 2009-2017

Groche, P., Pabst, C., 2015. Numerical Simulation of Impact Welding Processes with LS-DYNA. In: 10th European LS-DYNA Conference

Kakizaki, S., Watanabe, M., Kumai, S., 2011. Simulation and Experimental Analysis of Metal Jet Emission and Weld Interface Morphology in Impact Welding. In: Materials Transactions, Vol. 52, pp. 1003-1008

Kore, S. D., Date, P. P., Kulkarni, S. V., 2007. Effect of process parameters on electromagnetic impact welding of aluminum sheets. In: International Journal of Impact Engineering. Vol. 34, pp. 1327-1341

Koschlig, M., Veehmayer, M., Raabe, D., 2008. Production of Steel-Light Metal Compounds with Explosive Metal Cladding. In: 3rd International Conference on High Speed Forming, pp. 23-32

Pabst, C., Groche, P., 2014. Electromagnetic Pulse Welding: Process Insights by High Speed Imaging and Numerical Simulation. In: 6th International Conference on High Speed Forming, pp. 77-88

Schäfer, R., Pasquale, P., Elsen, A., 2011. Material hybrid joining of sheet metals by electromagnetic pulse technology. In: Key Engineering Materials, Vol. 473, pp. 61-68

Stern, A., Shribman, V., Ben-Artzy, A., Aizenshtein, M., 2014. Interface Phenomena and Bonding Mechanism in Magnetic Pulse Welding. In: Journal of Materials Engineering and Performance, Vol. 23, pp. 3449-3458

Turgutlu, A., Al-Hassani, S. T. S., Akyurt, M., 1995. Experimental investigation of deformation and jetting during impact spot welding. In: International Journal of Impact Engineering, Vol. 16, pp. 789-799

Wang, X., Zheng, Y., Liu, H., Shen, Z., Hu, Y., Li, W., Gao, Y., Guo, C., 2012. Numerical study of the mechanism of explosive/impact welding using Smoothed Particle Hydrodynamics method. In: Materials and Design, Vol. 35, pp. 210-219

Watanabe, M., Kumai, S., 2009. High-Speed Deformation and Collision Behavior of Pure Aluminum Plates in Magnetic Pulse Welding. In: Materials Transactions, Vol. 50, pp. 2035-2042

Zahn, A., Weppner, J., Widmann, H., Schlote-Holubek, K., Burger, B., Kühner, T., Franke, H., 2012. A fast and precise chemiluminescence ozone detector for eddy flux and airborne application. In: Atmospheric Measurement Techniques, Vol. 5, pp. 363–375

# A Study on the Critical Thickness of the Inner Tube for Magnetic Pulse Welding Using FEM and BEM

**H. Geng[1*], J. Cui[1,2], G. Sun[1,2], G. Li[1,2]**

[1] State Key Laboratory of Advanced Design and Manufacturing for Vehicle Body, Hunan University, Changsha, 410082, China
[2] Collaborative Innovation Center of Intelligent New Energy Vehicle, Shanghai, 201804, China
[*]Corresponding author. Email: genghuihui@hnu.edu.cn

## Abstract

*Due to high efficiency and quality in welding dissimilar metals, Magnetic Pulse Welding (MPW) has attracted much attention. In this study, 3A21 aluminium alloy used as outer tube was welded to 20Fe tube by MPW. In order to investigate the critical thickness of the inner tube (20Fe) which is subjected to huge impact pressure from the outer tube (3A21), both numerical simulations and experiments were carried out.*

*For the purpose of investigating the critical thickness of the inner tube under various impact velocities, four discharge voltages (9 kV, 11 kV, 13 kV and 14 kV) were employed in the MPW experiment. The diameters of inner tube at different locations were measured to obtain its plastic deformation at various discharge voltages. The simulations considering the coupled effects of the mechanical, thermal and electromagnetic process were performed to research the impact velocity and deformation of tubular fittings in the electromagnetic module (EM) in LS-DYNA. An inverse method was proposed to find the dynamic yield stress of inner tube, and the predicted yield stress was then employed in models with critical thickness. Both of the impact velocity and deformation were verified experimentally.*

## Keywords

Magnetic pulse welding, Dissimilar metals, Boundary element method

# 1 Introduction

With the globally increased energy prices and with strict environment regulations, severe limits have been made for industrial enterprises to increase energy efficiency and reduce carbon emissions. Thus energy-efficient and environmentally friendly technologies are becoming increasingly important in manufacturing. Due to its well controllability, no pollution and high efficiency, the use of magnetic force in industry has attracted much attention. For decades now, the application of magnetic force has been extended to areas such as forming, cutting, process combinations and magnetic pulse welding (MPW) (Psyk et al., 2011).

As a solid phase welding process, MPW is usually used for the welding of dissimilar metals. Due to the complexity of the multi-field coupling of MPW, many efforts have been made to investigate the electromagnetic process with numerical simulations. Meng et al. (2015) investigated the effect of process parameters of MPW on the mechanical and microstructure properties of dissimilar metal joints of 6063-O and 20 Fe, and finite element method (FEM) was used to find the proper discharge voltages. Simulations based on ANSYS/LS-DYNA software platform were carried out by Fan et al. (2016) to study the deformation of bi-metal tubes in MPW cladding; results have showed that the plastic deformation of flyer tube was mainly decided by the inclined angles. FEM was employed by J. Y. Shim et al. (2011) to analysis the interaction of work-piece and coil in MPW process. According to Xu et al. (2013), the impact velocity of MPW of pipe-fitting was simulated using ANSYS/LS-DYNA and the simulation was verified by experiments. Kore S D et al. (2010) used the commercial software ANSYS/EMAG and ABAQUS to study the impact velocity and pressure profile on the work-piece, and a criterion for the weld formation in the MPW process was obtained based on the simulation.

Previous studies mentioned above were mainly using FEM to investigate the effect of process parameters on the forming of MPW. Few reports have been found to study the effect of structural parameters, especially the thickness of the tube of MPW with a boundary element method (BEM). In the present study, the critical thickness of inner tube suffering impact load was explored through numerical simulations and experiments. Numerical simulations were performed with a combined FEM-BEM method through an electromagnetic (EM) module in LS-DYNA, and the impact velocities of the outer tubes and deformation of the inner tubes in the MPW process at different discharge voltages were studied. A reverse method was proposed to obtain the material parameters of the inner tubes suffering impact pressure, and the predicted yield stress was then employed in simulations. The impact velocities of the outer tubes and deformation of the inner tubes were verified experimentally.

# 2 Experiment and Method

20Fe and 3A21 (Al alloy) were selected as materials of the inner and outer tubes, respectively. The thickness of outer tube was 1 mm with external diameter of 20 mm. In

order to acquire the critical thickness of inner tubes under various discharge voltages, the inner tubes were prepared with thicknesses ranging from 1.5mm to 4.0mm and the interval was 0.1mm. Table 1 shows the size of the inner and outer tubes.

To perform the MPW experiment, a 20 kJ electromagnetic forming machine with a capacitance of 100 μF and maximum charging voltage 20 kV was employed. Fig. 1(a) shows the MPW equipment. The outer tube was driven by magnetic force generated by current in the coil and induced current in the outer tube, then the inner tube and outer tube were bonded together. Fig. 1(b) is the size of the coil and field shaper and their assembly relationships. For the purpose of simplifying experiments, gap between the inner tube and outer tube was fixed to 1.4mm and length of overlapped joint was 15mm.

| Materials | Outer diameter（mm） | Inner diameter (mm) | Thickness (mm) |
|---|---|---|---|
| 3A21 | 20.0 | 18.0 | 1.0 |
| 20Fe | 15.2 | 7.2-12.2 | 1.5-4.0 |

***Table 1**: Size of the inner and outer tubes*

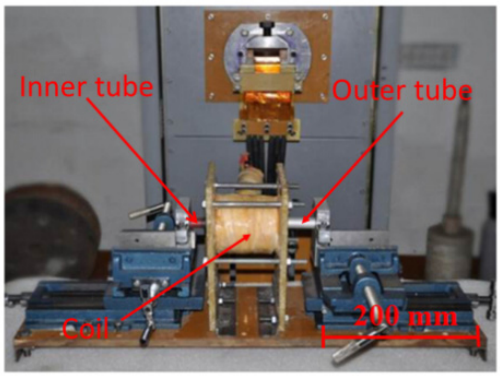


*(a) picture of the equipment*

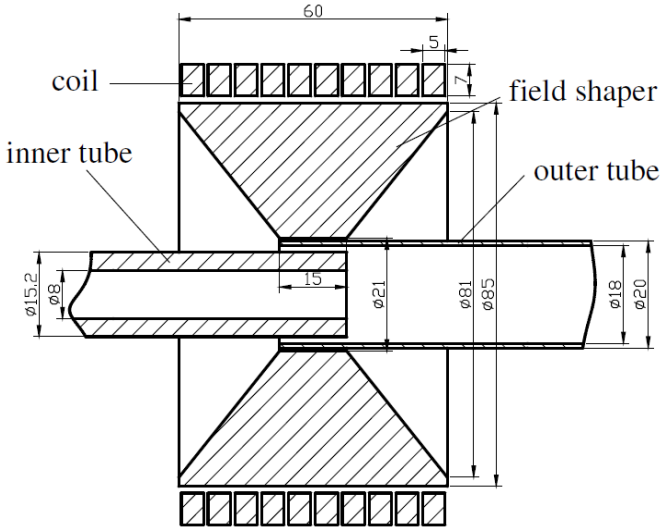


*(b) dimensions of the setup and work-pieces*

***Figure 1**: The MPW setup*

A high-speed camera system (FASTCAM SA5 1000 K-M2) was used to obtain the impact velocities of outer tubes at various discharge voltages, and the FASTCAM SA5 1000 K-M2 system could shoot at a speed of one million frames per second at most. In order to find out the critical thickness of inner tube, MPW experiments were carried out at various discharge voltages. To obtain accurate and reliable results, three repeat experiments were carried out at each thickness of the inner tube. Fig. 2(a) shows the MPW pipe fittings under voltage of 14 kV. The inner diameter of inner tube would show no change after experiments when the thickness reached a certain value, then the value was considered as the critical thickness. The deformation of inner tube was evaluated by measuring its inner diameter at different locations, which was shown in Fig. 2(b).

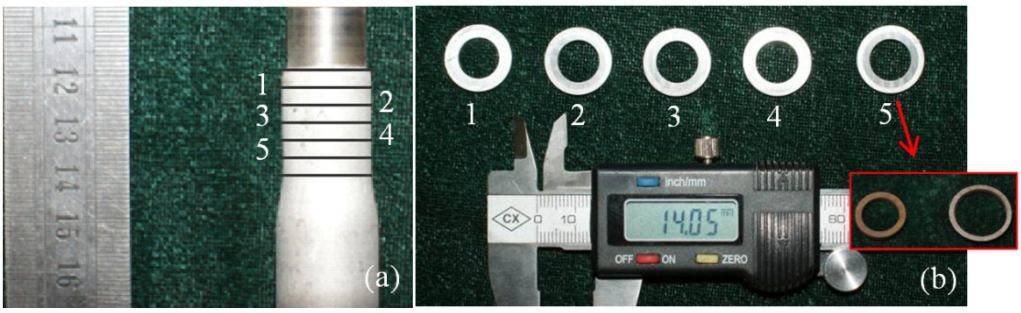


***Figure 2**: MPW pipe fittings and Measurements of the inner diameter: (a) MPW pipe fittings under voltage of 14 kV; (b) cross-sections at measurement locations*

The variations of diameters of inner tubes after MPW are shown in Fig. 3. $\bar{t}$ is dimensionless and represents the ration of thickness to external radius and $\Delta d$ denotes the deformation of inner diameter of inner tube. The deformation of inner tubes decreases with the increase of thickness at a certain discharge voltage, and thicker tube is needed to restrict its deformation when the discharge voltage increases.

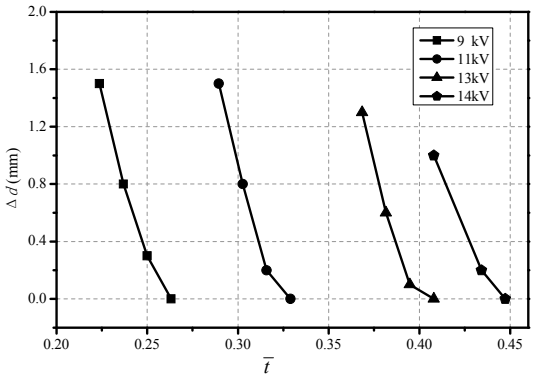


***Figure 3**: Deformation of inner tube under various discharges*

# 3 Numerical Simulation

## 3.1 Establishment of Coupled Numerical Model

MPW is a very complex transient impact process which involves the coupling effects of mechanical field, thermal field and electromagnetic field. Xu et al. (2013) employed a loose coupling method to study the changes of mechanical field and magnetic field, which ignored the effect of deformation of work-piece on electromagnetic field. However, deformation of work-piece has a significant influence on the precision of simulation (Bartels G et al., 2009).

In this study, a model was established in the electromagnetism module (EM) in LS-DYNA which coupling the mechanical, thermal and electromagnetic process. This module allows introducing source electrical current into coils to solve the coupled electric field, magnetic field and structural field. FEM was selected for the analysis of solid structures which was coupled with a Boundary Element Method (BEM) for air. Fig. 4 shows the established numerical model of the MPW.

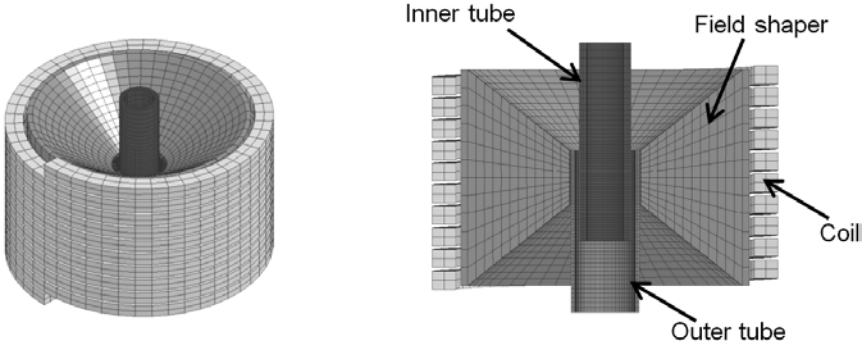


***Figure 4**: The established 3D model for the coupled-field analysis*

## 3.2 Inverse Method on the Acquisition of Mechanic Parameters of Inner Tube

MPW as a transient impact process, the inner tube suffers very high pressure in a short time. The mechanic properties of material such as yield stress, breaking strength in this situation show huge difference compared to that under static loading (Johnson G R and Cook W H, 1983). Rusinek et al. (2007) reported that under the shock of several hundred meters speed, the yield stress could be several times of that at quasi-static process.

Due to critical situation caused by extremely high pressure, the material's dynamic property is hard to obtain experimentally. An inverse method was introduced to acquire the dynamic yield stress of inner tubes in this paper. The critical thickness of inner tube obtained experimentally at every discharge voltage was employed. The inner tube was set to an ideal elastic-plastic material with high yield strength, and then the maximum stress distributed in the inner tube in the process of collision was considered to be its modified dynamic yield stress. The modified yield stress was regarded as a value related to the

discharge voltage. Finally, the predicted modified yield stress of inner tube was used in the simulation and the results were verified experimentally. The flow chart to acquire the critical thickness of inner tube is shown in Fig. 5.

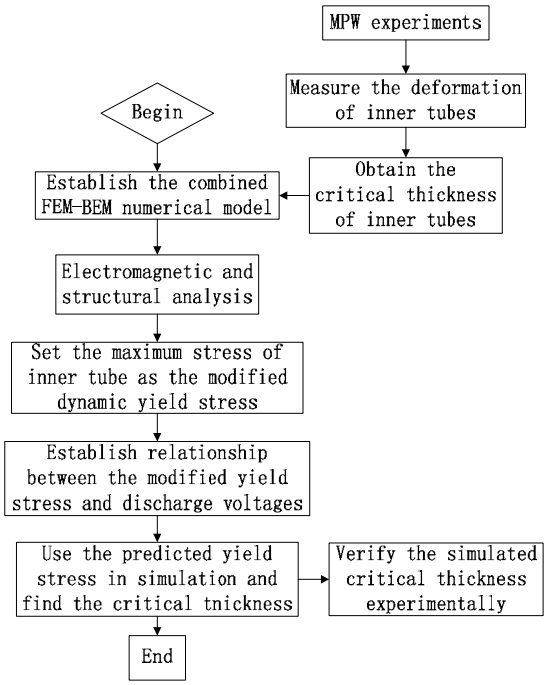


***Figure 5**: Flow chart of the acquisition of critical thickness of inner tube*

# 4 Results and Discussion

## 4.1 Distribution of Magnetic Field and Deformation of the Outer Tube

Due to the reason that magnetic force is proportion to magnetic field strength, the distribution of magnetic field of the outer tube in this period was studied in the simulation. Fig. 6 shows the distribution of magnetic field under a discharge voltage of 14 kV. It could be see that the magnetic field was mainly focused in the area closed to the field shaper, which means that the maximum magnetic force occurs at the end face of the outer tube. The process of collision and their deformation are shown in Fig. 7.

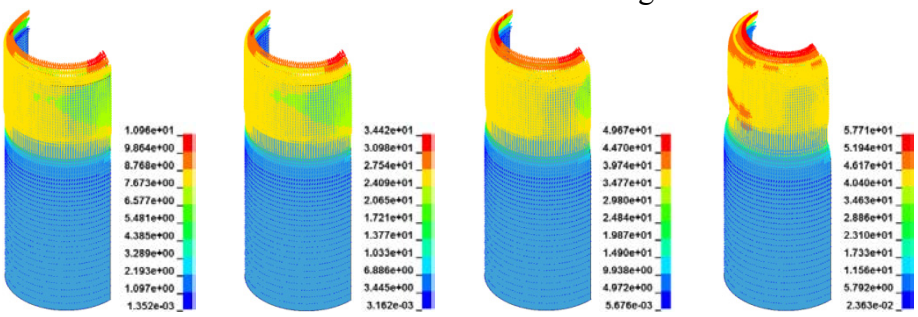


*(a) 6 μs* *(b) 10 μs* *(c) 13 μs* *(d) 16 μs*

***Figure 6**: Magnetic field distribution of inner tube*

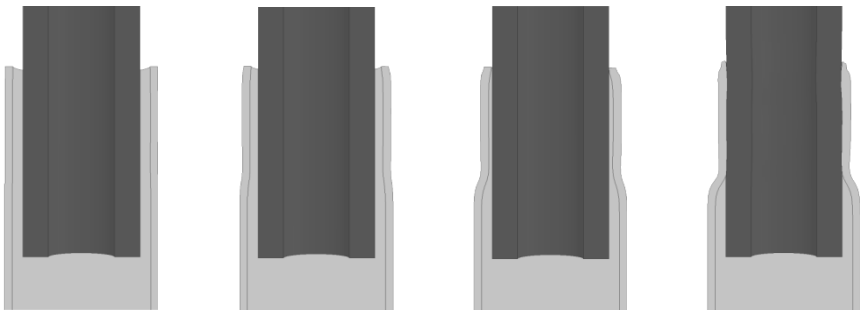

*(a) 10 μs* *(b) 13 μs* *(c) 16 μs* *(d) 18 μs*

***Figure 7**: The impact process at a discharge voltage of 14 kV*

## 4.2 Impact Speed of Outer Tube

Impact velocity is a very important process parameter in MPW. A numerical simulation was employed here to study the impact velocities under various discharge voltages. Regardless of the slightly uneven velocities caused by the slot in the field shaper, the simulated velocities of end face of outer tubes under different discharge voltages is shown in Fig. 8.

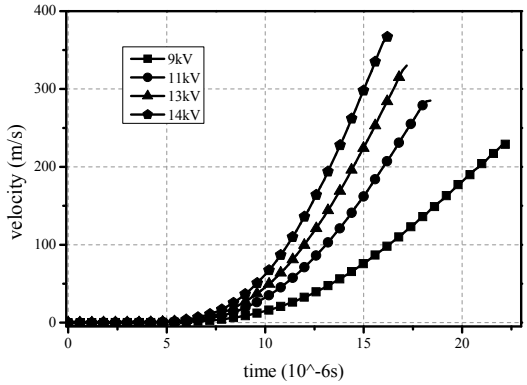


***Figure 8**: Simulated velocities of outer tubes under different discharge voltages*

The FASTCAM SA5 1000 K-M2 system was employed to measure the movement of the out tube and detailed information was shown by Xu et al. (2013). The impact velocity obtained through experiment and simulation is shown in Table 2.

| Voltage (kV) | $v_{experiment}$ (m/s) | $v_{simulation}$ (m/s) |
|---|---|---|
| 9 | 226 | 229 |
| 11 | 278 | 285 |
| 13 | 322 | 330 |
| 14 | 355 | 367 |

***Table 2:** Impact velocity of outer tube obtained thorough experiments and simulation*

Where $V_{experiment}$ represents experimental impact velocity and $V_{simulation}$ represents simulated impact velocity. It can be see that the simulated velocities agree well with experimental results and the maximum relative error is less than 4%.

## 4.3 Study on the Critical Thickness of Inner Tube

When the inner tube suffers higher pressure, thicker tube is needed to resist the plastic deformation. As demonstrated by Johnson (1972), the impact pressure is proportional to the impact velocity. The maximum stress in inner tube which had the critical thickness was regarded as the modified yield stress. Since von mises yield criterion was used in the simulation, the modified dynamic yield criterion could be expressed as below:

$$f = \sqrt{1/2[(\sigma_1 - \sigma_2)^2 + (\sigma_2 - \sigma_3)^2 + (\sigma_3 - \sigma_1)^2]} - N(v)\sigma_s \quad (1)$$

Where $\sigma_1, \sigma_2, \sigma_3$ represent the principal stresses, $\sigma_s$ is the yield strength of inner tube, $N(v)$ is the dynamic factor and $v$ is the impact velocity. When $f \geq 0$, material yields.

The maximum stress of inner tube in the whole impact process was obtained through simulation and Fig. 9 shows the stress distribution under the voltage of 11 kV while the thickness of inner tube was 2.4 mm. The maximum stress occurred in the inner surface of the tube, which means that the plastic deformation was first happened in the inner surface, and plastic deformation zoon would propagate from the inner surface to the outer surface.

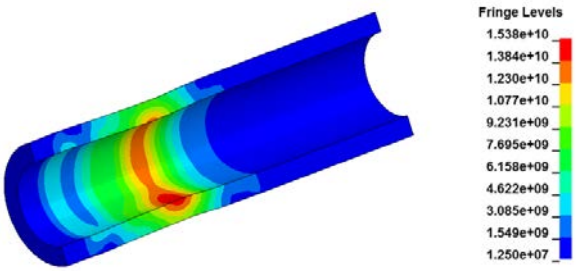


***Figure 9**: The stress distribution in the inner tube under voltage of 11 kV*

Four discharge voltages were used to obtain the relationship of dynamic factor $N(v)$ and impact velocity $v$ and the data through simulation are listed in table 3.

| Voltage (kV) | $v$ simulation (m/s) | N($v$) |
|---|---|---|
| 9 | 229 | 44.6 |
| 11 | 285 | 59.6 |
| 13 | 330 | 70.5 |
| 14 | 367 | 81.0 |

***Table 3**: Dynamic factors under various voltages*

Based on the given data, the relationship of $N(v)$ and $v$ was established as below:

$$N(v) = 0.2615v - 15.24 \quad (2)$$

Fig. 10 shows the comparison of the fitting curve with experimental value, the fitting curve shown a well linear relationship of dynamic factor and impact velocity.

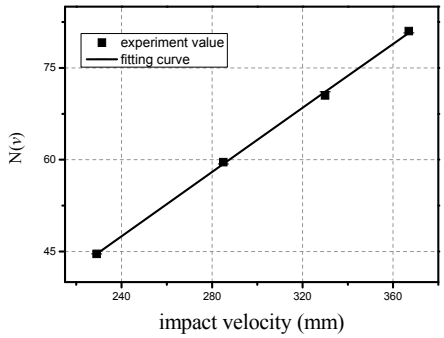


***Figure 10**: Relationship of dynamic factor $N(v)$ and impact velocity $v$*

In order to verify the model, the predicted dynamic yield stress under the voltage of 10 kV and 12 kV were used in the simulation. Fig. 11 shows the plastic strain distribution of inner tube under different discharge voltages. The maximum plastic strains in the two pictures are less than 0.12%, which means that model can predict the deformation of inner tube accurately.

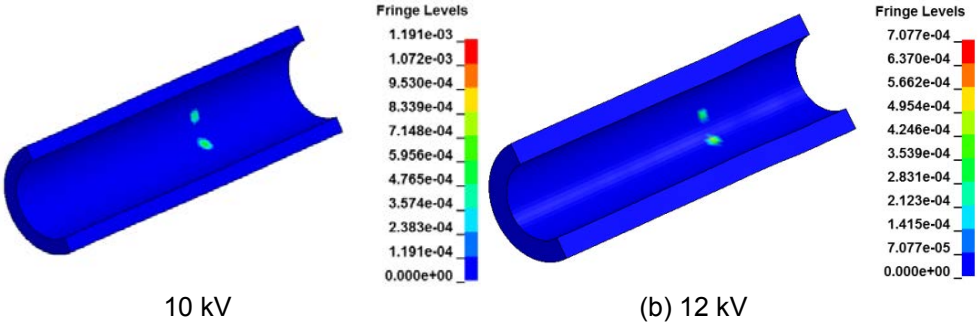


***Figure 11:** Plastic strain distribution of inner tube under different voltages*

The results show that the value of N related to impact velocity was suitable to the material 3A21 in our investigation. It is not fully considered whether it is valid in general. Further study considering this question is recommended.

# 5 Conclusions

In this study, both experiments and simulation were used to explore the critical thickness of inner tube in MPW process. The conclusions can be summarized as follows:

(1) A combined FEM-BEM method was used to investigate the electromagnetic process of MPW. The simulated impact velocity under various discharge voltages agreed

well with the experiment values. The error of simulated impact velocity increased with the increasing of discharge voltages while the maximum relative error was less than 4%. Maximum impact velocity occurred at the end surface of the outer tube.

(2) End surface of the outer tube suffered the maximum magnetic force, and the impact velocity also achieved the peak value in this area. Higher impact velocity caused larger impact pressure in the interface. As a consequence, deformation of inner tube was first occurred in area closed to the end surface of outer tube, then transferred to the free end.

(3) An inverse method was proposed to find the dynamic yield stress of the inner tube, and the predicted yield stress was then employed to obtain the critical thickness. The plastic deformation of inner tubes with critical thickness was less than 0.12%.

# References

Bartels, G., Schätzing, W., Scheibe, H. P., Leone, M., 2009. Comparison of two different simulation algorithms for the electromagnetic tube compression[J]. International Journal of Material Forming 2(1), pp. 693-696.

Fan, Z., Yu, H., Li, C., 2016. Plastic deformation behavior of bi-metal tubes during magnetic pulse cladding: FE analysis and experiments[J]. Journal of Materials Processing Technology 229, pp. 230-243.

Johnson, G. R., Cook, W. H., 1983. A constitutive model and data for metals subjected to large strains, High Strain Rates and High Temperatures 1983，Proceedings of the 7th International Symposium on Ballistics 21, pp. 541-547.

Johnson, W., 1972. Impact Strength of Materials. Hodder Arnold Publishers, London, pp. 79-86.

Kore, S. D., Dhanesh P, Kulkarni S V, Date P P, 2010. Numerical modeling of electromagnetic welding[J]. International Journal of Applied Electromagnetics and Mechanics 32, pp. 1-19.

Meng, Z., Lei, Y., Huang, S., Hua, L., 2015. Effects of process parameters on the mechanical properties and microstructure of Al-steel joint by magnetic pulse welding. MATEC Web of Conferences 2015. EDP Sciences 21.

Psyk, V., Risch, D., Kinsey, B. L., Tekkaya, A.E., Kleiner, M., 2011. Electromagnetic forming-a review[J]. Journal of Materials Processing Technology 211(5), pp. 787-829.

Rusinek, A., Zaera, R., Klepaczko, J. R., 2007. Constitutive relations in 3-D for a wide range of strain rates and temperatures–application to mild steels[J]. International Journal of Solids and Structures 44(17), pp. 5611-5634.

Shim, J. Y., Kim, I .S., Lee, K. J., Kang, B .Y., 2011. Experimental and numerical analysis on aluminum/steel pipe using magnetic pulse welding[J]. Metals and Materials International 17(6), pp. 957-961.

Xu, Z., Cui, J., Yu, H., Li, C., 2013. Research on the impact velocity of magnetic impulse welding of pipe fitting[J]. Materials & Design 49, pp. 736-745.

# Sponsors and Partners

Bmax

power to shape

# ADVANCED

## METAL PROCESSING SOLUTIONS

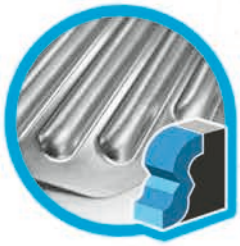

MAGNETIC PULSE
FORMING

MAGNETIC PULSE
WELDING

MAGNETIC PULSE
CRIMPING

www.Bmax.com

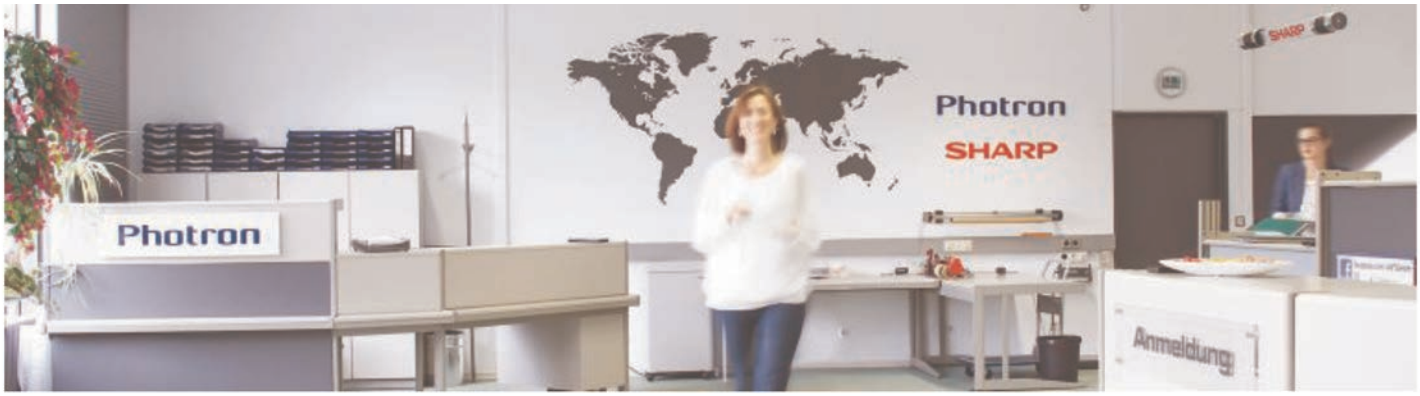


**VKT GmbH**
In der Highspeed-Technik arbeitet VKT eng mit Photron zusammen und setzt so Meilensteine in Deutschland, Österreich und der Schweiz. Die Highspeed-Kameras nehmen bis zu 2,1 Millionen Bilder pro Sekunde auf und erfassen so Bewegungen und komplexe Abläufe, die das menschliche Auge sonst nicht wahrnehmen könnte. Eingesetzt werden sie in unterschiedlichsten Bereichen, vom Werbefilm über die Luft- und Raumfahrt bis zur Partikelgeschwindigkeitsmessung (PIV) oder Qualitätssicherung.

Ebenso vielfältig wie die Aufgabenstellungen ist die Kundenstruktur: Bildungs- und Forschungseinrichtungen, Industrieunternehmen sowie Öffentliche Einrichtungen bedienen sich seit Jahren an dem fundierten Wissen und der Erfahrung der Mitarbeiter.

Neben dem Verleih und Verkauf von Produkten bietet VKT auch komplette Leistungspakete an und ist somit Ihr zuverlässiger Partner für die Zukunft.

**PHOTRON**
Photron is a trusted supplier of high-speed cameras to leading research and industrial groups around the world, delivering quality, reliability and high-performance for the most challenging imaging applications. Please visit the Photron stand to see the Photron's extensive range of solutions.

VKT Video Kommunikation GmbH
Technisches Fernsehen
Daimlerstr. 23, 72793 Pfullingen / Deutschland
Tel.: 07121 9797-0, Fax 07121 9797-97
E-Mail: hs@vkt.de, Internet: www.vkt.de

VKT
Video Kommunikation GmbH
Technisches Fernsehen

# RESSOURCEN EFFIZIENT NUTZEN. MIT ALUMINIUM.

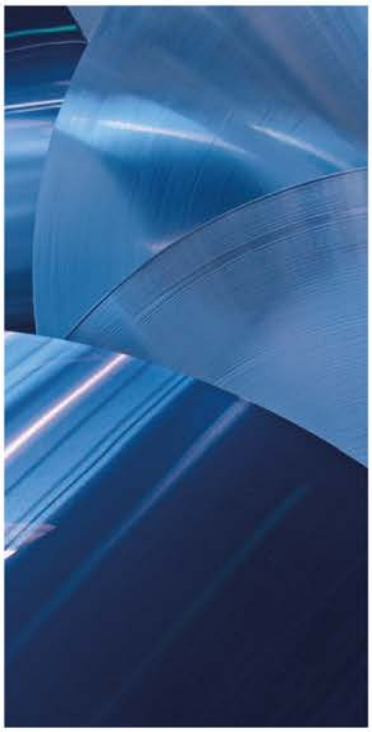


GDA GESAMTVERBAND DER ALUMINIUMINDUSTRIE e.V.

Am Bonneshof 5
40474 Düsseldorf

Tel.: +49 211 4796-0
Fax: +49 211 4796-408

information@aluinfo.de
www.aluinfo.de


## SO LEICHT UND HÖCHST EFFIZIENT: ALUMINIUM LÄSST SICH IMMER WIEDER VERWERTEN

Die Wiederverwertung von Aluminiumschrotten ist ein wichtiger Beitrag zu einem schonenden, intelligenten und sparsamen Umgang mit Ressourcen.

Der Energieeinsatz liegt hierfür nur bei 5 % des ursprünglichen Wertes. Und Produkte, die durch Aluminium leichter werden können, sparen in der Nutzungsphase zusätzlich Energie.

→ www.aluinfo.de

I2FG.ORG

# International Impulse Forming Group

The International Impulse Forming Group e.V. (I²FG) is a non-profit society that promulgates the advantages of impulse forming and processing technologies. It aims to encourage and coordinate national and international cooperations by instigating research so that knowledge of the relevant processes and sciences can be disseminated. The ICHSF and the I²FG have a common history as the founding of the I²FG was announced during the 3rd ICHSF, in 2008. Since then, both parties maintain a close partnership.

For more information (e.g., regarding memberships) please visit our webpage www.i2fg.org

## Contact


### I²FG secretary's office

Institute of Forming Technology and Lightweight Construction
TU Dortmund University
Baroper Straße 303
44227 Dortmund, Germany

+49 (0)231 755 2660
+49 (0)231 755 2489
office@i2fg.org